Dynamic Nuclear Polarization

in Liquids at 9.4 T

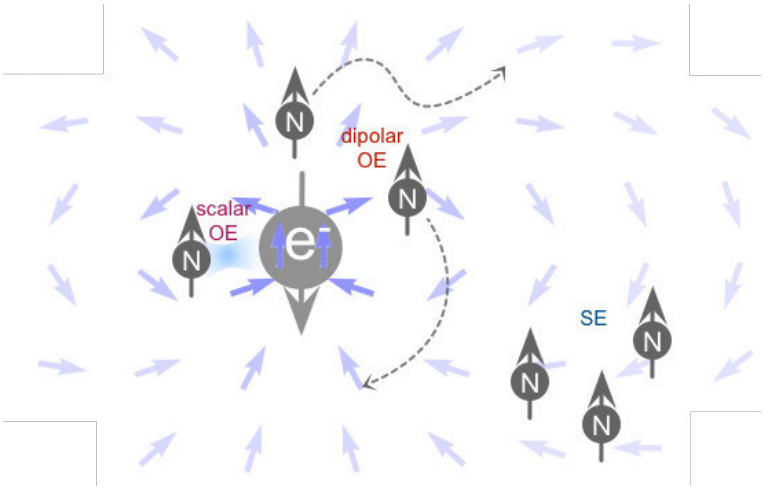

Dissertation

zur Erlangung des Doktorgrades

der Naturwissenschaften

vorgelegt beim Fachbereich 14

der Johann Wolfgang Goethe-Universität

in Frankfurt am Main

von

Danhua Dai

aus Zhejiang, China

Frankfurt am Main 2023

(D30)

Accepted by Department 14: Biochemistry, Chemistry and Pharmacy

of Goethe University Frankfurt as a dissertation

Dean:	Prof. Dr. Clemens Glaubitz
First expert assessor:	Prof. Dr. Thomas Prisner
Second expert assessor:	Prof. Dr. Clemens Glaubitz

Date of disputation: .....

Acknowledgements

I would like to start the dissertation with the acknowledgements.

First, I want to express my gratitude to Prof. Thomas Prisner for giving me this chance to start my journey in the field of liquid-state DNP and for his supports during my whole PhD study. The five-year duration of this study has been truly joyful, owing to his constructive suggestions of experimental plans and interpretations, coupled with the open atmosphere of our research group.

My special thanks go to Dr. Vasyl Denysenkov, the expert truly know the microwave resonator and the gyrotron, who taught me how to work with the instruments already during my master studies. Without his work on the probeheads none of my experimental progress would be possible.

Prof. Jiafei Mao is greatly acknowledged for the nice collaboration of the scalar DNP on small biomolecules, and for sharing me his knowledge in liquid-state NMR and his scientific perspectives, which are truly helpful for me.

My thanks go to Dr. Andrei Kuzhelev for the long-term experimental collaboration with fruitful outcomes. He is also profoundly acknowledged for his credits of the high-field solid effect DNP in viscous liquids.

My thanks also go to Dr. Deniz Sezer for helping me figured out plenty of theoretical questions, especially the autocorrelation function and spectral densities. His knowledge, not limited to DNP theories alone, impresses me all the time.

The computational work performed by our collaborator, Prof. Xiao He and his research group, to understand the observed scalar DNP enhancements is also profoundly acknowledged.

Dr. Burkhard Endeward is acknowledged for maintaining the functionality of our group's computers and network, and for his explanations and assistance in the operation of the EPR spectrometer.

I would like to thank Prof. Clemens Glaubitz for his clear introductions about the lipid structure and the relevant NMR experiments.

I also want to thank Dr. Orawan Jakdetchai for sharing her knowledge about the lipid sample preparation and the related experimental techniques at the beginning of my PhD study.

Manfred Strupf, Bernhard Thiem and Dr. Johanna Baldus are acknowledged for their supports in maintaining the functionality of the DNP/NMR spectrometers.

Bisera Krstić, Dr. Jörn Plackmeyer and Sigrid Kämmerer are acknowledged for the arrangement of chemicals.

Thanks go to Dr. Alberto Collauto for his help during the first step of my PhD study.

Thanks go to Silke Schneider for her administrative work and her warm-hearted support in various ways, such as checking the accuracy of my German-written emails, assisting in finding accommodations, and always being willing to have a short, relaxed conversation.

My thanks also go to the following individuals for their valuable suggestions to improve this dissertation: Prof. Thomas Prisner, Matthias Bretschneider, Dr. Andrei Kuzhelev, Dr. Burkhard Endeward, Dr. Deniz Sezer and Dr. Vasyl Denysenkov.

Finally, I want to dedicate this thesis to my family: to my fiancée, Chujing, for the consistent understanding and encouragement already started from my Bachelor study; to my mom, Xingbao, for always being considerate and consistently supportive of my decisions; and to my dad, Xianggao, though you have left this world in 2019, your love never fades in our family.

Table of Contents

1. Introduction and Overview

1.1 Introduction

Since its discovery over seven decades ago[1-3], Nuclear Magnetic Resonance (NMR) spectroscopy has established itself as a powerful analytical tool with versatile applications across multiple scientific disciplines and industrial areas including chemistry, biology, materials science and medicine[4-7]. It provides a non-invasive access to the properties of matter at the atomic scale and offers valuable insights into molecular structure, interaction and dynamics. However, NMR involves a minuscule interaction energy between the nuclear spins and the external magnetic field, which holds particularly true at ambient temperature. This inherent nature of NMR makes it a non-destructive method but also imposes limitations on its sensitivity, thereby restricts its capabilities in advanced applications. In order to address the sensitivity issue of NMR, enormous efforts have been devoted to enhancing NMR signal intensities. Beside the work on instrumentation and experimental procedure,[8] diverse hyperpolarization methods were constantly developed during the past decades, such as Dynamic Nuclear Polarization (DNP)[9], Photochemically-induced Dynamic Nuclear Polarization (Photo-CIDNP)[10], Parahydrogen-induced Polarization (PHIP)[11-13] and optical pumping of noble gases[14].

Among these hyperpolarization techniques, DNP, specifically continuous-wave (cw) DNP in liquids, will be the sole focus of this thesis. Combing aspects from both NMR and Electron Paramagnetic Resonance (EPR), DNP enhances NMR sensitivity by transferring the polarization from unpaired electron spins to their adjacent nuclear spins. Multiple DNP mechanisms have been proposed to explain the observed DNP enhancements in various sample systems. As first posed by Overhauser in 1953[9] and experimentally verified later in lithium[15], the initial discovered DNP mechanism relying on the cross-relaxation processes of the coupled

electron-nuclear (e-N) spins, is commonly referred to as Overhauser effect (OE) DNP. It is necessary to modulate the e-N hyperfine interaction (HFI) through stochastic processes to induce such cross-relaxation. This modulation is achievable in molecular systems with dynamical e-N spin pairs such as metal with mobile electrons or solution doped with radicals. Another DNP mechanism named solid effect (SE) was experimentally validated later in dielectric solids.[16,17] The SE relies on the mixing of nuclear spin states in the presence of an anisotropic HFI field. Therefore, it is typically exploited in solid samples because the anisotropic interactions are completely averaged out in non-viscous liquids. In solid-state samples, alternative DNP mechanisms were discovered involving one nuclear spin coupled with two electron spins or multiple electron spins, which were respectively termed cross effect (CE)[18,19] and thermal mixing (TM)[20].

Before 1990s, scientific curiosity was mainly restricted to low-field DNP studies, deviating from the trend of NMR research moving towards higher fields. This is due to theoretical predications indicating an unfavored DNP efficiency of all known DNP mechanism at high magnetic fields along with the lack of high frequency microwave (mw) sources to efficiently drive the electron spin transition.[21-24]

In the past three decades, DNP experienced a renaissance after the availability of high power gyrotron mw source as demonstrated by the Griffin group.[25] Combined with magic angle spinning, solid-state DNP has found many applications ranging from biomolecules to materials at high fields.[26,27] Dissolution DNP, taking advantage of the high DNP efficiency achieved at low temperature and moderate fields, are able to provide significant signal enhancements by a subsequent fast dissolution and NMR detection at high magnetic fields.[28,29] Apart from the approaches with cw mw irradiation, various pulsed DNP techniques were also developed to avoid the efficiency limitations of different DNP mechanisms, such as Nuclear Spin Orientation via Electron Spin Locking (NOVEL),[30,31] DNP in the nuclear rotating frame[32], time-optimized pulsed DNP[33].

Compared to its advancements in solid state, DNP is less explored in solution at high fields.[34] The primary challenge is the sample stability posed by excessive heating caused by the dielectric losses of liquids with high frequency mw. This technical issue can be effectively addressed by optimizing the design of the DNP probe from several perspectives, such as utilizing a mw resonator, namely separating the mw E- and B-components, improving the heat conductivity of the sample holder and applying active sample cooling methods.[35,36] These modifications, while compromising the sample volume to some extent, also enable the separation of the temperature influences from the DNP efficiency. Additionally, similar as the other DNP mechanisms, the predicted OE DNP efficiency drops rapidly with increasing magnetic fields. The spectral density function (SDF), which theoretically determines the OE DNP efficiency, was derived from the e-N spin interactions under molecular rotational and translational motions.[37-40] These motions described by the classical Stokes-Einstein model with a typical correlation time of tens to hundreds ps, which sufficiently explains the observed OE DNP at low field (< 1.5 T), are however unable to produce considerable spectral density at high fields (> 3 T).

Though the initial observations exhibits dropped DNP efficiency as expected[41-43], the progress of DNP in solutions in the past decade has revealed its potential at high field. Already before the initiation of this doctoral research work, it has been acknowledged that the simple molecular rotational and translational model could be inadequate to describe the high-field DNP efficiency, which is particularly sensitive to fast fluctuations.[44] The most demonstrative instance is the dipolar HFI-driven ^{1}H OE DNP with an enhancement factor of -10 observed on oriented lipid bilayers doped with nitroxide radicals at ambient temperatures and 9.4 T.[45] A fluctuation with a correlation time $\tau \approx 0.6$ ps, comparable to the inverse electron Larmor frequency $1/\omega_e$, is required to achieve efficient DNP polarization transfer at this magnetic field. Yet the characterization times of the lipid lateral diffusion or axial rotation are at least three orders of magnitudes slower,[46-48] suggesting an driving

force of DNP from local fast dynamics. Another promising approach at high field is scalar HFI-driven OE DNP. Theoretically, scalar HFI contributes predominantly to the e-N zero-quantum cross-relaxation and has neglectable impacts on the nuclear single-quantum relaxation for organic radicals in liquids.[23] Therefore, DNP efficiency can remain sizable with increased fields in molecular systems where scalar HFI-induced relaxation dominates over the counteracting dipolar relaxation. A computational approach with density functional theory (DFT) calculations and molecular dynamics (MD) simulations also predicted this potential of scalar DNP at high fields.[49] The initial and also most representative experimental evidences are the ^{13}C OE DNP observed with an enhancement up to 930 in CCl_4 solution at 3.4 T[50] and up to 600 in CBr_4 solution at 9.4 T[51]. The dynamics responsible for scalar DNP is also not limited to molecular motions. Though the mechanism is still under discussion, experimental observations show that OE DNP is effective in insulating solids at high fields and low temperatures.[52,53] Such a fast dynamic modulation of the scalar HFI responsible for the OE DNP exists even at 1.2 K.[54]

1.2 Overview of the thesis

Compared to researches conducted in solids, liquid-state DNP-NMR measurements provide the complementary insight to the molecular conformation, dynamics and substrate-radical interactions of molecules in solutions or even in their native environment. The manifold of current OE DNP strategies suggests that liquid-state DNP holds great potential even with limitation in sample volume and selectivity towards molecular systems. It motivated this research work for continuously exploration of the possibilities for DNP methods in liquids at high fields.

As the research outcome encompasses distinct aspects of liquid-state DNP including results already published and results to be published, this thesis is written in a cumulative manner.

Following this introductory chapter, Chapter 2 explains the theoretical background which is necessary for understanding the liquid-state DNP mechanisms along with relevant NMR and EPR principles. Chapter 3 introduces the aspects of hardware including the DNP spectrometer, probeheads and temperature control. The new experimental evidences of high-field DNP obtained in liquids during the research period are presented in Chapter 4-8. A summary of the research work as well as the outlook are given in Chapter 9. A German Summary is given in Chapter 10. The author's contributions to individual research work are summarized in Chapter 11.

The scalar OE DNP enhancement previously achieved at high magnetic fields are limited in organic solvents.[50,51] As presented in Chapter 4, one of the intriguing findings during the research period was the observation of high-field ^{13}C scalar OE DNP of small biomolecules for the first time in aqueous solution with considerable enhancements up to 50. In this work, the scalar DNP capabilities were extended to a series of biologically relevant molecules including amino acids and carbon hydrates.

Another novel discovery in high-field DNP shown in Chapter 5 was the SE DNP-enhanced ^{1}H NMR spectra of fluid liposome doped with BDPA (1,3-bisdiphenylene-2-phenylallyl) radical observed at ambient temperature with an enhancement factor of 12, which opens up new perspectives for DNP of large molecules or in viscous solutions.

Chapter 6 presents the further study of DNP on liposome doped with spin-labeled nitroxides at ambient temperature. Further mechanistic investigations of the ^{1}H dipolar OE DNP in lipids were performed including study of the site-specific DNP enhancements, experimentally determination of coupling factor, and an approach to obtain the DNP coupling factor via MD simulations. A recent theoretical approach with the dynamical modulated SE and g-anisotropy-broadened OE in liquids is attached.

Chapter 7 shows the interpretation of OE DNP enhancements with the classical models considering the molecular translational and rotational motion. A systematic study on the contribution of inner-sphere rotation to the coupling factor is presented. The existing experimental data were further reconsidered by incorporating the off-centered rotation of radicals into the outer-sphere model.

Triple-resonance (e^-, ^1H, ^{13}C) DNP experiments in solutions, including ^{13}C OE DNP measurements under ^1H decoupling and ^{13}C NMR signal enhancement achieved via a ^1H-^{13}C INEPT (Insensitive Nuclei Enhanced by Polarization Transfer) pulse sequence combining ^1H SE DNP, are presented in Chapter 8.

The multiple high-field DNP pathways in liquids covered by these studies are demonstrated in Figure 1. 1.

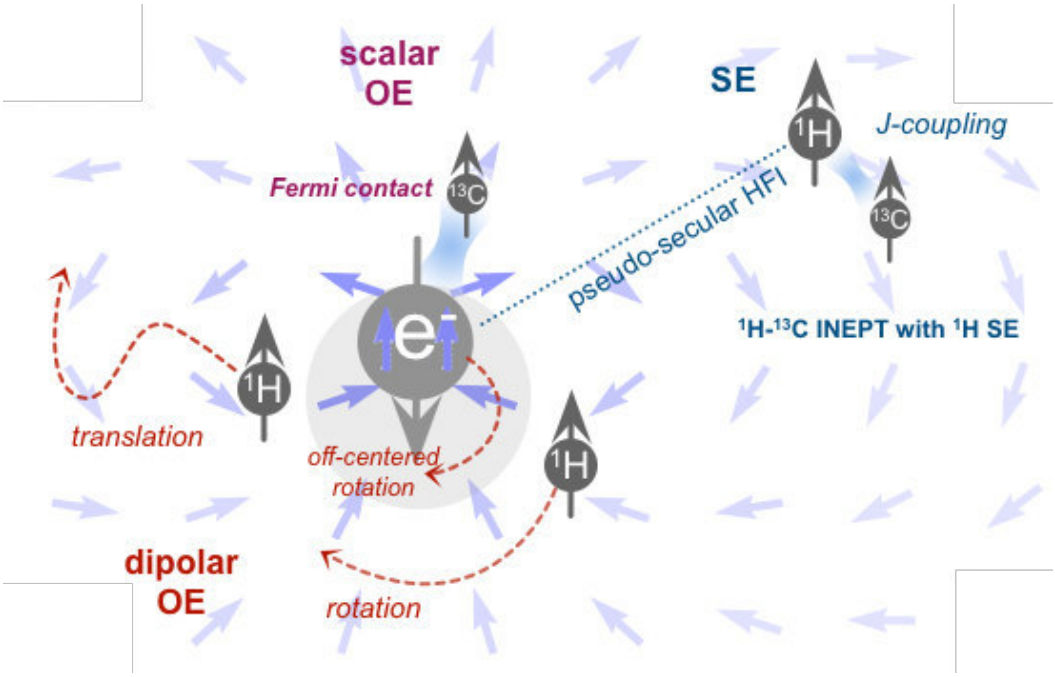

Figure 1. 1 Different high-field DNP pathways in liquids covered in this thesis

2. Theoretical background

In this chapter, the fundamental principles which are necessary to understand the liquid-state DNP are introduced. They are separated into four parts: Section 2.1 introduces the basic knowledge of magnetic resonance. Subsequently, the principles of NMR and EPR spectroscopy relevant to this work are briefly explained in Section 2.2 and Section 2.3, respectively; Section 2.4 explains thoroughly the liquid-state DNP mechanism, specifically Overhauser effect and solid effect.

2.1 Principles of Magnetic Resonance

2.1.1 Spin Property and Spin Hamiltonian

All spectroscopic method of magnetic resonance is based on the intrinsic *spin* property of the elementary particles. While the name "spin" may imply the particles undergoing a spinning process, it is important to note that the spin is an abstract property based on experimental observations and theoretical calculations. Analogous to the angular momentum of a rotating object, particles with non-zero spin possess the spin angular momentum. Unlike the classical angular momentum, spin angular momentum is quantized and only take certain discrete values. The possession of spin confers the particles a magnetic moment $\boldsymbol{\mu}$ proportional to its spin angular momentum $\boldsymbol{J}$, which can be written as[55],

$$\boldsymbol{\mu} = \gamma \boldsymbol{J} \tag{2. 1}$$

where γ is the gyromagnetic ratio describing the relations between $\boldsymbol{\mu}$ and $\boldsymbol{J}$. The value of γ is specific for each type of particles. γ can be positive, such as ^{1}H and ^{13}C, or negative, including electrons, ^{15}N, ^{17}O, etc. The negative γ will result a magnetic moment $\boldsymbol{\mu}$ opposite to the angular momentum $\boldsymbol{J}$. With the reduced Planck constant $\hbar$, the conversion between the spin angular momentum and the spin quantum number $\boldsymbol{S}$ is given by $\boldsymbol{J} = \hbar \boldsymbol{S}$. A dimensionless parameter g can also be used to

describe the magnetic moment resulted by spin. Since nuclear spins and electron spins are both involved in this work, it is convenient to denote nuclear spin with the quantum number $\boldsymbol{I}$ and electron spin with the quantum number $\boldsymbol{S}$. With this notation the magnetic moment of the nuclear spin $\boldsymbol{I}$ and electron spin $\boldsymbol{S}$ can be given as:[55]

$$\boldsymbol{\mu_N} = \hbar\gamma_I \boldsymbol{I} = g_I \mu_I \boldsymbol{I} \tag{2. 2}$$

$$\boldsymbol{\mu_e} = \hbar\gamma_e \boldsymbol{S} = -g_e \mu_B \boldsymbol{S} \tag{2. 3}$$

where μ_I, μ_B are respectively nuclear magneton and Bohr magneton, g_I, g_e are respectively g factor of nuclear spin and electron spin.

The time-dependent Schrödinger equation can be used for quantum-mechanical description of the time evolution of a spin system, which is given as:[56]

$$\frac{d}{dt}\left|\psi_{spin}(t)\right\rangle = -i\mathcal{H}_{spin}\left|\psi_{spin}(t)\right\rangle \tag{2. 4}$$

where ψ_{spin} is the wave function describing the spin system, also known as spin states, $\mathcal{H}_{spin}$ is the Hamiltonian operator describing the interactions energy involved in the spin system of interest. By knowing the spin Hamiltonian $\mathcal{H}_{spin}$ and solving the time-dependent Schrödinger equation, it is possible to predict the experimental observations. One thing to note is that the spin Hamiltonian can be expressed in either natural unit without $\hbar$ or in the SI (Système International) unit with $\hbar$, which depends on whether we are referring to the angular frequency in radian/s or the energy of the system.

2.1.2 The Zeeman Splitting and Bulk Magnetization

For a spin with quantum number $\boldsymbol{I}$, its spin azimuthal quantum number m_I can take the value of $+I, +(I-1), \ldots, -(I-1), -I$, which means the particles can have 2I +1 sublevels. In the absence of an external field, the states with the same value of I but different values of m_I are degenerate, meaning that they are at the same energy level. The degeneracy is broken under application of an external magnetic field,

resulting in the different energies of the sublevels. This phenomenon is called Zeeman effect. The energy separation between the sublevels is called Zeeman splitting.

For a spin with magnetic moment $\boldsymbol{\mu}$ with an external static magnetic field $\boldsymbol{B_0}$, the Hamiltonian of Zeeman effect is given by:[55]

$$\mathcal{H}_Z = -\boldsymbol{\mu} \cdot \boldsymbol{B_0} \tag{2. 5}$$

The negative sign on the right side indicates a preferred state where the magnetic moment is aligned with the external magnetic field. Conventionally, the external magnetic field $\boldsymbol{B_0}$ is taken along the z-direction of the laboratory frame. The magnetic moment $\boldsymbol{\mu}$ (in the non-zero case) can either aligned parallel or antiparallel to the external magnetic field. The Zeeman term for nuclear spin can therefore be written as:

$$\mathcal{H}_{Z_I} = -\hbar\gamma_I B_0 I = -g_I \mu_I B_0 I \tag{2. 6}$$

which holds true also for electron spins:

$$\mathcal{H}_{Z_S} = -\hbar\gamma_S B_0 S = g_e \mu_B B_0 S \tag{2. 7}$$

The spin interactions relevant for the present thesis will be introduced in most cases in the context of spin-1/2 systems, because the target nuclear in this research are limited to ^{1}H and ^{13}C, and the unpaired electron spin is from organic radicals such as nitroxide and BDPA. In the case of a 1/2 nuclear spin, the Zeeman splitting between the $\left|+\frac{1}{2}\right\rangle$ and the $\left|-\frac{1}{2}\right\rangle$ state (referred to as $|+\rangle$, $|-\rangle$ for convenience) is $\hbar\gamma_I B_0$.

By applying an oscillating field perpendicular to $\boldsymbol{B_0}$, it is possible to induce transition between different spin states, when the oscillating frequency is in resonance with the frequency of the spin precession. The Hamiltonians can also be represented in unit of Hz or radian/s as the resonance condition is determined by the

frequency. The frequency of the spin precession is termed Larmor frequency, which is given by:

$$\omega_0 = -\gamma B_0 \tag{2. 8}$$

The resonance can be detected only if there exists a population difference between different spin states. The population at different Zeeman energy levels can be described with the Maxwell-Boltzmann distribution:[57]

$$P_{m_I} = \frac{exp(\hbar\gamma_I B_0 m_I / k_B T)}{\sum_{m=-I}^{+I} exp(\hbar\gamma_I B_0 m_I / k_B T)} \tag{2. 9}$$

For nuclear spins with I = 1/2, the population ratio of two sublevels is:

$$\frac{N_{|+\rangle}}{N_{|-\rangle}} = \exp(\frac{\hbar\gamma_I B_0}{k_B T}) \tag{2. 10}$$

The Zeeman interaction energy results in a slight excess of spins in the $|+\rangle$ state. It gives rise to a small temperature-dependent macroscopic bulk magnetization, which is also called the magnetization at thermal equilibrium.

With the factor that $\hbar\gamma B_0 \ll k_B T$, the bulk magnetization for N_A particles at ambient temperature is given by:[57]

$$M = \mu_0 \frac{\hbar^2 {\gamma_I}^2}{4 k_B T} N_A \tag{2. 11}$$

where μ_0 is the vacuum permeability, N_A is the Avogadro constant. The bulk magnetization per mole is also termed magnetic susceptibility.

2.2 Relevant Principles of NMR Spectroscopy

This section introduces the principles of NMR detection relevant for the liquid-state DNP, including relevant NMR techniques such as ^{1}H decoupling and ^{1}H-^{13}C INEPT.

2.2.1 Hamiltonian of the radiofrequency field

The bulk magnetization of the nuclear spins is nearly impossible for direct detection as it is several orders of magnitude smaller compared with the diamagnetism resulted in the same sample. In practice, NMR spectroscopy applies a radiofrequency (rf) pulse to excite the nuclear spins, rotates the bulk magnetization by 90 degree and records the signals in the x-y plane of the laboratory frame. To explain this process, it is necessary to include the concept of rotating frame. When a rf field is resonant with the nuclear Larmor frequency, the nuclear spin "sees" the rf field as if it were stationary. As depicted in Figure 2. 1, the frame rotates around the laboratory z-axis with the frequency of the oscillating field is the rotating frame. The field strength of the rf pulse acts as a secondary magnetic field causing the spin to precess around the new magnetic field in the rotating frame.

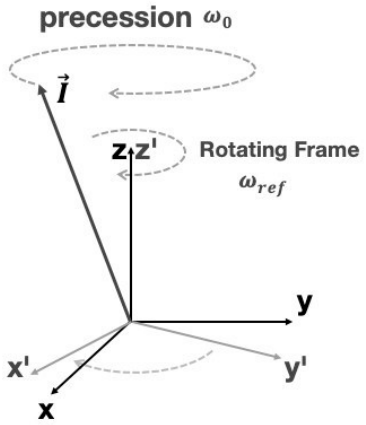

Figure 2. 1 Schematic representation of a rotation frame with frequency ω_{ref} where the frequency of spin precession is ω_0. When the offset $\omega_0 - \omega_{\mathrm{ref}}$ is zero, the spin "sees" the rotating frame as static.

Hamiltonian $\mathcal{H}_1$ of an oscillating rf field with the angular frequency ω_{ref} is given as:[56]

$$\mathcal{H}_1(\mathrm{t}) = \omega_1[cos(\omega_{\mathrm{ref}}t + \phi_p)I_x + sin(\omega_{\mathrm{ref}}t + \phi_p)I_y] - \omega_{\mathrm{ref}}B_0 \qquad (2.\ 12)$$

where ω_1 is the nutation frequency and represents the amplitude of the rf field B_1, ϕ_p is the phase of the pulse with respect to y-axis, I_x, I_y are respectively the x, y component of the spin $\boldsymbol{I}$.

By denote the frequency offset $\omega_0 - \omega_{\mathrm{ref}}$ with Ω_{off}, in the rotating frame, the spin Hamiltonian under static field with rf pulse is simplified to $\mathcal{H}_1(\mathrm{t}) = \omega_1[I_x cos\phi_p + I_y sin\phi_p] + \Omega_{off}B_0$. The exact on-resonance condition is $\Omega_{off} = 0$. To rotate the magnetization on x-y plane, a pulse with length τ_{pulse} satisfying $\omega_1\tau_{pulse} = \pi/2$ is applied.

2.2.2 Spin Relaxation and Bloch Equation

The bulk magnetization is referred to as longitudinal magnetization because it is established along the B_0 field, namely the z-axis of laboratory frame. The establishment of this magnetization after applying an external field or the re-establishment after the rf-pulse irradiation are known as longitudinal spin relaxation or spin-lattice relaxation. This phenomenon is attributed to the transient local magnetic field created by the surrounding environment ("lattice"), which causes the magnetization to return to its thermal equilibrium state via non-radiative transition. An exponential time constant T_1 used to characterize the longitudinal relaxation is known as the longitudinal relaxation time constant.

The net magnetization perpendicular to the external magnetic field after a $\pi/2$ rf pulse is called transverse magnetization. After the rf field is turned off, the transverse magnetization continues precessing but gradually decays. Due to the slight fluctuation of the microscopic magnetic fields, the precessing nuclear magnets gradually get out of phase with each other. The loss of the spin coherence in the x-y-plane is termed transverse relaxation or spin-spin relaxation. The transverse relaxation time constant T_2 is used to describe the transverse relaxation process.

Relaxation is a crucial process in magnetic resonance spectroscopy. It allows the spin system to regain its equilibrium state, enabling reproducible measurement. It also provides valuable insights into microscopic motional processes which generating the spin-interacting transient magnetic field. To describe the relaxation process of the bulk magnetization in the presence of an external B_0-field and an oscillating B_1-field, a set of differential equations known as the Bloch equations are used:[3]

$$\frac{\partial}{\partial t}\begin{pmatrix} M_x \\ M_y \\ M_z \end{pmatrix} = \begin{pmatrix} 0 & -\Omega_{off} & \omega_1 \sin\phi_p \\ \Omega_{off} & 0 & -\omega_1 \cos\phi_p \\ -\omega_1 \sin\phi_p & \omega_1 \cos\phi_p & 0 \end{pmatrix} \begin{pmatrix} M_x \\ M_y \\ M_z \end{pmatrix} - \begin{pmatrix} M_x/T_2 \\ M_y/T_2 \\ (M_z - M_0)/T_1 \end{pmatrix} \quad (2.\ 13)$$

where M_x, M_y and M_z are magnetizations along the x, y, z axis in the rotating frame, M_0 is the longitudinal magnetization at thermal equilibrium. The steady-state solution of Bloch equations allows prediction of the magnetization associated with T_1 and T_2 relaxation processes at on-resonance and off-resonance frequency. The importance of Bloch equation is less pronounced in NMR spectroscopy performed nowadays mostly with pulse techniques. However, it remains particularly useful to predict steady-state magnetization in the scenario of cw irradiation.

2.2.3 Fourier Transform NMR Signal

After the rf pulse is turned off, the nuclear spin magnetization undergoes precession, resulting in oscillation until it diminishes over time by the T_2 relaxation process. This oscillation is recorded by the detector on the laboratory x-y plane and gives rise to a rf NMR signal, which is known as free induction decay (FID). FID is a convoluted signal of the oscillation and the T_2 exponential decay. To convert the signal into a more intuitive manner, Fourier transformation (FT) as a mathematical method to present information in frequency domain is commonly employed in NMR spectroscopy. The FT formula is given by:[56]

$$S_{spectrum}(\Omega) = \int_0^\infty S_{FID}(t)\exp(-i\Omega t)\mathrm{d}t \quad (2.\ 14)$$

where $S_{FID}(t)$ is the FID signal as a function of time, the output spectrum $S_{spectrum}(\Omega)$ is a function of frequency.

FT of the FID itself doesn't add any additional information to the recorded FID. Other strategies such as applying weighting functions, truncations or line broadening prior to FT, are frequently used in NMR spectroscopy to suppress the signal noise.[58] In practice, FID is recorded as digital points evenly distributed in time. The sampling rate of these points have to be larger than the minimum Nyquist frequency of the detective oscillating.

With $\omega_1\tau_{pulse} = \pi/2$ and $\phi_p = \pi/2$, the resulted x- and y-components of the magnetization after rf pulse is given as $M_x = M_0\cos\Omega_{off}t$ and $M_y = M_0\sin\Omega_{off}t$. Using S_0 representing the initial FID intensity, $S_{FID}(t)$ can be represented as:[56]

$$S_{FID}(t) = S_0\exp(\mathrm{i}\Omega_{off}t)\exp(-t/T_2) \quad (2.\ 15)$$

where Ω_{off} is the frequency offset of the oscillating magnetization in the rotating frame. FT of the FID signal gives:

$$S_{spectrum}(\Omega) = \int_0^\infty S_0\exp\left(\mathrm{i}\Omega_{off}t\right)\exp\left(-\frac{t}{T_2}\right)\exp(-i\Omega t)\,\mathrm{d}t$$

$$\ldots = \frac{S_0/T_2}{1/{T_2}^2+(\Omega-\Omega_{off})^2} + i\,\frac{-S_0(\Omega-\Omega_{off})}{1/{T_2}^2+(\Omega-\Omega_{off})^2} \quad (2.\ 16)$$

The real part of the signal is often referred to as the absorption Lorentzian while the imaginary part is known as dispersion Lorentzian. The absorption Lorentzian $L(\Omega)$ is a common lineshape in NMR spectroscopy (Figure 2. 2 A). The maximum is at the frequency of Ω_{off} and the full width at the half maximum (FWHM) is $2/T_2$ (or $1/\pi T_2$ in Hz).

$$L(\Omega) = Re[S_{spectrum}(\Omega)] = S_0\frac{T_2}{1+{T_2}^2(\Omega-\Omega_{off})^2} \quad (2.\ 17)$$

Another commonly observed lineshape of NMR signal is Gaussian (Figure 2. 2 B), which often occurs with instrumental or random statistical effects. The Gaussian lineshape $G(\Omega)$ is given as:[59]

$$G(\Omega) = \sqrt{2\pi} T_2 e^{-\frac{1}{2}T_2^2(\Omega-\Omega_{off})^2} \quad (2.\ 18)$$

Gaussian has a $2/T_2$ width at the points of maximum slope. Compared to Gaussian shape, Lorentzian lines drop off much more slowly in the outer wings of the line. Notably, both expressions give the lineshape under enough low irradiation power without the effect of "saturation" and therefore depend only on T_2. The saturation term is vital for electron spins in the context of DNP and is introduced later.

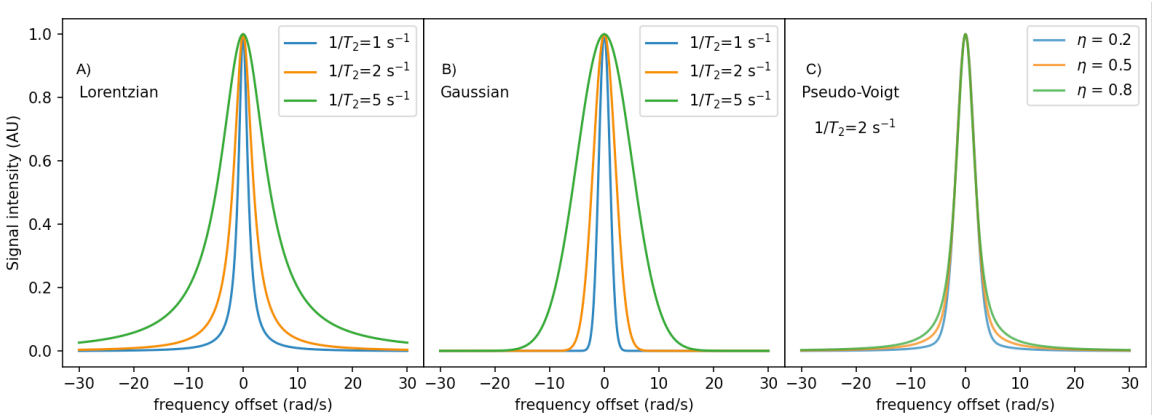

Figure 2. 2 (A) Demonstrative Lorentzian lineshape with different T_2; (B) Demonstrative Gaussian lineshape with different T_2; (C) Demonstrative pseudo-Voigt lineshape with different weight parameter η of Lorentzian with $1/T_2 = 2\ s^{-1}$.

Voigt lineshape as the convolutional function of the two complementary shape, Lorentzian and Gaussian, is also used frequently to describe the spectroscopic curves. In the case of signal centered at zero, the general Voigt profile is expressed as:

$$V(x;\sigma,\gamma) \equiv \int_{-\infty}^{\infty} G(x';\sigma)L(x-x';\gamma)\mathrm{d}x' \quad (2.\ 19)$$

where x is the shift from the center, σ and γ are the parameters determining the Gaussian signal width at the points of maximum slope and the Lorentzian FWHM,

respectively. A pseudo-Voigt approximation is commonly used in the determination of experimental spectral lineshape (Figure 2. 2 C). A simple form is given as:[60]

$$V_{pseudo}(\Omega;\eta) = (1-\eta)\exp(-\frac{T_2^2(\Omega-\Omega_{off})^2}{2}) + \eta\frac{T_2}{1+T_2^2(\Omega-\Omega_{off})^2} \qquad (2.\ 20)$$

where η is the weight parameter of the Lorentzian component.

An essential information obtainable from the FT NMR signal is the chemical shift denoted as δ, which is specific for different nucleus precessing with their own Larmor frequency, thereby revealing the surrounding chemical environment. For example, in diamagnetic molecules, the electrons in the outer atomic shells or the bonding electrons can generate small magnetic fields opposing to the external field B_0, thereby provides a shielding to the nuclear spin. To describe the chemical shielding in an anisotropic environment, the chemical shift anisotropy (CSA) is used. In non-viscous solution, the CSA is usually not observable due to isotropic averaging.[56]

An important aspect related to this thesis is the presence of paramagnetic radical molecules in solution, which provide a magnetic field to their surrounding nucleus in addition to B_0. This results in a paramagnetic shift to the observed nucleus. The paramagnetic molecules also introduce additional relaxation pathway to the nucleus, which is extensively discussed in Section 2.4.

2.2.4 Heteronuclear Decoupling and INEPT

Heteronuclear decoupling is a technique widely used in NMR spectroscopy to increase the signal intensity by avoiding the J-coupled splitting and to simplify complicated spectrum for signal assignment.[58] Figure 2. 3 illustrates an example of ^{13}C NMR pulse sequence with ^{1}H-decoupling, utilizing a strong cw rf field at the ^{1}H Larmor frequency.

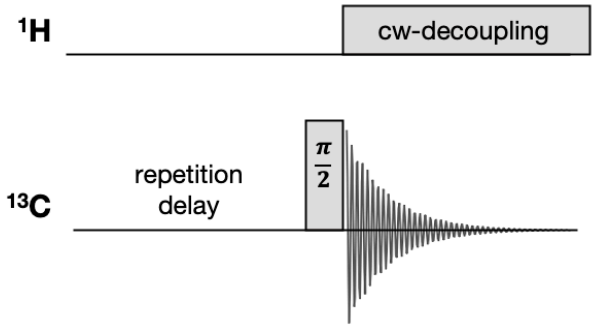

Figure 2. 3. ^{13}C NMR pulse sequence with ^{1}H-decoupling

Insensitive Nuclei Enhancement by Polarization Transfer (INEPT) is a NMR technique to enhance the signal of the low-γ nuclei by transferring the magnetization from a high-γ nuclei, which is achieved via coherence transfer under the evolution with the scalar coupling.[58] The pulse sequence of a ^{1}H-^{13}C INEPT experiment is demonstrated in Figure 2. 4.

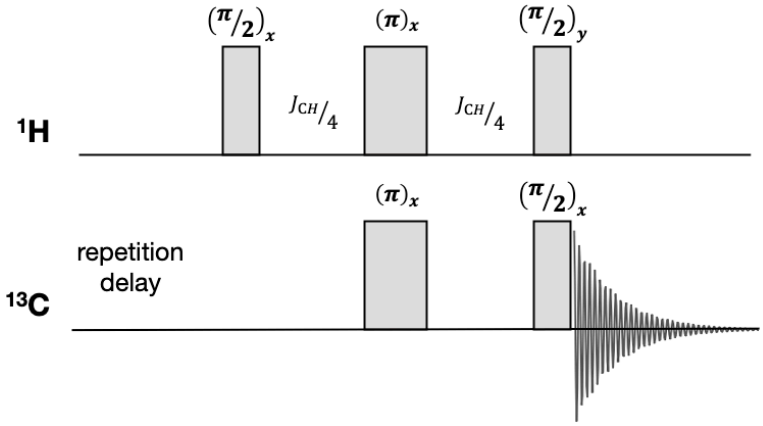

Figure 2. 4. ^{1}H-^{13}C INEPT pulse sequence

With an evolution time of $J_{\mathrm{CH}}/4$, the resulted spectrum is an anti-phase ^{13}C NMR doublet. Further modifications of the presented INEPT pulse sequence, such as applying an additional refocused pulse to detect the in-phase signal and simultaneously implementation of ^{1}H decoupling, are also available.

2.3 Relevant Principles of EPR spectroscopy

EPR shares the same basic principles with NMR. Their differences originate from the magnitude of the spin magnetization, thereby leads to variations in the experimental techniques. While NMR relies on the non-zero spin of the nucleus, EPR request the presence of unpaired electron spins in the matter. There are different sources of unpaired spins, including stable organic radicals, metal ion complexes, and transient radicals formed during chemical processes. In the scope of this work, stable organic compound such nitroxides, BDPA, triphenylmethyl (trityl) radicals, and their derivatives were used. As representatives, organic radicals TEMPO (2,2,6,6-Tetramethylpiperidinyloxy) nitroxide, BDPA and Finland trityl are shown in Figure 2. 5.

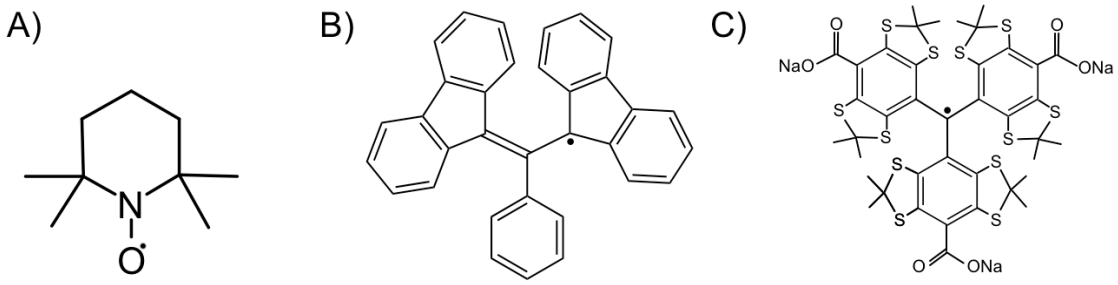

Figure 2. 5. Chemical structure of stable organic radicals relevant for this work: (A) TEMPO, (B) BDPA and (C) Finland trityl

2.3.1 g-tensor

Unlike the nucleus, where any corrections to the Zeeman energy are attributed to CSA, the electron spin angular moment is associated with its orbital, which may impose an additional angular momentum $\boldsymbol{L}$ contributed from orbital to the total spin magnetic moment. The Hamiltonian for the spin-orbit coupling is given by:[55]

$$\mathcal{H}_{S,L} = \mu_{\mathrm{B}} \boldsymbol{L} \cdot \boldsymbol{B_0} \qquad (2.\ 21)$$

As $\boldsymbol{B_0}$ is aligned with the laboratory z-axis and the $\boldsymbol{L}$ depends on the molecular axis, the interaction Hamiltonian $\mathcal{H}_{S,L}$ is orientation dependent. Combined with the Zeeman interaction of free electron spins, the total Zeeman Hamiltonian of a electron spin is expressed as:[55]

$$\mathcal{H}_{Z_S} = \mu_{\mathrm{B}}(g_e\boldsymbol{S} + \boldsymbol{L}) \cdot \boldsymbol{B_0} \tag{2. 22}$$

A convenient way is to define a tensor g which couples the magnetic moment S with the external magnetic moment. The tensor g in the laboratory axis is given as:

$$g_{lab} = \begin{pmatrix} g_{xx} & g_{xy} & g_{xz} \\ g_{yx} & g_{yy} & g_{yz} \\ g_{zx} & g_{zy} & g_{zz} \end{pmatrix} \tag{2. 23}$$

The value of g-tensor depends on the orientation of the molecule. It can be determined by studying an oriented single crystal. The g-tensor can be presented in its own principal directions with matrix diagonalization $g = \mathcal{L}^{-1} g_{lab} \mathcal{L}$. Therefore, the g-tensor is given with 3 principal values:

$$g = \begin{pmatrix} g_{xx} & 0 & 0 \\ 0 & g_{yy} & 0 \\ 0 & 0 & g_{zz} \end{pmatrix} \tag{2. 24}$$

which can also be expressed as $g = (g_{xx}, g_{yy}, g_{zz})$. When the spin-orbit coupling is axial symmetric with respect to the z-axis, namely $g_{xx} = g_{yy}$, the g-tensor can also be expressed with $g = (g_{\perp}, g_{\parallel})$.

In non-viscous solution where the radicals are tumbling rapidly and randomly, only the isotropic g-value is observed:

$$g_{iso} = \frac{1}{3}(g_{xx} + g_{yy} + g_{zz}) \tag{2. 25}$$

2.3.2 Hyperfine Interaction

The interaction between electron spins and nuclear spins was first discussed by Fermi to explain the hyperfine structure of atomic spectra.[61] The e-N HFI has two

major contributions, namely the isotropic and the anisotropic part. The isotropic HFI, also known as the Fermi contact interaction, arises from the finite probability of the unpaired electrons to be found on the nucleus, which is the case of the unpaired electron occupies an s orbital or has contributions to s orbitals of the molecules. The anisotropic HFI is the dipole-dipole interaction between e-N spins. The Hamiltonian of the e-N HFI is given as the sum of the dipolar HFI Hamiltonian $\mathcal{H}_{\mathrm{DD}}$ and the isotropic HFI Hamiltonian $\mathcal{H}_{\mathrm{iso}}$:[59]

$$\mathcal{H}_{\mathrm{HFI}} = \mathcal{H}_{\mathrm{DD}} + \mathcal{H}_{\mathrm{iso}} = -D_{eN}\left[\frac{3(\boldsymbol{I}\cdot\boldsymbol{r})(\boldsymbol{S}\cdot\boldsymbol{r})}{r^5} - \frac{\boldsymbol{I}\cdot\boldsymbol{S}}{r^3}\right] + A_{iso}\boldsymbol{I}\cdot\boldsymbol{S} \tag{2. 26}$$

where μ_0 is the vacuum permeability, $\boldsymbol{r}$ is the vector connecting the e-N spin, D_{eN} is the e-N dipolar coupling constant, which is given as $D_{eN} = \frac{\mu_0 \hbar \gamma_S \gamma_I}{4\pi} \approx -2\pi(79\ \mathrm{kHz\ nm^3})$, and the isotropic hyperfine constant A_{iso} is given as a function of the probability $\psi(0)$ of the unpair electron on the nucleus:

$$A_{iso} = \frac{8\pi}{3} D_{eN} |\psi(0)|^2 \tag{2. 27}$$

Similar as the g-anisotropy, the dipolar hyperfine interaction is orientation dependent and can be expressed with a tensor. Nevertheless, the components of the dipolar HFI Hamiltonian is more conveniently expressed with the spin operators in the spherical coordinates with the polar angle θ, azimuthal angle φ and radial distance r (Figure 2. 6) for subsequent discussions:[62]

$$\mathcal{H}_{\mathrm{DD}} = \frac{D_{eN}}{r^3}(\hat{A} + \hat{B} + \hat{C} + \hat{D} + \hat{E} + \hat{F}) \tag{2. 28}$$

where the dipolar alphabet in the bracket is given as:

$$\hat{A} = (1 - 3\cos^2\theta)\hat{S}_z\hat{I}_z$$

$$\hat{B} = -\frac{1}{4}(1 - 3\cos^2\theta)(\hat{S}^+\hat{I}^- + \hat{S}^-\hat{I}^+)$$

$$\hat{C} = -\frac{3}{2}\sin\theta cos\theta \exp(-\mathrm{i}\varphi)(\hat{S}^{+}\hat{I}_z + \hat{S}_z\hat{I}^{+})$$

$$\hat{D} = -\frac{3}{2}\sin\theta cos\theta \exp(\mathrm{i}\varphi)(\hat{S}^{-}\hat{I}_z + \hat{S}_z\hat{I}^{-})$$

$$\hat{E} = -\frac{3}{4}\sin^2\theta \exp(-2\mathrm{i}\varphi)\hat{S}^{+}\hat{I}^{+}$$

$$\hat{F} = -\frac{3}{4}\sin^2\theta \exp(2\mathrm{i}\varphi)\hat{S}^{-}\hat{I}^{-}$$

The ladder operators are given as:

$$\hat{S}^{+} = \hat{S}_x + i\hat{S}_y, \hat{S}^{-} = \hat{S}_x - i\hat{S}_y, \hat{I}^{+} = \hat{I}_x + i\hat{I}_y, \hat{I}^{-} = \hat{I}_x - i\hat{I}_y$$

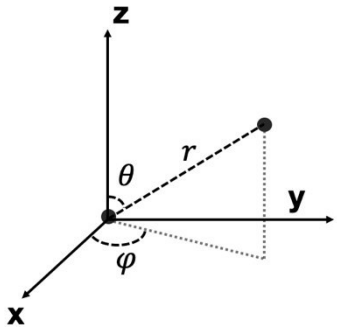

Figure 2. 6. Schematic representation of the spherical coordinates (r, θ, φ) in a Cartesian coordinate (x, y, z)

2.3.3 cw EPR spectrum

Valuable information of the g-tensor, hyperfine interaction and radical motions can be obtained from cw EPR spectra. Given the mw pulse phase $\phi_p = 0$, the resulted signal can be calculated as the steady-state solution with Bloch equation (Equation 2.13):

$$M_x = \frac{\omega_{\mathrm{mw}} T_2}{1+\omega_{\mathrm{mw}}{}^2 T_1 T_2 + \Omega_{off}{}^2 T_2{}^2} M_0 \quad (2.\ 29)$$

$$M_y = \frac{\omega_{\mathrm{mw}} \Omega_{off} T_2{}^2}{1+\omega_{\mathrm{mw}}{}^2 T_1 T_2 + \Omega_{off}{}^2 T_2{}^2} M_0 \quad (2.\ 30)$$

$$M_z = \frac{1+{\Omega_{off}}^2{T_2}^2}{1+{\omega_{\mathrm{mw}}}^2T_1T_2+{\Omega_{off}}^2{T_2}^2} M_0 \quad (2.\ 31)$$

The mw nutation frequency is denoted as ω_{mw} to avoid ambiguity of the rf and mw oscillating field. The saturation of the allowed EPR transition is defined as:

$$s \equiv \frac{M_0 - M_z}{M_0} = \frac{{\omega_{\mathrm{mw}}}^2T_1T_2}{1 + {\omega_{\mathrm{mw}}}^2T_1T_2 + {\Omega_{off}}^2{T_2}^2} \quad (2.\ 32)$$

The saturation factor has a maximum value of 1 when ${\omega_{\mathrm{mw}}}^2T_1T_2 \gg 1$. The absorption signal M_x can be simplified to a Lorentzian curve when the electron spin population is far from saturation, namely ${\omega_{\mathrm{mw}}}^2T_1T_2 \ll 1$. The electron saturation is avoided in cw EPR measurements to ensure the lineshape distortions do not occur. On the other hand, a sizable saturation is a prerequisite for OE DNP measurement, which is discussed in the next section.

cw EPR spectra can be calculated by solving the stochastic Liouville equation.[63] In practice, the EPR lineshape of radicals is not only determined by the T_2 relaxation, but also g-tensor, HFI tensor, and dynamic processes such as rotational motion of radicals and Heisenberg-spin exchange, etc. Specially, the Zeeman interaction determined by the g-tensor exhibits field dependence whereas the HFI splitting doesn't. Also, EPR curves are sensitive to motions of different time scales at different magnetic fields. Spectra at 9.4 T (J-band) simulated with easyspin[64] are shown in Figure 2. 7 to demonstrate the dependence of the cw EPR lineshape on g-tensor, hyperfine-tensor and rotational motion of radicals. The powder spectrum is simulated with *pepper* function and others with *chili* function of easyspin. The simulation parameters are presented in the figure caption.

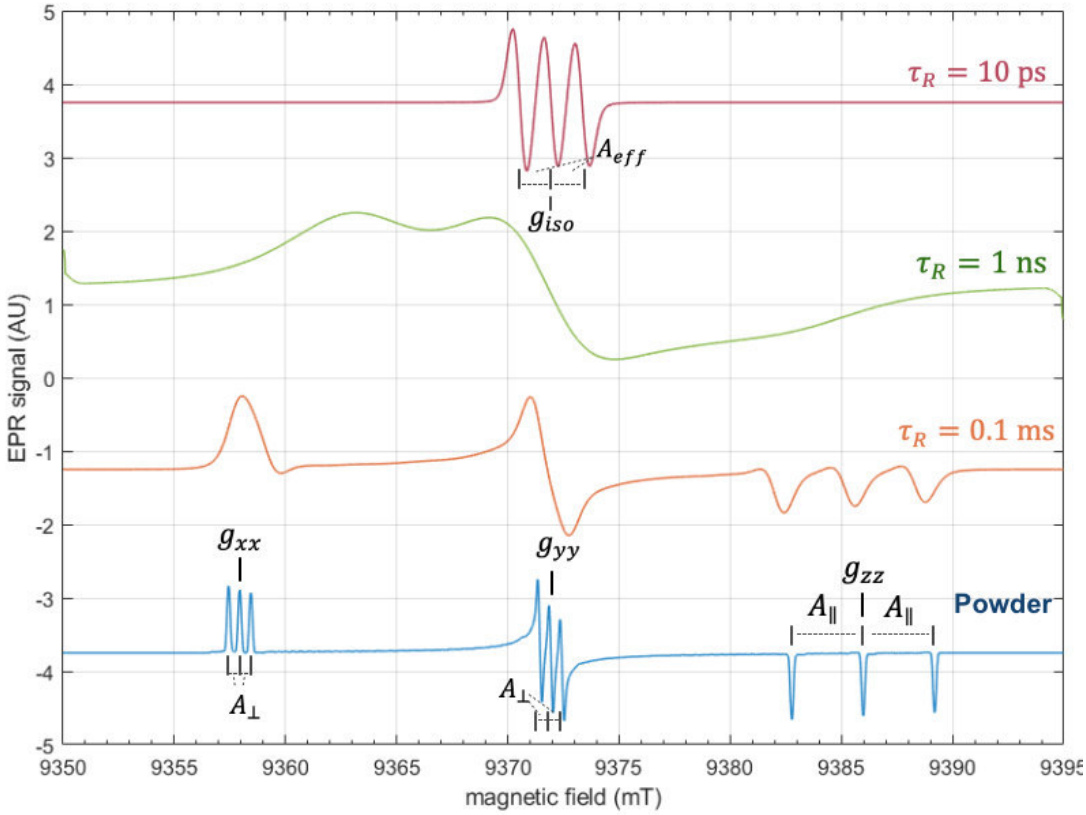

Figure 2. 7. EPR spectra simulated with (g_{xx}, g_{yy}, g_{zz})=(2.008, 2.005, 2.002), $(A_\perp, A_\parallel)$=(14, 90) MHz, which are typical values of nitroxide radicals. $T_2 = 50$ ns corresponding to a FWHM=20 MHz is used. The hyperfine tensor assumed to have the same principal axis as g-tensor. The curves from bottom to top showing: (blue curve) powder-like spectrum; (orange curve) spectra simulated with rotational correlation time of the radicals $\tau_R = 0.1$ ms; (green curve) spectra simulated with $\tau_R = 1$ ns; (red curve) spectra simulated with $\tau_R = 10$ ps

2.4 Liquid-State Dynamic Nuclear Polarization

In liquids, there are currently two pathways of DNP available, namely OE and SE. This section introduces the unique DNP mechanism in non-viscous liquids, namely OE, and the method newly explored in viscous liquids at high fields, that is SE.

Both OE or SE rely on the existence of the HFI between an electron spin and a nuclear spin. For subsequent discussions, it is necessary to provide the Hamiltonian expression for an e-N spin system:

$$\mathcal{H}_{\mathrm{e-N}} = \mathcal{H}_{Z_I} + \mathcal{H}_{Z_S} + \mathcal{H}_{mw}(\mathrm{t}) + \mathcal{H}_{\mathrm{HFI}} + \mathcal{H}_{II} + \mathcal{H}_{\mathrm{SS}} \qquad (2.\ 33)$$

2.4.1 Introduction of Overhauser Effect

OE relies on the cross-relaxation processes of one electron spin coupled to one nuclear spin. To discuss its mechanisms, we can focus on a system of spin 1/2. The energy level diagram for such a system is shown in Figure 2. 8.

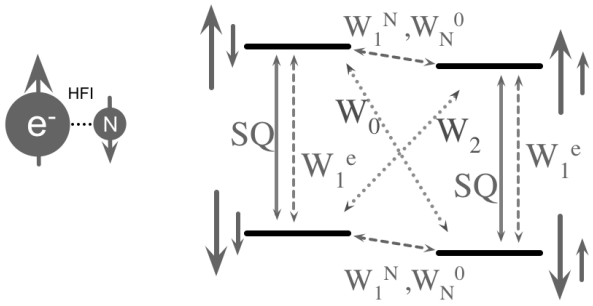

Figure 2. 8. Energy level diagram of a two-spin system of one nuclear spin coupled with one electron spin illustrating the OE. SQ denotes the allowed EPR single-quantum mw-driven transition. W denotes different relaxation rates.

Analogous to the Bloch equation, the differential equations for such a coupled system are formulated by Solomon[37], which are expressed as:

$$\frac{\partial I_Z}{\partial t} = -R_I(I_Z - I_0) - (W_2 - W_0)(S_Z - S_0) \qquad (2.\ 34)$$

$$\frac{\partial S_Z}{\partial t} = -(W_2 - W_0)(I_Z - I_0) - R_S(S_Z - S_0) \qquad (2.\ 35)$$

where I_Z and S_Z are the population differences of electron spin and nuclear spin during mw irradiation, respectively; I_0 and S_0 are the Boltzmann populations of electron spin and nuclear spin at thermal equilibrium, respectively; $R_I = 2W_1^N + W_0 + W_2 + W_N^0$ denotes the total nuclear relaxation rate; $R_S = 2W_1^S + W_0 + W_2 + W_S^0$ denotes the total electron relaxation rate; W_2 and W_0 are respectively

the double-quantum (DQ) and zero-quantum (ZQ) cross-relaxation rates; W_1^N and W_N^0 are respectively the nuclear single-quantum (SQ) relaxation with and without contributions from electron spin.

The enhancement by solving the steady-state differential equation is given as:

$$\varepsilon \equiv \frac{I_Z - I_0}{I_0} = \frac{W_2 - W_0}{R_I} * \frac{S_0 - S_Z}{S_0} * \frac{S_0}{I_0} \tag{2. 36}$$

By replacing the terms in Equation 2.36 with $\frac{\gamma_e}{\gamma_N} = \frac{S_0}{I_0}$, $s \equiv \frac{S_0 - S_Z}{S_0}$, and

$$\xi = \frac{W_2 - W_0}{2W_1^N + W_0 + W_2} \tag{2. 37}$$

$$f = \frac{2W_1^N + W_0 + W_2}{R_I} \tag{2. 38}$$

the general formula of OE DNP enhancement is expressed as:

$$\varepsilon = s \cdot \xi \cdot f \cdot \frac{\gamma_e}{\gamma_N} \tag{2. 39}$$

where s is the saturation factor, ξ is the coupling factor, f is the leakage factor. These parameters are introduced in the following sections.

2.4.2 OE Leakage Factor and Saturation Factor

The OE leakage factor *f* is defined as the ratio of the nuclear relaxation induced by the electronic spin and the total nuclear relaxation. It can be experimentally determined by measuring the nuclear relaxation time in the absence (T_{1W}) and in the presence (T_{1R}) of the radicals:

$$f = 1 - \frac{W_N^0}{R_I} = 1 - \frac{T_{1R}}{T_{1W}} \tag{2. 40}$$

The leakage factor relies on the nuclear relaxation induced in the presence of unpaired electrons. It is rather an experimental parameter and can reach the theoretical maximum, namely unity, with a sufficient concentration of radicals.

Saturation factor describes the microwave efficiency to saturate the electron population differences. When the mw B_1 strength is sufficiently high, the electron population differences gradually vanish, and a saturation close to 1 can be achieved. In practice, the mw B_1 may not always be adequate. The saturation factor can be affected by various factors beyond the simple solution of the steady-state Bloch equation shown in Equation 2.32. For example, the g- and HFI-anisotropy can result in an energy separation of electron spin states, thereby produce splitting and shift in resonance frequency. Moreover, the electron-electron Heisenberg exchange and dipolar interaction can change the populations of the spin states,[65] which also complicated the determination of the saturation factor.[66] Experimental approaches to the saturation factors include detection of the FID by pulsed ELDOR (Electron Double Resonance) experiments at low fields[67], and monitoring the suppression of Knight shift[68] or paramagnetic shifts.[69]

2.4.3 Perturbation Theory and Spectral Density Function

Unlike the leakage factor and saturation factor which can be experimentally optimized by using sufficient radical concentration and mw B_1 field strength, the coupling factor determined by the differences of two cross-relaxation rates, denoted with $W_2 - W_0$, reflects the intrinsic property of a sample system and defines the highest achievable OE enhancements. The cross-relaxation rates are theoretically determined by the spectral density function (SDF) dispersed at the corresponding DQ and ZQ frequency, namely $\omega_{0,\mathrm{S}} \pm \omega_{0,\mathrm{I}}$.

As already discussed, the relaxation is caused by the stochastic change of the local magnetic fields. When the frequency spectrum of these stochastic processes matches the transition frequencies between the spin states, relaxation happens, as described by the Redfield theory.[70] As the basis for the perturbation theory, the time derivative of the density matrix $\rho(\mathrm{t})$ is given with the Liouville-von Neumann equation:[57]

$$\frac{\partial}{\partial \mathrm{t}}\rho(\mathrm{t}) = -i[\mathcal{H}_0 + \mathcal{H}_1(\mathrm{t}), \rho(\mathrm{t})] \quad (2.\ 41)$$

where $\rho(\mathrm{t}) = |\psi\rangle\langle\psi|$, $\mathcal{H}_0$ is the time-independent spin Hamiltonian, and the time-dependent $\mathcal{H}_1(\mathrm{t})$ is also termed as the perturbation.

In the *interaction picture* with time evolution operator $U = e^{i\mathcal{H}_0 t}$, the density matrix becomes $\tilde{\rho}(\mathrm{t}) = U\rho(\mathrm{t})U^{\dagger}$ and the time-dependent Hamiltonian becomes $\widetilde{\mathcal{H}_1}(\mathrm{t}) = U\mathcal{H}_1(\mathrm{t})U^{\dagger}$. Equation 2.41 in the interaction picture is therefore expressed as:

$$\frac{\partial}{\partial \mathrm{t}}\tilde{\rho}(\mathrm{t}) = -i[\widetilde{\mathcal{H}_1}(\mathrm{t}), \tilde{\rho}(\mathrm{t})] \quad (2.\ 42)$$

Its integration gives:

$$\tilde{\rho}(\mathrm{t}) = \tilde{\rho}(0) - i\int_0^t [\widetilde{\mathcal{H}_1}(\mathrm{t}'), \tilde{\rho}(\mathrm{t})]\, d\mathrm{t}' \quad (2.\ 43)$$

Substitute it back to the right side of Equation 2.42, we have

$$\frac{\partial}{\partial \mathrm{t}}\tilde{\rho}(\mathrm{t}) = -i\left[\widetilde{\mathcal{H}_1}(\mathrm{t}), \tilde{\rho}(0)\right] - \int_0^t d\mathrm{t}' \left[\widetilde{\mathcal{H}_1}(\mathrm{t}), \left[\widetilde{\mathcal{H}_1}(\mathrm{t}'), \tilde{\rho}(\mathrm{t})\right]\right] \quad (2.\ 44)$$

Replacing with $\tau = t - t'$, it is expressed as:

$$\frac{\partial}{\partial \mathrm{t}}\overline{\tilde{\rho}(\mathrm{t})} = -i\overline{\left[\widetilde{\mathcal{H}_1}(\mathrm{t}), \tilde{\rho}(0)\right]} - \int_0^t d\tau \overline{\left[\widetilde{\mathcal{H}_1}(\mathrm{t}), \left[\widetilde{\mathcal{H}_1}(\mathrm{t}-\tau), \tilde{\rho}(\mathrm{t})\right]\right]} \quad (2.\ 45)$$

While any non-perturbative part should belong to $\mathcal{H}_0$, the ensemble average of the perturbation $\overline{\mathcal{H}_1(\mathrm{t})}$ is expected to be 0. In liquids, as the correlation time of $\mathcal{H}_1$ is of several orders shorter as the nuclear relaxation time, it is permissible to assume $\int_0^t \overline{\widetilde{\mathcal{H}_1}(\mathrm{t}')\tilde{\rho}(\mathrm{t})}\, d\mathrm{t}' = 0$ and the integral upper limit to be ∞. $\tilde{\rho}(\mathrm{t})$ in the right side of the equation is replaced by $\Delta\tilde{\rho}(\mathrm{t}) = \tilde{\rho}(\mathrm{t}) - \tilde{\rho}_{eq}(\mathrm{t})$, where $\tilde{\rho}_{eq}(\mathrm{t})$ is the thermal equilibrium of the density matrix with $\mathcal{H}_0$.

Therefore, Equation 2. 45 becomes[71]

$$\frac{\partial}{\partial \mathrm{t}}\overline{\tilde{\rho}(\mathrm{t})} = -\int_0^{\infty} d\tau \overline{\left[\widetilde{\mathcal{H}_1}(\mathrm{t}), \left[\widetilde{\mathcal{H}_1}(\mathrm{t}-\tau), \Delta\tilde{\rho}(\mathrm{t})\right]\right]} \quad (2.\ 46)$$

$\mathcal{H}_1(\mathrm{t})$ can be expressed as a linear combination of different operators:[57]

$$\mathcal{H}_1(\mathrm{t}) = \sum_P F_P(\mathrm{t})\mathrm{A}_P \tag{2. 47}$$

where $F_P(\mathrm{t})$ is a random function of time and A_P is an operator chosen from the eigenoperators of $\mathcal{H}_0$, so that $[\mathcal{H}_0, \mathrm{A}_P] = \omega_P \mathrm{A}_P$. In the interaction representations, the expansion of $\mathcal{H}_1(\mathrm{t})$ is given as $U\mathrm{A}_P U^\dagger = \widetilde{\mathrm{A}}_P(\mathrm{t}) = \mathrm{A}_P \exp(\mathrm{i}\omega_P \mathrm{t})$. As a physical operator, $\mathcal{H}_1(\mathrm{t})$ is a Hermitian. Therefore, ${F_P}^*(\mathrm{t})\mathrm{A}_P^\dagger$ as the conjugate transpose of $F_P(\mathrm{t})\mathrm{A}_P$ also exists in $\mathcal{H}_1(\mathrm{t})$.

Equation 2.46 is thereby given as:

$$\frac{\partial}{\partial \mathrm{t}}\overline{\tilde{\rho}(\mathrm{t})} = -\sum_{P,Q}\int_0^\infty d\tau \left[\widetilde{\mathrm{A}}_P(\mathrm{t}), \left[\widetilde{\mathrm{A}}_Q^\dagger(\mathrm{t}-\tau), \Delta\tilde{\rho}(\mathrm{t})\right]\right]\overline{F_P(t){F_Q}^*(t-\tau)} \tag{2. 48}$$

Now switching back to laboratory picture with $\rho(\mathrm{t}) = U^\dagger \tilde{\rho}(\mathrm{t}) U$, it becomes:

$$\frac{\partial}{\partial \mathrm{t}}\rho(\mathrm{t}) = -i[\mathcal{H}_0, \rho(\mathrm{t})] - \sum_{P,Q}\int_0^\infty d\tau \left[\mathrm{A}_P, \left[\widetilde{\mathrm{A}}_Q^\dagger(-\tau), \Delta\tilde{\rho}(\mathrm{t})\right]\right] G_{PQ}(\tau) \tag{2. 49}$$

where $G_{PQ}(\tau)$ is introduced as the correlation function with the definition:

$$G_{PQ}(\tau) = \overline{F_P(t){F_Q}^*(t-\tau)} \tag{2. 50}$$

Finally, with $\widetilde{\mathrm{A}}_Q^\dagger(-\tau) = \widetilde{\mathrm{A}}_Q^\dagger \exp(-\mathrm{i}\omega\tau)$, Equation 2.49 can be expressed as

$$\frac{\partial}{\partial \mathrm{t}}\rho(\mathrm{t}) = -i[\mathcal{H}_0, \rho(\mathrm{t})] - \sum_{P,Q}\left[\mathrm{A}_P, \left[\widetilde{\mathrm{A}}_Q^\dagger, \Delta\tilde{\rho}(\mathrm{t})\right]\right] J_{PQ}(\omega) \tag{2. 51}$$

where the SDF $J_{PQ}(\omega)$ is defined as

$$J_{PQ}(\omega) = \int_0^\infty G_{PQ}(\tau)\exp(-\mathrm{i}\omega\tau)d\tau \tag{2. 52}$$

2.4.4 OE Coupling Factor

With the spin Hamiltonians shown in Equation 2.33, the perturbative interactions include $\mathcal{H}_{\mathrm{SS}}$, $\mathcal{H}_{II}$, and $\mathcal{H}_{\mathrm{HFI}}$. The first term belongs to the electron spin density matrix and the second term contributes to the nuclear relaxation in the absence of electron spin. Both will not be considered in the cross-relaxation of one electron and one nuclear spin. Only the last term is concerned in the context of liquid-state DNP.

$\mathcal{H}_{\mathrm{HFI}}$ contribute to the nuclear spin relaxations with two different kinds, dipolar and scalar kind, which are discussed separately.

With the dipolar Hamiltonian presented with the dipolar alphabets in Equation 2.28, the transition rates of different e-N relaxation pathways can be calculated. As an instance, the ZQ cross-relaxation rate W_0 is expressed with $\hat{B}$ containing the $\hat{S}^+\hat{I}^-$ and $\hat{S}^-\hat{I}^+$:[72]

$$W_0 = {D_{eN}}^2 \int_{-\infty}^{\infty} \frac{\overline{\langle +-|\hat{B}(t)|-+\rangle}}{r^3(t)} \frac{\overline{\langle -+|\hat{B}^\dagger(t-\tau)|+-\rangle}}{r^3(t-\tau)} \exp[-\mathrm{i}(\omega_{0,S} - \omega_{0,I})\tau] d\tau \quad (2.\ 53)$$

With the spectral density J as a function of the correlation time τ_c and the corresponding pre-factor k_{dip}, the dipolar HFI-driven transition rates of the relevant e-N relaxation pathways are given as:[23,73]

$$W_{0,\mathrm{dip}} = k_{\mathrm{dip}} J_{\mathrm{dip}}(\omega_{0,I} - \omega_{0,S}, \tau_c) \quad (2.\ 54)$$

$$W_{2,\mathrm{dip}} = 6k_{\mathrm{dip}} J_{\mathrm{dip}}(\omega_{0,I} + \omega_{0,S}, \tau_c) \quad (2.\ 55)$$

$$W^N_{1,\mathrm{dip}} = \frac{3}{2} k_{\mathrm{dip}} J_{\mathrm{dip}}(\omega_{0,I}, \tau_c) \quad (2.\ 56)$$

As SDF is always non-negative, dipolar HFI has a stronger contribution to the DQ cross-relaxation pathway than the ZQ pathway, leading to a negative DNP enhancement.

Two models were commonly implemented to quantitatively explain the dynamical modulation of e-N dipolar HFI in liquids, namely the "inner-sphere"[37,39] and the "outer-sphere" model.[38,40]

In the inner-sphere model, distance r between e-N is assumed to be static and the angle parameters θ and φ are stochastic functions of time. As demonstrated in Figure 2. 9 A, the physical picture would be a bounded transient complex formed by the target molecule and the radical-bearing molecule undergoing reorientation processes. Within the lifetime of the coupling system, the dipolar coupling is

modulated by the rotational correlation time of the complex. The pre-factor k_{in} and a Lorentzian SDF $J_{in}(\omega, \tau_r)$ of the inner-sphere model are given by:[24,73]

$$k_{in} = \mathrm{f}_M \frac{{D_{eN}}^2}{r^6} S(S+1) \tag{2. 57}$$

$$J_{in}(\omega, \tau_r) = \frac{\tau_r}{1+(\omega\tau_r)^2} \tag{2. 58}$$

where S is the electron spin quantum number, f_M is the mole fraction of target nuclei in bound positions. The correlation time τ characterize the inner-sphere dynamics is given by ${\tau^{-1}} = {\tau_r}^{-1} + {\tau_M}^{-1} + {\tau_e}^{-1}$. To assume τ equals the rotational correlation time τ_r of the inner-sphere complex, the lifetime of the complex τ_M and the electron relaxation time τ_e should be much longer than the τ_r.

Similar to the inner-sphere model, another approach to the relaxation behavior proposed by Lipari and Szabo combining two Lorentzian SDFs was used frequently to describe macromolecules undergoing a slow macroscopic reorientation and a fast internal averaging both with a fixed r.[74,75]

In the outer-sphere model, which is also known as force-free hard sphere (FFHS) or hard sphere with centered spin (HSCS) model, the relative translational diffusion between the radical molecule and the target molecule stochastically modulates the dipolar HFI.[57] As shown in Figure 2. 9 B, it is assumed that the target nuclear spin can access the electron spin-bearing molecule from every direction equally. The FT of the correlation time of such model with an spatial exclusion of the radical itself has been introduced by Hwang and Freed, [24] and Ayant *et al*.[38] The pre-factor and SDF of the outer-sphere model are given as:

$$k_{out} = \frac{6400\pi}{81} \frac{N_A[M_e]{D_{eN}}^2}{bD} S(S+1) \tag{2. 59}$$

$$J_{out}(\omega, \tau_D) = \frac{1+5z/8+z^2/8}{1+z+z^2/2+z^3/6+4z^4/81+z^5/81+z^6/648} \tag{2. 60}$$

where N_A is the Avogadro's constant, $[M_e]$ is the molar concentration of the radicals in [mol/L], b is the distance of closest approach, D is the relative diffusion

coefficient between the radicals and target molecules, and $z = (2\omega\tau_D)^{0.5}$ with the diffusional correlation time $\tau_D = b^2/D$.

Both models have some assumptions to simplify the system. For example, both nuclear and electron spins are assumed to be localized at the center of the spin-bearing molecules, and any local or internal motions or molecular packing effect are ignored. Despite the simplifications, experimentally determined coupling factor and nuclear relaxivity can be well explained by combining the contributions from both inner- and outer-sphere model.[69,73,76-78] Nevertheless, there are small inconsistencies existing in the b and r values determined at different fields, and the fast inner-sphere rotation of a solvent- or solute-radical complex is also uncertain in terms of its physical significance in some molecular systems.

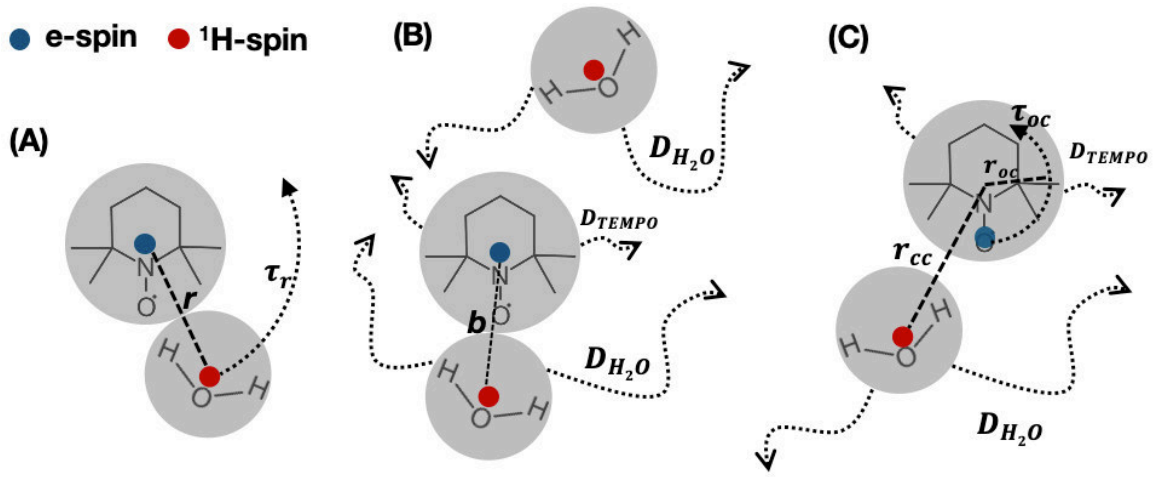

Figure 2. 9. Schematic demonstration of (A) inner-sphere model, (B) out-sphere model, and (C) HSOS model: outer-sphere model with off-centered rotation of radicals. All demonstrated with TEMPO as the polarizing agent and water as target molecule

In a consequent work from Ayant *et al.*,[79] the SDF of the modified outer-sphere model, where molecules were treated as hard spheres with off-centered spins (HSOS), is given. Of our interest, a system containing the off-centered rotation of the radical molecule and the translation of its surrounding target molecules is shown in Figure 2. 9 C. The pre-factor k_{HSOS} and SDF J_{HSOS} in this case are given as:[79]

$$k_{HSOS} = \frac{6400\pi}{81}\frac{N_A[M_e]D_{eN}{}^2}{rD}S(S+1) \quad (2.\ 61)$$

$J_{HSOS}(\omega, \tau_D, r, \tau_{oc}, r_{oc}) =$

$$\frac{9}{32}\sum_{l=0}^{\infty}\frac{(2l+4)!}{(2l+2)!}\left(\frac{r_{oc}}{r_{cc}}\right)^{2l}\mathrm{Re}\left[\frac{1}{\upsilon^2}\left[\frac{1}{2l+3}-\frac{l+3}{\upsilon^2}\left(1+\frac{l+3}{\upsilon}\frac{K_{l+5/2}(\upsilon)}{K_{l+3/2}(\upsilon)}\right)^{-1}\right]\right] \quad (2.\ 62)$$

where $K_n(\upsilon)$ is the modified Bessel function of the second kind for real order n, l is the degree of the spherical harmonic, r_{oc} is the radius of the off-centered rotation, r_{cc} is the center-to-center distance between the radical and target molecules, and $\upsilon = [i\omega\tau_D + l(l+1)\tau_D/6\tau_{oc}]^{0.5}$ with diffusion correlation time $\tau_D = r_{cc}{}^2/D$ and correction time τ_{oc} of the off-centered rotation. The parameters without any explanation carry the same meaning as in Equation 2.59 and Equation 2.60. Notably, the distance of the closest approach in this model is thereby given as $b_{HSOS} = r_{cc} - r_{oc}$ and the access possibilities for the target nuclears to the electron spins is inconsistent from every direction.

Scalar HFI contributes to the ZQ cross-relaxation but not to DQ, which is given as $W_{0,\mathrm{sc}} = k_{sc}J(\omega_{0,I} - \omega_{0,S}, \tau_{sc})$. The scalar SDF has been described with the *Pulse* model by Müller-Warmuth *et al.*,[24,80] where an encounter frequency $1/\tau_p$ (τ_p: Poisson time) and several collisional correlation time τ_i are used to characterize the scalar HFI modulation. The induced ZQ cross-relaxation rate is given as:[50,51]

$$W_{0,\mathrm{sc}} = \frac{2}{3}S(S+1)\frac{1}{\tau_p}\sum_i\left(\frac{\langle A_i\rangle}{\hbar}\tau_i\exp\left(-(\omega_{0,I}-\omega_{0,S})\tau_i\right)\right)^2 \quad (2.\ 63)$$

where $\langle A_i\rangle$ is the mean amplitude of the scalar HFI over time.

As discussed by Hausser and Stehlik, the scalar HFI may also contribute to the nuclear SQ longitudinal relaxation.[23,81] This contribution can be neglected if the lifetime τ_M of the radical-target molecule complex is much shorter as the electron relaxation time which is common for radicals in solutions.

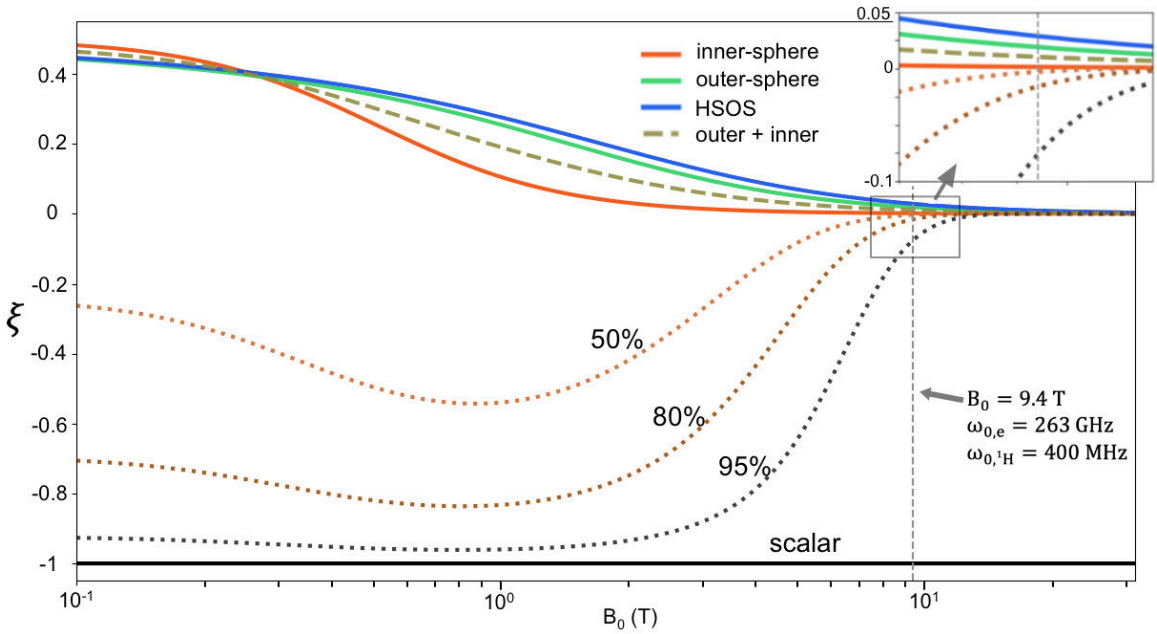

Figure 2. 10. B_0 field dependence of the coupling factor ξ simulated with:(red curve) *inner-sphere* model with $\tau_r = 20\ ps$; (green curve) *outer-sphere* model with $\tau_D = 20\ ps$, which corresponds to $b = 2.4$ Å with water diffusion coefficient at 308 K, namely 2.9 μm^2/ms; (olive dashed curve) *outer-sphere and inner-sphere* model with $\tau_D = 20\ ps$ and $\tau_r = 20\ ps$, assuming both contribute equally to the total nuclear longitudinal relaxation rate at low field; (blue curve) *HSOS* model with $\tau_D = 40\ ps$, which corresponds to $r_{cc} = 3.4$ Å with water diffusion coefficient 2.9 μm^2/ms, and $\tau_{oc} = 5\ ps$ with $r_{oc} = 1$ Å ; (black curve) scalar *Pulse model* with a single correlation time of $\tau = 2\ ps$; The dotted curves marked with percentages shows the coupling factor simulated with both *Pulse model* ($\tau = 2\ ps$) and *inner-sphere* rotational ($\tau_r = 20\ ps$). The percentage numbers beside the curves denote the ratio of scalar induced nuclear relaxation to the total nuclear relaxation at low field.

Figure 2. 10 illustrates the field dependence of the OE coupling factor calculated using the models just discussed. The simulation parameters are explained in the figure caption. As can be seen, ξ determined by pure scalar HFI (black curve) is field independent and with the competitive dipolar coupling, ξ (dotted curves) show strong field dependence. The coupling factor modulated by inner-sphere rotation (red solid curve) shows a steeper decrease with increasing magnetic field compared with the outer-sphere translation (green solid curve) with a same correlation time. The coupling factor simulated with a diffusion coefficient of water at 308 K and a

distance of closest approach of 2.4 Å (green solid curve) increases if a fast off-centered rotation the electron spin of the radical molecules ($\tau_{oc} = 5\ ps$, $r_{oc} = 1$ Å, $r_{cc} = 3.4$ Å) is included (blue solid curve).

2.4.5 Introduction of Solid Effect

The mechanism of solid effect is based on the theory of state mixing in the presence of a dipolar HFI field.[20] Similar as OE, SE is based on a scheme of one nuclear spin coupled to one electron spin. Unlike OE relying on the relaxation processes driven by the perturbative spin Hamiltonian, SE occurs when a transverse magnetic field induced by unpaired electron spins is presented on the nucleus and mixes the adjacent nuclear spin states as shown in Figure 2. 11.

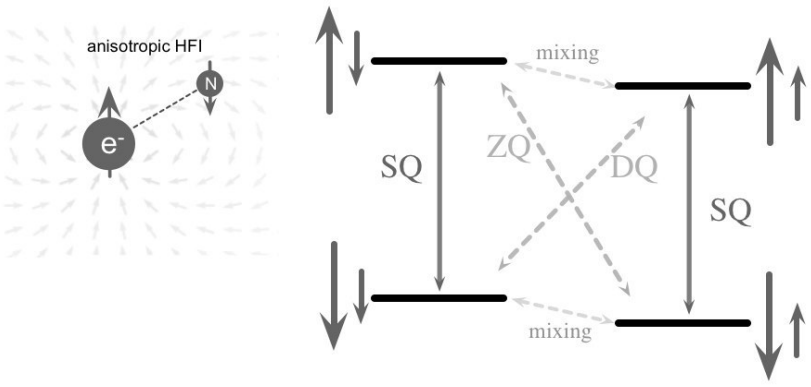

Figure 2. 11. Energy level diagram of a coupled e-N spin system both with spin-1/2. SE occurs when the transverse part of the anisotropic HFI presents on the nucleus. SQ denotes the allowed EPR single-quantum mw-driven transition. ZQ and DQ denotes the e-N ZQ and DQ forbidden transition pathways, respectively.

The e-N HFI tensor responsible for the transverse field is given with the pseudo-secular terms $\hat{C}$ and $\hat{D}$ in Equation 2.28. In a solid-like environment, the assumptions to simplify Equation 2.45 is no longer valid. In the presence of the off-diagonal terms $\hat{C}$ and $\hat{D}$, the eigenstates of the coupled e-N spins deviate from their original expressions in the laboratory frame. The new eigenstates can be obtained from the diagonalization by unitary transformation $\mathcal{H}_{\text{new}} = U\mathcal{H}U^{\dagger}$.[82] The degree

of the deviation depends on the energy difference between the mixed states. Therefore, the mixing of the states with different electron quantum number m_s is neglected and only the mixing of the adjacent nuclear spin states with same m_s is considered. With an approximation up to first order, the mixed states are given as:[20,83]

$$|\lambda_1\rangle = p|+-\rangle - q|++\rangle$$
$$|\lambda_2\rangle = p|++\rangle + q|+-\rangle$$
$$|\lambda_3\rangle = p|--\rangle - q|-+\rangle$$
$$|\lambda_4\rangle = p|-+\rangle + q|--\rangle \quad (2.\ 64)$$

where the state mixing factor q is given as

$$q = -\frac{3}{4}\frac{1}{\omega_{0,N}}\frac{D_{eN}}{r^3} sin\theta\ cos\theta \quad (2.\ 65)$$

and $p = \sqrt{1-q^2}$. The approximation $p \approx 1$ is valid for $\frac{D_{eN}}{r^3} \ll \omega_{0,N}$.

e,N	$\langle +- \|$	$\langle ++ \|$	$\langle -- \|$	$\langle -+ \|$
$\|+-\rangle$	$\hat{H}_z, \hat{A}$	$\hat{C}$	$\hat{D}$	$\hat{B}$
$\|++\rangle$	$\hat{D}$	$\hat{H}_z, \hat{A}$	$\hat{F}$	$\hat{D}$
$\|--\rangle$	$\hat{C}$	$\hat{E}$	$\hat{H}_z, \hat{A}$	$\hat{C}$
$\|-+\rangle$	$\hat{B}$	$\hat{C}$	$\hat{D}$	$\hat{H}_z, \hat{A}$

Figure 2. 12. The Hamiltonian matrix of a coupled e-N spin pair considering the Zeeman interaction $\hat{H}_z$ and HFI. $\hat{C}$ and $\hat{D}$ as off-diagonal terms mix the states $|-+\rangle$ with $|--\rangle$, and $|++\rangle$ with $|+-\rangle$.

The ZQ and DQ irradiative transitions with $\Delta m_s = \pm 1$ and $\Delta m_I = \pm 1$ are formally forbidden but are allowed in the presence of the state mixing. Analogous to the OE DNP, by solving the rate equation describing the transition process of a coupled e-N spin pair with the new eigenstates, the SE DNP enhancement can be expressed as:[21,84]

$$\varepsilon_{SE} \equiv \frac{I_Z - I_0}{I_0} = \frac{\pm W^{\pm}(1-s)\frac{\gamma_e}{\gamma_N} - W^{\pm}}{W^{\pm} + W_{N,total}} \tag{2. 66}$$

where s, γ_e, γ_N carry the same meaning in the OE enhancement expression, W^+ and W^- denote the ZQ and DQ forbidden transition rates, respectively. The forbidden transition rates $W^{\pm}$ are given as:

$$W^{\pm} = 2\pi q^2 {\omega_{1e}}^2 \mathrm{g}(\omega_{0,e} \pm \omega_{0,N}) \tag{2. 67}$$

where ω_{1e} is the mw nutation frequency and $\mathrm{g}(\omega)$ is the electron paramagnetic resonance (EPR) line shape centered at ω and normalized according to $\int_{-\infty}^{+\infty} \mathrm{g}(\omega)\mathrm{d}\omega = 1$.

3. Hardware

This chapter introduces the DNP setup necessary for the DNP/NMR measurements.[35,85] The development on hardware doesn't belong to this doctoral thesis. The author performed the test of the sample temperature stability of a recent improved Fabry–Pérot (FP) probe (Figure 3. 2 B-D). As a stable sample temperature is the prerequisite for a quantitative analysis of the liquid-state DNP enhancements, the relevant results are also presented in this chapter.

3.1 DNP Spectrometer

The liquid-state DNP/NMR experiments involved in this work were performed on a homebuilt DNP-NMR spectrometer comprising a Commercial NMR spectrometer (Bruker Avance II) operating at 9.4 T and a gyrotron (Gycom, Russia) as mw source operating at 264 GHz.[35] The gyrotron can provide a mw power up to about 5.5 W at the probehead inlet.

3.2 DNP Probeheads and Temperature Control

Depending on the experiments, two homebuilt probeheads were used in the work.

As demonstrated in Figure 3. 1, the homebuilt helical-cylindrical (HC) DNP probehead has a double-resonance structure consisting of a cylindrical mw cavity for EPR excitation which also serves as RF coil for NMR excitation and detection.[35] The mw cavity can be tuned to TE_{011}, TE_{012} and TE_{013} mode for different purpose. At TE_{011} mode, the mw conversion factor is 0.45 mT W-1/2 and the quality factor is about 400.[69] The liquid samples were introduced into quartz capillaries with an inner diameter ranging from 30 μm to 100 μm, which results in an effective sample volume of 3-35 nL. By keeping the sample diameter within this range, the excessive

heating can be significantly alleviated, keeping the sample temperature remains within an acceptable range.[69,76]

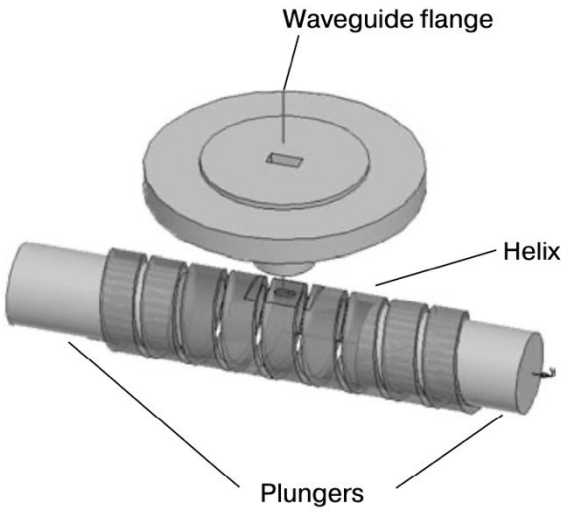

Figure 3. 1 Schematic representation of the helical-cylindrical double resonance structure[35]

Another homebuilt probehead was designed based on the FP mw resonance structure (Figure 3. 2 A).[86] The probehead combines the FP structure with a coplanar stripline for both NMR excitation and detection operating at 400 MHz (^{1}H) and 100 MHz (^{13}C). Attributed to the excellent heat conductivity of the plane mirror substrate, the sample temperature is only slightly elevated under full power mw irradiation. By further implementation of a nitrogen gas flow blowing against the backside of the sample substrate, the sample temperature can be controlled almost independent of the applied mw irradiation in the temperature range of 310 - 340 K. As can be seen in (Figure 3. 2 B-D), the temperature rise of the sample under heated nitrogen gas flow monitored by the ^{1}H NMR chemical shift difference between the CH_2 and OH group of ethylene glycol, results in a difference less than 10 K with and without mw irradiation.

Notably, both probeheads are equipped with mw modulation coil to enable cw EPR measurements.

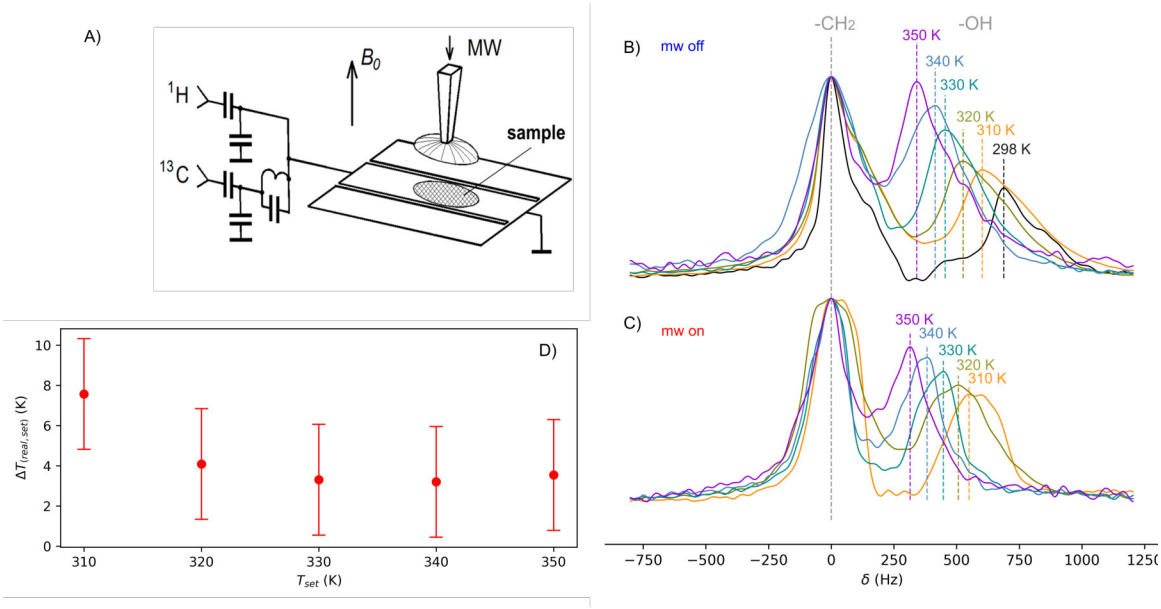

Figure 3. 2 (A) Schematic representation of the triple resonance structure comprising a Fabry–Pérot mw resonator and a coplanar stripline.[86] (B) NMR spectra of ethylene glycol in the probehead at different temperatures up to 350 K set with help of nitrogen gas flow (without mw heating); (C) the same sample in the probehead at similar gas flow conditions as in B), and with mw power of 5.5 W. In both experiments the gas flow rate was 1070 L/h; (D) calculated temperature increase of the sample due to the mw heating. Positions of CH_2 signal of all the spectra were centered for illustrative purpose.

4. ^{13}C Scalar OE DNP on small biomolecules

4.1 Introduction

The encouraging ^{13}C NMR enhancements observed in CCl_4 and CBr_4 solutions underscore the potential of scalar DNP at high magnetic fields.[50,51] Nonetheless the research targets were still limited to non-biological samples. In order to extend the capability of scalar DNP to biologically relevant molecular systems while avoiding the arbitrary "trial-and-error" approaches, a strategy to prescreen the potential DNP target molecules via their paramagnetic NMR shift is proposed and verified. Apart from the dynamics determining the spectral density, a substantial e-N HFI strength is also a prerequisite for a successful DNP experiment. Similar connection between the OE DNP enhancements and the hyperfine constant obtained from EPR has been examined at low fields.[87]

Imidazole and indole, exhibiting strong paramagnetic ^{13}C NMR shifts namely strong electron-^{13}C interactions in the presence of nitroxide,[88] were selected as the initial DNP candidates. A considerable ^{13}C NMR enhancement ε_{13C} up to 50 were observed on single labeled imidazole molecules in its aqueous solution doped with 100 mM 4-hydroxy-2,2,6,6-tetramethylpiperidinyloxyl (TEMPOL), as well as site-specific ε_{13C} ranging from -2 to 26 on uniformly labeled indole doped with the same concentration of TEMPO in CCl_4. Encouraged by these results, further paramagnetic NMR and OE DNP measurements were performed on various small biomolecules including glycine, alanine, serine, proline and glucose. A qualitatively relation between the two quantities were presented including the previously published results[50,51]. A quantitative match is not anticipated for several reasons. First of all, the paramagnetic NMR shift directly reflects the HFI strength and lacks information about the e-N dynamics, which is crucial for the DNP coupling factor. Secondly, other DNP pathways can also impact the observed DNP enhancements. For example, the counteractive dipolar HFI-driven OE can lead to a negative enhancement of

NMR signal, which was also observed in this study. Besides, paramagnetic shift in liquids can also comprise contributions from the dipolar HFI termed pseudo contact shift.

Computational approaches has been used to predict[49] and rationalize[50,51] the scalar OE DNP enhancements. Instead of the fast encounter-disassociation process ddescribed by the Pulse model, a quantum mechanical MD studies performed by our collaborators on the mechanisms of the observations suggests that the modulation originates from the fast intermolecular hydrogen-bond dynamics of the long-living radical-substrate complex.

4.2 Corresponding Publication:

The following publication together with the supporting information

"Dai, D., Wang, X., Liu, Y., Yang, X.-L., Glaubitz, C., Denysenkov, V., He, X., Prisner, T. and Mao, J., Room-temperature dynamic nuclear polarization enhanced NMR spectroscopy of small biological molecules in water. *Nat. Commun.* 12, 6880 (2021)"

is attached in the following pages.

The work was prepared in a collaborative manner. The connection between the paramagnetic NMR shift and scalar DNP enhancement was initially proposed by Prof. Jiafei Mao (Institute of Chemistry, Chinese Academy of Sciences). The author performed of the major part of the DNP/NMR experiments with the assistance from Prof. Jiafei Mao and Dr. Vasyl Denysenkov. The analysis of the DNP enhancements was performed by the author together with Prof. Jiafei Mao. The quantum mechanical MD simulation and DFT calculations were performed by Prof. Xianwei Wang (Zhejiang University of Technology), Dr. Yiwei Liu (East China Normal University) and Prof. Xiao He (East China Normal University).

nature COMMUNICATIONS

ARTICLE

https://doi.org/10.1038/s41467-021-27067-0 OPEN

Room-temperature dynamic nuclear polarization enhanced NMR spectroscopy of small biological molecules in water

Danhua Dai[1,2,9], Xianwei Wang[3,4,9], Yiwei Liu[3], Xiao-Liang Yang[5,6], Clemens Glaubitz[2,7], Vasyl Denysenkov[1,2], Xiao He[3,8✉], Thomas Prisner[1,2] & Jiafei Mao[2,7✉]

Nuclear magnetic resonance (NMR) spectroscopy is a powerful and popular technique for probing the molecular structures, dynamics and chemical properties. However the conventional NMR spectroscopy is bottlenecked by its low sensitivity. Dynamic nuclear polarization (DNP) boosts NMR sensitivity by orders of magnitude and resolves this limitation. In liquid-state this revolutionizing technique has been restricted to a few specific non-biological model molecules in organic solvents. Here we show that the carbon polarization in small biological molecules, including carbohydrates and amino acids, can be enhanced sizably by in situ Overhauser DNP (ODNP) in water at room temperature and at high magnetic field. An observed connection between ODNP ^{13}C enhancement factor and paramagnetic ^{13}C NMR shift has led to the exploration of biologically relevant heterocyclic compound indole. The QM/MM MD simulation underscores the dynamics of intermolecular hydrogen bonds as the driving force for the scalar ODNP in a long-living radical-substrate complex. Our work reconciles results obtained by DNP spectroscopy, paramagnetic NMR and computational chemistry and provides new mechanistic insights into the high-field scalar ODNP.

[1] Institute of Physical and Theoretical Chemistry, Goethe University Frankfurt, 60438 Frankfurt am Main, Germany. [2] Center for Biomolecular Magnetic Resonance, Goethe University Frankfurt, 60438 Frankfurt am Main, Germany. [3] Shanghai Engineering Research Center of Molecular Therapeutics and New Drug Development, School of Chemistry and Molecular Engineering, East China Normal University, Shanghai 200062, China. [4] College of Science, Zhejiang University of Technology, Hangzhou, Zhejiang 310023, China. [5] Jiangsu Key Laboratory of Advanced Organic Materials, School of Chemistry and Chemical Engineering, Nanjing University, Nanjing 210023, China. [6] State Key Laboratory of Coordination Chemistry, School of Chemistry and Chemical Engineering, Nanjing University, Nanjing 210023, China. [7] Institute of Biophysical Chemistry, Goethe University Frankfurt, 60438 Frankfurt am Main, Germany. [8] NYU-ECNU Center for Computational Chemistry at NYU Shanghai, Shanghai 200062, China. [9] These authors contributed equally: Danhua Dai, Xianwei Wang. ✉email: xiaohe@phy.ecnu.edu.cn; j.mao@em.uni-frankfurt.de

Nuclear magnetic resonance (NMR) spectroscopy is an indispensable powerful technique for probing the molecular structure, dynamics, and chemical properties at or even beyond the atomic resolution. It has strong impacts on a broad range of applications in chemistry, biology, material science, environmental science as well as chemical and pharmaceutical industries. However, all these applications are limited by the low inherent sensitivity of this technique. Since the early days of NMR spectroscopy, the demands for higher sensitivity have been driving the developments in instrumentation, methodology, and the understanding of NMR spin dynamics[1]. One of the popular approaches for boosting NMR sensitivity is dynamic nuclear polarization (DNP), in which nuclear spins are hyperpolarized via the polarization transfer from unpaired electron spins under microwave irradiation[2–9]. In most DNP schemes, the unpaired electron spins are introduced as paramagnetic radicals or metal centers. Since the electron spin has a much higher gyromagnetic ratio than any nuclear spins, that is −658-fold of ^{1}H nucleus and −2617-fold of ^{13}C nucleus, tremendous sensitivity enhancements can be anticipated. Such a remarkable potential has sparked enthusiasms on developing DNP techniques for numerous NMR applications[5,10–27].

The past decade has already witnessed the transformation of solid-state NMR (ssNMR) spectroscopy by DNP[2,5,6,9]. Solid-state DNP experiments are carried out mostly at cryogenic temperatures (usually below 120 K), at which the electron spin relaxation times are long enough for the efficient microwave saturation in solids. Such low operation temperatures quench most molecular dynamics, prohibit chemical processes, and in many cases compromise the spectral resolution. An alternative approach, namely the dissolution DNP, combines the low-temperature solid-state DNP and the room-temperature liquid-state NMR via a rapid dissolution/melting step. However, it is a single-shot experiment and a freeze-thaw procedure has to be applied to the samples[17,28–32]. Different from all the abovementioned approaches, the in situ liquid-state Overhauser DNP (ODNP) process permits to hyperpolarize the target molecules directly in solution at room-temperature[4,10,12,13,16,18,20,22,23,25,33].

In liquid-state DNP the electron-nucleus (e-N) polarization transfer is mediated by the electron-nucleus Overhauser effect (OE) driven by molecular motions. The physical principle of OE is the e-N cross-relaxation caused by dynamic fluctuations of the e-N spin−spin interactions. Unpaired electron spins interact with nuclear spins via dipolar interaction and scalar hyperfine interactions, both of which can contribute to the ODNP. The ODNP efficiency relies on both the magnitude and the dynamics of the e-N interactions. A more detailed introduction on the theoretical background of ODNP can be found in Supplementary Note 1. At high magnetic fields (e.g., 9.4 T), molecular motions at the sub-ps time scale, or in the THz frequency regime, are required for efficient ODNP. In aqueous solutions of nitroxide radicals, translational and rotational motions, which drive the stochastic e-N dipolar crosstalk upon the radical-water encounter events, occur within this time scale. These motions lead to a remarkable negative ODNP-enhancement of the water ^{1}H NMR signal at 9.4 T[34]. However, such molecular motions become significantly retarded upon increasing the molecular sizes. Consequentially the efficiency of ODNP driven by dipolar interactions drops significantly on more complex molecules[35].

Distinct from the dipolar ODNP, the scalar ODNP depends on the fluctuation of the e-N Fermi contact interactions. The *chemical* interaction between the radical and the substrate molecule permits the dispersion of spin density from the radical to the specific nuclear positions in the substrate molecule. This scalar e-N Fermi contact fluctuates upon the radical-substrate chemical encounter-disassociation events and/or during the structural rearrangement of the radical-substrate complex in solution[20,25,36,37]. The recently observed tremendous positive liquid-state ODNP enhancements on ^{13}C signals of various organic compounds show the great potential of this mechanism at high magnetic field[20,25]. However, these work has been limited on a few non-biological model compounds so far, for example, halogenated hydrocarbons, diketones, and benzene derivatives[19,20,25]. Moreover, all the previous studies have been restricted to organic solvents with lower microwave absorption at high magnetic field in order to reduce the sample heating by microwave, a major challenge for high-field room-temperature ODNP. Here, we have successfully polarized a number of structurally and chemically diverse small biological molecules in water directly at room-temperature and at high magnetic field (9.4 T, 263 GHz electron Larmor frequency). Motivated by the observed trend between scalar ODNP enhancement and paramagnetic NMR shift, we have also expanded our ODNP target list to biologically relevant heterocyclic compound indole. Extensive density functional theory (DFT) calculations and quantum mechanics/molecular mechanics molecular dynamics (QM/MM MD) simulations have provided new mechanistic insights into scalar ODNP in various small biological molecules as well as in a long-living H-bonded radical-substrate complex.

Results

Room-temperature ODNP ^{13}C NMR of imidazole in water. The sample heating under microwave irradiation poses one major challenge on room-temperature liquid-state ODNP spectroscopy. In some previous work, this problem was alleviated partially by restricting the experiments to organic solvents of low polarity[19,20,25]. However, on the aqueous samples relevant to biological applications, the microwave heat deposition becomes inevitably more severe (loss tangent of water tanδ = 1.05 at 20 °C and 0.26 THz)[38]. For tackling this issue, we have chosen a home-built liquid-state DNP instrumentation platform based on a Fabry–Pérot microwave double resonance structure (Fig. 1b)[39] that permits efficient excitation of the radical electron spin with an excellent temperature management. In the Fabry–Pérot microwave resonator, a highest microwave B-field strength is reached at the sample position, which is required for the microwave saturation of the radical electron spin transition in DNP experiments. At the same time, the microwave electric field component, which leads to sample heating, is near zero on the metal surface where the thin flatdisc-like sample (10^{1} μm thickness, Fig. 1b) is located. In addition, since the samples are situated directly onto a heat-conducting flat metal mirror (Fig. 1b), the heat dissipation from the sample to its environment is rather efficient. Previously this design has already been successfully used for dipolar ODNP ^{1}H NMR experiments on water and on hydrated lipid bilayers[16,39].

Although our setting reduces substantially the sample heating, it remains rather technically challenging to perform the ODNP NMR experiments. Here, instead of the blind "trial-and-error" search for molecules with large scalar ODNP enhancements, we have first sought a potential indicator of the scalar ODNP performance. The scalar ODNP relies on the Fermi contact mediated by the chemical interactions between radical and substrate molecules. The Fermi contact leads to three distinct but closely related spectroscopic consequences, namely the signal enhancement in scalar ODNP NMR spectroscopy, the hyperfine pattern in EPR spectroscopy, and the well-known Fermi contact shift in paramagnetic NMR spectroscopy. The hyperfine interactions in radical-substrate complexes have been explored extensively by EPR spectroscopy and computational chemistry. Indeed it has been shown that the hyperfine constant, which quantifies the magnitude of the Fermi contact, is correlated with the scalar

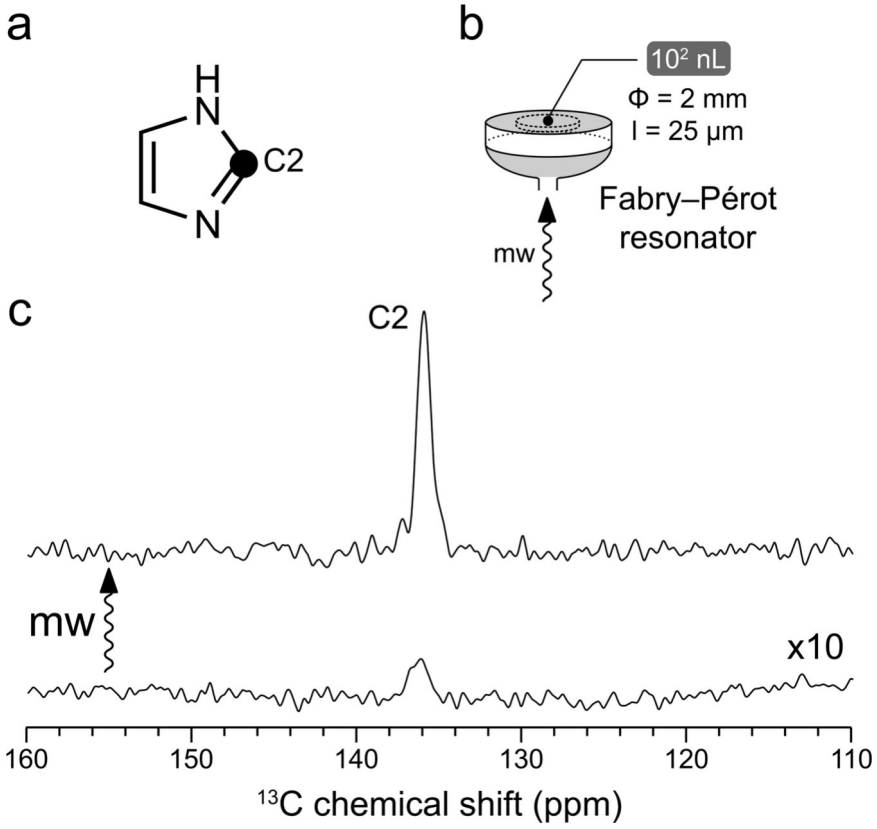

Fig. 1 Room-temperature ODNP-enhanced ^{13}C NMR of ^{13}C2 imidazole in D_2O at 9.4 T. a The chemical structure of imidazole molecule. The black circle indicates ^{13}C labeled position. **b** Scheme of Fabry-Pérot resonator[16,39]. The sample (10^2 nL) has been laid as a thin layer on the flat mirror (gray). The sample diameter (Φ) and thickness (*l*) are shown. The microwave beam (shown as mw arrow) enters the resonator via a hole in the middle of a spherical mirror (gray). **c** Spectra obtained with (up) and without (down) microwave (mw) are presented. A 50-fold ODNP enhancement on ^{13}C signal has been obtained. TEMPOL (100 mM) was used as the hyperpolarizing agent. The spectra are scaled with number of scans for visualizing directly the enhancement factor. The microwave-off spectra are further scaled up by 10-fold for the better visualization.

ODNP enhancement[40]. In this work, inspired originally by a Google search (Supplementary Note 6), we have recalled the link between paramagnetic NMR and ODNP spectroscopy. As the contact shift also reports the magnitude of the Fermi contact, it could be taken presumably as an NMR indicator for the ODNP performance similar to the hyperfine coupling constant explored in the previous work[40]. In particular, the molecules that do not interact chemically with radicals should show little paramagnetic NMR shift. Such molecules could be excluded efficiently prior to the technically challenging ODNP experiments, which improves the winning rate of our initial search for promising scalar ODNP targets.

The Fermi contact shift has been one of the major topics in paramagnetic NMR spectroscopy over many decades[41–45]. We have revisited the rich collection of literatures covering this topic and have identified a series of paramagnetic NMR studies, in which a wide range of radical-interacting molecules have been reported[46–53]. Interestingly some halogenated compounds showing large ODNP enhancements as reported recently[20,25] also exhibit large ^{13}C paramagnetic NMR shifts[54]. In this work, we have taken the molar-free ^{13}C paramagnetic NMR shifts ($\overline{\delta_{para}}$) for the comparison of various compounds, which normalize the scale of the paramagnetic NMR shift over the radical concentration. Within these paramagnetic NMR literatures, a water-soluble heterocyclic compound imidazole, which is the sidechain moiety of the amino acid histidine, is reported to interact with TEMPO-type radicals via an intermolecular H-bond and exhibits some of the most remarkable carbon $\overline{\delta_{para}}$[53]. We have therefore selected this compound as a candidate for ODNP ^{13}C NMR experiments in water on our high-field liquid-state DNP setup.

The solution of ^{13}C2-imidazole (Fig. 1a) in D_2O has been loaded as a thin layer into the Fabry–Pérot microwave resonator (Fig. 1b). The water-soluble radical TEMPOL (100 mM) has been used as the ODNP polarization agent. Pleasingly a large ODNP ^{13}C enhancement of 50 has been obtained with this sample (Fig. 1c and Supplementary Table 3). This finding has encouraged us to explore other families of water-soluble molecules for ODNP experiments.

Room-temperature ODNP ^{13}C NMR of small biological molecules in water. Encouraged by the initial success on imidazole, we moved on to structurally more complex small biological molecules. In this work, we have focused on carbohydrate and amino acids (Fig. 2) bearing amine and/or hydroxyl groups that could serve potentially as H-bond donor to TEMPO-type radicals. In particular, we have targeted the highly water-soluble glucose (Fig. 2e) and amino acids (Fig. 2a–d, glycine, serine, alanine and proline). As indicated by the significant carbon $\overline{\delta_{para}}$ (Supplementary Fig. 2 and Supplementary Table 4), all these small biological molecules interact chemically with TEMPOL in water. We have further subjected all these compounds to ODNP ^{13}C NMR experiments in H_2O using the same instrumentation setting for imidazole. Sizable ODNP ^{13}C enhancements have been obtained on all these molecules (Fig. 2a–e). Notably, our spectral resolution even permits to resolve the signal splitting by $^1J_{CH}$ couplings (Fig. 2a–e and Supplementary Table 3), which

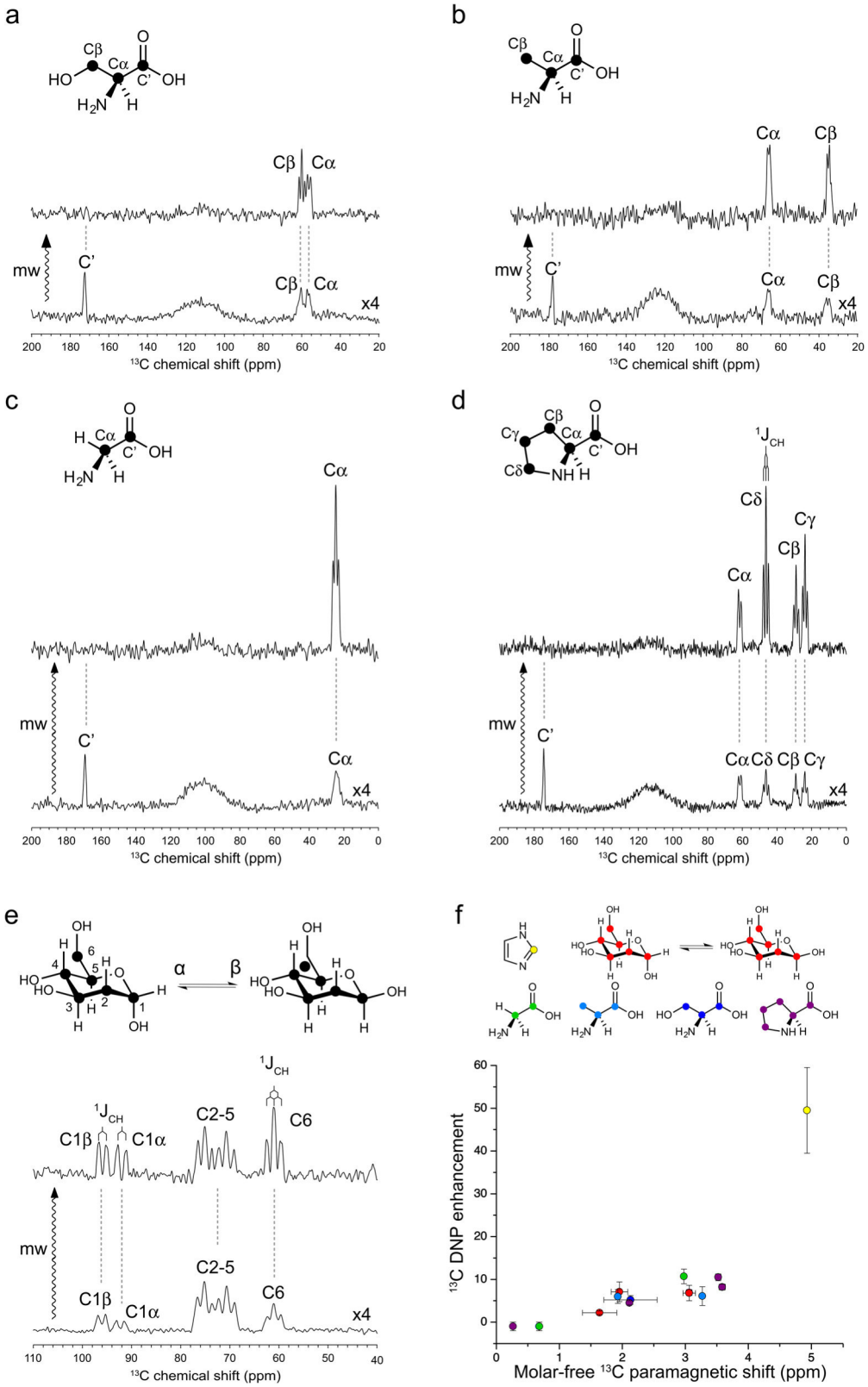

Fig. 2 Room-temperature ODNP NMR of small biological molecules in H_2O at 9.4 T. TEMPOL (100 mM) was used as the hyperpolarizing agent. The ODNP-enhanced ^{13}C NMR spectra of U-^{13}C serine (**a**), alanine (**b**), glycine (**c**), proline (**d**), and glucose (**e**) are scaled with the number of scans for visualizing directly the enhancement factor. All the microwave (mw)-off spectra in (**a**–**e**) are further scaled up by four-fold for the better visualization. The resolved $^{1}J_{CH}$ are showcased in spectral (**d**, **e**). **f** A positive trend of ODNP ^{13}C enhancement over molar-free paramagnetic ^{13}C NMR shift $\overline{\delta_{para}}$ is visualized. The data on various molecules are presented in colors. The error of $\overline{\delta_{para}}$ is defined as fitting error or standard deviation of $\overline{\delta_{para}}$ values on carbons showing overlapping signals on ODNP spectra. The error of ODNP enhancement is determined from signal-to-noise ratio. More details about the error calculations can be found in "Methods". Source data are provided as a Source Data file.

significantly outperforms the DNP ssNMR spectroscopy on a frozen solution sample at the same magnetic field (Supplementary Fig. 1d).

The excellent spectral resolution also permitted to detect the site-specific ODNP ^{13}C enhancement for most of the carbons in these small biological molecules. The chemical shift assignment of the ODNP-enhanced ^{13}C spectra of these molecules can be found in Fig. 2a–e. The corresponding site-specific ODNP enhancement factors are summarized in Supplementary Table 3 and Fig. 2f. Up to 11-fold ODNP enhancement of ^{13}C signals have been obtained on these small biological molecules. The site-specific ODNP enhancement has been observed on all these molecules. As expected, a qualitative positive trend has been observed between the carbon $\overline{\delta_{para}}$ and the ODNP enhancement factor within and across the tested water-soluble molecules (Fig. 2f and Supplementary Table 4).

In glucose, the C1 and C6 carbons show larger ODNP enhancements than the other carbons (Fig. 2e and Supplementary Table 3). These two carbons are less sterically hindered than other carbons and are therefore more likely accessible by TEMPOL radical as also indicated by their larger $\overline{\delta_{para}}$. In the four tested amino acids, the carboxylate carbons all show negative ODNP enhancements (Fig. 2a–d and Supplementary Table 3), which evidences the dominating role of dipolar ODNP mechanism on these carbons similar to that found on carbonyl and ester carbons in various organic compounds[25]. As indicated by their small $\overline{\delta_{para}}$ (Supplementary Table 4), these carboxylate groups are not involved in the direct interactions with TEMPOL radical. In contrast, the aliphatic carbons in amino acids and glucose all show positive ODNP enhancements, which supports the prevailing scalar ODNP mechanism on these sites. Interestingly the aliphatic carbons amino acids that are not directly linked to amino or hydroxyl groups also show sizable scalar ODNP enhancement (Fig. 2a–d). It seems that, besides the amino and hydroxyl groups that are well-known for their H-bonding capacities, aliphatic C−H groups also participate in the intermolecular interactions with TEMPOL radical.

To further resolve the molecular mechanism of the observed site-specific ODNP enhancement in these amino acids, we have performed DFT calculations of these TEMPOL-amino acid complexes (Fig. 3 and Supplementary Table 5). For each amino acid, the amine group-mediated TEMPOL-amino acid complex has been taken as the reference for deriving the relative Gibbs free energy ($\Delta\Delta G$) of the other binding configurations. Our simulations support the binding of TEMPOL to the amino groups as shown by the lower Gibbs energy of the corresponding complexes (Fig. 3a–d). For serine, the complex organized by the sidechain hydroxyl group is significantly more stable than that via the amino group ($\Delta\Delta G = -15.7$ kJ/mol, Fig. 3c), which demonstrates the stronger H-bonding capacity of hydroxyl groups. This binding site preference agrees with the higher scalar ODNP enhancement of Cβ than that of Cα carbon in serine (Fig. 2a and Supplementary Table 3). The aliphatic C-H groups in all the explored amino acids also show certain radical-binding capacities (Fig. 3a–d, ΔΔG in the range of 0.8−8.7 kJ/mol) in line with the generally observed scalar ODNP enhancement on these carbons (Fig. 2a–d and Supplementary Table 3). For serine and proline, the aliphatic CH-organized TEMPOL-amino acid complexes only show slightly higher energies ($\Delta\Delta G < 5$ kJ/mol) than the NH-mediated complexes (Fig. 3c, d). Interestingly, our structure optimization of the TEMPOL-proline (CγHγ1) complexes has led consistently to a binding configuration to the neighboring CβHβ1 group, suggesting a competition or cooperativity between these two sites. Similarly, in the TEMPOL-proline(CβHβ2) complex the neighboring Cγ carbon also carries significant spin density (Fig. 3d and Supplementary Table 5). The relative Gibbs energies of the TEMPOL-glycine/alanine(C−H) complexes ($\Delta\Delta G$ is close to 8 kJ/mol) are higher than those of the TEMPOL-serine/proline complexes. It has been reported that the methyl groups form weak H-bond with TEMPO-type radicals[55]. Our results agree with this previous finding and demonstrate that such methyl-radical interactions could lead to scalar ODNP enhancement. Compared to other amino acids, glycine shows significantly both higher $\overline{\delta_{para}}$ (Supplementary Fig. 2f) and ODNP enhancement (Fig. 2c) on its Cα carbon (Fig. 2f and Supplementary Table 4). This is likely due to the lack of competing radical binding sites (sidechain carbons) in glycine. In summary, our simulations support that a wide range of chemical moieties, including the amine, hydroxyl, methyl, and aliphatic CH_2 and CH groups, show binding capacity towards TEMPOL radical and therefore could all mediate the chemical engagement with the radicals for scalar ODNP.

ODNP ^{13}C NMR of biologically relevant heterocyclic compound indole. Biological molecules often bear heterocyclic moieties, such as imidazole in histidine, indole ring in tryptophan, and nucleobases in nucleic acids. Encouraged by the successful selection of imidazole as a scalar ODNP candidate from the previous paramagnetic NMR literature[53], we decided to expand this endeavor to other biologically relevant heterocyclic compounds. In the original paramagnetic NMR work, from which imidazole has been sourced, a full list of nitrogenous heterocyclic compounds have been shown to interact with TEMPO radical via intermolecular H-bonds[53]. In particular indole (Fig. 4b, c), the sidechain moiety of tryptophan, interacts with TEMPO and shows rather large paramagnetic ^{13}C NMR shifts (Supplementary Table 4)[53]. We, therefore, selected this compound for ODNP ^{13}C NMR experiments. Due to the poor solubility of indole in water, we switched to the apolar CCl_4 solvent. Previously we have developed another liquid-state ODNP NMR resonator at 9.4 T featuring a cylindrical microwave structure (Fig. 4a)[56] that is highly suitable for the volatile CCl_4 solvent[25]. We have therefore selected this setting for the ODNP ^{13}C NMR experiments on indole. TEMPO at 100 mM has been used as the DNP agent in this experiment.

As shown in Fig. 4c, in the uniformly–^{13}C ([U–^{13}C]) labeled indole significant positive ODNP enhancements have been observed on all except the two bridge carbons (C3a and C7a). The positive enhancements point to a dominating scalar ODNP mechanism on the peripheral carbons, while the negative ^{13}C enhancements indicate the prevailing dipolar ODNP mechanism on the bridge carbons. The ^{13}C–^{13}C homonuclear and ^{1}H–^{13}C heteronuclear J-coupling network in [U–^{13}C] indole leads to rather complex spectroscopic patterns (Fig. 4c). Nevertheless, with the help of conventional ^{1}H-decoupled liquid-state ^{13}C NMR spectrum (Fig. 4d), an unambiguous assignment of most of the signals on the ODNP ^{13}C NMR spectrum of [U–^{13}C] indole can be achieved. To further resolve the spectroscopic complexity caused by the ^{13}C–^{13}C homonuclear J-coupling, we have turned to another labeling scheme with a single ^{13}C site ($^{13}C2$ indole, Fig. 4b). The ODNP-enhanced ^{13}C NMR spectrum of $^{13}C2$-indole shows one ^{13}C doublet (Fig. 4b). The resolution of the spectrum (33 Hz without ^{1}H decoupling) permits to resolve the splitting of this ^{13}C doublet and to quantify the corresponding H2-C2 $^{1}J_{CH}$-coupling (181 Hz) (Fig. 4c). In addition, we have even detected the ODNP-enhanced NMR signal of CCl_4 carbon (Fig. 4b) at its natural isotope abundance (ca. 0.15 M ^{13}C spins) in the same sample.

The spectral resolution also allowed us to derive the site-specific ODNP enhancement factor for different carbons in the

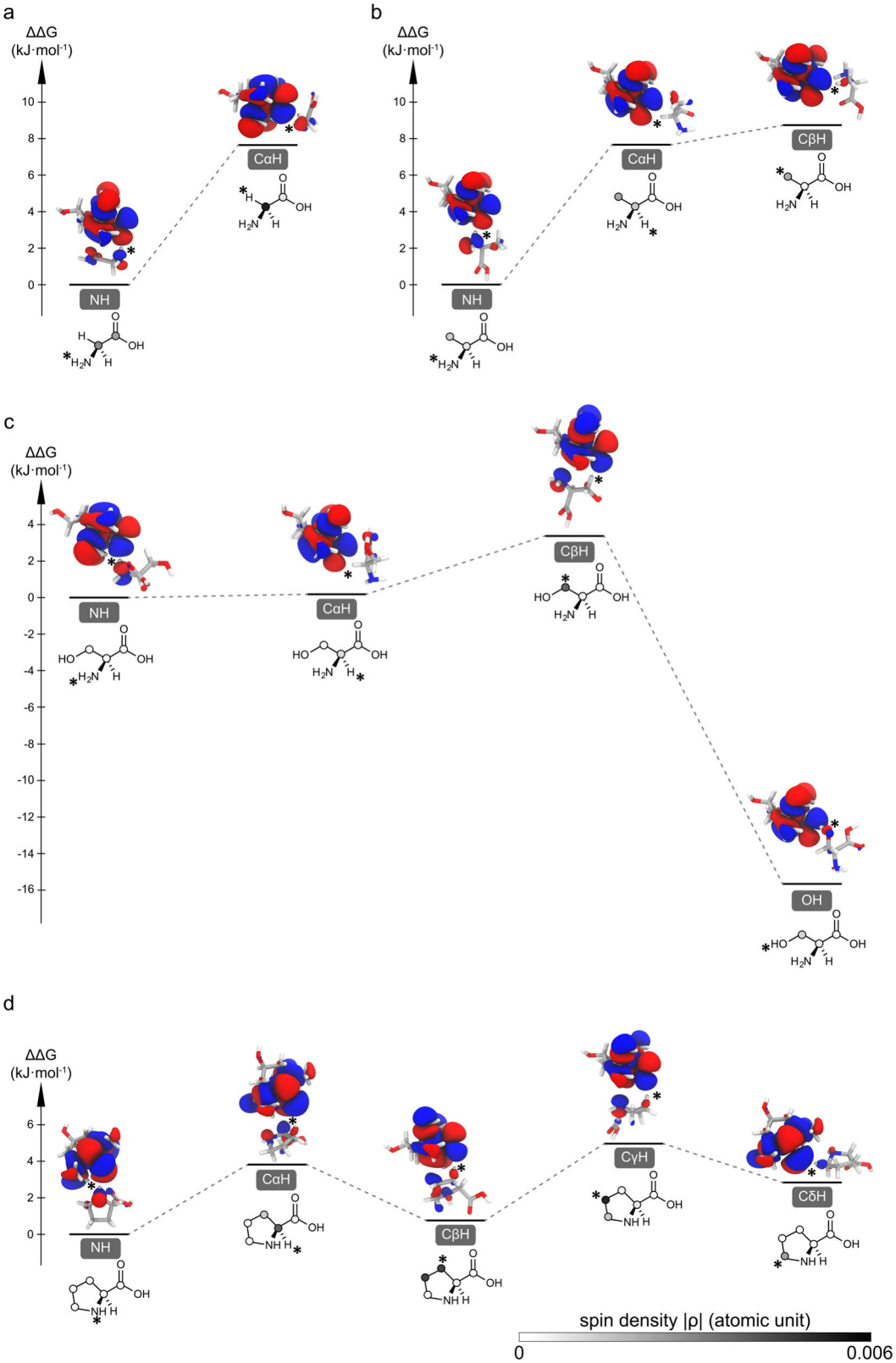

Fig. 3 Chemical interactions between TEMPOL radical and amino acids mapped by DFT calculations. The structural and energy landscapes of H-bonded glycine (**a**), alanine (**b**), serine (**c**), proline (**d**)-TEMPOL complexes are presented. The relative Gibbs free energies (ΔΔ*G*) of the complexes involving different binding sites are referenced to the amino-binding state. The SOMO orbitals and the corresponding spin densities are presented along with the energy. The TEMPOL-substrate interaction sites are indicated with * symbol. The magnitude of spin densities on various carbons is presented in gray scale as shown in (**d**).

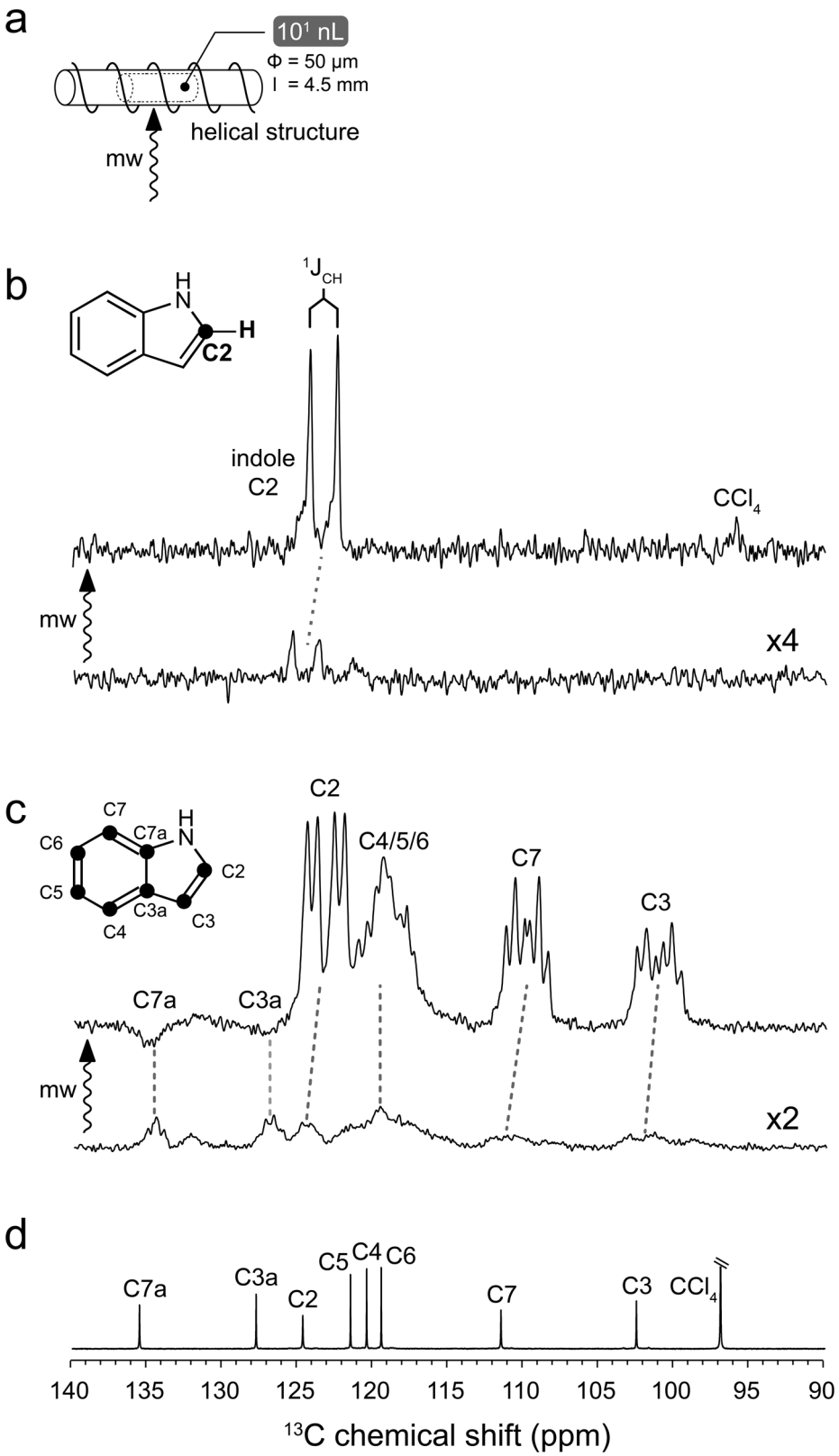

indole ring (Supplementary Table 4). Qualitatively the indole carbons exhibiting large $\overline{\delta_{para}}$ values also show more evident ODNP enhancements except the two bridge carbons (Supplementary Fig. 3c and Supplementary Table 4). We have further expanded this analysis to other compounds (Supplementary Fig. 3a) previously studied by ODNP ^{13}C NMR spectroscopy in organic solvents at the same magnetic field (9.4 T)[25]. Due to the recent in-house modification of the helical microwave structure (different plungers), we could only reach, though reproducibly, a moderately lower ODNP enhancement on the TEMPONE/$^{13}CCl_4$

Fig. 4 Room-temperature liquid-state ODNP NMR of indole in CCl_4 at 9.4 T. TEMPO (100 mM) has been used as the hyperpolarizing agent. CCl_4 has been chosen as the solvent. **a** Scheme of helical resonator[56]. The solution samples (10^1 nL) have been loaded into a capillary of 50 μm diameter (Φ). The sample length (*l*) is about 4.5 mm. The microwave beam (mw arrow) enters the cavity from side. **b** Spectra of ^{13}C2 indole obtained with (up) and without (down) microwave (mw arrow) are presented. The resolved J-coupling is indicated. **c** Spectra of U-^{13}C indole obtained with (up) and without (down) microwave are presented. The molecular structures of ^{13}C2 indole and U-^{13}C indole are shown in the insets of panels (**b**) and (**c**) respectively. The ^{13}C labeled positions are indicated by black circles. The spectra in (**b**) and (**c**) are scaled with the number of scans for visualizing directly the enhancement factor. The microwave (mw)-off spectra in (**b**) and (**c**) are further scaled up by four-fold and two-fold respectively for the better visualization. **d** The conventional ^{1}H-decoupled liquid-state ^{13}C NMR spectrum of indole without the ^{13}C enrichment.

sample compared to the previous work (Supplementary Fig. 1c)[25]. The ODNP enhancement of this new experimental result was used for rescaling the previous results in order to match the current instrumentation condition. As shown in Supplementary Fig. 3b and Supplementary Table 4, a correlation of ODNP enhancement over $\overline{\delta_{\mathrm{para}}}$ remains visible in this expanded molecular scheme. However, the data points seem more scattered than those shown in Fig. 2f. This could be due to the distinct nature (e.g., the halogen-bond and H-bond) of the radical-substrate interactions presented by this more diverse scheme of organic compounds. In addition, both the magnitude and the dynamics of hyperfine interactions determine the ODNP enhancement, while the paramagnetic NMR shift only indicates the average scale of hyperfine interactions. Since the dynamics of the H-bonded radical-substrate complexes had not been well explored, we decided to further explore such dynamics in the TEMPO-indole complex by advanced computational chemistry approaches.

Molecular dynamics permits scalar ODNP in the indole-TEMPO complex. Since the binding chemistry between indole and TEMPO is well-defined, we selected this complex as our model system for a detailed investigation on the molecular dynamics relevant to scalar ODNP. The sub-ps dynamics of the TEMPO-indole complex can neither be accessed directly by EPR/paramagnetic NMR spectroscopy nor be depicted by conventional single-point QM calculations. In previous studies, the "pulse model" has been used to describe the microscopic mechanism of scalar ODNP[25,55]. In such a model the fluctuations of hyperfine interactions that drive ODNP are associated primarily with the transient formation-disassociation of radical-substrate complexes, which can be approximated as "pulses"[36,37]. We have estimated that the lifetime of the TEMPO-indole complex is longer than 100 ps (Supplementary Note 2), a time scale mismatching with high-field ODNP. To resolve the molecular mechanism of the Fermi contact fluctuations in the long-living TEMPO-indole complex, we have carried out an extensive in silico simulation.

Since the Fermi contact is determined by the electronic structure of the complex, QM/MM MD simulation has been selected rather than the conventional MD approach based on classical mechanics. This ab initio approach also covers the contribution of the unpaired electron in the radical-substrate chemical interaction that cannot be depicted faithfully by empirical force fields. The TEMPO-indole complex (45 atoms) was included in the QM region set at the M06-2X/6-311G** level and the explicit solvent CCl_4 bath (498 molecules, 2490 atoms) were treated using classical mechanics (Fig. 5a). We have chosen M06-2X functional for the QM simulation of H-bonded TEMPO-indole complex due to its excellent radical/nonradical trade-off, namely the balanced accuracy on both the open and closed-shell molecules[57]. For resolving the hyperfine fluctuations at the sub-ps time scale, we have simulated the QM/MM trajectory of 10 ps (1×10^4 h CPU time). This extensive computational effort has yielded new structural, chemical, and dynamic insights into the molecular mechanism of high-field scalar ODNP.

First, our simulation reveals both the intermolecular and the intramolecular structural dynamics in the indole-TEMPO complex. The intermolecular H-bond in this complex fluctuates drastically and samples a large space of local geometry (Fig. 5b-d). In addition, the benzene and the pyrrole ring of the indole molecule also undergo fast intramolecular structural fluctuations (Fig. 5b, c). It has been reported that TEMPO-type radicals also interact chemically with CCl_4 via halogen-mediated interactions[20,54]. In our simulation the average TEMPO oxygen–CCl_4 chlorine distance (3.42 Å) remains significantly longer than that in TEMPONE–CCl_4 complex (2.96 Å), suggesting a negligible role of nearby CCl_4 molecules in competing for direct chemical interactions with the TEMPO radical within the time window of our simulation. The fluctuations of the surrounding CCl_4 molecules may reshape the solvent environment for accommodating the dynamic TEMPO-indole complex.

Second, the structural fluctuations within the TEMPO-indole complex are coupled with the spin density dynamics on indole carbons. As shown on a representative conformation of the TEMPO-indole complex (Fig. 6a), the singly occupied molecular orbital (SOMO) of the TEMPO radical overlaps with its indole counterpart in the H-bonded complex. The front lobe of the TEMPO SOMO located at the NO moiety overlaps with the indole SOMO in a head-to-side anti-π/anti-π configuration (Fig. 6a). In this configuration, the orbital overlap is sensitive to the intermolecular H-bond geometry. In addition, the indole SOMO orbital is also tuned by the indole ring structure (Fig. 6a). Through the intermolecular SOMO overlap, the electron spin density delocalizes from the TEMPO radical to the indole anti-π orbital (Fig. 6a). These spin densities further propagate to the indole ^{13}C nuclear positions via the local anti-π/σ ortibal overlap. The structural fluctuations of both the TEMPO-indole H-bond and the indole ring itself contribute to the spin density dynamics on the indole carbons (Fig. 6c). Notably, the two bridge carbons in the indole molecule are located at the node position of its SOMO (Fig. 6a, c). Indeed they exhibit negligible ODNP ^{13}C enhancements compared to the other carbons.

Third, the spin density dynamics within the TEMPO-indole complex present ODNP-relevant sub-ps features. The covariance between the spin density dynamics of various nuclei in the TEMPO-indole complex shows only a weekly correlated pattern (Fig. 6b). The individuality of the spin density dynamics on different indole carbons reflects the structural and chemical complexity of the Fermi contact in this complex as described above. To extract the time scale features of such complex spin density dynamics, we have performed a comprehensive analysis of the spin density trajectories (Supplementary Fig. 5) derived from our QM/MM MD simulation. Some detailed introductions on the theoretical and mathematical background of our data analysis can be found in Supplementary Information (Supplementary Note 4 and Supplementary Fig. 4) along with the full data presentation (Supplementary Figs. 5–11). The representative

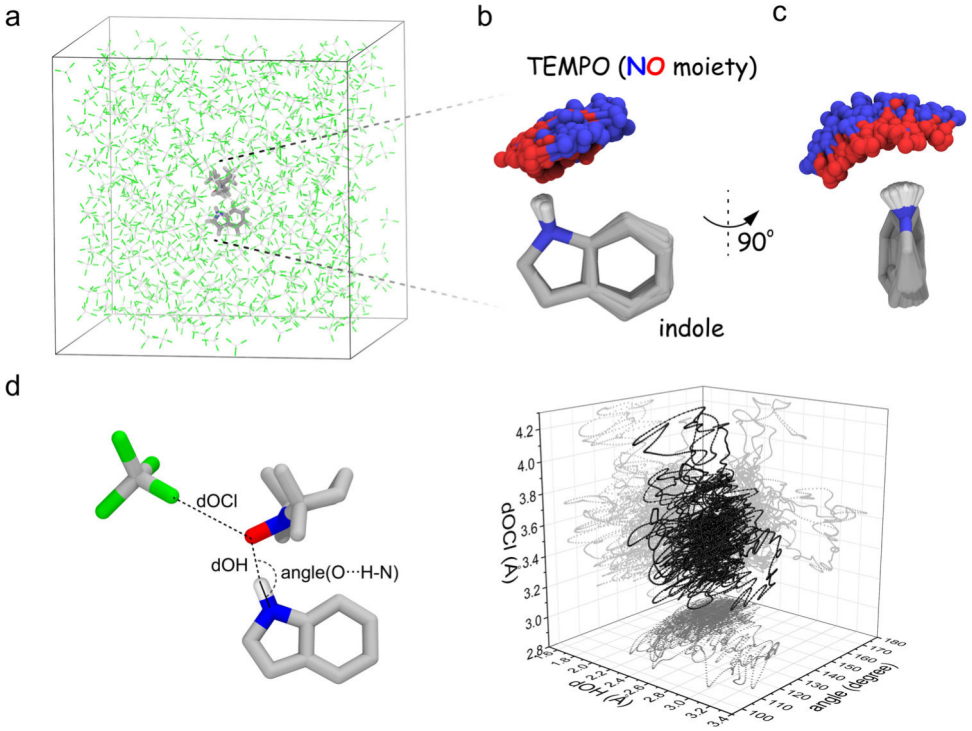

Fig. 5 QM/MM MD simulation captures the structure dynamics of the H-bonded TEMPO-indole complex. a The TEMPO-indole complex (QM) is immerse in CCl_4 solvent (MM) for the simulation. **b**, **c** Both the intermolecular H-bond and the indole ring undergo the structural fluctuations. **d** Both the H-bond (length and angle) and the radical-solvent distance undergo the dynamic fluctuations. Source data are provided as a Source Data file.

results of the spin density dynamics at the indole C2 position are shown in Fig. 6d–g.

The spin density autocorrelation functions (ACFs) of all indole carbons exhibit an initial decay followed by the sub-ps waves (Fig. 6e and Supplementary Fig. 6). The correlation times presented by the initial ACF decay are below 0.1 ps as extracted by the inverse Laplace transformation (Supplementary Fig. 8a–j). For most of the indole carbons, a second slower decaying component in the 0.5−1.0 ps range is also detectable (Supplementary Fig. 8b–j). The fast ACF decay at the similar time scale (0.1 ps) can be found on the intermolecular H-bond dynamics (Supplementary Fig. 8q, r) but not on the TEMPO-CCl_4 (solute-solvent) fluctuation or on the TEMPO methyl rotation (Supplementary Figs. 5m–p, s, S7m–p, s). This further supports that the spin density dynamics in the TEMPO-indole complex is associated primarily with the intermolecular H-bond dynamics. The complex features of spin-density ACFs (Fig. 6e and Supplementary Fig. 6) fit neither the "pulse" models[36,37] nor the commonly used memory-free Ornstein−Uhlenbeck process[58]. The spin density dynamics here can be better described by a more generalized autoregressive (AR) data model widely used in the time series analysis (Supplementary Note 4)[59]. The order of the AR model for describing the spin density dynamics in the TEMPO-indole complex is at least 6 (Supplementary Fig. 11q–t). This suggests a short "memory" of 6 fs (6 steps with 1 fs/step interval in our simulation) of the non-Markovian spin density dynamics, which aligns nicely with memory time at the 10 fs time scale as detected by the spin density memory functions. The detailed introduction and analysis of the memory function can be found in Supplementary Note 4 and Supplementary Figs. 9, 10 respectively.

Despite the highly complex nature of the spin density dynamics in the TEMPO-indole complex, we could derive the spectral density functions by Fourier transforming the spin density ACFs (Fig. 6f, g and Supplementary Figs. 4, 7). The spectral density at the e-^{13}C ZQ frequency (0.263 * $2\pi = 1.65$ THz) infers the ODNP performance. Indeed the e-^{13}C ZQ relaxation rates estimated from the e-^{13}C ZQ spectral density are in the order of magnitude of 10^{-1} to 10^{1} s^{-1} (Supplementary Note 5 and Supplementary Table 6), which agrees qualitatively with the order of magnitude of the observed DNP ^{13}C enhancements.

Discussion

In this work, we have discovered a full scheme of new molecular targets for scalar ODNP ^{13}C NMR spectroscopy ranging from structurally and chemically diverse small biological molecules (carbohydrates and amino acids) to biologically relevant heterocyclic compounds (imidazole and indole). In particular, we have achieved sizable ODNP ^{13}C enhancement on small biological molecules in water at room temperature and at high field (9.4 T). The paramagnetic NMR shift, a parameter that is rather easily accessible, has served us as an indicator for our initial search for such target molecules. Our data also identify a rather broad range of scalar ODNP-friendly chemical groups that interact with TEMPO-type radicals. The methyl groups, which are widely used NMR probes especially for large biomolecular complexes, form weak H-bonds with the TEMPO-type radicals and are eligible for room-temperature scalar ODNP. More generally, the H-bonding capacity of CH, OH, and NH groups with TEMPO-type radicals[55], suggests that a broad range of organic molecules could be explored by scalar ODNP ^{13}C NMR spectroscopy. We expect that paramagnetic NMR will continue to serve as a tool for facilitating the future ODNP target discovery. The spectral resolution achieved in our room-temperature ODNP ^{13}C NMR experiments, even in the presence of high concentration (100 mM) of paramagnetic species, is already sufficient for

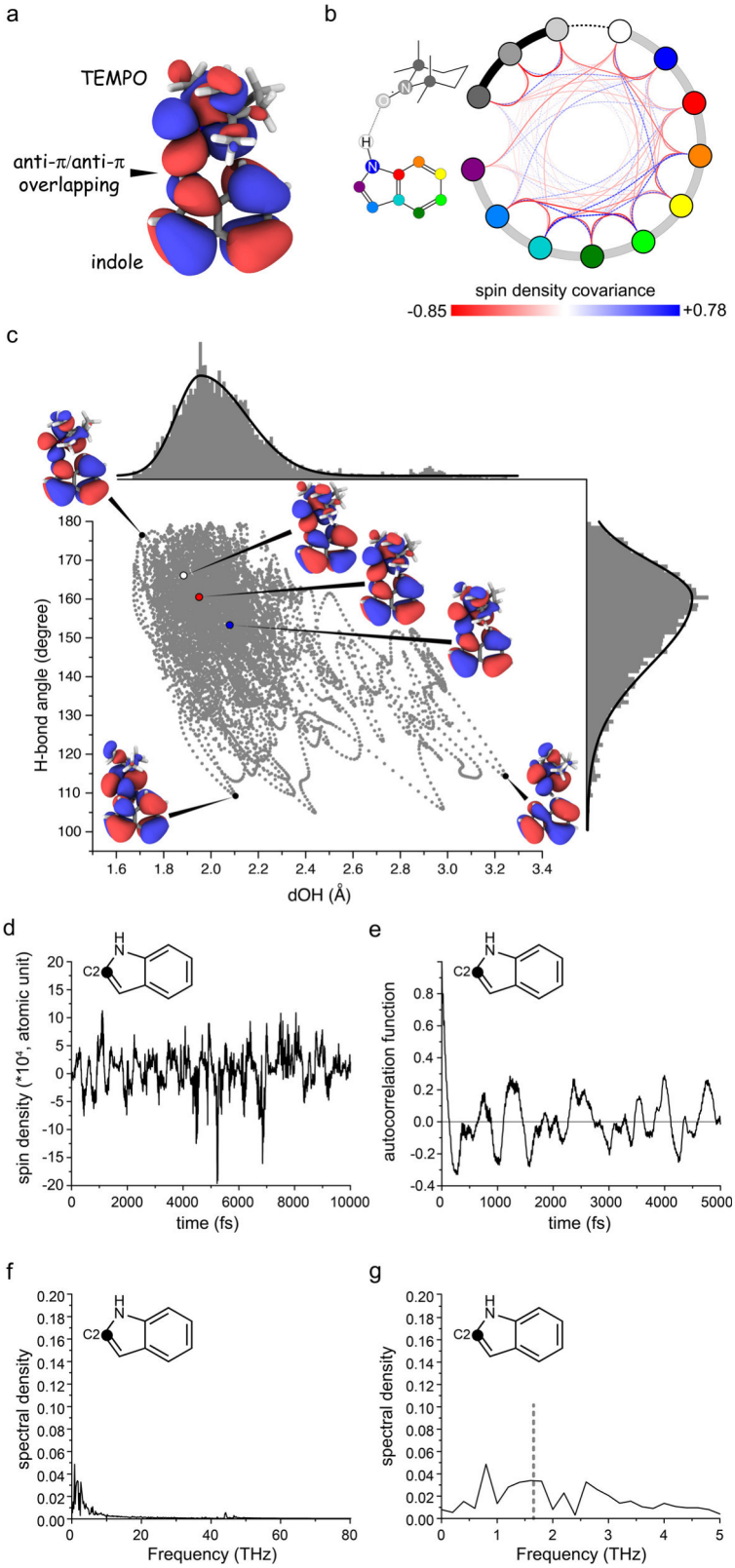

Fig. 6 The dynamic electronic structures of the TEMPO-indole complex. a The SOMO of a representative conformation of the complex. **b** The covariance of spin density fluctuations at the various positions in the complex. The atoms are represented as the colored circles. The red and blue links indicate the negative and positive covariance respectively. **c** The SOMO of several states sampling distinct H-bond structures (length and angle) are shown. **d** The spin density trajectory of indole C2. **e** The autocorrelation function of the spin density dynamics at indole C2 position. **f**, **g** The unnormalized spectral density function of the spin density dynamics at indole C2 position. The dashed line in (**g**) indicates e-^{13}C zero-quantum frequency at 9.4 T. Source data are provided as a Source Data file.

resolving some ^{1}J couplings. This opens the door towards more challenging ODNP 2D NMR experiments on such samples.

In previous ODNP studies[20,25,37], the radical-substrate chemical encounter-disassociation events were considered as the main driving-force of scalar ODNP. In the halogen-bonded radical-substrate systems such events indeed occur frequently at the sub-ps time scale suitable for high-field scalar ODNP (Supplementary Note 3). In contrast, the lifetime of the indole-TEMPO H-bond complex is drastically longer than those halogen-bond complexes (Supplementary Note 2). The long lifetime in the 100 ps regime has also been proposed on some other H-bonded radical-substrate complexes[55]. This trend is in line with the generally stronger H-bond interaction than the halogen-bond in radical-substrate complexes as indicated by the binding constants (Supplementary Notes 2 and 3, 10^{-1} to 10^{0} M^{-1} for the H-bonded radical-substrate complexes and 10^{-2} M^{-1} for the halogen-bonded complexes). At low magnetic fields (e.g., 0.33 T, 10 GHz electron Larmor frequency), radical-substrate interaction-disassociation processes at 10^2 ps time scale are fast enough for a good ODNP efficiency[40,55]. At high magnetic fields (e.g., 9.4 T in this study, 263 GHz electron Larmor frequency), molecular events at 10^2 ps time scale is two orders of magnitude slower than those required for promoting efficient e-^{13}C cross-relaxation. Rather the dynamic fluctuation within the long-living radical-substrate complex serves as the main driving force of scalar ODNP at such high magnetic field. Our simulation reveals that the intermolecular H-bond dynamics together with the intramolecular structural fluctuations are responsible for the high-field scalar ODNP in the long-living H-bonded TEMPO-indole complex. These molecular dynamics impact directly the intermolecular and intramolecular SOMO and are coupled with the spin density dynamics of the indole carbons. Such distinct molecular mechanisms in the H-bonded and halogen-bonded radical-substrate complexes could complicate the tentative correlation between ODNP enhancement and $\overline{\delta_{para}}$. A more detailed discussion on additional factors that may also cause such deviations can be found in Supplementary Discussion.

Our QM/MM MD simulation also unfolds the sub-ps features of the spin density dynamics in a H-bonded radical-substrate complex. In the framework of an AR model, the sub-ps sinusoidal-like waves presented in the spin density ACFs are determined by the much shorter "memory" of the dynamic process. The origin of this memory, namely the intra-complex quantum mechanical interactions and other potential latent degrees of freedoms, will be explored in our future work. Molecular dynamics at the sub-ps time scale has been found in many H-bonded molecules by terahertz (THz) spectroscopy[60–66]. Our data analysis framework based on QM/MM MD trajectories offers a new approach for exploring the ODNP potential of such fast THz modes in the H-bonded molecular systems.

In summary, we show that the carbons in structurally and chemically diverse small biological and biologically-relevant molecules, ranging from heterocyclic compounds, carbohydrates to amino acids, can be hyperpolarized via scalar ODNP at room temperature. In particular, sizable DNP ^{13}C enhancements, along with sufficient spectral resolution, can be obtained on small biological molecules in water directly at room-temperature and at high-field (9.4 T). All these observed scalar ODNP enhancements are based on intermolecular H-bonds in the radical-substrate complexes, suggesting a broad applicability of liquid-state ODNP ^{13}C NMR spectroscopy. Paramagnetic NMR spectroscopy, a technique strongly related to DNP, can facilitate the ODNP target search. In addition, QM/MM MD simulations offer mechanistic insights into the fast sub-ps dynamics in such H-bonded radical-substrate complexes. We expect that our work will promote the exploration of other families of molecules for room-temperature liquid-state ODNP NMR applications and will encourage further developments in high-field DNP instrumentation, QM/MM MD simulations, and the use of other complementary approaches for detecting and describing ultrafast H-bond dynamics in liquids.

Methods

Materials and sample preparation. U-^{13}C indole, U-^{13}C glucose, and $^{13}CCl_4$ were purchased from Cambridge Isotope Laboratory (Tewksbury, U.S.). ^{13}C-imidazole was obtained from Toronto Research Chemicals TRC (I350204, North York, Canada). ^{13}C-labeled amino acids and D_2O (> 99%) were obtained from CortecNet (Les Ulis, France). TEMPO, TEMPOL and TEMPONE were obtained from Aldrich-Sigma and were used without further purification. The solvent CCl_4 was purchased form ABCR (Karlsruhe, Germany). Radical and ^{13}C-enriched compounds were dissolved together in a specific solvent and all samples were used as soon as prepared or immediately stored at −80 °C before the further use. We have found that imidazole could not reach a good concentration in CCl_4. Therefore chloroform was used instead of CCl_4 for this compound. The details about all ODNP NMR samples are listed in Supplementary Table 1.

For paramagnetic NMR titration experiments, all samples were prepared using compounds of natural ^{13}C abundance at the concentrations in Supplementary Table 1 or reported previously[25]. The concentrations of radicals were varied between 0 and 200 mM. The samples were loaded to brown-colored 5 mm NMR tubes for the solution NMR measurements. The frequency locking on the deuterium-free sample (e.g., CCl_4) was achieved by placing an external DMSO-d_6 sample sealed in 1.0 mm (outer diameter) capillary into the solution NMR tubes.

ODNP experiments and data analysis. All liquid-state DNP experiments were performed on a homebuilt DNP NMR spectrometer operating at 9.4 T (^{1}H Larmor frequency 400 MHz, electron Larmor frequency 263 GHz)[56]. Microwave (MW) irradiation was generated in a customized 4.7 T gyrotron (Gycom, Russia) operating at the second harmonic mode and was directed to DNP NMR probe via corrugated waveguides. The maximal microwave power from the MW bridge was 5.5 W. A commercial Bruker Avance 9.4 T spectrometer was used for the NMR experiments.

DNP experiments on aqueous samples were carried out on a stripline Fabry–Pérot (FP) DNP NMR probehead modified from the previous design[39]. The Fabry–Pérot cavity offered high microwave efficiency on thin flat samples while restricting the sample heating. The stripeline served as the RF component for the NMR experiment. The sample solution was first loaded onto the stripline using a 1 μL microsyringe (Hamilton) and then sealed with a flat Teflon ring (2 mm inner diameter, 15 μm thickness) under a quartz plate (Stellar Industries Corp), which corresponds to an effective sample volume of 50 nL. The Teflon ring was pre-lubricated with proton-free grease (Crytox, DuPont) to prevent the leakage of the sample solution. The grease was not compatible with an organic solvent. Therefore the current setup is mostly suitable for aqueous samples. After being sealed, the samples were inspected carefully under microscope for the bubbles. Thanks to the small sample dimension (thickness) and high-heat conductance of metal stripeline, this FP probehead shows excellent heat management capacity, which permits the stable DNP NMR measurements on aqueous samples. The NMR spectra with thermal polarization ("Boltzmann" condition) were acquired without microwave irradiation. The DNP-enhanced NMR spectra were acquired under maximal MW power (5.5 W) obtainable from our gyrotron. The DNP working condition was optimized using a two-step procedure similar as that used on HC probehead (Supplementary Fig. 1a), with the exception that the distance between the stripeline and spherical mirror was adjusted for tuning the FP cavity. We noticed that the control of sample dimension could be helpful for maintaining the quality factor of the current FP cavity. The saturation factor under our experimental condition was estimated to be about 0.6 based on the observed DNP enhancement of water ^{1}H (about −10 at 320 K). The RF channel can be switched to either ^{1}H or ^{13}C Larmor frequency. The ^{13}C and ^{1}H 1D NMR spectra were acquired and processed as described above. All ^{1}H and ^{13}C chemical shifts were referenced indirectly to TMS.

DNP experiments on samples with organic solvents were performed on a home-built helix-cylindrical (HC) ODNP NMR probehead, which features a cylindrical MW cavity and a helical radiofrequency (RF) coil[56]. Liquid samples were loaded in a quartz capillary (Polymicro, 50 or 100 μm inner diameter, 150 μm outer diameter) via the capillary effect and were sealed with wax on both ends. An air gap was left between the sample solution and the wax in order to prevent the direct contact between the organic solvent and the wax sealing. Before each measurement, the capillaries were carefully inspected for ensuring the absence of bubbles inside the sample volume. The sample heating could generate bubbles inside the sample or even cause the sample leakage. Such sample deteriorations were indicated by the loss of NMR signals. We observed that polar solvents in particular water with a high dielectric constant can be heated rapidly by MW in HC probehead. Small sample size (capillary diameter) would alleviate partially this heating issue. However, this would severely compromise the NMR sensitivity. Therefore on polar solvent samples, only qualitative results can be obtained on this probehead. The

sample capillaries were placed horizontally along the axis of helix coil. The MW resonator was tuned to TE_{013} mode by adjusting the distance between two plungers made of Kel-F with silver-coated caps. The length of the MW cavity was about 4.5 mm, which corresponds to the active sample volume of 35 nL or 9 nL for 100 µm or 50 µm capillaries respectively. The NMR spectra with thermal polarization ("Boltzmann" condition) were acquired without microwave irradiation. The DNP-enhanced NMR spectra were acquired under 1.4 W microwave power. The best DNP working condition for each sample was located in two steps. First, the microwave frequency was first tuned preliminarily by scanning the gyrotron cavity temperature for the best DNP-enhancement on a standard TEPONE-$^{13}CCl_4$ sample. (Supplementary Fig. 1a) In the second step, the target sample was loaded and the cylinder microwave cavity was fine-tuned for each specific sample by adjusting the distance between plungers following the ^{1}H signal of the sample. The RF channel was switched manually between ^{1}H and ^{13}C Larmor frequencies by reconfiguring the RF circuit inside probehead. For the ^{13}C direct excitation NMR experiments, a "hard" ^{13}C pulse $\pi/2$ pulse of 22.7 kHz RF strength was used for excitation. The carrier frequency for ^{13}C RF pulse was set to 104 ppm. No ^{1}H decoupling was applied during the acquisition. The recycle delay was set to 1 s that is long enough for the full ^{13}C magnetization recovery. The ^{13}C spectral window was set to 140 ppm (14.1 kHz) and the FID was digitalized with 8192 points. The FID was processed with 16k points with Gaussian window function (lb = −5 Hz, gb = 0.04). For the ^{1}H NMR experiments, a ^{1}H pulse $\pi/2$ pulse of 25.0 kHz RF strength was applied. The carrier frequency for ^{1}H RF pulse was set to 6 ppm. The recycle delay was set to 1 s. The spectral window was set to 40 ppm (16.0 kHz) and the FID was digitalized with 4096 points. The FID was processed with 16k points without applying window functions. All ^{1}H and ^{13}C chemical shifts were referenced indirectly to TMS.

The ODNP enhancement factor was calculated with the following equation:

$$\varepsilon_{OE} = \frac{I_{DNP}}{I_{Boltzmann}} \cdot \frac{n_{Boltzmann}}{n_{DNP}} - 1$$

where I is the integral of the signal and n is the number of scans.

The error of DNP enhancement was calculated by the signal-to-noise ratio of the NMR spectra using Gaussian error propagation law:

$$\Delta\varepsilon_{OE} = \sqrt{\left(\frac{\partial\varepsilon_{OE}}{\partial I_{DNP}}\right)^2 \Delta I_{DNP}{}^2 + \left(\frac{\partial\varepsilon_{OE}}{\partial I_{Boltz}}\right)^2 \Delta I_{Boltz}{}^2}$$

where ΔI is the reciprocal of signal-to-noise ratio.

We found that the achievable ODNP enhancement on the same $^{13}CCl_4$/TEMPONE sample had dropped significantly from the previous record obtained on the sample HC probehead[25]. Since the radical concentration was identical in all samples, we derived a scaling factor from the DNP enhancements of $^{13}CCl_4$/TEMPONE sample under different HC probehead conditions and applied this scaling factor on previously reported results for a fairer comparison.

Determination of molar-free paramagnetic chemical shifts ($\overline{\delta_{para}}$). Solution 1D ^{13}C NMR experiments were performed on a Bruker 400 MHz spectrometer (Institute for Organic Chemistry and Chemical Biology, Goethe University of Frankfurt am Main). All ^{1}H and ^{13}C NMR experiments were performed using the standard setups at room temperature. ^{13}C FIDs were acquired with ^{1}H decoupling. All these solution experiments on the commercial instrument including the data processing were automated. The resonance assignment was performed manually and the molar-free paramagnetic shifts were obtained from the slope of the linear fitting of observed paramagnetic shift versus the radical concentration. The error of $\overline{\delta_{para}}$ is defined as the data fitting error of this linear regression. For the cases where several carbon signals are overlapped on OD NP NMR spectra, we calculated the standard deviations of $\overline{\delta_{para}}$ of these carbons and present this deviation as the error.

Single point DFT, QM/MM MD simulation, and trajectory data extraction. The structures of TEMPOL-amino acid complexes were optimized in water phase at the M06-2X/6–311G** level using Gaussian16[67]. All the molecular orbitals were described by cubegen module of Gaussian program. The solvation effect was introduced via polarizable continuum model (PCM). We performed an exhaustive configurational search for the TEMPOL-amino acid complexes at each binding site, and kept the lowest-energy configuration. The vibrational frequencies were calculated to confirm the local minima with all positive frequencies. The Gibbs free energies (including the solvation energy) of the TEMPOL-amino acid complexes are given in Supplementary Table 5.

The quantum mechanics/molecular mechanics molecular dynamics (QM/MM MD) simulation of indole-TEMPO complex was performed with the explicit CCl_4 solvent environment. The initial TEMPO-indole complex was constructed starting from the TEMPO-$CHCl_3$ complex[20] by replacing $CHCl_3$ with indole. Subsequently, the TEMPO-indole complex was optimized in a carbon tetrachloride solvent environment at the M06-2X/6–311 G** level[68] using the Gaussian16 program[67,68]. Polarizable Continuum Model (PCM) was applied to mimic the solvent environment.

Next, the TEMPO-indole complex was placed at the center of a rectangular box containing 498 carbon tetrachloride molecules. Force field parameters for carbon tetrachloride and the TEMPO-indole complex were taken from the Generalized Amber force field (GAFF)[69] with the HF/6–31G* RESP charges. Minimization using the Amber force field was first performed to relax the system with a weak constraint. Then the system was brought to room temperature (300 K) in 100 ps with a weak constraint. After that, 100 ps classical MD simulation of the weakly restrained TEMPO-indole complex was carried out to further relax the system with the periodic boundary condition at 300 K and 1 atm. The integration time step was set to 1.0 fs.

Finally, 10 ps QM/MM MD simulation was performed after the pre-equilibrium simulation.

Currently, this simulation is set as a long-run task on the computational platform and a glimpse into the 20 ps result can be found in Supplementary Figs. 5t and 6t. The TEMPO-indole complex was partitioned into the QM region and the rest of the system was treated by MM. The QM region was calculated by M06–2X/6–311G**[68]. The electronic coupling between the QM and MM regions was treated by including the MM charges in the QM Hamiltonian. A 15 Å cutoff was utilized to treat QM/MM electrostatic interactions. The integration time step for QM/MM MD simulation was also set to 1.0 fs. The atomic spin densities of the TEMPO-indole complex were obtained from the QM/MM calculations. The Amber18 program[70] was utilized to perform the MD simulations, and the Sander module with an interface to the Gaussian16 program was employed to carry out QM/MM MD simulations. The 10 ps trajectory calculation took 1×10^4 h CPU (Intel Xeon E5–2650 2.30 GHz) time on our cluster. The time evolutions of the spin density and molecular geometry (H-bond length, H-bond angle, TEMPO-CCl_4 distance, methyl rotation angle) were extracted from the QM/MM MD trajectory using in-house scripts. The 3D profiles of SOMO of selected conformations/frames were generated using GaussView. The QM/MM simulation was conducted on 20-core Intel Xeon E5–2650 2.30 GHz processors at the Supercomputer Center of East China Normal University (ECNU).

Data analysis of QM/MM MD trajectory. A general introduction of the data analysis procedure is shown in Supplementary Fig. 4. The normalized auto-correlation functions (ACF) $g(t)$ were calculated from the QM/MM MD trajectory data following the definition below:

$$g(t) = \frac{<\rho(t_0)\rho(t_0+t)>}{<\rho(t_0)\rho(t_0)>}$$

where $\rho(t)$ presents the specific target parameter (e.g., spin density, distance, angle) at time t. ACFs were computed from the corresponding trajectory data by a in-house written python script. In order to prevent the artificial "convergence" to zero caused by the finite length of trajectories, we only calculated ACF up to half of the trajectory time duration. High precision (100 decimals) was set for the ACFs in order to reduce the propagation of numerical errors from ACF to the later computed memory functions. In a test calculation, we also removed two methyl groups on TEMPO in QM/MM calculations and found that the spin density ACF shows similar pattern on indole in complex with this hypothetical radical.

All Fourier transforms were performed using Origin (OriginLab Corporation). The covariances of spin density variations between different atoms were calculated using StatPlus:mac (AnalystSoft Inc.) and were visualized using Circos–0.69–3[71]. The inverse Laplace transform of ACF was computed using CONTIN[72] as a plug-in of Origin (https://www.originlab.com/fileExchange/details.aspx?fid=456).

The memory function $K(t)$ was defined as below:

$$\frac{\partial}{\partial t}g(t) = -\int_0^t K_g(\tau)g(t-\tau)\mathrm{d}\tau$$

where $g(t)$ is the ACF and $K(\tau)$ is its memory kernel. This definition is in the form of Volterra integral equation of the second type, in which the right side of the equation is also called Bromwich integral. The solution of this integral equation takes the form of Laplace and inverse Laplace transform:

$$K_g(\tau) = \mathcal{L}^{-1}[(\mathcal{L}[g(t)])^{-1} - t]$$

where $\mathcal{L}$ and $\mathcal{L}^{-1}$ presents the Laplace and inverse Laplace transform.

Initially, we attempted to compute the memory function by discrete Z-transform and inverse Z-transform. However, the computational burden became astronomical for a 10^4 data sequence. Only the truncation of up to 20 terms was affordable for the initial points of the memory function on a normal PC. However, the error induced by such truncation escalated rapidly with increasing time (Supplementary Fig. 8p). Therefore the memory functions were eventually computed numerically following the protocol proposed by Berne and co-workers[73] using a python script written in house. The Gregory formula was taken for approximating the integration in Day's method for solving the linear Volterra integral equation[74]. To reduce the numerical error accumulated in the iteration, the decimal module was used for suppressing the rounding error of binary representation. We also calculated the memory function by reverting the Berne's approach for deriving g(t) from K(t)[73]. With the decimal module, this approach yields the result similar to that obtained from the direct treatment of Volterra integral equation. Though the deviation between two numerical memory functions yielded by these two approaches indeed propagates with time/iteration, its absolute value remains negligible (Supplementary Fig. 9q). In this work, we still used the approach by solving the Volterra integral equation. It should be noticed that even with the best numerical treatment we can afford, the

numerical error still propagates significantly on several sites as shown in Supplementary Fig. 9b, k, l, n, o.

The autoregressive AR-model-based time series analysis was performed using Mathematica (version 10.3.0.0). The function "TimeSeriesModelFit" was used and the model was set to "AR". We have also tested more general models (Supplementary Fig. 11q–t). The best candidate was ARMA(6,1) (AR(6) with moving average MA(1)), the Akaike information criterion (AIC) of this model was −236421, which is just slightly better than AR(6) model (AIC −235660). Since the physical meaning of MA is difficult to be interpreted in our case and AR(6) model already captures the feature of the trajectory, we finally selected AR(6) model to represent the trajectory. We have also confirmed the stationarity of this model using the "WeakStationarity" function. Our analysis also shows that the AR models of orders p higher than 6 do not further improve the fitting quality and the six time-point correlation parameters along with the noise level are already converged at $p = 6$. Therefore $p = 6$ shows the minimal order of RA for representing our trajectory data. However, high order $p > 6$ still yields essentially non-zero time-point correlation parameters. Therefore $p = 6$ only defines the minimal order of time-point correlation in our data.

Data availability

The ODNP NMR data have been deposited in Figshare (https://doi.org/10.6084/m9.figshare.14774433, https://doi.org/10.6084/m9.figshare.14774415). The results of DFT calculations have been deposited in GitHub (https://github.com/xiaohegroup/Simulations-of-Tempol). The full QM/MM trajectory is available from the corresponding authors upon reasonable requests. Source data are provided with this paper.

Code availability

All input files for the DFT calculations and QM/MM simulations are available via GitHub (https://github.com/xiaohegroup/Simulations-of-Tempol, https://doi.org/10.5281/zenodo.5150908[75]). The codes for analyzing the QM/MM trajectory are available from the corresponding authors upon reasonable requests.

Received: 3 March 2021; Accepted: 1 November 2021;
Published online: 25 November 2021

References

1. Ardenkjaer-Larsen, J. H. et al. Facing and overcoming sensitivity challenges in biomolecular NMR spectroscopy. *Angew. Chem. Int. Ed.* **54**, 9162–9185 (2015).
2. Ni, Q. Z. et al. High frequency dynamic nuclear polarization. *Acc. Chem. Res.* **46**, 1933–1941 (2013).
3. Lelli, M. et al. Solid-State dynamic nuclear polarization at 9.4 and 18.8 T from 100 K to room temperature. *J. Am. Chem. Soc.* **137**, 14558–14561 (2015).
4. Biller, J. R., Barnes, R. & Han, S. Perspective of Overhauser dynamic nuclear polarization for the study of soft materials. *Curr. Opin. Colloid Interface Sci.* **33**, 72–85 (2018).
5. Saliba, E. P., Sesti, E. L., Alaniva, N. & Barnes, A. B. Pulsed electron decoupling and strategies for time domain dynamic nuclear polarization with magic angle spinning. *J. Phys. Chem. Lett.* **9**, 5539–5547 (2018).
6. Zhao, L., Pinon, A. C., Emsley, L. & Rossini, A. J. DNP-enhanced solid-state NMR spectroscopy of active pharmaceutical ingredients. *Magn. Reson. Chem.* **56**, 583–609 (2018).
7. Denysenkov, V. P. & Prisner, T. F. Liquid-state Overhauser DNP at high magnetic fields. *Emagres* **8**, 41–54 (2019).
8. Jannin, S., Dumez, J. N., Giraudeau, P. & Kurzbach, D. Application and methodology of dissolution dynamic nuclear polarization in physical, chemical and biological contexts. *J. Magn. Reson.* **305**, 41–50 (2019).
9. Corzilius, B. High-field dynamic nuclear polarization. *Annu. Rev. Phys. Chem.* **71**, 143–170 (2020).
10. Prandolini, M. J., Denysenkov, V. P., Gafurov, M., Endeward, B. & Prisner, T. F. High-field dynamic nuclear polarization in aqueous solutions. *J. Am. Chem. Soc.* **131**, 6090–6092 (2009).
11. Lesage, A. et al. Surface enhanced NMR spectroscopy by dynamic nuclear polarization. *J. Am. Chem. Soc.* **132**, 15459–15461 (2010).
12. Lumata, L., Merritt, M. E., Hashami, Z., Ratnakar, S. J. & Kovacs, Z. Production and NMR characterization of hyperpolarized (107,109)Ag complexes. *Angew. Chem. Int. Ed.* **51**, 525–527 (2012).
13. Franck, J. M., Pavlova, A., Scott, J. A. & Han, S. Quantitative cw Overhauser effect dynamic nuclear polarization for the analysis of local water dynamics. *Prog. Nucl. Magn. Reson. Spectrosc.* **74**, 33–56 (2013).
14. Takahashi, H., Hediger, S. & De Paepe, G. Matrix-free dynamic nuclear polarization enables solid-state NMR 13C-13C correlation spectroscopy of proteins at natural isotopic abundance. *Chem. Commun.* **49**, 9479–9481 (2013).
15. Can, T. V. et al. Overhauser effects in insulating solids. *J. Chem. Phys.* **141**, 064202 (2014).
16. Jakdetchai, O. et al. Dynamic nuclear polarization-enhanced NMR on aligned lipid lilayers at ambient temperature. *J. Am. Chem. Soc.* **136**, 15533–15536 (2014).
17. Harris, T., Szekely, O. & Frydman, L. On the potential of hyperpolarized water in biomolecular NMR studies. *J. Phys. Chem. B* **118**, 3281–3290 (2014).
18. Valentine, K. G. et al. Reverse micelles as a platform for dynamic nuclear polarization in solution NMR of proteins. *J. Am. Chem. Soc.* **136**, 2800–2807 (2014).
19. Wang, X. et al. Optimization and prediction of the electron-nuclear dipolar and scalar interaction in H-1 and C-13 liquid state dynamic nuclear polarization. *Chem. Sci.* **6**, 6482–6495 (2015).
20. Liu, G. Q. et al. One-thousand-fold enhancement of high field liquid nuclear magnetic resonance signals at room temperature. *Nat. Chem.* **9**, 676–680 (2017).
21. Bielytskyi, P. et al. 13C → 1H transfer of light-induced hyperpolarization allows for selective detection of protons in frozen photosynthetic reaction center. *J. Magn. Reson.* **293**, 82–91 (2018).
22. Dubroca, T. et al. A quasi-optical and corrugated waveguide microwave transmission system for simultaneous dynamic nuclear polarization NMR on two separate 14.1 T spectrometers. *J. Magn. Reson.* **289**, 35–44 (2018).
23. Dubroca, T., Wi, S., van Tol, J., Frydman, L. & Hill, S. Large volume liquid state scalar Overhauser dynamic nuclear polarization at high magnetic field. *Phys. Chem. Chem. Phys.* **21**, 21200–21204 (2019).
24. Narasimhan, S. et al. DNP-supported solid-state NMR spectroscopy of proteins inside mammalian cells. *Angew. Chem. Int. Ed.* **58**, 12969–12973 (2019).
25. Orlando, T. et al. Dynamic nuclear polarization of C-13 nuclei in the liquid state over a 10 Tesla field range. *Angew. Chem. Int. Ed.* **58**, 1402–1406 (2019).
26. Olsen, G. L. et al. Sensitivity-enhanced three-dimensional and carbon-detected two-dimensional NMR of proteins using hyperpolarized water. *J. Biomol. NMR* **74**, 161–171 (2020).
27. Wang, Y., Kim, J. & Hilty, C. Determination of protein-ligand binding modes using fast multi-dimensional NMR with hyperpolarization. *Chem. Sci.* **11**, 5935–5943 (2020).
28. Ardenkjaer-Larsen, J. H. et al. Increase in signal-to-noise ratio of > 10,000 times in liquid-state NMR. *Proc. Natl Acad. Sci. USA* **100**, 10158–10163 (2003).
29. Dzien, P. et al. Following metabolism in living microorganisms by hyperpolarized H-1 NMR. *J. Am. Chem. Soc.* **138**, 12278–12286 (2016).
30. Novakovic, M. et al. A 300-fold enhancement of imino nucleic acid resonances by hyperpolarized water provides a new window for probing RNA refolding by 1D and 2D NMR. *Proc. Natl Acad. Sci. USA* **117**, 2449–2455 (2020).
31. Otikovs, M., Olsen, G. L., Kupce, E. & Frydman, L. Natural abundance, single-scan C-13-C-13-based structural elucidations by dissolution DNP NMR. *J. Am. Chem. Soc.* **141**, 1857–1861 (2019).
32. Szekely, O., Olsen, G. L., Novakovic, M., Rosenzweig, R. & Frydman, L. Assessing site-specific enhancements imparted by hyperpolarized water in folded and unfolded proteins by 2D HMQC NMR. *J. Am. Chem. Soc.* **142**, 9267–9284 (2020).
33. Krummenacker, J. G., Denysenkov, V. P. & Prisner, T. F. Liquid state DNP on metabolites at 260 GHz EPR/400 MHz NMR frequency. *Appl. Magn. Reson.* **43**, 139–146 (2012).
34. Neugebauer, P. et al. Liquid state DNP of water at 9.2 T: an experimental access to saturation. *Phys. Chem. Chem. Phys.* **15**, 6049–6056 (2013).
35. Neugebauer, P. et al. High-field liquid state NMR hyperpolarization: a combined DNP/NMRD approach. *Phys. Chem. Chem. Phys.* **16**, 18781–18787 (2014).
36. Noack, F., Krüger, G. J., Müller-Warmuth, W. & Van Steenwinkel, R. Stochastische Prozesse in Spinsystemen. *Z. Naturforsch. A* **22**, 2102–2108 (1967).
37. Müller-Warmuth, W., Van Steenwinkel, R. & Noack, F. Dynamic nuclear polarization experiments on 19F in solutions and their interpretation by the 'pulse model' of molecular collisions. *Z. Naturforsch. A* **23**, 506–513 (1968).
38. Liebe, H. J., Hufford, G. A. & Manabe, T. A model for the complex permittivity of water at frequencies below 1 THz. *Int. J. Infrared Millim. Waves* **12**, 659–675 (1991).
39. Denysenkov, V. & Prisner, T. Liquid state dynamic nuclear polarization probe with Fabry−Perot resonator at 9.2 T. *J. Magn. Reson.* **217**, 1–5 (2012).
40. Dorn, H. C., Gu, J., Bethune, D. S., Johnson, R. D. & Yannoni, C. S. The nature of fullerene solution collisional dynamics—a C-13 DNP and NMR-study of the C60/C6D6/TEMPO system. *Chem. Phys. Lett.* **203**, 549–554 (1993).
41. Banci, L., Camponeschi, F., Ciofi-Baffoni, S. & Piccioli, M. The NMR contribution to protein−protein networking in Fe−S protein maturation. *J. Biol. Inorg. Chem.* **23**, 665–685 (2018).

42. Bertini, I. et al. Ultrafast MAS solid-state NMR permits extensive C-13 and H-1 detection in paramagnetic metalloproteins. *J. Am. Chem. Soc.* **132**, 5558–5559 (2010).
43. Bertini, I., Luchinat, C. & Parigi, G. *Solution NMR of Paramagnetic Molecules: Applications to Metallobiomolecules and Models* (Elsevier Science Ltd., 2001).
44. Pell, A. J., Pintacuda, G. & Grey, C. P. Paramagnetic NMR in solution and the solid state. *Prog. Nucl. Magn. Reson. Spectrosc.* **111**, 1–271 (2019).
45. Westler, W. M., Lin, I. J., Perczel, A., Weinhold, F. & Markley, J. L. Hyperfine-shifted C-13 resonance assignments in an iron-sulfur protein with quantum chemical verification: Aliphatic C-H center dot center dot center dot S 3-center-4-electron interactions. *J. Am. Chem. Soc.* **133**, 1310–1316 (2011).
46. Morishima, I., Endo, K. & Yonezawa, T. Nuclear magnetic resonance contact shifts induced by hydrogen bonding with organic radicals. I. Proton and carbon-13 contact shifts of protic molecules in the presence of the nitroxide radical. *J. Am. Chem. Soc.* **93**, 2048–2050 (1971).
47. Morishima, I., Inubushi, T., Endo, K., Yonezawa, T. & Goto, K. Interaction between closed- and open-shell molecules. VII. Carbon-13 contact shift and molecular or obital studies on the charge-transfer interaction between halogenated molecules and nitroxide radical. *J. Am. Chem. Soc.* **94**, 4812–4818 (1972).
48. Morishima, I., Inubushi, T. & Yonezawa, T. Stable free-radicals as NMR spin probe for studying intermolecular interactions .12. C-13 contact shifts and electron-spin delocalization induced by charge-transfer interaction between halogenated molecules and stable free-radicals. *J. Am. Chem. Soc.* **98**, 3808–3814 (1976).
49. Morishima, I., Inubushi, T., Yonezawa, T. & Kyogoku, Y. Proton magnetic-resonance studies of specific association of nucleic-acid constituent bases in a non-aqueous solvent—utility of DTBN radical to probe affinity of hydrogen-bonding involved in complementary base-pairs. *J. Am. Chem. Soc.* **99**, 4299–4305 (1977).
50. Morishima, I., Okada, K. & Yonezawa, T. Nuclear magnetic resonance contact shifts, and electron spin distribution. Proton and carbon-13 contact-shift studies of azanaphthalenes. *J. Am. Chem. Soc.* **94**, 1425–1430 (1972).
51. Morishima, I., Toyoda, K., Yoshikawa, K. & Yonezawa, T. Interaction between closed-shell and open-shell molecules—nuclear nagnetic-resonance contact shift studies on Pi-hydrogen bonding involving stable hydrocarbon Pi radicals. *J. Am. Chem. Soc.* **95**, 8627–8630 (1973).
52. Morishima, I., Yonezawa, T., Goto, K., Imanari, M. & Kawakami, K. Interactions between closed-shell and open-shell molecules—C-13 contact shift studies on interaction between aromatic-hydrocarbons and nitroxide radical. *J. Am. Chem. Soc.* **94**, 6555–6557 (1972).
53. Qiu, Z. W., Grant, D. M. & Pugmire, R. J. Paramagnetic C-13 shifts induced by the free-radical Tempo .2. nitrogen-heterocycles. *J. Am. Chem. Soc.* **106**, 557–563 (1984).
54. Brintzinger, H. H. & Marvich, R. H. Metastable form of titanocene—formation from a hydride complex and reactions with hydrogen, nitrogen, and carbon monoxide. *J. Am. Chem. Soc.* **93**, 2046–2048 (1971).
55. Russ, J. L. et al. Nitroxide/substrate weak hydrogen bonding: attitude and dynamics of collisions in solution. *J. Am. Chem. Soc.* **129**, 7018–7027 (2007).
56. Denysenkov, V. P. et al. High-field DNP spectrometer for liquids. *Appl. Magn. Reson.* **34**, 289–299 (2008).
57. Janesko, B. G., Verma, P., Scalmani, G., Frisch, M. J. & Truhlar, D. G. M11plus, a range-separated hybrid meta functional incorporating nonlocal rung-3.5 correlation, exhibits broad accuracy on diverse databases. *J. Phys. Chem. Lett.* **11**, 3045–3050 (2020).
58. Abragam, A. *The Principles of Nuclear Magnetism* (Clarendon Press, 1961).
59. Cryer, J. D. & Chan, K. S. *Time Series Analysis: With Applications in R* 2nd edn (Springer-Verlag, 2008).
60. Ebbinghaus, S. et al. An extended dynamical hydration shell around proteins. *Proc. Natl Acad. Sci. USA* **104**, 20749–20752 (2007).
61. He, X., Sode, O., Xantheas, S. S. & Hirata, S. Second-order many-body perturbation study of ice Ih. *J. Chem. Phys.* **137**, 204505 (2012).
62. Nibali, V. C. & Havenith, M. New insights into the role of water in biological function: studying solvated biomolecules using terahertz absorption spectroscopy in conjunction with molecular dynamics simulations. *J. Am. Chem. Soc.* **136**, 12800–12807 (2014).
63. Sun, J. et al. Understanding THz spectra of aqueous solutions: glycine in light and heavy water. *J. Am. Chem. Soc.* **136**, 5031–5038 (2014).
64. Xu, Y. & Havenith, M. Perspective: Watching low-frequency vibrations of water in biomolecular recognition by THz spectroscopy. *J. Chem. Phys.* **143**, 170901 (2015).
65. Liu, J. F., He, X., Zhang, J. Z. H. & Qi, L. W. Hydrogen-bond structure dynamics in bulk water: insights from ab initio simulations with coupled cluster theory. *Chem. Sci.* **9**, 2065–2073 (2018).
66. Grechko, M. et al. Coupling between intra- and intermolecular motions in liquid water revealed by two-dimensional terahertz-infrared-visible spectroscopy. *Nat. Commun.* **9**, 885 (2018).
67. Frisch, M. J. b. et al. Gaussian 16, revision A.03. (Gaussian, Inc.: Wallingford, CT, USA, 2016).
68. Zhao, Y. & Truhlar, D. G. The M06 suite of density functionals for main group thermochemistry, thermochemical kinetics, noncovalent interactions, excited states, and transition elements: two new functionals and systematic testing of four M06-class functionals and 12 other functionals. *Theor. Chem. Acc.* **120**, 215–241 (2008).
69. Wang, J., Wolf, R. M., Caldwell, J. W., Kollman, P. A. & Case, D. A. Development and testing of a general amber force field. *J. Comput. Chem.* **25**, 1157–1174 (2004).
70. Case, D. A. et al. *Amber 2018* (University of California, 2018).
71. Krzywinski, M. et al. Circos: an information aesthetic for comparative genomics. *Genome Res.* **19**, 1639–1645 (2009).
72. Provencher, S. W. CONTIN: a general purpose constrained regularization program for inverting noisy linear algebraic and integral equations. *Comput. Phys. Commun.* **27**, 229–242 (1982).
73. Berne, B. J. & Harp, G. D. in *Advances in Chemical Physics* 63−227 (John Wiley & Sons Ltd., 1970).
74. Day, J. T. On the numerical solution of linear Volterra integral equations. *BIT Numer. Math.* **7**, 71–72 (1967).
75. Dai, D. et al. Room-temperature DNP NMR spectroscopy of small biological molecules in water, simulations of TEMPOL. *Zenodo* https://doi.org/10.5281/zenodo.5150908 (2021).

Acknowledgements

J.M. thanks FOCUS program funded by Goethe University of Frankfurt for some initial financial supports for this project. V.D., D.D. and T.P. acknowledge the DFG (Deutsche Forschungsgemeinschaft, Grant No. 405972957) for financial support. X.H. and C.G. acknowledge the support by NSFC-DFG collaborative research grant (NSFC Grant No. 21761132022, DFG Grant No. GL 307/12-1). X.H. acknowledges the NSFC (National Natural Science Foundation of China, Grant Nos. 21922301, 21673074), the National Key R&D Program of China (Grant Nos. 2016YFA0501700, 2019YFA0905201), Shanghai Municipal Natural Science Foundation (Grant No. 18ZR1412600), and the Fundamental Research Funds for the Central Universities. The Supercomputer Center of East China Normal University (ECNU Multifunctional Platform for Innovation 001) is acknowledged for providing computer resources. X.W. acknowledges the National Natural Science Foundation of China (Grant No. 21703206) for financial supports. X.-L.Y. is funded by the China Scholarship Council (CSC), China-Thailand International Cooperation Project (Grant No. 2071101213), Horizontal scientific research fund (Grant No. 0205151583). Gabriele Sentis and Sridhar Sreeramulu (Goethe University of Frankfurt, FB14) are thanked for their kind helps on some solution NMR experiments, and Signals GmbH & Co is thanked for assisting the data management.

Author contributions

J.M. and X.H. conceived the project. D.D., V.D., and J.M. performed the NMR experiments. X.W., Y.L., and X.H. performed the DFT calculations and QM/MM simulations. J.M. analyzed paramagnetic NMR data. D.D., J.M., and T.P. analyzed ODNP NMR data. J.M., X.H. X.W., and Y.L. analyzed and interpreted DFT and QM/MM MD data. J.M., X.H., and T.P. supervised the overall project. C.G. and X.Y. offered additional expertize on ODNP and solution NMR spectroscopy. J.M., X.H., D.D., and T.P. wrote the manuscript.

Funding

Open Access funding enabled and organized by Projekt DEAL.

Competing interests

The authors declare no competing interests.

Additional information

Supplementary information The online version contains supplementary material available at https://doi.org/10.1038/s41467-021-27067-0.

Correspondence and requests for materials should be addressed to Xiao He or Jiafei Mao.

Peer review information *Nature Communications* thanks the anonymous reviewer(s) for their contribution to the peer review of this work.

Supplementary Information

Room-Temperature Dynamic Nuclear Polarization Enhanced NMR Spectroscopy of Small Biological Molecules in Water

Danhua Dai[†],[1,2] Xianwei Wang[†],[3,4] Yiwei Liu,[3] Xiaoliang Yang,[5,6,] Clemens Glaubitz,[2,7]

Vasyl Denysenkov,[1,2] Xiao He[*],[3,8] Thomas Prisner,[1,2] Jiafei Mao[*2,7]

[1.] Institute of Physical and Theoretical Chemistry, Goethe University Frankfurt, 60438 Frankfurt am Main, Germany

[2.] Center for Biomolecular Magnetic Resonance, Goethe University Frankfurt, 60438 Frankfurt am Main, Germany

[3.] Shanghai Engineering Research Center of Molecular Therapeutics and New Drug Development, School of Chemistry and Molecular Engineering, East China Normal University, Shanghai, 200062, China

[4.] College of Science, Zhejiang University of Technology, Hangzhou, Zhejiang, 310023, China

[5.] Jiangsu Key Laboratory of Advanced Organic Materials, School of Chemistry and Chemical Engineering, Nanjing University, Nanjing, 210023, China

[6.] State Key Laboratory of Coordination Chemistry, School of Chemistry and Chemical Engineering, Nanjing University, Nanjing, 210023, China

[7.] Institute of Biophysical Chemistry, Goethe University Frankfurt, 60438 Frankfurt am Main, Germany

[8.] NYU-ECNU Center for Computational Chemistry at NYU Shanghai, Shanghai, 200062, China

[†] These authors contributed equally to the work

* Corresponding authors. Email addresses: xiaohe@phy.ecnu.edu.cn (X.H., https://orcid.org/0000-0002-4199-8175), j.mao@em.uni-frankfurt.de (J.M., https://orcid.org/0000-0003-1547-325X)

Supplementary Note 1. Brief introduction of ODNP theory for the general audience

ODNP is a result of e-N cross-relaxation. In the case of a spin pair by one electron and one ^{13}C nucleus spins, we consider an energy diagram 2*2 states (electron α and β states and ^{13}C α and β states). The spin dynamics of I (^{13}C) and S (electron) are coupled in this system via cross-relaxation rates R_{IS} and can be described phenomenologically by Solomon equation:

$$\frac{d}{dt}\begin{bmatrix} S_z(t) \\ I_z(t) \end{bmatrix} = \begin{bmatrix} -R_{1S} & -R_{IS} \\ -R_{IS} & -R_{1I} \end{bmatrix} \begin{bmatrix} S_z(t) - S_z(0) \\ I_z(t) - I_z(0) \end{bmatrix}$$

where R_{1S}, R_{1I} and R_{IS} are longitudinal relaxation rates of S-spin, I-spin and the I-S spin pair cross-relaxation rates, respectively.

In a steady state and assuming the electron spin S is only partially saturated by microwave, the explicit form of Solomon equation can be simplified as:

$$\begin{bmatrix} 0 \\ 0 \end{bmatrix} = \begin{bmatrix} -R_{1S} & -R_{IS} \\ -R_{IS} & -R_{1I} \end{bmatrix} \begin{bmatrix} -s \cdot S_z(0) \\ I_z(t) - I_z(0) \end{bmatrix}$$

where *s* stands for the saturation factor.

The ODNP enhancement (of steady state that assumes adequately long interscan delay) can be obtained from this equation:

$$\varepsilon_{ODNP} = \frac{I_z(t \to \infty)}{I_z(0)} = 1 + s \cdot \frac{R_{IS}}{R_{13C}} \cdot \frac{S_z(0)}{I_z(0)} = 1 - s \cdot \frac{R_{IS}}{R_{13C}} \cdot \left|\frac{\gamma_e}{\gamma_{13C}}\right|$$

where the ^{13}C relaxation rate R_{13C} contains the paramagnetic contributions.

$$R_{13C} = R_{13C}^{dia} + R_{13C}^{para}$$

We than rewrite the above equation as

$$\varepsilon_{ODNP} = 1 - s \cdot \frac{R_{IS}}{R_{13C}^{para}} \cdot \frac{R_{13C}^{para}}{R_{13C}} \cdot \left|\frac{\gamma_e}{\gamma_{13C}}\right|$$

$$\zeta = \frac{R_{IS}}{R_{13C}^{para}} \quad f = \frac{R_{13C}^{para}}{R_{13C}}$$

where ζ is coupling factor and f is leakage factor. When the ^{13}C T1 relaxation is dictated by the paramagnetic effect, leakage factor f is close to 1. The coupling factor presents the

competition between e-^{13}C cross-relaxation and paramagnetic-enhanced ^{13}C T1 relaxation. The cross-relaxation rate R_{IS} can be further dissected as below:

$$R_{IS}=R_{DQ}-R_{ZQ}=R_{DQ}^{dipolar}-R_{ZQ}^{dipolar}-R_{ZQ}^{scalar}$$

As shown by the scalar spin-spin interaction Hamiltonian, the scalar interaction only drives ZQ relaxation here. Therefore, the ODNP enhancement on ^{13}C is always positive if scalar interaction is dominating.

This equation links the macroscopic relaxation rates with microscopic spin-spin fluctuations. All these cross-relaxations are driven by the fluctuation of respect spin-spin interactions. In the case of rapid isotropic fluctuation, the macroscopic ZQ scalar relaxation can be linked to the microscopic fluctuations as below[1,2]:

$$\widehat{\mathcal{H}}_{IS}^{S}=\frac{1}{2}A(t)(\hat{I}_{+}\hat{S}_{-}+\hat{I}_{-}\hat{S}_{+})$$

$$J_{IS}^{S}(\omega)=\int_{-\infty}^{\infty}\overline{A(t)A(t+\tau)}\,e^{-i\omega\tau}d\tau=\int_{-\infty}^{\infty}|A|^{2}e^{-t/\tau_{s}}\,e^{-i\omega\tau}d\tau=\frac{2\tau_{s}}{\omega^{2}\tau_{s}^{2}+1}$$

$$R_{IS}^{S}=\frac{1}{3\hbar^{2}}J_{IS}^{S}(\omega_{ZQ})=\frac{2}{3}\cdot\left(\frac{A}{\hbar}\right)^{2}\cdot S(S+1)\cdot\frac{\tau_{s}}{\omega_{ZQ}^{2}\tau_{s}^{2}+1}$$

where A stands for the scale of hyperfine interaction, S is the quantum spin number and τ_s is the autocorrelation time of fluctuation of spin-spin scalar interaction. The spectral density function should be in dimension T^{-1}. Here the Lorentzian spectral density function is yielded from the exponential autocorrelation function. These forms can only be held for the idea Ornstein-Uhlenbeck process (**S9**). While the mode of the fluctuation does not match this simplest picture, the modification of the spectral density is required. One simple modification of the above model is so-called "pulse" model[3,4], in which the pulse-composed Poisson process yields an exponential spectral density function:

$$J_{IS}^{S}(\omega)=\frac{4\langle a\rangle^{2}\tau_{w}^{2}}{\tau_{p}}\exp\left(-\omega^{2}\tau_{w}^{2}\right)$$

where $\langle a\rangle$ is the amplitude of the scalar hyperfine pulse, τ_p^{-1} is the frequency of pulses and τ_w is the width (similar to correlation time) of the pulse.

In our long-living radical-substrate complexes, the mode of the Fermi contact fluctuation driving the scalar cross-relaxation processes is even much more complex. In particular, the autocorrelation function of the fluctuation is not simple exponential forms and the

corresponding spectral density function is very complex. The processes featuring the complex auto-correlation functions can be described more precisely via the autoregressive model (see **S9** below for more details). Here we derive an approximated version to link the spectral density of such complex processes with scalar ZQ relaxation time. In our systems the memory time (10^1 fs) is relative shorter than the Fermi contact fluctuation (spin-density fluctuation, 10^{-1} ps) and both are much shorter than the e-^{13}C cross-relaxation time (10^{-1} to 10^1 s).

$$\tau_{memory} < \tau_{Fermi} \ll T_{IS}^{scalar}$$

So we have taken the scalar relaxation theory in [1] as an approximation and incorporated an "arbitrary" form of spectral density:

$$J_{IS}^{s}(\omega) = \int_{-\infty}^{\infty} \overline{A(t)A(t+\tau)}\, e^{-i\omega\tau} d\tau = \int_{-\infty}^{\infty} \overline{X\rho(t)X\rho(t+\tau)}\, e^{-i\omega\tau} d\tau$$
$$= X^2 \cdot \mathcal{F}[G_\rho(t)] = X^2 \cdot G_\rho(0) \cdot j_\rho(\omega)$$

$$R_{IS}^{s} = \frac{1}{3\hbar^2} J_{IS}^{s}(\omega_{ZQ}) = \frac{1}{3} \cdot \left(\frac{X}{\hbar}\right)^2 \cdot S(S+1) \cdot G_\rho(0) \cdot j_\rho(\omega_{ZQ})$$

where X is the conversion factor from spin density to hyperfine coupling constant, $G_\rho(0)$ is the spin-density autocorrelation function at zero time shift, $j_\rho(\omega_{ZQ})$ is the spectral density at the ZQ frequency.

Supplementary Note 2. Lifetime of indole-TEMPO complex

Here we consider the reaction

$$\text{indole + TEMPO} \underset{k_{-1}}{\overset{k_1}{\rightleftharpoons}} \text{indole} \cdots \text{TEMPO}$$

The rate constants k_1 and k_{-1} defines equilibrium constant K:

$$K = \frac{k_1}{k_{-1}}$$

The up-limit of the formation rate of indole-TEMPO complex is defined by the diffusion-limited molecular collision in solution:

$$\max(k_1) = k_{Diff} = \frac{2RT}{3\eta}(r_{indole} + r_{TEMPO})(\frac{1}{r_{indole}} + \frac{1}{r_{TEMPO}})$$

in which η is the viscosity of solvent and r presents the molecular radius.

The radius of indole and TEMPO molecules are 3.4 Å[5,6]. Therefore the up-limit of k_1 in CCl_4 at 300 K is:

$$\max(k_1) = \frac{8RT}{3\eta} = 7.4\times10^9\ L \cdot mol^{-1} \cdot s^{-1}$$

The equilibrium constant K was reported in Ref. [7]. Taking this value, the minimal lifetime of indole-TEMPO complex can be obtained:

$$\min(\tau_{complex}) = \frac{1}{\max(k_{-1})} = \frac{\mathrm{K}}{\max(k_1)} = \frac{0.89}{7.4\times10^9} s = 120\ ps$$

Since the equilibrium constant of the indole-TEMPO complex was determined from the paramagnetic effects, the estimated minimal lifetime of indole-TEMPO should be qualified enough for the discussions in this work.

Supplementary Note 3. Binding affinity and lifetime of CCl_4-TEMPONE complex

First, the binding affinity of CCl_4-TEMPONE complex was approximated from the experimental molar-free carbon paramagnetic shift ($\overline{\delta_{para}}$) and carbon Fermi contact hyperfine constant A/h (4.65 MHz) from the previous DFT calculations in Gauss.[8] The Fermi contact shift δ_{con} of CCl_4 in CCl_4-TEMPONE complex can be calculated as:

$$\frac{A}{h}(^{13}C) = \frac{\mu_0\mu_e g_e \mu_N g_{13C}}{3S * h}\rho = 1.124\times10^3\ \rho$$

$$\delta_{con} = \frac{\mu_0\mu_B^2 g_e^2 (S+1)}{9kT}\rho = 1.186\times10^5\ \rho$$

where hyperfine coupling constant A/h is in MHz and spin density ρ is in atomic unit (Bohr radius as the distance unit) as also used in the Gaussian program. The contact shift δ_{con} is in ppm and the δ_{con} – ρ conversion applies ubiquitously for any types of nuclear spins. We take S = ½ and T = 298 K for our case.

Using the above equations, we have the spin density on CCl_4 carbon is $4.14*10^{-3}$ and the corresponding Fermi contact shift would be $1.57*10^3$ ppm. The $\overline{\delta_{para}}$ is only 25.7 ppm,

which is much smaller than the Fermi contact shift, and could contain a dipolar contribution. We can therefore estimate the up-limit of the binding affinity of CCl_4-TEMPONE complex as

$$K \approx \frac{\overline{\delta_{para}}}{\delta_{con}} = 1.6\times10^{-2}M^{-1}$$

Similar to S7, we take the radius of CCl_4 (2.45 Å[9]) and TEMPONE (3.5 Å[10]), we estimate the lifetime of indole-TEMPO complex as 2.1 ps, which is line with the magnitude of previous results[11].

Supplementary Note 4. Brief introduction on the spin density fluctuation - autocorrelation function, spectral density, autoregressive AR model

The spin density trajectory from QM/MM MD trajectory of a single molecular complex *ρ(t)* can be Fourier transformed to a frequency spectral the profile of which is the spectral density function of the random process (Supplementary Figure 4). Alternatively, *the autocorrelation function $G_\rho(t)$ and the normalized form $g_\rho(t)$ of ρ(t)* can be calculated following:

$$G_\rho(t) = < \rho(t_0)\rho(t_0 + t) >$$

$$g_\rho(t) = \frac{< \rho(t_0)\rho(t_0 + t) >}{< \rho(t_0)\rho(t_0) >}$$

The Fourier transform of autocorrelation function yields spectral density function $J_\rho(t)$ and its normalized form $j_\rho(t)$ (Supplementary Figure 4)

$$J_\rho(\omega) = \mathcal{F}[G_\rho(t)] = \mathcal{F}[g_\rho(t) \cdot G_\rho(0)] = G_\rho(0) \cdot \mathcal{F}[g_\rho(t)] = G_\rho(0) \cdot j_\rho(\omega)$$

$$j_\rho(\omega) = \mathcal{F}[g_\rho(t)]$$

If the distribution of ρ(t) follows a normal distribution, the corresponding process is called a *Gaussian (random) process*. While a Gaussian process shows *an exponential correlation function*, this special process is also called *Ornstein-Uhlenbeck process* that is the most common model of the random fluctuations adapted in the majority of relaxation theories in magnetic resonance field. The Ornstein-Uhlenbeck process is a *Markovian process*, namely the evolution of the current state of the system is solely determined by the current status of the state. A Markovian process has no memory effect ("memoryless"). The spectral density function of an exponential autocorrelation function is a Lorentzian function, which is the

most seen form in NMR relaxation theories. However, the deviation of $\rho(t)$ from the ideal Ornstein-Uhlenbeck process would break down the simplified Lorentzian spectral density function. A simple example is the so-called pulse model[3,4], in which the fluctuation is in the format of a pulse-composed Poisson process, yields a peak at a non-zero frequency. The deviation from the ideal Ornstein-Uhlenbeck can occur more generally than the pulse model. First, if the distribution of $\rho(t)$ in may not follows a symmetric normal distribution, which can be caused by e.g. *an asymmetry barrier* governing the dynamic process. Second, a random process can possess a memory effect e.g. in the presence of restraints defined by the previous steps or under the "slow" impacts that require certain time to propagate to the interested site. Such behaviors often emerge in highly coupled systems. A random process with memory effect is called a *non-Markovian process*. To describe this *memory effect*, the so-called *memory function* $K_g(t)$ can be derived following:

$$\frac{\partial}{\partial t} G_\rho(t) = -\int_0^t K_g(\tau)\, g_\rho(t-\tau)\, d\tau$$

Here $K_g(t)$ is also sometimes called *memory kernel*. The solution $K_g(t)$ of the above Volterra integral equation for an exponential $g_\rho(t)$ is a δ-function, which indicates a zero-memory effect. While $g_\rho(t)$ describes a non-Markovian process, the corresponding $K_\rho(t)$ shows a finite decay. (Supplementary Figure 4)

In a highly simplified picture, a random Ornstein-Uhlenbeck process drives the spin relaxation when the correlation time of the random process approaches the characteristic frequency (e.g. e-^{13}C ZQ frequency for the scalar cross-relaxation) of the specific spin Hamiltonian responsive for the relaxation. In this picture, *the random process (e.g. a molecular motion) opens the relaxation channel for dissipating the spin energy to the environment (or so-called "lattice")*. The stochastic feature often indicates that such a process is coupled to a large degree of freedom and therefore ensures the presence of a lattice to which the spin energy can dissipate efficiently. Here, the stochastic process can be viewed as a "superposition" of a large number of individual processes that seems coupled due to the complexity (high degrees of freedom) of the system ("lattice").

In our QM/MM simulations, peaks appear in low THz frequency regime that also hits e-^{13}C ZQ frequency. Conceivably the local coupling of spin interactions and the low THz motion takes place. Different from the IR modes that are often originated from highly localized molecular motions, THz modes arise commonly from the collective motions involve higher degrees of freedom IR motions. The presence of THz oscillation features at various molecular interfaces (indole/TEMPO, TEMPO/CCl_4) suggests the further extension of the coupling network.(Supplementary Figure 7m-a) In our system, the coupling of certain low-

THz modes to the environment is likely present as indicated by the significant breath of the modes that are beyond the resolution of the Fourier transform.(Supplementary Figure 7)

To resolve the complex pattern of autocorrelation functions derived from our QM/MM MD simulations, we have turned to the time series analysis with a rather generally used model called autoregressive model (AR). AR model describes the time evolution of spin density *ρ(t)* following the hypothesis:

$$\rho(t_n) = \sigma(t_n) + \sum_{i=1}^{p} \theta_i \, \rho(t_{n-i})$$

where $\rho(t_n)$ is related to p previous steps with coefficient θ_1(previous point) to θ_p(previous p^{th} point) and $\sigma(t)$ is the random noise with zero average and variance σ^2. In a discrete form such as the QM/MM MD simulation, an Ornstein-Uhlenbeck process can be described by memoryless AR(1) model. AR of higher orders contains a memory effect.

We can apply Z-transform to AR(p) model:

$$P(z)(1 + \sum_{i=1}^{p} \theta_i \, z^{-k}) = E(z)$$

$$z = \exp\,(i\omega T_s)$$

where T_s is the sampling period, and ω is frequency.

The spectral density function (square root of power spectrum) can be expressed in the following form:

$$G(\omega) = \left| \frac{\sigma}{1 + \sum_{i=1}^{p} \theta_i \exp\,(-ip\omega T_s)} \right|$$

The AR(p>1) models show three unique characteristics relevant to our data analysis. First, the autocorrelation function of an AR(p>1) model shows both an initial decay and the sinusoidal waves. Second, the spectral density function (or its squared power spectrum) of AR(p>1) model show p/2 peaks. Third, the damping factor D, frequency Ω and phase φ of the sinusoidal waves in power spectrum are determined by the factors θ_i. For example, in a simple AR(2) model, we have[12]:

$$D = \sqrt{-\theta_2}\,, \quad \Omega = cos^{-1}\left(\frac{\theta_1}{\sqrt{-2\theta_2}}\right), \quad \varphi = tan^{-1}\left(\frac{1-\theta_2}{1+\theta_2}\right)$$

Supplementary Note 5. Estimation of zero-quantum e-^{13}C scalar cross-relaxation rates from QM/MM MD simulation

In indole-TEMPO complex $\tau_{memory} < \tau_{Fermi} \ll T_{ZQ}$, so we use the conventional relaxation theory of the isotropic fluctuation of spin-spin scalar coupling[1] as an approximation for evaluating the impact of spin density fluctuation obtained from QM/MM MD in driving e-^{13}C ZQ cross-relaxation. We have

$$R_{ZQ} = \left(\frac{2\mu_0\mu_e g_e \mu_N g_{13C}}{3\hbar}\right)^2 \cdot G(0) \cdot j(\omega_{ZQ})$$

where the first term scales the spin density to Fermi hyperfine constant as defined $A/\hbar$ (= $2\pi A/h$). The $G(0) * j(\omega)$ is essentially equal to the spectral density of spectral density function $J(\omega)$ of unnormalized spin density autocorrelation function $G_\rho(t)$. The ZQ frequency ω_{ZQ} is equal to $2\pi * f_{ZQ}$ (1.652 THz). The spectral density functions presented in Supplementary Figure 7 are in the unit of fs (10^{-15} s). The estimated ZQ scalar cross-relaxation rates are listed in Supplementary Table 6. These reates are mostly in the order of magnitude of 10^{-1} to 10^{1} s^{-1}, which agrees qualitatively with the observed DNP enhancement factors.

Supplementary Note 6. The relevance of paramagnetic NMR in DNP inspired by a Google search

By taking the molecules "halogenated solvent" and "radical" investigated in a previous seminal ODNP work[8] as the key words, a Google search returned a collection of EPR and computational chemistry studies on these catalogues of molecules. Interestingly this search, likely "biased" by the personal search history, also suggested a paramagnetic NMR work on relevant molecular systems,[13] which immediately enlightened us about an overlooked link between paramagnetic NMR and ODNP spectroscopy.

Supplementary Discussion. Additional factors that may complicates the derivation of ODNP enhancement from paramagnetic NMR and QM/MM MD results

It appears that a simple correlation between $\overline{\delta_{para}}$, the spectral density function of Fermi contact fluctuation and the ODNP enhancement is not straightforward (Supplementary Table 6), which is likely due to multiple factors. The $\overline{\delta_{para}}$ parameter contains also the dipolar contribution and is impacted by macroscopic magnetic susceptibility, therefore only provides a qualitative rather than the quantitative measure of spin density. The frequency-resolution of the spectral density function derived from our QM/MM MD trajectory is still limited by the total duration (10 ps) of the simulation. A follow-up *ab initio* computational

study aiming a trajectory beyond 100 ps is currently underway. Our first glimpse into the more extended 20-ps trajectory shows that the oscillations at 10^2 fs time scale indeed persist (Supplementary Figure 5t, S6t). Beside the complexities in $\overline{\delta_{para}}$ and computed spectral density, the observed ODNP enhancement also contains contributions from the other hyperpolarization transfer pathways including the direct dipolar e-^{13}C ODNP and the indirect e-^{1}H-^{13}C polarization transfer. The direct dipolar e-^{13}C ODNP yields negative ^{13}C enhancement that could neutralize partially the positive scalar ODNP enhancement. This contribution is especially profound on the bridge carbons in indole and the carboxylate carbons in amino acids. Similar to the scalar e-N interaction, the dipolar e-N crosstalk in a long-living radical-substrate complex also presents rather complex dynamic features, not to mention the breaking-down of the point-dipole approximation in the closely engaged radical-substrate complexes with delocalized spin densities (Supplementary Figure 11j-p). We have also observed in general the negative ^{1}H enhancement in our systems (Supplementary Figure 1e-f, Supplementary Table 3-S4). In fast-tumbling small molecules, the negatively enhanced ^{1}H polarization could interconvert with the positive ^{13}C hyperpolarization via ^{1}H-^{13}C heteronuclear NOE (hNOE) effect (Supplementary Figure 11u-v).[14-16] All the abovementioned mechanistic complexities perplex the quantitative prediction of ODNP enhancement, which consolidates the value of $\overline{\delta_{para}}$ as a qualitative but highly practical indicator of scalar ODNP performance.

Supplementary Table 1. ODNP NMR samples used in this work

Target molecule	Target concentration (M)	Radical*	Solvent
Indole (U-^{13}C)	2.0	TEMPO	CCl_4
Indole (2-^{13}C)	2.0	TEMPO	CCl_4
$^{13}CCl_4$	≈ 20	TEMPONE	$^{13}CCl_4$
imidazole (2-^{13}C, U-^{15}N)	1.0	TEMPO	$CDCl_3$
imidazole (2-^{13}C, U-^{15}N)	2.0 (pH* = 11.0)	TEMPOL	D_2O
glucose (U-^{13}C)	2.0 (pH = 7.3)	TEMPOL	H_2O
glycine (U-^{13}C)	2.0 (pH = 6.1)	TEMPOL	H_2O
alanine (U-^{13}C)	1.4 (pH = 6.0)	TEMPOL	H_2O
serine (U-^{13}C)	2.0 (pH = 5.7)	TEMPOL	H_2O
proline (U-^{13}C)	2.0 (pH = 6.2)	TEMPOL	H_2O

* radical concentration was 100 mM for all samples

Supplementary Table 2. Summary of ODNP NMR spectra of indole, imidazole and CCl_4 acquired on HC probehead

compound	solvent	radical	site	chemical shift* (ppm, - mw)	chemical shift* (ppm, + mw)	$^1J_{CH}$ (Hz)	$^1J_{CC}$ (Hz)	DNP Enhancement
indole	**CCl_4**	**TEMPO**	C2	124.6	123.3	181	67	14.1 ± 2.5 ($^{13}C_2$) 26.2± 2.4 (U-^{13}C)
			C3	102.2	101.4	170	62	11.6 ± 1.1
			C3a	127.0	127.0†	-	-	-1.8 ± 0.5
			C4/5/6	119.7	119.5	n.r.‡	n.r.‡	5.4 ± 0.2
			C7	111.0	109.9	157	62	20.7 ± 2.5
			C7a	134.5	135.0	-	-	-2.1 ± 0.5
			H_N¶	7.23	7.04	-	-	-9.5 ± 0.0
			H2¶	6.61	6.31	n.r.‡	-	-1.5 ± 0.1
			H3¶	6.41	6.17	n.r.‡	-	-8.7 ± 0.0
			H4¶	7.57	7.30	n.r.‡	-	-8.9 ± 0.1
			H5/6¶	7.07	6.83	n.r.‡	-	-10.9 ± 0.0
			H7¶	6.87	6.60	n.r.‡	-	-11.8 ± 0.0
CCl_4	**CCl_4**	**TEMPONE**	C	97.9	91.7	-	-	92.4 ± 19.4
imidazole§	**$CDCl_3$**	**TEMPO**	H2	7.86	7.57	n.r.‡	-	-5.2 ± 0.4
			H4/5	7.30	7.02	n.r.‡	-	-4.0 ± 0.2
imidazole§	**D_2O**	**TEMPOL**	C2	-	136.2	n.r.‡	-	> 0 (low S/N)
			H2	7.70	7.36	n.r.‡	-	-12.3 ± 4.0
			H4/5	7.33	7.02	n.r.‡	-	-18.7 ± 1.7
			HDO	4.70	3.34	-	-	-39.2 ± 2.4

* all chemical shifts are referenced indirectly to TMS
† this peak is assigned tentatively
‡ not resolved (n.r.)
¶ values extracted from spectral deconvolution
§ no stable enhancement values can be obtained due to the severe sample heating

Supplementary Table 3. Summary of ODNP NMR spectra of water-soluble compounds acquired on FP probehead

compound	solvent	radical	site	chemical shift* (ppm, - mw)	chemical shift* (ppm, + mw)	$^1J_{CH}$ (Hz)	$^1J_{CC}$ (Hz)	DNP Enhancement
imidazole	**D_2O**	**TEMPOL**	C2	136.2	136.0	n.r.‡	n.r.‡	50 ± 10
			H2/4/5	7.12 (broad)	7.64	n.r.‡	n.r.‡	-5.0 ± 0.3
			HDO	4.70	5.18	-	-	-9.5 ± 0.2
glucose	**H_2O**	**TEMPOL**	C1 (β)	96.1	95.9	154	n.r.‡	5.9 ± 1.9
			C1 (α)	92.2	92.0	156	n.r.‡	6.9 ± 2.2
			C3 (β)	76.0	75.9	n.r.‡	59	
			C2 (β)	74.2	74.2	n.r.‡	59	2.2 ± 0.4
			C3 (α)	73.0	73.1	n.r.‡	50	(C2/3/4/5)
			C2 (α)/C4 (α+β)	71.5	71.5	n.r.‡	65	
			C5(α+β)	69.8	69.9	n.r.‡	74	
			C6 (α+β)	61.1	61.1	136	n.r.‡	6.8 ± 1.8
			$H_{glucose}$ + H_2O	4.70	4.65	n.r.‡	-	-8.3 ± 0.2
glycine	**H_2O**	**TEMPOL**	Cα	41.8	41.9	141	n.r.‡	10.7 ± 1.7
			C’	172.5	n.r.‡	-	n.r.‡	ca. -1†
			Hα	3.16¶	3.22¶	n.r.‡	n.r.‡	10.0 ± 0.1¶
			H_2O	4.70	5.02	n.r.‡	-	-9.8 ± 0.1
alanine	**H_2O**	**TEMPOL**	Cα	50.8	50.8	134	n.r.‡	6.0 ± 1.6
			Cβ	16.7	16.4	131	n.r.‡	6.1 ± 2.2
			C’	175.9	n.r.‡	-	n.r.‡	ca. -1†
			Hβ	1.19	n.r.‡	n.r.‡	n.r.‡	n.r.‡
			Hα + H_2O	4.70	4.48	n.r.‡	n.r.‡	-10.2 ± 0.1
serine	**H_2O**	**TEMPOL**	Cα	56.5	56.2	155	n.r.‡	6.0 ± 0.1
			Cβ	60.3	60.0	145	n.r.‡	6.5 ± 0.1
			C’	172.5	n.r.‡	-	n.r.‡	ca. -1†
			H_{serine} + H_2O	4.70	4.03	n.r.‡	n.r.‡	-7.0 ± 0.1

Supplementary Table 3. continue

compound	solvent	radical	site	chemical shift* (ppm, - mw)	chemical shift* (ppm, + mw)	$^1J_{CH}$ (Hz)	$^1J_{CC}$ (Hz)	DNP Enhancement
proline	**H_2O**	**TEMPOL**	Cα	61.3	61.5	144	n.r.‡	4.5 ± 0.5
			Cδ	46.3	46.3	145	n.r.‡	10.5 ± 0.8
			Cβ	29.1	29.0	128	n.r.‡	6.9 ± 0.7
			Cγ	23.8	23.8	133	n.r.‡	8.2 ± 0.7
			C’	174.5	n.r.‡	-	n.r.‡	ca. -1†
			Hβ2/γ	1.78	1.98	n.r.‡	n.r.‡	-2.9 ± 0.2
			$H_{\alpha/\beta1/\delta}$ + H_2O	4.70	3.39	n.r.‡	n.r.‡	-7.0 ± 0.1

* all chemical shifts are referenced indirectly to TMS

† this value is estimated by the disappearance of C’ signal on ODNP NMR spectrum

‡ not resolved (n.r.)

¶ values extracted from spectral deconvolution

Supplementary Table 4. Summary of paramagnetic shifts and ODNP enhancements*

compound	solvent	radical	site	Molar-free paramagnetic chemical shift (ppm)	DNP Enhancement
indole	**CCl_4**	**TEMPO**	C2	16.21 ± 0.09	14.1 ± 2.5 ($^{13}C_2$)
					26.2± 2.4 (U-^{13}C)
			C3	14.65 ± 0.07	11.6 ± 1.1
			C3a	11.66 ± 0.07	-1.8 ± 0.5
			C4/5/6	8.17 ± 0.38	5.4 ± 0.2
			C7	14.42 ± 0.09	20.7 ± 2.5
			C7a	10.19 ± 0.07	-2.1 ± 0.5
CCl_4	**CCl_4**	**TEMPONE**	C	25.69 ± 0.07	92.4 ± 19.4
					(430 ± 50)†
CBr_4	**CCl_4**	**TEMPONE**	C	120.4 ± 0.7	128.9 ± 12.9‡
					(600 ± 60)†
$CHCl_3$	**$CHCl_3$**	**TEMPONE**	C	46.13 ± 0.63	68.8 ± 12.9‡
					(320 ± 60)†
diethyl malonate	**diethyl malonate**	**TEMPONE**	C2	13.38 ± 0.11	6.4 ± 2.1‡ (30 ± 10)†
ethyl acetoacetate	**ethyl acetoacetate**	**TEMPONE**	C2	11.36 ± 0.09	3.9 ± 0.2‡ (18 ± 1)†
			C4	10.85 ± 0.08	2.8 ± 0.4‡ (13 ± 2)†
pyruvic acid	**pyruvic acid**	**TEMPONE**	C3	6.28 ± 0.15	2.8 ± 0.4‡ (13 ± 2)†
imidazole	**D_2O**	**TEMPOL**	C2	4.93 ± 0.02	50 ± 10
glucose	**H_2O**	**TEMPOL**	C1 (β)	1.86 ± 0.02	5.9 ± 1.9
			C1 (α)	2.05 ± 0.02	6.9 ± 2.2
			C3 (β)	1.78 ± 0.02	
			C2 (β)	1.43 ± 0.02	2.2 ± 0.4 (C2/3/4/5)
			C3 (α)	1.27 ± 0.01	
			C2 (α)/C4 (α+β)	1.87 ± 0.02	
			C5(α+β)	1.47 ± 0.02	
			C6 (α+β)	3.06 ± 0.02	6.8 ± 1.8

Supplementary Table 4. Continue

compound	solvent	radical	site	Molar-free paramagnetic chemical shift (ppm)	DNP Enhancement
glycine	**H_2O**	**TEMPOL**	Cα	2.98 ± 0.03	10.7 ± 1.7
			C’	0.68 ± 0.01	ca. -1
alanine	**H_2O**	**TEMPOL**	Cα	1.93 ± 0.02	6.0 ± 1.6
			Cβ	3.27 ± 0.02	6.1 ± 2.2
			C’	0.68 ± 0.01	ca. -1
serine	**H_2O**	**TEMPOL**	Cα	1.83 ± 0.01	6.0 ± 0.1
			Cβ	2.43 ± 0.01	6.5 ± 0.1
			C’	0.68 ± 0.01	ca. -1
proline	**H_2O**	**TEMPOL**	Cα	2.11 ± 0.04	4.5 ± 0.5
			Cδ	3.52 ± 0.04	10.5 ± 0.8
			Cβ	3.06 ± 0.04	6.9 ± 0.7
			Cγ	3.59 ± 0.05	8.2 ± 0.7
			C’	0.27 ± 0.01	ca. -1

* DNP enhancements in organic solvents (white background) or water (gray background) were measured on HC probehead.or FP probehead respectively. All enhancement values are determined at 9.4 T.

† the DNP enhancement in parenthesis was reported in Ref. [1].

‡ the DNP enhancement value was scaled from the results reported in Ref. [1] via the DNP enhancements determined on CCl_4.

Supplementary Table 5. Summary of spin density and hyperfine coupling of TEMPOL-amino acid complexes by DFT calculations

substrate	binding site	H-bond length (Å)	H-bond angle (°)	ΔΔG† (kJ/mol)	spin density |ρ|*10⁴ (atomic unit)					
					N	C'	Cα	Cβ	Cγ	Cδ
glycine	NH_2	2.092	158.0	0	68.6	23.2	27.7	-	-	-
	Cα	2.400	118.5	7.65	1.26	7.44	52.8	-	-	-
alanine	NH_2	2.076	164.8	0.00	71.8	1.33	6.88	12.6	-	-
	Cα	2.326	131.3	7.67	0.33	2.95	13.3	21.9	-	-
	Cβ (CH_3)	2.447	165.5	8.74	1.36	0.18	1.19	20.3	-	-
serine	NH_2	2.098	155.9	0.00	96.4	0.09	2.00	2.30	-	-
	Cα	2.294	125.0	0.18	1.71	5.5	9.09	1.40	-	-
	Cβ	2.452	163.0	3.37	4.24	0.64	3.88	36.9	-	-
	OH	1.815	161.6	-15.7	0.22	0.24	5.90	11.1	-	-
proline	NH	2.125	162.5	0.00	15.7	4.22	2.62	0.74	0.59	1.43
	Cα	2.307	137.6	3.82	0.27	0.05	37.6	13.22	1.26	1.20
	Cβ	2.453 (Hβ1)	137.8	3.42	0.76	29.5	6.42	70.03	1.34	7.14
		2.381 (Hβ2)	161.7	0.76	1.13	0.52	5.39	45.2	44.7	2.33
	Cγ	3.018 (Hγ1)*	93.9	3.84	0.50	7.48	4.02	60.9	3.15	9.80
		2.640 (Hγ2)	153.9	4.96	3.01	0.31	6.41	1.30	51.9	14.4
	Cδ	2.661 (Hδ1)	161.6	8.31	0.26	1.35	0.27	1.18	0.41	1.15
		2.384 (Hδ2)	157.6	2.84	0.37	0.16	0.26	1.26	0.33	22.9

† referenced to the energy of TEMPO-substrate(NH) complex

* the optimization consistently yields a structure similar to the Hβ1 complex as indicated by the much higher spin density on Cβ than Cγ

Supplementary Table 6. Summary of the mechanistic analysis of indole ODNP behaviors based on paramagnetic NMR and QM/MM MD

site	molar-free $\overline{\delta_{para}}$ (ppm)	Average spin density $\lvert\rho\rvert*10^4$ (atomic unit)	average A/h (MHz)	$G(0)*10^4$	$j_{ZQ}*10^2$ † (fs)	$Rs_{,ZQ}(s^{-1})$ ‡ QM/MM MD	^{13}C T1 (- radical)	^{13}C T1 (+ radical)	leakage factor
C2	16.21 ± 0.09	3.26	0.367	4.55	2.4	0.77	2.63 ± 0.07	0.85 ± 0.08	0.68 ± 0.05
C3	14.65 ± 0.07	0.664	$7.46*10^{-2}$	12.0	1.9	1.1	3.01 ± 0.09	1.19 ± 0.03	0.60 ± 0.00
C3a	11.66 ± 0.07	1.35	0.152	5.45	5.2	1.4	15.3 ± 1.0	1.05 ± 0.03	0.93 ± 0.04
C4/5/6	8.17 ± 0.38	5.83 (C4)	0.655 (C4)	2.05 (C4)	2.1	0.26 (C4)	2.62 ± 0.08 (C4)	1.46 ± 0.03 (C4)	0.44 ± 0.00 (C4)
		32.3 (C4)	3.63 (C5)	1.48 (C4)		0.098 (C5)	2.67 ± 0.05 (C5)	1.28 ± 0.02 (C5)	0.52 ± 0.00 (C5)
		8.19 (C4)	0.921 (C6)	12.6 (C4)		1.4 (C6)	2.34 ± 0.10 (C6)	1.68 ± 0.04 (C6)	0.28 ± 0.01 (C6)
C7	14.42 ± 0.09	1.83	0.205	785	2.2	85	2.62 ± 0.08	1.37 ± 0.04	0.48 ± 0.00
C7a	10.19 ± 0.07	0.579	$6.51*10^{-2}$	98.3	2.4	12	14.8 ± 1.0	1.07 ± 0.02	0.93 ± 0.05

† j_{ZQ} presents the "spectral density" at ω_{ZQ} on the spectral density function Fourier transformed from the normalized spin density autocorrelation function.
$\omega_{ZQ} = \omega_e - \omega_{13C}$ = (263-0.1)*2π GHz = 1.652 THz
‡ $Rs_{,ZQ}$ is the scalar coupling-driven relaxation

site	molar-free $\overline{\delta_{para}}$ (ppm)	$Rs_{,ZQ}$ (s^{-1}) QM/MM MD	^{13}C T1 (+ radical)	leakage factor	coupling factor	R_{DQ} - R_{ZQ} (s^{-1}) (back-fitted)	ODNP enhancement
C2	16.21 ± 0.09	0.77	0.85 ± 0.08	0.68	-0.013 ($^{13}C_2$) -0.024 (U-^{13}C)	-0.015 ($^{13}C_2$) -0.029 (U-^{13}C)	14.1 ± 2.5 ($^{13}C_2$) 26.2± 2.4 (U-^{13}C)
C3	14.65 ± 0.07	1.1	1.19 ± 0.03	0.60	-0.012	-0.010	11.6 ± 1.1
C3a	11.66 ± 0.07	1.4	1.05 ± 0.03	0.93	0.0020	0.002	-1.8 ± 0.5
C4/5/6	8.17 ± 0.38	0.26 (C4) 0.098 (C5) 1.4 (C6)	1.46 ± 0.03 (C4) 1.28 ± 0.02 (C5) 1.68 ± 0.04 (C6)	0.44 (C4) 0.52 (C5) 0.28 (C6)	-0.0065(C4) -0.0056 (C5) -0.010 (C6)	-0.005 (C4) -0.004 (C5) -0.006 (C6)	5.4 ± 0.2
C7	14.42 ± 0.09	85	1.37 ± 0.04	0.48	-0.027	-0.020	20.7 ± 2.5
C7a	10.19 ± 0.07	12	1.07 ± 0.02	0.93	0.0022	0.002	-2.1 ± 0.5

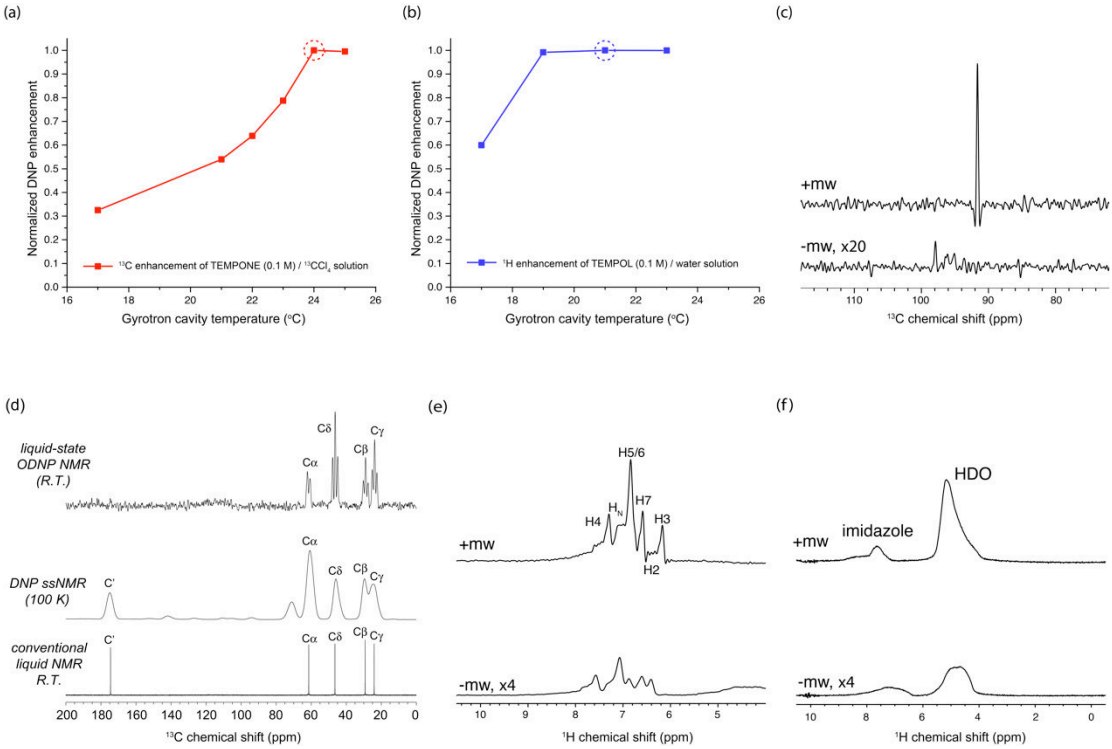

Supplementary Figure 1. ODNP NMR spectra of various compounds in organic solvent or water acquired on a 9.4 T spectrometer. (a-b) The initial search for the proper DNP working condition was performed by scanning the gyrotron cavity temperature and monitoring the signal intensity of the DNP enhanced signals of particular standard samples. (c) The ODNP enhanced ^{13}C NMR spectrum of $^{13}CCl_4$. The microwave (mw) off spectrum was accumulated with 512 scans and the mw on spectrum was acquired with 1 scan. (d) A comparison of the ODNP-enhanced R.T. liquid-state ^{13}C NMR spectrum, DNP-enhanced MAS ssNMR ^{13}C spectrum (CP-based, 110 K) and the conventional ^{1}H-decoupled liquid-state ^{13}C NMR spectra of proline acquired at 9.4 T. (e-f) ODNP-enhanced ^{1}H NMR spectra of indole and imidazole. For the spectra shown in (j), 128 and 8k scans were accumulated for the mw-on and mw-off conditions. For the spectra shown in (k), 64 and 2k scans were accumulated for the mw-on and mw-off conditions. The phase of the DNP-enhanced ^{1}H spectra are inverted here. Here, all the paired mw-on and mw-off spectra were scaled by the number of scans so that the enhancement-factors can be visualized directly despite the distinct noise level due to the very different numbers of scans used for mw-on and mw-off spectra.

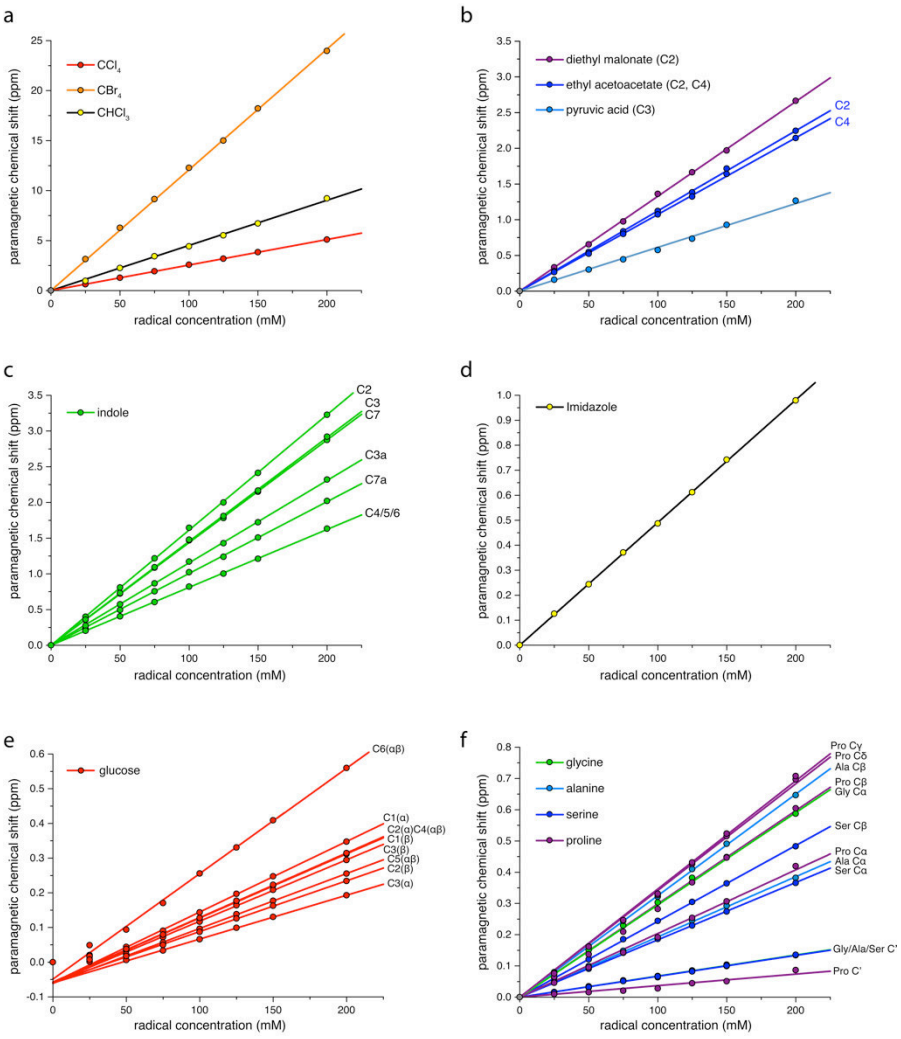

Supplementary Figure 2. Fitting of ^{13}C chemical shifts in the presence of radical at various concentrations. The molar free paramagnetic chemical shift $\overline{\delta_{para}}$ was obtained as the slope of the linear fitting of observed ^{13}C chemical shift versus the concentration of radical. The data shown in a-c were collected in organic solvents and the data in d-f were obtained in water.

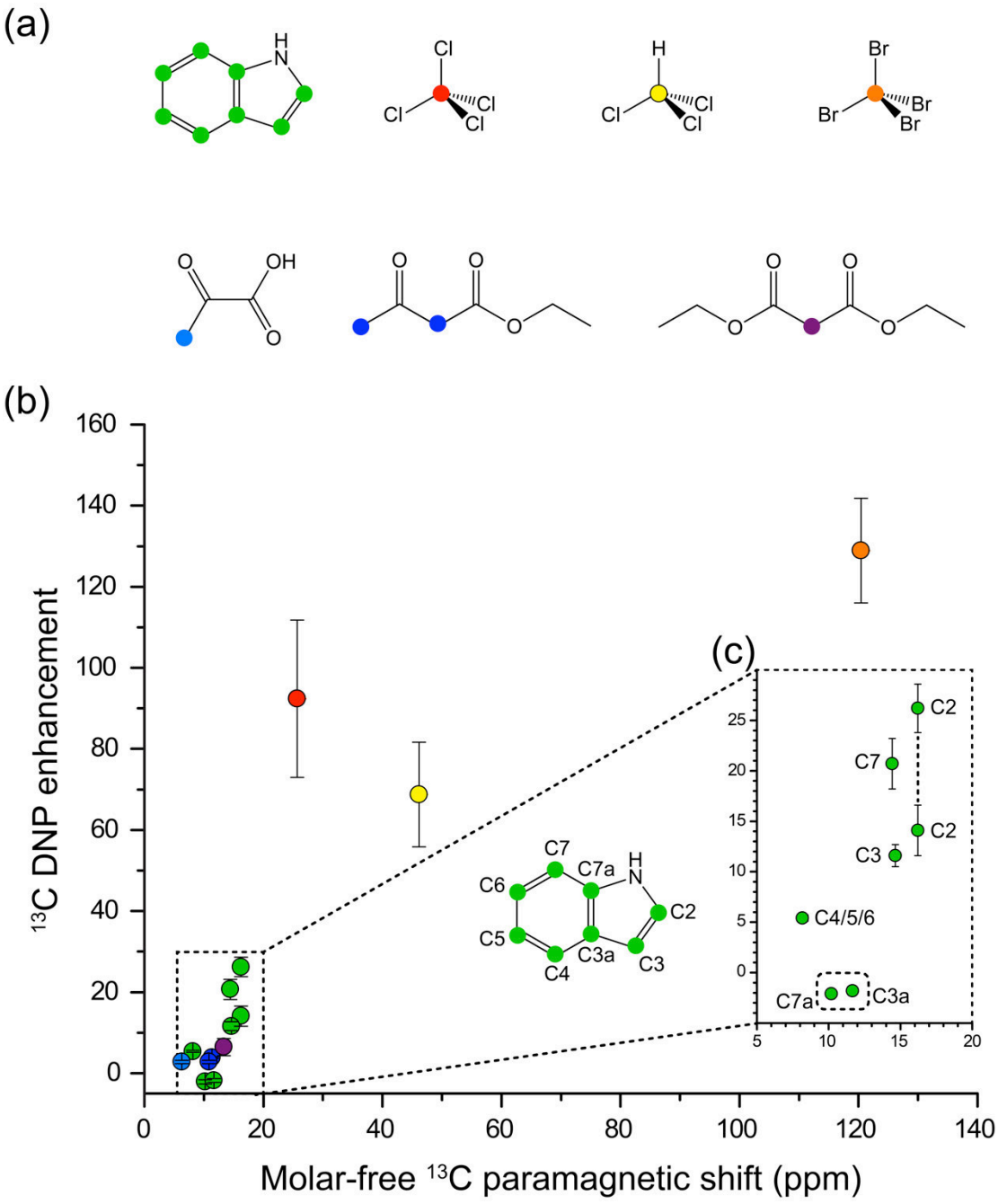

Supplementary Figure 3. ODNP ^{13}C NMR enhancement and the molar free ^{13}C paramagnetic NMR shift of various organic compounds in organic solvents. (a) The structures of the compounds. (b) A trend is visible though more deviated than that shown in Fig. 2f. (c) Data points of different ^{13}C sites in indole. Data obtained on different molecules are shown in various colors. The error of $\overline{\delta_{para}}$ is defined as fitting error or standard deviation of $\overline{\delta_{para}}$ values on carbons showing overlapping signals on ODNP spectra. The error of ODNP enhancement is determined from signal-to-noise ratio. More details about the error calculations can be found in 'Methods'.

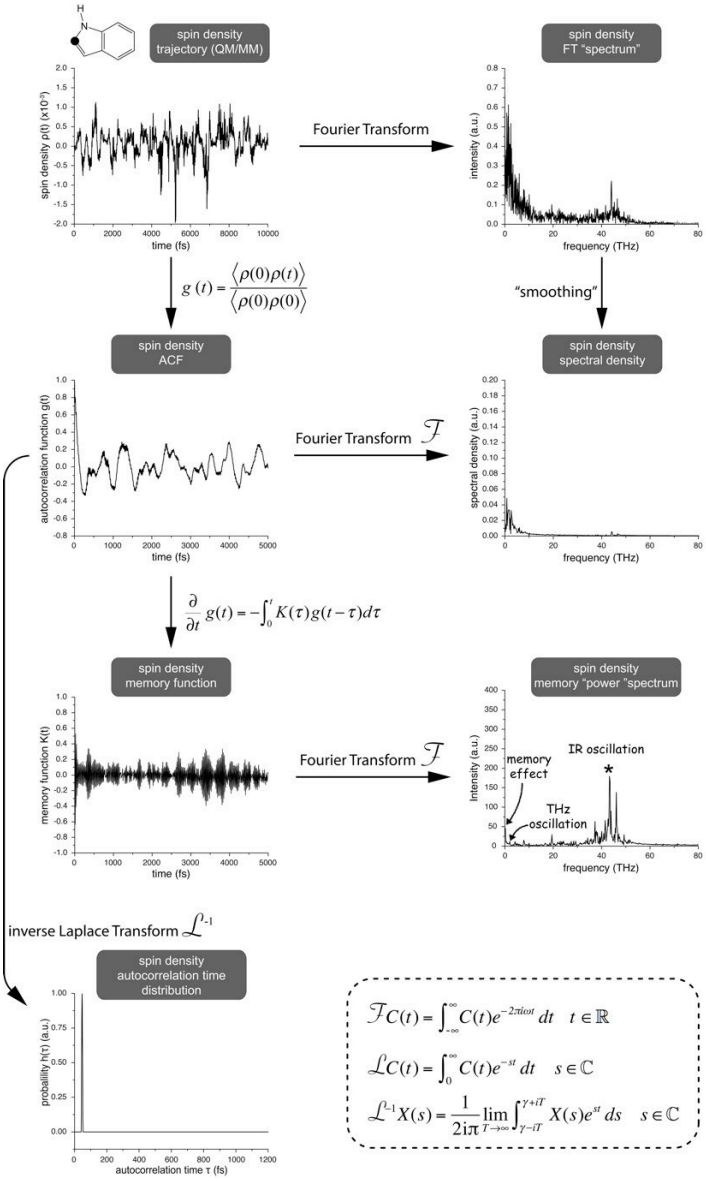

Supplementary Figure 4. Flow chart of the data analysis procedure of QM/MM MD trajectory. The detailed theoretical and mathematical grounds can be found in **S9**. The autocorrelation function $g(t)$ was computed from the trajectory data $\rho(t)$. The Fourier transform of normalized $g(t)$ gives rise to the spectral density function $j(\omega)$. The spectral density function also presents the profile of the frequency spectrum obtained by the direct Fourier transform of the trajectory time-series $\rho(t)$. The time constant of initial decay of $g(t)$ can be estimated by performing the inverse Laplace transform of $g(t)$. This fits the decay to a distribution of rates of the highly simplified exponential decay, therefore can only be taken as an estimation of the true decay kinetics of $g(t)$. The memory function $K(t)$ was further computed from $g(t)$ and the Fourier transform of $K(t)$ yields an amplitude spectrum of $K(t)$. The fast oscillations in $\rho(t)$ can be visualized in $g(t)$ and be better detected in $j(\omega)$, $K(t)$ and the Fourier transformed $K(t)$.

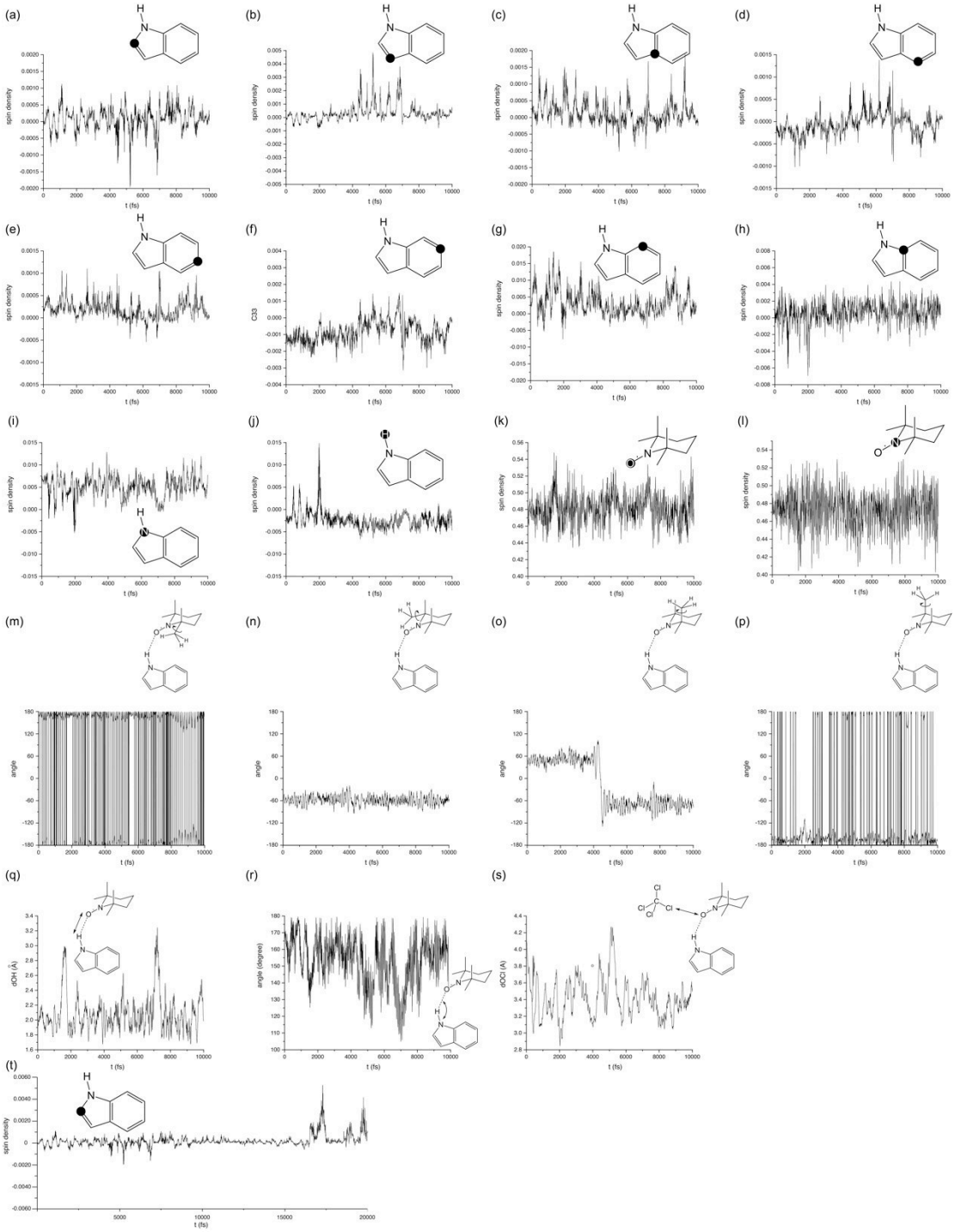

Supplementary Figure 5. Spin density (a-l) and geometry trajectories (m-s) extracted from the QM/MM MD simulation of indole-TEMPO complex in explicit CCl_4 solvent. The time duration of all trajectories is 10 ps. The spin density fluctuations at various atoms on indole and TEMPO are shown in (a-l). The rotation of TEMPO methyl groups are presented by the H(methyl)-C(methyl)-C(TEMPO ring)-N(TEMPO) torsion angle in (m-p). The fluctuations of indole-TEMPO H-bond length and the TEMPO(oxygen)-Cl(chlorine) distance are shown in (q) and (s), while the dynamics of the intermolecular H-bond angle in indole-TEMPO complex is shown in (r). For indole C2, a longer 20 ps spin density trajectory is presented in (t).

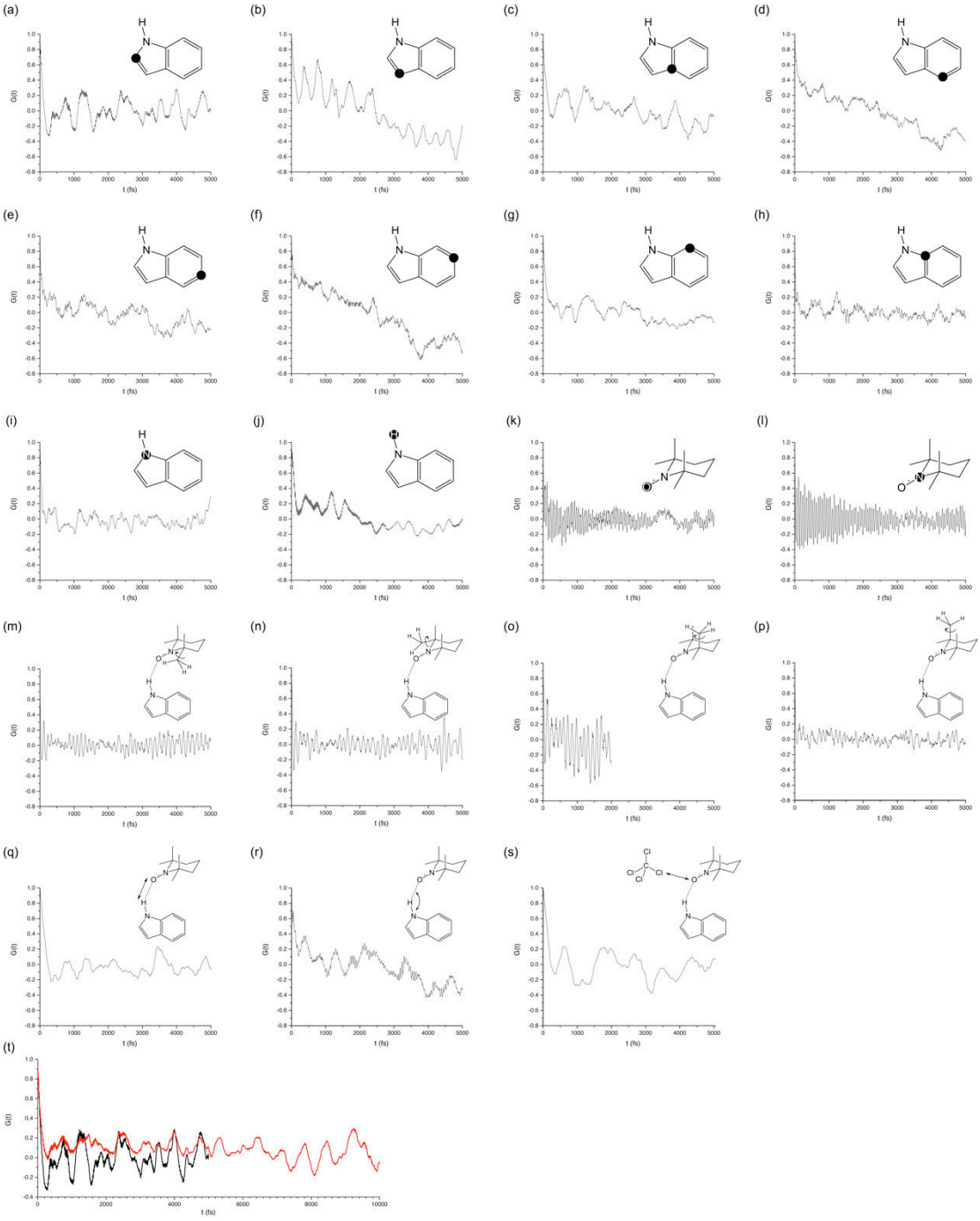

Supplementary Figure 6. Spin density (a-l) and geometry (m-s) autocorrelation functions $G(t)$ derived from the QM/MM MD simulation of indole-TEMPO complex in explicit CCl_4 solvent. The time duration is 5 ps. The spin density autocorrelation functions at various atoms on indole and TEMPO are shown in (a-l). The autocorrelation functions of the TEMPO methyl rotation process are presented in (m-p). The autocorrelation function shown in (o) is truncated due to the "intermittent" jumping in the corresponding trajectory. (Supplementary Figure 3o) The autocorrelation functions of indole-TEMPO H-bond length, indole-TEMPO H-bond angle and TEMPO(oxygen)-Cl(chlorine) distance are shown in (q-s). All autocorrelation functions feature

an initial decay compounded with oscillations components. The spin autocorrelation functions of indole atoms (a-j) and the autocorrelation functions of intermolecular geometry (q-s) show clearly the sub-ps oscillations. The spin density autocorrelation functions of TEMPO NO moiety (k-l) show more significant fs oscillations. The methyl rotation autocorrelation functions also show some fs oscillations. The spin density ACF of indole C2 derived from the extended 20 ps trajectory (Supplementary Figure 4t) is presented in (t). The major features of the ACF pattern, namely the initial decay and the oscillations, remains on this longer ACF.

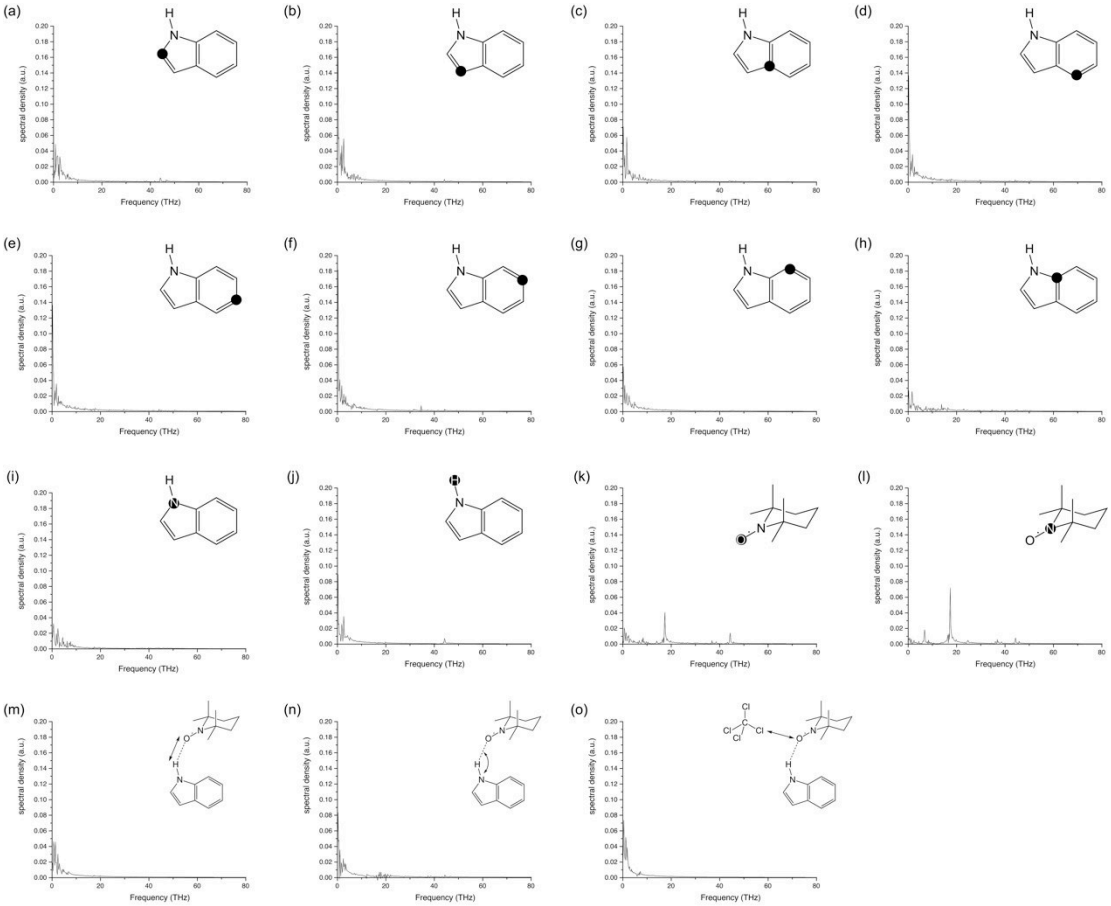

Supplementary Figure 7. Spectral density function $j(\omega)$ of spin density fluctuation (a-l) and the intermolecular dynamics (m-o) in indole-TEMPO complex. All these spectral density functions are obtained by the Fourier transform of the corresponding normalized autocorrelation functions. The spectral density functions of TEMPO NO moiety show coherent process(es) in the IR frequency range. All the spectral density functions feature the initial decay together with oscillations in the low THz regime. The low THz region of the spectral density functions is shown in the next session of Supplementary Figure 5 on the following page.

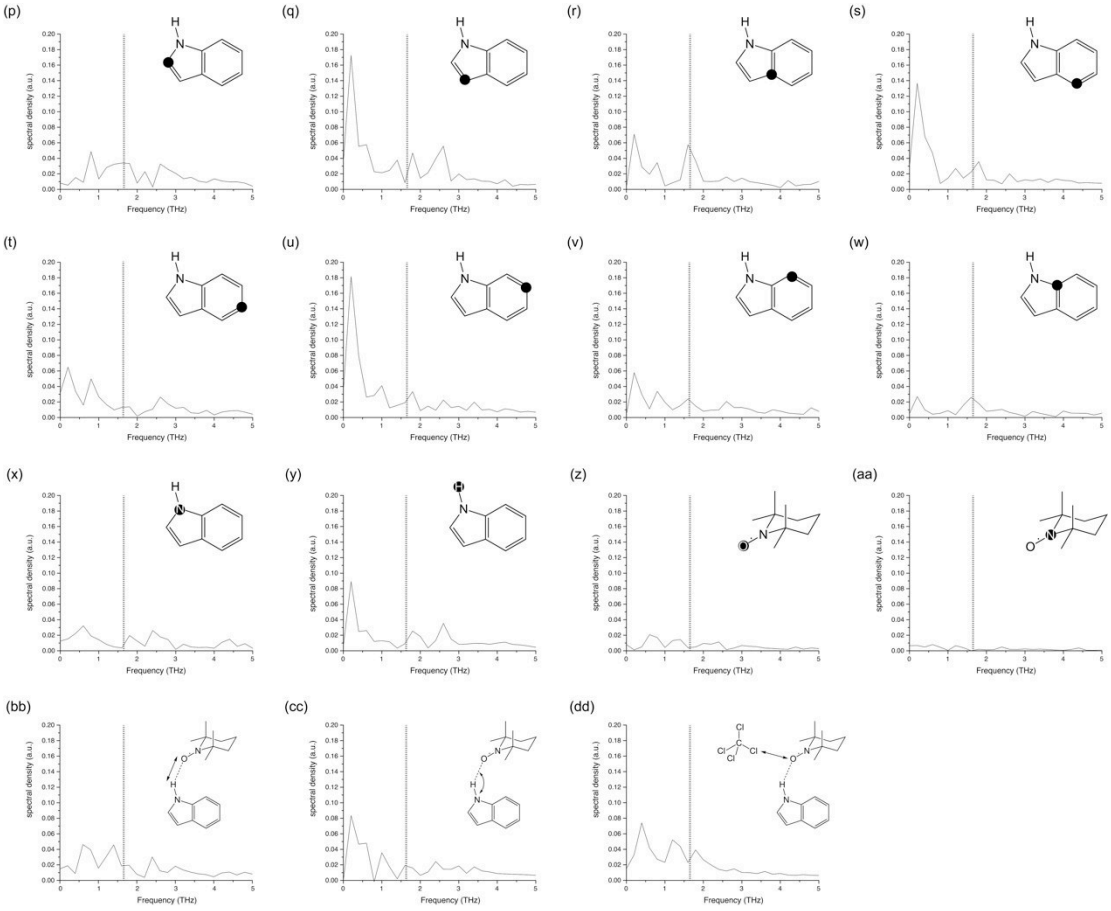

Supplementary Figure 7. (continue) Low THz region (p-dd) of the spectral density function shown in (a-o). The dashed line shows the position of e-^{13}C ZQ transition frequency at 9.4 T.

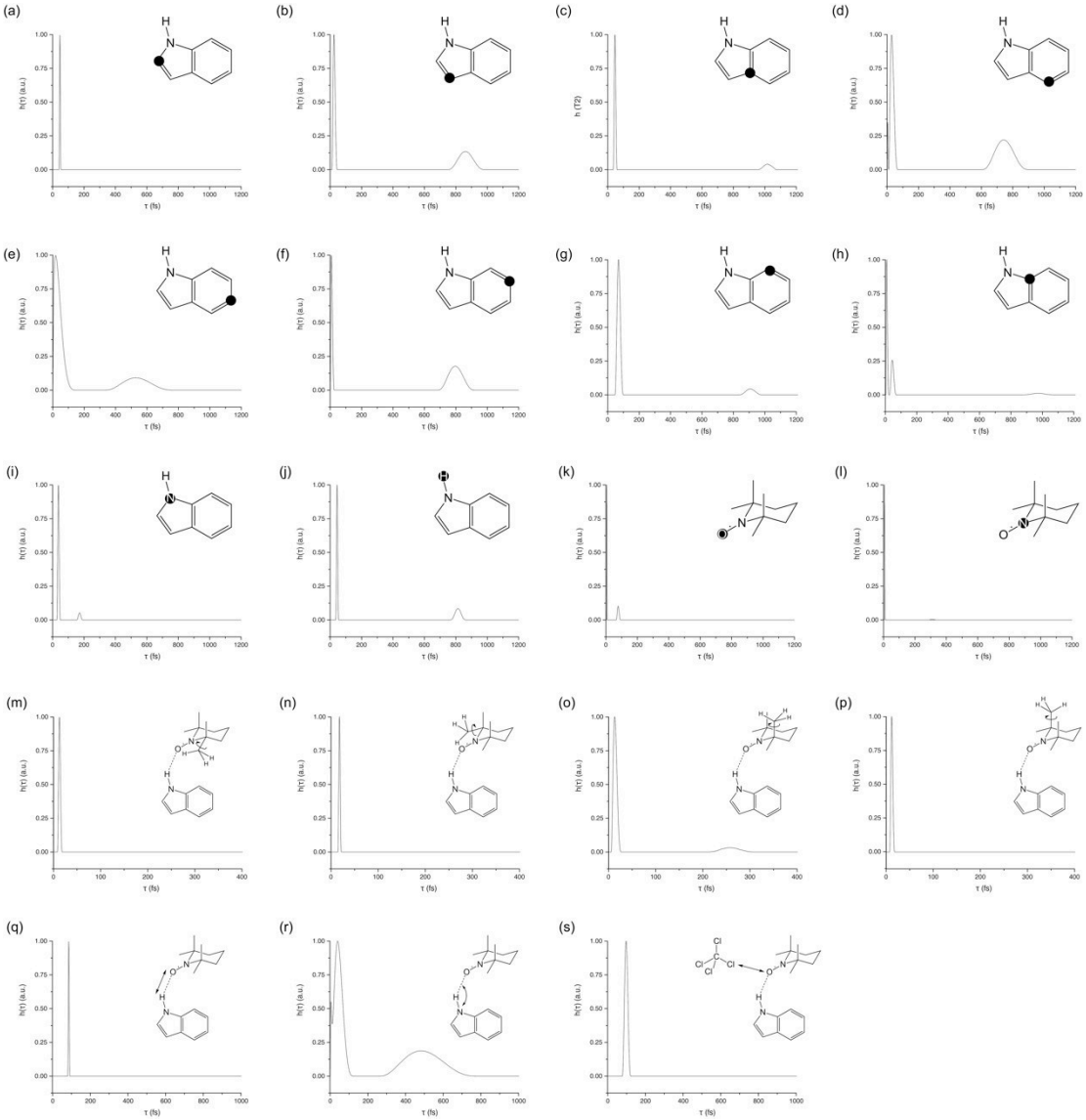

Supplementary Figure 8. Decay time constant of autocorrelation functions calculated by the inverse Laplace transform using CORTIN[17]. This protocol fits the decay of autocorrelation function as a distribution of decay time constants following the highly simplified exponential decay model. Therefore the results here only present the semi-quantitative description of the decay of autocorrelation function due to the random process. All results are normalized for clarity.

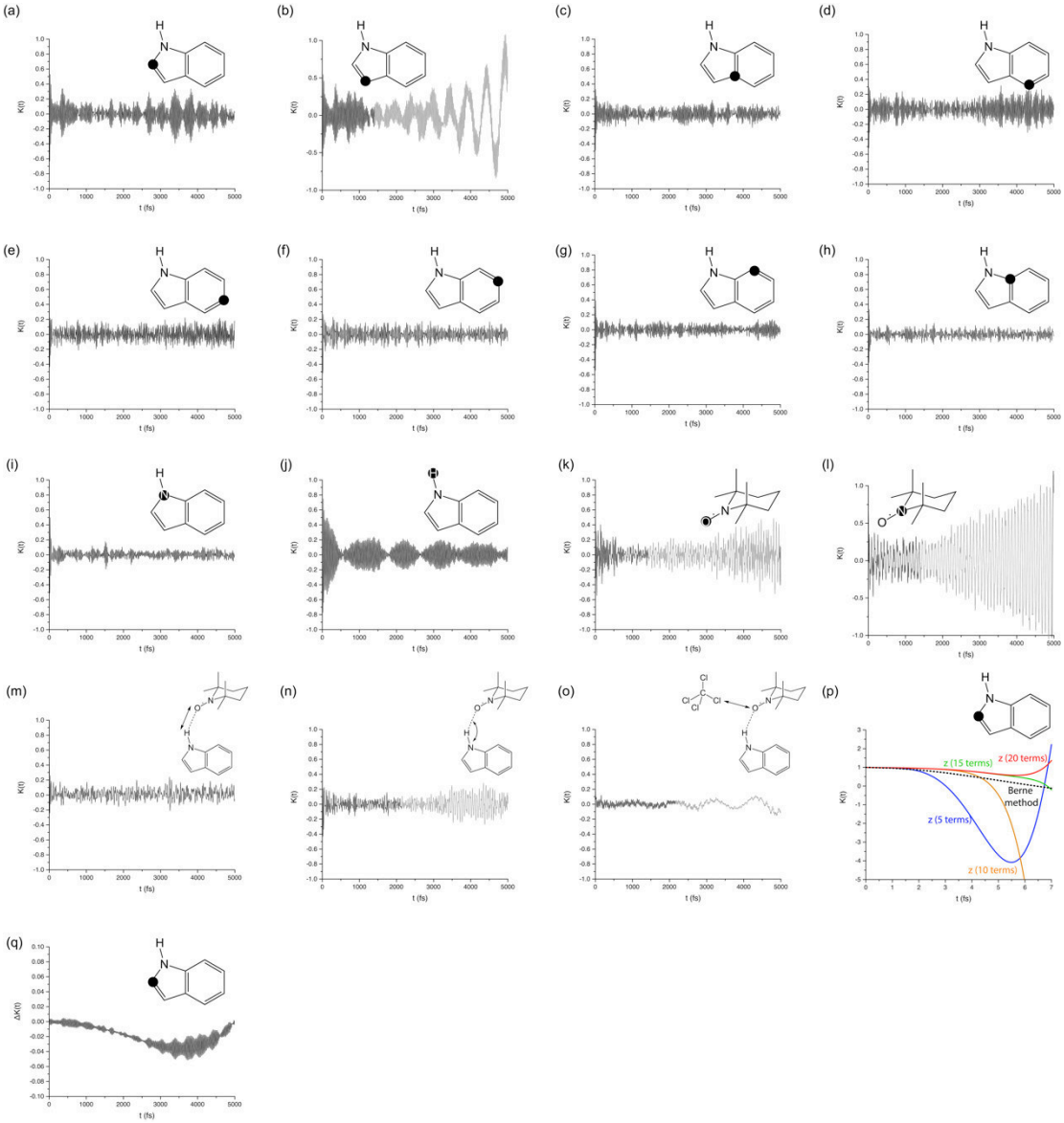

Supplementary Figure 9. Memory functions $K(t)$ of spin density fluctuations (a-k) and intermolecular dynamics (m-o) in indole-TEMPO complex. All memory functions are calculated using a numerical approach described by Berne et al.[18]. More details about the computation of memory function can be found in **S5**. The decay of $K(t)$ presents the length of the memory effect. The oscillation components are originated from the oscillations of corresponding $G(t)$ or $\rho(t)$, which are better visualized in $K(t)$. The truncated Z-transform was also use for calculating $K(t)$. However, as shown in (p), all levels of truncation (colored curves) lead to the significant deviation from the proper numerical solution (dashed black curve) and even to the rapid divergence in a few fs. Memory functions $K(t)$ can also be computed using an alternative numerical approach as described in **S5**. The deviation between two numerical approaches is shown in (q). The differences between these two numerical solutions escalate slowly and remain at a small scale. For some specific autocorrelation function $G(t)$, the numerical approach still leads to the observable divergence after more than 1000 steps (b,k,l,n.o, gray part). Nevertheless such divergence does not mask the fundamental features of those memory functions.

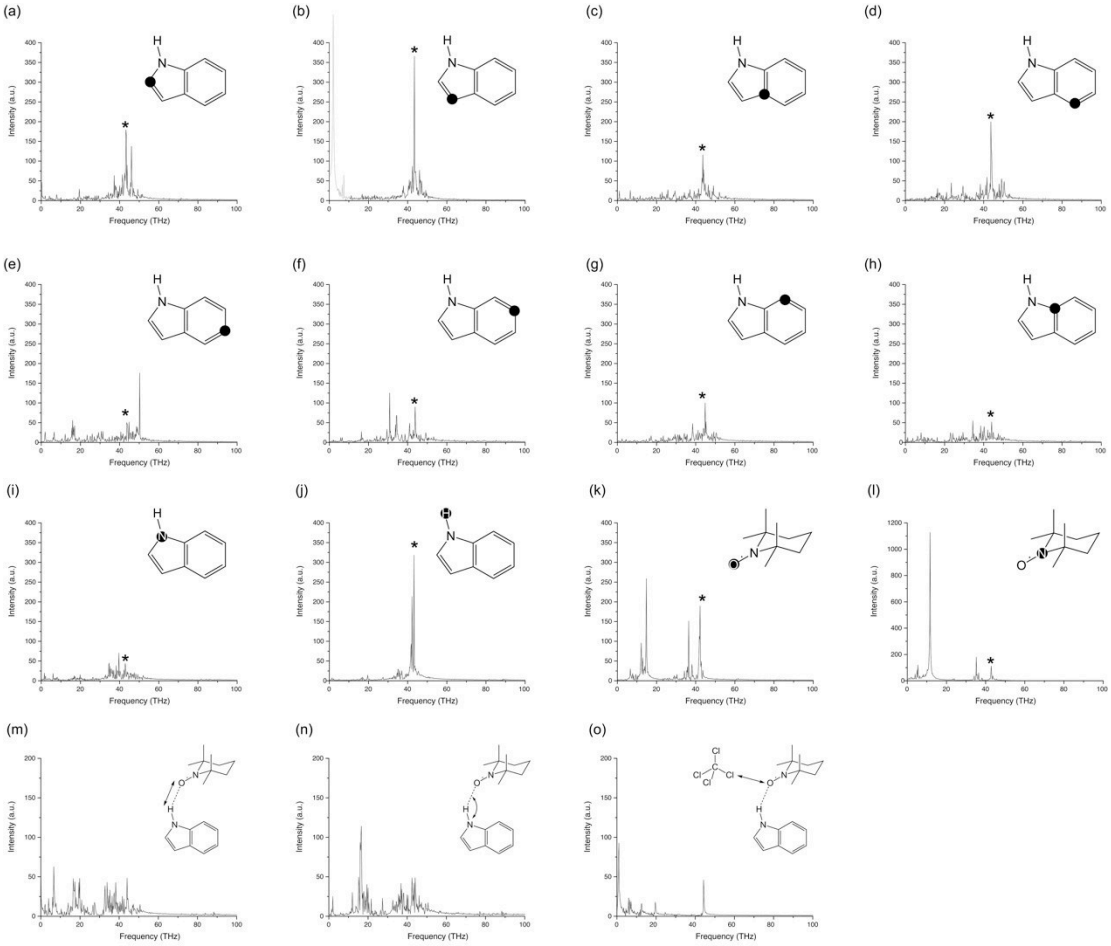

Supplementary Figure 10. Fourier transformed amplitude spectrum of memory functions $K(t)$ of the spin density fluctuation (a-l) or intermolecular dynamics (m-o) in indole-TEMPO complex. The presence of memory effect is indicated by the non-zero values at the zero frequency. The peaks in these spectra shows the presence of coherent dynamics in the original trajectory $\rho(t)$. The * symbol in (a-l) suggest a shared coherent component in the IR frequency range within the fluctuations of spin density within the whole complex, which suggests certain IR modes could modulate the electronic structure of the whole complex.

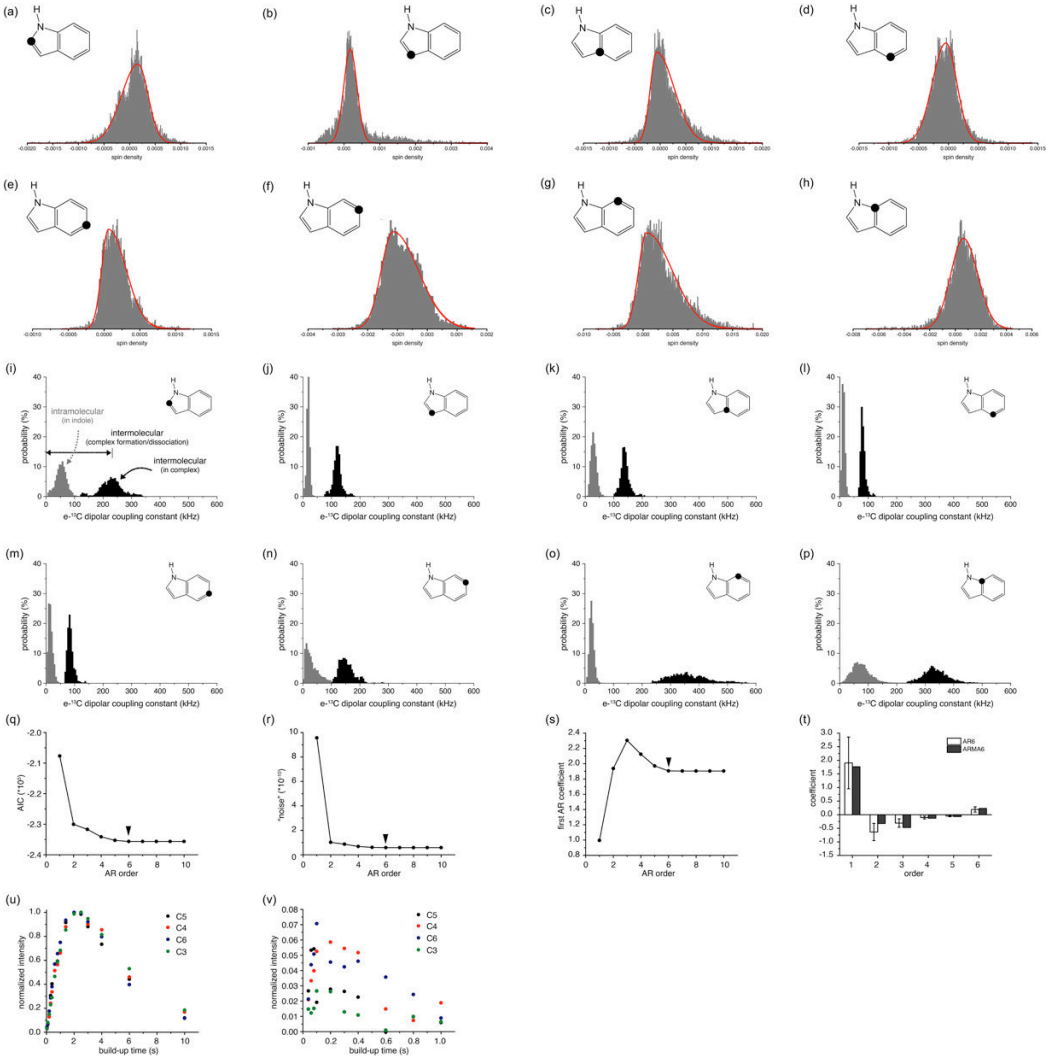

Supplementary Figure 11. Mechanistic complexity of ODNP in TEMPO-indole complex. (a-h) Most carbon spin density distribution in indole shows asymmetric distribution with significantly crossing of zero-spin density condition. (i-p) Beside the intermolecular dipolar coupling, the intramolecular dipolar coupling originated from the spin density on other indole carbons also could contribute to the dipolar ODNP. (q-s) The spin-density trajectory of indole C2 was fitted using AR(p) models of different order *p*. The fitted parameters, namely AIC (indicator of fitting quality), the noise level in the model and the scale of the first (main) component, show that the fitting quality does not improve beyond the *p* order 6. Therefore, the trajectory shows the "memory" of at least 6 steps (6 fs). (t) The trajectory was also fitting using a more complicated ARMA model, which shows that two models converge at higher orders ($p \geq 6$). The errors presented in panel (t) are from the model fitting directly. (u-v). ^{1}H-^{13}C hNOE build-up kinetics of indole (2 M) in the absence (u) and presence (v) of TEMPO (100 mM) in CCl_4 solvent. All these kinetics were extracted from on a series of 2D ^{1}H-^{13}C HOESY spectra. The maximum signal intensity of each indole carbon in the absence of TEMPO (u) was normalized. The signal intensities in the presence of TEMPO (v) were scaled according to the normalized diamagnetic signal intensity.

Supplementary References

1 Abragam, A. *The principles of nuclear magnetism*. (Clarendon Press, Oxford, 1961).

2 Bertini, I., Luchinat, C. & Parigi, G. *Solution NMR of Paramagnetic Molecules : Applications to Metallobiomolecules and Models*. (Elsevier Science Ltd., Amsterdam, 2001).

3 Noack, F., Krüger, G. J., Müller-Warmuth, W. & Van Steenwinkel, R. Stochastische Prozesse in Spinsystemen. *Z. Naturforsch. A* **22**, 2102-2108 (1967).

4 Müller-Warmuth, W., Van Steenwinkel, R. & Noack, F. Dynamic nuclear polarization experiments on 19F in solutions and their interpretation by the 'pulse model' of molecular collisions. *Z. Naturforsch. A* **23**, 506-513 (1968).

5 Gladchenko, L. F. & Pikulik, L. G. Dipole moment of the excited state in indole and tryptophan. *Zh. Prikl. Spektrosk.* **6**, 355-360 (1967).

6 Terazima, M., Tenma, S., Watanabe, H. & Tominaga, T. Translational diffusion of chemically stable and reactive radicals in solution. *J. Chem. Soc., Faraday Trans.* **92**, 3057-3062 (1996).

7 Qiu, Z. W., Grant, D. M. & Pugmire, R. J. Paramagnetic C-13 shifts induced by the free-radical Tempo .2. nitrogen-heterocycles. *J. Am. Chem. Soc.* **106**, 557-563 (1984).

8 Liu, G. Q. et al. One-thousand-fold enhancement of high field liquid nuclear magnetic resonance signals at room temperature. *Nat. Chem.* **9**, 676-680 (2017).

9 Iiyama, T. et al. Molecular assembly structure of CCl4 in graphitic nanospaces. *J. Phys. Chem. B* **101**, 3037-3042 (1997).

10 Merunka, D. & Peric, M. Measuring radical diffusion in viscous liquids by electron paramagnetic resonance. *J. Mol. Liq.* **277**, 886-894 (2019).

11 Orlando, T. et al. Dynamic nuclear polarization of C-13 nuclei in the liquid state over a 10 Tesla field range. *Angew. Chem. Int. Ed.* **58**, 1402-1406 (2019).

12 Cryer, J. D. & Chan, K. S. *Time Series Analysis: With Applications in R, second edition*. (Springer-Verlag, New York, 2008).

13 Cavallotti, C., Metrangolo, P., Meyer, F., Recupero, F. & Resnati, G. Binding energies and F-19 nuclear magnetic deshielding in paramagnetic halogen-bonded complexes of TEMPO with haloperfluorocarbons. *J. Phys. Chem. A* **112**, 9911-9918 (2008).

14 Kucuk, S. E., Biktagirov, T. & Sezer, D. Carbon and proton Overhauser DNP from MD simulations and ab initio calculations: TEMPOL in acetone. *Phys. Chem. Chem. Phys.* **17**, 24874-24884 (2015).

15 Daube, D. et al. Heteronuclear cross-relaxation under solid-state dynamic nuclear polarization. *J. Am. Chem. Soc.* **138**, 16572-16575 (2016).

16 Hoffmann, M. M. et al. Directly vs indirectly enhanced C-13 in dynamic nuclear polarization magic angle spinning NMR experiments of nonionic surfactant systems. *J. Phys. Chem. C* **121**, 2418-2427 (2017).

17 Provencher, S. W. CONTIN: A general purpose constrained regularization program for inverting noisy linear algebraic and integral equations. *Comput. Phys. Commun.* **27**, 229-242 (1982).

18 Berne, B. J. & Harp, G. D. On the Calculation of Time Correlation Functions in *Advances in Chemical Physics*, 63-227 (John Wiley & Sons Ltd., New York, 1970).

5. ^{1}H Solid Effect DNP on liposome doped with BDPA

5.1 Introduction

For a long period, DNP performed in the liquid state has been primarily referred to as OE DNP. Although some observations at low fields have shown the availability of SE in viscous or anisotropic medium,[89-91] the research interest on SE is limited due to the quadratic drop of the efficiency with increased fields as well as the dynamically averaged efficiency of the state mixing in liquids. As a consequence, OE has been the unique DNP pathway utilized in solution at elevated magnetic fields. In this work, a considerable ^{1}H DNP enhancement of 12 was observed on liposome doped with BDPA at ambient temperature and 9.4 T, which demonstrated the capability of SE DNP in an anisotropic liquid in the presence of a radical with narrow-line EPR and an efficient mw nutation field.

5.2 Corresponding Publication:

The following publication together with the supporting information

"Kuzhelev, A. A., Dai, D., Denysenkov, V. and Prisner, T. F., Solid-like Dynamic Nuclear Polarization Observed in the Fluid Phase of Lipid Bilayers at 9.4 T. *J. Am. Chem. Soc.*, 144, 1164–1168 (2022)"

is attached in the following pages.

The work was prepared in a collaborative manner. The measurement of DNP on viscous lipids with narrow-line radicals is initially proposed by Dr. Andrei Kuzhelev. The author performed of the DNP/NMR experiments together with Dr. Andrei Kuzhelev.

https://doi.org/10.1021/jacs.1c12837

JACS
JOURNAL OF THE AMERICAN CHEMICAL SOCIETY
pubs.acs.org/JACS
Communication

Solid-like Dynamic Nuclear Polarization Observed in the Fluid Phase of Lipid Bilayers at 9.4 T

Andrei A. Kuzhelev, Danhua Dai, Vasyl Denysenkov, and Thomas F. Prisner*

Cite This: J. Am. Chem. Soc. 2022, 144, 1164−1168
Read Online

ABSTRACT: Dynamic nuclear polarization (DNP) is a powerful method to enhance NMR sensitivity. Much progress has been achieved recently to optimize DNP performance at high magnetic fields in solid-state samples, mostly by utilizing the solid or the cross effect. In liquids, only the Overhauser mechanism is active, which exhibits a DNP field profile matching the EPR line shape of the radical, distinguishable from other DNP mechanisms. Here, we observe DNP enhancements with a field profile indicative of the solid effect and thermal mixing at ∼320 K and a magnetic field of 9.4 T in the fluid phase of 1,2-dimyristoyl-*sn*-glycero-3-phosphocholine (DMPC) lipid bilayers doped with the radical BDPA (1,3-bis(diphenylene)-2-phenylallyl). This interesting observation might open up new perspectives for DNP applications in macromolecular systems at ambient temperatures.

Dynamic nuclear polarization (DNP) is a method for NMR signal enhancement. It transfers the larger polarization of unpaired electron spins of paramagnetic molecules via resonant microwave excitation to the nuclear spins of the surrounding sample.[1,2] Different mechanisms have been explored to perform the polarization transfer: the Overhauser effect,[3] which is active in liquids and metals,[4] and the solid effect (SE),[5] the cross effect (CE),[6] and thermal mixing (TM),[7] which are functional in solid, nonconducting materials. In the last years, much progress has been made to optimize DNP efficiencies for solid state samples at high magnetic fields,[1] which are necessary for applications in biomolecular,[8−10] medical,[11] and surface and material sciences.[12−15] In these applications, mostly the SE and CE DNP have been exploited. They work best at low sample temperatures of 100 K or below. Only a few demonstrations[16−20] that also liquid samples at room temperature can be efficiently hyperpolarized by DNP at high magnetic fields exist. In liquids, only the Overhauser mechanism is active,[4] which relies on an efficient electron−nuclear cross-relaxation. Recently, Overhauser-like DNP enhancements have been observed with BDPA[21,22] or similar mixed valence compounds[23] in frozen solutions of nonconducting solvents, even at temperatures as low as 1.2 K.[24] This showed up as a positive NMR signal enhancement by microwave excitation directly at the EPR spectral position. These experimental results created much interest because it was found that much less microwave power was necessary to drive this polarization transfer, that it has a favorable dependence on the magnetic field strength,[22] that it survives with and without MAS conditions,[25] and that it works up to room temperature if the BDPA radical is embedded in solid matrices like *ortho*-terphenyl.[26]

In the present study, we report sizable DNP enhancements of lipid protons doped with BDPA radicals at a magnetic field of 9.4 T and a temperature of ∼320 K. Surprisingly, we only found DNP enhancement arising from the SE and from TM.

Liquid-state DNP measurements were performed with a home-built DNP spectrometer[27] working at 9.4 T magnetic field, corresponding to an EPR resonance frequency of 263 GHz for $g \approx 2$ radicals and a proton NMR frequency of 400 MHz. The central component of the liquid-state DNP spectrometer is a double resonance DNP structure[28] consisting of a Fabry−Pérot resonator for the microwave excitation (B_{mw}) and a stripline resonant structure for the NMR excitation and detection (B_{rf}) as shown in Figure 1. A gyrotron with a power of 5 W was used for the microwave excitation. The lipid/water/BDPA mixture consisting of 1,2-dimyristoyl-*sn*-glycero-3-phosphocholine (DMPC), deuterated water, and BDPA in molar ratio of 10/500/1 (more details for the sample preparation in the SI) was placed on top of the stripline in a sample container with a thickness of about 20 μm and a diameter of 1.5 mm, corresponding to the beam waist of the Gaussian microwave beam at the sample. This sample geometry and position ensures a maximum magnetic field component B_1 at the sample, necessary to saturate the electron spin transitions and at the same time minimize the electrical field component E_1 within the sample, minimizing sample heating. The flat mirror with a high heat conductivity was additionally cooled by a flow of room temperature nitrogen gas. The microwave heating of the 5 W microwave power led to an estimated sample temperature of about 310−330 K under DNP conditions.

We studied the BDPA radicals in the lipid samples by EPR spectroscopy at X-band (9 GHz) and J-band (260 GHz). For the concentrations of BDPA radicals optimal for the DNP

Received: December 7, 2021
Published: January 14, 2022

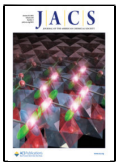

https://doi.org/10.1021/jacs.1c12837
J. Am. Chem. Soc. 2022, 144, 1164−1168

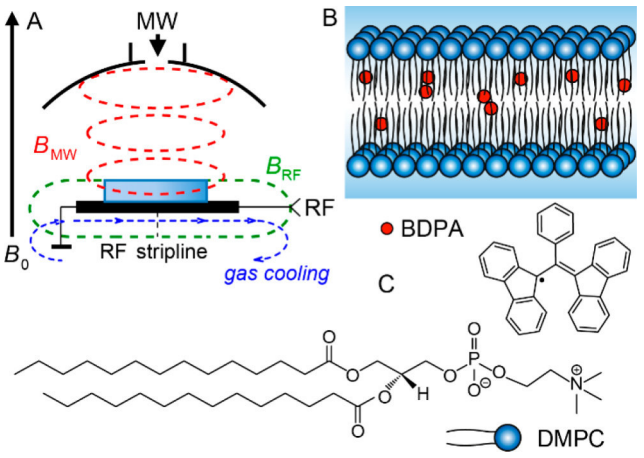

Figure 1. (A) Stripline Fabry–Pérot double-resonance probehead used for the DNP measurements. (B) Schematic picture of the assumed location of BDPA molecules and clusters inside the lipid bilayers. (C) Structure of the BDPA (1,3-bis(diphenylene)-2-phenylallyl) radical and the used DMPC (1,2-dimyristoyl-*sn*-glycero-3-phosphocholine).

experiments (BDPA/DMPC ratio of 1/10) an exchange narrowing of the hyperfine resolved EPR line from 1 mT to about 0.2 mT was observed at both magnetic field strengths (upper trace in Figure 2; more EPR characterization in the SI).

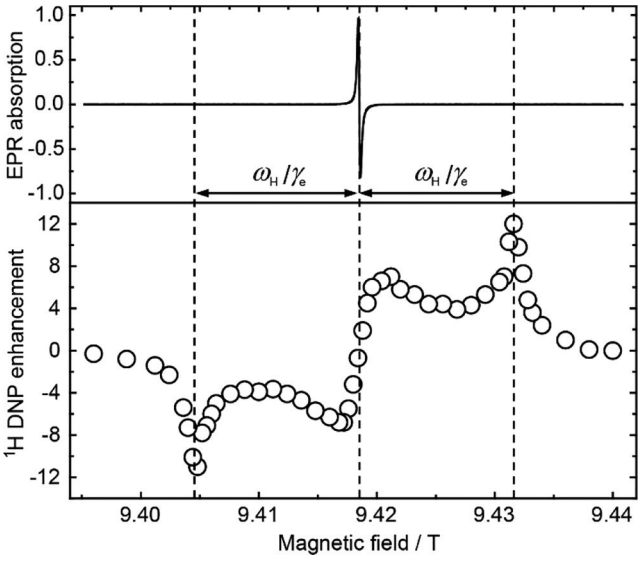

Figure 2. Field profile of the ^{1}H acyl chain DNP enhancement at a temperature of ~320 K. An antisymmetric DNP profile with respect to the narrow BDPA EPR resonance field position is observed.

The gel-to-liquid phase transition temperature of the BDPA/DMPC sample between 293 and 298 K, as confirmed by EPR and NMR measurements (see SI), ensures that the sample is in the fluid phase under DNP conditions. In the lower trace of Figure 2, the DNP field profile of the acyl chain protons is shown, which is totally antisymmetric with respect to the narrow BDPA EPR resonance position. The outermost peaks are located at magnetic field strengths displaced by $\pm\omega_H/\gamma_e$ compared to the EPR resonance field position. In addition, a second antisymmetric enhancement pattern, much closer to the EPR resonance field position, is visible. The maximal enhancements of both features correspond to ±12 and ±8, respectively. The outer two peaks appear at the field positions expected for a solid-state DNP mechanism and are quantitatively reproducible, whereas the inner peaks vary in their amplitude from sample to sample (see SI). We attributed the outer peaks to a SE driven DNP and the inner peaks to TM, resulting from clusters of BDPA molecules in the lipid (see below). Different from DNP experiments performed at lower microwave frequencies (X- or Q-band) at our high microwave frequencies (J-band), the features arising from Overhauser effect, TM, and SE can easily be distinguished and are well separated.

The solid-state mechanism is driven by excitation of "forbidden" electron spin transitions, where simultaneously a hyperfine coupled proton spin is inverted. This is only possible, if the anisotropic part of the hyperfine interaction is not averaged out, as usual is the case in liquid samples by fast rotational and translational motion of the radical. It has been shown at X-band frequencies that for viscous samples a transition from Overhauser effect to SE DNP can be observed if the rotational correlation time of the radical–target complex becomes slow enough.[29−32] The lateral diffusion of lipid molecules and the lipid reorientation in the bilayers are indeed slow enough even in the fluid phase of DMPC at our experimental conditions. A second important requirement to observe efficient SE DNP is a high enough microwave B_1 field strength. With our microwave resonant Fabry–Pérot structure large B_1 field strengths of up to 0.6 mT can be achieved with 5 W of microwave power. This allows a very efficient and fast driving of the allowed (and forbidden) electron-spin transitions, different from typical nonresonant DNP setups. Indeed, we observed a linear dependence of the SE DNP enhancement as a function of the applied microwave power (see SI).

In Figure 3, the NMR signal with and without applied microwave at the field position corresponding to the upper SE

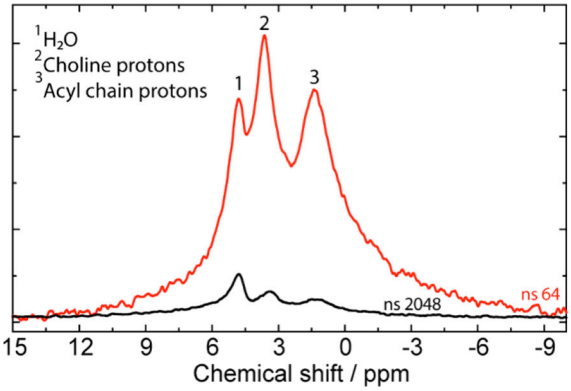

Figure 3. Normalized ^{1}H NMR spectra to single scan of a BDPA/DMPC/D_2O sample with molar ratio 1/10/500 with (red, 64 scans) and without (black, 2048 scans) microwave excitation at a magnetic field of 9.432 T.

maximum is shown. Our double resonant DNP probe and the high magnetic field enables enough spectral resolution to distinguish the signals from the residual water protons from the lipid tail and headgroup protons. Note that we observed similar DNP enhancements for the lipid tail and headgroup protons, while for the residual water protons, the DNP enhancement was negligible (Figure 3 and SI).

https://doi.org/10.1021/jacs.1c12837
J. Am. Chem. Soc. 2022, 144, 1164−1168

The antisymmetric feature much closer to the allowed electron-spin resonance position in the field profile of Figure 2 resembles the pattern expected for TM DNP. Different from the SE, the TM requires simultaneous interactions with several electron spins.[33] Therefore, this enhancement pattern could be due to small BDPA clusters in the lipid, as visualized in Figure 1. Such clusters have been observed in low temperature DNP experiments of BDPA in an *ortho*-terphenyl matrix.[34] Different from the DNP enhancement observed at $\omega_S/\gamma_e \pm \omega_H/\gamma_e$, attributed to the SE, this enhancement varied from sample to sample considerably (see SI). Previous EPR and UV−vis spectroscopy studies revealed that BDPA radicals, and especially BDPA clusters, have a limited thermal stability.[35] This observation could explain the variation of the inner part of the DNP field profiles in our BDPA doped lipid bilayers. The stability of the BDPA X-band EPR signal in the BDPA/DMPC samples was studied at 330 K (see SI). It showed indeed a biexponential behavior, with a fast-decaying component attributed to the decomposition of radical clusters and another component attributed to BDPA monomers that is quite stable over the typical DNP measurement time (3−5 h), leading to a stable SE DNP.

Our earlier high field DNP experiments with nitroxide mono- and biradicals as polarizing agents with lipid bilayers showed very different behavior.[36] In these samples, an Overhauser effect DNP enhancement of about −10 was observed at ambient temperatures with a DNP enhancement profile matching the nitroxide EPR spectral shape. No asymmetric DNP enhancement that could be attributed to the SE or to TM could be observed in this case. There are several reasons for this different behavior. First of all, the smaller size of nitroxides leads to a faster rotational motion inside the lipid bilayer well-known from EPR studies.[37−39] Second, the electron spin relaxation times of nitroxides are much shorter compared to BDPA at room temperature in fluid solutions. Additionally, the much broader EPR spectra of nitroxides compared to BDPA further reduces SE DNP contributions. In fact, the EPR line width of a slowly tumbling nitroxide radical at a magnetic field of 9.4 T spans 600 MHz, larger that the proton Larmor frequency. This will on the one hand significantly reduce the possibility of efficiently saturating allowed and forbidden EPR transitions and on the other hand lead to much less defined field profiles for the SE. A similar trend has been observed at X-band in ionic liquids using nitroxide and BDPA radicals as polarizing agents.[32]

Surprisingly, we did not observe any Overhauser DNP enhancement in the BDPA/DMPC samples under our experimental conditions, differently from observations of Overhauser-like positive DNP enhancements observed at lower temperatures in solids.[21−26] Indeed, the negative dipolar-coupling induced proton Overhauser DNP of BDPA in liquid solutions is much less efficient at high magnetic fields compared to nitroxide radicals.[40] This is due to the more bulky molecular structure and less exposure of the unpaired electron spin. This strongly reduces the spectral density of the dynamic modulation of the dipolar hyperfine coupling at high microwave frequencies, which is essential to observe an Overhauser DNP effect at high magnetic fields. The positive Overhauser DNP enhancement arises from the BDPA protons having an intense scalar Fermi-contact hyperfine coupling.[22,41,42] In solid state samples, the scalar Overhauser hyperpolarization propagates from the BDPA protons to the solvent by spin-diffusion. Under our DNP conditions in the fluid phase of the lipid, this polarization transfer pathway is inefficient. This might explain the fact that we did not observe Overhauser DNP under our experimental conditions. In contrast, our observed SE DNP on the lipid protons starts by a direct polarization transfer step from the BDPA electron spin to the lipid proton followed by a dispersion of the polarization mediated by lateral diffusion of the lipids. Our observation of DNP enhancements with the field profile of TM could also indicate that indeed such effects could contribute to the DNP enhancements observed at low temperatures in solid samples, as proposed recently.[34]

In conclusion, in this work we described the first high field DNP experiments in the liquid phase of DMPC at ambient temperatures, with field profiles indicative of the SE and TM. The essential steps to achieve this were (i) the use of stripline/Fabry−Pérot double resonance DNP structure, allowing us to perform the measurements in the liquid phase with a very high microwave B_1 field, (ii) the use of the polarizing agent BDPA with a narrow EPR line, and (iii) the use of DMPC lipid bilayers as an environment having much slower molecular motions in the aqueous medium compared to the BDPA radical alone. This together allowed the sample to behave like a solid on the nanosecond time scale necessary for the polarization transfer step from the unpaired electron to the proton nuclear spins of the lipid. DNP enhancement up to ±12 has been achieved at high temperatures and high magnetic fields by the SE. A full quantitative description and optimization of these new DNP results will require more detailed studies, including variation of radical and macromolecular environment and sample temperature and examination of the DNP enhancement on other nuclei, such as ^{13}C, ^{15}N, and ^{31}P. These experiments are under way in our laboratory at the moment.

■ ASSOCIATED CONTENT

Supporting Information

The Supporting Information is available free of charge at https://pubs.acs.org/doi/10.1021/jacs.1c12837.

More details on the sample preparation and the EPR, NMR, and DNP experimental details and additional EPR and DNP data (PDF)

■ AUTHOR INFORMATION

Corresponding Author

Thomas F. Prisner − *Goethe University Frankfurt am Main, Institute of Physical and Theoretical Chemistry and Center for Biomolecular Magnetic Resonance, 60438 Frankfurt am Main, Germany;* orcid.org/0000-0003-2850-9573; Email: prisner@chemie.uni-frankfurt.de

Authors

Andrei A. Kuzhelev − *Goethe University Frankfurt am Main, Institute of Physical and Theoretical Chemistry and Center for Biomolecular Magnetic Resonance, 60438 Frankfurt am Main, Germany*

Danhua Dai − *Goethe University Frankfurt am Main, Institute of Physical and Theoretical Chemistry and Center for Biomolecular Magnetic Resonance, 60438 Frankfurt am Main, Germany*

Vasyl Denysenkov − *Goethe University Frankfurt am Main, Institute of Physical and Theoretical Chemistry and Center*

https://doi.org/10.1021/jacs.1c12837
J. Am. Chem. Soc. 2022, 144, 1164−1168

for Biomolecular Magnetic Resonance, 60438 Frankfurt am Main, Germany

Complete contact information is available at: https://pubs.acs.org/10.1021/jacs.1c12837

Notes

The authors declare no competing financial interest.

■ ACKNOWLEDGMENTS

This work was supported by the Deutsche Forschungsgemeinschaft (DFG, grant 405972957) and by the Center of Biomolecular Magnetic Resonance (BMRZ).

■ REFERENCES

(1) Denysenkov, V. P.; Prisner, T. F. Liquid-State Overhauser DNP at High Magnetic Fields. *eMagRes.* **2019**, *8* (1), 41−54.
(2) Corzilius, B. High-Field Dynamic Nuclear Polarization. *Annu. Rev. Phys. Chem.* **2020**, *71*, 143−170.
(3) Overhauser, A. W. Polarization of Nuclei in Metals. *Phys. Rev.* **1953**, *92* (2), 411−415.
(4) Hausser, K. H.; Stehlik, D. Dynamic Nuclear Polarization in Liquids. *In Advances in Magnetic and Optical Resonance* **1968**, *3*, 79−139.
(5) Jeffries, C. D. Polarization of Nuclei by Resonance Saturation in Paramagnetic Crystals. *Phys. Rev.* **1957**, *106* (1), 164−165.
(6) Hwang, C. F.; Hill, D. A. New Effect in Dynamic Polarization. *Phys. Rev. Lett.* **1967**, *18* (4), 110−112.
(7) Abragam, A.; Goldman, M. Principles of Dynamic Nuclear Polarisation. *Rep. Prog. Phys.* **1978**, *41* (3), 395−467.
(8) Su, Y.; Andreas, L.; Griffin, R. G. Magic Angle Spinning NMR of Proteins: High-Frequency Dynamic Nuclear Polarization and 1H Detection. *Annu. Rev. Biochem.* **2015**, *84*, 465−497.
(9) Kaplan, M.; Cukkemane, A.; Van Zundert, G. C. P.; Narasimhan, S.; Daniëls, M.; Mance, D.; Waksman, G.; Bonvin, A. M. J. J.; Fronzes, R.; Folkers, G. E.; Baldus, M. Probing a Cell-Embedded Megadalton Protein Complex by DNP-Supported Solid-State NMR. *Nat. Methods* **2015**, *12* (7), 649−652.
(10) Mao, J.; Aladin, V.; Jin, X.; Leeder, A. J.; Brown, L. J.; Brown, R. C. D.; He, X.; Corzilius, B.; Glaubitz, C. Exploring Protein Structures by DNP-Enhanced Methyl Solid-State NMR Spectroscopy. *J. Am. Chem. Soc.* **2019**, *141* (50), 19888−19901.
(11) Ardenkjær-Larsen, J. H.; Golman, K.; Gram, A.; Lerche, M. H.; Servin, R.; Thaning, M.; Wolber, J.; et al. Increase of Signal-to-Noise of More than 10,000 Times in Liquid State NMR. *Proc. Natl. Acad. Sci. U. S. A.* **2003**, *100*, 10158.
(12) Rossini, A. J.; Zagdoun, A.; Lelli, M.; Lesage, A.; Copéret, C.; Emsley, L. Dynamic Nuclear Polarization Surface Enhanced NMR Spectroscopy. *Acc. Chem. Res.* **2013**, *46* (9), 1942−1951.
(13) Kobayashi, T.; Perras, F. A.; Slowing, I. I.; Sadow, A. D.; Pruski, M. Dynamic Nuclear Polarization Solid-State NMR in Heterogeneous Catalysis Research. *ACS Catalysis* **2015**, *5*, 7055−7062.
(14) Thankamony, A. S. L.; Knoche, S.; Bothe, S.; Drochner, A.; Jagtap, A. P.; Sigurdsson, S. T.; Vogel, H.; Etzold, B. J. M.; Gutmann, T.; Buntkowsky, G. Characterization of V-Mo-W Mixed Oxide Catalyst Surface Species by 51V Solid-State Dynamic Nuclear Polarization NMR. *J. Phys. Chem. C* **2017**, *121* (38), 20857−20864.
(15) Wolf, T.; Kumar, S.; Singh, H.; Chakrabarty, T.; Aussenac, F.; Frenkel, A. I.; Major, D. T.; Leskes, M. Endogenous Dynamic Nuclear Polarization for Natural Abundance 17 O and Lithium NMR in the Bulk of Inorganic Solids. *J. Am. Chem. Soc.* **2019**, *141* (1), 451−462.
(16) Prandolini, M. J.; Denysenkov, V. P.; Gafurov, M.; Endeward, B.; Prisner, T. F. High-Field Dynamic Nuclear Polarization in Aqueous Solutions. *J. Am. Chem. Soc.* **2009**, *131* (17), 6090−6092.
(17) Liu, G.; Levien, M.; Karschin, N.; Parigi, G.; Luchinat, C.; Bennati, M. One-Thousand-Fold Enhancement of High Field Liquid Nuclear Magnetic Resonance Signals at Room Temperature. *Nat. Chem.* **2017**, *9* (7), 676−680.
(18) Yoon, D.; Dimitriadis, A. I.; Soundararajan, M.; Caspers, C.; Genoud, J.; Alberti, S.; De Rijk, E.; Ansermet, J. P. High-Field Liquid-State Dynamic Nuclear Polarization in Microliter Samples. *Anal. Chem.* **2018**, *90* (9), 5620−5626.
(19) Van Der Heijden, G. H. A.; Kentgens, A. P. M.; Van Bentum, P. J. M. Liquid State Dynamic Nuclear Polarization of Ethanol at 3.4 T (95 GHz). *Phys. Chem. Chem. Phys.* **2014**, *16* (18), 8493−8502.
(20) Dubroca, T.; Wi, S.; Van Tol, J.; Frydman, L.; Hill, S. Large Volume Liquid State Scalar Overhauser Dynamic Nuclear Polarization at High Magnetic Field. *Phys. Chem. Chem. Phys.* **2019**, *21* (38), 21200−21204.
(21) Haze, O.; Corzilius, B.; Smith, A. A.; Griffin, R. G.; Swager, T. M. Water-Soluble Narrow-Line Radicals for Dynamic Nuclear Polarization. *J. Am. Chem. Soc.* **2012**, *134* (35), 14287−14290.
(22) Can, T. V.; Caporini, M. A.; Mentink-Vigier, F.; Corzilius, B.; Walish, J. J.; Rosay, M.; Maas, W. E.; Baldus, M.; Vega, S.; Swager, T. M.; Griffin, R. G. Overhauser Effects in Insulating Solids. *J. Chem. Phys.* **2014**, *141*, 064202.
(23) Gurinov, A.; Sieland, B.; Kuzhelev, A.; Elgabarty, H.; Kühne, T. D.; Prisner, T.; Paradies, J.; Baldus, M.; Ivanov, K. L.; Pylaeva, S. Mixed-Valence Compounds as Polarizing Agents for Overhauser Dynamic Nuclear Polarization in Solids. *Angew. Chemie - Int. Ed.* **2021**, *60* (28), 15371−15375.
(24) Ji, X.; Can, T. V.; Mentink-Vigier, F.; Bornet, A.; Milani, J.; Vuichoud, B.; Caporini, M. A.; Griffin, R. G.; Jannin, S.; Goldman, M.; Bodenhausen, G. Overhauser Effects in Non-Conducting Solids at 1.2 K. *J. Magn. Reson.* **2018**, *286*, 138−142.
(25) Chaudhari, S. R.; Wisser, D.; Pinon, A. C.; Berruyer, P.; Gajan, D.; Tordo, P.; Ouari, O.; Reiter, C.; Engelke, F.; Copéret, C.; Lelli, M.; Lesage, A.; Emsley, L. Dynamic Nuclear Polarization Efficiency Increased by Very Fast Magic Angle Spinning. *J. Am. Chem. Soc.* **2017**, *139* (31), 10609−10612.
(26) Lelli, M.; Chaudhari, S. R.; Gajan, D.; Casano, G.; Rossini, A. J.; Ouari, O.; Tordo, P.; Lesage, A.; Emsley, L. Solid-State Dynamic Nuclear Polarization at 9.4 and 18.8 T from 100 K to Room Temperature. *J. Am. Chem. Soc.* **2015**, *137* (46), 14558−14561.
(27) Denysenkov, V.; Prandolini, M. J.; Gafurov, M.; Sezer, D.; Endeward, B.; Prisner, T. F. Liquid State DNP Using a 260 GHz High Power Gyrotron. *Phys. Chem. Chem. Phys.* **2010**, *12* (22), 5786−5790.
(28) Denysenkov, V.; Prisner, T. Liquid State Dynamic Nuclear Polarization Probe with Fabry-Perot Resonator at 9.2 T. *J. Magn. Reson.* **2012**, *217*, 1−5.
(29) Leblond, J.; Uebersfeld, J.; Korringa, J. Study of the Liquid-State Dynamics by Means of Magnetic Resonance and Dynamic Polarization. *Phys. Rev. A* **1971**, *4* (4), 1532−1539.
(30) Leblond, J.; Papon, P.; Korringa, J. Stochastic Theory of Dynamic Spin Polarization in Viscous Liquids with Anisotropic Electron-Spin Relaxation. *Phys. Rev. A* **1971**, *4* (4), 1539−1549.
(31) Neudert, O.; Reh, M.; Spiess, H. W.; Münnemann, K. X-Band DNP Hyperpolarization of Viscous Liquids and Polymer Melts. *Macromol. Rapid Commun.* **2015**, *36* (10), 885−889.
(32) Gizatullin, B.; Mattea, C.; Stapf, S. Molecular Dynamics in Ionic Liquid/Radical Systems. *J. Phys. Chem. B* **2021**, *125* (18), 4850−4862.
(33) Wind, R. A.; Duijvestijn, M. J.; van der Lugt, C.; Manenschijn, A.; Vriend, J. Applications of Dynamic Nuclear Polarization in 13C NMR in Solids. *Prog. Nucl. Magn. Reson. Spectrosc.* **1985**, *17* (C), 33−67.
(34) Li, Y.; Equbal, A.; Tabassum, T.; Han, S. 1H Thermal Mixing Dynamic Nuclear Polarization with BDPA as Polarizing Agents. *J. Phys. Chem. Lett.* **2020**, *11* (21), 9195−9202.
(35) Mandal, S.; Sigurdsson, S. T. On the Limited Stability of BDPA Radicals. *Chem. - A Eur. J.* **2020**, *26* (33), 7486−7491.
(36) Jakdetchai, O.; Denysenkov, V.; Becker-Baldus, J.; Dutagaci, B.; Prisner, T. F.; Glaubitz, C. Dynamic Nuclear Polarization-Enhanced NMR on Aligned Lipid Bilayers at Ambient Temperature. *J. Am. Chem. Soc.* **2014**, *136* (44), 15533−15536.
(37) Isaev, N. P.; Dzuba, S. A. Fast Stochastic Librations and Slow Rotations of Spin Labeled Stearic Acids in a Model Phospholipid

Bilayer at Cryogenic Temperatures. *J. Phys. Chem. B* **2008**, *112* (42), 13285−13291.
(38) Marsh, D.; Kurad, D.; Livshits, V. A. High-field Spin-label EPR of Lipid Membranes. *Magn. Reson. Chem.* **2005**, *43* (S1), S20−S25.
(39) Marsh, D. Molecular Motion in Phospholipid Bilayers in the Gel Phase: Long Axis Rotation. *Biochemistry* **1980**, *19* (8), 1632−1637.
(40) Loening, N. M.; Rosay, M.; Weis, V.; Griffin, R. G. Solution-State Dynamic Nuclear Polarization at High Magnetic Field. *J. Am. Chem. Soc.* **2002**, *124* (30), 8808−8809.
(41) Pylaeva, S.; Ivanov, K. L.; Baldus, M.; Sebastiani, D.; Elgabarty, H. Molecular Mechanism of Overhauser Dynamic Nuclear Polarization in Insulating Solids. *J. Phys. Chem. Lett.* **2017**, *8* (10), 2137−2142.
(42) Delage-Laurin, L.; Palani, R. S.; Golota, N.; Mardini, M.; Ouyang, Y.; Tan, K. O.; Swager, T. M.; Griffin, R. G. Overhauser Dynamic Nuclear Polarization with Selectively Deuterated BDPA Radicals. *J. Am. Chem. Soc.* **2021**, *143* (48), 20281−20290.

https://doi.org/10.1021/jacs.1c12837
J. Am. Chem. Soc. 2022, 144, 1164−1168

Supporting Information

Solid-like Dynamic Nuclear Polarization Observed in the Fluid Phase of Lipid Bilayers at 9.4 T

Andrei A. Kuzhelev, Danhua Dai, Vasyl Denysenkov, Thomas F. Prisner*

Goethe University Frankfurt am Main, Institute of Physical and Theoretical Chemistry and Center for Biomolecular Magnetic Resonance, Max von Laue Str. 7, 60438 Frankfurt am Main, Germany.

Sample preparation

1,2-dimyristoyl-*sn*-glycero-3-phosphocholine (DMPC) were purchased from Avanti Polar Lipids. The stable BDPA radical (1,3-bis(diphenylene)-2-phenylallyl 1:1 benzene complex) was purchased from Sigma-Aldrich. For the lipid bilayer DNP sample preparation, 200-400 µl of chloroform ($CHCl_3$) were added to the mixtures of dry phospholipid powder and the BDPA 1:1 benzene complex (Table S1). The solution was vortexed for at least 3-5 minutes until a macroscopically liquid phase was formed. The solvent was removed by a flow of argon or nitrogen gas yielding a lipid thin film at the surface of the bottom flask. To remove remaining traces of the solvent, the flask was evacuated for at least 3 h at a pressure of $3.5 \cdot 10^{-6}$ bar. Subsequently, the dry DMPC/BDPA lipid film was hydrated with D_2O (or H_2O) and was stored at room temperature for an hour to enable liposome formation in the presence of oxygen of air. Note, that the initial concentration of paramagnetic BDPA radical in the sample is only 50% of the given concentration. This has been determined by EPR and is also mention in reference [1]. This effect reduces the real molar ratio for BDPA/DMPC/D_2O of our sample approximately by a factor of 2.

Table S1: Composition of the different samples used for the DNP and NMR experiments

Molar ratio for BDPA/DMPC/D_2O	BDPA 1:1 benzene complex / mg	DMPC dry powder / mg	D_2O / mg
1:5:250	0.3	2.0	2.8
1:10:500	0.3	4.1	5.4
1:20:1000	0.2	5.5	7.3
1:50:2500	0.2	13.6	17.8
1:100:5000	0.2	27.3	35.6

EPR experiments

X-band (0.3 T) CW EPR measurements were performed at 273 K and 330 K using a commercial Bruker Elexsys E500 spectrometer. The X-band CW EPR parameters were as follows: frequency 9.331 GHz, sweep width 10 mT, microwave power 2 mW, modulation frequency 100 kHz, modulation amplitude 0.01-0.04 mT, time constant 40.96 ms, conversion time 40.96 ms, sweep time 41.94 s, number of points 1024 and number of scans 1. The EPR line broadening was analyzed with the Easyspin software package [2] assuming Lorentzian lineshapes.

Pulse EPR experiments were done using a home-built X-band (9 GHz) EPR spectrometer equipped with an arbitrary waveform generator [3]. The electron spin relaxation times were measured at 298 K. T_2 was measured using a two-pulse electron spin echo (ESE) sequence; T_1 was measured using an inversion−recovery experiment with an inversion π-pulse and a two-pulse ESE sequence or FID for detection. The experiments were carried out using a two-step phase cycling. The pulse lengths were 4/8 ns for the electron spin echo experiments and 4 ns for the FID experiments.

J-band (9.4 T) CW EPR measurements were carried out at room temperature using a Fabry-Perot/stripline DNP/EPR probehead. The magnetic field sweep (Figure S6 and S8) was accomplished by incrementing the z-cryo-shim coil current. The EPR parameters were as follows: microwave frequency 264 GHz, microwave power 10 mW, sweep width 8-44 mT, field modulation frequency 10 kHz, field modulation amplitude 0.1 mT, time constant 0.1 s, number of points 1101 and number of scans 1.

DNP/NMR experiments

All DNP enhanced ^{1}H NMR spectra were recorded on our home-built DNP spectrometer based on a Bruker Avance II wide-bore spectrometer operating at 9.4 T. Microwaves were generated by a gyrotron (Gycom, Russian Federation). The DNP probe used here is the home-built Fabry-Perot/stripline double resonance structure (260 GHz/400 MHz). The DNP enhanced and the reference (MW off) NMR FID signals were recorded with a standard 90° RF-pulse excitation. The 90° pulse length was 25 μs, the repetition time was one second. The DNP enhancement was measured by observing the intensity of the ^{1}H signals of the lipid acyl chain with and without microwave irradiation. The enhancement was then calculated according to $\varepsilon = (I/I_0) - 1$. ^{1}H longitudinal relaxation times without microwave (T_1) and DNP build-up times with microwave (T_B) were measured with a standard inversion recovery sequence (π — τ — $\pi/2$ — acquisition).

The temperature dependence of the proton NMR spectra (Figure S4) was measured between 273-323 K using a commercial Bruker probehead for BDPA/DMPC/D_2O samples with molar ratios of 1/10/500 and 1/100/5000.

X-band CW-EPR lineshape as a function of the BDPA/Lipid ratio

Figure S1 shows the X-band CW-EPR lineshape of the BDPA radical in the lipid sample as a function of the BDPA/lipid ratio. As can be seen a strong narrowing of the EPR linewidth appears for ratios smaller than 1/20. This is attributed to fast Heisenberg spin-exchange between closely located BDPA radicals.

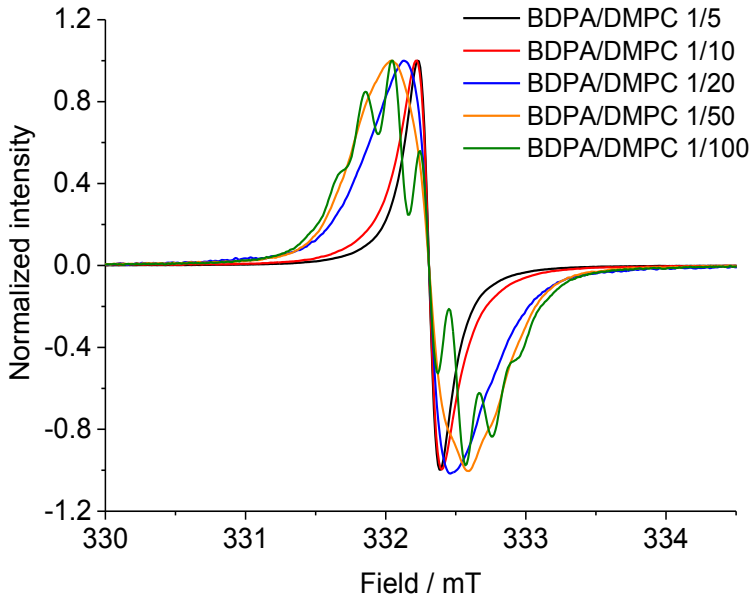

Figure S1. Room temperature X-band CW EPR spectra for BDPA/DMPC in aqueous medium with molar ratios: 1/5 (black curve), 1/10 (red curve), 1/20 (blue curve), 1/50 (orange curve), 1/100 (green curve).

Temperature dependence of X-band CW-EPR lineshape

Figure S2 shows the dependence of the X-band CW-EPR lineshape on the sample temperature for molar ratios of BDPA/DMPC 1/100 and 1/10. Figure S3 shows the temperature dependence of the linewidth determined by simulation of the CW-EPR spectra (Figure 2). The BDPA linewidth dependence with temperature in both cases clearly shows a phase transition from the gel phase (blue line) to the fluid phase (red line). The gel-fluid phase transition temperature of DMPC lipid bilayers doped with BDPA radicals is from these experiments determined to be between 293 K and 298 K.

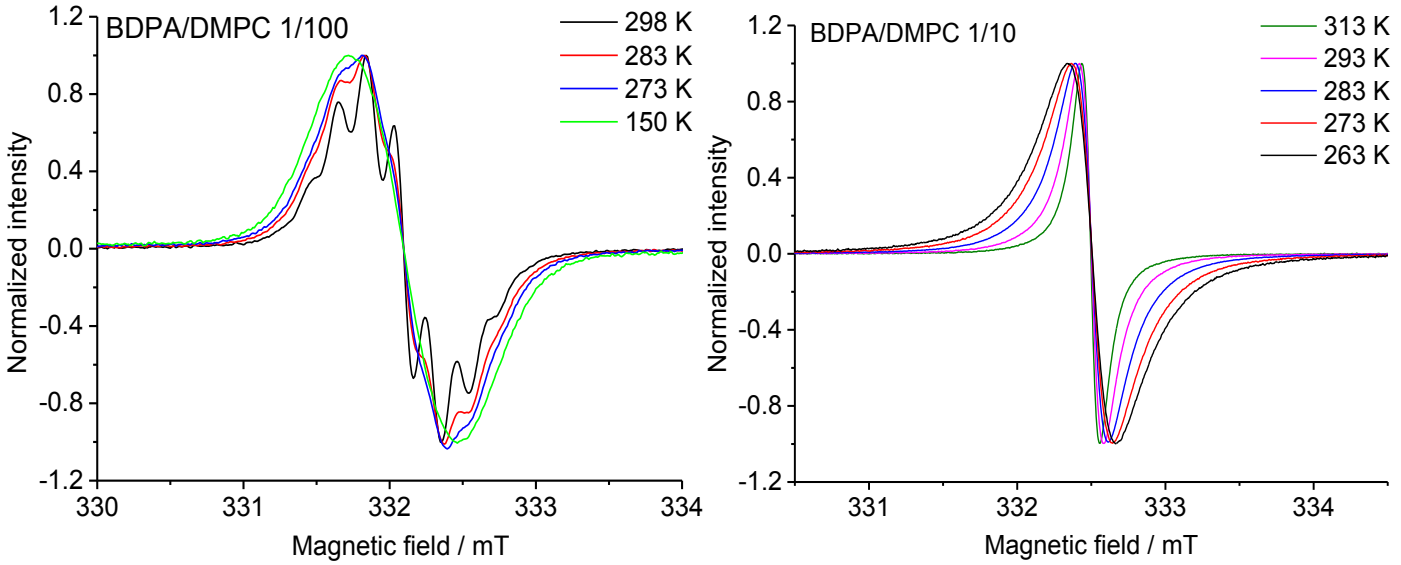

Figure S2. X-band CW EPR spectra for BDPA/DMPC (1/100 and 1/10) in aqueous medium at different temperatures.

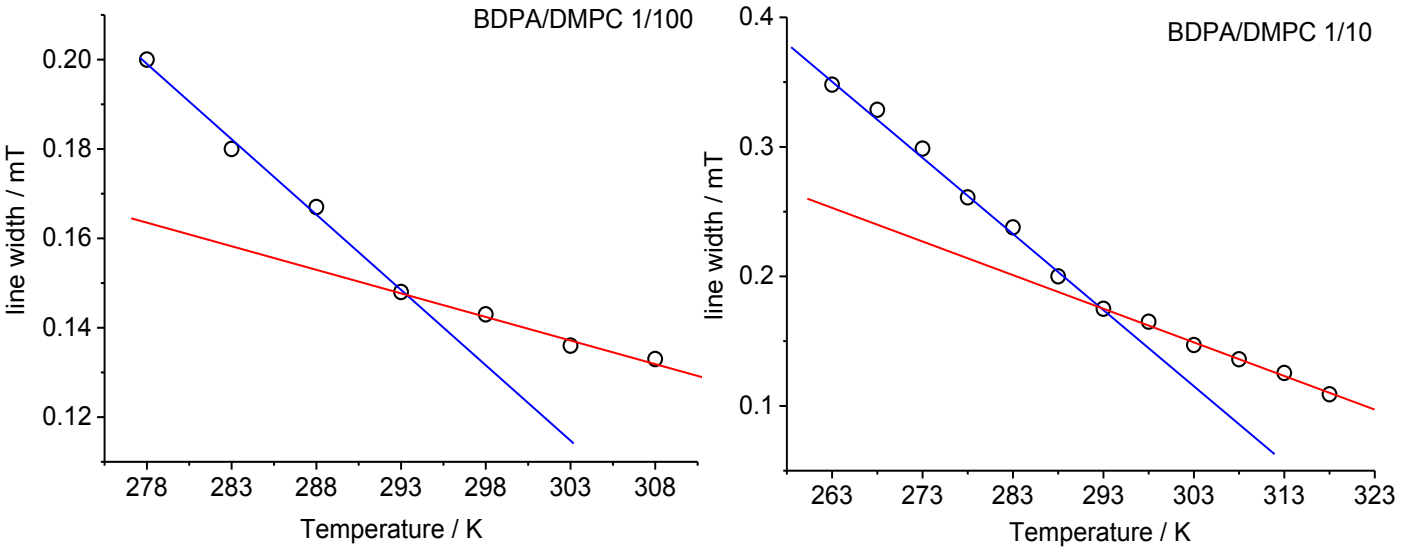

Figure S3. Temperature dependence of the linewidth for BDPA/DMPC (1/100 and 1/10) in aqueous medium. Two different slopes are observed corresponding to gel phase (blue curve) and fluid phase (red curve) with a transition temperature between 293 K and 298 K.

Temperature dependence of ^{1}H-NMR lineshape

Figure S4 shows the dependence of the 400 MHz proton NMR spectra as a function of the sample temperature for molar ratios of BDPA/DMPC 1/100 and 1/10. Figure S5 shows the temperature dependence of the intensity of the line at 1 ppm corresponding to the lipid acyl chain protons. As can be easily seen from the spectra a strong line broadening of the lipid proton signals appear as the temperature decrease from 298 to 293 K, related to the fluid-to-gel phase transition. The lipid-proton NMR results are in good agreement with the CW-EPR BDPA measurements and the literature value of the fluid-to-gel phase transition temperature of 297 K for pure DMPC. The ^{1}H-NMR spectral linewidth of the lipid in the fluid phase at our experimental temperature is very similar recorded with a commercial Bruker probehead (Figure S4) and our home-built Fabry-Perot/stripline double resonance structure (Figure 3 and Figure S9). This means that in this case the ^{1}H-NMR spectral linewidth is dominated mainly by the slow motion of the lipid bilayer and not by field inhomogeneity of the home-build Fabry-Perot resonance structure.

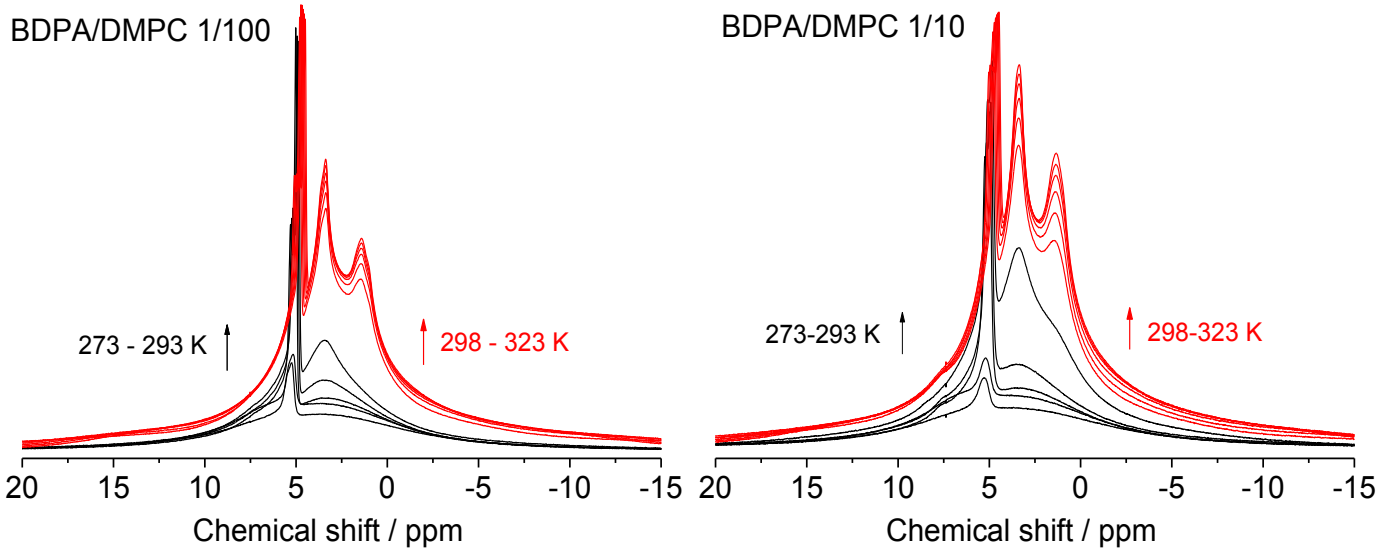

Figure S4. 400 MHz ^{1}H NMR spectra for BDPA/DMPC (1/100 and 1/10) in aqueous medium for temperatures in the temperature range of 273-323 K using a commercial Bruker probehead.

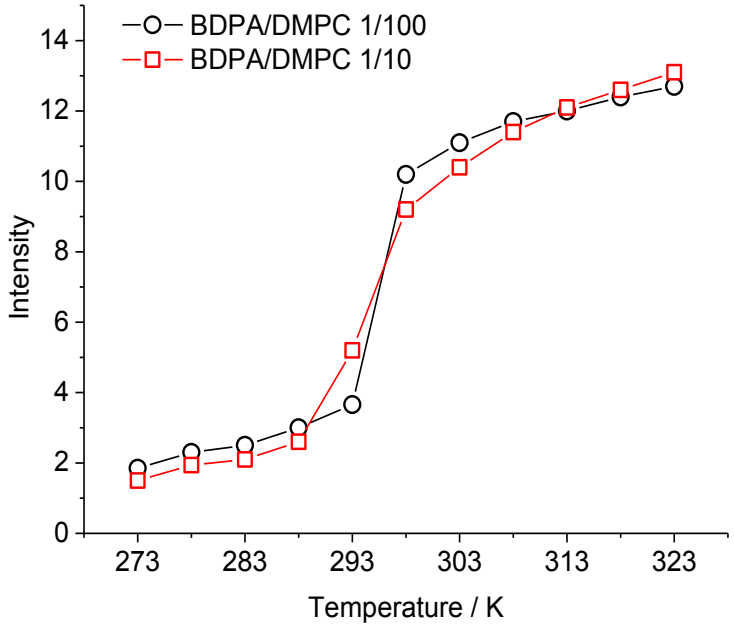

Figure S5. Temperature dependence of the acyl chain proton NMR line intensity at 1 ppm for BDPA/DMPC (1/100 and 1/10) in aqueous medium. As can be seen the gel-to-fluid phase transition temperature is between 293 K and 298 K.

Field dependence of the EPR spectra

Figure S6 shows the CW-EPR spectra of a BDPA/DMPC (1/10) sample measured at X-band (9.4 GHz) and at J-band frequencies (260 GHz). The Heisenberg narrowed line is very similar at both magnetic field strengths.

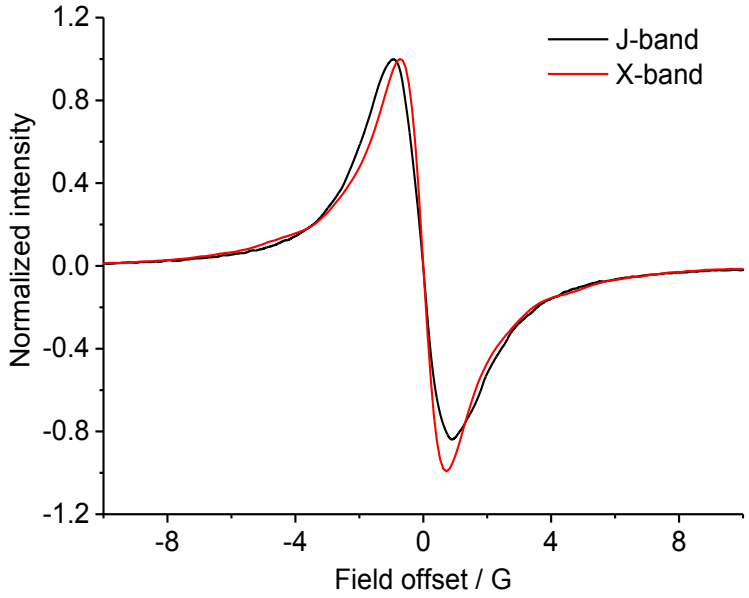

Figure S6. Room temperature CW-EPR spectra for BDPA/DMPC (1/10) in aqueous medium measured at X-band (red) and J-band (black) frequencies.

Stability of BDPA EPR signal in DMPC lipid bilayers at 330 K

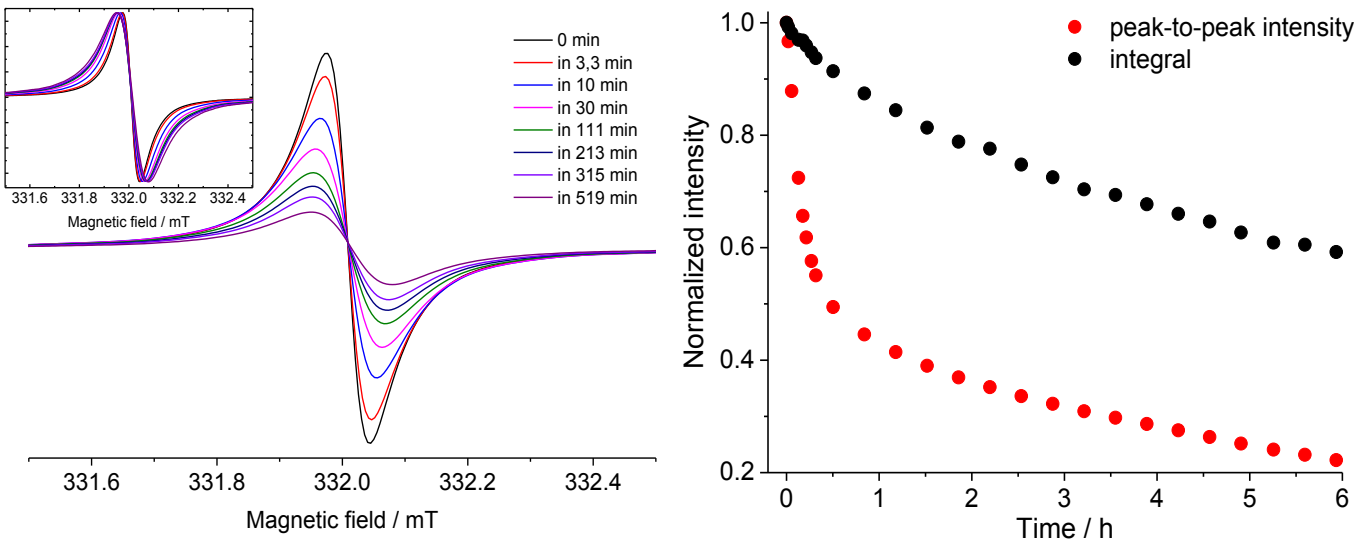

Figure S7. The decomposition of the radical BDPA in DMPC lipid bilayers with molar ratio of 1/10 measured by X-band CW EPR at 330 K. Left: Time dependent CW EPR spectra. The inset shows the EPR spectra normalized to the maximum cw-EPR intensity. With increasing observation time the EPR line broadens, related to the larger relative contribution of the BDPA monomer component. Right: Time dependence of peak-to-peak signal intensity (red curve) and integral intensity over the full EPR spectral width (black curve). A bi-exponential behavior is found, with a fast decaying component (within the first 60 min, related to the exchange narrowed EPR line) attributed to the decomposition of radical clusters and another slow decaying component attributed to BDPA monomers.

Variation of the TM efficiency

In Figure S8 the DNP field profile is shown for two independent sample preparations, both with a molar ratio of BDPA/lipid of 1/10. As can be seen the DNP enhancement observed at the solid effect field positions is very good reproducible, while the DNP enhancement resulting from thermal mixing varied strongly from sample to sample. We assume that this effect is related to varying amount of BDPA clusters in the samples and the thermal decomposition of these clusters by microwave heating within the experiments, as visible in Figure S7.

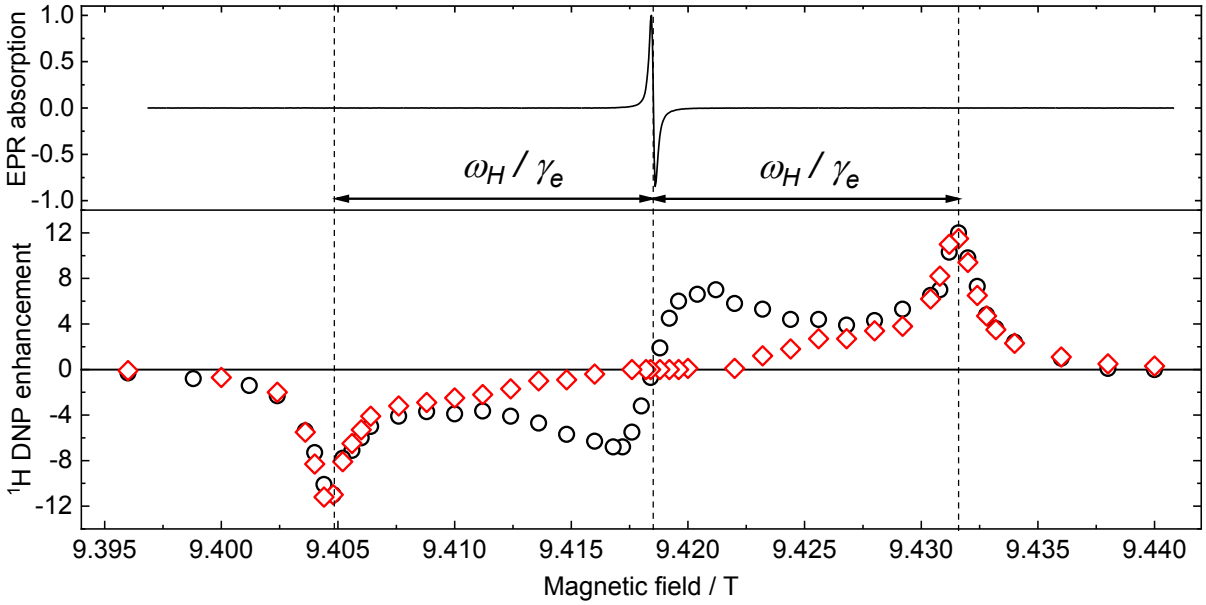

Figure S8. Variation of TM enhancements between two independently prepared samples. Shown is the acyl chain proton DNP field sweep profile for two BDPA/DMPC samples both with a molar ratio of 1/10. The central enhancement arising from thermal mixing is varying from sample to sample strongly (between 0 and ±8), while the DNP enhancement of ±12 at the solid effect field positions is very well reproducible.

DNP spectra at the low-field solid effect position

Figure S9 shows the FT-NMR spectra with (red) and without (black) microwave at the magnetic field position ω_S/γ_e - ω_H/γ_e corresponding to the solid effect maximum. We used protonated water (H_2O) for this experiments to better estimate the water proton DNP enhancement.

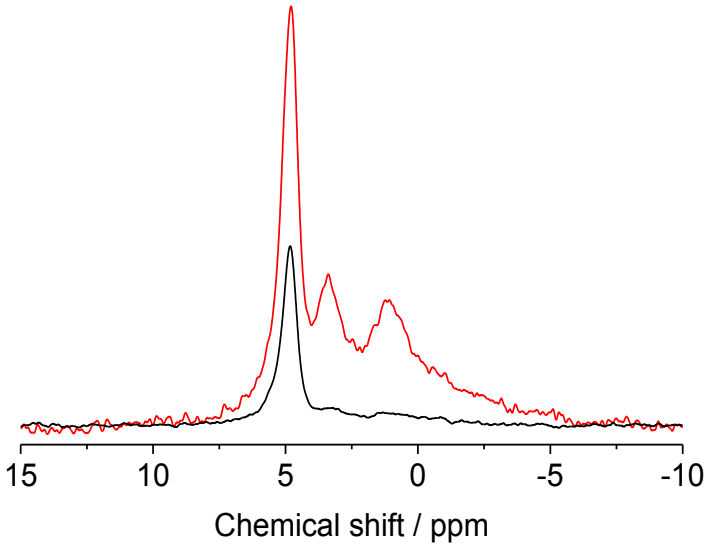

Figure S9. NMR signals of BDPA/DMPC/H_2O sample with molar ratios: 1/10/500 with microwave excitation power of 5 W (red) and without microwave excitation (black) at the magnetic field position corresponding to ω_S/γ_e - ω_H/γ_e. Both signals are normalized with respect to the number of acquisitions (with microwave 64, without microwave 256). The lipid signal peaks at 3.5 ppm (corresponds to the choline head group) and at 1 ppm (corresponding to the lipid acyl chain protons) show a DNP enhancement of about 12. The signals at 4.8 ppm corresponds to H_2O and is enhanced to about 1.

Table S2. DNP enhancements calculated for BDPA/DMPC (1/100, 1/50, 1/20, 1/10, 1/5) in aqueous medium. The error of the DNP enhancements is in all cases about 10%.

Molar ratio of BDPA to lipid	DNP enhancement		
	the lipid acyl chain protons	the choline head group	water
1/100	5	5	~1
1/50	7	7	~1
1/20	9	9	~1
1/10	12	12	~1
1/5	12	12	~1

Solid Effect DNP enhancements as a function of the molar ratio between BDPA/DMPC

Figure S10 shows the maximum obtained DNP enhancements with a microwave power of 5 W for different molar ratios of BDPA/DMPC. Optimum enhancements are obtained for 1/10 molar ratio. The DNP enhancement increases up to a BDPA/DMSO ratio of 1/10. This corresponds to the observed narrowing of the BDPA line by increasing this ratio (Figure S1), indicating the importance to have a narrow EPR line to efficiently drive the EPR transitions.

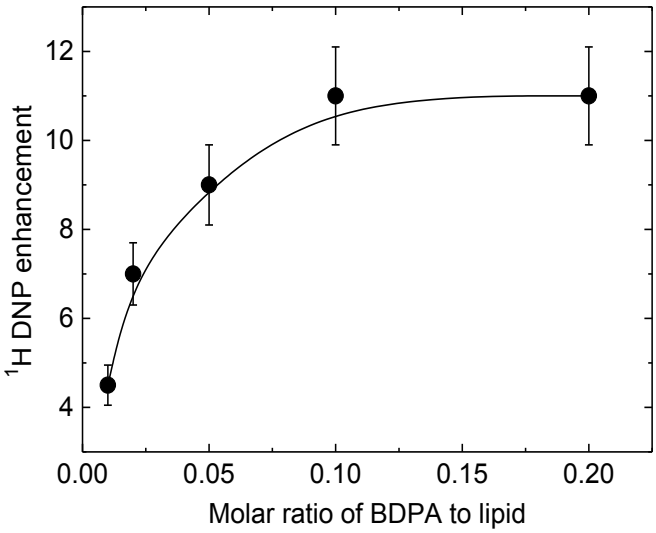

Figure S10. DNP enhancement as a function of the BDPA/DMPC molar ratio: 1/5, 1/10, 1/20, 1/50, 1/100 at the magnetic field position corresponding to ω_S/γ_e - ω_H/γ_e. The corresponding CW-EPR spectra for these samples are shown in Figure S1.

DNP enhancement as a function of applied mw power

Figure S11 shows the DNP enhancement at the high-field solid-effect position as a function of the applied microwave power. The microwave power dependence shows a linear increase with microwave power up to 3 W, with a slightly reduced slope at higher microwave power. The maximum enhancement of 12 is obtained for the maximum available microwave power of 5 W. The reduced increase at higher microwave power might be due to sample heating and related reductions in the solid effect efficiency.

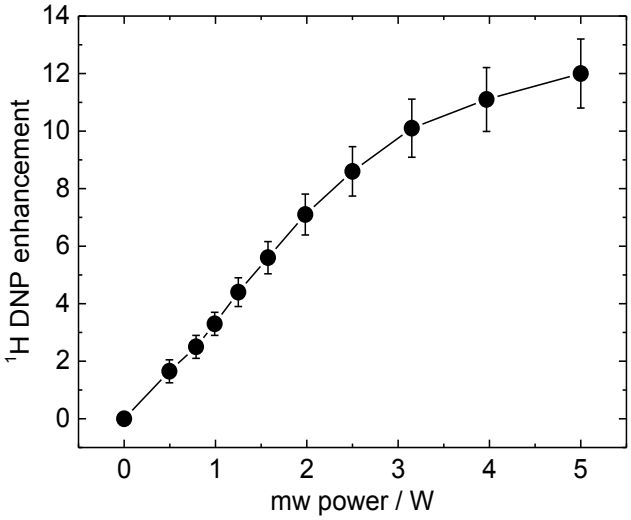

Figure S11: DNP enhancement as a function of the applied microwave power. The DNP enhancement is measured at a magnetic field position corresponding to ω_S/γ_e - ω_H/γ_e corresponding to the high-field solid-effect position.

Lipid proton relaxation times

Figure S12 shows the inversion recovery measurements of the longitudinal relaxation time of the lipid acyl chain protons both with and without BDPA radical present.

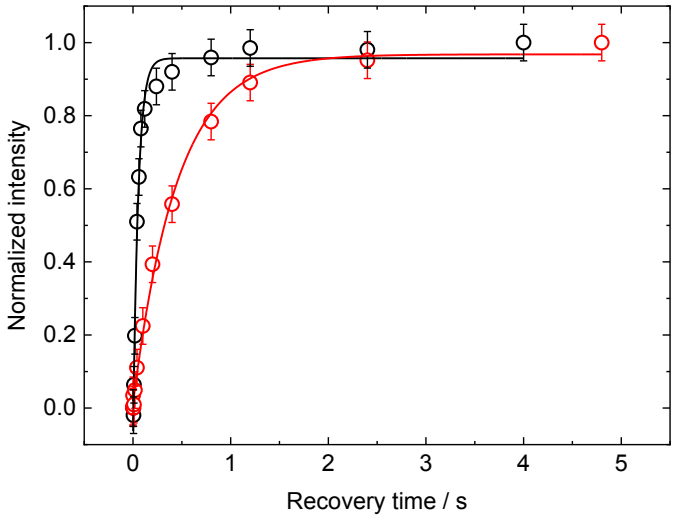

Figure S12. Experimental inversion recovery relaxation data for DMPC lipid acyl chain protons at 298 K. Black circles: experimental data in the presence of BDPA in DMPC lipid with molar ratio of 1/10. Red circles: experimental data in the absence of radical BDPA. The red and black lines show the fit of the data with a proton longitudinal relaxation time of $T_1 \approx 50$ ms for the sample with BDPA radical and $T_1 \approx 450$ ms for the lipid without radical.

DNP buildup time

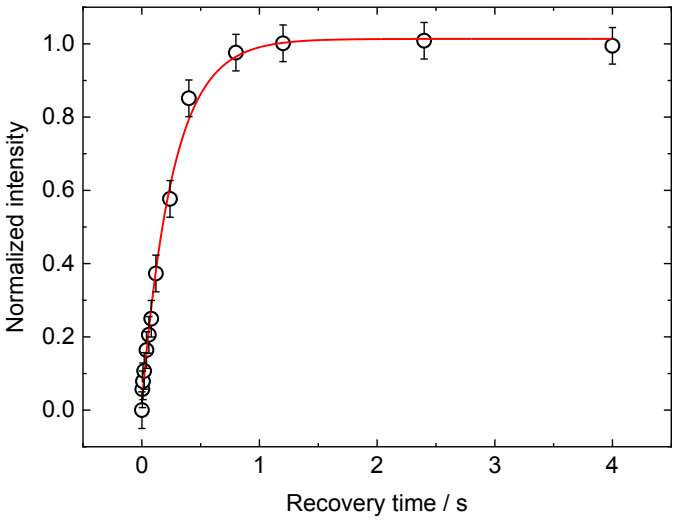

Figure S13. Experimental proton DNP buildup time for DMPC lipid acyl chain protons in the presence of BDPA with molar ratio of 1/10 and microwave power of 5 W. The black line shows the exponential fit of the data with a DNP buildup time of $T_B \approx 260$ ms. The DNP buildup time of T_B is slower than the proton longitudinal relaxation time T_1 (in the presence of radical DBPA) due to different temperatures for the experiments: 298 K for the T_1 measurement and ~330 K for the determination of T_B.

Electron spin relaxation times at X-band frequency

Figure S14 shows the two-pulse Hahn echo decay and inversion recovery measurements for determination of the electron spin transverse and longitudinal relaxation times (T_{2e} and T_{1e}) of a BDPA/DMPC sample with a molar ratio of 1/100 at 298 K at X-band frequency.

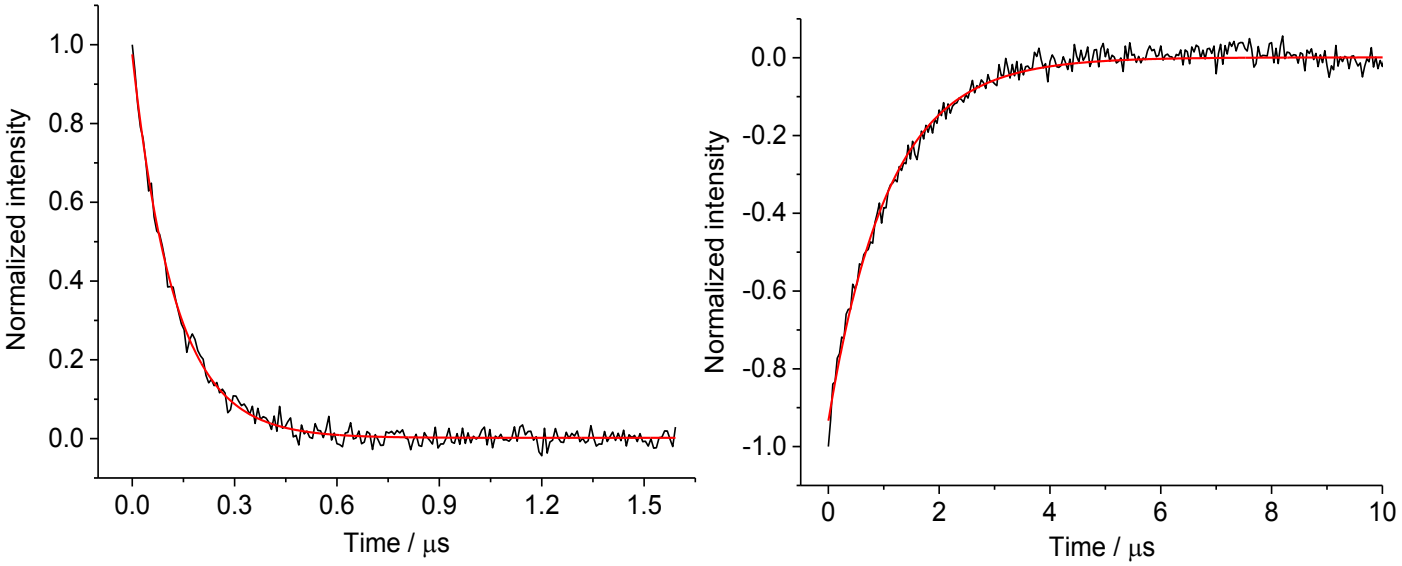

Figure S14. Experimental X-band electron spin relaxation data for BDPA in DMPC lipid bilayers with molar ratio of 1/100 at 298 K. Left: transverse electron spin relaxation time (T_{2e}). Right: longitudinal electron spin relaxation time (T_{1e}). The red lines show the exponential fit of the experimental data with a transverse relaxation time of $T_{2e} \approx 123$ ns and a longitudinal relaxation time of $T_{1e} \approx 1080$ ns.

Figure S15 shows the free induction decay (FID) and FID-detected inversion recovery measurement of the longitudinal relaxation time T_{1e} of the BDPA/DMPC sample with a molar ratio of 1/10 at 298 K at X-band frequency. For this sample with a higher BDPA concentration we could not observe a two-pulse Hahn echo signal anymore due to too short transverse electron spin relaxation time.

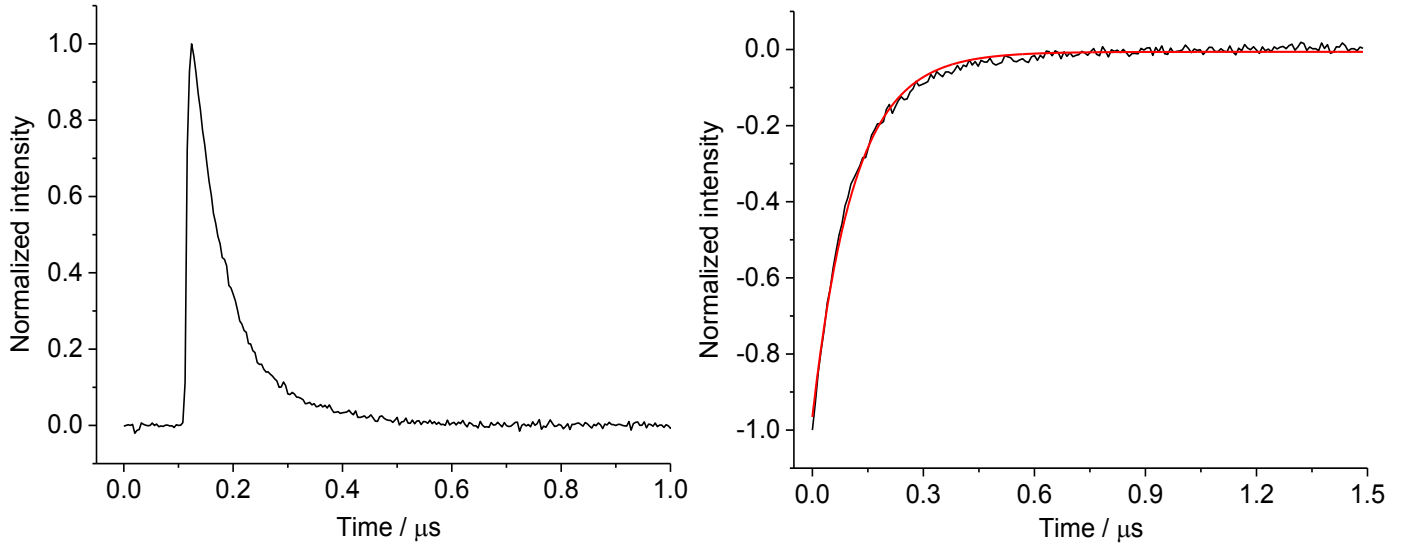

Figure S15. Experimental X-band electron spin relaxation data for BDPA in DMPC lipid bilayers with molar ratio of 1/10 at 298 K. Left: free induction decay (FID) signal. Right: FID-detected longitudinal electron spin relaxation time T_{1e}. The red line shows the exponential fit of the experimental data with a longitudinal relaxation time of $T_{1e} \approx 112$ ns.

Estimated solid effect DNP efficiency

The relative transition probability of the forbidden electron-nuclear spin transition $W_{forbidden}$ in comparison to the allowed EPR transition probability $W_{allowed}$ can be estimated as [4]:

$$u^2 = \frac{W_{forbidden}}{W_{allowed}} \approx \frac{A_{aniso}^2}{4 \cdot \omega_H^2}$$

We estimated the anisotropic interaction between the electron spin and lipid proton spins (A_{aniso}) as < 1 MHz considering previous ENDOR measurements of BDPA in polystyrene [5]. Typically this leads to a 10^{-6}-10^{-8} reduced transition probability driving such a coupled electron-nuclear spin transition under DNP conditions [6]. With our Fabry-Pérot microwave resonance structure and our available microwave power of 5 W we reach a microwave field strength B_1 of about 6 G at the sample, leading to a Rabi-Frequency ω_1 of about 10^8 rad·s^{-1}, resulting in an inversion time of about 28 ns and allowing saturation of the allowed EPR transitions. The transition rate for the forbidden transition can be calculated to [6]:

$$W^{\pm} = 2\pi \cdot u^2 \cdot \omega_1^2 \cdot g(\omega - \omega_s \pm \omega_I)$$

with $g(\omega)$ being the normalized EPR lineshape function. This leads to transition rates for the forbidden transition in the range of $W^{\pm} \approx$ 0.4-40 s^{-1}. With the rates W_I^x = 2 s^{-1} (lipid proton spin relaxation rate without BDPA) and W_I^S = 20 s^{-1} (lipid proton spin relaxation with BDPA) an overall solid-state DNP enhancement of:

$$\varepsilon_{DNP} = 1 + \frac{W^{\pm}}{W^{\pm} + W_I^S + W_I^x} \cdot \left(\frac{\gamma_S}{\gamma_I} - 1\right) \approx 14 - 440$$

can be expected. Thus, the observed DNP enhancement of ±12 by the solid-state mechanism seems feasible under our specific experimental condition for a BDPA-lipid complex.

References:

1. Delage-Laurin, L.; Palani, R. S.; Golota, N.; Mardini, M.; Ouyang, Y.; Tan, K. O.; Swager, T. M.; Griffin, R. G. Overhauser Dynamic Nuclear Polarization with Selectively Deuterated BDPA Radicals. *J. Am. Chem. Soc.* **2021**, *143* (48), 20281–20290.
2. Stoll S.; Schweiger A. EasySpin, a comprehensive software package for spectral simulation and analysis in EPR *J. Magn. Reson.* **2006**, 178(1), 42-55.
3. Bretschneider M.; Spindler P.; Rogozhnikova O.; Trukhin D.; Endeward B.; Kuzhelev A.; Bagryanskaya E.; Tormyshev V.; Prisner T. Multiquantum Counting of Trityl Radicals. *J. Phys. Chem. Lett.*, **2020**, 11(15), 6286-6290.
4. Mims W.B. Envelope modulation in spin-echo experiments. *Phys. Rev. B* **1972**, 5, 2409-2419.
5. Bennati M.; Farrar C.T.; Bryant J.A.; Inati S.J.; Weis V.; Gerfen G.J.; Riggs-Gelasco P.; Stubbe J.; Griffin R.G. Pulsed electron-nuclear double resonance (ENDOR) at 140 GHz. *J. Magn. Reson.* **1999**, 138 (2), 232-243.
6. Wind, R. A.; Duijvestijn, M. J.; van der Lugt, C.; Manenschijn, A.; Vriend, J. Applications of Dynamic Nuclear Polarization in 13C NMR in Solids. *Prog. Nucl. Magn. Reson. Spectrosc*. **1985**, 17, 33–67.

6. ^{1}H OE and SE DNP on liposome doped with nitroxides

6.1 Introduction

Encouraged by the dipolar OE DNP enhancements observed on lipid bilayers at 9.4 T,[45] further investigation was conducted on the liposome doped with site-specific nitroxide-based spin labels and shown in Section 6.2. To explain the observed OE DNP enhancements, coupling factors calculated with dipolar HFI from MD simulations[92] were compared with the experimental results. Though the MD simulations suggest a 10-30 % coupling factor of the experimental value, the fast dynamics of the lipid molecules comparable to the critical correlation time (0.6 ps) is well captured by MD. The observed SE indicated the presence of a non-averaged HFI field on lipid molecules which well supports the modulation responsible for the OE arising from the local fast dynamics in lipids.

A theoretical work studying the SE at high fields[93,94] with a g-tensor broadened OE saturation profile is presented in Section 6.3. Part of the OE DNP enhancements observed on lipids shown in Section 6.2 was interpreted within this theoretical frame. This theory will be implemented together with the MD simulations to rationalize our results in the near future.

6.2 Corresponding Manuscript

The results of the OE DNP on lipids doped with spin-labeled lipids are summarized in a draft attached in the following pages. The author performed the DNP/NMR and EPR experiment, deconvoluted the overlapped NMR signal and calculated the DNP coupling factor. The trajectories of MD simulations were provided by Dr. Deniz Sezer. The calculation of the dipolar acf and the resulted coupling factor from MD trajectories were performed by the author.

Overhauser and Solid Effect ^{1}H Dynamic Nuclear Polarization on Liposome at Ambient Temperature and 9.4 T

Abstract

In the past decades, dynamic nuclear polarization (DNP) as a technique to enhance NMR sensitivity has gained revived attention especially at high magnetic fields. Previously, DNP observed on oriented lipid bilayers at ambient temperature and 9.4 T demonstrates the potential of fast local dynamics to drive DNP process at high fields. In this work, DNP experiments were performed on liposome doped with site-specific spin labels above the lipid gel-to-liquid-crystalline phase transition temperature at 9.4 T. Appreciable ^{1}H DNP enhancements attributed to Overhauser effect (OE) and solid effect (SE) were observed on lipid molecules. The temperature (310 - 340 K) and spin-label position dependent OE DNP efficiencies of the lipid acyl chain, choline head group and the internal water molecules were experimentally investigated. The experimental DNP coupling factors were compared with the values calculated by the dipolar auto-correlation function obtained from MD simulations, which provides an insight into the fast dynamics inside lipid bilayers.

1. Introduction

Nuclear Magnetic Resonance (NMR) spectroscopy is a powerful tool to characterize molecules on the atomic level but is also limited by its intrinsically low sensitivity. Dynamic Nuclear Polarization (DNP) can potentially increase the nuclear spin polarization by at least three orders of magnitudes utilizing the comparatively large polarization of the unpaired electron spins. However, Overhauser effect (OE), which serves currently as the only active DNP mechanism in non-viscous solution, is predicted to be significantly less efficient at high fields with the dynamics described by the molecular translational and rotational motion.(Hausser and Stehlik 1968)

The OE DNP previously observed on oriented lipid bilayers at ambient temperature suggested a polarization transfer driven by the dipolar hyperfine interaction with a negative enhancement up to -10.(Jakdetchai et al. 2014) Yet the dynamics responsible for the fast dipolar modulations

could not be explained with the molecular motions described by the classical Stokes-Einstein model, as the characteristic time of the lipid lateral diffusion and axial rotation (Ellena, Lepore, and Cafiso 1993; Filippov, Orädd, and Lindblom 2004; Klauda et al. 2008) are at least three orders of magnitudes slower as the critical correlation time at this field ($1/\omega_e \approx 0.6$ ps). To understand the responsible polarization transfer mechanism, we extended this experiment to samples composed of liposomes doped with site-specific nitroxide-based spin labels under a systematic control of the sample temperature. Taking into account our recently observation of solid effect (SE) DNP in lipids doped with BDPA(Kuzhelev et al. 2022), we also measured the DNP profile to examine the existence of SE in the presence of the broad-line radicals. While the dynamic modulation of the electron-nuclear (e-N) hyperfine interaction modeled by the molecular translation and rotation is not adequate to describe the viscous and anisotropic lipid environment, an approach to predict the coupling factor by calculating the dipolar auto-correlation function (acf) from MD simulations is used to rationalize our observations.(Sezer, Prandolini, and Prisner 2009)

2. Experiments

2.1 Materials

Phospholipids: 1,2-dimyristoyl-sn-glycero-3-phosphocholine (DMPC; powder) and 1,2-dioleoyl-sn-glycero-3-phosphocholine (DOPC; powder) were obtained from Avanti polar lipids.

Spin-labeled lipids: 1-palmitoyl-2-stearoyl-(*n*-doxyl)-sn-glycero-3-phosphocholine (*n*-doxyl-PC, n=5, 10, 16; powder) and 1,2-dipalmitoyl-sn-glycero-3-phospho(tempo)choline (TEMPO-PC; powder) were obtained from Avanti polar lipids.

Others: 4-Hydroxy-2,2,6,6-tetramethyl-piperidin-1-oxyl (TEMPOL, purity: 97%) and Deuterium oxide (D2O, 99.990% D) were obtained from Sigma-Aldrich.

Note: The phospholipids and spin-labeled lipids used in this work are illustrated in Figure 1 B. For convenience, the spin-labeled lipids are abbreviated as n-PC according to their labeling position. For instance, the head group-labeled TEMPO-PC is abbreviated as 0-PC; the chain-labeled *n*-doxyl-PC with n = 5,10,16 are abbreviated as 5-,10-,16-PC, respectively (Fig. 1B). All radicals used are with natural abundance of nitrogen.

2.2 Sample preparation

The DNP/NMR/EPR samples were prepared as liposome in D_2O. Liposome samples were formed by one of the phospholipids (DMPC or DOPC) and doped with one of the spin-labeled lipids with a nitroxide moiety at either the phosphocholine (PC) head group or the hydrocarbon chain. A mixture of DMPC and n-PC with a desired molar ratio was dissolved by adding chloroform into a flask to form a homogeneous lipid solution with a concentration of ~10 mM. The majority of the solvent was removed by a nitrogen gas flow until a lipid thin film yielded at the bottom of the flask. Residual traces of chloroform were removed under vacuum (< 4 x 10^{-6} bar) for at least 4 hours. Subsequently, to enable the liposome formation, the dried DMPC/n-PC thin film was hydrated with D_2O for more than 40 minutes at room temperature (25 ˚C), which is above the phase transition temperature of DMPC (24 ˚C) and DOPC (-17 ˚C). The DNP sample is a mixture of lipid/n-PC/D_2O with a molar ratio of 20/1/1000. The n-PC molar concentration is calibrated as 43 ± 10 mM by cw EPR at X-band.

Liposome doped with TEMPOL nitroxide were prepared as a referential sample to compare with previous reported results (Jakdetchai et al. 2014). The DMPC thin film was prepared as in the previous procedure only without adding n-PC. Finally, TEMPOL D_2O solution was added to the dried DMPC film to enable liposome formation. All liposome samples were prepared without degassing, sonication or extrusion.

2.3 NMR/DNP experiments

All DNP/NMR experiments in this work were performed on a homebuilt DNP spectrometer operating at 9.4 T (electron 263 GHz/^{1}H 400 MHz).(Denysenkov et al. 2008) A gyrotron (Gycom, Russia) is used as mw source which can provide a mw power up to about 6 W at the probe inlet. A homebuilt stripline Fabry-Pérot (FP) DNP probehead was used in this work with the capability of both NMR and EPR excitation and detection.(Denysenkov, Dai, and Prisner 2021). Liposome samples were prepared and placed onto the heat-conducting flat metal mirror with a volume of ~50 nL in the resonator (Figure 1 A). The sample was subsequently sealed by a flat Teflon ring (20 μm thickness, 1.5 mm inner diameter) lubricated with grease and a quartz plate as the cover. Benefiting from the thin thickness of the disc-shaped sample and the high heat conductivity of the plane mirror substrate, the sample temperature under full mw power is only moderately increased (20 ~ 30 K) and can be controlled by blowing nitrogen gas against the backside of the substrate with an error < 10 K. The DNP measurements were

done at temperatures in the range from 310 K to 340 K, which are all above the lipid transition temperature. All ^{1}H NMR/DNP spectra were measured with an optimized single $\pi/2$ pulse, a repetition delay of 1 s and a scan number ranging from 64 to 1024 depending on the signal-to-noise ratio. ^{1}H T_1 relaxation times of lipid samples with and without radicals were measured with inversion recovery pulse sequences between 310 - 330 K with FP probehead.

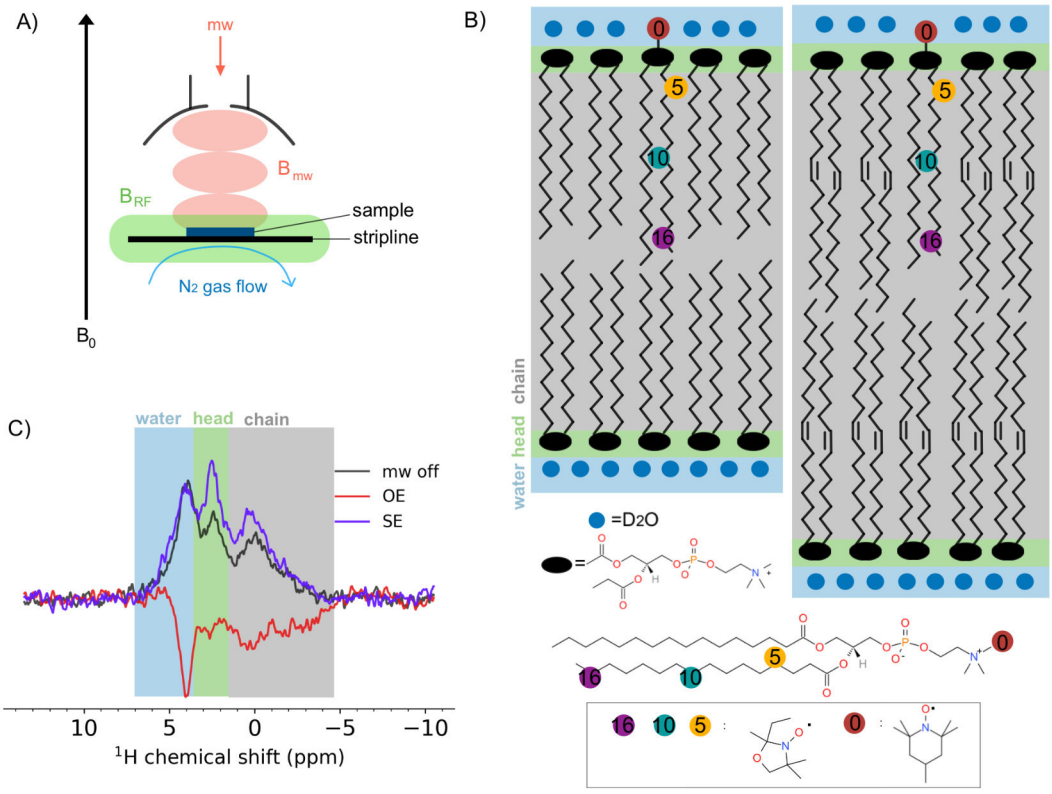

Figure 1. (A) Stripline Fabry-Pérot triple resonance structure with N_2 gas flow to control sample temperature. (B) Schematic picture of the DNP lipid sample: spin-labeled lipids (0-PC: TEMPO-PC; 5-,10-,16-PC: *5-,10-,16*-doxyl-PC) inside phosphatidylcholine (DMPC, DOPC) bilayer. (C) Demonstration of OE DNP-enhanced (observed at $B_0 = \omega_e/\gamma_e$, red curve), SE DNP-enhanced (observed at $B_0 = (\omega_e + \omega_{1H})/\gamma_e$, purple curve) and non-enhanced (black curve) ^{1}H NMR spectra of DMPC doped with 16-PC.

2.4 NMR/DNP signal deconvolution and enhancements calculation

With a moderate sample temperature, the liposome samples were stable during the DNP experiment up to 10 h. As demonstrated in Figure 1 C, NMR spectrum of DMPC at thermal equilibrium (black curve) are compared with OE enhanced signal at field position $B_0 = \omega_e/\gamma_e$

(red curve) and SE enhanced signal at $B_0 = (\omega_e + \omega_{1H})/\gamma_e$ (purple curve). The spectral resolution of the obtained NMR/DNP spectra was good enough to resolve the ^{1}H signal of lipid acyl chain (abbr. chain), lipid choline head group (abbr. head) and residual H_2O (abbr. water), respectively. Since the glycerol signal is much weaker compared with the water and choline head group and is overlapped with both of them, it was neglected in the analysis. To deconvolute the individual contributions of three signals (chain, head, water), a home-written MATLAB script based on its optimization toolbox was used. The lineshape of the signals is assumed to be a pseudo-Voigt function (V) which is a linear combination of Gaussian (G) and Lorentzian (L) function, and is given as $V(\delta, k, \Gamma_G, \Gamma_L) = k \cdot G(\delta, \Gamma_G) + (1-k) \cdot L(\delta, \Gamma_L)$, where δ is the chemical shift of the NMR signal, Γ is the full width at half maximum and k is the weighted contribution of Gaussian function.

The DNP enhancements ε were calculated with the formula

$$\varepsilon = (I_{DNP}/I_{Bol}) \cdot (N_{Bol}/N_{DNP}) - 1$$

where I_{DNP} and I_{Bol} are respectively the signal integral of NMR signal under DNP condition or Boltzmann thermal equilibrium, and N_{DNP} and N_{Bol} are respectively the scan numbers of NMR experiments under DNP condition or Boltzmann thermal equilibrium. Notably, the signal of choline head protons is partially overlapped with signal of water and lipid chain. To estimate the error, the deconvolution was performed repeatedly with slightly varying initial fitting conditions.

2.5 EPR measurements

The EPR measurements in this work were performed on a commercial Bruker Elexsys E500 spectrometer at 0.34 T and the DNP spectrometer with FP probe at 9.4 T. Both spectrometers are equipped with a temperature control unit. The magnetic field sweep at 9.4 T was accomplished by using a z-cryoshim coil, which supports a sweep range of current up to $\pm$ 20 A corresponding to $\mp$ 80 mT of the magnetic field.

3. Results and discussion

3.1 Solid-effect/Overhauser-effect ^{1}H DNP profile of lipid acyl chain

DNP enhancements attributed to OE and SE mechanisms were observed on lipids. As shown in Figure 2 A-F, the ^{1}H DNP field profile of lipid chain together with the corresponding EPR absorption spectrum were measured at 320 K. The two different DNP patterns can be characterized by their field dependences on ω_e, where OE DNP, has a maximum efficiency at the maximal EPR signal position $B_0 = \omega_e/\gamma_e$ and SE DNP was observed at the field position $B_0 = (\omega_e \pm \omega_{1H})/\gamma_e$. The OE and SE DNP profile are partially overlapped with each other because of the broad EPR profile of nitroxide. To obtain individual contributions, the enhancement profiles (ε) are fitted with the equation:

$$\varepsilon = \varepsilon_{OE} \cdot \mathrm{g}(B_0) \; - \; \varepsilon_{SE} \cdot \mathrm{g}(\frac{\omega_e}{\omega_e + \omega_{1H}} B_0) + \varepsilon_{SE} \cdot \mathrm{g}(\frac{\omega_e}{\omega_e - \omega_{1H}} B_0)$$

where ε_{OE} (red dashed curve), ε_{SE} (purple dashed curve) are respectively the DNP enhancements of OE and SE to fit. $\mathrm{g}(B_0)$ is the experimental-determined EPR absorptive line shape as a function of external magnetic field B_0 normalized by its maximum amplitude. The simulated field profiles qualitatively match the experimental data with some inconsistency in the field range between the fitted OE and SE profile. The obtained OE and SE DNP enhancements of individual samples are shown in Figure 2 G. The observed enhancements on lipid chain attributed to SE (0.5 to 1.5) are generally smaller than the OE (-1 to -3) for all radicals.

3.2 temperature-dependent OE ^{1}H DNP

To understand the temperature dependence of the fast dynamics driven the OE DNP on lipids, DNP experiment was further studied at the temperatures from 310 K to 340 K at the OE field position ($B_0 = \omega_e/\gamma_e$). Since the SE DNP enhancement is small compared to OE and has a negative dependence on the dynamics which is faster with increased temperatures, it was not further studied at other temperatures.

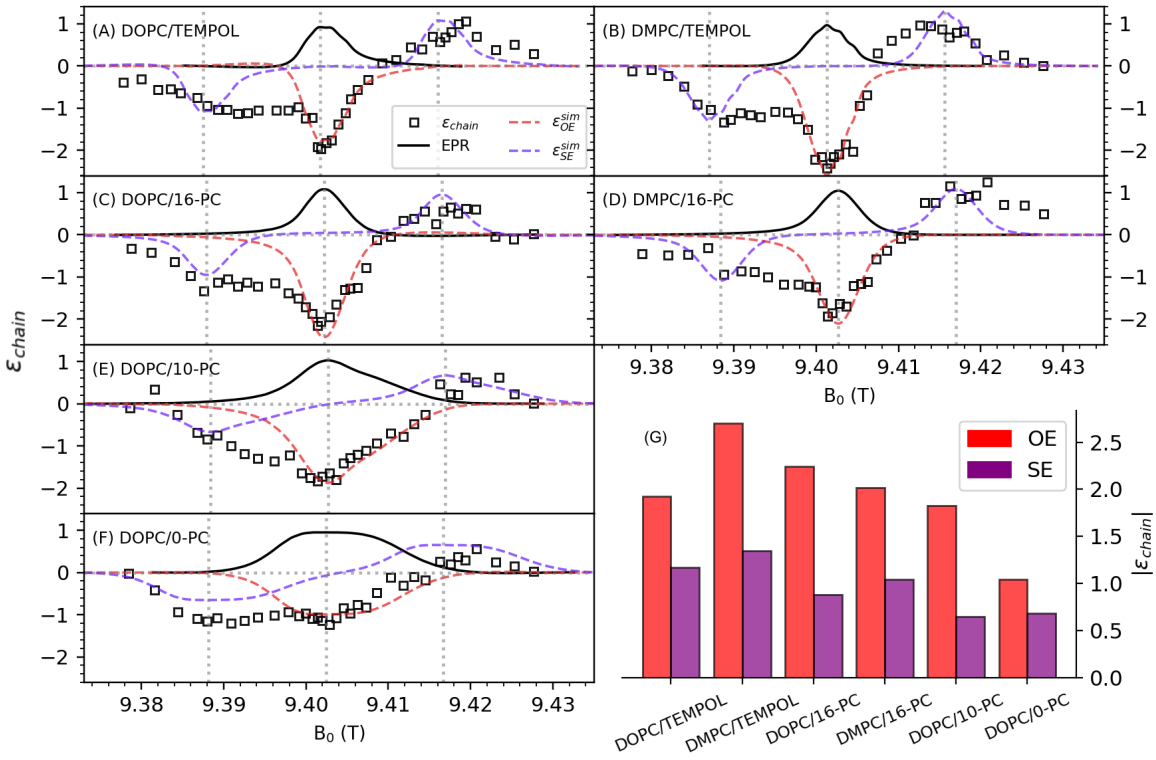

Figure 2 (A)-(F): DNP field profile (open squares) of lipid (DMPC or DOPC) doped with various radicals (TEMPOL, 16-PC, 10-PC and 0-PC) compared with corresponding EPR absorptive spectra (black curve) measured at 320 K. The DNP field profile was fitted to show the individual contributions of OE (red dashed curve) and SE (purple dashed curve); (G) Absolute OE/SE enhancement of different lipid/radical (A-F) determined by fitting.

3.2.1 OE DNP leakage factor *f* and saturation factor *s*

It is necessary to determine the leakage factor and saturation factor before extracting the coupling factor from the OE DNP enhancements. ^{1}H longitudinal relaxation time of liposome consisting of DMPC or DOPC with and without radicals were measured at 310 K and 330 K to determine the leakage factor *f*. As shown in Figure 3 A-C, leakage factors of lipid chain, head and internal water were determined in the sample with a lipid/radical ratio (L/R) of 20/1. Furthermore, leakage factors were also measured on liposome sample doped with different radical concentration, such as TEMPOL with a L/R ranging from 40/1 to 5/1 (Figure 3 D-F) or doped with 16-PC with a L/R ranging from 40/1 to 10/1 (Figure 3 G-I). With the radical concentration used for our DNP measurements (lipid/n-PC=20/1), a leakage factor of appr. 0.9 can be reached for all protons of lipid acyl chain, choline head and internal water.

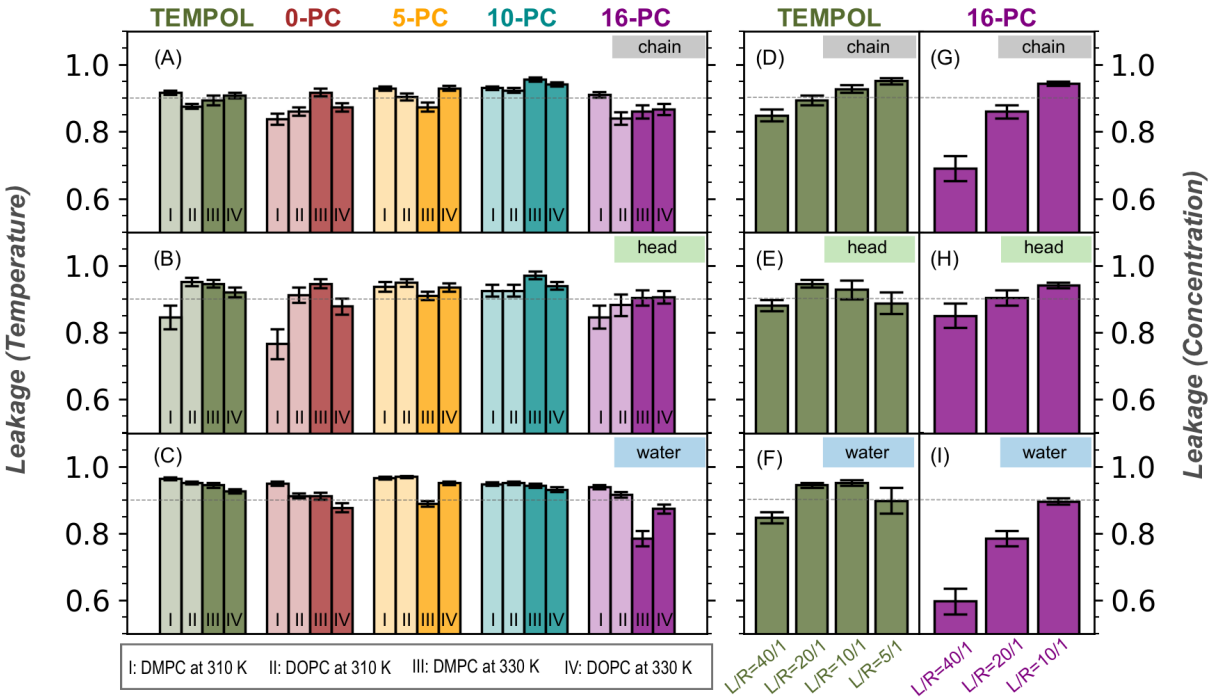

Figure 3. **(A-C)**: DNP leakage factor of (A) chain (B) head and (C) water were determined inside two kinds of lipid matrix (DMPC or DOPC) at two temperatures (310 K or 330 K) doped with various radicals (TEMPOL: green, 0-PC: red, 5-PC: yellow, 10-PC: cyan, 16-PC purple) with a lipid/radical ratio (L/R) of 20/1; Measurement temperature and type of lipid matrix are indicated by the indices on the bar. **(D-F)**: DNP leakage factor of (D) chain, (E) head and (F) water of DMPC doped with TEMPOL with different L/R measured at 330 K. **(G-I)**: DNP leakage factor of (G) chain, (H) head and (I) water of DMPC doped with 16-PC with different L/R measured at 330 K.

The DNP saturation factor of liquid sample at 9.4 T is hard to be directly accessed. This is owing to the very fast relaxation time of the electron spins of the nitroxide radicals at room temperature at high fields. In addition, the saturation behavior of nitroxide radicals with three ^{14}N hyperfine EPR transitions is further complicated by the Heisenberg exchange and ^{14}N spin relaxation. Here, we experimentally estimated the saturation factor without determination of the electron relaxation time. First, as shown in Figure 4 A, the OE DNP enhancements of DMPC doped with 16-PC were measured as mw power dependent with a temperature stabilized at 320 K. Theoretically, other factors except saturation factor were kept constant at this condition. The power dependent DNP ε were fitted with the equation:

$$\varepsilon(P_{mw}) = \varepsilon_{max} \frac{P_{mw}}{P_{mw} + K}$$

where ε_{max} is the maximal achievable DNP enhancement, equals to $f_{320K} \cdot \xi_{320K} \cdot \frac{\gamma_e}{\gamma_{1H}} \cdot s_{max}$ and s_{max} is the maximal achievable saturation factor. K is a fitting parameter reflects the EPR lineshape. As the fitting result shown in Figure 4 B, the ε_{max} of lipid chain and internal water were determined both as -3. As indicated by the achieved enhancements under a 6 W mw irradiation of lipid chain and internal water (-2 and -2.4, respectively), the saturation of spin-labeled lipids can reach about 70% and 80% of s_{max} within lipid chain and internal water, respectively.

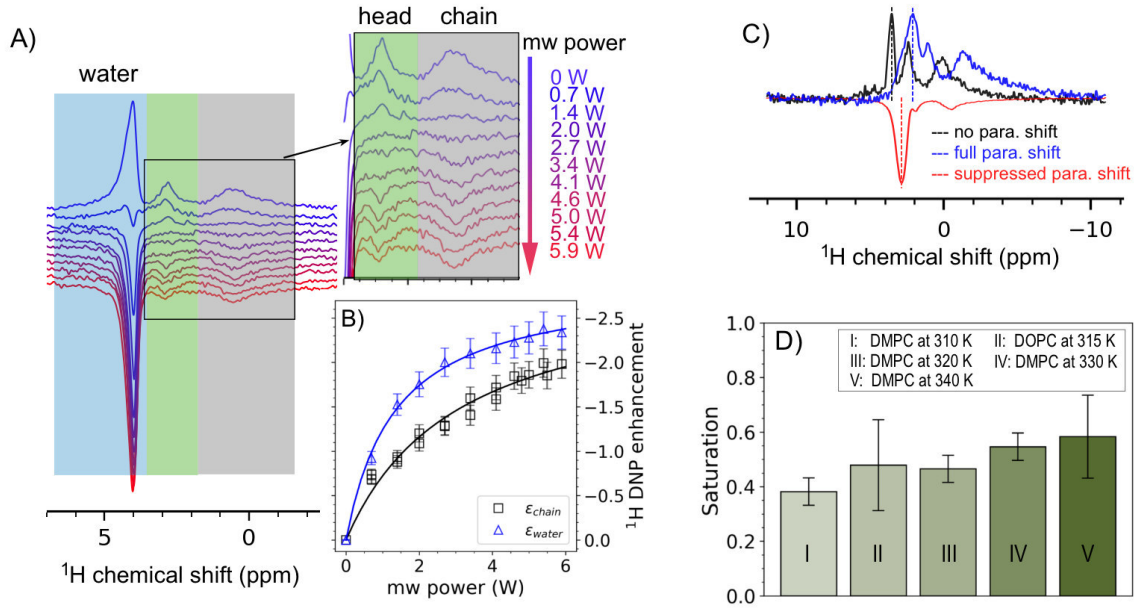

Figure 4. (A) The build-up process of ODNP enhancement of DMPC/16-PC with increased mw power; (B) mw power dependent ODNP enhancement of DMPC chain (black open squares) and water (blue open triangles) and their corresponding fitting results (black curve and blue curve, respectively); (C) Schematic introduction of access to saturation of TEMPOL in DMPC via suppressed paramagnetic shift; (D) Saturation factor of TEMPOL in lipid bilayers estimated from the suppression of the paramagnetic shift of water ^{1}H signal

As demonstrated in Figure 4 C, the saturation factor *s* can be approached by monitoring the suppressed paramagnetic shift of the NMR signal under mw irradiation (Neugebauer et al. 2013). Here, the ^{1}H NMR signal position of water internal water in liposome was monitored at different temperatures. The samples were doped with TEMPOL with a lipid/radical ratio of 5/1.

As can be seen in Figure 4 D, the determined saturation factors were in the range of 0.4 to 0.6 and show a positive tendency with increased temperature. By assuming a same saturation achieved for TEMPOL and all spin labeled n-PCs, a saturation factor of 0.5 ± 0.1 is used for further calculations for all samples.

3.2.2 OE ^{1}H DNP coupling factor ξ of water in lipids

As can be seen from the DNP field profile shown in Figure 5 A-F, OE DNP is the only observed DNP mechanism on water protons in all measured liposome samples. The minor SE feature at field corresponds to $\omega_e \pm \omega_{1H}$ is due to the error of experiments and signal deconvolution which can be neglected. The absence of SE DNP can be explained by the fast rotational and translational motion of water molecules which averages the anisotropic e-N HFI efficiently in contrast to the lipids. We also observed an offset between the field position of the maximal EPR absorption and DNP enhancements for lipids doped with TEMPOL radicals (Figure 5A-B), which can be explained by the radicals partitioned in hydrophobic phase in lipids and hydrophilic phase in water. The partitioning of TEMPO radicals in lipids has been observed by EPR measurements at other magnetic fields.(Smirnov, Smirnova, and Morse 1995)

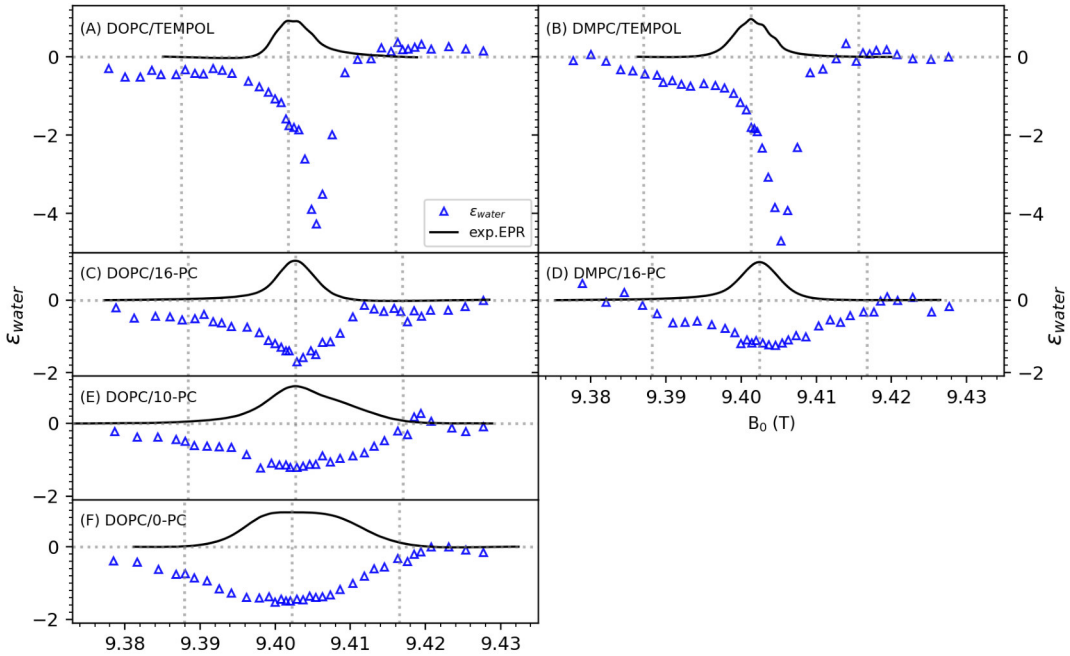

Figure 5. (A)-(F): DNP field profile (blue triangles) of internal water inside lipid (DMPC or DOPC) doped with various radicals (TEMPOL, 16-PC, 10-PC and 0-PC) compared with EPR spectra (black curve) measured at 320 K.

With the independent experiment determination of the leakage factor *f*, the saturation factor *s* and the OE DNP enhancement ε, coupling factors ξ of the internal water protons were calculated. As can be seen from the green bars in Figure 6, the largest enhancement and therefore also the largest coupling factor, is seen for TEMPOL radicals. To compare with the OE DNP studies performed on spin-labeled lipids at 0.34 T(Kausik and Han 2011), these coupling factors were analyzed using the same model only considering the out-sphere translation of water molecules with a distance of closest approach of 2.88 Å. We obtain a diffusion coefficient of water in DMPC/TEMPOL samples similar as the literature value of the bulk water (Easteal, Price, and Woolf 1989)(blue dots in Figure 6). Water in DOPC sample shows reduced diffusion coefficients compared to DMPC sample. The coupling factors ξ between the water protons and the spin-labeled n-PCs are also experimentally determined and shown in Figure 6 (left axis). By keeping the same distance of closest approach, the deduced coupling factors imply reduced water self-diffusion coefficients of D = 1.7 - 3.4 x 10^{-9} m^2s^{-1} (right blue axis), which is about 30% to 40% less compared with the bulky water. Compared with the OE DNP efficiency obtained at low field, we observed a same trend of decreased water diffusion but with a different reduced factor comparing to the water diffusion of 0.3 - 0.6 x 10^{-9} m^2s^{-1} obtained at 0.34 T(Kausik and Han 2011).

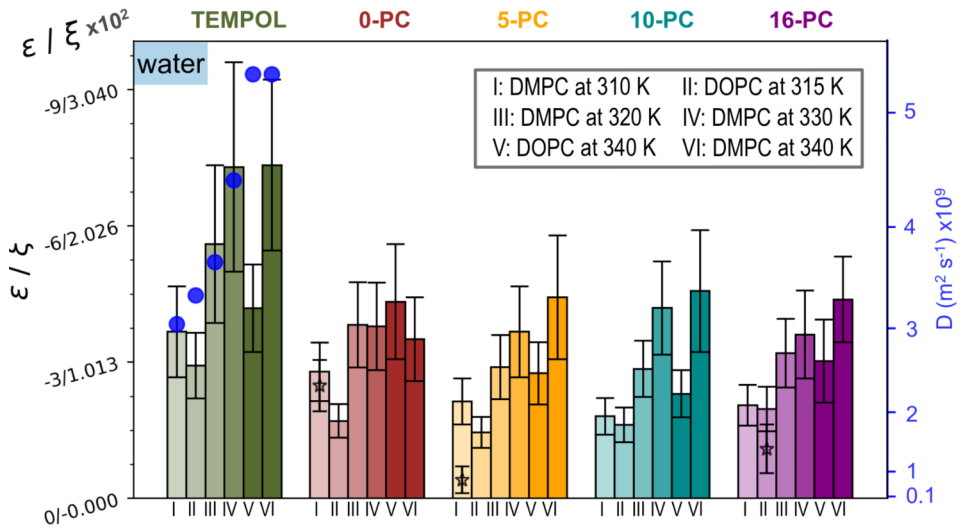

Figure 6. Temperature dependent coupling factors of water in lipid sample at different temperatures (indicated by the indices on the bottom) with different radicals (indicated by the colored labels on the top). Right axis: the diffusion coefficient D that corresponds to the coupling factor on left axis calculated with the outer-sphere translation with a distance of closest approach of 2.88 Å. Blue circles: coupling factor simulated with translational motion

of free water molecules at different temperatures. Black open stars: coupling factor calculated from the auto-correlation function deduced from the MD simulations compared with the experimental data bar at the similar temperature

To investigate this difference, we extracted the coupling factor of water molecules in lipid samples determined by the dipolar acf from the MD trajectories (Figure 6, black open stars). We have determined the coupling factor from the averaged dipolar acf (averaging of several 0.5 ns files) as shown in Figure 7-9 A. To enable the estimation of the error of MD-resulted coupling factor, we have also determined the coupling factor from individual MD trajectories as shown in Figure 7-9 B.

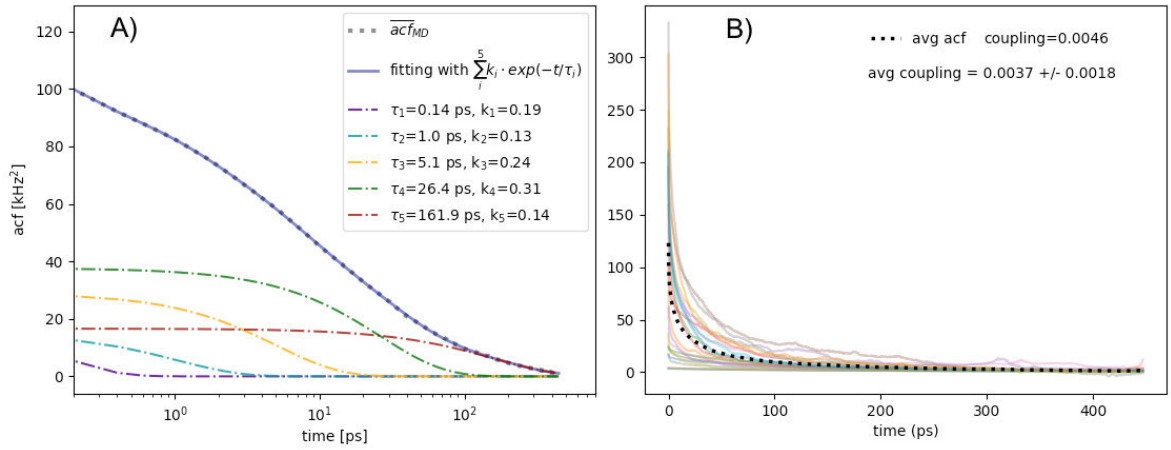

Figure 7. (A) Fitting of the averaged dipolar acf of water protons in DOPC/16-PC simulated by MD at 323 K with 5 components of exponential decays. (B) Schematic representation of the averaged dipolar acf (dashed black curve) and the dipolar acf from individual MD trajectories; the resulted coupling factor are shown as texts

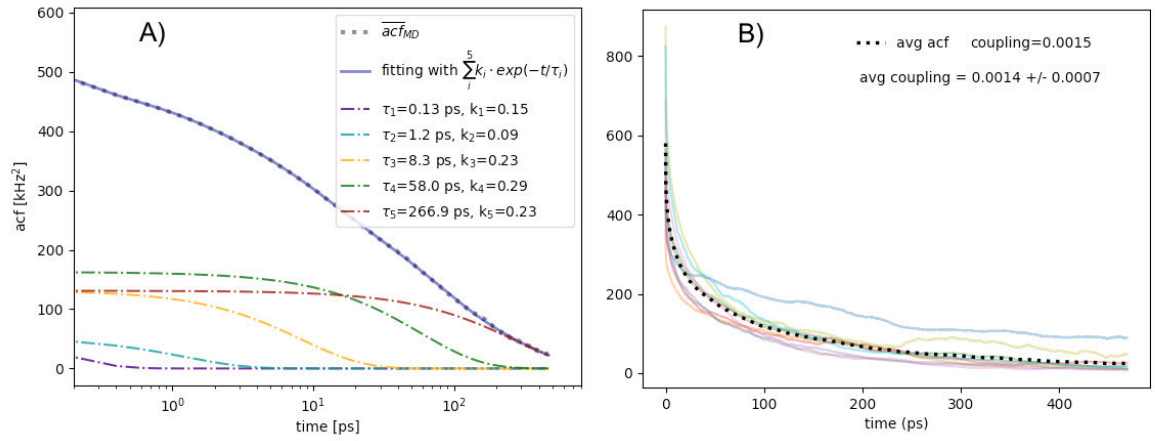

Figure 8 (A) Fitting of the averaged dipolar acf of water protons in DMPC/5-PC simulated by MD at 303 K with 5 components of exponential decays. (B) Schematic representation of the averaged dipolar acf (dashed black curve) and the dipolar acf from individual MD trajectories; the resulted coupling factor are shown as texts

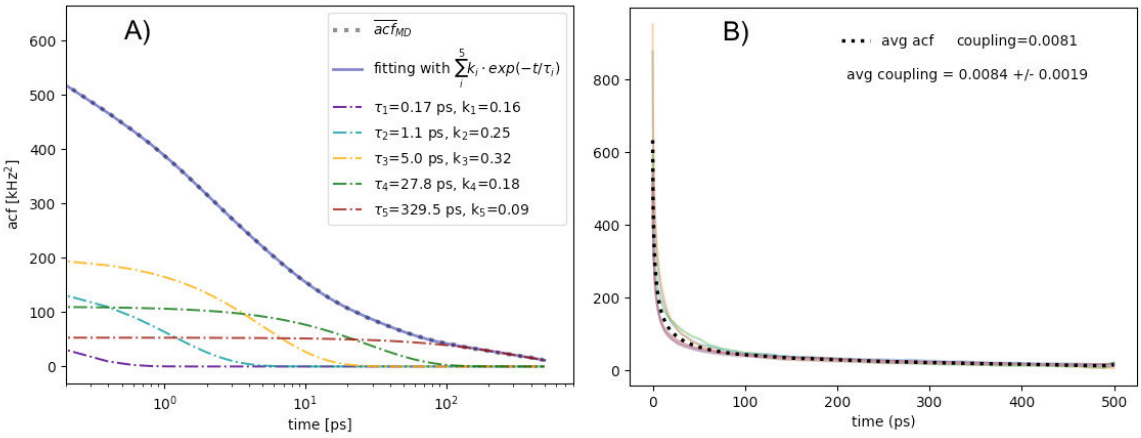

Figure 9. (A) Fitting of the averaged dipolar acf of water protons in DMPC/0-PC simulated by MD at 303 K with 5 components of exponential decays. (B) Schematic representation of the averaged dipolar acf (dashed black curve) and the dipolar acf from individual MD trajectories; the resulted coupling factor are shown as texts

To further investigate whether this coupling factor between water proton and the spin-labels comes from the water inside the lipids or water outside lipids, we have distinguished the spin-labels by its duration of stay inside or outside the lipid boundary. The boundary is determined as the location on the z-axis of the lipid bilayers (axis along the lipid molecules in bilayers) where 99.9% water protons according to the MD trajectories were outside this boundary as shown in Figure 10. And the corresponding boundary-separated coupling factor is given in Figure 11-13. The coupling factors (Fig11-13 A) inside boundary are significantly smaller than the values outside the boundary (Fig 11-13 B), which indicates the coupling factor is mainly determined by the spin interaction happened outside or close to the lipid boundary.

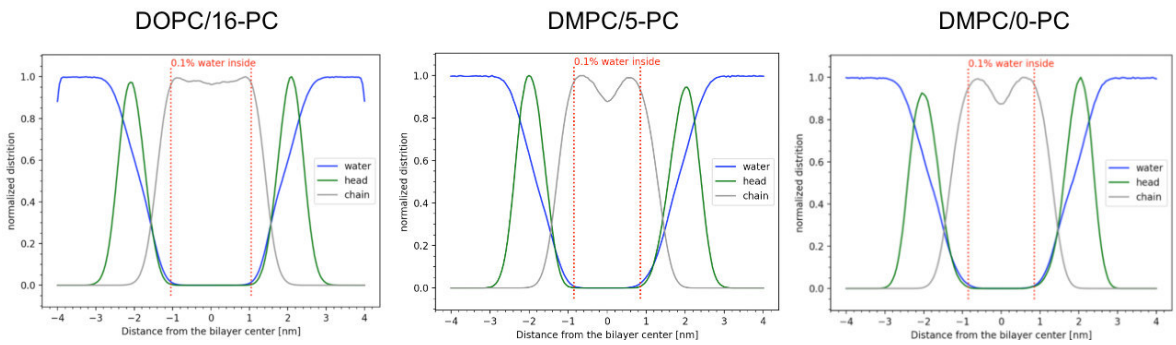

Figure 10. z-axis distribution of different protons inside (left) DOPC/16-PC sample; (middle) DMPC/5-PC sample; (right) DMPC/0-PC sample;

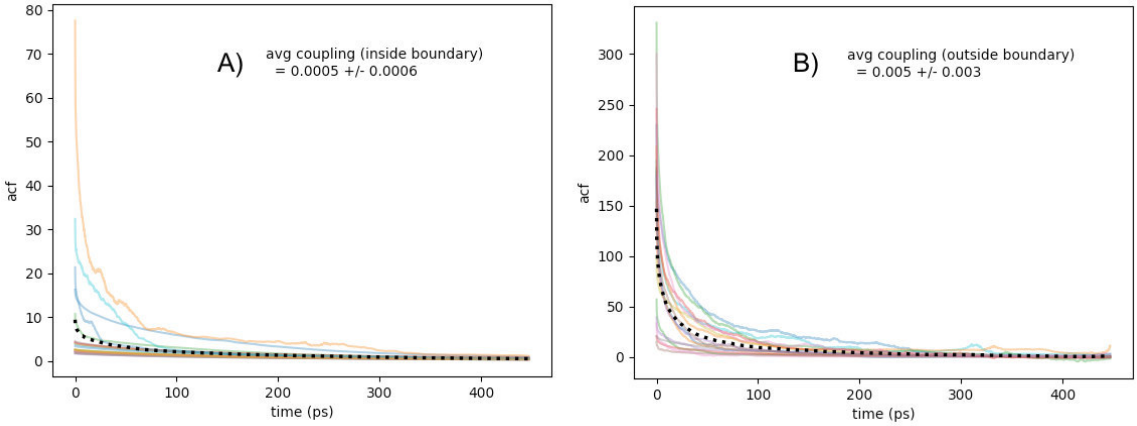

Figure 11. Coupling factor of water atoms in DOPC/16-PC determined by MD simulation at 323 K (A) inside the lipid boundary and (B) outside the lipid boundary

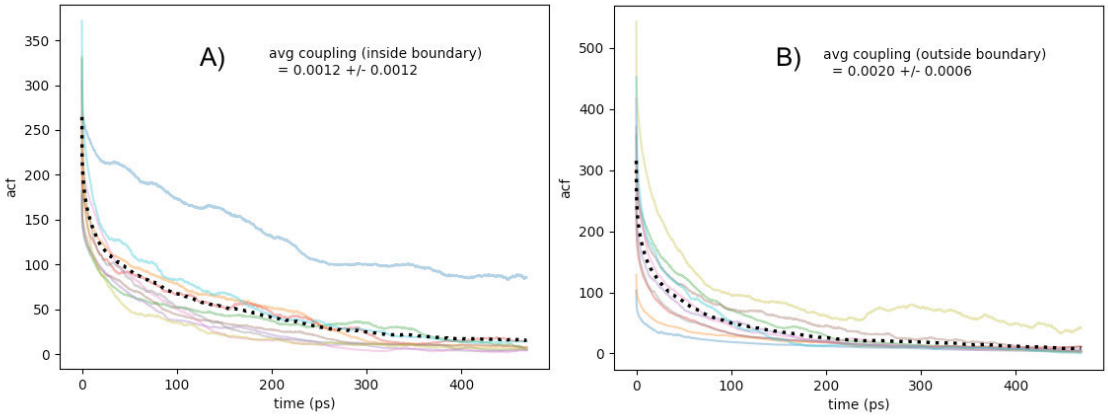

Figure 12. Coupling factor of water atoms in DMPC/5-PC determined by MD simulation at 303 K (A) inside the lipid boundary and (B) outside the lipid boundary

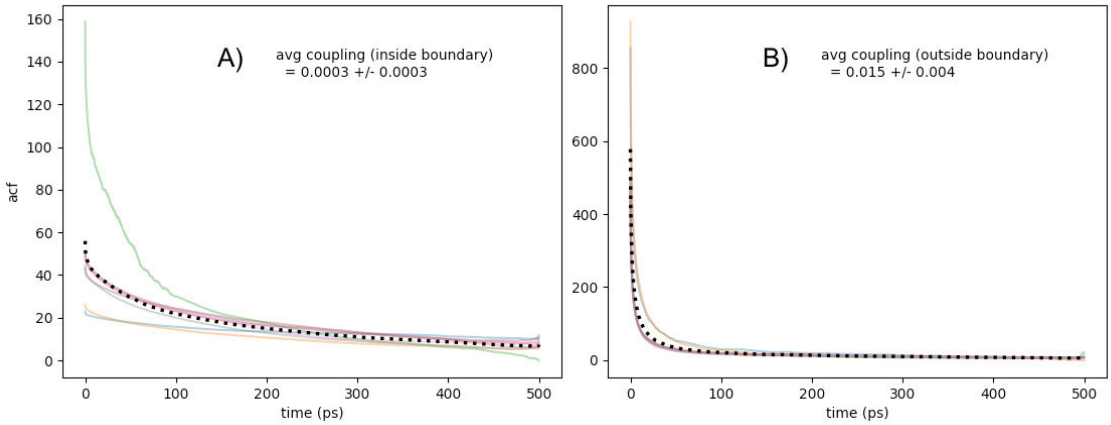

Figure 13. Coupling factor of water atoms in DMPC/0-PC determined by MD simulation at 303 K (A) inside the lipid boundary and (B) outside the lipid boundary

3.2.2 OE ^{1}H DNP coupling factor ξ of lipid

Figure 14 shows the OE DNP enhancements and the deduced coupling factors ξ of the lipid protons (A: acyl chain, B: choline head) determined at different temperatures and with different spin-label positions. The acyl chain and choline head protons of the DMPC lipid show the largest DNP enhancements and deduced coupling factors with the TEMPOL radical as polarizing agent. For the spin-labeled n-PCs as polarizing agents, a small but systematic dependence on the spin-label position is visible as indicated by the grey shadow in Figure 14. Here, the largest DNP polarization of the choline head protons (Figure 14 B, red bars) is observed for 0-PC, whereas for the acyl chain protons of DMPC the largest DNP enhancement is observed for 16-PC (Figure 14 A, purple bars), which is located in the center of the lipid bilayer. The small effect of site-specific position of spin labels on the DNP efficiency indicates the structural flexibility of the lipid molecules, so that the spin labels tethered at the head or chain terminus have contact possibility of the lipid tail or head, respectively. The conformational flexibility of lipid molecule itself(Chen and Stark 1996; Huster and Gawrisch 1999) and the spin-labeled lipids inside the bilayer structure(Kyrychenko and Ladokhin 2013) has already been well discussed. The coupling factors predicted by the MD simulations are also presented in Figure 14 (black open stars).

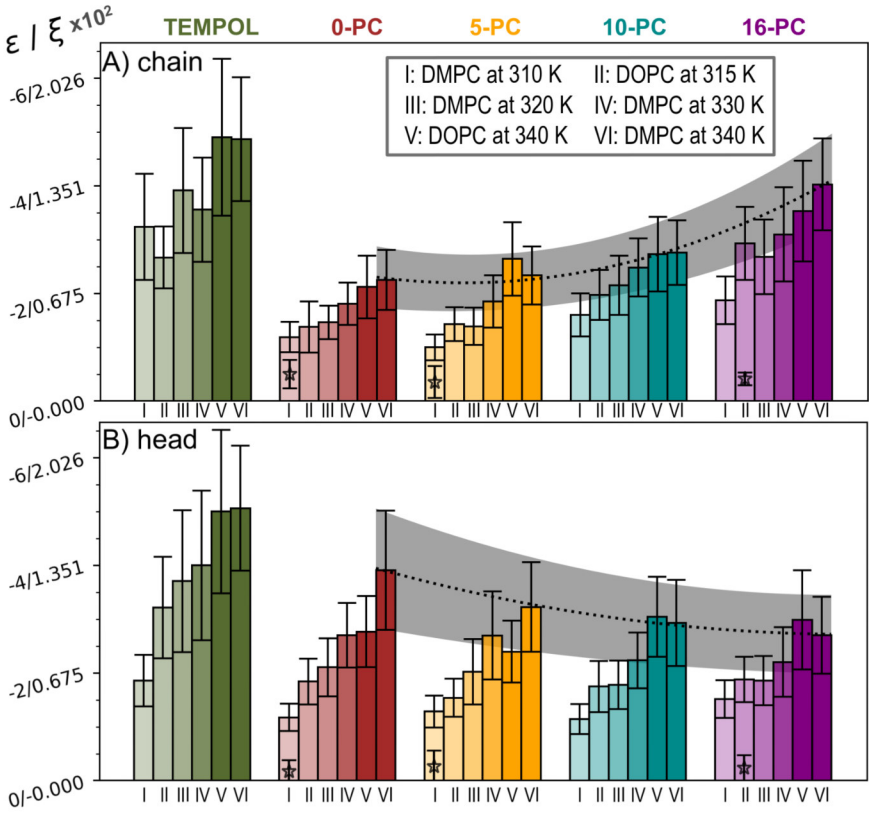

Figure 14. Temperature dependent coupling factor of lipid choline head group (A) and acyl chain (B). Sample temperature in K are indicated by the indices on the bars. The dashed lines and the grey shadows are used to indicate the slight dependence of the DNP enhancements on the site-specific position of spin labels at 340 K. Black open stars: coupling factor calculated from the auto-correlation function deduced from the MD simulations compared with the experimental data bar at its closest temperature

3.2.3 OE ^{1}H DNP coupling factor ξ determined by MD simulations

The coupling factor determined by MD simulation are summarized in the following page. ξ_{exp} is the experimentally determined DNP coupling factor, ξ_{MD} is the coupling factor determined by the dipolar acf from MD simulations. For water protons, a boundary is determined as the location on the z-axis of the lipid bilayers, namely the axis along the lipid molecules in bilayers, where 99.9% water protons were outside this position. By distinguishing the duration of individual spin-label inside or outside the lipid boundary, the coupling factor of the water protons to the inside-boundary and inside-boundary spin-labels and can be calculated respectively.

For DOPC/16-PC at 323 K:

Target nuclear	ξ_{exp}	ξ_{MD} (all acf)	ξ_{MD}/ξ_{exp}	ξ_{MD} inside boundary	ξ_{MD} outside boundary
chain	0.01	0.0014 ± 0.0004	14±4%		
head	0.007	0.0008 ± 0.0008	11±11%		
water	0.008	0.0037 ± 0.0018	46±23%	0.0005±0.0006	0.006±0.003

For DMPC/5-PC at 303 K:

Target nuclear	ξ_{exp}	ξ_{MD} (all acf)	ξ_{MD}/ξ_{exp}	ξ_{MD} inside boundary	ξ_{MD} outside boundary
chain	0.005	0.0012 ± 0.001	24±20%		
head	0.005	0.0009 ± 0.001	18±20%		
water	0.008	0.0014 ± 0.001	18±13%	0.0012±0.0012	0.002±0.0006

For DMPC/0-PC at 303 K:

Target nuclear	ξ_{exp}	ξ_{MD} (all acf)	ξ_{MD}/ξ_{exp}	ξ_{MD} inside boundary	ξ_{MD} outside boundary
chain	0.005	0.0017 ± 0.0009	34±18%		
head	0.006	0.0006 ± 0.0007	10±12%		
water	0.01	0.0084 ± 0.0019	84±19%	0.0003±0.0003	0.015±0.004

Summary

In this work, we have performed DNP experiments on liposome with a systematic control of the sample temperature and the spin-labeled positions. With the satisfied NMR signal resolution, the individual coupling factor of water, lipid choline head, and acyl chain protons were determined by a curve deconvolution. OE DNP efficiency was observed on lipid molecules, but with an insignificant Site-specific effect. This site-specific character was totally absent in OE DNP on the water molecules. This suggests the structural flexibility of lipid molecules.

The coupling factors of water, as determined by MD, fall within the range of 20-80% of the experimentally obtained values. On the other hand, for lipid molecules, the coupling factors determined by MD are approximately 10-30% of the experimental values. The cause of the discrepancy might come from the experimental errors and the current force-field could not adequately describe e-N encounter events. Despite the discrepancies, dynamics characterized by the time comparable to 0.6 ps, which is required for the OE DNP at this field, were captured well by the MD simulations. The co-existence of SE proves the slow global motion of lipid molecules didn't averaged out the anisotropic dipolar hyperfine interaction, which also suggests a responsible modulation for the DNP originating from the local fast dynamics inside lipids.

The OE DNP efficiency of water molecules determined by MD suggests that the DNP efficiency mainly originated from the events of the spin labels flipped to the boundary of lipid bilayers. This is contradicted to the interpretations of previous low-field result (Kausik and Han 2011) and requires further investigations.

References

Chen, Z. J., and R. E. Stark. 1996. 'Evaluating spin diffusion in MAS-NOESY spectra of phospholipid multibilayers', *Solid State Nucl Magn Reson*, 7: 239-46.

Denysenkov, V., D. Dai, and T. F. Prisner. 2021. 'A triple resonance (e, 1H, 13C) probehead for liquid-state DNP experiments at 9.4 Tesla', *Manuscript submitted for publication*.

Denysenkov, V. P., M. J. Prandolini, A. Krahn, M. Gafurov, B. Endeward, and T. F. Prisner. 2008. 'High-field DNP spectrometer for liquids', *Appl. Magn. Reson.*, 34: 289-99.

Easteal, Allan J., William E. Price, and Lawrence A. Woolf. 1989. 'Diaphragm cell for high-temperature diffusion measurements. Tracer Diffusion coefficients for water to 363

K', *Journal of the Chemical Society, Faraday Transactions 1: Physical Chemistry in Condensed Phases*, 85: 1091-97.

Ellena, Jeffrey F., Leslie S. Lepore, and David S. Cafiso. 1993. 'Estimating lipid lateral diffusion in phospholipid vesicles from carbon-13 spin-spin relaxation.', *J. Phys. Chem. A*, 97: 2952–57.

Filippov, Andrey, Greger Orädd, and Göran Lindblom. 2004. 'Lipid lateral diffusion in ordered and disordered phases in raft mixtures', *Biophysical journal*, 86: 891-96.

Hausser, K.H., and D. Stehlik. 1968. 'Dynamic nuclear polarization in liquids', *Adv. Magn. Reson.*, 3: 79-139.

Huster, Daniel, and Klaus Gawrisch. 1999. 'NOESY NMR Crosspeaks between Lipid Headgroups and Hydrocarbon Chains: Spin Diffusion or Molecular Disorder?', *Journal of the American Chemical Society*, 121: 1992-93.

Jakdetchai, O., V. Denysenkoy, J. Becker-Baldus, B. Dutagaci, T. F. Prisner, and C. Glaubitz. 2014. 'Dynamic nuclear polarization-enhanced NMR on aligned lipid lilayers at ambient temperature', *J. Am. Chem. Soc.*, 136: 15533-36.

Kausik, Ravinath, and Songi Han. 2011. 'Dynamics and state of lipid bilayer-internal water unraveled with solution state 1H dynamic nuclear polarization', *Physical Chemistry Chemical Physics*, 13: 7732-46.

Klauda, Jeffery B., Mary F. Roberts, Alfred G. Redfield, Bernard R. Brooks, and Richard W. Pastor. 2008. 'Rotation of Lipids in Membranes: Molecular Dynamics Simulation, 31P Spin-Lattice Relaxation, and Rigid-Body Dynamics', *Biophysical journal*, 94: 3074-83.

Kuzhelev, Andrei A., Danhua Dai, Vasyl Denysenkov, and Thomas F. Prisner. 2022. 'Solid-like Dynamic Nuclear Polarization Observed in the Fluid Phase of Lipid Bilayers at 9.4 T', *Journal of the American Chemical Society*, 144: 1164-68.

Kyrychenko, Alexander, and Alexey S. Ladokhin. 2013. 'Molecular Dynamics Simulations of Depth Distribution of Spin-Labeled Phospholipids within Lipid Bilayer', *The Journal of Physical Chemistry B*, 117: 5875-85.

Neugebauer, P., J. G. Krummenacker, V. P. Denysenkov, G. Parigi, C. Luchinat, and T. F. Prisner. 2013. 'Liquid state DNP of water at 9.2 T: an experimental access to saturation', *Phys. Chem. Chem. Phys.*, 15: 6049-56.

Sezer, D., M. J. Prandolini, and T. F. Prisner. 2009. 'Dynamic nuclear polarization coupling factors calculated from molecular dynamics simulations of a nitroxide radical in water', *Phys. Chem. Chem. Phys.*, 11: 6626-37.

Smirnov, A. I., T. I. Smirnova, and P. D. Morse. 1995. 'Very high frequency electron paramagnetic resonance of 2,2,6,6-tetramethyl-1-piperidinyloxy in 1,2-dipalmitoyl-sn-glycero-3-phosphatidylcholine liposomes: partitioning and molecular dynamics', *Biophysical journal*, 68: 2350-60.

6.3 Corresponding Manuscript

The following manuscript submitted to *Magn. Reson*. and under revision

"Sezer, D., Dai, D., and Prisner, T. F., The solid effect of dynamic nuclear polarization in liquids II: Accounting for g-tensor anisotropy at high magnetic fields, *Magn*. *Reson*., in review (2023), doi:10.5194/mr-2023-10"

is attached in the following pages.

The work was prepared in a collaborative manner. The project was proposed by Dr. Deniz Sezer. The author provided the experimental DNP field profiles and cw EPR spectra, and performed the easyspin simulation. The theoretical work was performed by Dr. Deniz Sezer.

https://doi.org/10.5194/mr-2023-10
Preprint. Discussion started: 31 July 2023

Open Access MAGNETIC RESONANCE Discussions

The solid effect of dynamic nuclear polarization in liquids II: Accounting for g-tensor anisotropy at high magnetic fields

Deniz Sezer, Danhua Dai, and Thomas F. Prisner
Institute of Physical and Theoretical Chemistry, Goethe University, 60438 Frankfurt am Main, Germany
Correspondence: Deniz Sezer (dzsezer@gmail.com)

Abstract. In spite of its name, the solid effect of dynamic nuclear polarization (DNP) is operative also in viscous liquids, where the dipolar interaction between the polarized nuclear spins and the polarizing electrons is not completely averaged out by molecular diffusion. Under such slow-motional conditions, it is likely that the tumbling of the polarizing agent is similarly too slow to efficiently average the anisotropies of its magnetic tensors. Here we extend our previous analysis of the solid effect in liquids to account for the effect of g-tensor anisotropy at high magnetic fields. Building directly on the mathematical treatment of slow-tumbling in electron spin resonance (Freed et al., 1971), we calculate solid-effect DNP enhancements in the presence of both translational diffusion of the liquid molecules and rotational diffusion of the polarizing agent. To illustrate the formalism, we analyze high-field (9.4 T) DNP enhancement profiles from nitroxide-labeled lipids in fluid lipid bilayers. By properly accounting for power-broadening and motional-broadening, we successfully decompose the measured DNP enhancements into their separate contributions from the solid and Overhauser effects.

1 Introduction

The sensitivity of NMR experiments is greatly increased by dynamic nuclear polarization (DNP),[1] where the much larger static polarization that is available to electronic spins is transferred to nuclear spins (Wenckebach, 2016). For the transfer to take place, the electronic and nuclear spins should be able to flip simultaneously (Abragam and Goldman, 1978). Such concerted flips correspond to the zero-quantum (ZQ) and double-quantum (DQ) transitions of the electron-nucleus spin system, which are enabled by the inter-spin interactions. Among the four DNP mechanisms, namely the Overhauser effect (OE), the solid effect (SE), the cross effect, and thermal mixing, only the first two are operative in the liquid state, where the spin-spin interactions change randomly in time due to the thermal motions of the molecules.

In OE-DNP, the ZQ and DQ transitions are in fact possible because the dipole-dipole and contact interactions are modulated by the molecular motions. In SE-DNP, on the other hand, the ZQ and DQ transitions are driven directly by the microwave (mw) excitation, and the modulation of the dipolar interaction is detrimental because it constantly modifies the matching condition that the mw frequency should satisfy in order to resonantly drive these transitions.

[1] Abbreviations used in the text: continuous wave (cw), 1,2-dioleoyl-sn-glycero-3-phosphocholine (DOPC), double quantum (DQ), dynamic nuclear polarization (DNP), electron paramagnetic resonance (EPR), force-free hard sphere (FFHS), microwave (mw), nuclear magnetic resonance (NMR), Overhauser effect (OE), 1-palmitoyl-2-stearoyl-sn-glycero-3-phosphocholine (PSPC), solid effect (SE), stochastic Liouville equation (SLE), zero quantum (ZQ).

https://doi.org/10.5194/mr-2023-10
Preprint. Discussion started: 31 July 2023


Open Access MAGNETIC RESONANCE Discussions

The initial theoretical treatments of OE (Solomon, 1955) and SE (Abragam and Proctor, 1958) modeled the ZQ and DQ transitions by expressing the transition probabilities per unit time using Fermi's golden rule. As the mathematical description of (semi-classical) relaxation theory matured around the same time (Redfield, 1957; Abragam, 1961), the Fermi golden rule was promptly replaced in the theory of OE-DNP in liquids (Hausser et al., 1968) by the correlation function of the dipolar interaction (or its Laplace transform, which is known as spectral density). Because the time-domain description of relaxation leads to a correlation function in a very general way (Abragam, 1961), the same formalism works naturally with different spectral densities (e.g., for rotational or translational diffusion). As an example, the improved analytical treatment of translational diffusion achieved in 1975 was immediately applied to paramagnetic relaxation in liquids (Ayant et al., 1975; Hwang and Freed, 1975).[2]

During the same time period, it also became possible to account for spin dephasing and relaxation beyond second order (Anderson, 1954; Kubo, 1954), which is important for understanding spectral line shapes outside the regime of fast averaging (Kubo, 1969). These initial ideas were transformed into a powerful tool for the calculation and analysis of slow-motional EPR spectra by Freed et al. (1971).

When first presented, Abragam's quantitative description of SE-DNP in terms of mixing of the Zeeman energy levels by the dipolar interaction (Abragam and Proctor, 1958) conclusively explained that the NMR signal is maximally enhanced when the mw frequency is shifted from the electronic resonance by $\pm\omega_I$, where ω_I is the Larmor frequency of the polarized nuclear spin. Abragam's perturbative analysis also correctly predicted that the effect should drop quadratically with the magnitude of the static magnetic field, which has lasting implications for SE-DNP at high magnetic fields. In spite of these successes, however, the perturbative approach to SE is practically impossible to integrate with other relevant spin phenomena whose mathematical treatment matured subsequently.

Recently, Sezer (2023a) presented a time-domain description of SE which, like semi-classical relaxation theory, allows for different dynamical processes to modulate the relevant spin interactions. By interfacing this description with the spectral density of translational diffusion (Ayant et al., 1975; Hwang and Freed, 1975), it was possible to treat SE-DNP in the presence of molecular translation (Sezer, 2023b), as relevant to liquids. The requirement that the dipolar interaction should not be completely averaged out by the molecular dynamics restricts liquid-state SE-DNP to viscous media, where the tumbling of the polarizing agent may similarly be too slow to average the anisotropies of its magnetic tensors. The current paper accounts for the effect of g-tensor anisotropy on SE in this slow-tumbling regime. To this end, the time-domain description of SE-DNP in liquids is interfaced here with the established mathematical treatment of slow-motional EPR spectra (Freed et al., 1971).

To motivate the presented theoretical study, in Sec. 2 we formulate one specific practical problem that it addresses. There we also introduce the experimental EPR and DNP data that are analyzed subsequently in Sec. 5 using the developed theory. The needed background from Sezer (2023a, b) is presented in Sec. 3. Building on it, in Sec. 4 we adapt the slow-motional formalism of Freed et al. (1971) to the treatment of SE in the liquid state. Our conclusions are in Sec. 6, and several supporting figures are left to the appendix.

[2]Surprisingly, this improved treatment is not mentioned by Müller-Warmuth et al. (1983), who continue to use the older, deficient expression of the spectral density for translational diffusion.

https://doi.org/10.5194/mr-2023-10
Preprint. Discussion started: 31 July 2023

Open Access MAGNETIC RESONANCE Discussions

2 Motivation

DNP aims to increase the longitudinal nuclear magnetization, i_z, beyond its equilibrium Boltzmann value, i_z^{eq}. This is done by doping the sample with unpaired electrons, whose spins are then subjected to near-resonance microwave irradiation. In continuous-wave (cw) DNP, which is the only variety that we consider here, a steady state magnetization i_z^{ss} is reached after the microwaves have been applied for sufficiently long time. The enhancement of i_z under such steady-state conditions is

$$\epsilon = \frac{i_z^{\mathrm{ss}}}{i_z^{\mathrm{eq}}} - 1, \tag{1}$$

where $\epsilon = 0$ corresponds to the absence of DNP.

In both OE and SE, ϵ is directly proportional to the ratio of the gyromagnetic factors of the electronic and nuclear spins, γ_S and γ_I. For OE (Hausser et al., 1968; Müller-Warmuth et al., 1983),

$$\epsilon_{\mathrm{OE}} = scf\frac{|\gamma_S|}{\gamma_I}, \tag{2}$$

where s, c and f are, respectively, the electronic saturation factor, the coupling factor and the leakage factor. The former is defined as

$$s = 1 - s_z^{\mathrm{ss}}/s_z^{\mathrm{eq}} \tag{3}$$

and reflects the deviation of the longitudinal electronic magnetization at steady state, s_z^{ss}, from its equilibrium value, s_z^{eq}. The other two factors, c and f, quantify the interaction between the electronic and nuclear spins. Specifically,

$$f = 1 - T_{1I}/T_{1I}^0 \tag{4}$$

compares the nuclear T_1's in the presence (T_{1I}) and in the absence (T_{1I}^0) of the polarizing agent. In DNP, the former is typically (much) shorter than the latter due to the elevated concentration of the electronic spins, hence $f \approx 1$.

Similarly, the SE enhancement can be expressed as (Sezer, 2023a)

$$\epsilon_{\mathrm{SE}} = pv_-T_{1I}\left(\frac{1}{1+v_+T_{1I}}\right)\frac{|\gamma_S|}{\gamma_I}, \tag{5}$$

where $p = 1 - s$ quantifies how "non-saturated" the electronic transition is, and the rate constants $v_\pm$ are related to the ability of the microwaves to excite simultaneous flips of the electronic and nuclear spins. These concerted flips correspond to the "forbidden" ZQ and DQ transitions, which are enabled by the dipolar interaction. In fact,

$$v_\pm = v_2 \pm v_0, \tag{6}$$

where v_0 and v_2 denote, respectively, the ZQ and DQ transition rates. In liquids, where the dipolar interaction is partially averaged, the contribution of the mw excitation to the nuclear relaxation rate $R_{1I} = 1/T_{1I}$, which is quantified by v_+, is generally negligibly small. As a result, $v_+/R_{1I} \ll 1$ and the expression in parenthesis in (5) is essentially one. Then the SE enhancement acquires the multiplicative form

$$\epsilon_{\mathrm{SE}} \approx pv_-T_{1I}\frac{|\gamma_S|}{\gamma_I} \qquad (v_+ \ll R_{1I}), \tag{7}$$

https://doi.org/10.5194/mr-2023-10
Preprint. Discussion started: 31 July 2023


Open Access MAGNETIC RESONANCE Discussions

which is analogous to ϵ_{OE} with the factors s, c and f being replaced by the factors p, v_- and T_{1I}, respectively. In the numerical work presented in Sec. 5 we use the approximation (7). The condition $v_+ T_{1I} \ll 1$ is validated at the end of the analysis by comparing the estimated v_+ to the measured T_{1I}.

In the current paper we study the dependence of the DNP enhancement on the displacement from the electronic resonance. Following Gizatullin et al. (2022), we call the profile of ϵ against the offset from resonance a "DNP spectrum". Because DNP experiments in the liquid state are carried out with a mw resonator (Erb et al., 1958a, b; Leblond et al., 1971b; Neudert et al., 2016; Gizatullin et al., 2021a; Kuzhelev et al., 2022, 2023), off-resonance conditions are achieved by varying the stationary magnetic field at constant mw frequency (i.e., field sweep). In theoretical analysis, however, it is more convenient to work with a fixed B_0 and a variable mw frequency. Thus, when comparing calculations and experiments, we will convert the horizontal axis of the experiments from magnetic field to offset frequency.

In the case of ϵ_{OE} (eq. (2)), the entire offset dependence is due to the saturation factor s, as the factors c and f are practically constant over such narrow frequency range. In the case of ϵ_{SE} (eq. (5)), both pv_- and v_+ are functions of the offset. For a single, homogeneously-broadened EPR line the saturation factor can be obtained in closed analytical form from the Bloch equations (as we review below in Sec. 3.1). Recently Sezer (2023a) showed that the SE spin dynamics is described by two coupled Bloch equations, whose steady state can similarly be solved analytically to obtain closed-form expressions for the rate constants $v_\pm$ (reviewed in Sec. 3.2). In liquids, where the random molecular motion modulates the dipolar interaction between the electronic and nuclear spins, these rate constants are no longer available analytically but can be calculated numerically for motional models with known dipolar spectral densities (Sezer, 2023b), as reviewed below in Sec. 3.3.

Liquid-state SE-DNP is restricted to viscous media, where the dipolar interaction is not averaged out completely by the molecular motions. Under these conditions, the tumbling of the polarizing agent is also expected to be too slow to average the anisotropies of its magnetic tensors. One thus expects substantial deviations from the Lorentzian EPR line shape of the Bloch equations. Such deviations are unavoidable in the case of nitroxide-based polarizing agents whose g and A tensors are rather anisotropic. A recent SE-DNP study at 9.4 T demonstrated that even the narrow-line radical trityl exhibited g-tensor broadening in liquid glycerol (Kuzhelev et al., 2023).

This paper extends the theoretical description of SE-DNP to the regime of slow radical tumbling where the cw-EPR spectrum deviates from a Lorentzian line. Given our longstanding efforts in liquid-state DNP at 9.4 T, here we focus on high magnetic fields, where the width of the EPR spectrum is dominated by the anisotropy of the g tensor. We will thus completely neglect the hyperfine tensor. This possibility will greatly simplify the needed adjustments to the Lorentzian case (Sec. 4).

To illustrate the practical problem that motivated this theoretical work, we now turn to the experimental data in fig. 1. The characterized samples comprised liposomes of hydrated lipid bilayers composed of DOPC (1,2-dioleoyl-sn-glycero-3-phosphocholine) lipids. As the phase transition temperature of DOPC is about $-17\,^{\circ}\mathrm{C}$, the lipids were in their fluid, liquid-crystalline phase in the experiments at ≈ 320 K. The DOPC lipids were mixed at a ratio of 20:1 with PSPC lipids spin-labeled either at position 10 (1-palmitoyl-2-stearoyl-(10-doxyl)-sn-glycero-3-phosphocholine) or at position 16 along one of their aliphatic chains. Both the EPR spectra (fig. 1a,b) and the DNP enhancements (fig. 1c,d) were recorded in our home-built Fabry-Pérot resonator at 9.4 T, equipped with temperature control (Denysenkov et al., 2022). While the target temperature of

https://doi.org/10.5194/mr-2023-10
Preprint. Discussion started: 31 July 2023

Open Access MAGNETIC RESONANCE Discussions

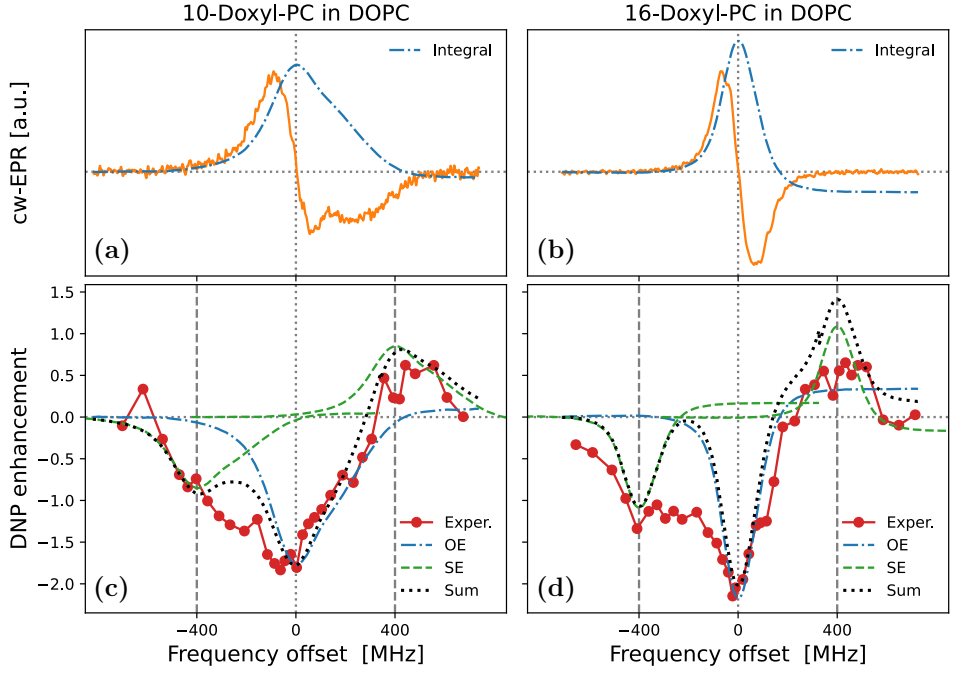

Figure 1. Experimental cw-EPR spectra (**a**, **b**) and DNP spectra (**c**, **d**) of spin-labeled lipids in DOPC lipid bilayers at 9.4 T and ≈ 320 K. The nitroxide spin label (Doxyl) is either at position 10 (**a**, **c**) or at position 16 (**b**, **d**) of the aliphatic lipid chain. The integrated cw-EPR spectra (dashed-dotted blue lines in **a** and **b**) are used to decompose the DNP spectra (**c** and **d**) into contributions from OE (dashed-dotted blue lines) and SE (dashed green lines).

the experiments was 320 K, an extra temperature rise of less than $10\,^{\circ}$C can be expected at the maximum mw power of 5.5 W that was used for DNP (Denysenkov et al., 2022). Details about the experiments and the sample preparation will be published elsewhere.

The cw-EPR spectrum of 10-Doxyl-PC in fig. 1a (orange line) is seen to deviate substantially from (the derivative of) a Lorentzian line shape. At this high magnetic field, the EPR line width is expected to be dominated by the large anisotropy of the nitroxide g tensor, with comparatively much smaller contribution from the nitroxide hyperfine tensor. (These expectations are tested and verified below in Sec. 5.1.) For comparison, in fig. 1b we show the cw-EPR spectrum of the sample doped with 16-Doxyl-PC. Visually, this narrower spectrum more closely resembles a homogeneous Lorentzian line, although it still deviates from it (as discussed in Sec. 5.2).

In fig. 1c we show the DNP spectrum (filled red circles) of the sample containing 10-Doxyl-PC as a polarizing agent. The enhanced NMR signal belongs to the acyl chain protons of the lipids. Thanks to the high magnetic field of the experiment, it was possible to resolve the NMR signal of these non-polar protons from the polar protons of water and of the lipid head groups. The DNP spectrum is seen to have a complex line shape, with the positive enhancement values at offsets of about $+400$ MHz demonstrating contribution from SE. At the same time, the comparatively larger negative enhancements in the vicinity of the

https://doi.org/10.5194/mr-2023-10
Preprint. Discussion started: 31 July 2023


Open Access MAGNETIC RESONANCE Discussions

electronic resonance (i.e., around 0 MHz) point to a contribution from OE. Such coexistence of SE and OE is well documented for nitroxide free radicals at the classical EPR fields of about 0.35 T (Leblond et al., 1971b; Neudert et al., 2017; Gizatullin et al., 2021a, b). Evidently, it also persists at 9.4 T. The DNP spectrum of 16-Doxyl-PC in fig. 1d also exhibits a mixture of SE and OE.

More than half a century ago Korringa and coworkers developed a rigorous theoretical framework to predict such mixed DNP spectra in viscous liquids (Papon et al., 1968; Leblond et al., 1971a). Likely because of its complexity, as well as its neglect of translational diffusion, their formal analysis has not been applied to recent DNP data. As a simple and practical alternative, Neudert et al. (2017) disentangle the OE and SE components of such mixed DNP spectra using only the integral of the measured cw-EPR signal. Their approach is based on the following insightful observations: (i) up to an overall scaling factor the EPR line shape is equal to the saturation factor and thus to the OE enhancement (eq. (2)); (ii) up to an overall scaling factor the SE enhancement lines at $\pm\omega_I$ are shifted versions (and flipped for the ZQ transition) of the same EPR line shape. One can thus identify the contributions of OE and SE to the DNP spectrum by placing the integrated cw-EPR spectrum at, respectively, zero and $\pm\omega_I$ offsets, and independently adjusting the magnitudes of the two components.

This approach is illustrated in figs. 1c and 1d, where the dashed-dotted blue lines are the integrals of the cw-EPR spectra from figs. 1a and 1b, respectively (flipped here to reflect the dipolar nature of OE), and the dashed green lines are the same EPR spectra but centered at -400 MHz and +400 MHz. The sum of the OE and SE contributions determined in this way is shown with a dotted black line. This sum is seen to agree closely with the DNP spectrum of 10-Doxyl-PC (fig. 1c) and to capture well the overall shape of the DNP spectrum of 16-Doxyl-PC (fig. 1d).

In spite of the good general agreement between the experimental DNP spectra and the dotted black lines in figs. 1c and 1d, some persistent differences remain. In particular, (i) the OE feature in the experiment appears to be consistently broader than the EPR line and (ii) the enhancement between the central OE feature and the negative SE feature is consistently larger than what is predicted by the overlap of the two copies of the EPR line shape. Both of these aspects are especially clear in the case of 16-Doxyl-PC (fig. 1d)

The first deficiency is easy to rationalize. Cw-EPR spectra are recorded at low mw power and their widths reflect mechanisms contributing to the electronic T_2 relaxation. The DNP spectrum, on the other hand, is recorded at high mw power, where the EPR line width experiences power-broadening that also depends on the electronic T_1 relaxation. That the OE-DNP spectrum "represents an indirect observation of the electron resonance when greatly saturated" was understood early on (Carver and Slichter, 1956, fig. 6). To properly model the contribution of OE to mixed DNP spectra, therefore, it is necessary to calculate the cw-EPR spectrum under saturating conditions. How to rigorously do that in the regime of slow radical tumbling is known (Freed et al., 1971).

While power-broadening affects OE, it is not immediately clear whether one should also take it into account when modeling SE. (We address this point in Sec. 4.4.) Even leaving power-broadening aside, however, we know that in liquids the SE lines of the DNP spectrum should also be broader than the EPR line width because of the fluctuations of the dipolar interaction (Sezer, 2023b). Although Sezer (2023b) showed how to quantify this additional motional broadening in the case of translational molecular diffusion, the theoretical treatment there assumed a Lorentzian EPR line and is thus not directly applicable to the

https://doi.org/10.5194/mr-2023-10
Preprint. Discussion started: 31 July 2023

Open Access MAGNETIC RESONANCE Discussions

experiments in fig. 1. In the current paper, we extend the formalism to slow radical tumbling and g-tensor anisotropy (Sec. 4). In Sec. 5 we apply the developed theory to the analysis of the experimental spectra in fig. 1. The needed theoretical background is reviewed next.

3 Theoretical background

3.1 Bloch equations

The evolution of the expectation values of the electronic spin operators S_i ($i = x, y, z$), which we denote by s_i, is described by the classical Bloch equations (in the rotating frame)

$$\begin{bmatrix} \dot{s}_x(t) \\ \dot{s}_y(t) \\ \dot{s}_z(t) \end{bmatrix} = -\begin{bmatrix} R_2 & \Delta & 0 \\ -\Delta & R_2 & \omega_1 \\ 0 & -\omega_1 & R_1 \end{bmatrix} \begin{bmatrix} s_x(t) \\ s_y(t) \\ s_z(t) \end{bmatrix} + R_1 \begin{bmatrix} 0 \\ 0 \\ s_z^{\mathrm{eq}} \end{bmatrix}. \tag{8}$$

Here, the dot above the variable indicates differentiation with respect to time, R_2 and R_1 are the reciprocals of the electronic relaxation times T_2 and T_1, respectively, and[3]

$$\Delta = \omega_0 - \omega \tag{9}$$

is the offset between the Larmor frequency of the electronic spins, ω_0, and the (angular) frequency of the oscillating magnetic field, ω. In the case of an isotropic g-factor, g_0,

$$\omega_0 = g_0 \mu_{\mathrm{B}} B_0 / \hbar, \tag{10}$$

where μ_{B} is the Bohr magneton.

At steady state

$$\begin{bmatrix} R_2 & \Delta & 0 \\ -\Delta & R_2 & \omega_1 \\ 0 & -\omega_1 & R_1 \end{bmatrix} \begin{bmatrix} s_x^{\mathrm{ss}} \\ s_y^{\mathrm{ss}} \\ s_z^{\mathrm{ss}} \end{bmatrix} = R_1 \begin{bmatrix} 0 \\ 0 \\ s_z^{\mathrm{eq}} \end{bmatrix}. \tag{11}$$

Solving these algebraic equations for the variables s_i^{ss}, one can calculate the cw-EPR spectrum and the electronic saturation profile. Making use of the zeros in the first and last rows of the Bloch matrix in (11), we first express s_x^{ss} and s_z^{ss} in terms of s_y^{ss}:

$$s_x^{\mathrm{ss}} = -\Delta T_2 s_y^{\mathrm{ss}}, \qquad s_z^{\mathrm{ss}} = \omega_1 T_1 s_y^{\mathrm{ss}} + s_z^{\mathrm{eq}}. \tag{12}$$

The middle row of the matrix then yields

$$s_y^{\mathrm{ss}} = -\omega_1 P_0^{-1} s_z^{\mathrm{eq}}, \tag{13}$$

[3] In Sezer (2023a, b) the frequency offset was denoted by Ω. Here we reserve this symbol for the orientation of the polarizing agent (Sec. 4).

https://doi.org/10.5194/mr-2023-10
Preprint. Discussion started: 31 July 2023

Open Access MAGNETIC RESONANCE Discussions

where we defined

$$P_0 = R_2 + \omega_1^2 T_1 + \Delta^2 T_2. \tag{14}$$

The in-phase (absorptive) and the out-of-phase (dispersive) components of the cw-EPR signal are then found to be

$$\begin{aligned} \mathrm{abs} &= s_y^{\mathrm{ss}}/s_z^{\mathrm{eq}} = -\omega_1 P_0^{-1} \\ \mathrm{dsp} &= s_x^{\mathrm{ss}}/s_z^{\mathrm{eq}} = -\Delta T_2\,\mathrm{abs}. \end{aligned} \tag{15}$$

From the longitudinal component at steady state we similarly find

$$s = 1 - s_z^{\mathrm{ss}}/s_z^{\mathrm{eq}} = -\omega_1 T_1\,\mathrm{abs}, \tag{16}$$

which shows that the saturation factor is directly proportional to the absorptive EPR line shape. This proportionality holds for all mw powers, including the large powers used in DNP. In Sec. 4.3 we show that it remains valid also in the case of g-tensor anisotropy.

When generalizing the Bloch equations to non-isotropic g tensor, we will need to work with high-dimensional abstract vectors. To distinguish these vectors from the vectors in 3D space, we will denote the latter by placing an arrow above their symbols, and will use bold symbols for the former. (A 3D unit vector will be indicated with a hat rather than an arrow.) Additionally, we will use capital hollow letters to denote 3×3 matrices that act on the 3D vectors. With this understanding, we will write the Bloch equations (8) as

$$\dot{\vec{s}}(t) = -\mathbb{B}_0 \vec{s}(t) + R_1 \hat{k} s_z^{\mathrm{eq}}, \tag{17}$$

where

$$\vec{s}(t) = \begin{bmatrix} s_x(t) \\ s_y(t) \\ s_z(t) \end{bmatrix}, \qquad \hat{k} = \begin{bmatrix} 0 \\ 0 \\ 1 \end{bmatrix}, \tag{18}$$

$$\mathbb{B} = \begin{bmatrix} R_2 + \mathrm{i}\omega_I & \Delta & 0 \\ -\Delta & R_2 + \mathrm{i}\omega_I & \omega_1 \\ 0 & -\omega_1 & R_1 + \mathrm{i}\omega_I \end{bmatrix}, \tag{19}$$

and $\mathbb{B}_0 = \mathbb{B}(\omega_I = 0)$. (The subscript of $\mathbb{B}_0$ is a reminder that $\mathbb{B}$ is evaluated at $\omega_I = 0$, where ω_I is the Larmor frequency of the polarized nuclear spin.)

3.2 Solid effect in solids

SE relies on the dipolar interaction between the electronic and nuclear spins whose coupling is

$$A_1 = D_{\mathrm{dip}} \frac{-3\cos\theta\sin\theta}{r^3} \mathrm{e}^{\mathrm{i}\phi}. \tag{20}$$

https://doi.org/10.5194/mr-2023-10
Preprint. Discussion started: 31 July 2023

Open Access MAGNETIC RESONANCE Discussions

Here $D_{\mathrm{dip}} = (\mu_0/4\pi)\hbar\gamma_S\gamma_I$ is the dipolar constant, which equals approximately $2\pi(79\,\mathrm{kHz\,nm^3})$ for protons, and (r, θ, ϕ) are the spherical polar coordinates of the inter-spin vector.

In liquids, A_1 changes in time because of molecular diffusion. The treatment of SE-DNP for time-dependent A_1 in Sezer (2023b) was developed under the assumption that the nuclear T_1 is orders of magnitude larger than the correlation time of the dipolar interaction, which is practically always the case in liquids. For the same analysis to apply to solids, spin diffusion should be much faster than the nuclear T_1, which is not necessarily true in practice. When accounting for g-tensor anisotropy below, we will similarly assume that the tumbling of the radical is much faster than the nuclear T_1. This assumption is clearly violated in solids where "tumbling" is infinitely slow. Nevertheless, for the purposes of comparison, we will refer in the following to 'solids' with the understanding that the correlation time of the dipolar interaction is infinitely long (but still much shorter than the nuclear T_1). Because we will keep all other parameters, including the time scale of radical tumbling, the same when comparing 'solids' and liquids, it should be kept in mind that our treatment is not a good model for the solid state (hence the quotation marks).

For SE-DNP, in addition to the Bloch equations it is necessary to consider the following dynamical equations of the electron-nucleus coherences $g_i = \langle S_i I_+ \rangle$ $(i = x, y, z)$ (Sezer, 2023a):

$$\begin{bmatrix} \dot{g}_x(t) \\ \dot{g}_y(t) \\ \dot{g}_z(t) \end{bmatrix} = -\mathbb{B} \begin{bmatrix} g_x(t) \\ g_y(t) \\ g_z(t) \end{bmatrix} - \frac{1}{4}A_1 \begin{bmatrix} s_y(t) \\ -s_x(t) \\ 0 \end{bmatrix} - \mathrm{i}\frac{1}{4}A_1 \begin{bmatrix} 0 \\ 0 \\ i_z(t) \end{bmatrix}. \tag{21}$$

Again, we are only interested in the steady state of the dynamics where

$$\mathbb{B} \begin{bmatrix} g_x^{\mathrm{ss}} \\ g_y^{\mathrm{ss}} \\ g_z^{\mathrm{ss}} \end{bmatrix} = -\frac{1}{4}A_1 \begin{bmatrix} s_y^{\mathrm{ss}} \\ -s_x^{\mathrm{ss}} \\ 0 \end{bmatrix} - \mathrm{i}\frac{1}{4}A_1 \begin{bmatrix} 0 \\ 0 \\ i_z^{\mathrm{ss}} \end{bmatrix}. \tag{22}$$

The rate constants pv_- and v_+ needed to calculate the SE enhancement (eq. (5)) are determined from g_z^{ss} using the following equality, which combines (Sezer, 2023a, eq. (31)) and (Sezer, 2023b, eq. (42)):

$$\dot{i}_z|^{\mathrm{ss}}_{\mathrm{coh}} = -\mathrm{Re}\{\mathrm{i}A_1^* g_z^{\mathrm{ss}}\} = -R_{1I}^A i_z^{\mathrm{ss}} - v_+ i_z^{\mathrm{ss}} - pv_- s_z^{\mathrm{eq}}. \tag{23}$$

(Re{} takes the real part of its argument.) The term proportional to R_{1I}^A on the right-hand side of (23) accounts for the contribution of the coherences g_i to the nuclear T_1 relaxation in the absence of mw excitation. This contribution should be removed when calculating the mw-related rates v_+ and pv_-.

To a good approximation the electronic spin dynamics is independent from the dipolar interaction with the nuclear spins, as other mechanisms are more efficient in causing electronic relaxation, especially in liquids. As a result, the steady-state expressions from Sec. 3.1 can be used when solving (22) for g_z^{ss}.

Inverting the matrix $\mathbb{B}$ in (22), and using $s_{x,y}^{\mathrm{ss}}$ from before, we find

$$\begin{aligned} g_z^{\mathrm{ss}} = {} & \omega_1 \frac{1}{4}A_1([\mathbb{B}^{-1}]_{zx} + \Delta T_2[\mathbb{B}^{-1}]_{zy})P_0^{-1}s_z^{\mathrm{eq}} \\ & - \mathrm{i}\frac{1}{4}A_1[\mathbb{B}^{-1}]_{zz}i_z^{\mathrm{ss}}, \end{aligned} \tag{24}$$

https://doi.org/10.5194/mr-2023-10
Preprint. Discussion started: 31 July 2023

Open Access MAGNETIC RESONANCE Discussions

where $[\mathbb{B}^{-1}]_{ij}$ is the ijth matrix element of $\mathbb{B}^{-1}$. Substituting this $g_z^{\rm ss}$ into (23) we identify the desired SE rate constants

$$\begin{aligned} R_{1I}^A &= \delta^2 \mathrm{Re}\{[\mathbb{B}^{-1}_{\omega_1=0}]_{zz}\} \\ v_+ &= \delta^2 \mathrm{Re}\{[\mathbb{B}^{-1}]_{zz}\} - R_{1I}^A \\ pv_- &= -\delta^2 \omega_1 P_0^{-1} \mathrm{Im}\{[\mathbb{B}^{-1}]_{zx} + \Delta T_2 [\mathbb{B}^{-1}]_{zy}\}, \end{aligned} \tag{25}$$

where

$$\delta^2 = (A_1^* A_1)/4 \tag{26}$$

reflects the strength of the dipolar interaction. (Im{} takes the imaginary part of its argument.)

In liquids, where A_1 is time-dependent, we will need to modify the matrix $\mathbb{B}^{-1}$ in (25) without changing the structure of these expressions (Sec. 3.3). In the case of solids (i.e., when A_1 does not change with time), it is possible to carry out the inversion of $\mathbb{B}$ by expressing $g_x^{\rm ss}$ and $g_z^{\rm ss}$ in terms of $g_y^{\rm ss}$, analogously to our treatment of the Bloch equations in the previous subsection.

From the upper and lower rows of $\mathbb{B}$ in (22) we find

$$\begin{aligned} g_x^{\rm ss} &= -\Delta (R_2 + \mathrm{i}\omega_I)^{-1} g_y^{\rm ss} - \frac{1}{4} A_1 (R_2 + \mathrm{i}\omega_I)^{-1} s_y^{\rm ss} \\ g_z^{\rm ss} &= \omega_1 (R_1 + \mathrm{i}\omega_I)^{-1} g_y^{\rm ss} - \mathrm{i}\frac{1}{4} A_1 (R_1 + \mathrm{i}\omega_I)^{-1} i_z^{\rm ss}. \end{aligned} \tag{27}$$

Substituting this $g_z^{\rm ss}$ into (23) we obtain

$$\begin{aligned} \dot{i}_z|_{\rm coh}^{\rm ss} &= -\omega_1 \mathrm{Re}\{\mathrm{i} A_1^* (R_1 + \mathrm{i}\omega_I)^{-1} g_y^{\rm ss}\} \\ &\quad - \delta^2 \mathrm{Re}\{(R_1 + \mathrm{i}\omega_I)^{-1}\} i_z^{\rm ss}. \end{aligned} \tag{28}$$

The first term on the right-hand side of the equality in (28) vanishes when $\omega_1 = 0$. In contrast, the term in the second line is independent of ω_1 and thus contributes also in the absence of mw excitation. We thus identify this second term with the thermal relaxation rate

$$R_{1I}^A = \delta^2 \mathrm{Re}\{(R_1 + \mathrm{i}\omega_I)^{-1}\}. \tag{29}$$

Since we are not interested in this rate, the second summand in (28) can be dropped at this stage. The rate constants v_+ and pv_- will thus be identified using only the first line in (28):

$$\omega_1 \mathrm{Re}\{\mathrm{i} A_1^* (R_1 + \mathrm{i}\omega_I)^{-1} g_y^{\rm ss}\} = v_+ i_z^{\rm ss} + pv_- s_z^{\rm eq}. \tag{30}$$

Substituting $g_x^{\rm ss}$ and $g_z^{\rm ss}$ from (27) into the middle equation in (22), and using the electronic steady state, we find

$$\begin{aligned} g_y^{\rm ss} &= \frac{1}{4} A_1 \omega_1 \Delta P_0^{-1} [R_2^{-1} + (R_2 + \mathrm{i}\omega_I)^{-1}] P^{-1} s_z^{\rm eq} \\ &\quad + \mathrm{i}\frac{1}{4} A_1 \omega_1 (R_1 + \mathrm{i}\omega_I)^{-1} P^{-1} i_z^{\rm ss}, \end{aligned} \tag{31}$$

https://doi.org/10.5194/mr-2023-10
Preprint. Discussion started: 31 July 2023

Open Access MAGNETIC RESONANCE Discussions

where

$$P = R_2 + \mathrm{i}\omega_I + \omega_1^2 (R_1 + \mathrm{i}\omega_I)^{-1} + \Delta^2 (R_2 + \mathrm{i}\omega_I)^{-1} \tag{32}$$

generalizes (14) such that $P_0 = P(\omega_I = 0)$. Finally, using this g_y^{ss} in (30) we obtain

$$v_+ = -\delta^2 \omega_1^2 \,\mathrm{Re}\left\{ \frac{(R_1 + \mathrm{i}\omega_I)^{-2}}{R_2 + \mathrm{i}\omega_I + \frac{\omega_1^2}{R_1 + \mathrm{i}\omega_I} + \frac{\Delta^2}{R_2 + \mathrm{i}\omega_I}} \right\} \tag{33}$$

and

$$pv_- = -\delta^2 \omega_1^2 \frac{\Delta}{R_2 + \omega_1^2 T_1 + \Delta^2 T_2} \times \mathrm{Im}\left\{ \frac{[R_2^{-1} + (R_2 + \mathrm{i}\omega_I)^{-1}](R_1 + \mathrm{i}\omega_I)^{-1}}{R_2 + \mathrm{i}\omega_I + \frac{\omega_1^2}{R_1 + \mathrm{i}\omega_I} + \frac{\Delta^2}{R_2 + \mathrm{i}\omega_I}} \right\}. \tag{34}$$

In these expressions we have written down the combinations P and P_0 explicitly in order to show in closed form how v_+ and pv_- depend on all parameters. For example, we immediately see that pv_- is odd in the offset Δ while v_+ is even. Because the SE-DNP enhancement is proportional to the ratio of these two rates (eq. (5)), it has the characteristic odd (i.e., antisymmetric) dependence on the offset from the electronic resonance.

When generalizing the SE spin dynamics to g-tensor anisotropy, we will write the dynamical equations (21) as

$$\dot{\vec{g}}(t) = -\mathbb{B}\vec{g}(t) - \frac{1}{4} A_1 \mathbb{G}\vec{s}(t) - \mathrm{i}\frac{1}{4} A_1 \hat{k} i_z(t) \tag{35}$$

with

$$\vec{g}(t) = \begin{bmatrix} g_x(t) \\ g_y(t) \\ g_z(t) \end{bmatrix}, \qquad \mathbb{G} = \begin{bmatrix} 0 & 1 & 0 \\ -1 & 0 & 0 \\ 0 & 0 & 0 \end{bmatrix} = \frac{\partial \mathbb{B}}{\partial \Delta}. \tag{36}$$

3.3 Solid effect in liquids

The modulation of the dipolar interaction by translational diffusion was described in Sezer (2023b) on the level of the spectral density of the motional model, which was denoted by $J_{11}(s)$ since this is the Laplace transform of the auto-correlation function of the dipolar interaction A_1 (hence the double subscript of J). As an example, the spectral density of the force-free hard-sphere (FFHS) model of translational diffusion is (Ayant et al., 1975; Hwang and Freed, 1975)

$$J_{11}^{\mathrm{ffhs}}(s) = \langle \delta^2 \rangle \tau \frac{(s\tau)^{\frac{1}{2}} + 4}{(s\tau)^{\frac{3}{2}} + 4(s\tau) + 9(s\tau)^{\frac{1}{2}} + 9}. \tag{37}$$

Here, the parameter

$$\tau = b^2 / D_{\mathrm{trans}} \tag{38}$$

https://doi.org/10.5194/mr-2023-10
Preprint. Discussion started: 31 July 2023


Open Access MAGNETIC RESONANCE Discussions

is the diffusive time scale of the model, which depends on the contact distance of the electronic and nuclear spins, b, and on the coefficient of their relative translational diffusion, D_{trans}, and

$$\langle\delta^2\rangle = D_{\mathrm{dip}}^2 \frac{6\pi}{5} \frac{N}{3b^3}. \tag{39}$$

is the average of the dipolar interaction strength δ^2 over the sample volume, times the concentration of the electronic spins, N.

It is convenient to write J_{11}, which has units of angular frequency, as

$$J_{11}(s) = \langle\delta^2\rangle j_{11}(s), \tag{40}$$

where $j_{11}(s)$ has units of time. This factorization confines the effect of the parameters N, b and the constant D_{dip} to the scaling factor $\langle\delta^2\rangle$. The factor $j_{11}(s)$ then fully accounts for the line shape of the SE-DNP spectrum, which results from the interplay between the offset frequency and the time scale of the translational motion.

According to Sezer (2023b), the modification from solids to liquids amounts to replacing the matrix $\mathbb{B}^{-1}$ in (25) by the matrix

$$\mathbb{Q} = j_{11}(\mathbb{B}), \tag{41}$$

and also replacing δ^2 by $\langle\delta^2\rangle$. The desired SE rate constants in liquids are thus

$$\begin{aligned} R_{1I}^A &= \langle\delta^2\rangle \mathrm{Re}\{[\mathbb{Q}_{\omega_1=0}]_{zz}\} \\ v_+ &= \langle\delta^2\rangle \mathrm{Re}\{[\mathbb{Q}]_{zz}\} - R_{1I}^A \\ pv_- &= -\langle\delta^2\rangle \omega_1 P_0^{-1} \mathrm{Im}\{[\mathbb{Q}]_{zx} + \Delta T_2 [\mathbb{Q}]_{zy}\}. \end{aligned} \tag{42}$$

We now clarify the meaning of (41). Following the definition of a function of a matrix, one should first solve the eigenvalue problem of $\mathbb{B}$, i.e., $\mathbb{B}\mathbb{U} = \mathbb{U}\Lambda$, where the diagonal matrix $\Lambda = \mathrm{diag}(\lambda_1, \lambda_2, \lambda_3)$ contains the three eigenvalues and the columns of $\mathbb{U}$ contain the corresponding (right) eigenvectors. Then one should evaluate the spectral density at the three eigenvalues: $\ell_n = j_{11}(\lambda_n)$. Finally, one should form the diagonal matrix $\mathbb{L} = \mathrm{diag}(\ell_1, \ell_2, \ell_3)$ and calculate $\mathbb{Q} = \mathbb{U}\mathbb{L}\mathbb{U}^{-1}$. Comparing this expression of $\mathbb{Q}$ with $\mathbb{B}^{-1} = \mathbb{U}\Lambda\mathbb{U}^{-1}$ we see that in the transition from solids to liquids, where $\mathbb{B}^{-1}$ is replaced by $\mathbb{Q}$, we essentially "process" the eigenvalues of $\mathbb{B}$ with the spectral density function j_{11}. This step prevents us from eliminating the variables $g_{x,z}^{\mathrm{ss}}$ the way we did previously for solids (Sec. 3.2). Because of that, the rate constants in liquids (eq. (42)) need to be calculated numerically.

Nonetheless, it is still possible to simplify the expression for R_{1I}^A since when $\omega_1 = 0$ the zz component of $\mathbb{B}$ is decoupled from the rest of the matrix. One then finds

$$R_{1I}^A = \langle\delta^2\rangle \mathrm{Re}\{j_{11}(R_1 + \mathrm{i}\omega_I)\}. \tag{43}$$

Clearly, the time-dependence of the dipolar interaction modifies all rate constants, including R_{1I}^A (*cf.* eq. (29)).

https://doi.org/10.5194/mr-2023-10
Preprint. Discussion started: 31 July 2023

Open Access MAGNETIC RESONANCE Discussions

4 Slow-motional EPR and DNP spectra for anisotropic g tensor

In this section we show how to account for g-tensor anisotropies when the tumbling of the radical is slow. Because our description of SE is built around the Bloch equations (Sezer, 2023a, b), we first adapt the pioneering approach of Freed et al. (1971) to our needs (Secs. 4.1, 4.2 and 4.3) and then generalize it to SE-DNP (Secs. 4.4 and 4.5).

4.1 Stochastic Liouville equation

Following Freed et al. (1971), we account for the effect of tumbling on the EPR spectrum using the SLE formalism (Anderson, 1954; Kubo, 1954). We describe the rotational state of the radical statistically with the probability density $P(\Omega,t)$, which quantifies the likelihood that at time t the molecular system of coordinates attached to the radical has orientation Ω with respect to the laboratory system of axes. This probability evolves with the Fokker-Planck equation

$$\frac{\partial}{\partial t}p(\Omega,t|\Omega_0,t_0) = D_{\rm rot}\nabla_\Omega^2 p(\Omega,t|\Omega_0,t_0), \tag{44}$$

where $D_{\rm rot}$ is the rotational diffusion constant of the radical and the Laplacian differential operator ∇_Ω^2 acts on the orientation variable Ω. The operator

$$K_\Omega = -D_{\rm rot}\nabla_\Omega^2 \tag{45}$$

satisfies the following eigenvalue problem

$$K_\Omega \mathscr{D}^\ell_{mn}(\Omega) = D_{\rm rot}\ell(\ell+1)\mathscr{D}^\ell_{mn}(\Omega), \tag{46}$$

where the eigenfunctions $\mathscr{D}^\ell_{mn}(\Omega)$ are the Wigner rotation matrix elements, which are orthogonal to each other:

$$\int \mathscr{D}^{L*}_{MN}(\Omega)\mathscr{D}^\ell_{mn}(\Omega){\rm d}\Omega = \frac{8\pi^2}{2L+1}\delta_{L\ell}\delta_{Mm}\delta_{Nn}. \tag{47}$$

From (46) it is clear that the time derivative on the left-hand side of (44) vanishes for the equilibrium probability

$$p^{\rm eq}(\Omega) = \frac{1}{8\pi^2} = \frac{1}{8\pi^2}\mathscr{D}^0_{00}(\Omega). \tag{48}$$

In the presence of g-tensor anisotropy, the electronic Larmor frequency depends on the orientation Ω of the radical as follows:[4]

$$\omega(\Omega) = \omega_0 + \gamma_0^2\mathscr{D}^2_{00}(\Omega) + \gamma_2^2[\mathscr{D}^2_{-20}(\Omega) + \mathscr{D}^2_{20}(\Omega)], \tag{49}$$

where the angular frequencies

$$\begin{aligned}\gamma_0^2 &= \frac{2}{3}\left[g_{zz} - \frac{1}{2}(g_{xx}+g_{yy})\right]\mu_{\rm B}B_0/\hbar \\ \gamma_2^2 &= \frac{1}{\sqrt{6}}(g_{xx}-g_{yy})\,\mu_{\rm B}B_0/\hbar\end{aligned} \tag{50}$$

[4]We follow Freed et al. (1971) and consider the effect of the g-tensor anisotropy only on the secular terms in the electronic spin Hamiltonian, i.e., those proportional to the spin operator S_z. The response of the non-secular terms to the g anisotropy is neglected.

https://doi.org/10.5194/mr-2023-10
Preprint. Discussion started: 31 July 2023

Open Access MAGNETIC RESONANCE Discussions

are formed from the components g_{xx}, g_{yy} and g_{zz} of the g-tensor in the molecular frame.

Because the electronic Larmor frequency depends on Ω, the offset frequency Δ also becomes a function of the molecular orientation. As an example, for a fixed Ω the Bloch equations (17) should be modified as

$$\dot{\vec{s}}(t) = -[\mathbb{B}_0 + \mathbb{F}(\Omega)]\vec{s}(t) + R_1\hat{k}s_z^{\mathrm{eq}}, \tag{51}$$

where the orientation dependence is confined to the 3×3 matrix

$$\mathbb{F}(\Omega) = \{\gamma_0^2\mathscr{D}_{00}^2(\Omega) + \gamma_2^2[\mathscr{D}_{-20}^2(\Omega) + \mathscr{D}_{20}^2(\Omega)]\}\,\mathbb{G}. \tag{52}$$

(The matrix $\mathbb{G}$ was introduced in (36).) It should be stressed, however, that (51) is not a legitimate equation of motion, as it does not account for the dynamics of the orientation Ω.

The SLE formalism remedies this deficiency by introducing the orientation-conditioned averages $\vec{s}(\Omega,t)$, whose spatial part evolves according to the Bloch equations (51) and whose Ω dependence evolves according to the diffusion equation (44):

$$\begin{aligned}\frac{\partial}{\partial t}\vec{s}(\Omega,t) &= -(K_\Omega \otimes \mathbb{E} + E_\Omega \otimes \mathbb{B}_0)\,\vec{s}(\Omega,t) \\ &\quad - E_\Omega \otimes \mathbb{F}(\Omega)\,\vec{s}(\Omega,t) + R_1\hat{k}s_z^{\mathrm{eq}}p^{\mathrm{eq}}(\Omega).\end{aligned} \tag{53}$$

Here $\mathbb{E}$ is the 3×3 identity matrix in 3D space and E_Ω is the identity operator in the same abstract space as K_Ω. The outer product $\otimes$ is needed to create a combined operator that acts simultaneously in both of these spaces.

Since the functions $\mathscr{D}_{mn}^{\ell}(\Omega)$ form a complete set, we expand $\vec{s}(\Omega,t)$ as follows:

$$\vec{s}(\Omega,t) = \frac{1}{8\pi^2}\sum_{\ell=0}^{\infty}\sum_{m=-\ell}^{\ell}\sum_{n=-\ell}^{\ell}\mathscr{D}_{mn}^{\ell}(\Omega)\,\vec{s}_{mn}^{\ell}(t). \tag{54}$$

The coefficients $\vec{s}_{mn}^{\ell}$, which contain the time-dependence, can be obtained from $\vec{s}(\Omega,t)$ using the orthogonality of $\mathscr{D}_{mn}^{\ell}(\Omega)$ (eq. (47)):

$$\vec{s}_{MN}^{L}(t) = (2L+1)\int \mathscr{D}_{MN}^{L*}(\Omega)\,\vec{s}(\Omega,t)\,\mathrm{d}\Omega. \tag{55}$$

Ultimately, the only property that we care about is the integral of the SLE variable $\vec{s}(\Omega,t)$ over all orientations:

$$\int \vec{s}(\Omega,t)\,\mathrm{d}\Omega = \int \mathscr{D}_{00}^{0}(\Omega)\vec{s}(\Omega,t)\,\mathrm{d}\Omega = \vec{s}_{00}^{0}(t). \tag{56}$$

In that sense, the (vector) coefficient $\vec{s}_{00}^{0}(t)$ is the main object of interest, while all other coefficients $\vec{s}_{mn}^{\ell}(t)$ play an auxiliary, book-keeping role.

Substituting $\vec{s}(\Omega,t)$ from (54) into (53), multiplying both sides by $\mathscr{D}_{MN}^{L*}(\Omega)$ and integrating over Ω, we get

$$\begin{aligned}\dot{\vec{s}}_{MN}^{L}(t) &= R_1\hat{k}s_z^{\mathrm{eq}}\delta_{L0}\delta_{M0}\delta_{N0} \\ &- [D_{\mathrm{rot}}L(L+1) + \mathbb{B}_0]\vec{s}_{MN}^{L}(t) \\ &- \sum_{\ell mn}\left(\frac{2L+1}{8\pi^2}\int \mathscr{D}_{MN}^{L*}(\Omega)\mathscr{D}_{mn}^{\ell}(\Omega)\mathbb{F}(\Omega)\mathrm{d}\Omega\right)\vec{s}_{mn}^{\ell}(t).\end{aligned} \tag{57}$$

https://doi.org/10.5194/mr-2023-10
Preprint. Discussion started: 31 July 2023

Open Access MAGNETIC RESONANCE Discussions

Clearly, the terms proportional to K_Ω and $\mathbb{B}_0$ in the SLE (53) do not mix coefficients $\vec{s}^L_{MN}$ with different values of L, M and N. In other words, these two operators are diagonal in the selected representation. The term proportional to $\mathbb{F}(\Omega)$, on the other hand, mixes coefficients with different L and M (but not N, as we discuss below).

The integral in the last line of (57) contains the product of three Wigner rotation matrix elements. These can be expressed in therms of the Clebsch-Gordan coefficients $C^{LM}_{\ell_1 m_1 \ell_2 m_2}$. Specifically, for the $\mathscr{D}^2_{K0}(\Omega)$ in eq. (52), we have

$$\frac{2L+1}{8\pi^2}\int \mathscr{D}^{L*}_{MN}(\Omega)\mathscr{D}^2_{K0}(\Omega)\mathscr{D}^{\ell}_{mn}(\Omega)\mathrm{d}\Omega = C^{LM}_{2K\ell m}C^{LN}_{20\ell n}, \tag{58}$$

which leads to

$$\begin{aligned}\dot{\vec{s}}^L_{MN}(t) &= R_1\hat{k}s^{\mathrm{eq}}_z\delta_{L0}\delta_{M0}\delta_{N0}\\ &-[D_{\mathrm{rot}}L(L+1)+\mathbb{B}_0]\vec{s}^L_{MN}(t)\\ &-\sum_{\ell mn}[\gamma_0^2 C^{LM}_{20\ell m}+\gamma_2^2(C^{LM}_{2-2\ell m}+C^{LM}_{22\ell m})]C^{LN}_{20\ell n}\mathbb{G}\vec{s}^{\ell}_{mn}(t).\end{aligned} \tag{59}$$

In (59), the sum over ℓ mixes only expansion coefficients whose values ℓ differ by two from L, in both the positive and negative directions, because all three Wigner rotation matrix elements in $\mathbb{F}$ have $L=2$ (eq. (52)). Since we need $\vec{s}^0_{00}$ at the end, it is sufficient to consider only coefficients with even values of ℓ. Furthermore, as the Wigner rotation matrix elements in $\mathbb{F}$ have $M=0,\pm2$ and $N=0$, the sum over m mixes only coefficients whose values m are either equal to M or differ from it by two units, while the sum over n does not mix any coefficients with n different from N. These considerations imply that the triple sum in (59) will go only over $\vec{s}^{\ell}_{m0}$ with even ℓ and m. Finally, because the Wigner rotation matrix elements with $M=2$ and $M=-2$ appear in a symmetrical way in $\mathbb{F}$, it becomes possible to work with the symmetrized coefficients (Freed et al., 1971)

$$\vec{s}^{LM} = \frac{1}{2}(\vec{s}^L_{-M0}+\vec{s}^L_{M0}), \tag{60}$$

thus restricting M to non-negative values ($0\leqslant M\leqslant L$). The lowest-order coefficients that are coupled by the SLE dynamics are thus $\vec{s}^{00}$, $\vec{s}^{20}$, $\vec{s}^{22}$, $\vec{s}^{40}$, $\vec{s}^{42}$, $\vec{s}^{44}$, $\vec{s}^{60}$, etc.

4.2 Matrix representation of the SLE dynamics

While the above considerations greatly reduce the needed coefficients, there is still an infinite number left. In any practical work, this infinite set is truncated by selecting a maximum value of L to account for, and setting to zero the coefficients with $L>L_{\max}$. Since the total number of even L such that $L\leqslant L_{\max}$ is $n_L = L_{\max}/2+1$, the total number of remaining coefficients $\vec{s}^{LM}$ is $n_{\mathrm{tot}} = n_L(n_L+1)/2 = L^2_{\max}/8+3L_{\max}/4+1$. For the smallest non-trivial choice of $L_{\max}=2$, $n_{\mathrm{tot}}=3$ (with $\vec{s}^{00}$, $\vec{s}^{20}$ and $\vec{s}^{22}$). The number of coefficients increases quadratically with $L_{\max}$ (e.g., $n_{\mathrm{tot}}=15,28,45$ for $L_{\max}=8,12,16$, respectively).

https://doi.org/10.5194/mr-2023-10
Preprint. Discussion started: 31 July 2023

Open Access MAGNETIC RESONANCE Discussions

To compactly write down how these coefficients are mixed by the SLE dynamics, we introduce the following abstract vectors with n_{tot} elements:

$$\mathbf{1}^{00} = \begin{bmatrix} 1 \\ 0 \\ 0 \\ \vdots \end{bmatrix}, \qquad \boldsymbol{s}_i(t) = \begin{bmatrix} s_i^{00}(t) \\ s_i^{20}(t) \\ s_i^{22}(t) \\ \vdots \end{bmatrix} \quad (i = x, y, z), \tag{61}$$

where the former is needed for the first term on the right-hand side of (59). The SLE dynamics then becomes

$$\begin{bmatrix} \dot{\boldsymbol{s}}_x(t) \\ \dot{\boldsymbol{s}}_y(t) \\ \dot{\boldsymbol{s}}_z(t) \end{bmatrix} = -\mathcal{B}_0 \begin{bmatrix} \boldsymbol{s}_x(t) \\ \boldsymbol{s}_y(t) \\ \boldsymbol{s}_z(t) \end{bmatrix} + R_1 \begin{bmatrix} 0 \\ 0 \\ \mathbf{1}^{00} \end{bmatrix} s_z^{\mathrm{eq}}, \tag{62}$$

where

$$\mathcal{B}_0 = \begin{bmatrix} \mathbf{R}_2 & \boldsymbol{\Delta} & 0 \\ -\boldsymbol{\Delta} & \mathbf{R}_2 & \omega_1 \mathbf{E} \\ 0 & -\omega_1 \mathbf{E} & \mathbf{R}_1 \end{bmatrix} \tag{63}$$

is a $3n_{\mathrm{tot}} \times 3n_{\mathrm{tot}}$ matrix, and $\mathbf{E}$, $\mathbf{R}_1$, $\mathbf{R}_2$ and $\boldsymbol{\Delta}$ are $n_{\mathrm{tot}} \times n_{\mathrm{tot}}$ matrices.

The first three of these sub-matrices are purely diagonal: $\mathbf{E}$ is the identity matrix and

$$\mathbf{R}_{1,2} = R_{1,2}\mathbf{E} + D_{\mathrm{rot}}\mathbf{C}_D, \tag{64}$$

with the diagonal elements of $\mathbf{C}_D$ being equal to $L(L+1)$. For the simplest case of $L_{\max} = 2$ with only three coefficients ($\vec{s}^{00}$, $\vec{s}^{20}$ and $\vec{s}^{22}$),

$$\mathbf{E} = \begin{bmatrix} 1 & & \\ & 1 & \\ & & 1 \end{bmatrix}, \qquad \mathbf{C}_D = \begin{bmatrix} 0 & & \\ & 6 & \\ & & 6 \end{bmatrix}. \tag{65}$$

In (63), the diagonal matrices $\mathbf{R}_{1,2}$ and $\mathbf{E}$, which originate from the second line in (59), do not mix coefficients with different L and M. Only the sub-matrix $\boldsymbol{\Delta}$, which is of the form

$$\boldsymbol{\Delta} = \Delta\mathbf{E} + \gamma_0^2\mathbf{C}_0 + \gamma_2^2\mathbf{C}_2, \tag{66}$$

mixes coefficients of different orders. In fact, the mixing is due to the matrices $\mathbf{C}_{0,2}$, which modify the frequency offset Δ in proportion to the g-tensor anisotropies γ_0^2 and γ_2^2. For $L_{\max} = 2$,

$$\mathbf{C}_0 = \begin{bmatrix} 0 & \frac{1}{5} & 0 \\ 1 & \frac{2}{7} & 0 \\ 0 & 0 & -\frac{2}{7} \end{bmatrix}, \qquad \mathbf{C}_2 = \begin{bmatrix} 0 & 0 & \frac{1}{5} \times 2 \\ 0 & 0 & -\frac{2}{7} \times 2 \\ 1 & -\frac{2}{7} & 0 \end{bmatrix}. \tag{67}$$

https://doi.org/10.5194/mr-2023-10
Preprint. Discussion started: 31 July 2023

Open Access MAGNETIC RESONANCE Discussions

(The factors of two in the last column of $\mathbf{C}_2$ arise from the fact that coefficients with $M = 0$ pose an exception to the symmetrization (60).) The matrix elements of these two matrices in the most general case are

$$[\mathbf{C}_0]_{LM,\ell m} = C^{LM}_{20\ell m} C^{L0}_{20\ell 0}$$
$$[\mathbf{C}_2]_{LM,\ell m} = (C^{LM}_{2-2\ell m} + C^{LM}_{22\ell m} + \delta_{M0} C^{LM}_{22\ell m}) C^{L0}_{20\ell 0}, \tag{68}$$

where the summand proportional to δ_{M0} in the second line accounts for the factor of two that is needed by the coefficients $\vec{s}^{\,L0}$.

Selecting $L_{\max} = 0$ in the above formalism amounts to retaining only the (3D vector) coefficient $\vec{s}^{\,00}$. Then the matrix $\mathcal{B}_0$ in (63) reduces to $\mathbb{B}_0$, and (62) reduces to the classical Bloch equations for a homogeneous line. For $L_{\max} > 0$, the diagonal matrices $\mathbf{R}_1$ and $\mathbf{R}_2$ cause the coefficients s_z^{LM} and $s_{x,y}^{LM}$, respectively, to decay exponentially, with those with larger L being suppressed more strongly by the tumbling. Analogously to the Bloch equations, the mw excitation mixes the y and z components of $\vec{s}^{\,LM}$, without mixing their LM dependence. The latter is mixed only by the offset matrix $\mathbf{\Delta}$, as elaborated above.

By building the SLE dynamics on top of the classical Bloch equations, we have arrived at a rather intuitive picture of how the g-tensor anisotropy is incorporated into the spin dynamics. Specifically, every element of the Bloch matrix $\mathbb{B}_0$ (eq. (19) with $\omega_I = 0$) is replaced by a matrix in the space of LM indices (eq. (63)). In this replacement, all elements except the frequency offset become diagonal matrices in the LM space, with the mixing in this space being entirely due to the offset. Since we describe the solid effect by two coupled Bloch equations, this intuition about the effect of g-tensor anisotropy on the spin dynamics will be helpful when adapting the approach to SE-DNP.

4.3 EPR spectrum

The cw-EPR spectrum and the electronic saturation factor under g-tensor anisotropy are obtained from the steady state of (62),

$$\mathcal{B}_0 \begin{bmatrix} \boldsymbol{s}_x^{\mathrm{ss}} \\ \boldsymbol{s}_y^{\mathrm{ss}} \\ \boldsymbol{s}_z^{\mathrm{ss}} \end{bmatrix} = R_1 \begin{bmatrix} 0 \\ 0 \\ \mathbf{1}^{00} \end{bmatrix} s_z^{\mathrm{eq}}, \tag{69}$$

which can be solved by inverting the $3n_{\mathrm{tot}} \times 3n_{\mathrm{tot}}$ matrix $\mathcal{B}_0$ numerically. However, it is also possible to solve (69) by inverting a single matrix with dimensions that are three times smaller (i.e., $n_{\mathrm{tot}} \times n_{\mathrm{tot}}$), as we show next.

First, taking advantage of the zeros in $\mathcal{B}_0$ (eq. (63)), we express $\boldsymbol{s}_x^{\mathrm{ss}}$ and $\boldsymbol{s}_z^{\mathrm{ss}}$ in terms of $\boldsymbol{s}_y^{\mathrm{ss}}$:

$$\boldsymbol{s}_x^{\mathrm{ss}} = -\mathbf{R}_2^{-1} \mathbf{\Delta}\, \boldsymbol{s}_y^{\mathrm{ss}}$$
$$\boldsymbol{s}_z^{\mathrm{ss}} = \omega_1 \mathbf{R}_1^{-1} \boldsymbol{s}_y^{\mathrm{ss}} + R_1 \mathbf{R}_1^{-1} \mathbf{1}^{00} s_z^{\mathrm{eq}}. \tag{70}$$

Because only the first element of $\mathbf{1}^{00}$ is non-zero, and the diagonal matrix $\mathbf{R}_1$ does not mix coefficients with different values of LM, the second equality in (70) becomes

$$\boldsymbol{s}_z^{\mathrm{ss}} = \omega_1 \mathbf{R}_1^{-1} \boldsymbol{s}_y^{\mathrm{ss}} + \mathbf{1}^{00} s_z^{\mathrm{eq}}. \tag{71}$$

https://doi.org/10.5194/mr-2023-10
Preprint. Discussion started: 31 July 2023

Open Access MAGNETIC RESONANCE Discussions

For the 00th (i.e., first) element of $\boldsymbol{s}_z^{\mathrm{ss}}$ we thus have $s_z^{00} = \omega_1 T_1 s_y^{00} + s_z^{\mathrm{eq}}$, which is identical to the second equality in (12). We thus conclude that the proportionality between the electronic saturation factor and the in-phase EPR line shape (eq. (16)) is not limited to a homogenous line but applies also under g-tensor anisotropy.

Second, from the middle row of the matrix $\mathcal{B}_0$ (eq. (63)), and after substituting $\boldsymbol{s}_x^{\mathrm{ss}}$ and $\boldsymbol{s}_z^{\mathrm{ss}}$ from (70), we find

$$\boldsymbol{s}_y^{\mathrm{ss}} = -\omega_1 \mathbf{P}_0^{-1} \mathbf{1}^{00} s_z^{\mathrm{eq}}, \tag{72}$$

where we have introduced the $n_{\mathrm{tot}} \times n_{\mathrm{tot}}$ matrix

$$\mathbf{P} = (\mathbf{R}_2 + \mathrm{i}\omega_I) + \omega_1^2 (\mathbf{R}_1 + \mathrm{i}\omega_I)^{-1} + \boldsymbol{\Delta} (\mathbf{R}_2 + \mathrm{i}\omega_I)^{-1} \boldsymbol{\Delta} \tag{73}$$

and $\mathbf{P}_0 = \mathbf{P}(\omega_I = 0)$. The matrix $\mathbf{P}_0$ generalizes P_0 (eq. (14)) and (72) generalizes (13) to the case of g-tensor anisotropy.

From the 00th components of $\boldsymbol{s}_y^{\mathrm{ss}}$ and $\boldsymbol{s}_x^{\mathrm{ss}}$ we find

$$\mathrm{abs} = -\omega_1 [\mathbf{P}_0^{-1}]_{11}, \qquad \mathrm{dsp} = \omega_1 T_2 [\boldsymbol{\Delta} \mathbf{P}_0^{-1}]_{11}, \tag{74}$$

where we used the fact that $\mathbf{R}_2$ is a diagonal matrix. These expressions generalize eqs. (15) to the case of g-tensor anisotropy. The corresponding saturation factor as a function of the offset is then (from eqs. (16) and (74))

$$s(\Delta) = \omega_1^2 T_1 [\mathbf{P}_0^{-1}(\Delta)]_{11}. \tag{75}$$

As claimed, to solve for the steady state numerically we need to invert the matrix $\mathbf{P}_0$ whose dimensions are three times smaller than those of $\mathcal{B}_0$. (The two matrix inversions needed to calculate $\mathbf{P}_0$ itself involve the diagonal matrices $\mathbf{R}_{1,2}$.)

The cw-EPR spectrum in derivative mode can be calculated from the derivative of $\mathbf{P}_0$ with respect to the (scalar) frequency offset Δ:

$$\frac{\partial \mathbf{P}_0}{\partial \Delta} = \mathbf{R}_2^{-1} \boldsymbol{\Delta} + \boldsymbol{\Delta} \mathbf{R}_2^{-1}. \tag{76}$$

The in-phase and out-of-phase derivative spectra are then obtained from the first (i.e., 00th) components of the vectors

$$\begin{aligned} \frac{\partial \boldsymbol{s}_y}{\partial \Delta} &= \omega_1 \mathbf{P}_0^{-1} (\mathbf{R}_2^{-1} \boldsymbol{\Delta} + \boldsymbol{\Delta} \mathbf{R}_2^{-1}) \mathbf{P}_0^{-1} \mathbf{1}^{00} s_z^{\mathrm{eq}} \\ \frac{\partial \boldsymbol{s}_x}{\partial \Delta} &= -\mathbf{R}_2^{-1} (\boldsymbol{s}_y + \boldsymbol{\Delta} \frac{\partial \boldsymbol{s}_y}{\partial \Delta}). \end{aligned} \tag{77}$$

These expressions are used in Sec. 5 to fit the experimental EPR spectra from fig. 1.

In fig. 2 we show examples of (integral) EPR spectra calculated using the presented approach for different tumbling times τ_{rot}. The different columns in the figure correspond to different choices of L_{max}. The g-tensor values used in the simulations are characteristic of nitroxide spin labels. We also selected a small mw magnetic field ($B_1 = 0.02\,\mathrm{G}$) to mimic the low-power conditions typical for cw-EPR. The main message of this figure is that slower tumbling requires larger L_{max}. At the same time, we see that $L_{\mathrm{max}} = 8$ is already good enough for $\tau_{\mathrm{rot}} \leqslant 10\,\mathrm{ns}$, which is the range of rotational time scales of relevance to our experimental data (Sec. 5). By selecting $L_{\mathrm{max}} = 10$, to be on the safe side, we only need to invert a 21×21 matrix at every frequency offset, which makes the calculation of g-broadened EPR spectra very fast. This allows us to perform an automated search over the various parameters and fit the experimental cw-EPR spectra in less than a minute.

https://doi.org/10.5194/mr-2023-10
Preprint. Discussion started: 31 July 2023

Open Access MAGNETIC RESONANCE Discussions

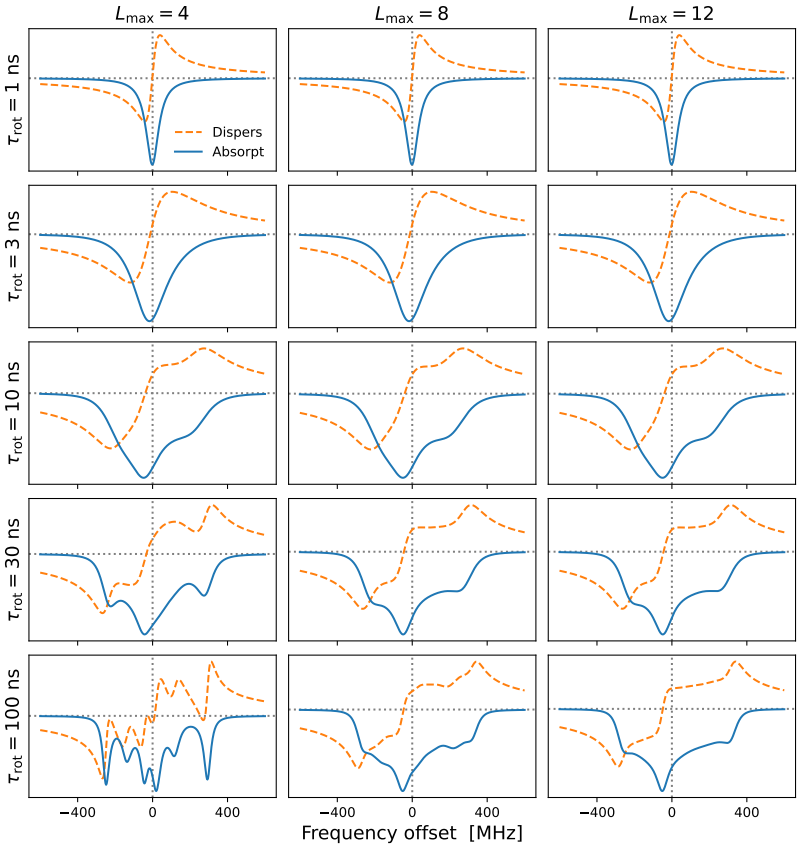

Figure 2. Continuous-wave EPR spectra for $g = \mathrm{diag}(2.00755, 2.00555, 2.0023)$ and different tumbling times τ_{rot}. Larger L_{max} is necessary for slower tumbling. The needed L_{max} also depends on the anisotropies, which are $(\gamma_0, \gamma_2) = (-373, 107)$ MHz for $B_0 = 9.403$ T. Other simulation parameters were $B_1 = 0.02$ G, $T_1 = 100$ ns, $T_2^{\mathrm{homog}} = 20$ ns.

4.4 Solid effect in 'solids'

Extending the above treatment to SE-DNP, we combine the spin dynamics in (35) with the rotational dynamics in (44) to form the following SLE:

$$\begin{aligned}\frac{\partial}{\partial t}\vec{g}(\Omega,t) &= -(K_\Omega \otimes \mathbb{E} + E_\Omega \otimes \mathbb{B})\vec{g}(\Omega,t) \\ &\quad - E_\Omega \otimes \mathbb{F}(\Omega)\vec{g}(\Omega,t) \\ &\quad - \frac{1}{4}A_1 \mathbb{G}\vec{s}(\Omega,t) - \mathrm{i}\frac{1}{4}A_1 \hat{k} i_z(t) p^{\mathrm{eq}}(\Omega).\end{aligned} \tag{78}$$

As before, we introduce the expansion

$$\vec{g}(\Omega,t) = \frac{1}{8\pi^2}\sum_{\ell=0}^{\infty}\sum_{m=-\ell}^{\ell} \mathscr{D}^2_{m0}(\Omega)\,\vec{g}^{\ell}_{m0}(t), \tag{79}$$

https://doi.org/10.5194/mr-2023-10
Preprint. Discussion started: 31 July 2023

Open Access MAGNETIC RESONANCE Discussions

where we have set $n = 0$ from the start, and find

$$\dot{\vec{g}}^{L}_{M0}(t) = -[D_{\rm rot}L(L+1) + \mathbb{B}]\vec{g}^{L}_{M0}(t)$$
$$-\sum_{\ell m}[\gamma_0^2 C^{LM}_{20\ell m} + \gamma_2^2(C^{LM}_{2-2\ell m} + C^{LM}_{22\ell m})]C^{L0}_{20\ell n}\mathbb{G}\vec{g}^{\ell}_{m0}(t)$$
$$-\frac{1}{4}A_1\mathbb{G}\,\vec{s}^{L}_{M0}(t) - \mathrm{i}\frac{1}{4}A_1\hat{k}\,i_z(t)\delta_{L0}\delta_{M0}. \tag{80}$$

Again, we switch to the symmetrized coefficients

$$\vec{g}^{LM} = \frac{1}{2}(\vec{g}^{L}_{-M0} + \vec{g}^{L}_{M0}) \tag{81}$$

and form the following three, $n_{\rm tot}$-dimensional vectors from the spatial components of the 3D vectors $\vec{g}^{LM}$:

$$\boldsymbol{g}_i = \begin{bmatrix} g_i^{00} \\ g_i^{20} \\ g_i^{22} \\ \vdots \end{bmatrix} \qquad (i = x, y, z). \tag{82}$$

The steady state of the resulting spin dynamics is then

$$\mathcal{B}\begin{bmatrix} \boldsymbol{g}_x^{\rm ss} \\ \boldsymbol{g}_y^{\rm ss} \\ \boldsymbol{g}_z^{\rm ss} \end{bmatrix} = -\frac{1}{4}A_1\begin{bmatrix} \boldsymbol{s}_y^{\rm ss} \\ -\boldsymbol{s}_x^{\rm ss} \\ 0 \end{bmatrix} - \mathrm{i}\frac{1}{4}A_1\begin{bmatrix} 0 \\ 0 \\ \mathbf{1}^{00} \end{bmatrix} i_z^{\rm ss}, \tag{83}$$

where

$$\mathcal{B} = \mathcal{B}_0 + \mathrm{i}\omega_I \tag{84}$$

generalizes the matrix $\mathcal{B}_0$ from (63).

Our goal is to solve for $\boldsymbol{g}_z^{\rm ss}$ since its 00th component should be used in (23) to calculate the rate constants pv_- and v_+. After inverting $\mathcal{B}$ in (83) we find

$$\boldsymbol{g}_z^{\rm ss} = -\frac{1}{4}A_1[\mathcal{B}^{-1}]_{zx}\boldsymbol{s}_y^{\rm ss} - \frac{1}{4}A_1[\mathcal{B}^{-1}]_{zy}(-\boldsymbol{s}_x^{\rm ss})$$
$$-\mathrm{i}\frac{1}{4}A_1[\mathcal{B}^{-1}]_{zz}\mathbf{1}^{00}i_z^{\rm ss}. \tag{85}$$

Note that now $[\mathcal{B}^{-1}]_{ij}$ denotes the $n_{\rm tot} \times n_{\rm tot}$ sub-matrix of $\mathcal{B}^{-1}$ at position ij, and not a scalar matrix element. Using $\boldsymbol{s}^{\rm ss}_{x,y}$ from the previous subsection, we find that the first component of $\boldsymbol{g}_z^{\rm ss}$ is

$$g_z^{00} = \omega_1\frac{1}{4}A_1[([\mathcal{B}^{-1}]_{zx} + [\mathcal{B}^{-1}]_{zy}\mathbf{R}_2^{-1}\boldsymbol{\Delta})\mathbf{P}_0^{-1}]_{11}s_z^{\rm eq}$$
$$-\mathrm{i}\frac{1}{4}A_1[[\mathcal{B}^{-1}]_{zz}]_{11}i_z^{\rm ss}. \tag{86}$$

https://doi.org/10.5194/mr-2023-10
Preprint. Discussion started: 31 July 2023

Open Access MAGNETIC RESONANCE Discussions

Substituting this result into (23) we obtain

$$
\begin{aligned}
R_{1I}^A &= \delta^2 \mathrm{Re}\{[[\mathcal{B}^{-1}_{\omega_1=0}]_{zz}]_{11}\} \\
v_+ &= \delta^2 \mathrm{Re}\{[[\mathcal{B}^{-1}]_{zz}]_{11}\} - R_{1I}^A \\
pv_- &= -\delta^2\omega_1 \mathrm{Im}\{[([\mathcal{B}^{-1}]_{zx} + [\mathcal{B}^{-1}]_{zy}\mathbf{R}_2^{-1}\boldsymbol{\Delta})\mathbf{P}_0^{-1}]_{11}\}.
\end{aligned}
\tag{87}
$$

These expressions, which require the inversion of the $3n_{\mathrm{tot}} \times 3n_{\mathrm{tot}}$ matrix $\mathcal{B}$, are directly generalizable to liquids (Sec. 4.5). In 'solids', it is possible to obtain alternative expressions that require the inversion of a smaller, $n_{\mathrm{tot}} \times n_{\mathrm{tot}}$ matrix. To this end, we express $\boldsymbol{g}_x^{\mathrm{ss}}$ and $\boldsymbol{g}_z^{\mathrm{ss}}$ in terms of $\boldsymbol{g}_y^{\mathrm{ss}}$ using the first and last rows of $\mathcal{B}$:

$$
\begin{aligned}
\boldsymbol{g}_x^{\mathrm{ss}} &= -(\mathbf{R}_2 + \mathrm{i}\omega_I)^{-1}\boldsymbol{\Delta}\boldsymbol{g}_y^{\mathrm{ss}} - \frac{1}{4}A_1(\mathbf{R}_2 + \mathrm{i}\omega_I)^{-1}\boldsymbol{s}_y^{\mathrm{ss}} \\
\boldsymbol{g}_z^{\mathrm{ss}} &= \omega_1(\boldsymbol{R}_1 + \mathrm{i}\omega_I)^{-1}\boldsymbol{g}_y^{\mathrm{ss}} - \mathrm{i}\frac{1}{4}A_1(\boldsymbol{R}_1 + \mathrm{i}\omega_I)^{-1}\mathbf{1}^{00}i_z^{\mathrm{ss}}.
\end{aligned}
\tag{88}
$$

Substituting the first (i.e., 00th) component of $\boldsymbol{g}_z^{\mathrm{ss}}$ in (23) we find

$$
R_{1I}^A = \delta^2 \mathrm{Re}\{[(\boldsymbol{R}_1 + \mathrm{i}\omega_I)^{-1}]_{11}\}. \tag{89}
$$

Because $\mathbf{R}_1$ is a diagonal matrix, this result is identical to (29), showing that R_{1I}^A is not affected by the anisotropy of the g tensor.

Similarly, from the middle part of $\mathcal{B}$ we obtain

$$
\begin{aligned}
\mathbf{P}\boldsymbol{g}_y^{\mathrm{ss}} = &\frac{1}{4}A_1[\boldsymbol{s}_x^{\mathrm{ss}} - \boldsymbol{\Delta}(\mathbf{R}_2 + \mathrm{i}\omega_I)^{-1}\boldsymbol{s}_y^{\mathrm{ss}}] \\
&+ \omega_1 \mathrm{i}\frac{1}{4}A_1(\boldsymbol{R}_1 + \mathrm{i}\omega_I)^{-1}\mathbf{1}^{00}i_z^{\mathrm{ss}}.
\end{aligned}
\tag{90}
$$

We first observe that $(\mathbf{R}_1 + \mathrm{i}\omega_I)^{-1}\mathbf{1}^{00} = \mathbf{1}^{00}(R_1 + \mathrm{i}\omega_I)^{-1}$ because $\mathbf{R}_1$ is diagonal. Then we substitute $\boldsymbol{s}_{x,y}^{\mathrm{ss}}$ from before to get

$$
\begin{aligned}
\boldsymbol{g}_y^{\mathrm{ss}} = &\omega_1\frac{1}{4}A_1\mathbf{P}^{-1}[\mathbf{R}_2^{-1}\boldsymbol{\Delta} + \boldsymbol{\Delta}(\mathbf{R}_2 + \mathrm{i}\omega_I)^{-1}]\mathbf{P}_0^{-1}\mathbf{1}^{00}s_z^{\mathrm{eq}} \\
&+ \omega_1\mathrm{i}\frac{1}{4}A_1\mathbf{P}^{-1}\mathbf{1}^{00}(R_1 + \mathrm{i}\omega_I)^{-1}i_z^{\mathrm{ss}}.
\end{aligned}
\tag{91}
$$

Finally, substituting the 00th element of $\boldsymbol{g}_y^{\mathrm{ss}}$ in (30) we find

$$
\begin{aligned}
v_+ &= -\delta^2\omega_1^2 \mathrm{Re}\{(R_1 + \mathrm{i}\omega_I)^{-2}[\mathbf{P}^{-1}]_{11}\} \\
pv_- &= -\delta^2\omega_1^2 \mathrm{Im}\{(R_1 + \mathrm{i}\omega_I)^{-1} \\
&\quad \times [\mathbf{P}^{-1}(\mathbf{R}_2^{-1}\boldsymbol{\Delta} + \boldsymbol{\Delta}(\mathbf{R}_2 + \mathrm{i}\omega_I)^{-1})\mathbf{P}_0^{-1}]_{11}\}.
\end{aligned}
\tag{92}
$$

Observe how these expressions generalize (33) and (34) to the case of g-tensor anisotropy.

In the last two rows of fig. 3 we show v_+/δ^2 and pv_-/δ^2, which have units of time. Although the electronic non-saturation factor p and the rate constant v_- always appear together as pv_-, it is helpful to separate these two factors when rationalizing

https://doi.org/10.5194/mr-2023-10
Preprint. Discussion started: 31 July 2023

Open Access MAGNETIC RESONANCE Discussions

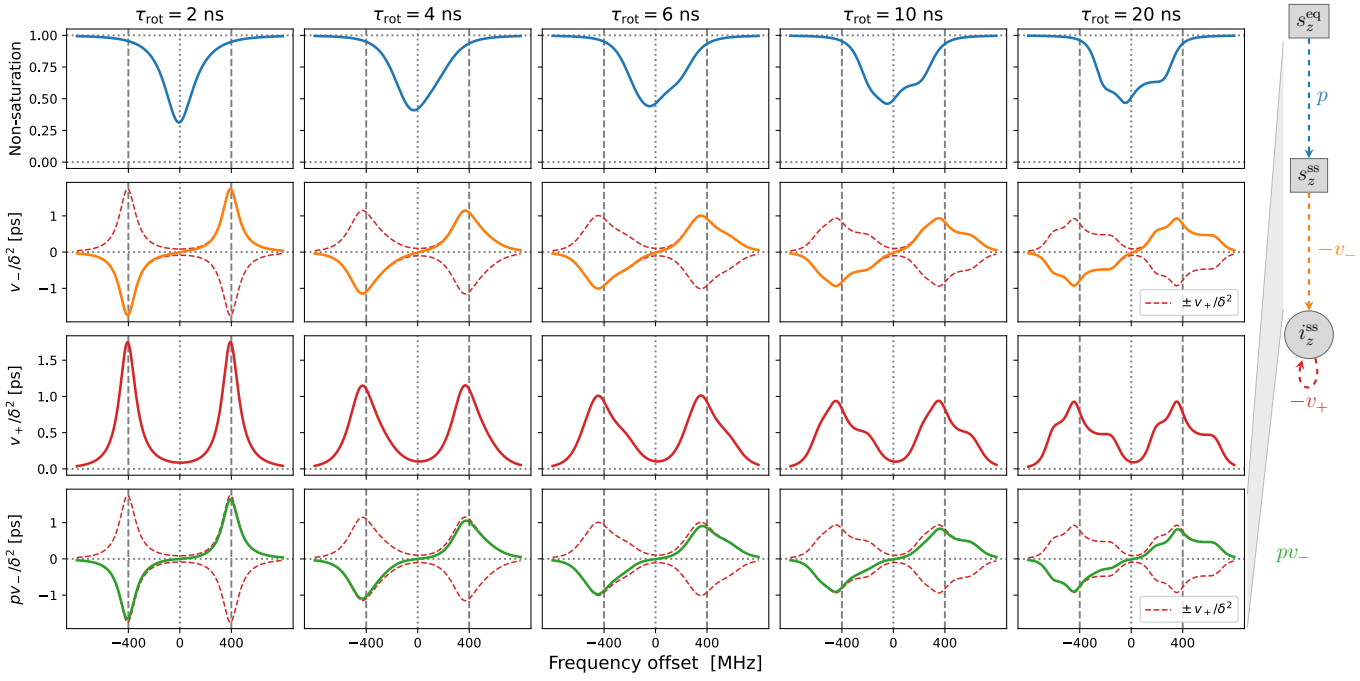

Figure 3. Solid-effect rates v_+ (red line) and pv_- (green line) calculated at high mw power ($B_1 = 5.5\,\mathrm{G}$) for static dipolar interaction (i.e., 'solid') and several different rates of rotational tumbling. The factorization of pv_- into p (blue line) and v_- (orange line) is also shown. All other parameters as in fig. 2 and $L_{\max} = 10$. In particular, $T_1 = 100\,\mathrm{ns}$.

SE. We show p and v_-/δ^2 in the first two rows of fig. 3. Note that v_+/δ^2 and pv_-/δ^2 were calculated directly from (92), whereas v_-/δ^2 was determined by dividing pv_-/δ^2 by $p = 1 - \omega_1^2 T_1 [\mathbf{P}_0^{-1}]_{11}$ (eq. (75)).

The columns in fig. 3 reveal the effect of the g-tensor anisotropy on the different factors relevant to SE. v_+/δ^2 in the third row of the figure is composed of two SE lines centered at $-\omega_I$ and $+\omega_I$. At the fastest tumbling (leftmost column), each of these two lines is symmetric and approximately Lorentzian. When the tumbling slows down, each line broadens and becomes asymmetric. At the slowest tumbling rate (rightmost column), each line resembles a powder EPR spectrum with anisotropic g tensor. We see that in the regime of slow tumbling the profile of v_+/δ^2 is no longer symmetric (i.e., even) with respect to the electronic resonance at zero offset frequency.

In the second row of fig. 3 we show v_-/δ^2 (orange line), which is also composed of two SE lines centered at $-\omega_I$ and $+\omega_I$, with the former flipped with respect to the horizontal axis. For comparison, in the second row we also plotted v_+/δ^2 and $-v_+/\delta^2$ (dashed red lines). We see that, for all tumbling rates, the two SE lines comprising v_-/δ^2 exactly match their counterparts in v_+/δ^2.

The first row of fig. 3 shows the electronic saturation under g-tensor anisotropy (we actually plot the "non-saturation" $p = 1 - s$). Because of the large B_1 used in the calculations ($B_1 = 5.5\,\mathrm{G}$) appreciable electronic saturation is achieved for

https://doi.org/10.5194/mr-2023-10
Preprint. Discussion started: 31 July 2023


Open Access MAGNETIC RESONANCE Discussions

all shown tumbling rates. From the perspective of the solid effect, it is noteworthy that the saturation is more localized to on-resonance conditions when the g-tensor anisotropy is averaged out by the tumbling, and spreads to larger off-resonance frequencies when the tumbling slows down. This spread broadens the saturation profile and reduces its maximum. However, in spite of the substantial increase of the spectral width of the saturation when going from $\tau_{\mathrm{rot}} = 2\,\mathrm{ns}$ to $\tau_{\mathrm{rot}} = 20\,\mathrm{ns}$, the maximum decreases only moderately, remaining close to 50% at the slower tumbling rate.

Of course, the amplitude of the saturation profile depends not only on B_1 but also on the electronic T_1 relaxation time. To illustrate this dependence, we recalculated all curves in fig. 3 after increasing T_1 five-fold to 500 ns. The result, which is shown in fig. A1, demonstrates larger saturation for all tumbling rates. At the same time, v_-/δ^2 and v_+/δ^2 (second and third rows) remain entirely unaffected. This demonstrates that the SE lines do not experience the power-broadening that affects the EPR spectrum.

Finally, the last row of fig. 3 shows pv_-/δ^2 (solid green line), which equals the product of the first and second rows. From (7) we know that pv_-/δ^2 basically gives the SE-DNP spectrum, up to an overall scaling factor. Since pv_- is suppressed by the electronic saturation compared to v_-, we see that pv_-/δ^2 is somewhat reduced at offsets between the canonical SE positions $\pm\omega_I$. Because both the electronic saturation profile and the profile of v_- are asymmetric in the slow motional regime where the EPR line exhibits clear g-broadening, the line shape of the SE-DNP spectrum (proportional to pv_-) is no longer antisymmetric (i.e., odd) with respect to the electronic resonance. This is most visible for the green line in the lower rightmost corner of fig. 3.

4.5 Solid effect in liquids

In the light of Sec. 3.3, the generalization to liquids consists of calculating the matrix

$$\mathcal{Q} = j_{11}(\mathcal{B}), \tag{93}$$

and using it instead of $\mathcal{B}^{-1}$ in (87):

$$\begin{aligned} R_{1I}^A &= \langle\delta^2\rangle \mathrm{Re}\{[[\mathcal{Q}_{\omega_1=0}]_{zz}]_{11}\} \\ v_+ &= \langle\delta^2\rangle \mathrm{Re}\{[[\mathcal{Q}]_{zz}]_{11}\} - R_{1I}^A \\ pv_- &= -\langle\delta^2\rangle \omega_1 \mathrm{Im}\{[([\mathcal{Q}]_{zx} + [\mathcal{Q}]_{zy}\mathbf{R}_2^{-1}\boldsymbol{\Delta})\mathbf{P}_0^{-1}]_{11}\}. \end{aligned} \tag{94}$$

Because the zz sub-block of $\mathcal{B}$ is diagonal and does not couple to the rest when $\omega_1 = 0$, we deduce that

$$R_{1I}^A = \langle\delta^2\rangle \mathrm{Re}\{j_{11}(R_1 + \mathrm{i}\omega_I)\}, \tag{95}$$

which is identical to (43). Thus, as we already observed for 'solids', the expression for R_{1I}^A is not affected by the anisotropy of the g tensor and the slow tumbling of the radical.

In fig. 4 we show the same properties as in fig. 3 but now in the presence of translational diffusion treated by the FFHS model with motional time scale $\tau_{\mathrm{ffhs}} = 6\,\mathrm{ns}$. Several changes compared to 'solids' (fig. 3) are worth pointing out.

https://doi.org/10.5194/mr-2023-10
Preprint. Discussion started: 31 July 2023

Open Access MAGNETIC RESONANCE Discussions

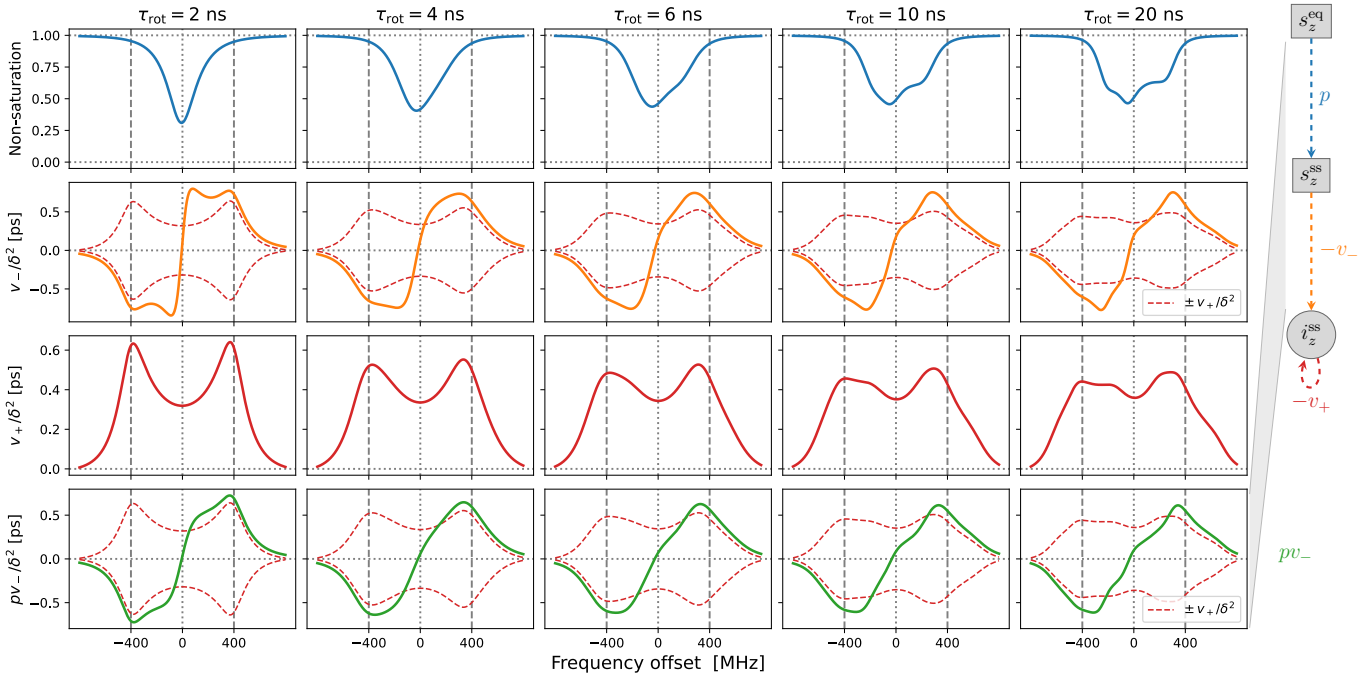

Figure 4. Same as fig. 3 for the FFHS model of translational diffusion with $\tau_{\mathrm{ffhs}} = 6$ ns.

In line with our previous understanding (Sezer, 2023b), the SE lines comprising $v_+/\langle\delta^2\rangle$ are broadened by the translational motion that modulates the dipolar interaction (red lines in the third row of fig. 4). This motional broadening reduces their maximum intensities compared to 'solids' (fig. 3, third row). Previously, in the case of Lorentzian lines, the reduction of intensity in the transition from solids to liquids was dramatic, by more than a factor of ten (Sezer, 2023b, figs. 3, 4 and 5). In contrast, the reduction in the presence of g-tensor broadening is about a factor of two (compare third rows of figs. 3 and 4). This observation may help rationalize why the maximum SE-DNP enhancement in liquids, e.g., about 50 for trityl in glycerol at 320 K (Kuzhelev et al., 2023), is not negligibly smaller compared to the enhancements that are obtained in the solid state. We also point out that, while reducing the maximum SE intensities in the vicinity of $\pm\omega_I$, the motional broadening substantially increases the intensities at the smaller offsets around the electronic resonance.

Besides the motional broadening, the progression from left to right in the third row of fig. 4 demonstrates additional g-tensor broadening, which was present also in 'solids'. However, now the two SE lines are affected differently by the g-tensor anisotropy, making the profile of $v_+/\langle\delta^2\rangle$ at slow tumbling rates rather irregular.

Moving on to the second row in fig. 4, we see that the SE lines that make up $v_-/\langle\delta^2\rangle$ (orange) are now completely different from their counterparts in $v_+/\langle\delta^2\rangle$ (dashed red). The increased intensity in the vicinity of the electronic resonance due to motional broadening is also manifested by $v_-/\langle\delta^2\rangle$. For the fastest tumbling in the figure (leftmost column), the fluctuations of the dipolar interaction not only broaden the SE lines but also enable a new phenomenon, which is manifested as near-resonance

https://doi.org/10.5194/mr-2023-10
Preprint. Discussion started: 31 July 2023


Open Access MAGNETIC RESONANCE Discussions

peaks that are comparable in magnitude to the peaks at $\pm\omega_I$ but clearly distinct from them (orange line). These peaks reflect the multiplicative contribution of the dispersive EPR signal to v_- (Sezer, 2023a, b). For faster translational diffusion the near-resonance peaks may become larger than the peaks at $\pm\omega_I$, as can be seen in the leftmost column of fig. A3a (orange line). Because they are more strongly suppressed by the electronic saturation, however, these peaks do not exceed the SE peaks in the final enhancement profile (fig. A3a, leftmost column, green line).

Up to an overall scaling factor, the green lines in the last row of fig. 4 correspond to the SE-DNP enhancement profile. Because its middle part is suppressed by the electronic saturation, this profile in the presence of g-tensor broadening becomes very non-symmetric and responds sensitively to the tumbling of the polarizing agent. To further illustrate the influence of the electronic saturation on the SE-DNP spectrum, in fig. A2 we show the same curves but calculated with five-fold longer electronic spin-lattice relaxation time ($T_1 = 500\,\mathrm{ns}$), which leads to larger saturation. Similarly, to illustrate the effect of translational diffusion, we recalculated the curves in fig. 4 for $\tau_{\mathrm{ffhs}} = 3\,\mathrm{ns}$ (two times faster) and $\tau_{\mathrm{ffhs}} = 12\,\mathrm{ns}$ (two times slower). The results are presented in fig. A3. These additional simulations show that the SE-DNP line shape is very sensitive to the times scales of molecular motion.

In the next section, we systematically vary the degrees of power broadening and motional broadening to match the experimental DNP profiles from fig. 1.

5 Disentangling the solid and Overhauser DNP effects

Using the developed methodology, we now analyze the experiments from fig. 1. In the light of eqs. (2) and (7) for the OE and SE enhancements, we will identify the profile of the electronic saturation (fig. 4, first row) with ϵ_{OE} and the profile of $pv_-/\langle\delta^2\rangle$ (fig. 4, last row, green line) with ϵ_{SE}. The tumbling times to be used in the DNP calculations will be obtained by fitting the experimental cw-EPR spectra. We start with 10-Doxyl-PC (fig. 1a,c) as its experimental spectra were more amenable to unrestricted fits of all parameters.

5.1 10-Doxyl-PC

5.1.1 Fit to the cw-EPR spectrum

Derivative EPR spectra were calculated from the first (i.e., 00th) components of the expressions in (77) for different values of the fitting parameters. In the fit, we varied the time scale of tumbling, τ_{rot}, as well as the g-tensor anisotropies γ_0^2 and γ_2^2 (eq. (50)). As we have no precise knowledge of the field B_0 at the sample, we freely shifted the calculated spectra along the horizontal axis to achieve best match with experiment. Since this leaves one of the g-tensor components undetermined we took $g_{zz} = 2.0023$, which is typical for nitroxides.

The numerical integrals of the derivative EPR spectra in figs. 1a and 1b (dotted-dashed blue lines) do not come down exactly to zero at the end of the integration range at high frequency offsets. This points to the possibility that the in-phase component, s_y, is mixed slightly with the out-of-phase component, s_x. To account for this possibility, we fitted the derivative EPR spectra

https://doi.org/10.5194/mr-2023-10
Preprint. Discussion started: 31 July 2023

Open Access MAGNETIC RESONANCE Discussions

by calculating

$$\frac{\partial s_y^{00}}{\partial \Delta}\cos\phi + \frac{\partial s_x^{00}}{\partial \Delta}\sin\phi, \tag{96}$$

where the angle ϕ controlled the degree of mixing.

All in all, not counting the shift along the horizontal axis, we had four fitting parameters: γ_0^2, γ_2^2, τ_{rot} and ϕ. The best fit to the cw-EPR spectrum of 10-Doxyl-PC is shown in fig. 5a. The corresponding fitting parameters are given in the upper half of Table 1.

Encouragingly, our fitted spectrum shows rather good agreement with experiment, in spite of the simplifying assumptions of the theoretical model, namely isotropic rotational diffusion and absence of hyperfine interaction. To check the effect of the latter on the cw-EPR spectrum, we used Easyspin (Stoll and Schweiger, 2006) to simulate spectra with our fitted parameters but now also including a nitroxide hyperfine tensor, $A = \mathrm{diag}(14, 14, 90)$ MHz. The result is given in fig. A4a. The modification due to the hyperfine interaction, although small as expected at high magnetic fields, is clearly visible. Nevertheless, the comparison of the integrals of the cw-EPR spectra in fig. A4b suggests that the error made by neglecting the hyperfine interaction when calculating the DNP spectrum should be small.

Regarding the values of the fitted parameters, it was encouraging to see that the fit resulted in a negligibly small mixing angle of $\phi = -1.3°$, indicating that the measured spectrum correctly reflects the in-phase EPR component. With $B_0 = 9.4029\,\mathrm{T}$ and $g_{zz} = 2.0023$, the fitted g-tensor anisotropies that are given in Table 1 implied

$$g_{xx} = 2.00755, \qquad g_{zz} = 2.00555. \tag{97}$$

These values are rather reasonable for a nitroxide spin label. Finally, the fitted time scale of rotational diffusion was $\tau_{\mathrm{rot}} = 5.2\,\mathrm{ns}$. For comparison, the same time scale for the nitroxide free radical TEMPOL in water is about 20 ps (Sezer et al., 2009). However, unlike TEMPOL, our spin label is covalently attached to the lipid chain.

5.1.2 Fit to the DNP spectrum

Fixing the g-tensor components and the tumbling time to the values obtained from the fit to the cw-EPR spectrum, we proceeded to fit the DNP spectrum of 10-Doxyl-PC (fig. 1c). In the calculations, we fixed the mw field to $B_1 = 5.5\,\mathrm{G}$, which is our best estimate for the home-built Fabry-Pérot resonator operating at maximum power (Denysenkov et al., 2022). During the fits, we again allowed for global shift of the calculation along the horizontal axis. In addition, we fitted the electronic T_1 time, which has a direct effect on the electronic saturation profile, as well as the time scale of translational diffusion, τ_{ffhs}, which is responsible for the motional broadening of the SE lines.

In the fit, we calculated the electronic saturation factor (eq. (75)) and the time scale $pv_-(\Delta)/\langle\delta^2\rangle$ (last equation in (94)) as functions of the offset frequency Δ. Up to unknown multiplicative factors, these correspond to, respectively, the OE and SE enhancement profiles (eqs. (2) and (7)). We then fit the experimental DNP spectrum by calculating

$$\epsilon(\Delta) = \sigma_{\mathrm{OE}} \times s(\Delta) + \sigma_{\mathrm{SE}} \times \frac{pv_-}{\langle\delta^2\rangle}(\Delta), \tag{98}$$

https://doi.org/10.5194/mr-2023-10
Preprint. Discussion started: 31 July 2023

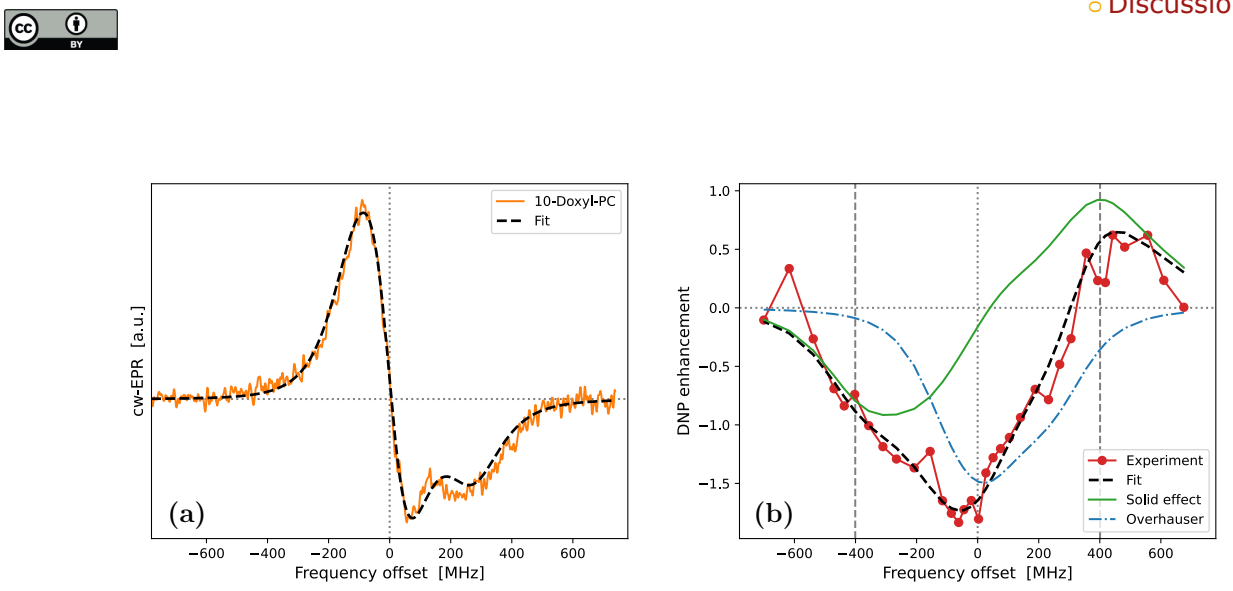

Figure 5. Fits to the experimental cw-EPR spectrum (**a**) and DNP spectrum (**b**) of 10-Doxyl-PC. In both cases, our best fits are shown with dashed black lines. The DNP spectrum in (**b**) is calculated by adding the contributions of SE (solid green line) and OE (dotted-dashed blue line), both of which are affected by the g-tensor anisotropy. The fit parameters are given in Table 1.

Table 1. Parameters obtained from the fits to the experimental data. $B_1 = 0.02$ G for EPR and 5.5 G for DNP. Homogeneous $T_2^{\mathrm{homog}} = 20$ ns was used for both EPR and DNP.

fit	parameter	10-Doxyl-PC	16-Doxyl-PC	
EPR	γ_0^2, γ_2^2 (MHz)	$-373, 107$	from 10-PC	
	τ_{rot} (ns)	5.2	1.9	
	ϕ (°)	-1.3	-2	
shown in figure		5a	6a	
DNP	τ_{ffhs} (ns)	6.4	from 10-PC	15.3
	T_1 (ns)	123	153	141
	σ_{OE} (-)	2.43	2.385	2.57
	σ_{SE} (ps^{-1})	1.51	1.35	1.09
shown in figure		5b	6b	7

where the scaling parameters σ_{OE} and σ_{SE} were also allowed to vary freely. As a result, not counting the shift along the horizontal axis, our fit contained four fitting parameters: τ_{ffhs}, T_1, σ_{OE} and σ_{SE}. The best fit to the DNP spectrum of 10-Doxyl-PC is shown in fig. 5b. It is noteworthy how the total DNP enhancement (dashed black line) emerges from the sum of the SE (green line) and OE (dotted-dashed blue line) contributions. The corresponding fitting parameters are given in the bottom half of Table 1.

In the case of 10-Doxyl-PC, the intuitive analysis of Neudert et al. (2017) for identifying the OE and SE components of a mixed DNP spectrum using the integrated cw-EPR line shape already performed very well (fig. 1c). It is, therefore, not surprising that our analysis, which has more fitting parameters, agrees better with the experimental DNP spectrum (fig. 5b).

https://doi.org/10.5194/mr-2023-10
Preprint. Discussion started: 31 July 2023


Open Access MAGNETIC RESONANCE Discussions

Both deficiencies of the intuitive approach, namely, too narrow OE and SE contributions due to the lack of, respectively, power broadening and motional broadening, appear to be satisfactorily addressed.

On a more fundamental level, our simulation shows that, due to the simultaneous power- and motional-broadening, the OE and SE contributions to the DNP enhancement are not only rather asymmetric but also overlap extensively. It should, therefore, be practically impossible to extract any molecular information from the mixed DNP spectrum without a complex, quantitative analysis. In our specific case, the fit resulted in a translational time scale $\tau_{\mathrm{ffhs}} = 6.4\,\mathrm{ns}$, and suggested that the electronic relaxation time should be about $T_1 = 120\,\mathrm{ns}$. At the high magnetic field of the experiment ($B_0 = 9.4\,\mathrm{T}$) this spin-lattice relaxation time is practically impossible to measure in the liquid state.

In addition to τ_{ffhs} and T_1, the fit to the DNP spectrum of 10-Doxyl-PC also produced the following numerical values for the two scaling parameters in eq. (98): $\sigma_{\mathrm{OE}} = 2.4$ and $\sigma_{\mathrm{SE}} = 1.5\,\mathrm{ps}^{-1}$. These will be analyzed in Sec. 5.3 together with the corresponding values for 16-Doxyl-PC.

5.2 16-Doxyl-PC

Because the g-tensor anisotropies are largely averaged in the cw-EPR spectrum of 16-Doxyl-PC (fig. 1b), we did not attempt to fit them. Instead, we fixed all three components to the values obtained from 10-Doxyl-PC. This left only the rotational time, τ_{rot}, and the mixing angle, ϕ, as fitting parameters, not counting the shift along the horizontal axis. As the automated fitting did not behave well, we varied these two parameters manually. One satisfactory fit, obtained with the parameters that are given in Table 1, is shown in fig. 6a. We mention that the relative heights of the two lines in the calculation were slightly improved by using a small mixing angle of $\phi = -2^\circ$.

Although, overall, the fit is not bad, the middle part of the calculated spectrum changes too sharply and its high-frequency line is too narrow compared to experiment. We again used Easyspin to check whether these deficiencies are due to the lack of hyperfine interaction. The spectra for $\tau_{\mathrm{rot}} = 1.9\,\mathrm{ns}$ with and without hyperfine interaction are shown in fig. A5a. As the whole spectrum is narrower than that of 10-Doxyl-PC, the effect of the hyperfine tensor is comparatively larger. Nonetheless, the integrated EPR lines in fig. A5b show that the extra width due to the hyperfine tensor should not compromise our subsequent analysis of the DNP spectrum, which will experience additional power-broadening and motional-broadening.

Moving on to the DNP spectrum, we observed that the free fit of all parameters resulted in τ_{ffhs} that was more than two times larger than that of 10-Doxyl-PC, as we explain below. Considering this to be unrealistic, we fixed τ_{ffhs} to the value that was obtained from 10-Doxyl-PC. Thus, not counting the horizontal translation of the calculated DNP spectrum, our automated fit had three fitting parameters: T_1, σ_{OE} and σ_{SE}. The outcome is shown in fig. 6b. The corresponding parameters are given in the second-last column of the lower half of Table 1.

At 9.4 T the electronic Larmor precession time scale is about half a picosecond, which is three orders of magnitude less than the rotational time scales inferred from the cw-EPR spectra. On such sub-ps time scales, the local dynamics of the spin labels at positions 10 and 16 should not be very different from each other. Since the spin-lattice relaxation is determined by dynamics on the electronic Larmor time scale, we were satisfied that the fitted $T_1 = 150\,\mathrm{ns}$ was close to that from 10-Doxyl-PC.

https://doi.org/10.5194/mr-2023-10
Preprint. Discussion started: 31 July 2023

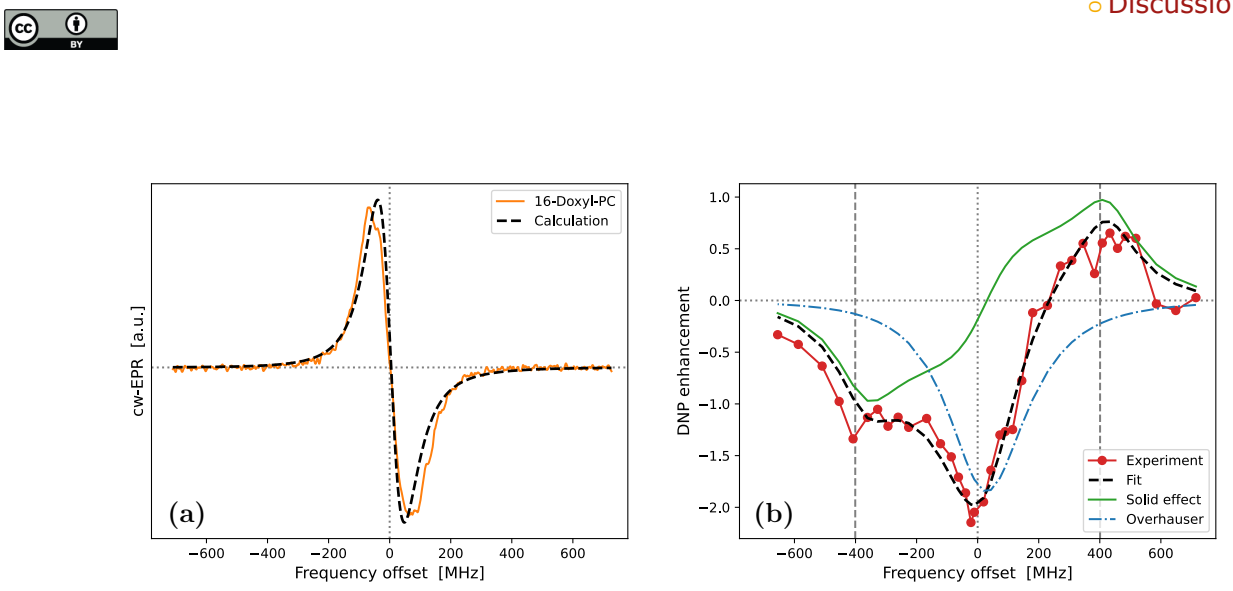

Figure 6. Same as fig. 5 but for 16-Doxyl-PC. The fitted parameters are given in the second to last column of Table 1. Because all fitted lines in figs. 5, 6 and 7 are calculated only at the experimental offsets, the green SE lines are not perfectly smooth.

The performance of the simple analysis of Neudert et al. (2017) was poorer for 16-Doxyl-PC (fig. 1d). Compared to it, our fit to the DNP enhancement profile is excellent (fig. 6b). The only part of the DNP spectrum that our calculation systematically underestimates are the five leftmost experimental points. Although there are other individual experimental points that lie further from the calculated spectrum, these five points are persistently lower by about 0.2 enhancement units.

Observe that the downward shift of the fifth experimental point (together with the first four points) produces an enhancement peak at around -400 MHz. The only way our automated fit can create a pronounced peak at this offset is by making the SE contribution (green line) more "solid-like", i.e., by increasing τ_{ffhs} and reducing the motional broadening. (The lower left corner of fig. A3b provides an example of such more solid-like SE line shape.) We thus identify the systematic displacement of the leftmost five points to be responsible for the increase of τ_{ffhs} when it is allowed to vary freely during the fit.

The best fit that we obtained when τ_{ffhs} was included among the other fitting parameters is shown in fig. 7. (The resulting fit parameters are given in the last column of the lower half of Table 1.) Indeed, with $\tau_{\mathrm{ffhs}} = 15.3$ ns, the SE lines (green) have become sharper and a small enhancement peak at -400 MHz has emerged (dashed black line). Although the enhancement around $+400$ MHz has been compromised in the process, the overall fit to all experimental points is improved compared to fig. 6b.

The two alternative fits in figs. 6b and 7 correspond to very different time scales of translational diffusion. Nevertheless, within the variability of the measurements, they both agree with the DNP data. Considering the experimental challenges of liquid-state DNP at such high magnetic fields and large mw powers, further decreasing the experimental variability will be very hard. It is, therefore, important to analyze together several different experimental constructs, like our 10- and 16-Doxyl-PC. The final decision of which fit to the DNP spectrum of 16-Doxyl-PC is "better" can only be based on the overall consistency of the fitted parameters across all analyzed data. We return to this point in Sec. 5.3.

https://doi.org/10.5194/mr-2023-10
Preprint. Discussion started: 31 July 2023

Open Access MAGNETIC RESONANCE Discussions

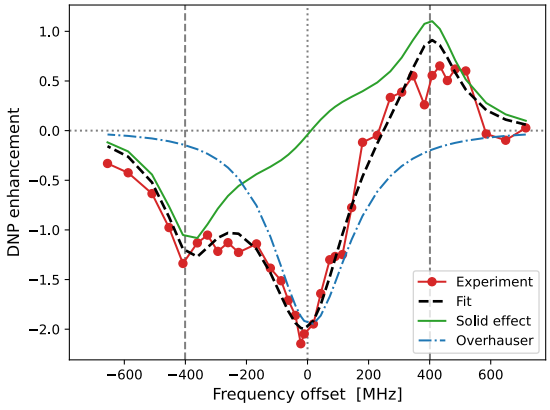

Figure 7. Same as fig. 6b but also fitting τ_{ffhs}. The fitted parameters are given in the last column of Table 1. Observe that the OE contribution to the DNP spectrum (dotted-dashed blue line) is narrower (i.e., more "liquid-like") than that of 10-Doxyl-PC (fig. 5b), while the SE contribution is more "solid-like" because the time scale τ_{ffhs} is 2.4 times longer.

The other two parameters that emerged from the fit to the DNP spectrum of 16-Doxyl-PC were σ_{SE} and σ_{OE}. These determine the amplitudes of the SE contribution (solid green lines in figs. 6b and 7) and OE contribution (dotted-dashed blue lines) to the DNP enhancement (dashed black lines). We now turn to the analysis of these scaling parameters.

5.3 Additional molecular parameters

Ultimately, the motivation to disentangle a mixed DNP spectrum into its OE and SE components lies in the desire to extract information about the molecular and spin properties that the respective DNP mechanism depends on. The main advantage of our procedure over the intuitive approach of Neudert et al. (2017) is that our decomposition produces physically interpretable parameters, like τ_{ffhs} and T_1. In addition, our scaling parameters σ_{OE} and σ_{SE} multiply, respectively, the saturation factor and $v_-/\langle\delta^2\rangle$, whose absolute magnitudes are part of the calculation (fig. 4, vertical axes). Thus, we can extract further information from the fitted values of σ_{OE} and σ_{SE}. In contrast, because the simple approach rescales the integrated cw-EPR spectrum whose amplitude is arbitrary, the values of its scaling factors are not informative.

Using eq. (2) for the OE enhancement, the coupling factor c is readily expressed in terms of σ_{OE}:

$$c = \frac{\sigma_{\mathrm{OE}}}{f}\frac{\gamma_I}{|\gamma_S|}, \tag{99}$$

where the leakage factor f can be obtained by measuring the nuclear spin-lattice relaxation times (eq. (4)).

We measured the T_1 values for the chain protons of DOPC (without spin-labeled lipids) at 310 K and 330 K using the Fabry-Pérot probe. These are given in the T_{1I}^0 column of Table 2. Additionally, we measured the nuclear spin-lattice relaxation times in the presence of either 10- or 16-Doxyl-PC (column T_{1I} of Table 2). The target temperature of the DNP experiments (320 K) lies between the two temperatures at which the nuclear T_1 times were measured. However, considering the possibility of mild

https://doi.org/10.5194/mr-2023-10
Preprint. Discussion started: 31 July 2023

Open Access MAGNETIC RESONANCE Discussions

Table 2. Analysis of the scaling parameters σ_{OE} and σ_{SE}. Nuclear spin-lattice relaxation times with (T_{1I}) and without (T_{1I}^0) spin labels were measured at two different temperatures. These determine the leakage factor f. The coupling factor c is obtained from f and σ_{OE} using eq. (99). The magnitude of the dipolar interaction responsible for SE ($\langle\delta^2\rangle$), obtained from σ_{SE} using eq. (100), provides information about the effective contact distance (b). Combining b with τ_{ffhs} from Table 1, we estimate the diffusion constant of the FFHS model (D_{ffhs}).

	Temp.	Nuclear T_1's		Overhauser			Solid effect			
Doxyl-PC	T (K)	T_{1I}^0 (ms)	T_{1I} (ms)	f	σ_{OE}	c (‰)	σ_{SE} (ps^{-1})	$\langle\delta^2\rangle T_{1I}$ (ns^{-1})	b (nm)	D_{ffhs} (nm^2/μs)
10	310	580	44	0.92	2.43	3.99	1.51	2.29	0.61	59
	330	910	52	0.94		3.92			0.65	66
16	310	580	93	0.84	2.385	4.32	1.35	2.05	0.81	104
	330	910	120	0.87		4.17			0.89	123
16*	310	"	"	"	2.57	4.65	1.09	1.66	0.87	50
	330	"	"	"		4.50			0.95	59

temperature rise by several degrees, we expect the values at 330 K to closely reflect the DNP conditions. Nonetheless, we carry out the following analysis using the T_1 values measured at both 310 K and 330 K.

The leakage factors obtained from (4) are shown in the column f of Table 2. Using the values of σ_{OE} from Table 1 in (99), we arrived at the coupling factors in column c of Table 2. In the case of 16-Doxyl-PC, the analysis was performed for the fit where τ_{ffhs} was fixed at 6.4 ns (denoted 16 in Table 2) as well as for the fit where τ_{ffhs} was free to change (denoted 16*). (These two alternatives correspond to the last two columns of Table 1.) For both choices, somewhat larger coupling factors were deduced for 16-Doxyl-PC compared to 10-Doxyl-PC. The estimated coupling factors are less than two times smaller than what we have obtained previously for TEMPOL in DMSO, and about four times smaller than the coupling factors between TEMPOL and the protons of toluene (Prisner et al., 2016; Sezer, 2013; Küçük et al., 2015).

Turning now to SE, using the enhancement in (7) we express the unknown strength of the dipolar interaction in terms of the scaling parameter σ_{SE} as follows:

$$\langle\delta^2\rangle T_{1I} = \sigma_{\mathrm{SE}} \frac{\gamma_I}{|\gamma_S|}. \tag{100}$$

The values of $\langle\delta^2\rangle T_{1I}$, which were calculated from the right-hand side of (100), are about 2 ns^{-1} for 10, 16 and 16* (Table 2). Since $v_+/\langle\delta^2\rangle$ is about 1 ps (fig. 4, third row), we conclude that $v_+ T_{1I} \ll 1$, which justifies our use of the approximation (7) throughout the analysis, including during the fit to the DNP spectra.

From the expression of $\langle\delta^2\rangle$ (eq. (39)), we can write the contact distance of the translational FFHS model as

$$b^3 = N \frac{2\pi}{5} D_{\mathrm{dip}}^2 \frac{T_{1I}}{\sigma_{\mathrm{SE}}} \frac{|\gamma_S|}{\gamma_I}, \tag{101}$$

where N is the number density of the electronic spins. Since, in principle, all parameters on the right-hand side of (101) are measurable, we can determine b. To estimate N, we note that the molecular volume of DOPC is 1.3 nm^3 (Greenwood et al., 2006). Since there are 20 unlabeled lipids for one labeled one, we estimate $N = (20 \times 1.3\,\mathrm{nm}^3)^{-1}$, which corresponds to a

https://doi.org/10.5194/mr-2023-10
Preprint. Discussion started: 31 July 2023


Open Access MAGNETIC RESONANCE Discussions

molar concentration of 64 mM. Using this number in (101), we obtained the values of b that are given in the second to last column of Table 2.

When the values of b are interpreted literally as "contact distance" between the nitroxide spin label and the protons of the lipid chains, their substantial variation between 10- and 16-Doxyl-PC is disturbing. From that perspective, it is clear that the parameter b of the FFHS model, which we used to account for the fluctuations of the dipolar interaction due to molecular translations, cannot reflect the actual molecular distances of closest approach.

Because b was obtained from the scaling parameter σ_{SE}, only information about the *amplitude* of the SE enhancement has been directly used in its estimate. In contrast, the motional time scale τ_{ffhs} (Table 1) encodes information about the *line shape* of the SE enhancement. From these complementary features of the SE contribution to the DNP spectrum, we have managed to determine both b and τ_{ffhs}. Having access to these two parameters, we can calculate the diffusion constant of the FFHS model from (38). The results are given in the last column of Table 2. To our surprise, we obtained very similar values for 10 and 16*, while the diffusion constant for 16 is two-fold larger. (Given the variability in the experimental data and the fact that the fits to the DNP spectra are not unique, the differences between D_{ffhs} of 10 and 16* should not be seen as meaningful.)

In an effort to identify a potential candidate for the physical motion that the FFHS model emulates, we observed that the coefficients of lateral translational diffusion for DOPC in oriented bilayers are 20 $\mathrm{nm}^2\ \mu\mathrm{s}^{-1}$ at 323 K, and 26 $\mathrm{nm}^2\ \mu\mathrm{s}^{-1}$ at 333 K (Filippov et al., 2003, fig. 6a). These, we expect, bracket the value at our DNP conditions. The diffusion in the FFHS model corresponds to the *relative* translation of the nuclear and electronic spins, i.e., $D_{\mathrm{ffhs}} = D_I + D_S$. Assuming that the lateral diffusion of spin-labeled PSPC in a DOPC bilayer is similar to that of DOPC, from the measured values given above we would expect D_{ffhs} between 40 and 52 $\mathrm{nm}^2\ \mu\mathrm{s}^{-1}$. This range is surprisingly close to the estimates of 10 and 16* in the last column of Table 2, which suggests that the FFHS model in our analysis likely accounts for the lateral diffusion of the lipids in the plane of the bilayer.

Since it leads to a diffusion constant that is similar to (i) the known lateral diffusion of DOPC and (ii) the estimate obtained for 10-Doxyl-PC, we conclude that the fit to the DNP spectrum of 16-Doxyl-PC that is shown in fig. 7 (i.e., the one that led to "unreasonably" large τ_{ffhs}) is more realistic than the one with fixed τ_{ffhs} (fig. 6b). From the perspective of the diffusion constant, the longer motional time scale of 16* compared to 10, which resulted in more solid-like SE line shape with less motional broadening, reflects the fact that the "contact distances" in the two cases are different. In retrospect, it is amazing how the independent estimates of b and τ_{ffhs} combine to yield practically identical diffusion constants for the two spin-labeling positions.

At the moment, it is not clear to us how to properly interpret the different values of b at positions 10 and 16. Atomistic molecular dynamics simulations (Oruç et al., 2016) could, in principle, be used to investigate whether these effective contact distances reflect differences in proton density along the normal of the lipid bilayer, or arise for some other reason.

https://doi.org/10.5194/mr-2023-10
Preprint. Discussion started: 31 July 2023


Open Access MAGNETIC RESONANCE Discussions

6 Conclusion

In the time-domain description of SE that we developed recently (Sezer, 2023a), the relevant spin dynamics is pictured in terms of two connected Bloch equations. Due to this central role of the Bloch equations in our formalism, we first rephrased Freed's treatment of slow tumbling as a generalization of the classical Bloch equations, where the scalar elements of the Bloch matrix became matrices in the space of the angular-momentum indices LM. For this reformulation to work, we had to neglect the hyperfine interaction, which is in fact treated by Freed et al. (1971). As a result, our analysis is formally deficient for nitroxide radicals. Nevertheless, it should be valid approximately at high magnetic fields where the influence of the hyperfine tensor is smaller than that of the g tensor. The experimental data that we analyzed fell into this regime.

DNP experiments with nitroxide free radicals in viscous liquids invariably manifest a mixture of SE and OE (Leblond et al., 1971b; Neudert et al., 2017). As these two DNP mechanisms are sensitive to molecular motions on vastly different time scales, it should be possible to obtain rich dynamical information by analyzing their contributions to the overall DNP enhancement. Disentangling the SE and OE contributions, however, has proven to be challenging (Leblond et al., 1971a). Here we fitted liquid-state DNP spectra by calculating enhancements that were affected by both the translational diffusion of the spins and the rotational diffusion of the free radical. Since different motions modify the amplitude and the shape of the DNP spectrum in a highly concerted manner, by fitting the entire line shape of the enhancement we also gained access to the absolute magnitudes of the SE and OE contributions.

Our current treatment of SE-DNP in liquids uses only the correlation function of the dipolar interaction to describe the translational motion of the spins (Sezer, 2023b). This is formally correct only when the diffusion is much faster than the nuclear T_1 relaxation. It should be possible to relax this condition and model slower spin diffusion, as relevant for SE in the solid state.

https://doi.org/10.5194/mr-2023-10
Preprint. Discussion started: 31 July 2023

Open Access MAGNETIC RESONANCE Discussions

Appendix A: Additional figures

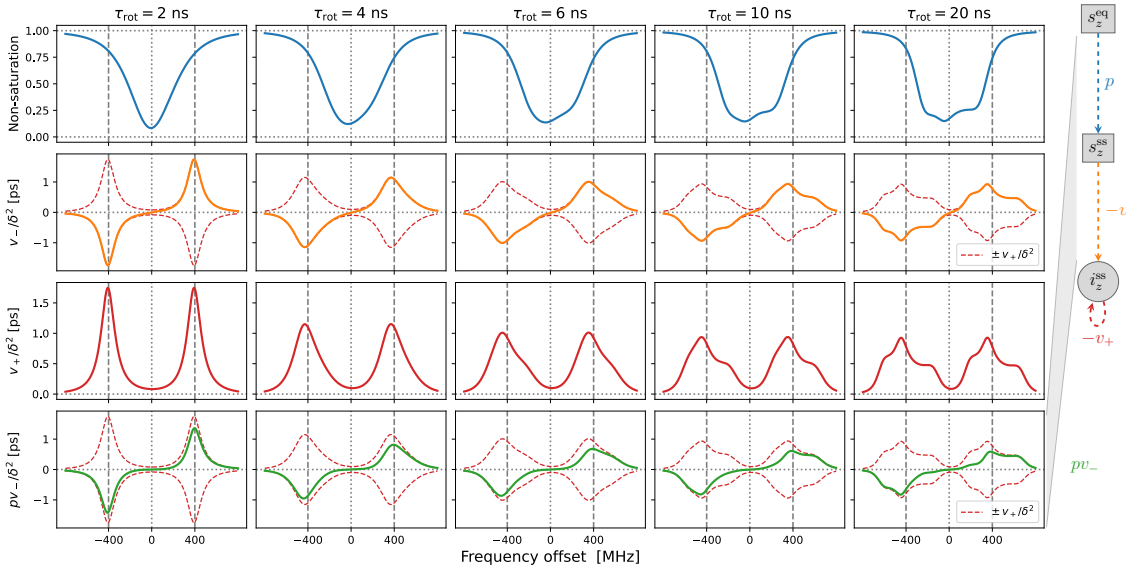

Figure A1. Same as fig. 3 but with $T_1 = 500$ ns (i.e., five-fold longer), which leads to larger saturation of the allowed electronic transition. Only the first and last rows are affected.

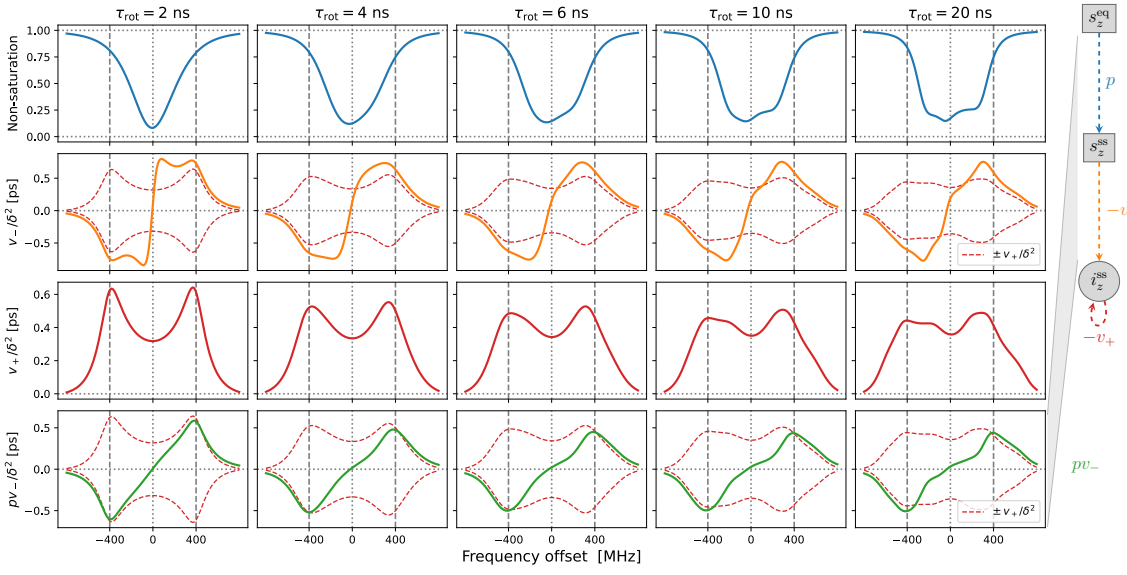

Figure A2. Same as fig. 4 but with $T_1 = 500$ ns, which leads to larger electronic saturation. As in the case of 'solids', only the first and last rows are affected.

https://doi.org/10.5194/mr-2023-10
Preprint. Discussion started: 31 July 2023

Open Access MAGNETIC RESONANCE Discussions

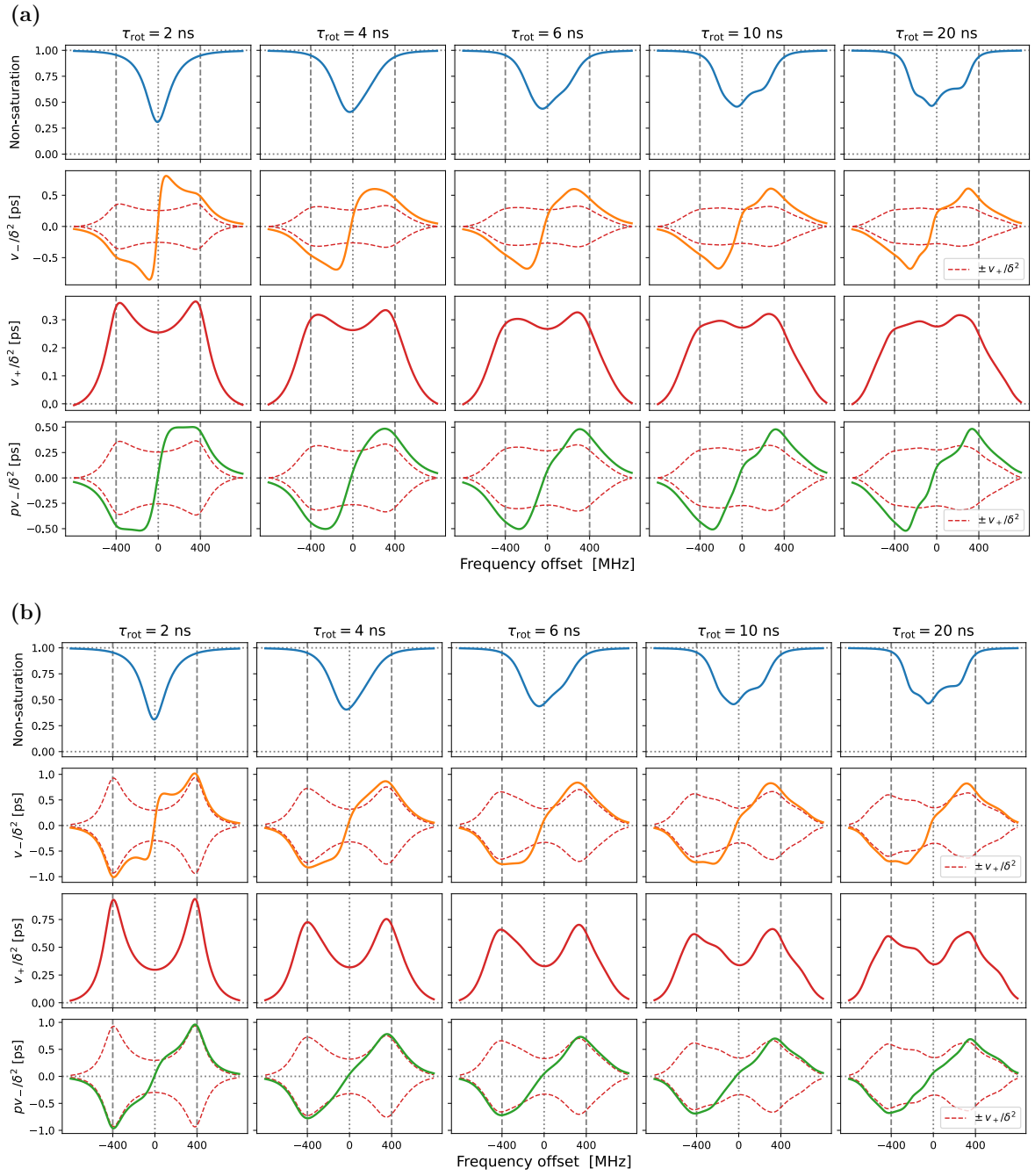

Figure A3. Same as fig. 4 but with (**a**) $\tau_{\mathrm{ffhs}} = 3\,\mathrm{ns}$, i.e., two-fold faster translational motion which broadens the SE lines to a larger extent, and (**b**) $\tau_{\mathrm{ffhs}} = 12\,\mathrm{ns}$, i.e., more solid-like behavior. Observe how the predicted SE-DNP line shape (green line in the last row) responds sensitively to the time scale of the translational motion that is responsible for averaging the dipolar interaction.

https://doi.org/10.5194/mr-2023-10
Preprint. Discussion started: 31 July 2023

Open Access MAGNETIC RESONANCE Discussions

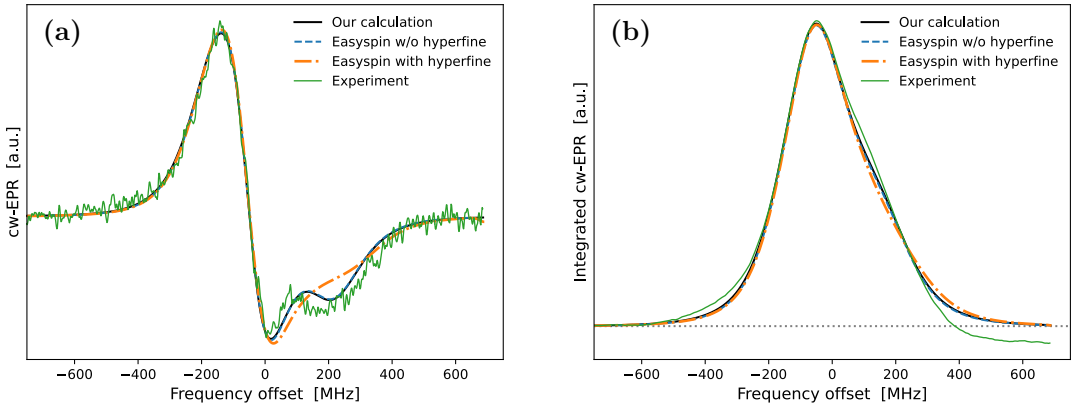

Figure A4. Effect of hyperfine tensor on the calculated EPR spectrum of 10-Doxyl-PC. Various derivative cw-EPR spectra (**a**) and their numerical integrals (**b**) are compared with each other. Our calculation (solid black line) agrees perfectly with the Easyspin (Stoll and Schweiger, 2006) simulation without a hyperfine tensor (dashed blue line). Including a hyperfine tensor with components $(14, 14, 90)$ MHz in the Easyspin calculation (dotted-dashed orange line) leads to visible changes in the derivative cw-EPR spectrum. However, the difference of the integrated EPR lines with and without a hyperfine tensor in (**b**) should be negligible as far as the simulation of the DNP spectrum is concerned.

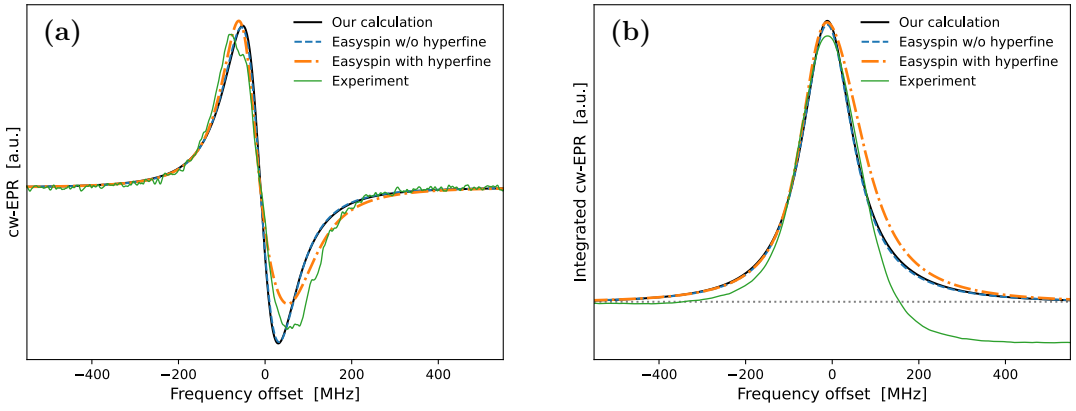

Figure A5. Same as fig. A4 but for 16-Doxyl-PC. Because the cw-EPR spectrum is narrower to begin with, the relative contribution of the hyperfine tensor with components $(14, 14, 90)$ MHz is larger than in the case of 10-Doxyl-PC. Considering that the EPR line will experience additional power-broadening and motional-broadening in DNP, it should still be possible to safely neglect the extra width that the hyperfine tensor brings to the integrated EPR line in (**b**).

https://doi.org/10.5194/mr-2023-10
Preprint. Discussion started: 31 July 2023

Open Access MAGNETIC RESONANCE Discussions

Author contributions. TFP envisioned the presented high-field DNP experiments in lipid bilayers and acquired funding for their execution. DD carried out these EPR and NMR experiments, deconvoluted the measured NMR signals to calculate the presented DNP spectra for the lipid chain protons, and performed the reported Easyspin simulations. DS conceived of the presented analysis of the experimental data, developed the reported theoretical and numerical framework, analyzed the data, and wrote the manuscript with feedback from all coauthors.

Competing interests. TFP is an associate editor of Magnetic Resonance.

Acknowledgements. We are grateful to Vasyl Denysenkov, without whom the analyzed high-field DNP experiments would have not been possible. This work was funded by grant 405972957 of the German Research Foundation (DFG).

https://doi.org/10.5194/mr-2023-10
Preprint. Discussion started: 31 July 2023

Open Access MAGNETIC RESONANCE Discussions

References

Abragam, A.: The Principles of Nuclear Magnetism, Oxford University Press, New York, 1961.

Abragam, A. and Goldman, M.: Principles of dynamic nuclear polarisation, Reports on Progress in Physics, 41, 395, https://doi.org/10.1088/0034-4885/41/3/002, 1978.

Abragam, A. and Proctor, W. G.: Une nouvelle méthode de polarisation dynamique des noyaux atomiques dans les solides, Compt. rend., 246, 2253–2256, 1958.

Anderson, P. W.: A Mathematical Model for the Narrowing of Spectral Lines by Exchange or Motion, Journal of the Physical Society of Japan, 9, 316–339, https://doi.org/10.1143/JPSJ.9.316, 1954.

Ayant, Y., Belorizky, E., Alizon, J., and Gallice, J.: Calcul des densités spectrales résultant d'un mouvement aléatoire de translation en relaxation par interaction dipolaire magnétique dans les liquides, J. Phys. (Paris), 36, 991–1004, 1975.

Carver, T. R. and Slichter, C. P.: Experimental Verification of the Overhauser Nuclear Polarization Effect, Physical Review, 102, 975–980, https://doi.org/10.1103/PhysRev.102.975, 1956.

Denysenkov, V., Dai, D., and Prisner, T. F.: A triple resonance (e, 1H, 13C) probehead for liquid-state DNP experiments at 9.4 Tesla, Journal of Magnetic Resonance, 337, 107 185, https://doi.org/https://doi.org/10.1016/j.jmr.2022.107185, 2022.

Erb, E., Motchane, J.-L., and Uebersfeld, J.: Effet de polarisation nucléaire dans les liquides et les gaz adsorbés sur les charbons, Compt. rend., 246, 2121–2123, 1958a.

Erb, E., Motchane, J.-L., and Uebersfeld, J.: Sur une nouvelle méthode de polarisation nucléaire dans les fluides adsorbés sur les charbons. extension aux solides et en particulier aux substances organiques irradiées., Compt. rend., 246, 3050–3052, 1958b.

Filippov, A., Orädd, G., and Lindblom, G.: The Effect of Cholesterol on the Lateral Diffusion of Phospholipids in Oriented Bilayers, Biophysical Journal, 84, 3079–3086, https://doi.org/https://doi.org/10.1016/S0006-3495(03)70033-2, 2003.

Freed, J. H., Bruno, G. V., and Polnaszek, C. F.: Electron spin resonance line shapes and saturation in the slow motional region, The Journal of Physical Chemistry, 75, 3385–3399, https://doi.org/10.1021/j100691a001, 1971.

Gizatullin, B., Mattea, C., and Stapf, S.: Field-cycling NMR and DNP –A friendship with benefits, Journal of Magnetic Resonance, 322, 106 851, https://doi.org/https://doi.org/10.1016/j.jmr.2020.106851, 2021a.

Gizatullin, B., Mattea, C., and Stapf, S.: Molecular Dynamics in Ionic Liquid/Radical Systems, The Journal of Physical Chemistry B, 125, 4850–4862, https://doi.org/10.1021/acs.jpcb.1c02118, 2021b.

Gizatullin, B., Mattea, C., and Stapf, S.: Three mechanisms of room temperature dynamic nuclear polarization occur simultaneously in an ionic liquid, Physical Chemistry Chemical Physics, 24, 27 004–27 008, https://doi.org/10.1039/D2CP03437A, 2022.

Greenwood, A. I., Tristram-Nagle, S., and Nagle, J. F.: Partial molecular volumes of lipids and cholesterol, Chemistry and Physics of Lipids, 143, 1–10, https://doi.org/https://doi.org/10.1016/j.chemphyslip.2006.04.002, 2006.

Hausser, K. H., Stehlik, D., and Waugh, J. S.: Dynamic Nuclear Polarization in Liquids, vol. 3, pp. 79–139, Academic Press, https://doi.org/https://doi.org/10.1016/B978-1-4832-3116-7.50010-2, 1968.

Hwang, L.-P. and Freed, J. H.: Dynamic effects of pair correlation functions on spin relaxation by translational diffusion in liquids, J. Chem. Phys., 63, 4017–4025, 1975.

Kubo, R.: Note on the Stochastic Theory of Resonance Absorption, Journal of the Physical Society of Japan, 9, 935–944, https://doi.org/10.1143/JPSJ.9.935, 1954.

https://doi.org/10.5194/mr-2023-10
Preprint. Discussion started: 31 July 2023

Open Access MAGNETIC RESONANCE Discussions

Kubo, R.: A Stochastic Theory of Line Shape, vol. XV, chap. 6, pp. 101–127, John Wiley & Sons. Inc., https://doi.org/https://doi.org/10.1002/9780470143605.ch6, 1969.

Küçük, S. E., Neugebauer, P., Prisner, T. F., and Sezer, D.: Molecular simulations for dynamic nuclear polarization in liquids: a case study of TEMPOL in acetone and DMSO, Physical Chemistry Chemical Physics, 17, 6618–6628, https://doi.org/10.1039/C4CP05832A, 2015.

Kuzhelev, A. A., Dai, D., Denysenkov, V., and Prisner, T. F.: Solid-like Dynamic Nuclear Polarization Observed in the Fluid Phase of Lipid Bilayers at 9.4 T, Journal of the American Chemical Society, 144, 1164–1168, https://doi.org/10.1021/jacs.1c12837, 2022.

Kuzhelev, A. A., Denysenkov, V., Ahmad, I. M., Rogozhnikova, O. Y., Trukhin, D. V., Bagryanskaya, E. G., Tormyshev, V. M., Sigurdsson, S. T., and Prisner, T. F.: Solid-Effect Dynamic Nuclear Polarization in Viscous Liquids at 9.4 T Using Narrow-Line Polarizing Agents, Journal of the American Chemical Society, 145, 10 268–10 274, https://doi.org/10.1021/jacs.3c01358, 2023.

Leblond, J., Papon, P., and Korringa, J.: Stochastic Theory of Dynamic Spin Polarization in Viscous Liquids with Anisotropic Electron-Spin Relaxation, Physical Review A, 4, 1539–1549, https://doi.org/10.1103/PhysRevA.4.1539, 1971a.

Leblond, J., Uebersfeld, J., and Korringa, J.: Study of the Liquid-State Dynamics by Means of Magnetic Resonance and Dynamic Polarization, Physical Review A, 4, 1532–1539, https://doi.org/10.1103/PhysRevA.4.1532, 1971b.

Müller-Warmuth, W., Meise-Gresch, K., and Waugh, J. S.: Molecular Motions and Interactions as Studied by Dynamic Nuclear Polarization (DNP) in Free Radical Solutions, vol. 11, pp. 1–45, Academic Press, https://doi.org/https://doi.org/10.1016/B978-0-12-025511-5.50007-4, 1983.

Neudert, O., Mattea, C., and Stapf, S.: A compact X-Band resonator for DNP-enhanced Fast-Field-Cycling NMR, Journal of Magnetic Resonance, 271, 7–14, https://doi.org/https://doi.org/10.1016/j.jmr.2016.08.002, 2016.

Neudert, O., Mattea, C., and Stapf, S.: Molecular dynamics-based selectivity for Fast-Field-Cycling relaxometry by Overhauser and solid effect dynamic nuclear polarization, Journal of Magnetic Resonance, 276, 113–121, https://doi.org/https://doi.org/10.1016/j.jmr.2017.01.013, 2017.

Oruç, T., Küçük, S. E., and Sezer, D.: Lipid bilayer permeation of aliphatic amine and carboxylic acid drugs: rates of insertion, translocation and dissociation from MD simulations, Physical Chemistry Chemical Physics, 18, 24 511–24 525, https://doi.org/10.1039/C6CP05278A, 2016.

Papon, P., Motchane, J. L., and Korringa, J.: Unitary Theory of Dynamic Polarization of Nuclear Spins in Liquids and Solids, Physical Review, 175, 641–649, https://doi.org/10.1103/PhysRev.175.641, 1968.

Prisner, T., Denysenkov, V., and Sezer, D.: Liquid state DNP at high magnetic fields: Instrumentation, experimental results and atomistic modelling by molecular dynamics simulations, Journal of Magnetic Resonance, 264, 68–77, https://doi.org/https://doi.org/10.1016/j.jmr.2015.11.004, 2016.

Redfield, A. G.: On the Theory of Relaxation Processes, IBM Journal of Research and Development, 1, 19–31, https://doi.org/10.1147/rd.11.0019, 1957.

Sezer, D.: Computation of DNP coupling factors of a nitroxide radical in toluene: seamless combination of MD simulations and analytical calculations, Physical Chemistry Chemical Physics, 15, 526–540, https://doi.org/10.1039/C2CP42430D, 2013.

Sezer, D.: Non-perturbative treatment of the solid effect of dynamic nuclear polarization, Magn. Reson., 4, 129–152, https://doi.org/10.5194/mr-4-129-2023, 2023a.

Sezer, D.: The solid effect of dynamic nuclear polarization in liquids, Magn. Reson., 4, 153–174, https://doi.org/10.5194/mr-4-153-2023, 2023b.

https://doi.org/10.5194/mr-2023-10
Preprint. Discussion started: 31 July 2023

Open Access MAGNETIC RESONANCE Discussions

Sezer, D., Gafurov, M., Prandolini, M. J., Denysenkov, V. P., and Prisner, T. F.: Dynamic nuclear polarization of water by a nitroxide radical: rigorous treatment of the electron spin saturation and comparison with experiments at 9.2 Tesla, Physical Chemistry Chemical Physics, 11, 6638–6653, https://doi.org/10.1039/B906719C, 2009.

Solomon, I.: Relaxation Processes in a System of Two Spins, Physical Review, 99, 559–565, https://doi.org/10.1103/PhysRev.99.559, 1955.

Stoll, S. and Schweiger, A.: EasySpin, a comprehensive software package for spectral simulation and analysis in EPR, Journal of Magnetic Resonance, 178, 42–55, https://doi.org/https://doi.org/10.1016/j.jmr.2005.08.013, 2006.

Wenckebach, T.: Essentials of Dynamic Nuclear Polarization, Spindrift Publications, The Netherlands, 2016.

7. Translational and Rotational Modulations on DNP efficiency

7.1 Introduction

In liquids, the stochastic modulation of the HFI responsible for the OE DNP are commonly modeled by the relative translational motion between polarizing agent and the target molecule, and the inner-sphere rotation of their transient complex.[67,69,95] Understanding the contributions of different models is advantageous for accurately prediction of the DNP efficiency, as well as the strategic design or modification of the chemical structures of polarizing agents for specific purpose.

In this work, DNP measurements were performed on dimethyl sulfoxide (DMSO) solution doped with nitroxide derivatives featuring different ring geometries and various substituents that influence the steric accessibility to the NO group. With the rotational correlation time of radicals determined from the cw EPR spectra and the DMSO diffusion coefficient from literature, the dynamic modulation by molecular translational and rotational motion can quantitatively predict the observed OE DNP efficiency.

In addition to the combined outer- and inner-sphere model presented with the published article in Section 7.2, a further analysis in Section 7.3 showed that the HSOS model with outer-sphere translation of DMSO and off-centered rotation of radical molecules also can predict DNP coupling factors closely agrees with the experimental observations and provides simulation parameters which agrees better with the MD simulations.

7.2 Corresponding Publication:

The following publication together with the supporting information

"Kuzhelev, A. A., Dai, D., Denysenkov, V., Kirilyuk, I. A., Bagryanskaya E. G. and Prisner, T. F., Influence of Rotational Motion of Nitroxides on Overhauser Dynamic Nuclear Polarization: A Systematic Study at High Magnetic Fields. *J. Phys. Chem. C*, 125, 25651–25659 (2021)"

is attached in the next pages.

The work was prepared in a collaborative manner. The author performed DNP/NMR measurements together with Dr. Andrei Kuzhelev. The EPR experiments were performed by Dr. Andrei Kuzhelev. The analysis and interpretation were performed mainly by Dr. Andrei Kuzhelev.

https://doi.org/10.1021/acs.jpcc.1c06979

THE JOURNAL OF PHYSICAL CHEMISTRY C
A JOURNAL OF THE AMERICAN CHEMICAL SOCIETY

pubs.acs.org/JPCC

Article

Influence of Rotational Motion of Nitroxides on Overhauser Dynamic Nuclear Polarization: A Systematic Study at High Magnetic Fields

Andrei A. Kuzhelev, Danhua Dai, Vasyl Denysenkov, Igor A. Kirilyuk, Elena G. Bagryanskaya, and Thomas F. Prisner*

Cite This: J. Phys. Chem. C 2021, 125, 25651−25659

Read Online

ACCESS | Metrics & More | Article Recommendations | Supporting Information

ABSTRACT: TEMPOL nitroxide radicals are frequently used as a polarizing agent for liquid-state Overhauser dynamic nuclear polarization. To achieve large signal enhancements at high magnetic fields (9.4 T), fast picosecond to sub-picosecond dynamics between nitroxide and the target solvent molecule are required. Such dynamics have been predicted by molecular dynamic studies and attributed to fast inner-sphere motions of a transient radical−solvent complex. Here, we systematically study a series of nitroxide radicals with different substituents around the electron spin-bearing NO moiety and different overall sizes to quantify the contribution of the rotational dynamics of the radical to these inner-sphere dynamics. The experiments are performed at a 9.4 T magnetic field, which exhibits high sensitivity to rotational motion contributions in a low picosecond time range. We can show that the observed enhancements can be quantitatively predicted taking the rotational motion of the radical into account.

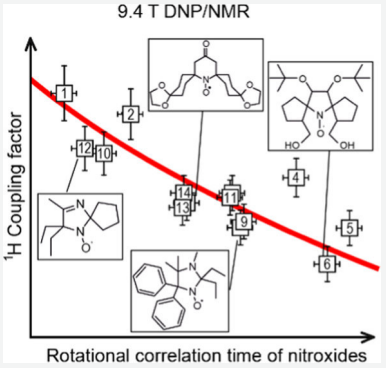

INTRODUCTION

Dynamic nuclear polarization (DNP) has received attention over the last years as a promising method to enhance nuclear magnetic resonance (NMR) signals.[1,2] It can be shown that considerable enhancements are also achieved at high magnetic fields if an efficient microwave (mw) irradiation in the sub-THz regime of the unpaired electron spin of the polarizing agent can be accomplished.[3,4] Most DNP experiments perform the polarization transfer from the radical electron spin to the target nuclear spin in the solid state, where the solid effect,[5] the cross effect,[6,7] and thermal mixing[8,9] are effective and where the electron spin relaxation times are reasonably long. Only a few DNP experiments at high magnetic fields have been performed in liquid solutions, where the electron−nuclear cross-relaxation processes generate signal enhancement.[10−14] The NMR signal enhancement ε by the Overhauser mechanism is described as[15]

$$\varepsilon = \frac{\langle I_z \rangle - I_0}{I_0} = \frac{\gamma_s}{\gamma_I} \cdot f \cdot s \cdot \xi \tag{1}$$

where γ_S and γ_I are the gyromagnetic ratios of the electron and the nucleus, respectively, f is the leakage factor that is equal to $1 - T_{1IS}/T_{1I}$ (T_{1IS} and T_{1I} are corresponding nuclear longitudinal relaxation times in the presence and in the absence of polarizing agents in solution), s is the saturation factor ranging from 0 (no saturation) to 1 (full saturation of the electron spin system by the mw), and ξ is the coupling factor, which describes the efficiency of the polarization transfer. In the Overhauser mechanism, the polarization transfer is accomplished by the cross-relaxation processes caused by the dynamic modulation of the hyperfine coupling between the electron and nuclear spin.

The major reason why liquid-state Overhauser DNP experiments at a high magnetic field fall behind the progress seen in solid-state DNP is of technical nature and related to the strong absorption of the electric field component of the microwave in liquids at high frequencies. To avoid strong heating of the liquid sample while at the same time achieving substantial saturation of the fast relaxing electron spins, mw resonance structures can be used.[16] They allow maximizing the mw magnetic field strength at the sample while at the same time minimizing the electrical field component at this position. Unfortunately, in this case, the size of the mw resonator severely limits the size of the sample to below 1 μL. Successful Overhauser DNP experiments on liquids have also been performed with oversized resonance structures or without such mw resonators, achieving larger sample volumes.[17,18] Additionally, similar to the polarization transfer mechanism active in solids, all of these efficiencies decrease rapidly at higher

Received: August 6, 2021
Revised: October 24, 2021
Published: November 11, 2021

https://doi.org/10.1021/acs.jpcc.1c06979
J. Phys. Chem. C 2021, 125, 25651−25659

magnetic fields. For Overhauser DNP in liquids at high magnetic fields, this is due to the lack of the necessary fast translational and rotational correlation times on a sub-ps time scale.[19]

Nevertheless, it could be shown experimentally that substantial ^{1}H DNP enhancements can be obtained in liquids at 9.4 T using nitroxide radicals as polarizing agents.[14,20] These surprisingly large enhancements were interpreted by additionally fast internal dynamics of the radical−solvent complex based on molecular dynamics (MD) simulations.[21,22] At high magnetic fields, such fast inner-sphere dynamics can substantially contribute to the DNP efficiency, in addition to the translational diffusion dynamics of the solvent and radical, which can easily be identified by NMR relaxation dispersion measurements.[14] However, the physical origins of these fast dynamics in the low to sub-picosecond time range are still unexplained.

Recent DNP experiments performed at X-band frequencies demonstrated how rotational motion of bulky fullerene-linked nitroxides with rotational correlation times in the 10−100 ps range can affect the Overhauser DNP coupling factor at a 0.3 T magnetic field.[23] Here, we systematically investigated a series of nitroxide radicals with different sizes and different substitutes close to the spin-bearing N−O group by EPR and DNP at 9.4 T to investigate the importance of the rotational motion of the nitroxides to the high-field DNP enhancements.

METHODS

A series of nitroxide derivatives based on piperidine (**1**, **2**, **3**), pyrrolidine (**4**, **5**, **6**, **7**, **8**), imidazolidine (**9**, **10**), pyrroline (**11**), imidazoline (**12**, **13**), and nitronyl (**14**) nitroxides with various substituents adjacent to a NO spin-bearing moiety (spyrocyclohexane, spirocyclopentane, tetramethyl, tetraethyl, phenyl, butyl, and *tert*-butyl) dissolved in DMSO were used for the DNP and EPR measurements (Figure 1).

Nitroxide **1** was obtained from Sigma-Aldrich. Nitroxides **2**,[24] **3** and **12**,[25] **5** and **11**,[26] **6**,[27] **7**,[28] **8**,[29] **9** and **10**,[30] **13**,[31] and **14**[32] were prepared according to the literature protocols. 3,3-Dicarboxy-2,2,5,5-tetramethylpyrrolidine-1-oxyl (**4**) was prepared in analogy to the original method[33] with some modifications described in ref 34.

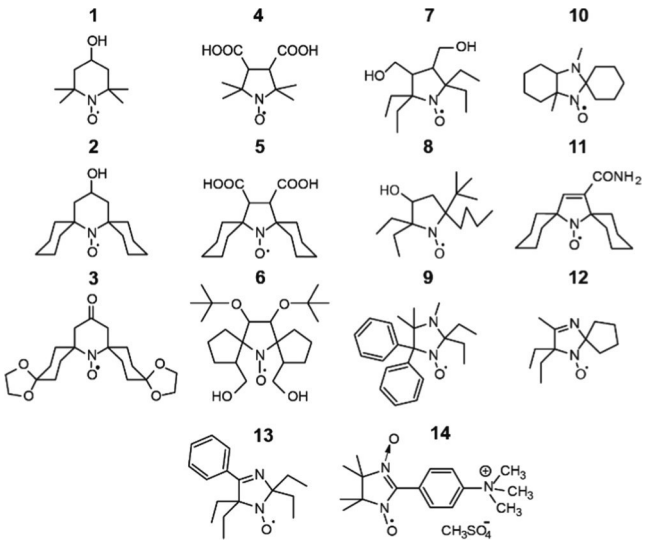

Figure 1. Structure of the investigated nitroxides.

X-band (9.4 GHz, 0.3 T) CW-EPR measurements to determine the rotational correlation times of all nitroxide radicals were performed in the temperature range of 295−383 K with nitroxide concentrations of 0.5 mM using a commercial Bruker Elexsys E500 spectrometer. High-field CW-EPR spectra were recorded at J-band frequencies (260 GHz, 9.4 T) at a temperature of 295 K using a Bruker Elexsys E780 spectrometer. In this case, the same nitroxide radical concentration of 50 mM was used as for the DNP experiments. ESEEM and ENDOR measurements to investigate the DMSO proton spins close to the electron spin-bearing NO group of the different nitroxides were performed using a Bruker Elexsys E580 spectrometer (more detailed in SI). The EPR spectra were simulated using EasySpin software.[35]

DNP experiments were carried out on our home-built liquid-state 400 MHz DNP spectrometer, consisting of a commercial 400 MHz NMR Bruker Advance spectrometer equipped with a home-built EPR bridge operating at 260 GHz for electron spin excitation and detection. Microwave excitation with a power of up to 0.5 W was achieved using a gyrotron source.[36] DNP samples with a 50 mM nitroxide concentration in DMSO were put in quartz capillaries with a 50 μm inner diameter and an outer diameter of 150 μm and sealed with wax at both ends. The DNP probe head has a double-resonance structure consisting of a helix that serves as a cylindrical TE_{011} cavity for EPR excitation and as an NMR coil for detection. Experimentally, a conversion factor of 0.27 mT/$\sqrt{W}$ was determined for the TE_{011} microwave resonance structure,[36] leading to a B_1 field strength of 1.5 G for an applied microwave power of 0.3 W. The DNP-enhanced and the reference NMR FID signals were recorded with a standard 90° RF-pulse excitation. The 90° pulse length was 20 μs, the repetition time was 1 s, and the number of scans was 8−16 for DNP (MW on) and 128 for NMR (MW off) FID signals. The DNP enhancements were determined by taking the ^{1}H FT-NMR spectra of the samples with and without cw mw irradiation of the central hyperfine line of the nitroxide spectra. Integrated proton NMR signals were used to calculate the DNP enhancement factor ε. Proton longitudinal relaxation times were measured with and without a polarizing agent using an inversion recovery experiment with FID detection at room temperature. Data were fitted with a single exponential function. The experimental values of longitudinal relaxation times were T_{1I} = 2.68 s for pure DMSO and T_{1IS} = 0.11−0.16 s for DMSO in the presence of nitroxides.

THEORETICAL DESCRIPTION OF OVERHAUSER DNP

For solutions containing nitroxides as polarizing agents and the molecules of the solvent as target molecules, the coupling factor can be expressed by two mechanisms: outer-sphere translational diffusion of the molecules and inner-sphere dynamics of the short-lived radical−solvent encounter complexes.[37] The coupling factor ξ can, in this case, be expressed as

$$\xi = \frac{5}{7}\left[1 - \frac{3k_{inner}J(\omega_I, \tau_c) + 3k_{outer}\tilde{J}(\omega_I, \tau_D)}{R_1^{inner} + R_1^{outer}}\right] \quad (2)$$

with the relaxation rates $R_1 = 1/T_1$ of the nuclear spin defined by

https://doi.org/10.1021/acs.jpcc.1c06979
J. Phys. Chem. C 2021, 125, 25651−25659

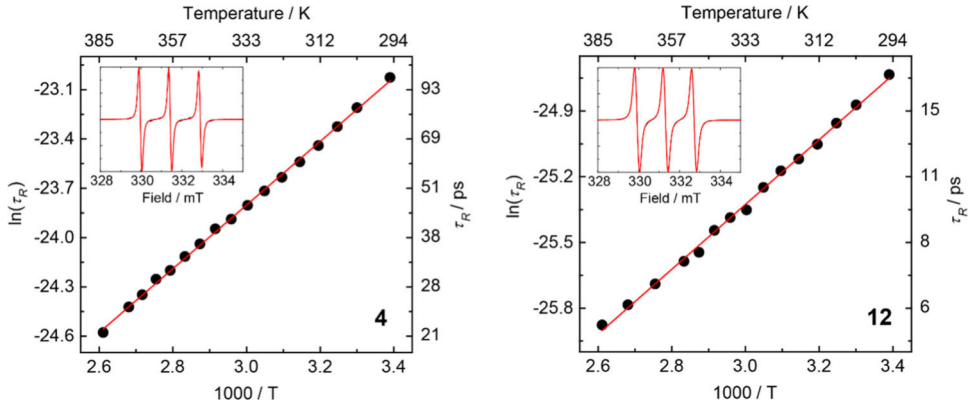

Figure 2. Temperature dependence of the rotational correlation time τ_R of the two nitroxides **4** and **12** in DMSO obtained from simulation of X-band CW-EPR spectra with isotropic rotational motion. Data are displayed as an Arrhenius plot. The solid red line obtained by linear regression yields the activation energy, which is given in the SI. The insets show the experimental CW-EPR spectra (black curve) and their simulation (red curve) at 383 K (better visible in the SI).

$$R_1^{\text{outer}} = k_{\text{outer}}(7\tilde{J}(\omega_s, \tau_D) + 3\tilde{J}(\omega_I, \tau_D)) \tag{3}$$

$$R_1^{\text{inner}} = k_{\text{inner}}(7J(\omega_s, \tau_c) + 3J(\omega_I, \tau_c)) \tag{4}$$

for outer-sphere and inner-sphere dynamics.

The two related amplitudes are defined by

$$k_{\text{outer}} = \frac{32\pi}{405}\left(\frac{\mu_0}{4\pi}\right)^2 \frac{N_A 1000[\text{M}]\gamma_I^2\gamma_s^2\hbar^2 S(S+1)}{Dd} \tag{5}$$

$$k_{\text{inner}} = \frac{2}{15}\frac{q\cdot[\text{M}]}{a\cdot[\text{M}_{\text{sol}}]}\left(\frac{\mu_0}{4\pi}\right)^2 \frac{\gamma_I^2\gamma_s^2\hbar^2 S(S+1)}{r^6} \tag{6}$$

where q is the number of DMSO protons per polarizing agent (in our case $q = 3$), [M] is the concentration of the paramagnetic agent (in mol/L), a is the number of all solvent protons (for DMSO $a = 6$), $[\text{M}_{\text{sol}}]$ is the concentration of DMSO (14.1 mol/L), ω_s and ω_I are the electron and nuclear spin Larmor frequencies, S is the electronic spin quantum number, r is the distance between the proton and the unpaired electron of the polarizing agent in the inner-sphere complex, d is the distance of the closest approach between the solvent protons and the polarizing agent electron spin within the translational diffusion process, and D is the sum of the diffusion coefficients for the solvent molecule and the polarizing agent. All other symbols describe natural constants: N_A is the Avogadro number, μ_0 is the permeability of vacuum, and $\hbar$ is the reduced Planck constant.

The outer-sphere dynamics described by the hard-sphere translational diffusive model of the solvent and radical molecules result in a spectral density function[38]

$$\tilde{J}(\omega, \tau) = \frac{1 + \frac{5z}{8} + \frac{z^2}{8}}{1 + z + \frac{z^2}{2} + \frac{z^3}{6} + \frac{4z^4}{81} + \frac{z^5}{81} + \frac{z^6}{648}} \tag{7}$$

with $z = \sqrt{2\omega\tau_D}$ and the translational correlation time given by $\tau_D = d^2/D$.

The inner-sphere spectral density function for rotational motion of the radical is defined by a Lorentzian function

$$J(\omega, \tau_R) = \frac{\tau_c}{1 + \omega^2\tau_c^2} \tag{8}$$

The correlation time τ_c as a characteristic time of the inner-sphere dynamical process is given by

$$\frac{1}{\tau_c} = \frac{1}{\tau_R} + \frac{1}{\tau_M} + \frac{1}{\tau_e} \tag{9}$$

where τ_R is the rotational correlation time of a bound complex of a polarizing agent and solvent molecules, τ_M is the lifetime of the radical−solvent complex (in our case nitroxide−DMSO), and τ_e is the longitudinal electron spin relaxation time of the nitroxide. The radical−solvent complex time τ_M and the electronic spin relaxation time τ_e of nitroxides at a J-band frequency and ambient temperature are in the nanosecond time range. Under the same conditions, the rotational correlation time τ_R is in the picosecond range, resulting in $1/\tau_R \gg 1/\tau_M, 1/\tau_e$. Therefore, further, we can assume $1/\tau_c = 1/\tau_R$.

The strategy to predict the high-field Overhauser DNP coupling factors ξ for the different radicals is as follows: the rotational correlation time τ_R has been measured by CW-EPR spectroscopy for all used radicals at the same temperature at which the high-field DNP experiments are performed. From these values, the inner-sphere contribution to the coupling factor ξ can be calculated if the distance r of the inner-sphere complex is known. We take this value from former MD studies and modeling of the coupling factor based on nuclear magnetic resonance dispersion (NMRD) measurements using the hard-sphere model.[14,22] Furthermore, we assume that this distance is the same for all radicals investigated, supported by electron−nuclear double resonance (ENDOR) and electron spin echo envelope modulation (ESEEM) measurements. The contribution of the translational motion of the DMSO to the coupling factor was calculated from the known diffusion coefficient D of DMSO[39] (and assuming that the diffusion coefficient of the radical itself is smaller).

Under our experimental conditions (magnetic field of 9.4 T, sample temperature above room temperature, and DMSO diffusion constant D), we found a significant dependence of the observed Overhauser DNP enhancement ε on the experimentally determined rotational correlation times τ_R of the different nitroxide radicals investigated. For a quantitative comparison of the calculated coupling factor profiles $\xi(\tau_R)$ with the experimentally determined DNP enhancements $\varepsilon(\tau_R)$ for the different radicals, the leakage factor f and the saturation factor s have to be known as well. The leakage factor f can easily be measured experimentally and was close to 1 for the

https://doi.org/10.1021/acs.jpcc.1c06979
J. Phys. Chem. C 2021, 125, 25651−25659

used radical concentrations of 50 mM. The saturation factor s is the most difficult parameter to access experimentally at high magnetic fields because increasing the mw excitation power also increases the sample temperature considerably. We used our previously proposed approach of measuring the reduction of the paramagnetic shift by the applied mw power to estimate the saturation factor of our samples under DNP conditions.[20] This procedure allowed quantitative comparison of the calculated and experimentally determined coupling factor profiles $\xi(\tau_R)$ at a magnetic field of 9.4 T.

EXPERIMENTAL RESULTS

Determination of the Rotational Correlation Time of Nitroxides by CW-EPR. The rotational correlation times of all nitroxides (Figure 1) were determined by simulation of CW-EPR spectra recorded at X-band frequencies in a temperature range of T = 295−383 K. The inlets in Figure 2 show thze CW-EPR spectra of the two radicals **4** and **12** (further spectra together with simulations performed with EasySpin software[35] are shown in the SI) and, as the main graph, the temperature dependence of the extracted rotational correlation time. The rotational correlation times τ_R for all radicals as well as the anisotropic g-tensor and ^{14}N hyperfine tensor values extracted from the field-swept high-field (G-band) EPR spectra are summarized in Table 1.

The rotational correlation times τ_R of all investigated nitroxides fall in the range of 5−30 ps at a temperature of 383 K. Increasing the molecular size of nitroxide affects the rotational correlation time, which ranges from $\tau_R \approx$ 5−6 ps for nitroxides **1**, **10**, and **12** to $\tau_R \approx$ 20−30 ps for nitroxides **4**, **5**, and **6** (Table 1).

Modeling of Inner-Sphere Rotational Contributions to the DNP Coupling Factor. With a diffusion coefficient of $D = 2.75 \times 10^{-9}$ m^2 s^{-1} for DMSO (at a temperature of 383 K) and an electron to proton spin distance of d = 3.75 Å for the translational motion and r = 3.60 Å for the inner-sphere complex (taken from MD and NMRD simulations),[14,22] the coupling factor profile shown in Figure 3 can be predicted. As can be seen, the DNP coupling factor at J-band (260 GHz) microwave frequencies is very sensitive to inner-sphere contributions for correlation times in this time range. The assumption that the distance of the closest approach is the same for all investigated nitroxides, despite their different substituents close to the NO group, is justified by pulsed ENDOR measurements performed at Q-band frequencies, which allow studying the hyperfine couplings of the unpaired electron of nitroxides to the surrounding solvent protons (see SI). In addition, the spectra obtained from the ESEEM time traces revealed similar ^{1}H signal intensities for all nitroxides within experimental error (see SI). Thus, we concluded that the distances between the nearest solvent proton and the electron spin are practically the same for all studied nitroxides.

Overhauser DNP Experiments at 9.4 T. We performed ^{1}H DNP experiments at a magnetic field strength of 9.4 T (corresponding to a proton resonance frequency of 400 MHz and an EPR resonance frequency of 260 GHz). To be able to quantitatively compare the experimentally obtained DNP enhancements of the different radicals, a radical concentration of 50 mM was used, which was found to be optimal to obtain good solubility for all radicals. The microwave irradiation was achieved using a gyrotron source with a maximum power of ∼5 W at the entrance of the probe head. Because the microwave excitation leads to the heating of the sample, the DNP measurements of all of the different radicals were performed with exactly the same mw power to achieve coupling factor profiles $\xi(\tau_R)$ at a fixed temperature T. Two representative DNP experiments for radicals **4** and **12** for a mw power between 0.15 and 0.47 W are shown in Figure 4. As can be seen in Table 1, negative DNP enhancements between −2.7 and −7.2 were obtained for a mw power of 0.23 W and a 50 mM radical concentration (the full set of the DNP measurements of all radicals is provided in the SI). The NMR signal intensities with and without mw irradiation are calculated by the integration of the NMR signal intensities, and the enhancement ε is defined as described in eq 1. The error of the experimental DNP enhancement ε can, due to several repetitions of the experiments, be estimated to be ±10%.

Determination of Sample Temperature under Microwave Irradiation. Notably, the enhanced DNP signal is significantly shifted compared to the initial NMR signal due to microwave heating of the sample. Many of the parameters influencing the Overhauser DNP enhancement, as the rotational and translational correlation times as well as the nuclear and electron spin relaxation times, are temperature-dependent. Therefore, it is very important to know the exact sample temperature for a quantitative comparison of our experimentally achieved DNP results with our calculations. We used the temperature dependence of the chemical shift of the

Table 1. Experimental Parameters for Different Nitroxides in DMSO[a]

nitroxides	ε	f	τ_R [ps]	A_{xx} A_{yy} A_{zz} [G]	g_{xx} g_{yy} g_{zz}
1	−7.2	0.96	4.9	5.7 5.7 36.0	2.00957 2.00625 2.00220
2	−6.6	0.96	7.5	5.5 5.5 35.5	2.00950 2.00630 2.00212
3	−4.3	0.96	10.8	4.5 4.5 35.0	2.00920 2.00620 2.00212
4	−5.0	0.96	21.6	4.4 4.4 34.9	2.00845 2.00612 2.00220
5	−3.7	0.96	30.4	4.5 4.5 34.1	2.00890 2.00610 2.00220
6	−2.7	0.96	26.4	3.6 3.6 34.6	2.00900 2.00595 2.00219
7	−4.5	0.95	14.4	3.6 3.6 34.5	2.00900 2.00585 2.00205
8	−3.7	0.96	15.2	4.2 4.2 34.5	2.00927 2.00603 2.00212
9	−3.8	0.96	15.5	4.8 4.8 34.4	2.00990 2.00610 2.00212
10	−5.6	0.96	6.4	4.6 4.6 35.7	2.00887 2.00592 2.00213
11	−4.5	0.96	14.2	4.5 4.5 34.7	2.00892 2.00600 2.00210
12	−5.6	0.94	5.6	4.0 4.0 33.5	2.00925 2.00602 2.00212
13	−4.1	0.95	10.5	4.2 4.2 33.4	2.00930 2.00598 2.00207
14	−4.6	0.96	10.6	1.8 1.8 19.3	2.01100 2.00670 2.00207

[a] ^{1}H DNP-NMR enhancements ε, achieved for 50 mM radical concentration at a temperature of T = 383 K. The experimental error of the DNP enhancement ε is 10%. The leakage factor f is determined at 298 K. The rotational correlation time τ_R determined with a radical concentration of 0.5 mM from X-band CW-EPR spectra is given for a temperature of T = 383 K. ^{14}N nitroxide hyperfine A- and g-tensors were determined from G-band echo-detected EPR spectra at 50 K (0.5 mM concentration of the radical in a DMSO/methanol 7:3 mixture).

https://doi.org/10.1021/acs.jpcc.1c06979
J. Phys. Chem. C 2021, 125, 25651−25659

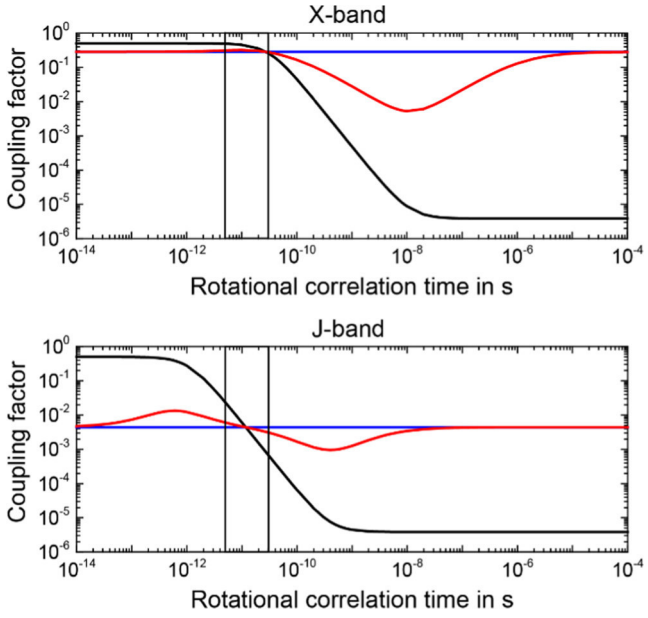

Figure 3. Dependence of the proton Overhauser DNP coupling factor on the rotational correlation time of the radical. The coupling factor calculations are shown for a rotational motion of an S−I complex (black), an intermolecular translational diffusional motion between radical and solvent molecules (blue), and a coupled outer- and inner-sphere dynamical model (red). Simulations at two different magnetic field strengths are compared. Upper diagram: calculations for a 0.3 T magnetic field. Lower diagram: calculations for a 9.4 T magnetic field. The two vertical black lines frame the rotational correlation time window of 5−30 ps of our studied nitroxides at a temperature of 383 K.

DMSO proton signal as an internal standard to calibrate the sample temperature under DNP conditions for a given mw power (see SI). Depending on the applied mw power (0.15−0.47 W), the sample temperature increases to 348−473 K.

Determination of the Leakage Factor *f*. For a microwave power of 0.23 W, the sample is heated to a temperature of 383 K, at which the rotational correlation times have been measured as well. Therefore, a direct comparison between the calculated coupling factor profile and the experimental NMR signal enhancement ε can be performed under these conditions if the leakage factor f and the saturation factor s are also determined at this temperature. The values for the leakage factor have been experimentally determined at room temperature for all radicals and are all close to 1 (see Table 1).

Estimation of the Electron Spin Transition Saturation Factor *s*. The saturation factor s is most difficult to access experimentally at high magnetic fields. Extrapolation of enhancements obtained by different microwave powers does not work due to the strong heating of the sample by high-frequency microwaves. Pulsed EPR methods, as electron double resonance (ELDOR),[40,41] which were used at lower frequencies, are difficult to realize due to the very fast relaxation times (<100 ns) of nitroxides in liquid solutions at high fields. Instead, we previously proposed to use the suppression of the paramagnetic shift as a function of the mw irradiation power to estimate the saturation factor.[20] Figure 5 demonstrates this procedure for nitroxide **1** dissolved at a concentration of 50 mM in DMSO. As can be seen from Figure 5, for a mw power above 0.3 W, the paramagnetic contribution to the chemical shift is fully suppressed, which we interpret as a full saturation $s \approx 1$ of the electron spin. The top horizontal axis shows the increasing sample temperature by the applied mw power. Therefore, sample properties as the translational and rotational correlation times of both the solvent and the radical, as well as the solvent proton spin and the radical electron spin relaxation times, are changing, as a function of the applied mw power. This hinders the quantitative interpretation of this saturation curve. Nevertheless, we believe that the saturation value for a mw power of 0.23 W is about $s \approx 0.9$. The suppression of the paramagnetic shift as a function of mw power for the nitroxides **1** and **14** with a rather different size and a different CW-EPR line width at a J-band frequency is identical (see SI). Therefore, we believe that the saturation factor s is very similar for all of the nitroxides investigated here at the same mw power.

Calculation of the Coupling Factor for the Different Nitroxide DNP Polarizing Agents. With the knowledge of the leakage and the saturation factor at this temperature, a coupling factor can be extracted from the measured DNP enhancements and compared to the values predicted from the hard-sphere model including an inner-sphere rotational contribution (Figure 6). The calculated coupling factor, taking the inner-sphere rotational contribution into account, fits very well to the experimental values given by the experimentally determined rotational correlation times and the measured

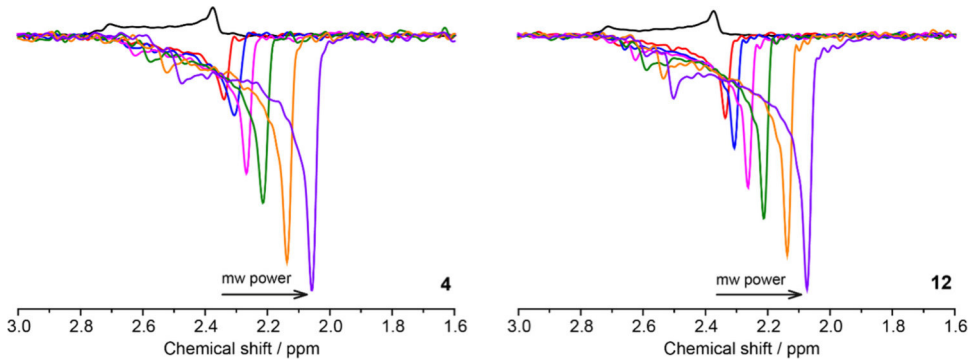

Figure 4. ^{1}H NMR spectra of the two nitroxides **4** and **12** dissolved with a concentration of 50 mM in DMSO. The black curve is the FT-NMR signal without mw excitation and the colored curves show the FT-NMR signals obtained with different amounts of mw power: (red) 0.15 W, (blue) 0.19 W, (purple) 0.23 W, (green) 0.30 W, (orange) 0.37 W, and (violet) 0.47 W. The ^{1}H NMR spectra for the other studied nitroxides are provided in the SI.

https://doi.org/10.1021/acs.jpcc.1c06979
J. Phys. Chem. C 2021, 125, 25651−25659

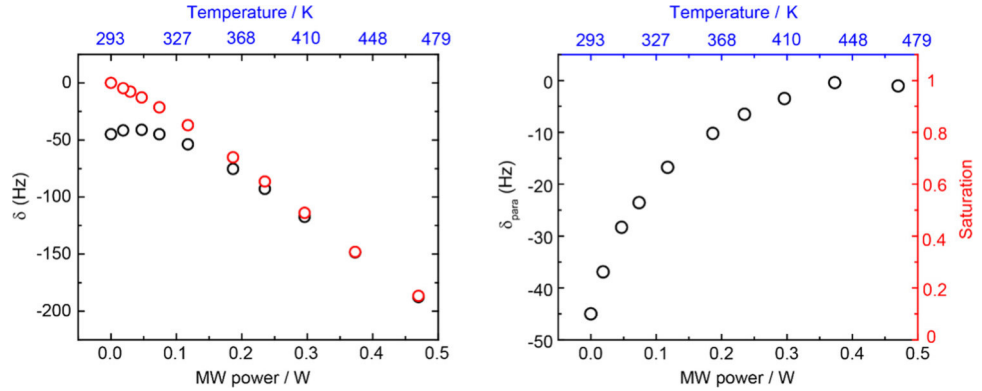

Figure 5. Suppression of the paramagnetic shift by mw excitation of the electron spin of the radical. On the left side, the paramagnetic shift is shown for pure DMSO (red) and 50 mM nitroxide **1** in DMSO (black). The chemical shift change of the DMSO sample as a function of mw power allows to calibrate the sample temperature for a given mw power. The difference of the line positions of the sample with and without a radical is the paramagnetic shift (shown in the right panel). For a mw power larger than 0.3 W, the paramagnetic shift is fully suppressed, resulting in a saturation factor of $s \approx 1$.

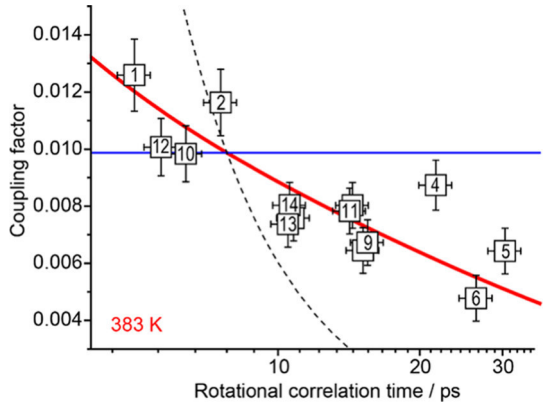

Figure 6. Comparison of the calculated proton coupling factors with the experimentally determined coupling factors at a sample temperature of 383 K. The proton coupling factor ξ of DMSO doped with different nitroxide derivatives is shown as a function of the rotational correlation time τ_R of the polarizing agent. The radical concentration was 50 mM for all samples. The coupling factor ξ was calculated using eq 2 for translational diffusional motion (blue curve), rotational motion (black dotted curve), and contribution from both translational and rotational motions (red curve). The experimental data points for nitroxides **3**, **7**, and **8** are overlapping with the nitroxides **13**, **11**, and **9**, respectively.

DNP enhancements. Also, the predicted slope of the coupling factor profile $\xi(\tau_R)$ follows the experimental data points very nicely. This quantitative agreement underlines that the observed differences in the DNP enhancements are primarily related to the different sizes and therefore rotational correlation times of the investigated nitroxides. Interestingly, the liquid-state Overhauser DNP efficiency at high magnetic fields seems neither dependent on the nature and the size of the ring (piperidine, pyrrolidine, imidazolidine, pyrroline, imidazoline) nor on the shielding of the unpaired electron spin by bulky substituents around the NO group.

DISCUSSION

The obtained DNP enhancement $\varepsilon = -7.2$ for nitroxide **1** reached under our experimental conditions (50 mM radical concentration, 0.23 W mw power, 50 μm capillary diameter, and sample temperature of 383 K) is less compared to experiments obtained previously (DNP enhancement $\varepsilon = -29$, 1 M TEMPOL concentration, 0.5 W mw power, 30 μm sample capillary, and a sample temperature of 453 K).[14] There are several reasons for this reduced value. First of all, a different mw B_1 field strength, which depends on the quality factor Q of the probe head and the applied mw power, results in a different sample temperature. At higher temperatures, larger DNP enhancement is accomplished due to faster translational and rotational correlation times. Here, we wanted to keep the sample temperature to a value where the rotational correlation times of all nitroxides have been experimentally determined by X-band CW-EPR. We also measured the temperature dependence of the rotational correlation times (see SI), but this did not allow the secure projection to a temperature as high as 473 K, corresponding to the sample temperature at a 0.47 W mw power. Another reason to stay at only slightly elevated temperatures is to achieve very accurate and reproducible DNP enhancements. This was very important to experimentally identify the slope of the coupling factor as a function of the different rotational correlation times (Figure 6). The errors of the experimental points in the graph (where each point reflects a different sample) become much larger for experiments at higher temperatures (see the SI). This is because at higher mw power, the finally reached temperature strongly depends on sample size and alignment within the mw resonator, which introduces a larger fluctuation in the DNP enhancements. Additionally, the rotational correlation times smaller than 10 ps become difficult to determine quantitatively by X-band CW-EPR, introducing an additional horizontal error. Furthermore, the procedure to calculate the DNP enhancement needs the comparison with the Boltzmann NMR signal, which is obtained at room temperature. So again, this procedure is safer if the increase in temperature is moderate.

Another reason for the difference of these measurements in comparison to earlier results is an unexpected concentration dependence of the DNP enhancement. Two times larger DNP enhancements are observed for a 1 M radical concentration compared to a 50 mM sample (see SI). Because the coupling factor itself is not concentration-dependent, this must reflect a variation in the saturation and/or leakage factor or might be due to a reduction of the Boltzmann signal by extensive paramagnetic relaxation. This concentration effect is presently under study in our lab.

https://doi.org/10.1021/acs.jpcc.1c06979
J. Phys. Chem. C 2021, 125, 25651−25659

Nevertheless, we also recorded DNP enhancements at higher mw power (up to 0.5 W), where the saturation factor is expected to reach 1. Even at such high temperatures, the predicted coupling factors fit well to the experimental data (but with larger error bars in enhancement and rotational correlation times). The rotational correlation times could not be accurately determined at these elevated temperatures, as discussed above. The coupling factor profiles $\xi(\tau_R)$ at these higher temperatures are given in the SI.

The coupling factor (and thus the DNP enhancement) is more sensitive to the rotational motion of typical nitroxide radicals (with rotational correlation times in the range of 1−30 ps) at high magnetic fields. As can be seen from Figure 3 at an X-band frequency, the coupling factor of the studied nitroxides with a rotational correlation time in a range of 1−30 ps is governed mainly by the translational diffusion. Therefore, we can predict that at low magnetic fields, the liquid-state Overhauser DNP efficiency will practically be the same for all of the nitroxides studied in the present work. This agrees well with previous studies, where relatively small polarizing agents (except BDPA and nitroxides attached to fullerene) showed very similar coupling factors at the X-band frequency.[23,42] Thus, experiments at 9.4 T are perfectly suited to observe the dependence of the Overhauser DNP effect on the inner-sphere rotational dynamics for the nitroxide radicals studied here.

CONCLUSIONS

Here, we report on a systematic study of the high-field Overhauser DNP efficiency of a series of nitroxides exhibiting different ring geometries and sterically differing substituents close to the NO group. Although we could show that the ring structure and the substituents close to the NO group do not affect the DNP performance, it is well known that they are crucial for their redox stability. Thus, for room-temperature applications in redox-active media, for example, for DNP experiments in cells, redox-stable nitroxides are mandatory. Among the studied nitroxides, the best ones as redox-stable polarizing agents are radicals **7** and **13** due to steric shielding of the NO moiety by the mobile ethyl groups.[43] Both of these radicals show somewhat lower Overhauser DNP enhancement due to the larger size, leading to a longer rotational correlation time.

In conclusion, we have studied how different structures of nitroxide as polarizing agents affect the efficiency of Overhauser DNP at high magnetic fields (9.4 T). We could show that the differences observed in the Overhauser DNP efficiency of these nitroxides can be explained rather well with the classical hard-sphere model by the different rotational correlation times of the nitroxides. These results are very helpful for the prediction of high-field Overhauser DNP efficiencies of nitroxides—the most efficient and the most commonly used class of DNP agents at high magnetic fields so far.

ASSOCIATED CONTENT

Supporting Information

The Supporting Information is available free of charge at https://pubs.acs.org/doi/10.1021/acs.jpcc.1c06979.

Details of the experimental setup, CW-EPR spectra at room temperature at X- and J-band frequencies, pulsed field-swept spectra at low temperature at G-band frequency, ENDOR and ESEEM measurements, and further DNP experiments and analysis (PDF)

AUTHOR INFORMATION

Corresponding Author

Thomas F. Prisner − *Goethe University Frankfurt am Main, Institute of Physical and Theoretical Chemistry and Center for Biomolecular Magnetic Resonance, 60438 Frankfurt am Main, Germany;* orcid.org/0000-0003-2850-9573; Email: prisner@chemie.uni-frankfurt.de

Authors

Andrei A. Kuzhelev − *Goethe University Frankfurt am Main, Institute of Physical and Theoretical Chemistry and Center for Biomolecular Magnetic Resonance, 60438 Frankfurt am Main, Germany*

Danhua Dai − *Goethe University Frankfurt am Main, Institute of Physical and Theoretical Chemistry and Center for Biomolecular Magnetic Resonance, 60438 Frankfurt am Main, Germany*

Vasyl Denysenkov − *Goethe University Frankfurt am Main, Institute of Physical and Theoretical Chemistry and Center for Biomolecular Magnetic Resonance, 60438 Frankfurt am Main, Germany*

Igor A. Kirilyuk − *N. N. Vorozhtsov Novosibirsk Institute of Organic Chemistry SB RAS, 630090 Novosibirsk, Russia*

Elena G. Bagryanskaya − *N. N. Vorozhtsov Novosibirsk Institute of Organic Chemistry SB RAS, 630090 Novosibirsk, Russia;* orcid.org/0000-0003-0057-383X

Complete contact information is available at: https://pubs.acs.org/10.1021/acs.jpcc.1c06979

Notes

The authors declare no competing financial interest.

ACKNOWLEDGMENTS

The authors thank Dr. Dmitry Akhmetzyanov for help with preliminary DNP experiments. This work was supported by the Deutsche Forschungsgemeinschaft (DFG) and by the Center of Biomolecular Magnetic Resonance (BMRZ). E.G.B. and I.A.K. thank the Ministry of Science and Higher Education of the Russian Federation (Grant no. 14.W03.31.0034) for financial support.

REFERENCES

(1) Ardenkjær-Larsen, J. H.; Golman, K.; Gram, A.; Lerche, M. H.; Servin, R.; Thaning, M.; Wolber, J. Increase of Signal-to-Noise of More than 10,000 Times in Liquid State NMR. *Proc. Natl. Acad. Sci. USA* **2003**, *3*, 37−379.

(2) Griesinger, C.; Bennati, M.; Vieth, H. M.; Luchinat, C.; Parigi, G.; Höfer, P.; Engelke, F.; Glaser, S. J.; Denysenkov, V.; Prisner, T. F. Dynamic Nuclear Polarization at High Magnetic Fields in Liquids. *Prog. Nucl. Magn. Reson. Spectrosc.* **2012**, *64*, 4−28.

(3) Corzilius, B. High-Field Dynamic Nuclear Polarization. *Annu. Rev. Phys. Chem.* **2020**, *71*, 143−170.

(4) Lelli, M.; Chaudhari, S. R.; Gajan, D.; Casano, G.; Rossini, A. J.; Ouari, O.; Tordo, P.; Lesage, A.; Emsley, L. Solid-State Dynamic Nuclear Polarization at 9.4 and 18.8 T from 100 K to Room Temperature. *J. Am. Chem. Soc.* **2015**, *137*, 14558−14561.

(5) Jeffries, C. D. Polarization of Nuclei by Resonance Saturation in Paramagnetic Crystals. *Phys. Rev.* **1957**, *106*, 164−165.

(6) Hwang, C. F.; Hill, D. A. New Effect in Dynamic Polarization. *Phys. Rev. Lett.* **1967**, *18*, 110−112.

(7) Hovav, Y.; Feintuch, A.; Vega, S. Theoretical Aspects of Dynamic Nuclear Polarization in the Solid State - The Cross Effect. *J. Magn. Reson.* **2012**, *214*, 29−41.
(8) Abragam, A.; Goldman, M. Principles of Dynamic Nuclear Polarisation. *Rep. Prog. Phys.* **1978**, *41*, 395−467.
(9) Wind, R. A.; Duijvestijn, M. J.; van der Lugt, C.; Manenschijn, A.; Vriend, J. Applications of Dynamic Nuclear Polarization in 13C NMR in Solids. *Prog. Nucl. Magn. Reson. Spectrosc.* **1985**, *17*, 33−67.
(10) Loening, N. M.; Rosay, M.; Weis, V.; Griffin, R. G. Solution-State Dynamic Nuclear Polarization at High Magnetic Field. *J. Am. Chem. Soc.* **2002**, *124*, 8808−8809.
(11) Prandolini, M. J.; Denysenkov, V. P.; Gafurov, M.; Endeward, B.; Prisner, T. F. High-Field Dynamic Nuclear Polarization in Aqueous Solutions. *J. Am. Chem. Soc.* **2009**, *131*, 6090−6092.
(12) Orlando, T.; Dervişoğlu, R.; Levien, M.; Tkach, I.; Prisner, T. F.; Andreas, L. B.; Denysenkov, V. P.; Bennati, M. Dynamic Nuclear Polarization of 13 C Nuclei in the Liquid State over a 10 Tesla Field Range. *Angew. Chem., Int. Ed.* **2019**, *58*, 1402−1406.
(13) Van Der Heijden, G. H. A.; Kentgens, A. P. M.; Van Bentum, P. J. M. Liquid State Dynamic Nuclear Polarization of Ethanol at 3.4 T (95 GHz). *Phys. Chem. Chem. Phys.* **2014**, *16*, 8493−8502.
(14) Neugebauer, P.; Krummenacker, J. G.; Denysenkov, V. P.; Helmling, C.; Luchinat, C.; Parigi, G.; Prisner, T. F. High-Field Liquid State NMR Hyperpolarization: A Combined DNP/NMRD Approach. *Phys. Chem. Chem. Phys.* **2014**, *16*, 18781−18787.
(15) Hausser, K. H.; Stehlik, D. Dynamic Nuclear Polarization in Liquids. In *Advances in Magnetic and Optical Resonance*; Royal Society of Chemistry, 1968; Vol. 3, pp 79−139.
(16) Denysenkov, V.; Prisner, T. Liquid State Dynamic Nuclear Polarization Probe with Fabry-Perot Resonator at 9.2 T. *J. Magn. Reson.* **2012**, *217*, 1−5.
(17) Yoon, D.; Dimitriadis, A. I.; Soundararajan, M.; Caspers, C.; Genoud, J.; Alberti, S.; De Rijk, E.; Ansermet, J. P. High-Field Liquid-State Dynamic Nuclear Polarization in Microliter Samples. *Anal. Chem.* **2018**, *90*, 5620−5626.
(18) Dubroca, T.; Smith, A. N.; Pike, K. J.; Froud, S.; Wylde, R.; Trociewitz, B.; McKay, J.; Mentink-Vigier, F.; van Tol, J.; Wi, S.; et al. A Quasi-Optical and Corrugated Waveguide Microwave Transmission System for Simultaneous Dynamic Nuclear Polarization NMR on Two Separate 14.1 T Spectrometers. *J. Magn. Reson.* **2018**, *289*, 35−44.
(19) Denysenkov, V. P.; Prisner, T. F. Liquid-State Overhauser DNP at High Magnetic Fields. *eMagRes* **2019**, *8*, 41−54.
(20) Neugebauer, P.; Krummenacker, J. G.; Denysenkov, V. P.; Parigi, G.; Luchinat, C.; Prisner, T. F. Liquid State DNP of Water at 9.2 T: An Experimental Access to Saturation. *Phys. Chem. Chem. Phys.* **2013**, *15*, 6049−6056.
(21) Sezer, D.; Prandolini, M. J.; Prisner, T. F. Dynamic Nuclear Polarization Coupling Factors Calculated from Molecular Dynamics Simulations of a Nitroxide Radical in Water. *Phys. Chem. Chem. Phys.* **2009**, *11*, 6626−6637.
(22) Küçük, S. E.; Neugebauer, P.; Prisner, T. F.; Sezer, D. Molecular Simulations for Dynamic Nuclear Polarization in Liquids: A Case Study of TEMPOL in Acetone and DMSO. *Phys. Chem. Chem. Phys.* **2015**, *17*, 6618−6628.
(23) Levien, M.; Hiller, M.; Tkach, I.; Bennati, M.; Orlando, T. Nitroxide Derivatives for Dynamic Nuclear Polarization in Liquids: The Role of Rotational Diffusion. *J. Phys. Chem. Lett.* **2020**, *11*, 1629−1635.
(24) Miura, Y.; Nakamura, N.; Taniguchi, I. Low-Temperature "Living" Radical Polymerization of Styrène in the Presence of Nitroxides with Spiro Structures. *Macromolecules* **2001**, *34*, 447−455.
(25) Kuzhelev, A. A.; Strizhakov, R. K.; Krumkacheva, O. A.; Polienko, Y. F.; Morozov, D. A.; Shevelev, G. Y.; Pyshnyi, D. V.; Kirilyuk, I. A.; Fedin, M. V.; Bagryanskaya, E. G. Room-Temperature Electron Spin Relaxation of Nitroxides Immobilized in Trehalose: Effect of Substituents Adjacent to NO-Group. *J. Magn. Reson.* **2016**, *266*, 1−7.
(26) Kirilyuk, I. A.; Polienko, Y. F.; Krumkacheva, O. A.; Strizhakov, R. K.; Gatilov, Y. V.; Grigor'ev, I. A.; Bagryanskaya, E. G. Synthesis of 2,5-Bis(Spirocyclohexane)-Substituted Nitroxides of Pyrroline and Pyrrolidine Series, Including Thiol-Specific Spin Label: An Analogue of MTSSL with Long Relaxation Time. *J. Org. Chem.* **2012**, *77*, 8016−8027.
(27) Morozov, D. A.; Kirilyuk, I. A.; Komarov, D. A.; Goti, A.; Bagryanskaya, I. Y.; Kuratieva, N. V.; Grigorev, I. A. Synthesis of a Chiral C2-Symmetric Sterically Hindered Pyrrolidine Nitroxide Radical via Combined Iterative Nucleophilic Additions and Intramolecular 1,3-Dipolar Cycloadditions to Cyclic Nitrones. *J. Org. Chem.* **2012**, *77*, 10688−10698.
(28) Dobrynin, S. A.; Glazachev, Y. I.; Gatilov, Y. V.; Chernyak, E. I.; Salnikov, G. E.; Kirilyuk, I. A. Synthesis of 3,4-Bis(Hydroxymethyl)−2,2,5,5-Tetraethylpyrrolidin-1-Oxyl via 1,3-Dipolar Cycloaddition of Azomethine Ylide to Activated Alkene. *J. Org. Chem.* **2018**, *83*, 5392−5397.
(29) Zhurko, I. F.; Dobrynin, S.; Gorodetskii, A. A.; Glazachev, Y. I.; Rybalova, T. V.; Chernyak, E. I.; Asanbaeva, N.; Bagryanskaya, E. G.; Kirilyuk, I. A. 2-Butyl-2-Tert-Butyl-5, 5-Diethylpyrrolidine-1-Oxyls: Synthesis and Properties. *Molecules* **2020**, *25*, 845.
(30) Zubenko, D.; Tsentalovich, Y.; Lebedeva, N.; Kirilyuk, I.; Roshchupkina, G.; Zhurko, I.; Reznikov, V.; Marque, S. R. A.; Bagryanskaya, E. Laser Flash Photolysis and CIDNP Studies of Steric Effects on Coupling Rate Constants of Imidazolidine Nitroxide with Carbon-Centered Radicals, Methyl Isobutyrate-2-Yl and Tert-Butyl Propionate-2-Yl. *J. Org. Chem.* **2006**, *71*, 6044−6052.
(31) Edeleva, M. V.; Kirilyuk, I. A.; Zubenko, D. P.; Zhurko, I. F.; Marque, S. R. A.; Gigmes, D.; Guillaneuf, Y.; Bagryanskaya, E. G. Kinetic Study of H-Atom Transfer in Imidazoline-, Imidazolidine-, and Pyrrolidine-Based Alkoxyamines: Consequences for Nitroxide-Mediated Polymerization. *J. Polym. Sci., Part A: Polym. Chem.* **2009**, *47*, 6579−6595.
(32) Woldman, Y. Y.; Khramtsov, V. V.; Grigorev, I. A.; Kiriljuk, I. A.; Utepbergenov, D. I. Spin Trapping of Nitric Oxide by Nitronylnitroxides: Measurement of the Activity of NO Synthase from Rat Cerebellum. *Biochem. Biophys. Res. Commun.* **1994**, *202*, 195−203.
(33) Mathew, A. E.; Dodd, J. R. Synthesis of Substituted, 2,2,5,5-tetramethylpyrrolidin-l-oxyl Spin Labels−PH Sensitivity Studies. *J. Heterocycl. Chem.* **1985**, *22*, 225−228.
(34) Gorodetsky, A. A.; Kirilyuk, I. A.; Khramtsov, V. V.; Komarov, D. A. Functional Electron Paramagnetic Resonance Imaging of Ischemic Rat Heart: Monitoring of Tissue Oxygenation and PH. *Magn. Reson. Med.* **2016**, *76*, 350−358.
(35) Stoll, S.; Schweiger, A. EasySpin, a Comprehensive Software Package for Spectral Simulation and Analysis in EPR. *J. Magn. Reson.* **2006**, *178*, 42−55.
(36) Denysenkov, V.; Prandolini, M. J.; Gafurov, M.; Sezer, D.; Endeward, B.; Prisner, T. F. Liquid State DNP Using a 260 GHz High Power Gyrotron. *Phys. Chem. Chem. Phys.* **2010**, *12*, 5786−5790.
(37) Ravera, E.; Luchinat, C.; Parigi, G. Basic Facts and Perspectives of Overhauser DNP NMR. *J. Magn. Reson.* **2016**, *264*, 78−87.
(38) Hwang, L. P.; Freed, J. H. Dynamic Effects of Pair Correlation Functions on Spin Relaxation by Translational Diffusion in Liquids. *J. Chem. Phys.* **1975**, *63*, 4017−4025.
(39) Holz, M.; Heil, S. R.; Sacco, A. Temperature-Dependent Self-Diffusion Coefficients of Water and Six Selected Molecular Liquids for Calibration in Accurate 1H NMR PFG Measurements. *Phys. Chem. Chem. Phys.* **2000**, *2*, 4740−4742.
(40) Hyde, J. S.; Chien, J. C. W.; Freed, J. H. Electron−Electron Double Resonance of Free Radicals in Solution. *J. Chem. Phys.* **1968**, *48*, 4211−4226.
(41) Türke, M. T.; Tkach, I.; Reese, M.; Höfer, P.; Bennati, M. Optimization of Dynamic Nuclear Polarization Experiments in Aqueous Solution at 15 MHz/9.7 GHz: A Comparative Study with DNP at 140 MHz/94 GHz. *Phys. Chem. Chem. Phys.* **2010**, *12*, 5893−5901.

https://doi.org/10.1021/acs.jpcc.1c06979
J. Phys. Chem. C 2021, 125, 25651−25659

(42) Levien, M.; Reinhard, M.; Hiller, M.; Tkach, I.; Bennati, M.; Orlando, T. Spin Density Localization and Accessibility of Organic Radicals Affect Liquid-State DNP Efficiency. *Phys. Chem. Chem. Phys.* **2021**, *23*, 4480−4485.
(43) Jagtap, A. P.; Krstic, I.; Kunjir, N. C.; Hänsel, R.; Prisner, T. F.; Sigurdsson, S. T. Sterically Shielded Spin Labels for In-Cell EPR Spectroscopy: Analysis of Stability in Reducing Environment. *Free Radical Res.* **2015**, *49*, 78−85.

https://doi.org/10.1021/acs.jpcc.1c06979
J. Phys. Chem. C 2021, 125, 25651−25659

Supporting Information

The Influence of Rotational Motion of Nitroxides to Overhauser Dynamic Nuclear Polarization: A Systematic Study at High Magnetic Fields

Andrei A. Kuzhelev,[a] Danhua Dai,[a] Vasyl Denysenkov,[a] Igor A. Kirilyuk,[b] Elena G. Bagryanskaya[b] and Thomas F. Prisner*[a]

[a] *Goethe University Frankfurt am Main, Institute of Physical and Theoretical Chemistry and Center for Biomolecular Magnetic Resonance, Max von Laue Str. 7, 60438 Frankfurt am Main, Germany. E-mail: prisner@chemie.uni-frankfurt.de*

[b] *N. N. Vorozhtsov Novosibirsk Institute of Organic Chemistry SB RAS, Lavrentiev Avenue 9, 630090 Novosibirsk, Russia.*

Content

1. Experimental EPR setting

CW EPR measurements were performed at X-band (C = 0.5 mM, at 295-383 K) and J-band (C = 50 mM, at 295 K) frequencies using commercial spectrometers (Bruker Elexsys E500 for X-band and Bruker E780 for J-band). The EPR parameters for the CW X-band measurements are: frequency 9.331 GHz, sweep width 8 mT, microwave power 2 mW, modulation frequency 100 kHz, modulation amplitude 0.06 to 0.1 mT, time constant 40.96 ms, conversion time 163.84 ms, sweep time 335.54 s, number of points 1024 and number of scans 1. The used experimental EPR parameters at J-band are: frequency 263.8002 - 264.1187 GHz, sweep width 20 mT, microwave power 0.024 mW, modulation frequency 5 kHz, modulation amplitude 0.05 mT, time constant 81.90 ms, conversion time 327.60 ms, sweep time 327.92 s, number of points 1001 and number of scans 1.

Echo-detected EPR spectra were carried out with our home built G-band EPR spectrometer (180 GHz, 6.4 T).[1,2] EPR spectra were recorded in a mixture of DMSO/Methanol (7:3) with nitroxide concentration of 0.5 mM at 50 K using pulse length of 46 and 72 ns (for $\pi/2$ and π pulses, respectively), and a pulse delay of 200 ns. To determine the g-values of the nitroxides accurately, we placed a $^{55}Mn^{2+}$ standard sample ($g_{Mn^{2+}}$=2.00101)[3] in the resonator, together with the studied sample.

The g- and hyperfine-tensors of all studied nitroxides were obtained from simulation of G-band EPR spectra with the EasySpin program[4] (using the function *pepper* for solids). The obtained EPR parameters of the nitroxides **1**-**14** are listed in Table 1 and the EPR spectra are shown in Figure S2. The molecular rotational correlation time τ_R was obtained by fitting the X-band EPR spectra with the Easyspin program,[4] using the routine *garlic* corresponding to liquids in the fast motion regime (Figures S3-S5). The rotational correlation times show a clear dependence on the temperature and can be fitted by: $\ln\left(\frac{\tau_R}{1\,s}\right) = \ln\left(\frac{\tau_0}{1\,s}\right) + \frac{E_A}{RT}$ (Figures S6-S8). The corresponding Arrhenius energies E_A and τ_0 are listed in Table S1.

Pulsed ENDOR and ESEEM measurements were recorded on a commercial X/Q-band Bruker Elexsys E580 spectrometer equipped with an Oxford flow helium cryostat and temperature control system. All pulsed experiments were performed with nitroxide concentrations of 0.5 mM. The pulsed ENDOR experiments were performed at Q-band frequencies at a temperature of 50 K in protonated and deuterated DMSO using the Davies[5] and Mims[6] ENDOR pulse sequences. ENDOR spectra were recorded at a magnetic field position corresponding to the maximum echo intensity. Davies ENDOR was done with FID detection ((π)-*RF pulse*-(π/2)-FID) using mw pulse lengths of 400 ns (π) and 200 ns (π/2) and a RF pulse length of 13-14 µs. Mims ENDOR spectra were collected with the stimulated-echo pulse sequence ((π/2)-τ-(π/2)-*RF pulse*-(π/2)-τ-*echo*) using mw pulse lengths of 12 ns (π/2), a RF pulse length of 16-17 µs and a time delay of τ = 150 – 390 ns.

ESEEM data were measured at 50 K at X-band frequency in DMSO using the three-pulse stimulated echo sequence ((π/2)-τ-(π/2)-*T*-(π/2)-τ-*echo*) with 16 ns long π/2 pulses. For suppression of unwanted echoes, a four-step phase cycle was used. The delay τ was adjusted to obtain sufficient modulation by nuclei ^{1}H (τ = 170 ns). The shot repetition time was 3 ms. The echo decay traces were normalized by division by the maximal value of a mono-exponential fit to them, followed by a subtraction of the normalized fit. Then, the data were further processed by Gaussian apodization, zero filling, and Fourier transformation to obtain frequency-domain magnitude spectra.

2. J-band CW EPR spectra of nitroxides at 298 K

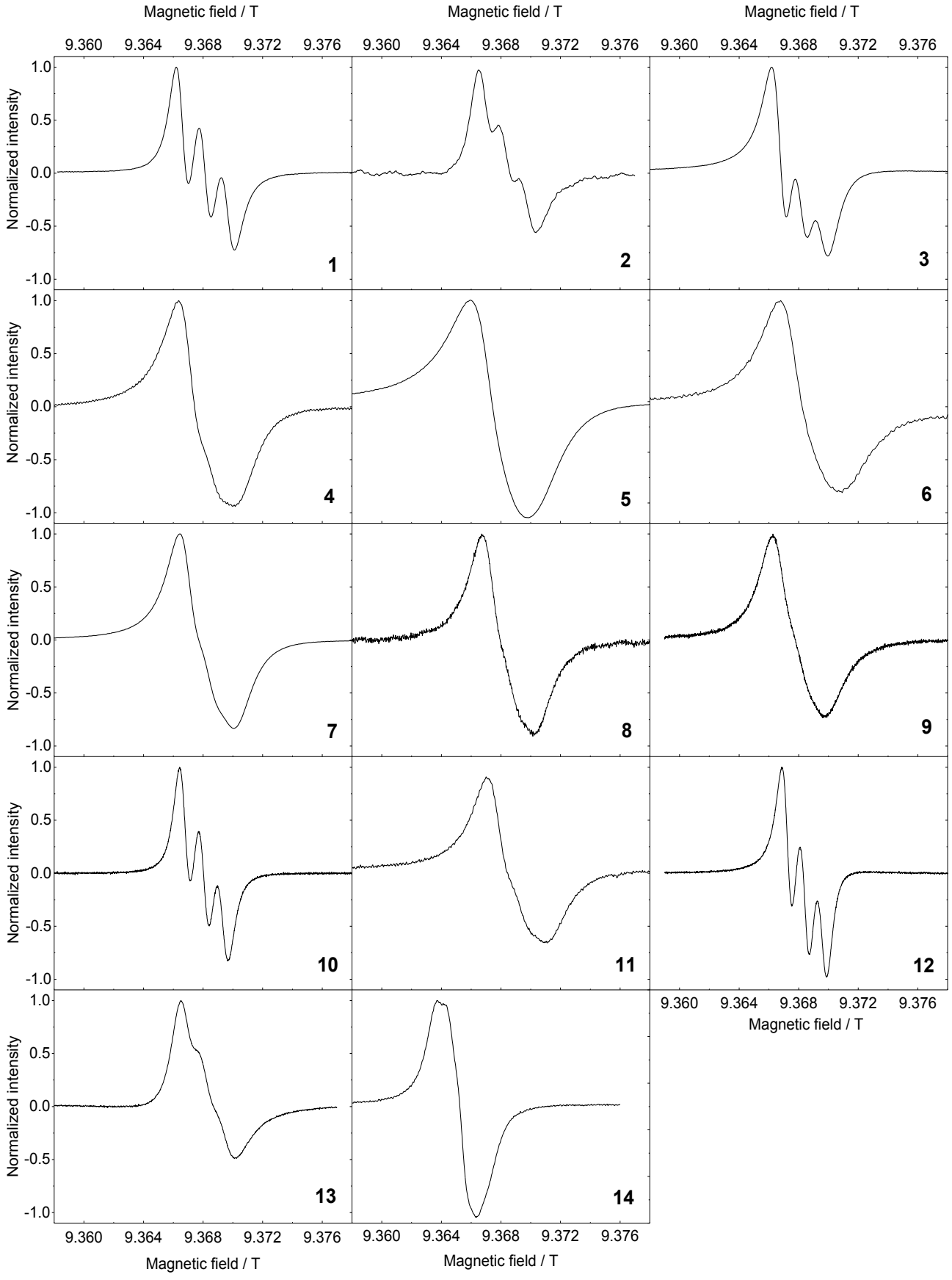

Figure S1. J-band CW EPR spectra of all studied nitroxides with concentration of 50 mM in DMSO at room temperature.

3. G-band EPR spectra of nitroxides at 50 K

Figure S2 shows the EPR spectra recorded at G-band frequency at 50 K in a DMSO/Methanol (7:3) mixture. The DMSO/Methanol mixture was used to avoid the aggregation of some of the nitroxides in pure DMSO at low temperatures. The differences of the simulated and experimental obtained echo-detected field-swept spectra probably have two different reasons: (i) some nitroxides still aggregate in the mixture of DMSO/Methanol solvents (as for example nitroxide **7**); (ii) the mixture of DMSO/Methanol is a soft matrix resulting in librational dynamics of the nitroxides in the frozen solution (as for example nitroxide **14**). However, this does not strongly influence the determination of the main g-tensor elements and of the A_{zz} hyperfine component from the experimental G-band EPR spectra. The other two components of the hyperfine tensor (A_{xx} and A_{yy}) were estimated from the isotropic hyperfine coupling constant obtained from cw-EPR spectra at X-band frequencies.

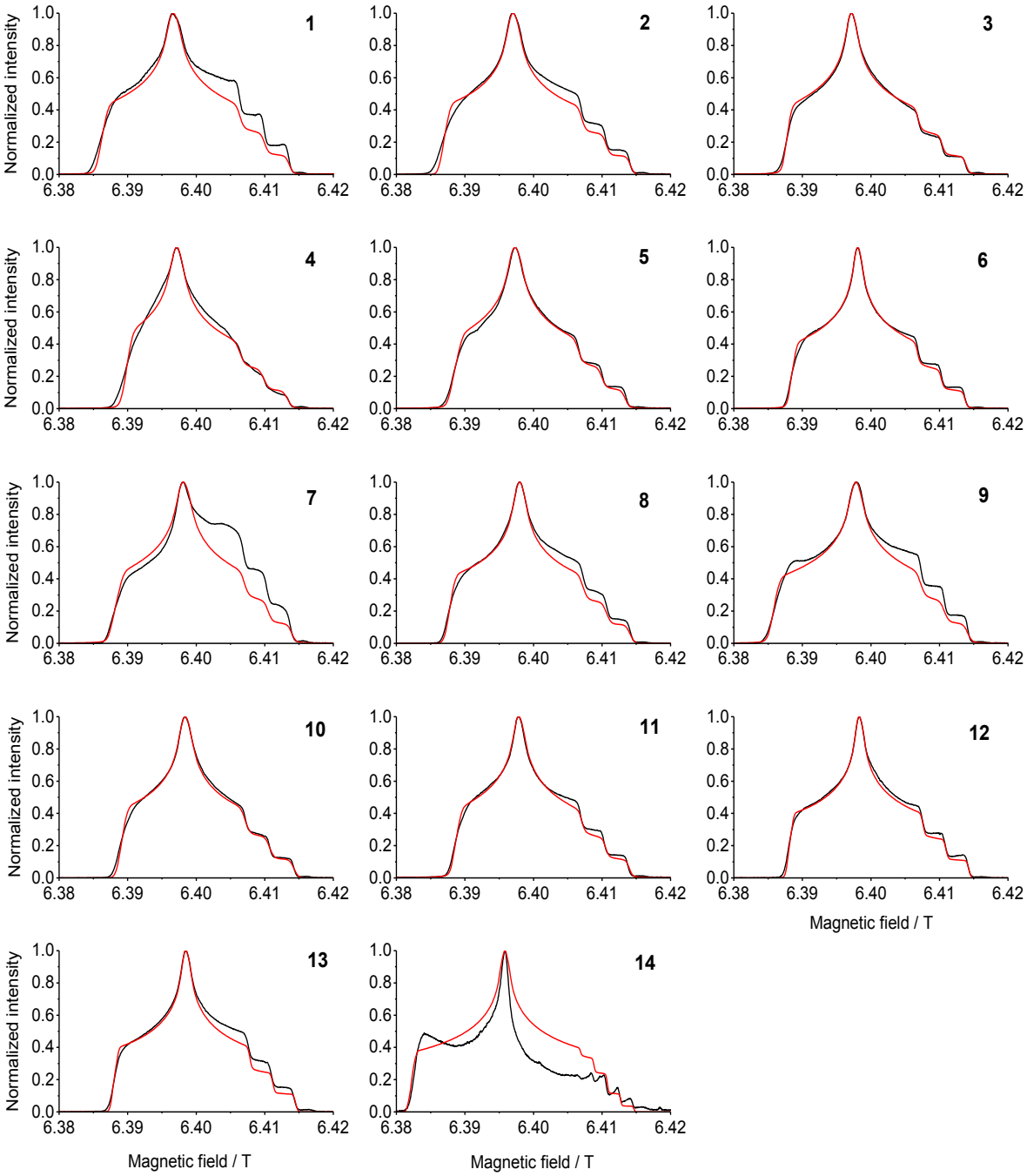

Figure S2. G-band echo-detected EPR spectra of the studied nitroxides **1-14.** Concentration was 0.5 mM and solvent was a mixture of DMSO and Methanol (7:3). The temperature was 50 K. Shown are the experimental data (black) and the simulations with the parameters of Table 1 (red).

4. X-band CW EPR spectra of nitroxides

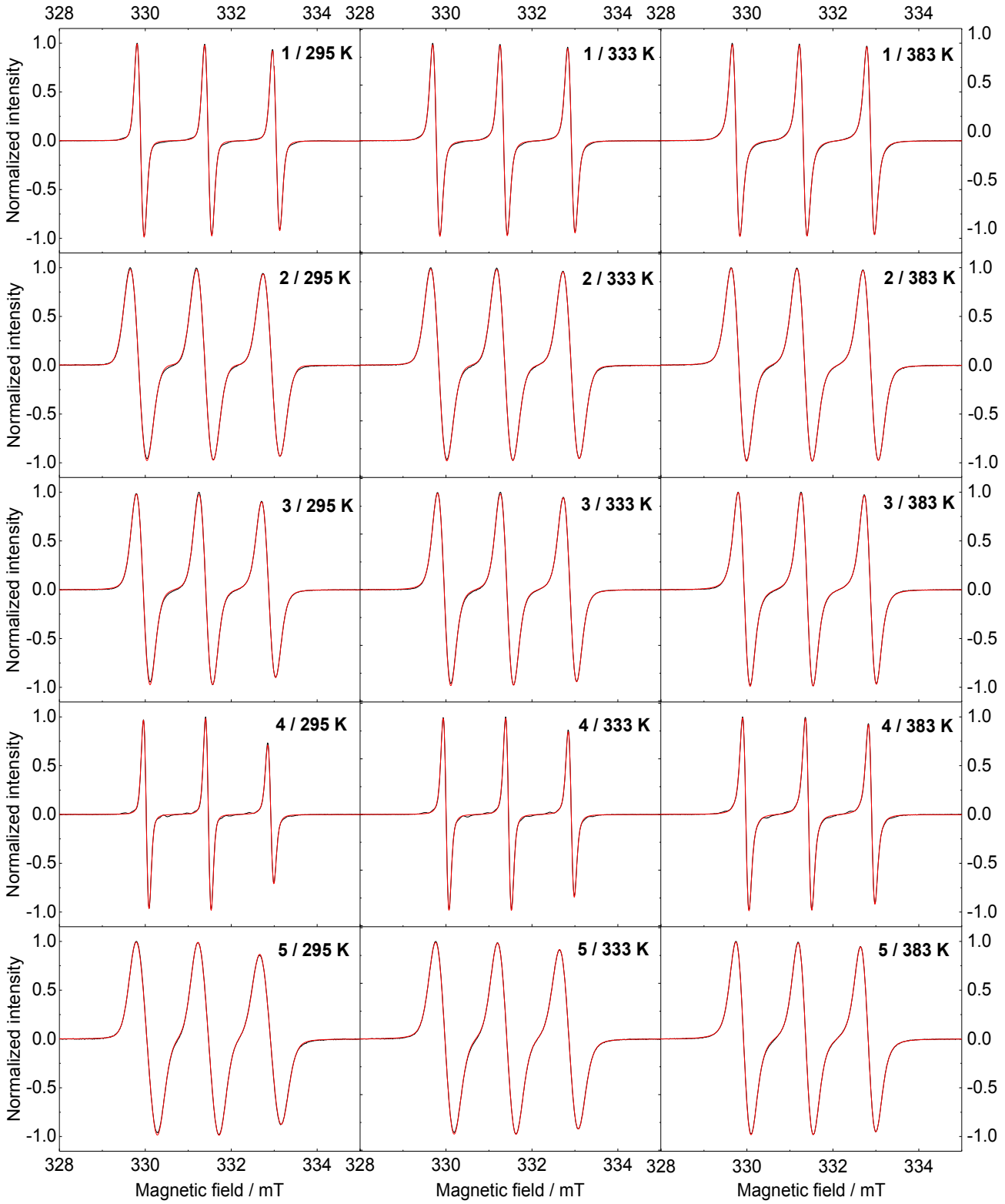

Figure S3. X-band CW EPR spectra of nitroxides **1-5** in DMSO (C = 0.5 mM) at 295, 333 and 383 K (black line) and their corresponding simulations (red line).

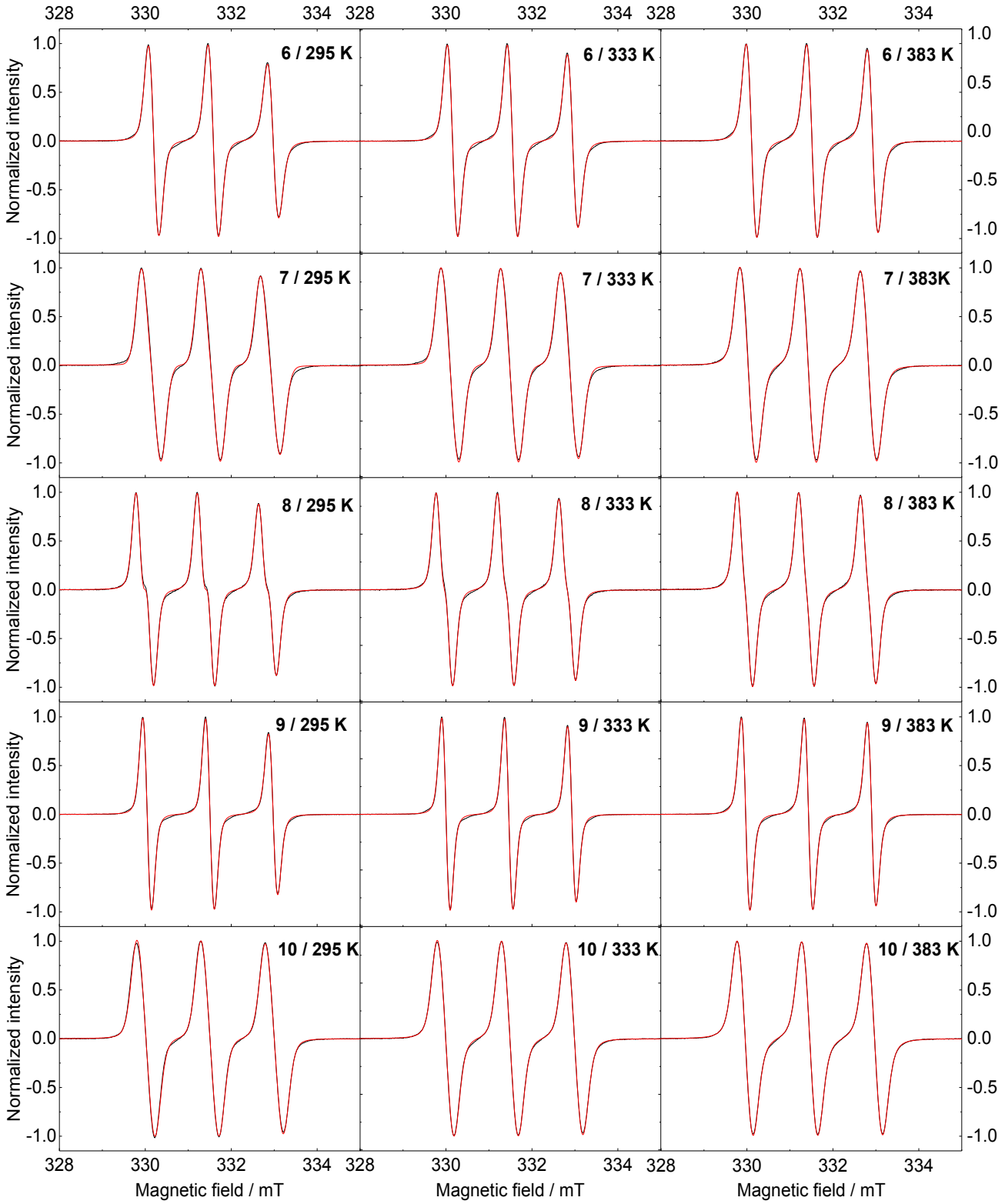

Figure S4. X-band CW EPR spectra of nitroxides **6-10** in DMSO (C = 0.5 mM) at 295, 333 and 383 K (black line) and their corresponding simulations (red line).

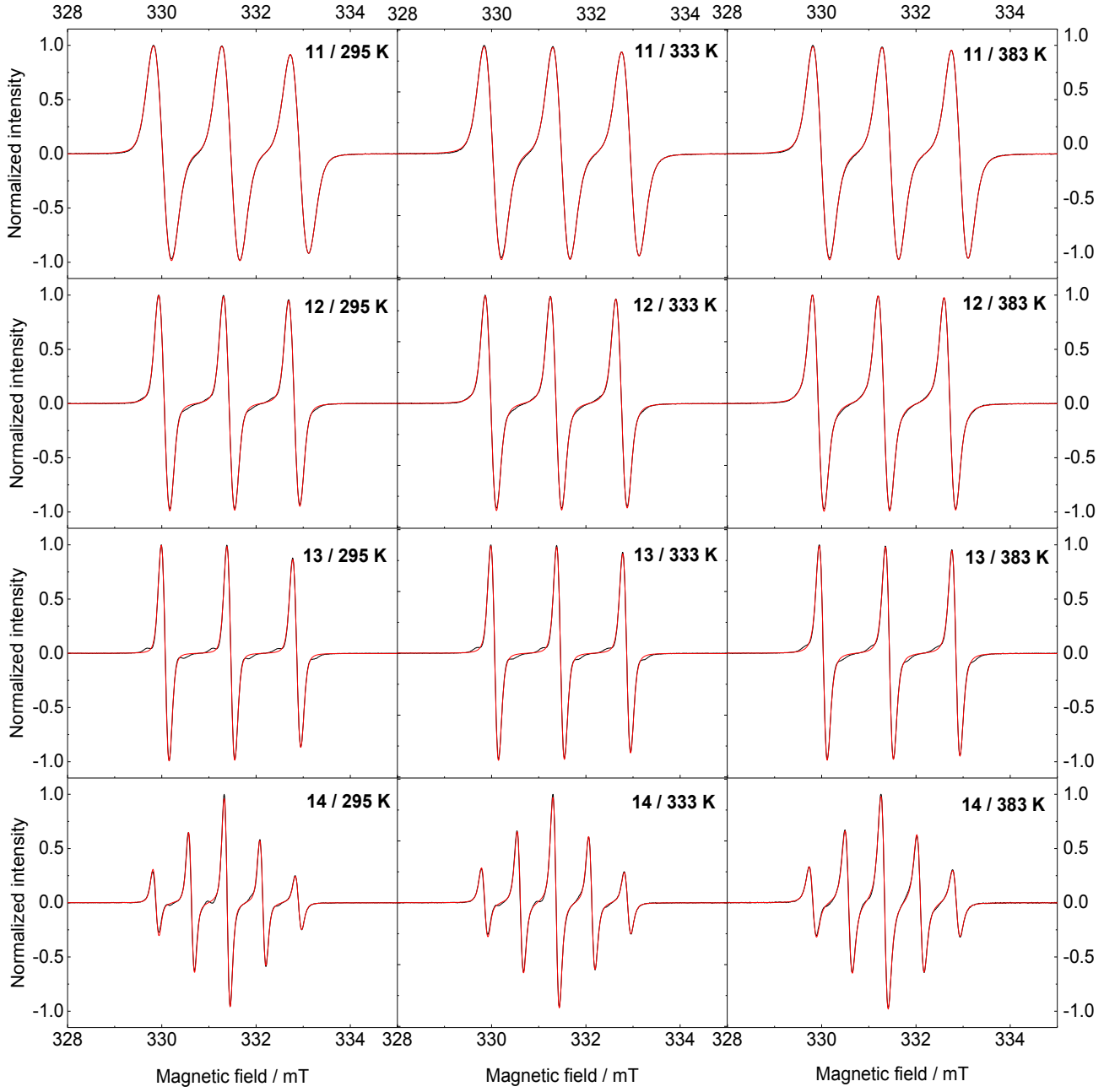

Figure S5. X-band CW EPR spectra of nitroxides **11**-**14** in DMSO (C = 0.5 mM) at 295, 333 and 383 K (black line) and their corresponding simulations (red line).

5. Temperature dependence of rotational correlation times of nitroxides

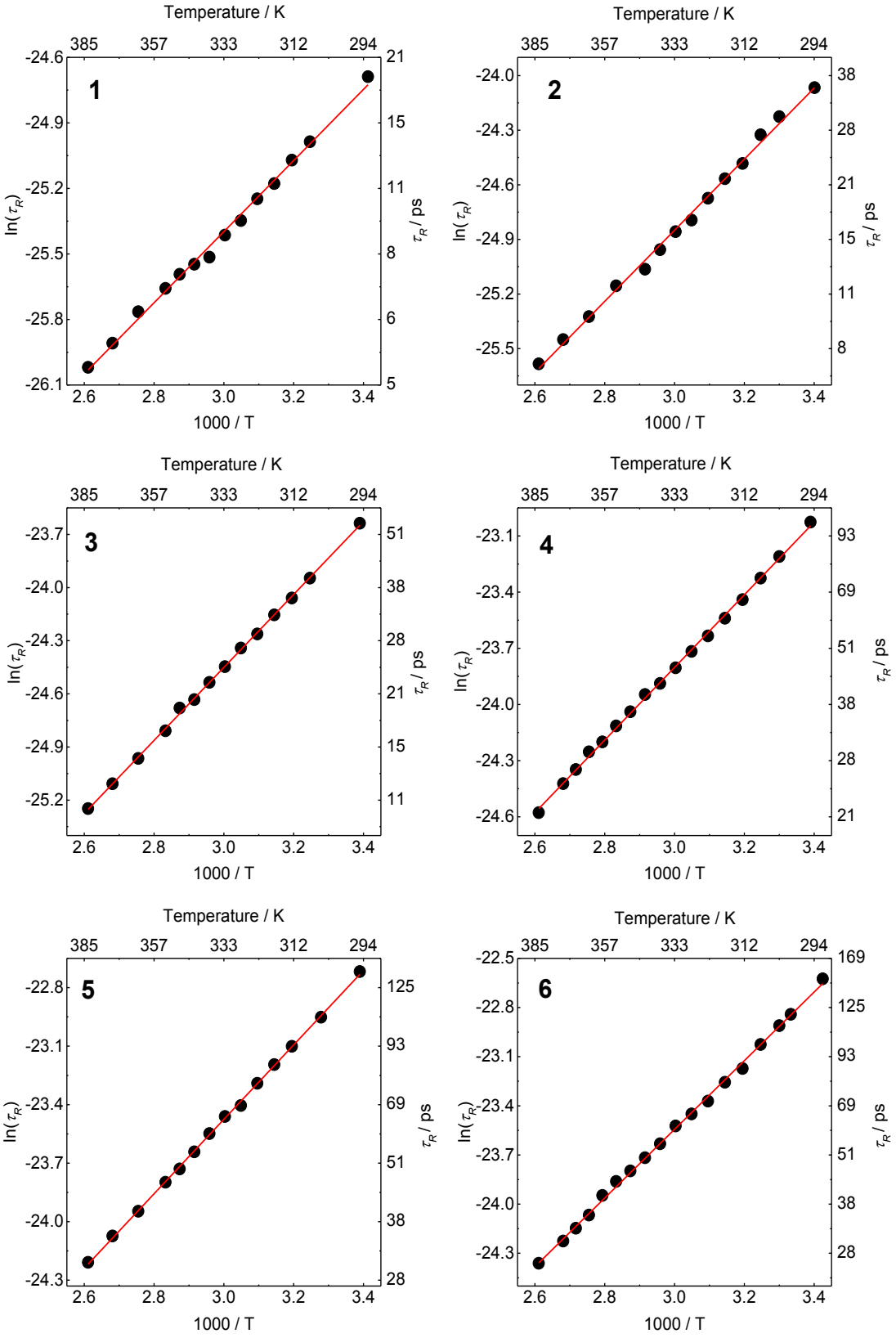

Figure S6. Temperature dependence of rotational correlation time, τ_R, for isotropic rotation of nitroxides **1-6** in DMSO obtained from simulation of X-band CW EPR spectra. Data displayed as Arrhenius plot; solid red line: linear regression giving activation energy shown in Table S1.

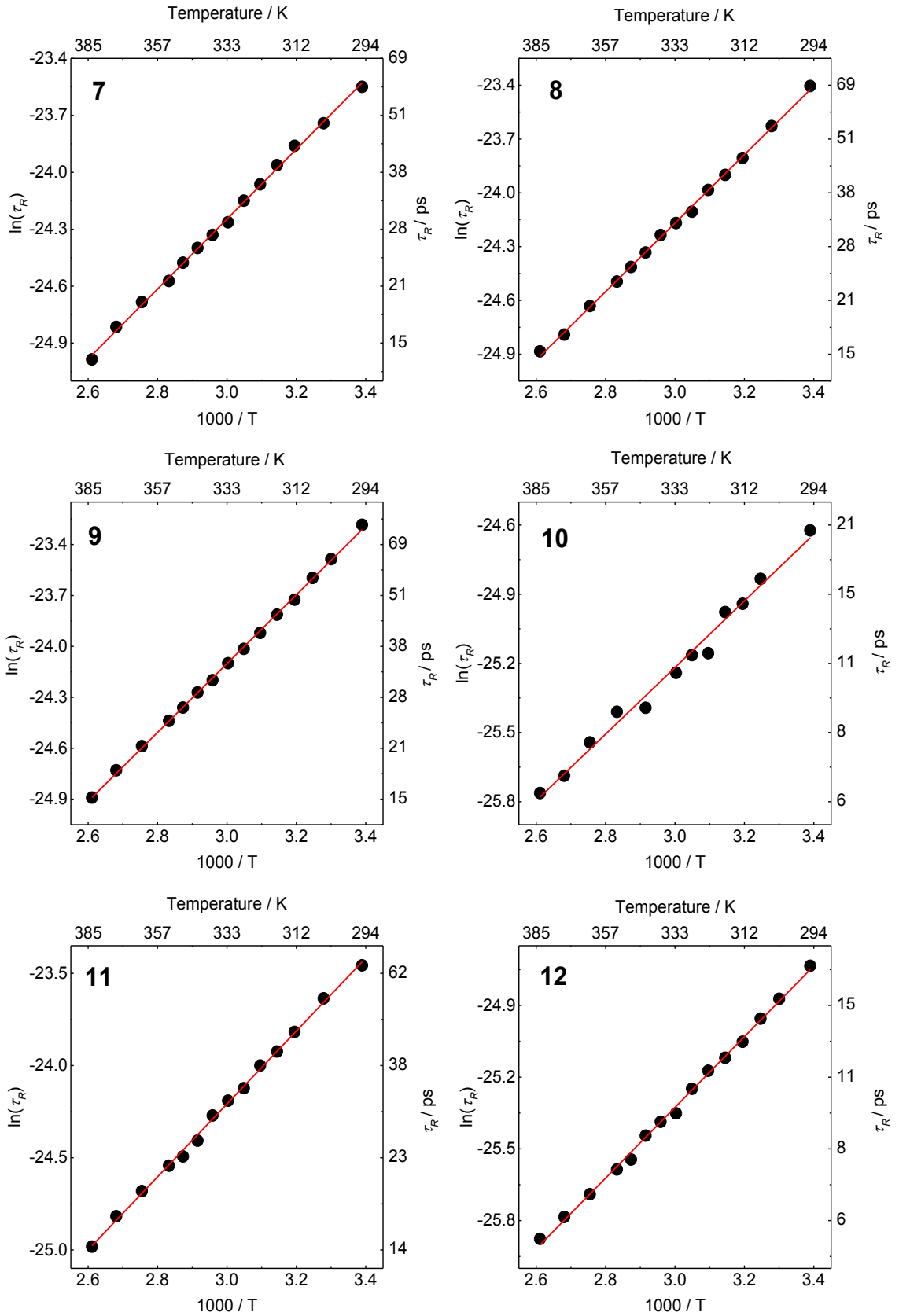

Figure S7. Temperature dependence of rotational correlation time, τ_R, for isotropic rotation of nitroxides **7**-**12** in DMSO obtained from simulation of X-band CW EPR spectra. Data displayed as Arrhenius plot; solid red line: linear regression giving activation energy shown in Table S1.

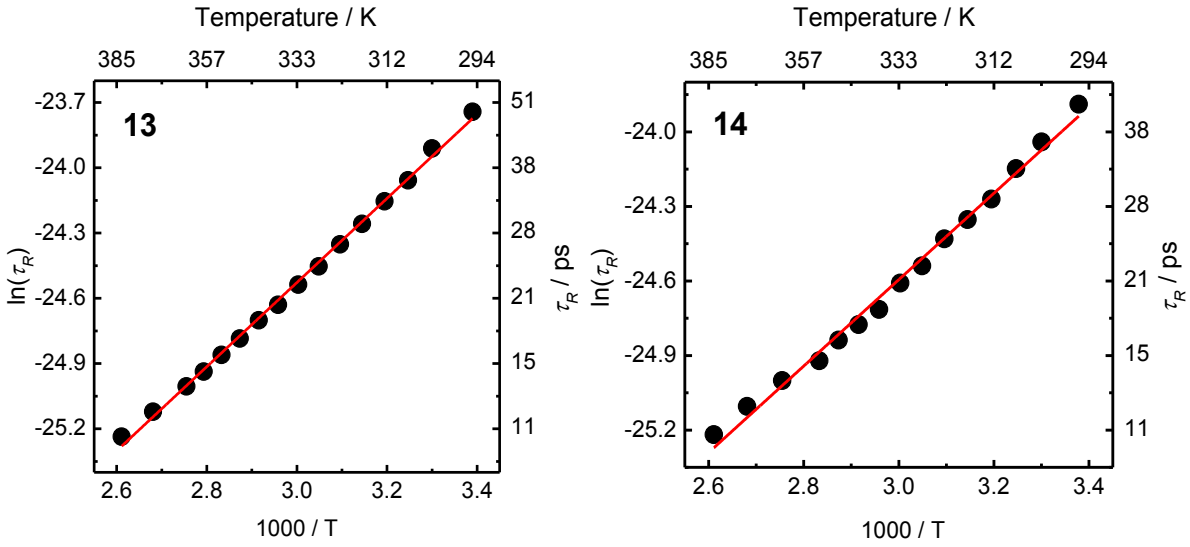

Figure S8. Temperature dependence of rotational correlation time, τ_R, for isotropic rotation of nitroxides **13** and **14** in DMSO obtained from simulation of X-band CW EPR spectra. Data displayed as Arrhenius plot; solid red line: linear regression giving activation energy shown in Table S1.

Table S1. Pre-exponent factor and Arrhenius energy for rotational correlation time of nitroxides obtained from X-band CW EPR spectra in the temperature range of 295-383 K in DMSO.

Nitroxides	$\ln(\tau_0$ / s)	E_a / kJ/mol
1	-30.28 ± 0.09	13.53 ± 0.25
2	-30.70 ± 0.10	16.23 ± 0.28
3	-30.63 ± 0.04	17.13 ± 0.12
4	-29.60 ± 0.05	16.08 ± 0.14
5[a]	-29.20 ± 0.04	15.86 ± 0.11
6	-29.83 ± 0.06	17.42 ± 0.16
7[a]	-29.77 ± 0.06	15.31 ± 0.18
8[a]	-29.90 ± 0.06	15.87 ± 0.15
9	-30.18 ± 0.05	16.85 ± 0.12
10[a]	-29.55 ± 0.15	12.01 ± 0.42
11	-30.14 ± 0.07	16.43 ± 0.20
12[a]	-29.76 ± 0.06	12.29 ± 0.16
13	-30.33 ± 0.07	16.08 ± 0.20
14	-29.81 ± 0.12	14.46 ± 0.34

[a] Additional isotropic proton HFI constants.

6. Q-band ENDOR measurements at 50 K in DMSO

Information about the hyperfine interaction of the electron spin of the nitroxide with the nuclear spins close by can be obtained by ENDOR spectroscopy. To detect the hyperfine coupling to the DMSO proton spins the Q-band pulsed ENDOR experiments were performed in protonated and deuterated solvents in order to separate the hyperfine signals resulting from the protons of the radical itself and the solvent protons. Q-band Davies ENDOR experiments were done at 50 K in pure DMSO and DMSO-d6. Most of the here studied nitroxides aggregate at low temperature in DMSO (see for example the echo detected field-swept spectra for nitroxides **2-5**, **7**, **12**, **14** in figures S9-12). In order to study the influence of radical aggregation on the pulsed ENDOR results we performed Davies ENDOR experiments also in a mixture of DMSO and ethylene glycol-d6 for the two representative radicals **12** and **14** (Figure S12). We observed the same shapes for the ENDOR spectra for nitroxides **12** and **14** and only different intensities of the lines in pure DMSO and the mixture of DMSO with ethylene glycol-d6. Thus, we concluded that nitroxide aggregation mainly effected the relative intensity of the ENDOR lines but did not change the hyperfine couplings strengths. Comparison of the Davies ENDOR spectra obtained in protonated and deuterated solvents showed that the observed large hyperfine couplings > 1.2 MHz corresponded to the radical protons and the smaller hyperfine couplings ≤ 1.2 MHz corresponded to the DMSO solvent protons. As can be seen, the hyperfine couplings between the electron spin and the protons of radical itself depend on the specific nitroxide structure, whereas the couplings between the electron spin and the solvent protons are practically the same for all studied nitroxide. Simulation of the observed pattern for the small hyperfine couplings ≤ 1.2 MHz resulted in dipolar coupling strengths of T = 1.2 MHz and 0.49 MHz and an isotropic couplings strength of a_{iso} = 0 (Figure S9). Assuming a localized electron spin (point-dipole model), the distance between the nitroxide and solvent proton is given by:

$$T = \frac{\mu_0}{4\pi h}\left(\frac{g_e g_N \mu_B \mu_N}{R^3}\right) = 79.2/R^3$$

where μ_0 is the vacuum permeability, h is the Planck constant, g_e and g_N are the electron and proton g-values, μ_B and μ_N are Bohr and nuclear magneton, R is the distance between electron and proton in Å. Therefore, a dipolar coupling of T = 1.2 MHz and 0.49 MHz corresponds to distances of 4.0 Å and 5.4 Å, respectively.

In order to confirm the small dipolar couplings between the electron spin of the radical and the solvent protons, we also performed Q-band Mims ENDOR measurements for five of the nitroxides (Figure S13), which are more sensitive to weakly coupled nuclei with small hyperfine coupling constants < 2 MHz. Since the Mims ENDOR experiment has blind spots dependent on the time τ (the delay between the first two $\pi/2$ pulses), we performed the measurements with different τ values and added all individual spectra (Figure S13). The Mims ENDOR spectra agree very well with the Davies ENDOR spectra. Thus, the ENDOR measurements confirm that the distances between the electron spin of the radical and the DMSO protons are very similar for all studied nitroxides. This agrees well with previous ^{1}H NMRD and molecular dynamics studies of piperidine and pyrroline nitroxides.[7]

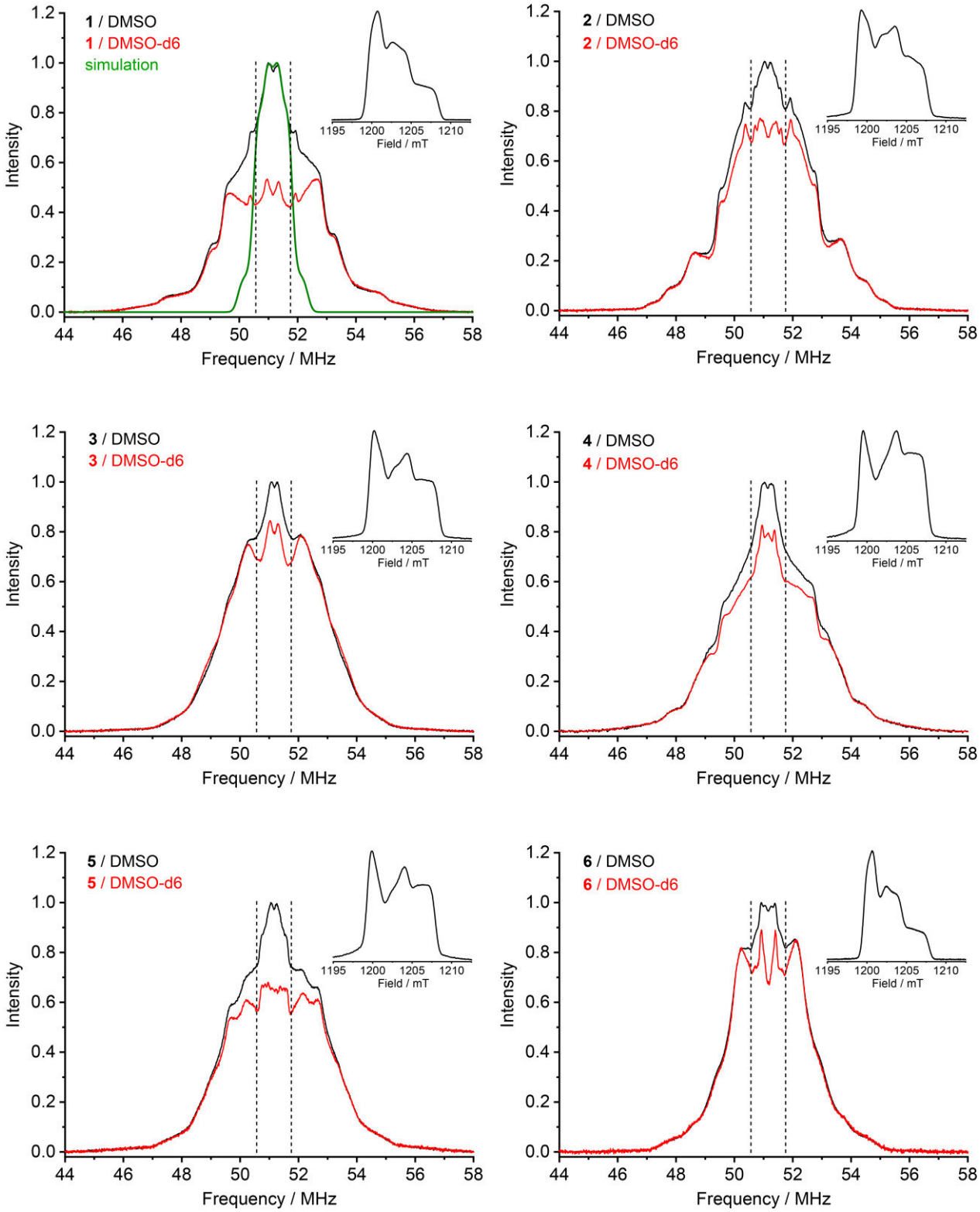

Figure S9. Q-band Davies ^{1}H ENDOR spectra at 50 K for nitroxides **1-6** in DMSO (black line), DMSO-d6 (red line) and simulated spectrum (green line). The vertical straight lines show the boundaries for solvent protons corresponding to 1.2 MHz. The inserts show the echo detected field-swept EPR spectra in DMSO.

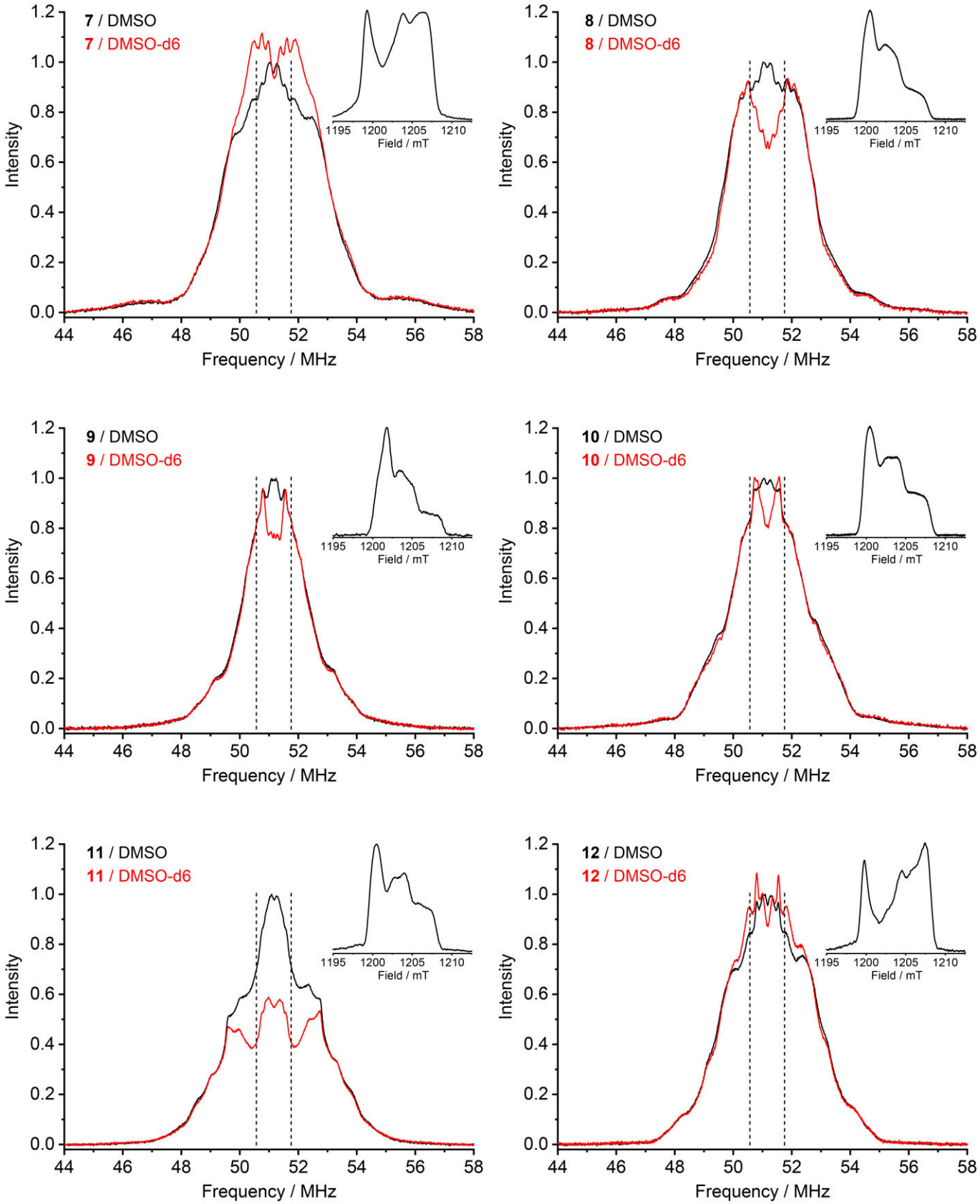

Figure S10. Q-band Davies ^{1}H ENDOR spectra at 50 K for nitroxides **7-12** in DMSO (black line) and DMSO-d6 (red line). The vertical straight lines show the boundaries for solvent protons corresponding to 1.2 MHz. The inserts show the echo-detected field-swept EPR spectra in DMSO.

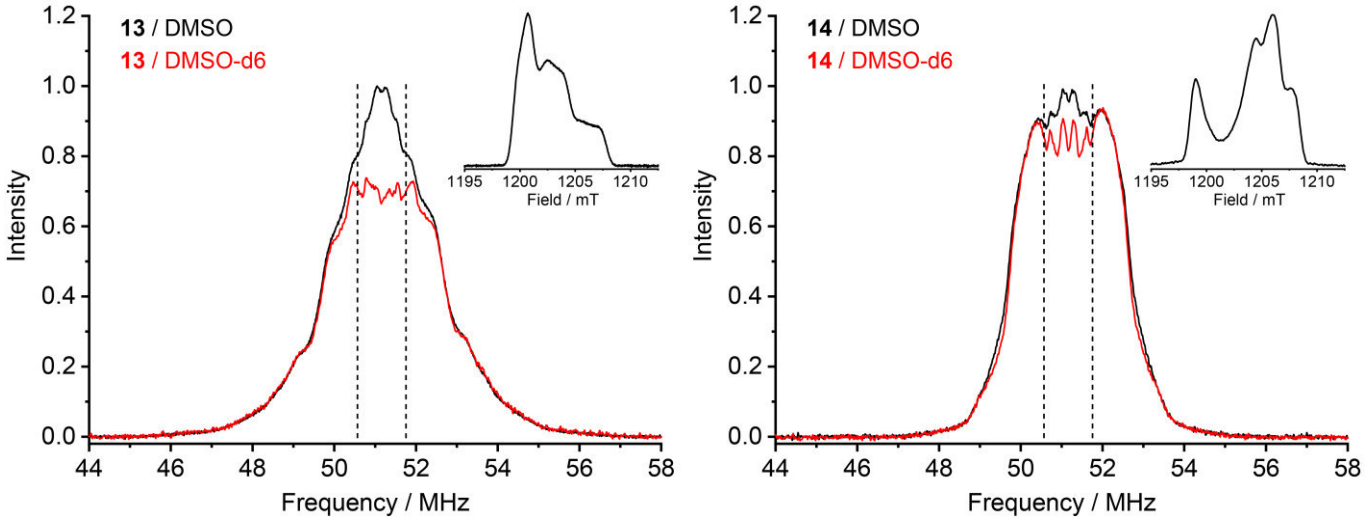

Figure S11. Q-band Davies ^{1}H ENDOR spectra at 50 K for **13** and **14** nitroxides in DMSO (black line) and DMSO-d6 (red line). The vertical straight lines show the boundaries for solvent protons corresponding to 1.2 MHz. The inserts show ED EPR spectra in DMSO.

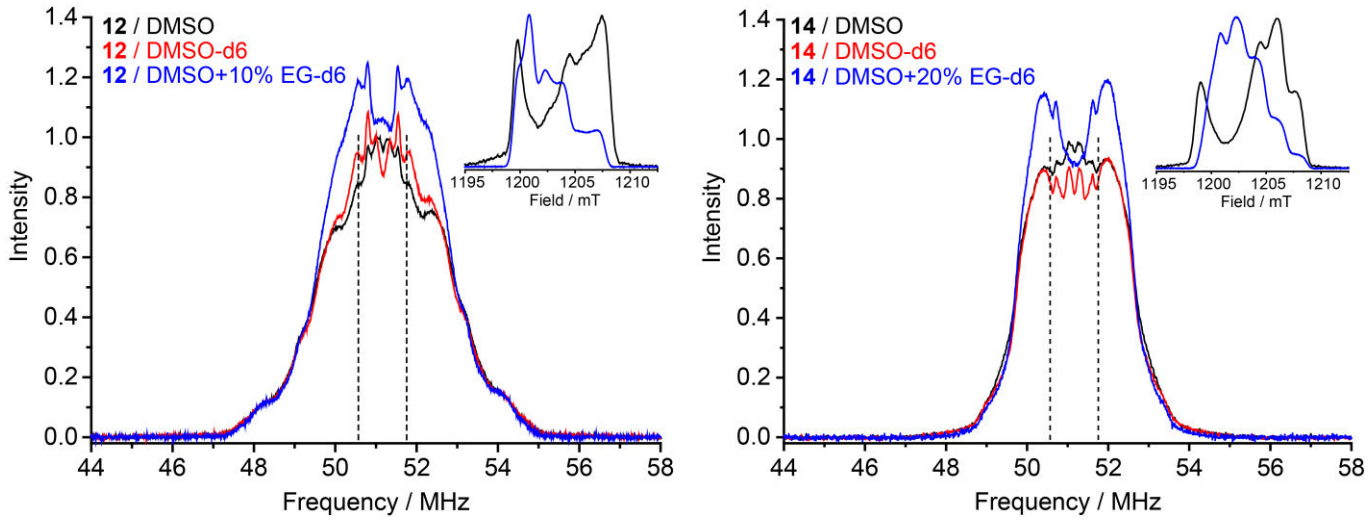

Figure S12. Q-band Davies ^{1}H ENDOR spectra at 50 K for nitroxides **12** and **14** in DMSO (black line), DMSO-d6 (red line) and DMSO + ethylene glycol-d6 (EG-d6) (blue line). The vertical straight lines show the boundaries for solvent protons corresponding to 1.2 MHz. The inserts show echo-detected field-swept EPR spectra in DMSO (black line) and in DMSO + ethylene glycol-d6 (blue line).

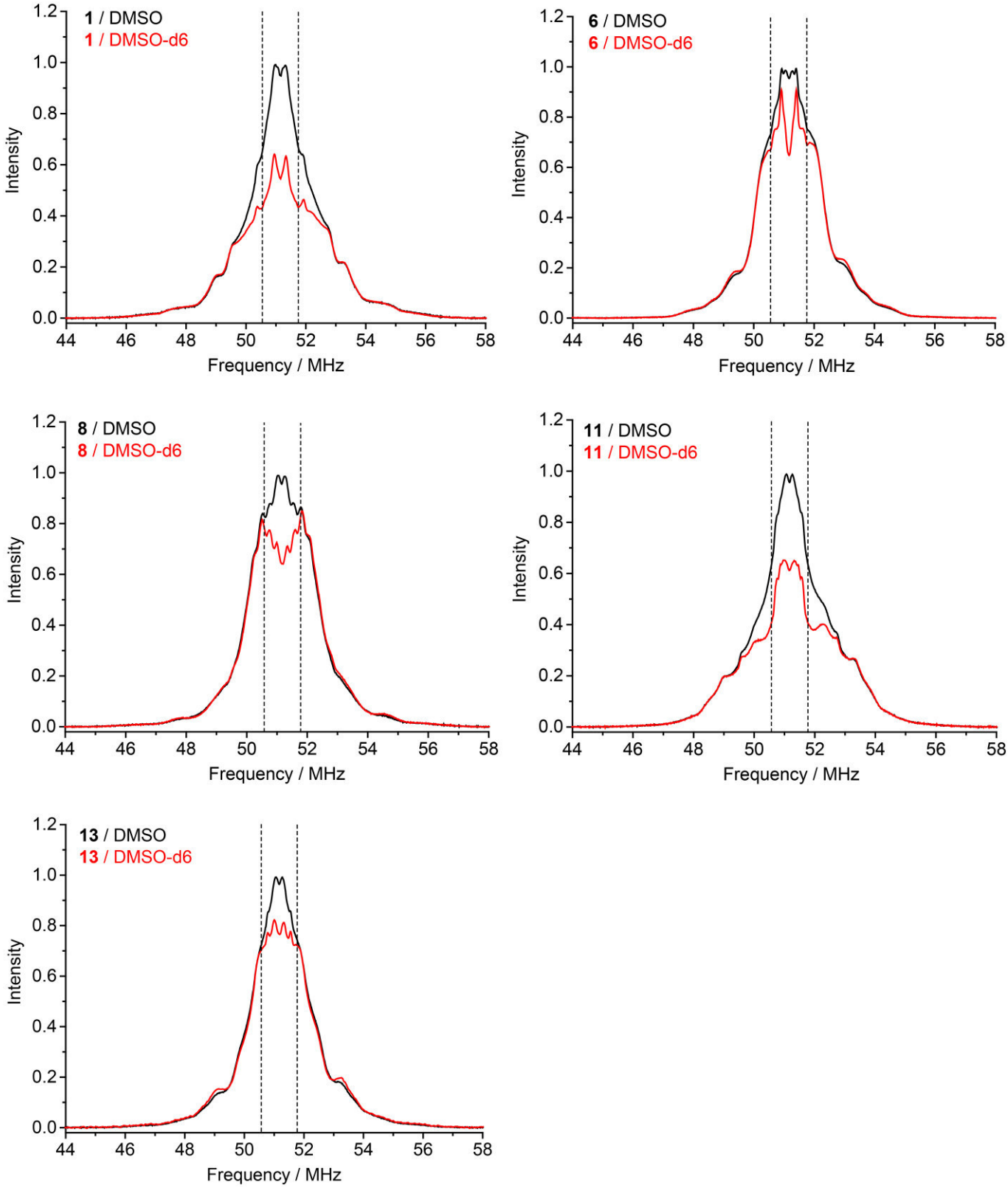

Figure S13. Q-band Mims ^{1}H ENDOR spectra at 50 K for nitroxides **1**, **6**, **8**, **11** and **13** in DMSO (black line) and DMSO-d6 (red line). The shown spectra are the sum of spectra measured with τ = 150 – 390 ns. The vertical straight lines show the boundaries for solvent protons corresponding to 1.2 MHz.

7. X-band ESEEM measurements at 50 K in DMSO

ESEEM measurements were performed at X-band frequencies using a stimulated echo sequence. The proton spin intensity resulting from the Fourier transformed time traces is show in Figure S14. For all nitroxide radicals the same proton modulation depth and, therefore, the same FT proton signal intensity close to the proton Larmor frequency, was observed. This is in agreement with the ENDOR results reported above in Section 6 and demonstrates that now, differences in the weak hyperfine coupling to solvent protons exist for all the investigated nitroxides.

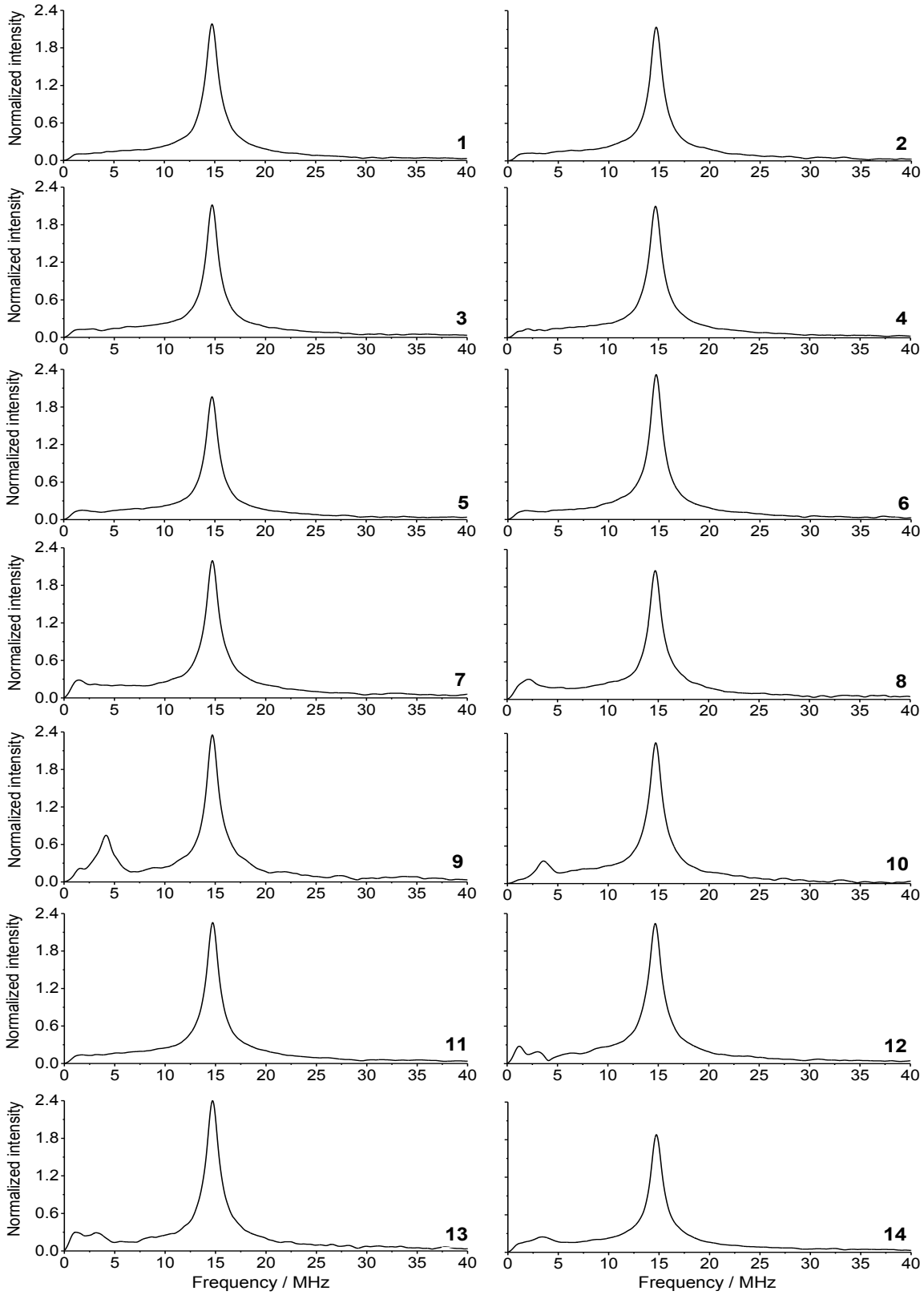

Figure S14. Normalized Fourier transformed ESEEM spectra at 50 K for the studied nitroxides (C = 0.5 mM) in DMSO.

Table S2. Intensity of ESEEM proton line for nitroxides in DMSO. Error of measurements is 10 %.

Nitroxide	ESEEM Intensity
1	2.15
2	2.13
3	2.12
4	2.10
5	1.96
6	2.32
7	2.19
8	2.06
9	2.35
10	2.25
11	2.26
12	2.24
13	2.40
14	2.07

8. DNP experiments

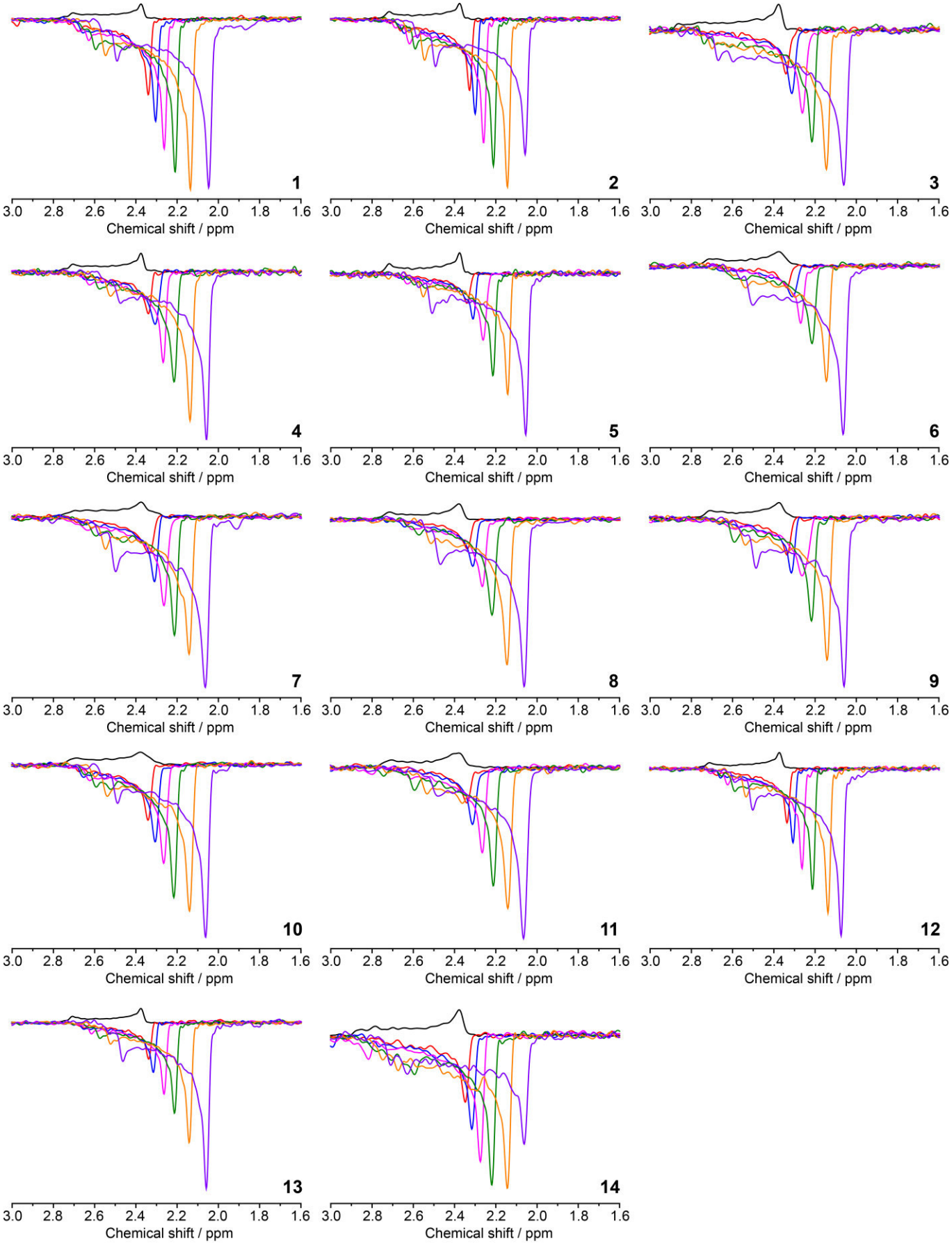

Figure S15. ^{1}H-NMR spectra for 50 mM nitroxide **1-12** in DMSO with (colored curve) and without (black curve) MW irradiation of the sample. DNP experiments were recorded at different mw power: 0.15 W, 0.19 W, 0.23 W, 0.30 W, 0.37 W and 0.47 W.

9. Sample temperature calibration

In order to determine the sample temperature under mw irradiation conditions we perform a temperature calibration using two different approaches. We used the relative shift (Δδ) between (i) the ethylene glycol peaks and (ii) the water and the DMSO peak (inset Figure S16). Figure S16a and S16d shows the evolution of Δδ (Δδ is shown in the inset) in a Bruker BBI liquid probe for DMSO with 10% of ethylene glycol and with 5% of water, respectively. The shifts Δδ(T) were fitted using linear fit for the mixture of DMSO with ethylene glycol and using a quadratic fit for the mixture of DMSO and water. Figure S16b and S16e show Δδ as a function of the mw power in the cylindrical DNP probe. It should be noted that due to the field inhomogeneity caused by the mw waveguide and the sample geometry, the solvent proton NMR signals show a distorted lineshape.[8] For each mw power, we can calculate the corresponding sample temperature using the temperature calibration Δδ(T) shown in Figure S16a and S16d. Figure S16c and S16f show the temperature dependence of the DMSO proton peak in the corresponding mixtures.

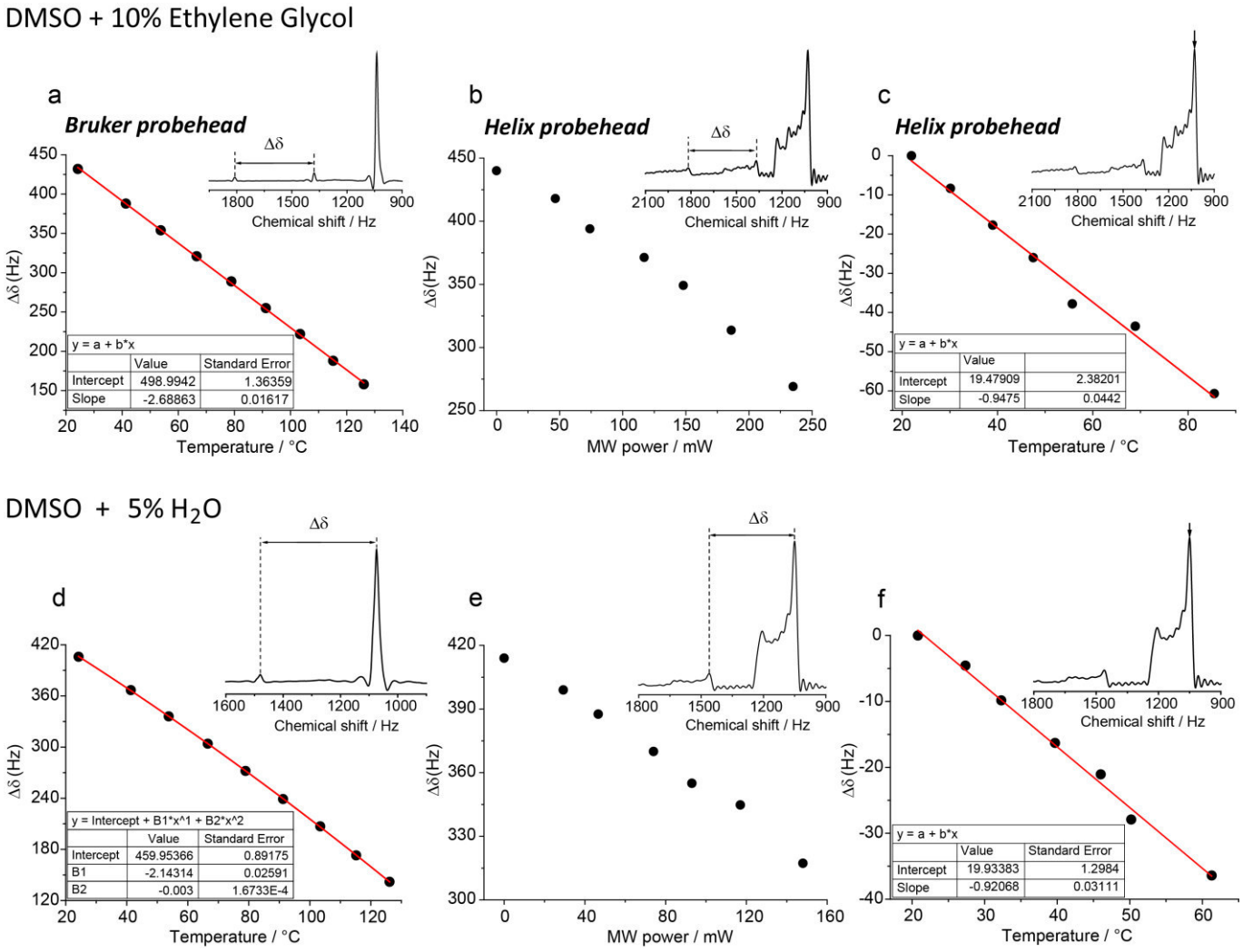

Figure S16. Temperature calibration curves for DMSO solvent. A) Differential chemical shift of 10% ethylene glycol in DMSO as a function of temperature. B) Differential chemical shift of the 10% ethylene glycol peaks as a function of applied mw power. C) Chemical shift of the DMSO proton signal as a function of temperature calibrated by the ethylene glycol partial chemical shift. D) Differential chemical shift between 5% water and DMSO as a function of temperature. E) Differential chemical shift of 5% water and DMSO peaks as a function of the applied mw power. F) Chemical shift of the DMSO proton signal as a function of temperature calibrated by using the differential chemical shift between DMSO and water. The inserts illustrate with arrows the peak positions used for the temperature calibration.

10. Saturation factor

The saturation factor was estimated via the suppression of the paramagnetic shift under mw irradiation.[9] In the DNP experiments, the NMR signal is shifted compared to the pure solvent signal, due to the paramagnetic shift, which depends on the concentration of polarizing agents. With increasing saturation of the electron spin transition, the paramagnetic shift is decreased, getting closer to the chemical shift of the pure solvent proton signal. At full saturation (s = 1) the paramagnetic shift fully disappears. Additionally, there is a shift of the DMSO proton signal under mw irradiation by the changed temperature of the solvent. A saturation curve can be obtained by subtracting the mw power dependent shift of the proton signal of the sample with 50 mM radical concentration from the curve obtained with pure solvent. The saturation curve was measured for the two nitroxides **1** and **14** with radical concentration of 50 mM in DMSO. We obtained very similar saturation curves for both nitroxides, which leads us to the conclusion that the saturation factor for a given mw power is similar for all nitroxides.

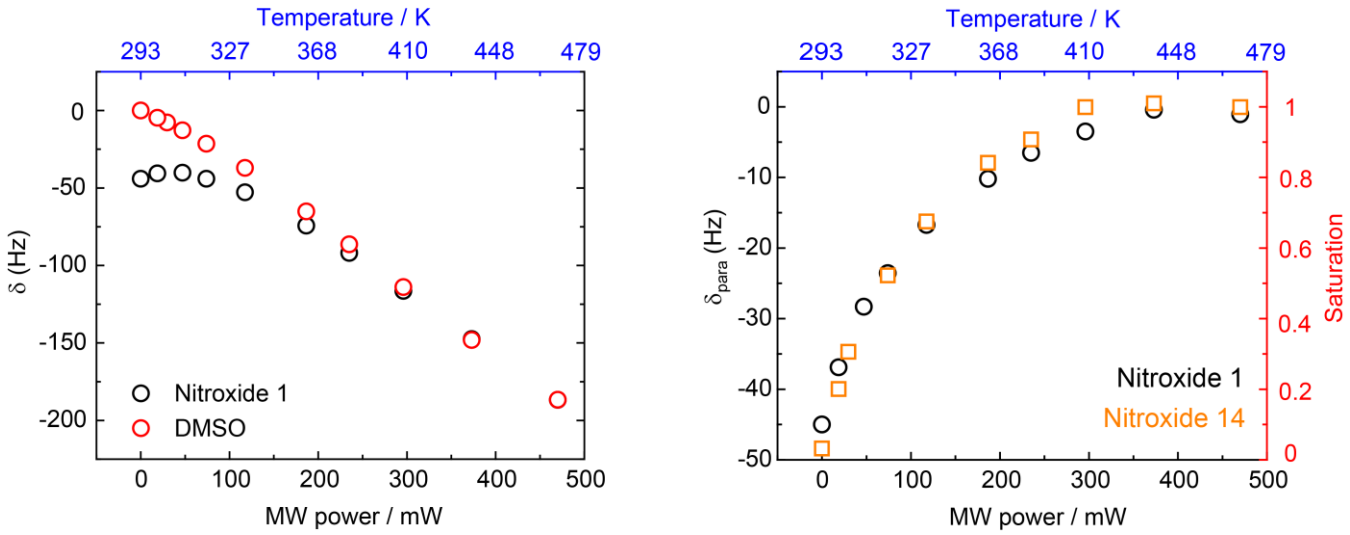

Figure S17. Suppression of the paramagnetic shift by mw excitation of the electron spin of the radical. On the left side the paramagnetic shift is shown for pure DMSO (red) and 50 mM nitroxide **1** in DMSO (black). The chemical shift change of the DMSO sample as a function of mw power allows to calibrate the sample temperature for each mw power. The difference of the line positions of the sample with and without radical is the paramagnetic shift (shown in the right panel) for 50 mM of nitroxide **1** (○) and **14** (□). For a mw power larger that 0.3 W the paramagnetic shift is fully suppressed resulting hence in a saturation factor of $s \approx 1$.

11. Concentration dependence of DNP enhancement

The concentration dependence of DNP enhancement was measured for nitroxide **1** in DMSO. The applied maximum microwave power of 0.75 W for this experiment is differed from the comparative measurements with all nitroxides **1**-**14** (0.47 W) since the quality factor *Q* of the probe head was reduced. We observed a factor of 3 larger DNP enhancements with increasing nitroxide concentration from 0.025 M to 1 M. Moreover, the obtained DNP enhancement of ε = -32 for 1 M concentration of nitroxide **1** reached under our experimental conditions (0.75 W, 50 µm capillary, T = 473 K) is comparable with previously reported results (ε = -29, 1 M, 0.5 W, 30 µm capillary, T = 453 K).[10] The slightly higher DNP enhancement under our experimental conditions is most likely related to the slightly higher sample temperature (473 K vs. 453 K) due to different capillary sizes (50 µm vs. 30 µm).

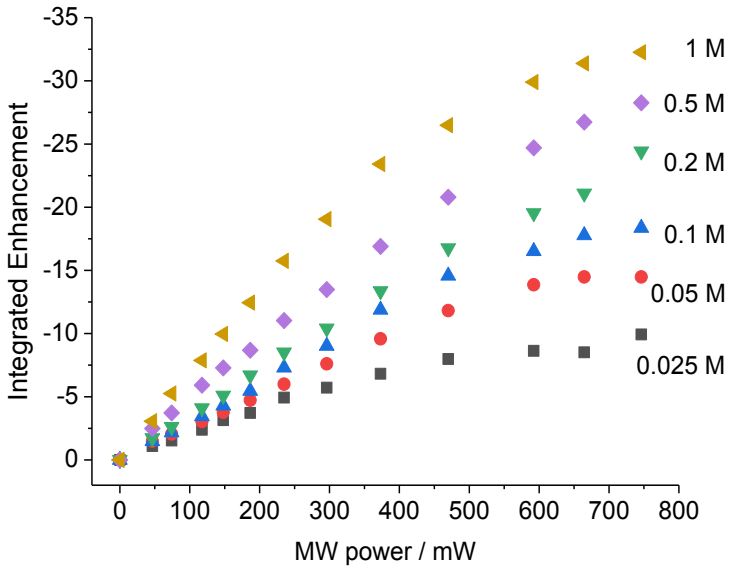

Figure S18. The DNP enhancement (from the integrated NMR line intensity) plotted against the incident MW power for nitroxide **1** in DMSO for six different radical concentrations. The capillary inner diameter is 50 µm.

12. Calculation of coupling factor

The coupling factor described by equation (2) results from two different mechanisms: the outer-sphere translational diffusion of the molecules and the inner-sphere rotational dynamics of the radical-solvent complex. For the calculation of the outer-sphere translational diffusion contribution, the overall diffusion coefficient $D = D_{Radical} + D_{DMSO}$ has to be known. Because the diffusion coefficient of the nitroxide radicals in DMSO is not known, we used two different approaches to calculate the overall diffusion coefficient D. In the first approach, we just multiplied the known diffusion coefficient of DMSO with a factor k, reflecting the translational dynamics of the nitroxide radical. For k=1 the nitroxide mobility is much lower than the mobility of the DMSO target molecule and for k=2 the nitroxide mobility is assumed to be as fast as the DMSO molecule. Here, we have chosen the same k value for all nitroxides at a given temperature (Table S3).

In a second approach, we used the Stokes-Einstein equation for rotational diffusion and the relation between translational D_t and rotational D_R diffusion coefficients to predict the nitroxide translational diffusion coefficient D_t from the experimentally determined rotational correlation time τ_R:

$$\tau_R = \frac{4\pi\eta R^3}{3k_bT}, \quad D_R = \frac{1}{6\tau_R}, \quad \frac{D_R}{D_t} = \frac{3}{4R^2}$$

where η is viscosity of the DMSO solvent[11] and R is the hydrodynamic radius of the nitroxide. In this case, the translational diffusion coefficient of the radicals (and therefore also the overall translational diffusion coefficient) depends on their rotational correlation time τ_R and on their hydrodynamic radius R.

The calculated contributions of the translational motion to the coupling factor by both methods are compared in Figure S19 for the temperature of 383 K. As can be seen, with both methods calculating the translation diffusion, an additional inner sphere rotational contribution is needed to fit the slope of the experimental data. Therefore, we have chosen the simple approach, assuming a constant translational diffusion coefficient for all nitroxides. Figure S20 shows the calculated coupling factors profiles which best fit the experimental data for different temperatures (from 348 K to 473 K). The parameters used for the calculation of the coupling factors are tabulated in Table S3. The experimentally determined coupling factors for all nitroxides follow the predicted curve rather well. Only the coupling factor determined for radical **14** at a temperature of T=473 K is rather far below the predicted curve (Figure S20).

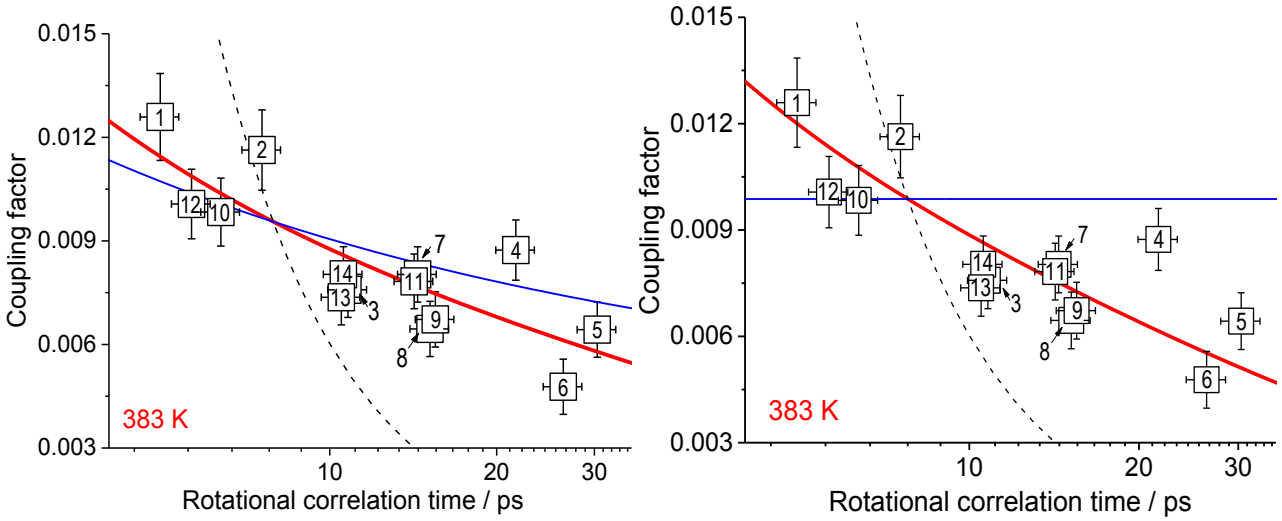

Figure S19. Comparison of calculated coupling factor with experimental measured DNP enhancements at 473 K. (left) with Stokes-Einstein equation; (right) without Stokes-Einstein equation. Coupling factor ξ^{1H} of DMSO doped with nitroxide derivatives plotted as a function of the rotational correlation time (τ_R) of the polarizing agent. Radical concentration was C ≈ 50 mM. ξ^{1H} was simulated with translational motion (blue curve), rotation motion (black dotted curve) and both translational and rotation motions (red curve).

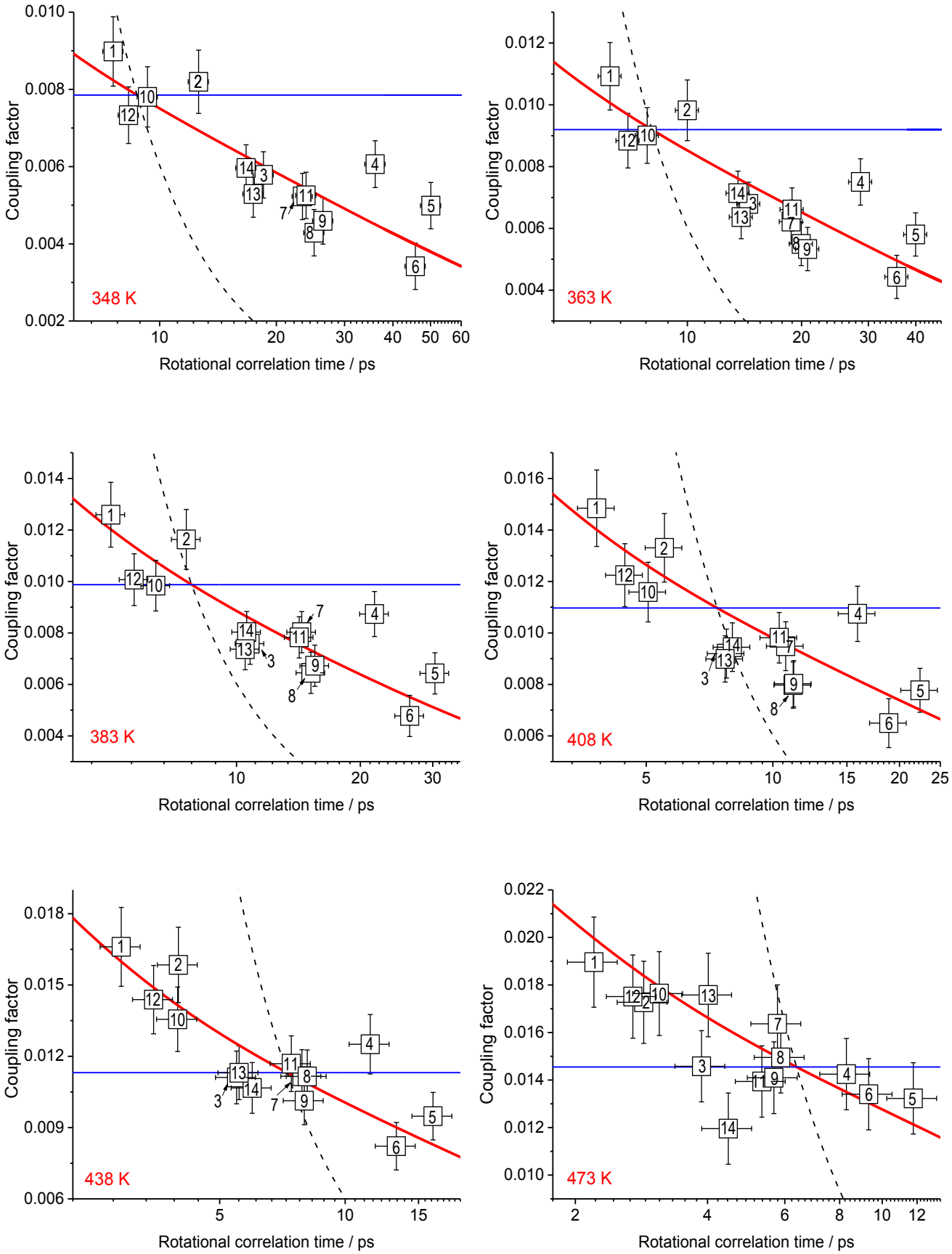

Figure S20. Comparison of calculated coupling factor with experimental measured DNP enhancements in the temperature range of 348-473 K. Coupling factor ξ^{1H} of DMSO doped with nitroxide derivatives plotted as a function of the rotational correlation time τ_R of the polarizing agent. The radical concentration was C ≈ 50 mM. The coupling factor ξ^{1H} was simulated with translational motion only (blue curve), rotation motion only (black dotted curve) and both translational and rotation motion (red curve).

Table S3. Parameters used for the calculation of the coupling factor using the hard sphere model with an inner sphere rotational contribution. The contribution of the translational diffusion to the coupling factor were calculated from the known diffusion coefficient *D* of DMSO[12] multiplied by an coefficient *k* assuming that the diffusion coefficient of the radical itself is smaller or equal (*k*=2) to DMSO.

Temperature / K	Outer-sphere translational model			Inner-sphere rotational model
	d / Å	D_{DMSO} / $\cdot 10^{-9}$ m^2/s	*k*	r / Å
348	3.68	1.85	2.00	3.60
363	3.75	2.22	1.90	3.60
383	3.75	2.75	1.65	3.50
408	3.70	3.70	1.30	3.60
438	3.80	4.90	1.00	3.60
473	3.93	6.10	1.00	3.80

For nitroxide **14** we observed a decreasing DNP signal applying very high mw power, while for all the other nitroxides the DNP enhancement still increased. Measuring the time dependence of the DNP enhanced signal (Figure S21) demonstrate that radical **14** degrades rapidly at elevated temperatures (473 K). As can been seen from Figure S21, nitroxide **1** is rather stable even at high mw power (0.47 W) and correspondently high temperature (473 K). The DNP signal decreases by 40 % within 20 min. At the same time nitroxide **14** at a mw power of 0.47 W decomposes within minutes. Therefore, at higher mw powers (resulting in higher temperatures) a quantitative comparison of the calculated coupling factor with the experimental data cannot be performed for nitroxide **14**.

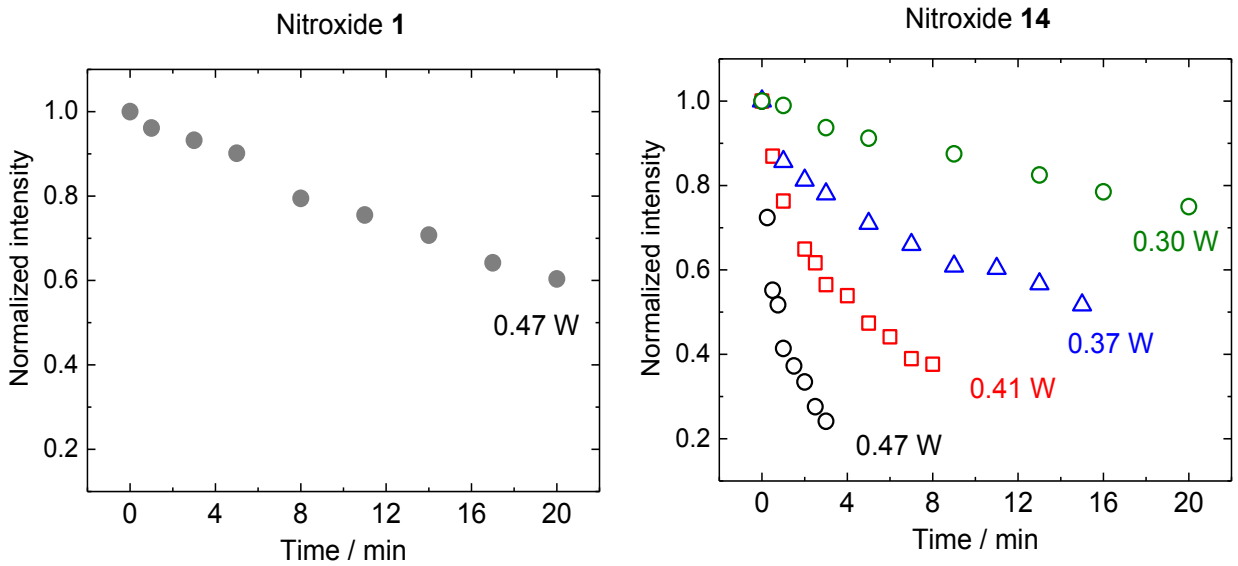

Figure S21. The stability of **1** and **14** nitroxides in DMSO at different mw power in the range of 0.3-0.47 W corresponding to the temperature from 408 K to 473 K.

References

(1) Rohrer, M.; Brügmann, O.; Kinzer, B.; Prisner, T. High-Field/High-Frequency EPR Spectrometer Operating in Pulsed and Continuous-Wave Mode at 180 GHz. *Appl. Magn. Reson.* **2001**, *21*, 257–274.

(2) Denysenkov, V. P.; Prisner, T. F.; Stubbe, J.; Bennati, M. High-Frequency 180 GHz PELDOR. *Appl. Magn. Reson.* **2005**, *29* (2), 375–384.

(3) Burghaus, O.; Rohrer, M.; Gotzinger, T.; Plato, M.; Mobius, K. A Novel High-Field/High-Frequency EPR and ENDOR Spectrometer Operating at 3 Mm Wavelength. *Meas. Sci. Technol.* **1992**, *3* (8), 765–774.

(4) Stoll, S.; Schweiger, A. EasySpin, a Comprehensive Software Package for Spectral Simulation and Analysis in EPR. *J. Magn. Reson.* **2006**, *178* (1), 42–55.

(5) Davies, E. R. A New Pulse ENDOR Technique. *Phys. Lett. A* **1974**, *47* (1), 1–2.

(6) Mims, W. B. Pulsed ENDOR Experiments. *Proc. R. Soc. London. Ser. A. Math. Phys. Sci.* **1965**, *283* (1395), 452–457.

(7) Armstrong, B. D.; Soto, P.; Shea, J. E.; Han, S. Overhauser Dynamic Nuclear Polarization and Molecular Dynamics Simulations Using Pyrroline and Piperidine Ring Nitroxide Radicals. *J. Magn. Reson.* **2009**, *200* (1), 137–141.

(8) Gafurov, M.; Denysenkov, V.; Prandolini, M. J.; Prisner, T. F. Temperature Dependence of the Proton Overhauser DNP Enhancements on Aqueous Solutions of Fremy's Salt Measured in a Magnetic Field of 9.2 T. *Appl. Magn. Reson.* **2012**, *43* (1–2), 119–128.

(9) Neugebauer, P.; Krummenacker, J. G.; Denysenkov, V. P.; Parigi, G.; Luchinat, C.; Prisner, T. F. Liquid State DNP of Water at 9.2 T: An Experimental Access to Saturation. *Phys. Chem. Chem. Phys.* **2013**, *15* (16), 6049–6056.

(10) Neugebauer, P.; Krummenacker, J. G.; Denysenkov, V. P.; Helmling, C.; Luchinat, C.; Parigi, G.; Prisner, T. F. High-Field Liquid State NMR Hyperpolarization: A Combined DNP/NMRD Approach. *Phys. Chem. Chem. Phys.* **2014**, *16* (35), 18781–18787.

(11) Messaâdi, A.; Dhouibi, N.; Hamda, H.; Belgacem, F. B. M.; Adbelkader, Y. H.; Ouerfelli, N.; Hamzaoui, A. H. A New Equation Relating the Viscosity Arrhenius Temperature and the Activation Energy for Some Newtonian Classical Solvents. *J. Chem.* **2015**, *2015*, 1–13.

(12) Holz, M.; Heil, S. R.; Sacco, A. Temperature-Dependent Self-Diffusion Coefficients of Water and Six Selected Molecular Liquids for Calibration in Accurate 1H NMR PFG Measurements. *Phys. Chem. Chem. Phys.* **2000**, *2* (20), 4740–4742.

7.3 Modelling with Off-centered Rotation

The combined model of outer-sphere translation and inner-sphere rotation predicts a clear trend of changes in OE coupling factor with varied molecular sizes and solution viscosities. Yet the physical interpretation of the obtained fitting parameters by the simplified modeling is not clear. Specifically, this model assumes a complex with a lifetime much longer as the rotational correlation time and ignores the relative locations of the spins to the molecular center, which is not necessarily applicable to all molecular systems. As presented by Okuno *et al.*,[96] the high-field ^{1}H DNP enhancements observed on the DMSO, acetone and toluene along with the NMRD (Nuclear Magnetic Relaxation Dispersion) results measured from 0.01 MHz to 950 MHz from the previous studies[76] can be readily explained using the HSOS model[40] instead of the linear combination of inner-sphere and outer-sphere model. Out of the same consideration, the HSOS model is further examined in this section.

Firstly, as shown in Figure 7. 1, the experimental DNP coupling factors of water doped with nitroxides determined at 0.34 T,[67] 3.4 T,[95] and 9.4 T[69] are compared with the values simulated with outer-sphere model and the HSOS model. The simulation parameters (*, #) are shown in the Table 5. 1. The HSOS model provides a closer match to the experimental results at 3.4 T compared with the outer-sphere model, whereas outer-sphere model better explains the results at 9.4 T. Interestingly, the coupling factor simulated with HSOS model is very close to the values predicted by the radian distribution functions (rdf) from MD simulations (△) as shown in Table 5. 1.[97]

Table 5. 1. Simulation parameters for the DNP coupling factor of TEMPOL aqueous solution with outer-sphere model[97] (*) and HSOS model (#). τ_{oc} takes the rotational correlation time of TEMPOL[98] calculated with the Stokes-Einstein equation with the viscosities of water at different temperatures[99]. Determined by the first peak appeared in the rdf from MD simulation (Δ)[97], the distance r_{H-O} between water ^{1}H and oxygen atom of TEMPOL and the distance r_{w-T} between the centers of mass of water and TEMPOL are also listed.

	298 K	308 K	318 K
D (μm^2/ms) *, #	2.7	3.4	4.2
b (Å) *	3		
r_{oc} (Å) #	2.65		
r_{cc} (Å) #	4.5		
b_{HSOS} (Å) #	1.85		
τ_{oc} (ps) #	16.6	14.4	12.5
r_{H-O} (Å) Δ	2		
r_{w-T} (Å) Δ	4.5		

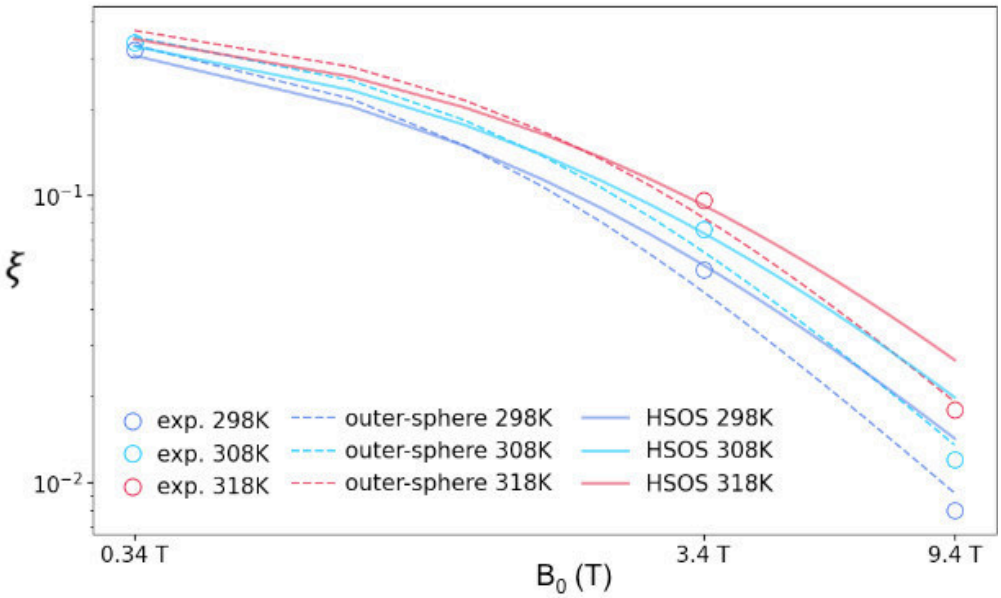

Figure 7. 1. Experimental DNP coupling factor of TEMPOL aqueous solutions measured at different temperatures and fields[67,69,95] (empty circles) compared with simulation with outer-sphere model (dashed curves) and HSOS models (solid curves).

Furthermore, the HSOS model is validated with the experimental results shown in Section 7.2. As depicted in Figure 7. 2, a quantitative match between the DNP coupling factor predicted by the HSOS model (red curve) and the experimental data, similar to what was achieved by the combined inner- and outer-sphere model (Figure 6 in the published paper), is obtained. Here the rotational correlation time determined by the cw EPR spectra is used to describe the off-centered rotation (τ_{oc}). The diffusional coefficient of DMSO at 383 K (D=2.75 μm^2/ms) used in the publication is applied. r_{oc}=3.8 Å, b_{HSOS}=2.7 Å and r_{cc}=6.5 Å is used for all radicals.

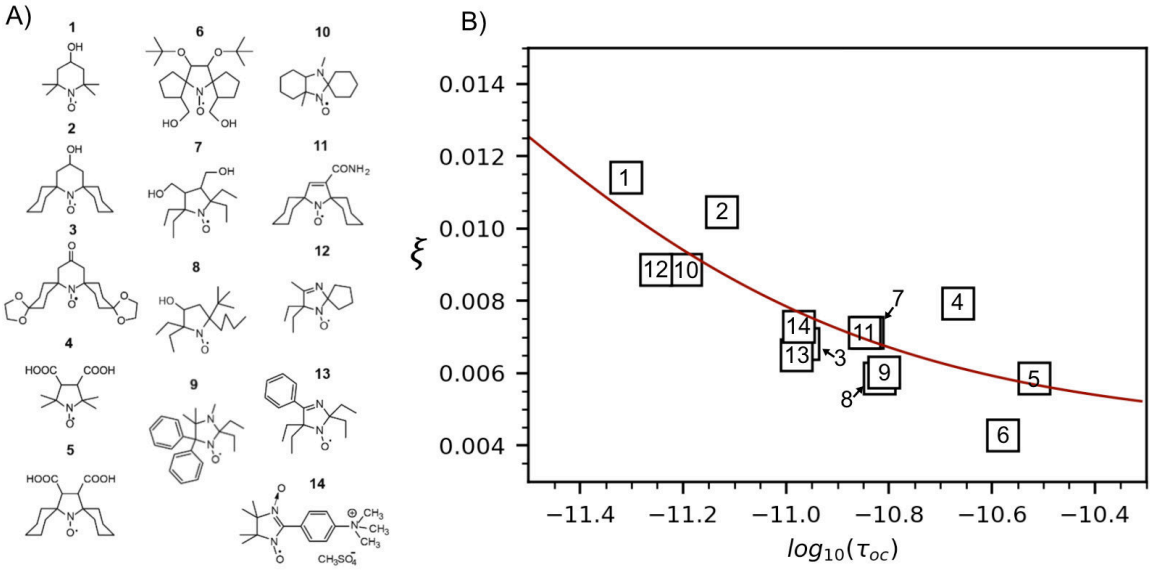

Figure 7. 2. (A) Structures of the different nitroxides used.[100] (B) Comparison of the experimental DNP coupling factors (black squares) of DMSO doped with different nitroxide radicals at 383 K with the values simulated with HSOS model (red curve)

The simulation parameters for the HSOS model, namely b_{HSOS}= 1.85 Å and r_{cc} = 4.5 Å for water, and b_{HSOS}=2.7 Å and r_{cc} = 6.5 Å for DMSO, reached a remarkably close agreement with the shortest distance between the radical oxygen and the target hydrogen as well as the distance between the centers of mass of target molecules and radical molecules determined from the rdf in MD simulations.[97,101] From these simulations, HSOS model can quantitatively predict the DNP coupling factor and provides information with more physical significance.

8. Triple-resonance DNP experiments

8.1 Introduction

With the availability of the triple-resonance (e^-, ^1H, ^{13}C) FP probehead, we have performed two experiments that combine DNP with other commonly used NMR double resonance techniques. In the paper describing the FP probeheads (Section 8.2), we have shown the ^{13}C OE DNP enhancements observed on 3-^{13}C-sodium pyruvate doped with TEMPOL under ^1H decoupling in aqueous solution. INEPT-DNP experiments were conducted on ^{13}C-labeled glycerol doped with Finland trityl as shown in Section 8.3. The ^{13}C NMR signal of glycerol was enhanced by transferring the SE DNP-enhanced ^1H spin polarization via a ^1H-^{13}C INEPT pulse sequence.

8.2 Corresponding Publication (1):

The following publication

"Denysenkov, V., Dai, D. and Prisner, T. F., A triple resonance (e, ^1H, ^{13}C) probehead for liquid-state DNP experiments at 9.4 Tesla. *J. Magn. Reson.* 337, 107185 (2022)"

is attached in the following pages.

The work was prepared in a collaborative manner. The development of the probehead and test of the DNP/NMR performance were performed by Dr. Vasyl Denysenkov. The author performed the ^1H-decoupling DNP/NMR experiments and the experiments to monitor sample temperature with/without mw irradiation.

Journal of Magnetic Resonance 337 (2022) 107185

Contents lists available at ScienceDirect

Journal of Magnetic Resonance

journal homepage: www.elsevier.com/locate/jmr

A triple resonance (e, ^{1}H, ^{13}C) probehead for liquid-state DNP experiments at 9.4 Tesla

Vasyl Denysenkov, Danhua Dai, Thomas F. Prisner *

Institute for Physical Chemistry, and Center of Biomolecular Magnetic Resonance, Goethe University Frankfurt, Max von Laue Str. 7, 60438 Frankfurt am Main, Germany

ARTICLE INFO

Article history:
Received 23 December 2021
Revised 24 February 2022
Accepted 27 February 2022
Available online 02 March 2022

Keywords:
Dynamic nuclear polarization
Nuclear magnetic resonance
Microwave resonator
Fabry-Pérot resonator

ABSTRACT

In DNP experiments, NMR signal intensity is increased by transferring the much larger electron spin polarization to nuclear spins via microwave irradiation. Here we describe the design and performance of a probehead that makes it possible to perform Overhauser DNP experiments at ^{1}H and ^{13}C in liquid samples with a volume of up to 100 nl. We demonstrate on a ^{13}C-labeled sodium pyruvate sample in water that proton decoupling under DNP conditions is possible with this new triple-resonance DNP probehead. In addition, the heat dissipation from the sample has been greatly improved with our new probe design. This makes it possible to keep liquid samples at a constant temperature under irradiation with a high-frequency 263 GHz microwave gyrotron with a few watts of output power. This improved performance opens up the possibility to disentangle the role of sample temperature and applied microwave power for DNP efficiency in liquids and to obtain a quantitative determination of EPR saturation by observing the suppression of paramagnetic shift as a function of microwave power.

1. Introduction

The sensitivity of nuclear magnetic resonance (NMR) can be improved several orders of magnitude by hyperpolarization methods. One of them, called Dynamic Nuclear Polarization (DNP), was first predicted by Albert Overhauser [1] and, shortly after, experimentally observed by Charles Slichter in metals [2]. DNP transfers the much higher spin polarization of unpaired electron spins to the target nucleus spin by microwave (mw) irradiation of electron spin transitions. It was later shown that DNP could also be applied to diamagnetic solids [3] and to liquids [4] by mixing them with paramagnetic molecules. In solid state samples, the mw drives 'forbidden' transitions to achieve polarization transfer (with a simultaneous electron and nuclear spin flip for the solid-effect or with a simultaneous flip of two electron spins and a nuclear spin for the cross effect). Such transitions become partially allowed due to the mixing of the nuclear spin states by the anisotropic dipolar interactions with the nearby unpaired electron spins. The early DNP experiments were all carried out at low magnetic field strengths (<1.5 T), where the mixing of nuclear spin states is very efficient. However, at higher external magnetic field strengths, the hyperfine field cannot compete anymore and the forbidden transitions become less efficient. Thus, high mw power (>1 W) from a gyrotron mw source and/or low temperatures (long electron and nuclear spin relaxation times) are required to efficiently drive these transitions at high magnetic fields. Substantial DNP enhancements of $\varepsilon > 300$ have been obtained for proton spins at a temperature of about 100 K with a mw power of few W at 5 T magnetic field under MAS conditions [5]. Overall enhancement factors of $\varepsilon > 10000$ have been achieved for ^{13}C spins with a mw power of 0.2 W at a magnetic field of 3.35 T and a very low temperature of 1.2 K for the hyperpolarization process [6].

In liquids at room temperature, the anisotropic dipolar interactions are averaged due to the rapid motion of the paramagnetic radical and the target molecule. Therefore, another DNP mechanism is active, in which the mw drives the allowed electron spin transitions, perturbing the electron spin populations from the Boltzmann equilibrium (saturates the EPR transitions in the optimal case). In this case, nuclear spin polarization is built up by the differences in the two cross-relaxation rates (zero quantum and double quantum transitions) between nuclear and electron spin. The cross-relaxation processes are initiated by a rapid modulation of the dipolar and scalar hyperfine interaction between electron and nuclear spin (on a time scale of the inverse electron spin resonance frequency). This process, which is effective in liquids and metals, is called Overhauser effect DNP (OE-DNP). At lower magnetic fields (<1.5 T), the translational and rotational motion of the radical and target molecules in typical liquid solutions is fast enough, which leads to a strong hyperpolarization effect [7]. Sim-

* Corresponding author.
E-mail address: Prisner@Chemie.Uni-Frankfurt.de (T.F. Prisner).

https://doi.org/10.1016/j.jmr.2022.107185
1090-7807/

ilar to solids, OE-DNP polarization transfer in liquids becomes less efficient at higher magnetic fields (>3 T), where the electron spin Larmor frequency increases into the sub-THz range (>100 GHz). The spectral density of the dynamics of the electron-nuclear spin hyperfine interaction becomes very small at such high frequencies for typical diffusion coefficients ($D < 5{\cdot}10^{-9}$ m^2s^{-1}) and rotation correlation times ($\tau_c > 10$ ps). Nevertheless, high OE-DNP enhancement of $\varepsilon > 50$ for ^1H [8] and $\varepsilon > 300$ for ^{13}C [9] at a magnetic field strength of 9.4 T and $\varepsilon \sim 1000$ at 3.4 T [10] were also achieved for liquids. They result from fast dynamics modulating the dipolar and isotropic part of the hyperfine interaction, which can be rationalized by molecular dynamics (MD) simulations [11].

However, OE-DNP in the liquid state at high magnetic fields still lags behind developments in the solid state due to technological difficulties. The main reason is the excessive mw heating of liquid samples. There are some ways to reduce this heating. One of them is to put the NMR sample in a MW resonator operating in the fundamental mode. One of the first resonators for OE-DNP at high fields was a cylindrical MW resonator in TE_{011} mode [12,13]. In this case, the sample is located at the maximum of the mw *B* field component along the resonator axis (which is necessary to drive the EPR transitions) and at the same time at the minimum of the mw *E* field component, which is responsible for the sample heating. However, this limits the sample size below the mw wavelength in 3 dimensions, which leads to a very small sample volume at high magnetic fields (few nl only at 9.4 T). This leads to an overall low NMR signal intensity and difficult sample handling. The amount of sample in the cylindrical resonator can be increased by increasing the sample tube diameter. However, this automatically exposes the sample to increasing values of the mw *E* field component, which leads to mw absorption and thus increased sample temperatures even at low mw power. Another option is to increase the mw cavity length to a higher mode, i.e. TE_{013}, which increases the active sample volume by almost 3 times [9]. However, such a modification leads to a reduced mw coupling efficiency.

Some other approaches to achieve larger sample volumes for DNP in the liquid state at high magnetic fields have been reported by other research groups. A photonic bandgap MW resonator which can handle a 5 µl aqueous sample was developed for EPR applications at magnetic field of 3.4 T [14] that can also be promising for DNP in liquids. Also a non-resonant probe head that suppresses the mw-E field by placing a Ph_3P-C_6H_5F liquid sample on a gold-plated aluminum nitrate surface with high thermal conductivity resulted in ^{31}P DNP enhancement of ~ 200 in an accessible sample volume of 10 µl at a magnetic field of 9.2 T [15]. In another publication, ^{13}C OE-DNP enhancements of 70 were reported for a slowly rotating 100 µl NMR sample tube directly exposed to 30 W of mw radiation for a solution of TEMPO in chloroform at a magnetic field of 14.1 T [16]. However, no significant proton enhancement in aqueous solution has been shown for these probes.

Another approach that we have already investigated in the past [17] and that we are also following here is the use of a semi-confocal Fabry-Pérot (FP) mw resonance structure. In this structure, only one dimension of the sample (the height) is limited to < 100 µm. In this case, the liquid sample is placed on the surface of the flat mirror, which can have a high thermal conductivity, which improves the heat dissipation from the sample to a heat sink and makes it possible to stabilize the sample temperature almost independently of the applied mw power, as we will demonstrate here. Aqueous sample volumes up to 100 nl can be used with such an oversized resonance structure, but a powerful mw source (i.e. gyrotron) is needed to efficiently saturate the electron spin transitions [17]. In such a resonance structure, the flat FP mirror can be combined with a stripline in order to excite and detect the NMR signal efficiently. Our first probehead designed in this way, consisting of an FP resonator for mw excitation and a stripline resonance structure for ^1H NMR excitation and detection, was successfully used to investigate the DNP polarization transfer from nitroxide radicals to proton core spins of ordered lipid bilayers [18]. Unfortunately, in this first version, the mw heating of the sample was still quite strong, which prevented the saturation of the EPR transitions while keeping the sample close to room temperature.

Classically, the OE-DNP enhancement ε can be described by the following formula:

$$\varepsilon = f \cdot \xi \cdot s \cdot \frac{\gamma_e}{\gamma_I} \tag{1}$$

where the leakage factor *f* depends on the radical concentration and the saturation factor *s* on the applied mw power. The DNP coupling factor ξ describing the efficiency of the polarization transfer process under ideal conditions ($f = s = 1$). For dipolar coupling the DNP coupling factor can in the best case (low magnetic fields) become $\xi = 0.5$, resulting in a DNP enhancement given by the ratios of the electron and nuclear gyromagnetic ratios (γ_e and γ_I respectively).

The leakage factor can easily be experimentally determined by measuring the nuclear spin relaxation time T_1 with and without the radical present. The saturation factor is typically determined by recording either the EPR signal intensity I_{EPR}, the DNP enhancement ε [4] or the paramagnetic shift δ_{para} of the NMR line (at high enough magnetic fields) [19] as a function of the applied mw power P_{mw}. Unfortunately, if the sample temperature rises as a function of the applied mw power, all these methods cannot provide quantitatively evaluable saturation curves and reliable saturation values. In addition, the other parameters (f, ε, ξ) also depend on the temperature. This makes it difficult to quantitatively compare the coupling factor ξ derived from the DNP experiments with predictions from the classical hard-sphere model [20], NMR dispersion measurements [21] or from MD simulations [22].

Here we present a newly developed triple resonance probe designed to perform OE-DNP experiments with two NMR channels. The probe operates at the resonant frequencies of 263 GHz (electron spin), 400 MHz (^1H) and 100 MHz (^{13}C), so that 2-D NMR experiments can be performed with other low-γ nuclei involved. In addition, this probe was developed for more efficient cooling of the liquid sample in order to keep the temperature of the sample stable regardless of the applied mw power. This also improves sample handling and makes the DNP experiments more reproducible.

2. Development of the triple-resonance probe for liquid samples

The new triple resonance structure is a combination of a coplanar line used as the actuator and detector at two RF frequencies (^1H and ^{13}C) and a semi-confocal Fabry-Pérot resonator at 263 GHz, as shown in Fig. 1. The coplanar line consists of 3 parallel metal strips: ground-signal-ground, designated as G-S-G in Fig. 1.

The surface of the 3 mm wide signal strip (S) also serves as a flat mirror of the Fabry-Pérot resonator. The plane of the flat mirror is orthogonal to the magnetic field direction B_0. Up to 100 nl of liquid sample can be placed on the flat mirror centered below the elliptically curved second mirror used for mw irradiation through a small iris of 0.5 mm diameter.

The volume of a liquid sample (Fig. 2) is defined by the height and inner diameter of the sample holder ring made of a 0.02 mm thin PTFE film (in this study OD 3 mm, ID 1.5 mm). The sample diameter is limited by the Gaussian profile of the mw field on the flat mirror (see Fig. 2). Its height must be chosen small enough to avoid excessive heating of the sample by microwaves due to the dielectric losses and to keep the mw coupling close to the critical

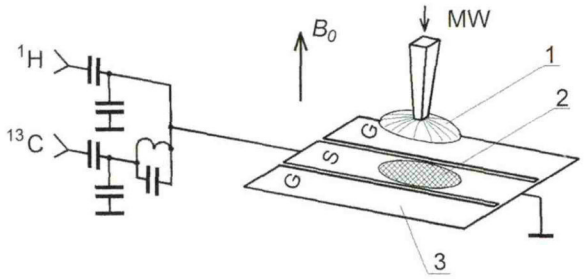

Fig. 1. Schematics of the probehead capable to resonantly excite the liquid sample at 3 frequencies simultaneously: ^{1}H nuclear spins at 400 MHz, ^{13}C nuclear spins at 100 MHz, and electron spins at 263 GHz. 1- elliptical mirror; 2- sample; 3- stripes of the coplanar line (GSG: ground-signal-ground). C1 and C2 are trimmer capacitors to tune the ^{1}H channel; C3 and C4 trimmers to tune the ^{13}C channel. The parallel circuit consisting of C5 and L1 is used as a notch-filter tuned to 400 MHz.

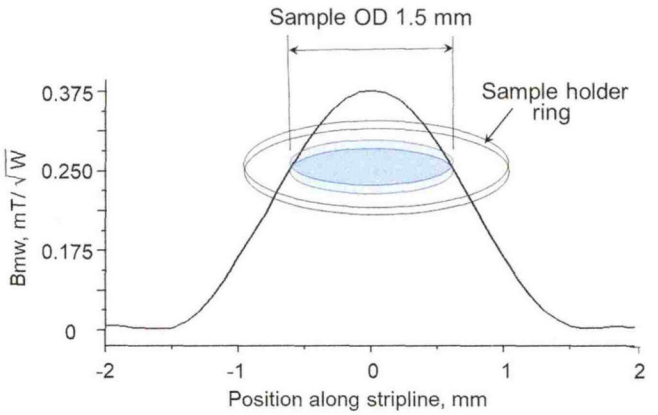

Fig. 2. Microwave magnetic field strength distribution over the disc shaped liquid sample on top of the flat mirror inside the Fabry-Pérot resonator. The aqueous sample has a diameter of 1.5 mm and a height of 20 μm. The sample diameter of 1.5 mm was chosen to be equal to the mw beam waist defined by the Gaussian distribution on the flat mirror.

value. For a liquid water sample, this was achieved with a film height of 20 μm. This gave a total volume of about 35 nl for the liquid sample. The sample holder ring is covered with a 0.15 mm thin quartz plate.

The design of the parts of the probehead close to the sample (Fig. 3a) was made of copper in an in-house machine shop. The new probe is designed to be compatible with our previously developed DNP probe [17]. Thus, we were able to use the existing probe frame and the oversized metal dielectric waveguide with the elliptical mirror of OD = 4 mm and the mw frequency tuning mechanics for the newly developed triple resonance probehead. Therefore, we were able to achieve a similar mw conversion factor as in the previous probehead. The coplanar line of a 6.5 μm copper/gold layer is deposited by thin-film metallization on a 1 mm thick aluminum nitride (AlN) substrate (Fig. 3) as a ceramic with high thermal conductivity (L.E.W. Techniques, UK). It has very low dielectric losses at high frequencies and much higher thermal conductivity (170–220 W/m * K) [23] compared to previously used alumina (20–30 W/m * K) and quartz glass (1.4–1.6 W/m * K). The back of the metallized ceramic substrate was soldered with indium to the copper support frame to further improve the heat dissipation. Thus, the sample temperature can be controlled by means of the variable temperature controller of the Bruker AVANCE NMR console, blowing nitrogen gas along the structure, as shown in Fig. 3a.

Finite element simulations using the CST Microwave Office showed that the two grounded stripes collinearly aligned with the rf currents can concentrate the B_{rf} field inside the space between the signal stripe and the spherical mirror (Fig. 3b) and that B_{rf} field amplitude is rather homogeneous over the disc-

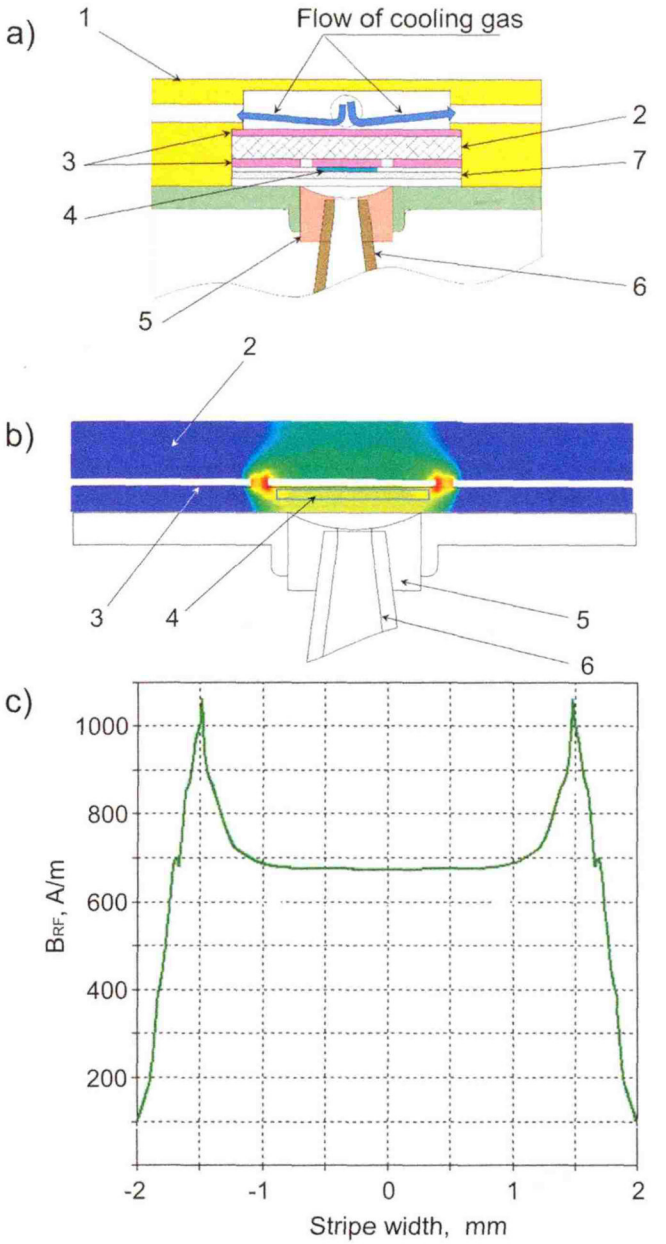

Fig. 3. Layout and radiofrequency magnetic field simulations (proton frequency) of the DNP probe: (a) design of the triple resonance structure. 1- housing, 2- ceramic AlN substrate, 3- copper/gold layer (the lower one is used as the coplanar stripline and the flat mirror of the FP, the higher one is used as ground) 4- sample, 5- elliptical mirror of the FP resonator, 6- mw waveguide taper and iris, 7- quartz cover plate for the sample. (b) CST simulated B_{rf} field distribution across the coplanar line inside the housing block. (c) B_{rf} field distribution at the surface of the stripe (shown above) for 1 W of applied rf power at 400 MHz.

shaped sample (Fig. 3c). The expected rf conversion factor at ^{1}H and ^{13}C frequencies is 10 kHz/W$^{1/2}$, and 2.5 kHz/W$^{1/2}$ respectively. The expected B_{mw} field strength of the Fabry-Pérot resonator with a mode of TEM_{004} is in the range of 4–4.5 G for the available mw power of 3 Watts at the resonator.

3. Experimental results and discussion

3.1. Performance of the rf and mw channels

The assembled probehead (Fig. 4) was experimentally tested on the home-built 9.4 Tesla DNP spectrometer, designed specifically for liquid samples [24].

Microwave power from a 12 W/263 GHz gyrotron source (GYCOM; Russia) is transmitted to the spectrometer over a 4 m long corrugated waveguide with total mw losses of 3 dB, resulting in about 4.5 W of mw power at the probe inlet, monitored by a PM-4 mw power meter (Virginia Diodes, USA). The Fabry-Pérot (FP) resonator described above was tuned to the TEM_{004} operation mode. The mw is coupled into the resonator through an iris with a fixed diameter of 0.5 mm, leading to a variable mw coupling depending on sample properties such as thickness and/or loss-tangent of the solvent at 263 GHz. The quality factor of the ^{1}H rf circuit and the ^{13}C rf circuit was determined to be 84, and 59 respectively, and for the FP mw resonator a $Q_{mw} = 150$ was achieved with the water sample, which is slightly below the calculated values, due to manufacturing imperfections. The ^{1}H NMR performance of the new probehead was tested also with a 300 mM ^{14}N-TEMPOL (Sigma Aldrich) solution in deionized water without degassing. A 35 nl droplet of the solution was placed on top of the signal stripe inside the sample holder. The optimal ^{1}H NMR $\pi/2$ pulse length has been determined to be 25 μs at 1 W of applied rf power, resulting in a rf conversion factor of $C_{rf} = 10$ kHz/$W^{1/2}$ that is a factor of two smaller in comparison with a typical Bruker BBI probe at this frequency. The measured ^{1}H NMR line width of 196 Hz for the sample is due to a magnetic susceptibility mismatch of materials chosen for the mw components near the sample and the paramagnetic line broadening of the high-concentrated TEMPOL solution.

3.2. Sample temperature

For Overhauser-DNP in the liquid state, the sample temperature strongly depends on the applied mw power, especially at high magnetic field strengths. This strongly hampers a quantitative evaluation of the electron spin saturation factor, because an increase of applied mw power changes the sample temperature and therefore the relaxation times of the coupled electron and nuclear spin system as well as the thermodynamic parameters such as viscosity, translational diffusion coefficients and rotational correlation times [12,17,19]. One goal of this new probe head design was to improve the heat dissipation from the sample to the housing of the probe in order to make the sample temperature almost independent of the applied mw power.

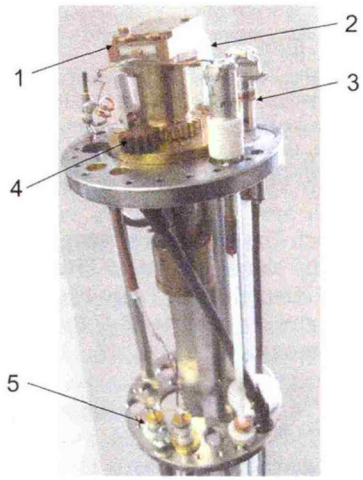

Fig. 4. Probehead assembly: 1- housing box containing the coplanar line and the Fabry-Pérot resonator; 2- tubing for cooling/heating gas; 3- trimmer capacitors to tune the RF structure to 400 MHz (^{1}H); 4- gears to tune the FP resonator to the gyrotron mw frequency of 263 GHz; 5- trimmer capacitors to tune the RF structure to 100 MHz (^{13}C channel).

The distribution of the electrical (E^2) and the magnetic field (B^2) component of the mw within the cylindrical sample placed on top of the flat mirror with a high thermal conductivity is shown in Fig. 5. Due to the standing mw inside of the Fabry-Pérot resonance structure, both field components are well separated. Most of the heating (proportional to E^2_{mw}) occurs at the top layer and in the center of the cylindrical liquid sample, whereas the largest contribution to the DNP enhanced signal (proportional to B^2_{mw} and the ring coverage $2\pi r$) arises from a more outer part of the sample. At the bottom of the sample efficient cooling is achieved by direct contact to the aluminum nitrate substrate. Therefore, the overall temperature rise of the sample is moderate.

The temperature rise of the sample by the mw heating was monitored by the chemical shift between CH_2 and OH components of proton NMR spectra of 100% ethylene glycol which is well known for temperature calibrations in NMR. [25,26,27]. First, the temperature dependent shift was calibrated by changing the sample temperature from 298 K to 350 K with heated nitrogen gas from a variable temperature controller (Fig. 6A). Then the shift between the CH_2 and OH lines was measured with an additional applied mw power of 6 W to the FP resonator keeping similar gas flow conditions as before (Fig. 6B). The temperature increase due to the mw heating was calculated by the difference in chemical shifts of corresponding spectra in Fig. 6A and B. This resulted in an average increase of the temperature of the sample by about 4 degrees above the set point as shown in Fig. 6C.

In more detail, as can be seen from Fig. 5, there is a temperature gradient occurring in the radial direction as well as along the height of the sample. The most elevated temperatures occur at the top and center of the sample, whereas the sample temperature at the bottom mirror is the same as adjusted by the thermocouple and the nitrogen gas flow due to the direct contact with the metal stripline as well as the ceramic substrate with high thermal conductivity.

3.3. Saturation of EPR line and ^{1}H OE-DNP enhancements

For the ^{1}H DNP experiments a 300 mM aqueous solution of ^{14}N TEMPOL was used. At these high radical concentrations, significantly broadened EPR spectra can already be observed at 260 GHz, resulting in a broad line instead of the 3 resolved ^{14}N hyperfine lines observed at lower concentrations.

The suppression of the paramagnetic shift of the ^{1}H water signal in the solution as a function of the applied mw power is shown in Fig. 7a for two sample temperatures (305 K and 315 K). In both cases the paramagnetic shift is completely suppressed when the mw power is applied above 2 W, which indicates an efficient saturation ($s = 1$) of the TEMPOL radical EPR transitions at these mw power levels [19]. Such a high saturation factor can be achieved despite the fact that only the center of the broad EPR spectrum (about 100 MHz) is resonantly excited by the mw, because of efficient Heisenberg exchange between the different hyperfine lines at such high radical concentrations [28]. We tested the temperature rise of the sample in response to applied mw power up to 3.3 W by the temperature dependent chemical shift of the NMR signal of pure water, assuming that mw absorption of 300 mM TEMPOL solution is similar to the absorption of pure water.

In support of these observations, the ^{1}H OE-DNP enhancements at both temperatures (305 K and 315 K) show almost no increase at mw power above 2 W (see Fig. 7b). That is an indication that the sample is under complete mw saturation and almost constant temperature conditions.

The reason for this behavior can be rationalized by taking into account the mw B_1 field strength profile along the disc shaped sample (see Fig. 2). Parts of the sample with different radial distances from the center saturate with different applied mw power

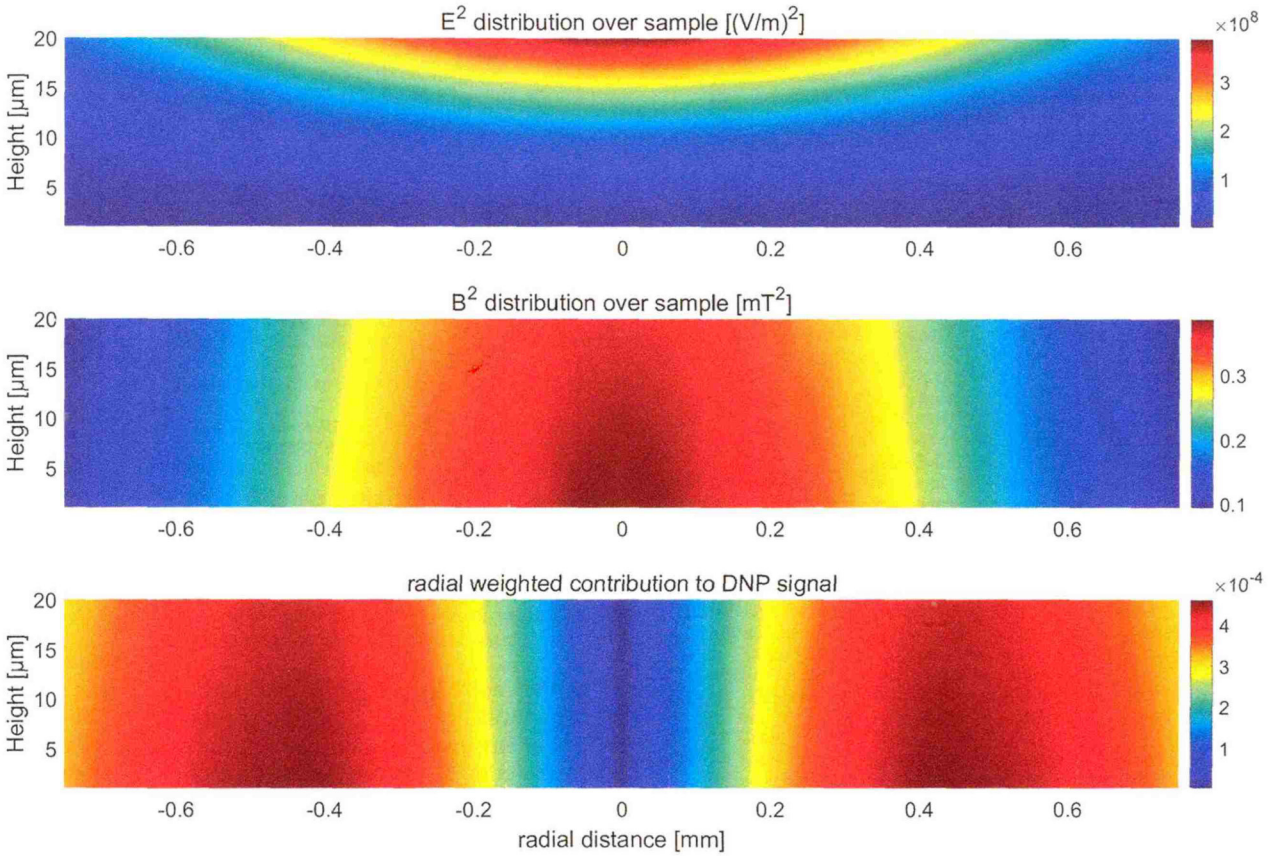

Fig. 5. Microwave field distribution within the sample, calculated with finite-element simulations of the Fabry-Pérot resonance structure (calculated with CST). Top: Distribution of E^2_{mw} within a liquid water sample which is responsible for the heating. The dimension of the cylindrical sample are 20 µm height and 1.5 mm diameter. Middle: Distribution of the squared mw magnetic field (B^2_{mw}) which is proportional to the saturation of the electron spin. Bottom: Relative radial contribution (weighted by the ring circumference) of the sample to the DNP enhanced NMR signal for a condition below full saturation of the EPR transitions.

and therefore have different paramagnetic shifts. In addition, the Gaussian mw power distribution over the sample implies a radial temperature gradient within the sample. This also leads to a radial variation of the DNP coupling factor ξ over the sample.

The maximum DNP enhancement of $\varepsilon = -21$ for the water proton NMR signal at a sample temperature of $T = 315$ K and $\varepsilon = -13$ at $T = 305$ K with 3 W of incident mw power is slightly lower compared to the maximum enhancement of $\varepsilon = -16$ achieved earlier for a 24 mM ^{15}N-TEMPOL aqueous sample with the older FP probehead [17]. The lower enhancement achieved here results from the lower sample temperatures of $T = 305$ K (with respect to 310 K) which can be stabilized with the new probe even under mw irradiation conditions, whereas with the former FP probe with lower heat conductivity of the flat mirror substrate made of quartz, a larger temperature rise of the sample under mw irradiation was observed. Indeed, an increase of the coupling factor ξ by a factor of 1.8 is predicted by a 20 K rise in temperature by MD, simulations for TEMPOL in water [22] and was also experimentally observed [19]. This further emphasizes the strong sensitivity of OE-DNP enhancements at high magnetic fields to the sample temperature and the importance of accurate control and precise measurement of the sample temperature within the DNP experiment.

3.4. OE-DNP experiments on ^{13}C with ^{1}H decoupling

Direct detection of scalar ^{13}C OE-DNP experiments was accomplished in an aqueous solution of 1 M 99% enriched 3-^{13}C -sodium pyruvate $C_3H_3NaO_3$ (Sigma Aldrich) and 100 mM TEMPOL. In this experiment a 20 µm thin PTFE holder ring of ID = 2.5 mm, and OD = 4 mm was used.

The optimal rf pulse length in the ^{13}C channel was 35 µsec for the $\pi/2$-pulse, with a rf attenuation of 10 dB. A short pulse repetition time $t_R = 1$ s could be chosen for the ^{13}C signal detection, due to the fast paramagnetic relaxation induced by the TEMPOL radicals. Fig. 8a) shows the Boltzmann background NMR signal recorded at ambient temperature (average of 220 k scans). In Fig. 8b) the OE-DNP enhanced NMR signal is shown with 6 W of mw power at 263 GHz applied (average of 8 k scans). Proton decoupling was accomplished in a final step by applying rf power in the ^{1}H channel of the new triple resonance FP-DNP probe with an attenuation level of 30 dB during the detection period (84 ms) under DNP conditions (Fig. 8c). Under these conditions we did not observe any additional sample heating by the decoupling RF power.

The observed scalar OE-DNP enhancement on the methyl carbons of pyruvate in aqueous solution is 16 (integral value). The enhancement was slightly smaller (about 12) under proton decoupling conditions. At the moment it is unclear whether this is due to technical reasons or results from the coupled/decoupled three spin system.

4. Summary and outlook

Our new triple resonance OE-DNP probe enables the measurement of scalar ^{13}C OE-DNP signals under proton decoupling with a well-defined sample temperature, almost independent of the applied mw power. This provides an opportunity to quantitatively

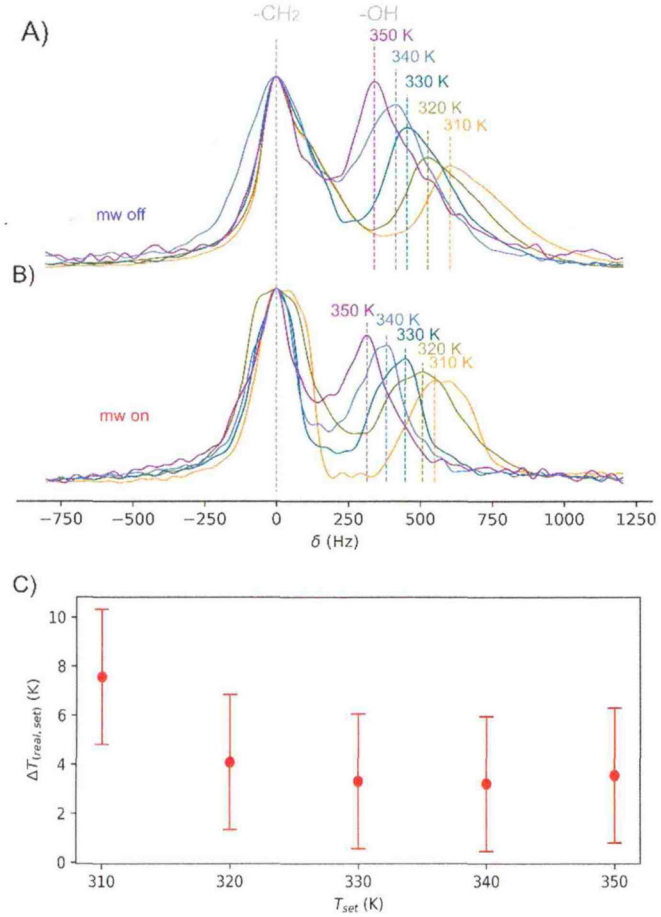

Fig. 6. (A) NMR spectra of 100% ethylene glycol sample recorded in the FP probehead at different temperatures up to 350 K set by the variable temperature gas flow (without mw); (B) the same sample in the probehead at similar gas flow conditions as in A) with 6 W mw power applied. In both experiments the gas flow rate was 1070 l/h; C) calculated temperature increase of the sample due to the mw heating. The positions of the CH_2 signal component of all spectra is set to 0 ppm for convenience.

study the interplay of scalar and dipolar Overhauser polarization efficiency and mechanism at a magnetic field of 9.4 T. The ^{13}C channel can also be easily tuned to other low-γ nuclei spins, as for example ^{15}N or ^{31}P.

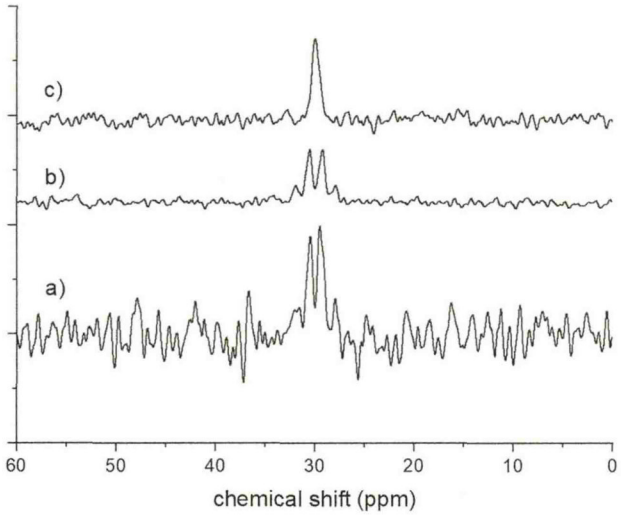

Fig. 8. ^{13}C NMR signal of an aqueous solution of 1 M ^{13}C-sodium pyruvate and 100 mM TEMPOL (a) Boltzmann equilibrium signal (220 k scans); (b) DNP enhanced signal (8 k scans); (c) ^{13}C DNP signal with proton decoupling (8 k scans). Temperature of the sample was set to be 340 K.

At the moment, the probe does not achieve high resolution NMR performance for ^{1}H, due to magnetic susceptibility discontinuities of the mw resonator parts in the sample vicinity. The ^{1}H NMR resolution can be improved by a careful choice and geometry of the probehead materials near the sample. The obtained dipolar ^{1}H DNP enhancement of $\varepsilon = -21$ for water with TEMPOL radicals varies slightly with the sample temperature. We plan to optimize the probe design, enabling more homogeneous sample conditions.

Furthermore, the triple resonance DNP probe will allow to perform 2D resolved DNP experiments of biologically interesting molecules in liquid solution. It will be interesting to investigate the polarization transfer schemes of such experiments under DNP conditions if both nuclear spins achieve (scalar and/or dipolar) OE-DNP enhancements directly.

Declaration of Competing Interest

The authors declare that they have no known competing financial interests or personal relationships that could have appeared to influence the work reported in this paper.

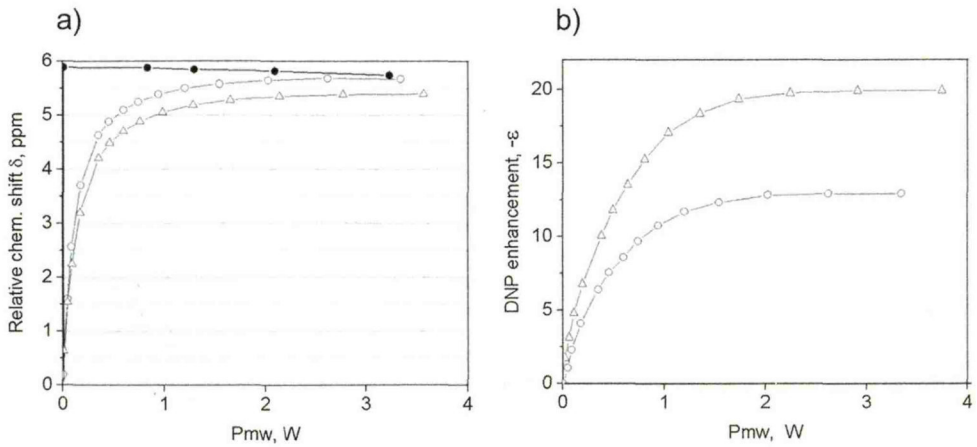

Fig. 7. (a) Chemical shift of the ^{1}H NMR line of pure water sample within housing kept at 305 K (solid circles) and of 300 mM aqueous TEMPOL solution at 305 K (open circles) and 315 K (open triangles) versus applied mw power. (b) ^{1}H OE-DNP enhancement measured versus the applied mw power at 305 K (open circles) and 315 K (open triangles) determined from the peak NMR intensities. The real sample temperature slightly increases with increasing mw power as described in the text.

Acknowledgement

The authors thank the DFG (Deutsche Forschungsgemeinschaft, Grant 405972957) for financial support and Dr. Andrei Kuzhelev for helpful discussions.

References

[1] A.W. Overhauser, Polarization of Nuclei in Metals, Phys. Rev. 92 (1953) 411–415.
[2] T.R. Carver, C.P. Slichter, Polarization of Nuclear Spins in Metals, Phys. Rev. 92 (1953) 212–213.
[3] A. Abragam, W.G. Proctor, Une Nouvelle Methode de Polarization Dynamique des Noyaux Atomiques dans les Solides, Comptes Rendus Hebdomadaries des Seances de L'Academia des Sciences 246 (1958) 2253–2256.
[4] K.H. Hausser, D. Stehlik, Dynamic nuclear polarization in liquids, Adv. Magn. Reson. 3 (1968) 79–139.
[5] B. Barnes, G. De Paepe, P.C.A. van der Wel, K.N. Hu, C.G. Joo, V.S. Bajaj, M.L. Mak-Jurkauskas, J.R. Sirigiri, J. Herzfeld, R.J. Temkin, R.G. Griffin, High-Field Dynamic Nuclear Polarization for Solid and Solution Biological NMR, Appl. Magn. Reson. 34 (2008) 237–263.
[6] J.H. Ardenkjær-Larsen, B. Fridlund, A. Gram, G. Hansson, L. Hansson, M.H. Lerche, R. Servin, M. Thaning, K. Golman, Increase in signal-to-noise ratio of >10,000 times in liquid-state NMR, Proc. Natl. Acad. Sci. USA 100 (2003) 10158–10163.
[7] X. Wang, W.C. Isley III, S.I. Salido, Z. Sun, L. Song, K.H. Tsai, C.J. Cramer, H.C. Dorn, Optimization and prediction of the electron–nuclear dipolar and scalar interaction in ^{1}H and ^{13}C liquid state dynamic nuclear polarization, Chem. Sci. 6 (2015) 6482–6495.
[8] M. Gafurov, V. Denysenkov, M.J. Prandolini, T.F. Prisner, Temperature Dependence of the Proton Overhauser DNP Enhancements on Aqueous Solutions of Fremy's Salt Measured in a Magnetic Field of 9.2 T, Appl. Magn. Res. 43 (2012) 119–128.
[9] T. Orlando, R. Dervisoglu, M. Levien, I. Tkach, T.F. Prisner, L. Andreas, V. Denysenkov, M. Bennati, Dynamic Nuclear Polarization of ^{13}C Nuclei in the Liquid State over a 10Tesla Field Range, Angew. Chem. Int. Ed. 58 (2019) 1402–1406.
[10] G. Liu, M. Levien, N. Karschin, G. Parigi, C. Luchinat, M. Bennati, One-thousand-fold enhancement of high field liquid nuclear magnetic resonance signals at room temperature, Nature Chem. 9 (2017) 676–680.
[11] S.E. Kücük, D. Sezer, Multiscale computational modeling of ^{13}C DNP in liquids, Phys. Chem. Chem. Phys. 18 (2016) 9353-9357.
[12] M. Prandolini, V. Denysenkov, M. Gafurov, B. Endeward, T. Prisner, High-Field Dynamic Nuclear Polarization in Aqueous Solutions, J. Am. Chem. Soc. 131 (2009) 6090–6092.
[13] G. Annino, J.A. Villanueva-Garibay, P.J.M. van Bentum, A.A.K. Klaassen, A.P.M. Kentgens, A. High-Conversion-Factor, Double-Resonance Structure for High-Field Dynamic Nuclear Polarization, Appl. Magn. Reson. 37 (2010) 851–864.
[14] S. Milikisiyants, A. Nevzorov, A. Smirnov, Photonic band-gap resonators for high-field/high-frequency EPR of microliter-volume liquid aqueous samples, J. Magn. Reson. 296 (2018) 152–164.
[15] D. Yoon, A.I. Dimitriadis, M. Soundararajan, C.h. Caspers, J. Genoud, S. Alberti, E. de Rijk, J.-P. Ansermet, High-Field Liquid-State Dynamic Nuclear Polarization in Microliter Samples, Anal. Chem. 90 (2018) 5620–5626.
[16] T. Dubroca, A.N. Smith, K.J. Pike, S. Froud, R. Wylde, B. Trociewitz, J. McKay, F. Mentink-Vigier, J. van Tol, S. Wi, W. Brey, J.R. Long, L. Frydman, S. Hill, A quasi-optical and corrugated waveguide microwave transmission system for simultaneous dynamic nuclear polarization NMR on two separate 14.1 T spectrometers, J. Magn. Reson. 289 (2018) 35–44.
[17] V. Denysenkov, T.F. Prisner, Liquid State Dynamic Nuclear Polarization Probe with Fabry-Perot Resonator at 9.2 Tesla, J. Magn. Reson. 217 (2012) 1–5.
[18] O. Jakdetchai, V. Denysenkov, J. Becker-Baldus, B. Dutagaci, T.F. Prisner, C. Glaubitz, Dynamic Nuclear Polarization-Enhanced NMR on Aligned Lipid Bilayers at Ambient Temperature, J. Am. Chem. Soc. 136 (2014) 15533–15536.
[19] P. Neugebauer, J. Krummenacker, V. Denysenkov, G. Parigi, C. Luchinat, T.F. Prisner, Liquid State DNP of Water at 9.2 T: an Experimental Access to Saturation, Phys. Chem. Chem. Phys. 15 (2013) 6049–6056.
[20] L.-P. Hwang, J.H. Freed, Dynamic effects of pair correlation functions on spin relaxation by translational diffusion in liquids, J. Chem. Phys. 63 (1975) 4017.
[21] M. Bennati, G. Parigi, C. Luchinat, M.-T. Türke, Water 1H relaxation dispersion analysis on a nitroxide radical provides information on the maximal signal enhancement in Overhauser dynamic nuclear polarization experiments, Phys. Chem. Chem. Phys. 12 (2010) 5902–5910.
[22] D. Sezer, Rationalizing Overhauser DNP of nitroxide radicals in water through MD simulations Phys, Chem. Chem. Phys. 16 (2014) 1022–1032.
[23] A. Franco Júnior, D.J. Shanafield, Thermal Conductivity of Polycrystalline Aluminum Nitride (AlN) Ceramics, Cerâmica 50 (2004) 315–319.
[24] V.P. Denysenkov, M.J. Prandolini, A. Krahn, M. Gafurov, B. Endeward, T.F. Prisner, High field DNP spectrometer for liquids, Appl. Magn. Reson. 34 (2008) 289–299.
[25] A.L. van Geet, Calibration of the methanol and glycol nuclear magnetic resonance thermometers with a static thermistor probe, Anal. Chem. 40 (1968) 2227–2229.
[26] C. Amman, P. Meier, A. Merbach, A simple multinuclear NMR thermometer, J. Magn. Reson. 46 (1982) 319–321.
[27] D. Rolford, C.h. Fisk, E. Becker, Calibration of methanol and ethylene glycol NMR thermometers, Anal. Chem. 51 (1979) 2050–2051.
[28] M.T. Türke, M. Bennati, Saturation factor of nitroxide radicals in liquid DNP by pulsed ELDOR experiments, Phys. Chem. Chem. Phys. 13 (2011) 3630–3633.

8.3 Corresponding Publication (2):

The following publication together with the supporting information

"Dai, D., Denysenkov, V., Bagryanskaya E. G., Tormyshev, V. M., Prisner, T. F. and Kuzhelev, A. A., ^{13}C Hyperpolarization of Viscous Liquids by Transfer of Solid-Effect ^{1}H Dynamic Nuclear Polarization at High Magnetic Field. *J. Phys. Chem. Lett.* 14, 31, 7059–7064 (2023)"

is attached in the next pages.

The work was prepared in a collaborative manner. The author performed the initial proof of the INEPT-DNP concept. The author performed the DNP/NMR experiments including sample preparation, spectra recording and spectra analysis together with Dr. Andrei Kuzhelev. The author participated in manuscript preparation including preparation of the figures of DNP spectra and supportive figures.

https://doi.org/10.1021/acs.jpclett.3c01732

THE JOURNAL OF PHYSICAL CHEMISTRY LETTERS
A JOURNAL OF THE AMERICAN CHEMICAL SOCIETY

pubs.acs.org/JPCL

Letter

^{13}C Hyperpolarization of Viscous Liquids by Transfer of Solid-Effect ^{1}H Dynamic Nuclear Polarization at High Magnetic Field

Danhua Dai, Vasyl Denysenkov, Elena G. Bagryanskaya, Victor M. Tormyshev, Thomas F. Prisner, and Andrei A. Kuzhelev*

Cite This: *J. Phys. Chem. Lett.* 2023, 14, 7059−7064

Read Online

ACCESS | Metrics & More | Article Recommendations | Supporting Information

ABSTRACT: Dynamic nuclear polarization (DNP) is routinely used as a method for increasing the sensitivity to nuclear magnetic resonance (NMR). Recently, high-field solid-effect DNP in viscous liquids on ^{1}H nuclei was demonstrated using narrow-line polarizing agents. Here we expand the applicability of DNP in viscous media to ^{13}C nuclei. To hyperpolarize ^{13}C nuclei, we combined solid-effect ^{1}H DNP with a subsequent transfer of the ^{1}H polarization to ^{13}C via insensitive nuclei enhanced by polarization transfer (INEPT). We demonstrate this approach using a triarylmethyl radical as a polarizing agent and glycerol-$^{13}C_3$ as an analyte. We achieved ^{13}C enhancement factors of up to 45 at a magnetic field of 9.4 T and room temperature.

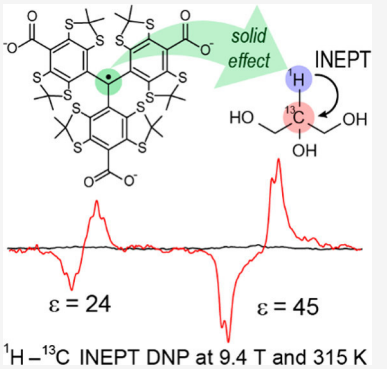

Nuclear magnetic resonance (NMR) is a powerful spectroscopic technique for the atomistic characterization of molecules. The intensity of the NMR signal depends on both the gyromagnetic ratio γ of the nucleus, which determines the Zeeman energy splitting and therefore the Boltzmann polarization of the nuclear spin, and the natural abundance of the nucleus. The low gyromagnetic ratio and small natural abundance of ^{13}C of only 1.1% lead to a poor sensitivity of the NMR spectra and therefore long acquisition times. The sensitivity problem of NMR can be overcome by using dynamic nuclear polarization (DNP). DNP allows to enhance an NMR signal by several orders of magnitude using the transfer of polarization from the unpaired electron spin of a polarizing agent to the nuclear spin of an analyte.[1]

In the solid state, the NMR signal can be enhanced by direct DNP, mostly for ^{1}H and ^{19}F nuclei,[2−4] or indirect DNP, for low-γ nuclei (e.g., ^{13}C, ^{15}N, ^{17}O, ^{27}Al, or ^{29}Si).[5−9] The indirect polarization pathway is commonly used in solid-state DNP because many analytes contain ^{1}H nuclei that can be easily polarized. Currently, the most efficient electron-to-proton polarization transfer mechanism in solids is the cross effect that operates at moderate magnetic fields (e.g., 9.4 T) and low temperature (e.g., 100 K).[10,11] The DNP hyperpolarization is then transferred from ^{1}H to other nuclei by Hartmann−Hahn cross-polarization (CP).[12,13] This approach has been successfully employed in structural biology and materials science.[14−22]

In liquids, direct DNP polarization is mainly applied to various nuclei (e.g., ^{1}H, ^{9}Li, ^{13}C, ^{15}N, ^{19}F, ^{23}Na, or ^{31}P),[23−29] where only one mechanism is operational: the Overhauser effect.[1,30] In liquid solutions, the electron spin interacts with the nuclear spin through dipolar and scalar interactions. If the scalar coupling dominates over the dipolar one (as commonly observed for ^{13}C, ^{15}N, ^{19}F, or ^{31}P nuclei), then the Overhauser DNP can yield outstanding signal enhancements at magnetic fields of ≥1 T,[31−34] although usually it requires specific chemical systems that involve a strong contact interaction between the electron and nuclear spins. On the other hand, the dipolar Overhauser effect (as in the case of ^{1}H) has only limited applications owing to low DNP efficiency at high magnetic fields.[35,36] Therefore, to increase the ^{1}H polarization, a technique was proposed recently for transferring ^{13}C hyperpolarization produced by scalar Overhauser DNP to the attached ^{1}H spins via the polarization transfer scheme.[37,38]

With regard to an intermediate state between solids and liquids, viscous media, only a few DNP measurements at high magnetic fields[39,40] and a number of DNP experiments at low magnetic fields exist.[41−45] These experiments have been so far performed only on proton and fluorine nuclei via the direct transfer of spin polarization from the electron spin to the nuclear spin through the Overhauser effect or solid effect.

Here we demonstrate a new approach to achieving ^{13}C DNP enhancements in viscous liquids by transferring the ^{1}H

Received: June 25, 2023
Accepted: July 28, 2023
Published: August 1, 2023

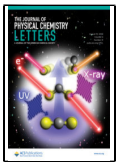

https://doi.org/10.1021/acs.jpclett.3c01732
J. Phys. Chem. Lett. 2023, 14, 7059−7064

hyperpolarization generated by the solid-effect DNP mechanism to ^{13}C spins by insensitive nuclei enhanced by polarization transfer (INEPT) (Figure 1C). We achieved enhancements of up to 45 for glycerol-$^{13}C_3$ in the presence of triarylmethyl radicals at a magnetic field of 9.4 T and above room temperature.

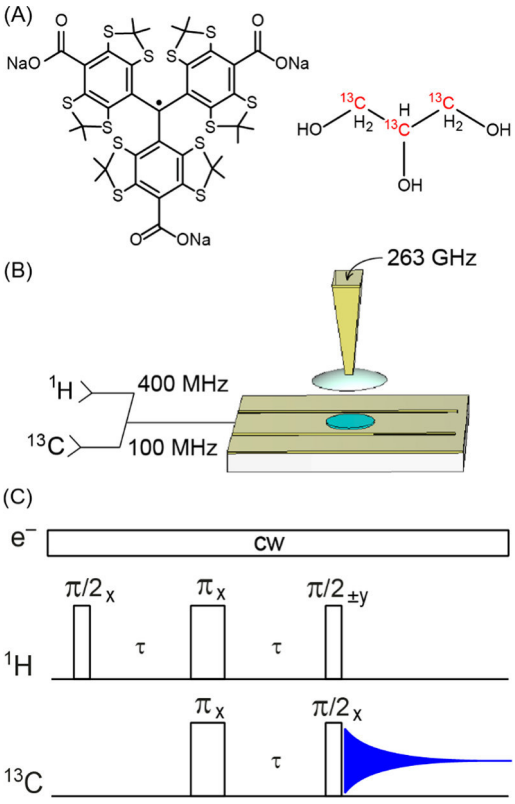

Figure 1. (A) Chemical structure of Finland trityl and glycerol-$^{13}C_3$. (B) Schematics of the triple-resonance probehead capable of exciting the liquid sample simultaneously at three frequencies: ^1H at 400 MHz, ^{13}C at 100 MHz, and electron spin at 263 GHz. (C) The pulse sequence used to attain ^{13}C hyperpolarization was solid-effect ^1H DNP combined with $^1H-^{13}C$ INEPT. The $\pi/2$ pulses were 34 and 80 μs for ^1H and ^{13}C, respectively, and the pulse delay τ was $1/4J_{CH}$, i.e., 1.7 ms. The microwave irradiation was applied in continuous wave.

To carry out $^1H-^{13}C$ INEPT solid-effect DNP in liquids, three experimental challenges have to be addressed: (i) the microwave power (the B_1 field) has to be strong enough to efficiently drive the forbidden electron−nuclear spin transition, (ii) the sample heating due to the microwave electric field has to be minimized, and (iii) the probehead has to simultaneously operate at resonant frequencies of 263 GHz (electron spin), 400 MHz (^1H), and 100 MHz (^{13}C). All these requirements can be fulfilled with our newly designed triple-resonance probehead.[46] The probehead is a combination of a coplanar strip line used as a transmitter and receiver at two radio frequencies (^1H and ^{13}C) and a Fabry−Pérot microwave resonator at 263 GHz as shown in Figure 1B. In addition, the probehead has another function: cooling and heating a liquid sample by flowing nitrogen gas.

We recently demonstrated that polarizing agents with a narrow EPR line can be utilized to polarize lipid bilayers in the fluid phase and tripeptides in glycerol through the solid effect at high magnetic fields and ambient temperatures.[39,40] ^1H DNP enhancement of up to ±45-fold was observed for the glycerol molecules in the presence of triarylmethyl radicals.[40] At the same time, the solid-effect ^{13}C DNP enhancements of glycerol-$^{13}C_3$ were around three times less compared to ^1H DNP enhancements under the same experimental conditions (see the Supporting Information). To find out whether this large ^1H hyperpolarization can be potentially transferred to other low-γ nuclei, we implemented $^1H-^{13}C$ polarization transfer experiments combined with solid-effect ^1H DNP of glycerol-$^{13}C_3$ solutions doped with Finland radicals (Figure 1A). These experiments can be accomplished using, for example, INEPT (Figure 1C)[47] or CP[13] pulse sequences. To choose the right polarization scheme in rigid or mobile molecular systems, a theoretical model for calculating INEPT and CP intensities as a function of rotational correlation time τ_c has been developed and verified on liquid crystals.[48] According to this model, the INEPT sequence affords signal enhancement for isotropic liquids with $\tau_c < 10$ ns, whereas CP is most efficient for media with $\tau_c > 10$ μs. The rotational correlation time of glycerol falls within the nanosecond time scale,[49] and therefore the INEPT pulse sequence is more efficient at ambient temperatures.

INEPT is a well-known method for enhancing the NMR sensitivity of low-γ nuclei in liquids. This method increases the signal intensity by transferring the larger polarization of a high-γ spin onto a coupled low-γ spin. For the INEPT experiment with a single coupling constant J_{CH} the signal enhancement can be expressed using equation slightly modified from ref 37:

$$\varepsilon_{INEPT} = \frac{I_{INEPT}}{I_{0,C}} = \frac{\gamma_H}{\gamma_C} n \sin(2\pi J_{CH}\tau) \exp\left(-\frac{2\tau}{T_2^H}\right) \exp\left(-\frac{\tau}{T_1^C}\right) \quad (1)$$

where I_{INEPT} and $I_{0,C}$ are the INEPT intensity and the thermal equilibrium ^{13}C intensity, respectively; γ_H and γ_C are the gyromagnetic ratios for ^1H and ^{13}C, respectively; n is the bond multiplicity (CH_n); τ is the pulse delay in the INEPT sequence and equals to $1/4J_{CH}$ (for glycerol-$^{13}C_3$, J_{CH} = 145 Hz and τ = 1.7 ms); and T_2^H and T_1^C are the transverse and longitudinal relaxation times of ^1H and ^{13}C, respectively.

According to eq 1, the ^1H spin polarization strengthens the ^{13}C signal by a factor given by the ratio of the gyromagnetic ratios (γ_H/γ_C = 4) multiplied by the number of protons coupled to the ^{13}C nucleus. The resulting INEPT spectrum of ^{13}C contains both a positive and a negative line with intensities of −4:4 for doublets (CH), −8:0:8 for triplets (CH_2), and −12:−12:12:12 for quartets (CH_3) after phase cycling. Moreover, in the INEPT experiments under hyperpolarization conditions, the overall sensitivity of the ^{13}C signal is additionally increased by the proton hyperpolarization, and thus the ^{13}C signal enhancement can be expressed as

$$\varepsilon_C = \varepsilon_{DNP}\varepsilon_{INEPT} = \frac{I_{DNP} - I_{0,H}}{I_{0,H}} \frac{I_{INEPT}}{I_{0,C}} \quad (2)$$

where ε_{DNP} and ε_{INEPT} are the ^1H DNP and ^{13}C INEPT NMR enhancements (see eq 1), respectively, and I and $I_{0,H}$ are the DNP and Boltzmann proton polarization levels, respectively.

The performance of the INEPT experiment is significantly affected by the nuclear spin relaxation (eq 1). During the τ delay of the pulse sequence (Figure 1C), the signal intensity decays with relaxation times of both ^1H (T_2) and ^{13}C (T_1). The coupling constant J_{CH} in glycerol-$^{13}C_3$ is 145 Hz, and τ was therefore set to $1/4J_{CH}$, i.e., 1.7 ms. Because the

https://doi.org/10.1021/acs.jpclett.3c01732
J. Phys. Chem. Lett. 2023, 14, 7059−7064

longitudinal relaxation time of ^{13}C is longer than τ (see Table 1) by at least 2 orders of magnitude, the effect of T_1 on the

Table 1. Transverse (T_2) and Longitudinal (T_1) Relaxation Times (in ms) of ^1H and ^{13}C for Glycerol-$^{13}C_3$ in the Presence of Finland Trityl (Concentrations Are Shown in the Table) Measured at a Magnetic Field of 9.4 T and 298 K[a]

concentration (mM) of Finland trityl in glycerol-$^{13}C_3$	^1H		^{13}C			
	T_2	T_1	T_2(CH)	T_1(CH)	T_2(CH_2)	T_1(CH_2)
0	44	222	113*	222	76*	132
5	6.4	210	48	245	42	140
10	3.8	205	34	230	31	135
20	1.8	188	24	233	21	136

[a]Nuclear relaxation times were measured for the CH/CH_2 groups for both nuclei. T_2 and T_1 were measured using a Carr−Purcell−Meiboom−Gill and an inversion recovery pulse sequence, respectively. Experimental error of all values is 10%. The asterisk (*) shows results for nonlabeled glycerol.

INEPT experiment can be ignored. For the sample without triarylmethyl radicals, the proton transverse relaxation time is longer than τ by an order of magnitude (Table 1), which means that the polarization of ^1H can be successfully transferred to ^{13}C with an INEPT efficiency of >90% as shown in Figure 2. When Finland radical is added to the

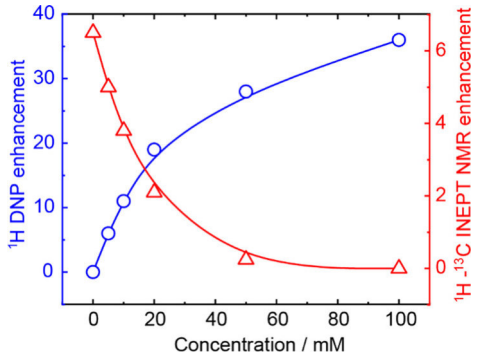

Figure 2. ^1H DNP (blue circles) and $^1H-^{13}C$ INEPT NMR (red triangles) enhancements as a function of the concentration of Finland trityl in glycerol-$^{13}C_3$ at a magnetic field of 9.4 T and a temperature of ~315 and 298 K, respectively. The ^1H DNP enhancements were measured at a magnetic field corresponding to the high-field solid-effect position. The ^1H ^{13}C INEPT NMR enhancements are shown for the CH_2 groups of glycerol-$^{13}C_3$.

sample at a concentration of 20 mM, the proton T_2 becomes comparable to τ (Table 1), and the efficiency of the INEPT transfer decreases significantly to ~15% (Figure 2) at room temperature.

The intramolecular coupling J_{CH} affects the ^{13}C longitudinal relaxation. There are two protons coupled to each $^{13}C(1,3)$ and only one to each $^{13}C(2)$; therefore, these two sites relax differently. For example, the ^{13}C longitudinal relaxation rates (R_1) of two sites were found to be in a ratio close to $R_1(CH_2)/R_1(CH) = 2$, consistent with the number of protons attached to the ^{13}C's. In contrast, for the ^{13}C transverse relaxation times, we obtained similar values for the CH_2 and CH groups (within the experimental error of 10%). The addition of the paramagnetic compound to the solution led to paramagnetic relaxation enhancement mostly for transverse relaxation time in a concentration-dependent manner (Table 1). The paramagnetic relaxation enhancement is often used for deducing a distance between an analyte nuclear spin and electron spin of a paramagnetic probe.[50] Nevertheless, this effect is not only inversely proportional to the sixth power of the distance between electron and nuclear spins (r^{-6}) but also proportional to the square of the nuclear gyromagnetic ratio (γ^2). For this reason, in our study, we noted that the transverse relaxation times of the ^1H nuclei are significantly shorter in the presence of Finland trityl radicals than the transverse relaxation times of the ^{13}C nuclei, as shown in Table 1.

Figure 2 presents both ^1H DNP and $^1H-^{13}C$ INEPT NMR enhancements as a function of the concentration of the Finland radical in glycerol-$^{13}C_3$ at a magnetic field of 9.4 T. With increasing concentration of the polarizing agent, the ^1H DNP enhancements go up, while the $^1H-^{13}C$ INEPT NMR enhancements decrease to zero. Consequently, an optimum concentration of the polarizing agent for the $^1H-^{13}C$ INEPT DNP experiment of about 20 mM was found, leading to a ^1H DNP enhancement of about 20 as well as an INEPT enhancement of about 2 for the CH_2 group.

Next, we aimed to measure $^1H-^{13}C$ INEPT DNP enhancements of glycerol-$^{13}C_3$ in the presence of triarylmethyl radicals at concentrations of 5, 10, and 20 mM (Figure 3C). To analyze the observed ^{13}C DNP enhancements, we additionally measured both solid-effect ^1H DNP and $^1H-^{13}C$ INEPT NMR enhancements using the triple-resonance probehead and the Bruker BBI probehead, respectively (Figure 3). Note that in the INEPT experiments without microwaves with the triple-resonance probehead, we observed similar enhancements to those seen with the Bruker BBI probehead (see the Supporting Information). For the sample of 10 mM Finland radical in glycerol-$^{13}C_3$, the ^1H DNP enhancement was 10 ± 1 and INEPT enhancements were 1.8 ± 0.2 and 3.6 ± 0.4 for CH and CH_2 groups, respectively (Figure 3A,B, middle). This corresponds to an overall increase in ^{13}C polarization by a factor of ~18 (for CH) and ~36 (for CH_2) according to eq 2. The expected ^{13}C DNP enhancements are in good agreement with the experimental values of 24 ± 3 (for CH) and 45 ± 5 (for CH_2), which were calculated taking into account the thermal equilibrium ^{13}C polarization ($\varepsilon = I_{INEPT\ DNP}/I_{0,C}$). For 5 and 20 mM Finland trityl in glycerol-$^{13}C_3$ (Figure 3, top and bottom), a quantitative transfer of polarization of ^1H to ^{13}C nuclei was also observed, with enhancements of 26 ± 3 and 39 ± 4 for CH_2 sites, respectively. Thus, using the INEPT pulse sequence, whose efficiency is limited only by the proton transverse relaxation time, we could successfully transfer the full DNP hyperpolarization of ^1H to the ^{13}C nuclei. In our approach, we used a relatively low concentration of the polarizing agent of ≤20 mM, which has only a slight effect on the line width via paramagnetic relaxation for both ^1H and ^{13}C nuclei. Note that using the triple-resonance probehead, we obtained slightly broader NMR lines as compared to the Bruker BBI probehead (Figure 3A,C). Nonetheless, the spectral resolution was high enough to observe the J_{CC} coupling at 40 Hz.

For larger molecules or more viscous liquids, where the molecular rotational correlation time exceeds the nanosecond time range, the INEPT pulse sequence will not be efficient any more due to too short nuclear transverse relaxation times. In this case, other polarization transfer techniques for slow-motion media can be used such as cross-correlated relaxation-

https://doi.org/10.1021/acs.jpclett.3c01732
J. Phys. Chem. Lett. 2023, 14, 7059−7064

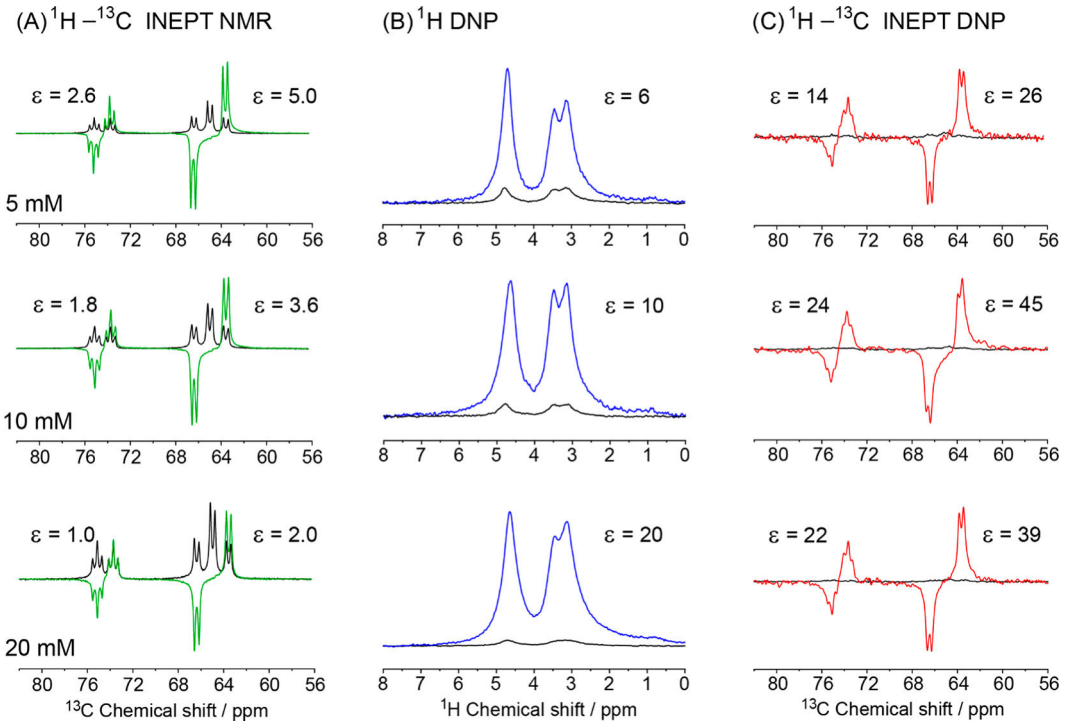

Figure 3. (A) ^{1}H–^{13}C INEPT NMR, (B) ^{1}H DNP, and (C) ^{1}H–^{13}C INEPT DNP spectra acquired at 9.4 T with (red, blue) or without (black, green) microwave irradiation using a 263 GHz gyrotron source for glycerol-$^{13}C_3$ in the presence of Finland trityl at a concentration of 5 mM (top), 10 mM (middle), or 20 mM (bottom). NMR or DNP experiments were conducted with the Bruker BBI probehead (A) or the triple-resonance probehead (B, (C). The spectra were normalized to a single scan. The enhancements were measured by examination of the signal intensity and were calculated according to $\varepsilon = I_{DNP}/I_{0,H} - 1$ for ^{1}H DNP and $\varepsilon = I_{INEPT}/I_{0,C}$ for ^{1}H–^{13}C INEPT NMR/DNP experiments, where $I_{0,H}$ and $I_{0,C}$ are Boltzmann ^{1}H/^{13}C polarization levels. The error in the measurements was 10%.

induced polarization transfer (CRIPT) and cross-correlated relaxation-enhanced polarization transfer (CRINEPT), which are less dependent on rotational correlation times.[51,52] These pulse sequences have been already implemented in NMR studies on large proteins (≥110000 Da) in an aqueous solution at 4 °C.[51] In principle, a combination of solid-effect ^{1}H DNP and CRIPT or CRINEPT could be potentially applied to solution-state NMR on supramolecular complexes, such as membrane proteins in micelles or lipid bilayers or large protein complexes.

In summary, we demonstrated an approach to attaining ^{13}C hyperpolarization in viscous liquids by efficiently transferring ^{1}H hyperpolarization generated by solid-effect DNP to ^{13}C nuclei using an INEPT pulse sequence. Here, this technique yielded an overall increase in ^{13}C polarization by factors of 24 ± 3 and 45 ± 5 for the CH and CH_2 groups of glycerol-$^{13}C_3$, respectively. It was only limited by the proton transverse relaxation time which is decreased by the addition of the radical. This approach may become an alternative method allowing the significant enhancement of ^{13}C NMR signals in liquids at temperatures >280 K and may also be extended to samples containing other low-γ nuclei such as ^{15}N, ^{17}O, or ^{29}Si.

■ ASSOCIATED CONTENT

Supporting Information

The Supporting Information is available free of charge at https://pubs.acs.org/doi/10.1021/acs.jpclett.3c01732.

Experimental methods, DNP field profiles, nuclear relaxation curves, ^{1}H–^{13}C INEPT NMR using the triple-resonance probehead, refocused and ^{1}H-decoupled INEPT (PDF)

■ AUTHOR INFORMATION

Corresponding Author

Andrei A. Kuzhelev − *Goethe University Frankfurt am Main, Institute of Physical and Theoretical Chemistry and Center for Biomolecular Magnetic Resonance, Frankfurt am Main 60438, Germany;* orcid.org/0000-0003-3445-2921; Email: kuzhelev@chemie.uni-frankfurt.de

Authors

Danhua Dai − *Goethe University Frankfurt am Main, Institute of Physical and Theoretical Chemistry and Center for Biomolecular Magnetic Resonance, Frankfurt am Main 60438, Germany*

Vasyl Denysenkov − *Goethe University Frankfurt am Main, Institute of Physical and Theoretical Chemistry and Center for Biomolecular Magnetic Resonance, Frankfurt am Main 60438, Germany*

Elena G. Bagryanskaya − *N. N. Vorozhtsov Institute of Organic Chemistry, Siberian Branch of Russian Academy of Sciences (SB RAS), Novosibirsk 630090, Russia;* orcid.org/0000-0003-0057-383X

Victor M. Tormyshev − *N. N. Vorozhtsov Institute of Organic Chemistry, Siberian Branch of Russian Academy of Sciences (SB RAS), Novosibirsk 630090, Russia*

Thomas F. Prisner − *Goethe University Frankfurt am Main, Institute of Physical and Theoretical Chemistry and Center for Biomolecular Magnetic Resonance, Frankfurt am Main 60438, Germany;* orcid.org/0000-0003-2850-9573

Complete contact information is available at: https://pubs.acs.org/10.1021/acs.jpclett.3c01732

https://doi.org/10.1021/acs.jpclett.3c01732
J. Phys. Chem. Lett. 2023, 14, 7059−7064

Notes

The authors declare no competing financial interest.

■ ACKNOWLEDGMENTS

A.A.K. acknowledges the DFG (Deutsche Forschungsgemeinschaft, Grant 518679424). D.D., V.D., T.F.P., and A.A.K. thank the Center for Biomolecular Magnetic Resonance for financial support.

■ REFERENCES

(1) Overhauser, A. W. Polarization of Nuclei in Metals. *Phys. Rev.* **1953**, *92* (2), 411−415.
(2) Becerra, L. R.; Gerfen, G. J.; Temkin, R. J.; Singel, D. J.; Griffin, R. G. Dynamic Nuclear Polarization with a Cyclotron Resonance Maser at 5 T. *Phys. Rev. Lett.* **1993**, *71* (21), 3561−3564.
(3) Chandrakumar, N.; Narasimhan, P. T. 1H and 19F Dynamic Nuclear Polarization Studies at X-Band: ^{19}F Differential Enhancements. *Mol. Phys.* **1982**, *45* (1), 179−187.
(4) Lu, M.; Wang, M.; Sergeyev, I. V.; Quinn, C. M.; Struppe, J.; Rosay, M.; Maas, W.; Gronenborn, A. M.; Polenova, T. ^{19}F Dynamic Nuclear Polarization at Fast Magic Angle Spinning for NMR of HIV-1 Capsid Protein Assemblies. *J. Am. Chem. Soc.* **2019**, *141* (14), 5681−5691.
(5) Lesage, A.; Lelli, M.; Gajan, D.; Caporini, M. A.; Vitzthum, V.; Miéville, P.; Alauzun, J.; Roussey, A.; Thieuleux, C.; Mehdi, A.; et al. Surface Enhanced NMR Spectroscopy by Dynamic Nuclear Polarization. *J. Am. Chem. Soc.* **2010**, *132* (44), 15459−15461.
(6) Vitzthum, V.; Miéville, P.; Carnevale, D.; Caporini, M. A.; Gajan, D.; Copéret, C.; Lelli, M.; Zagdoun, A.; Rossini, A. J.; Lesage, A.; Emsley, L.; Bodenhausen, G. Dynamic Nuclear Polarization of Quadrupolar Nuclei Using Cross Polarization from Protons: Surface-Enhanced Aluminium-27 NMR. *Chem. Commun.* **2012**, *48* (14), 1988−1990.
(7) Michaelis, V. K.; Markhasin, E.; Daviso, E.; Herzfeld, J.; Griffin, R. G. Dynamic Nuclear Polarization of Oxygen-17. *J. Phys. Chem. Lett.* **2012**, *3* (15), 2030−2034.
(8) Kobayashi, T.; Gupta, S.; Caporini, M. A.; Pecharsky, V. K.; Pruski, M. Mechanism of Solid-State Thermolysis of Ammonia Borane: A ^{15}N NMR Study Using Fast Magic-Angle Spinning and Dynamic Nuclear Polarization. *J. Phys. Chem. C* **2014**, *118* (34), 19548−19555.
(9) Lelli, M.; Gajan, D.; Lesage, A.; Caporini, M. A.; Vitzthum, V.; Miéville, P.; Héroguel, F.; Rascón, F.; Roussey, A.; Thieuleux, C.; Boualleg, M.; Veyre, L.; Bodenhausen, G.; Copéret, C.; Emsley, L. Fast Characterization of Functionalized Silica Materials by Silicon-29 Surface-Enhanced NMR Spectroscopy Using Dynamic Nuclear Polarization. *J. Am. Chem. Soc.* **2011**, *133* (7), 2104−2107.
(10) Kessenikh, A.; Lushchikov, V.; Manenkov, A.; Taran, Y. Proton Polarization in Irradiated Polyethylenes. *Sov. Phys.-Solid State* **1963**, *5*, 321−329.
(11) Hwang, C. F.; Hill, D. A. Phenomenological Model for the New Effect in Dynamic Polarization. *Phys. Rev. Lett.* **1967**, *19* (18), 1011−1014.
(12) Hartmann, S. R.; Hahn, E. L. Nuclear Double Resonance in the Rotating Frame. *Phys. Rev.* **1962**, *128* (5), 2042−2053.
(13) Pines, A.; Gibby, M. G.; Waugh, J. S. Proton-Enhanced NMR of Dilute Spins in Solids. *J. Chem. Phys.* **1973**, *59* (2), 569−590.
(14) Lafon, O.; Lilly Thankamony, A. S.; Rosay, M.; Aussenac, F.; Lu, X.; Trébosc, J.; Roumazeilles, V. B.; Vezine, H.; Amoureuxa, J. P. Indirect and Direct ^{29}Si Dynamic Nuclear Polarization of Dispersed Nanoparticles. *Chem. Commun.* **2013**, *49* (28), 2864−2866.
(15) Hall, D. A.; Maus, D. C.; Gerfen, G. J.; Inati, S. J.; Becerra, L. R.; Dahlquist, F. W.; Griffin, R. G. Polarization-Enhanced NMR Spectroscopy of Biomolecules in Frozen Solution. *Science* **1997**, *276* (5314), 930−932.
(16) Van Der Wel, P. C. A.; Hu, K. N.; Lewandowski, J.; Griffin, R. G. Dynamic Nuclear Polarization of Amyloidogenic Peptide Nanocrystals: GNNQQNY, a Core Segment of the Yeast Prion Protein Sup35p. *J. Am. Chem. Soc.* **2006**, *128* (33), 10840−10846.
(17) Sergeyev, I. V.; Day, L. A.; Goldbourt, A.; McDermott, A. E. Chemical Shifts for the Unusual DNA Structure in Pf1 Bacteriophage from Dynamic-Nuclear-Polarization-Enhanced Solid-State NMR Spectroscopy. *J. Am. Chem. Soc.* **2011**, *133* (50), 20208−20217.
(18) Renault, M.; Pawsey, S.; Bos, M. P.; Koers, E. J.; Nand, D.; Tommassen-Van Boxtel, R.; Rosay, M.; Tommassen, J.; Maas, W. E.; Baldus, M. Solid-State NMR Spectroscopy on Cellular Preparations Enhanced by Dynamic Nuclear Polarization. *Angew. Chemie - Int. Ed.* **2012**, *51* (12), 2998−3001.
(19) Moroz, I. B.; Leskes, M. Dynamic Nuclear Polarization Solid-State NMR Spectroscopy for Materials Research. *Annu. Rev. Mater. Res.* **2022**, *52*, 25−55.
(20) Biedenbänder, T.; Aladin, V.; Saeidpour, S.; Corzilius, B. Dynamic Nuclear Polarization for Sensitivity Enhancement in Biomolecular Solid-State NMR. *Chem. Rev.* **2022**, *122* (10), 9738−9794.
(21) Bothe, S.; Nowag, J.; Klimavičius, V.; Hoffmann, M.; Troitskaya, T. I.; Amosov, E. V.; Tormyshev, V. M.; Kirilyuk, I.; Taratayko, A.; Kuzhelev, A.; Parkhomenko, D.; Bagryanskaya, E.; Gutmann, T.; Buntkowsky, G. Novel Biradicals for Direct Excitation Highfield Dynamic Nuclear Polarization. *J. Phys. Chem. C* **2018**, *122* (21), 11422−11432.
(22) Chow, W. Y.; De Paëpe, G.; Hediger, S. Biomolecular and Biological Applications of Solid-State NMR with Dynamic Nuclear Polarization Enhancement. *Chem. Rev.* **2022**, *122* (10), 9795−9847.
(23) Carver, T. R.; Slichter, C. P. Experimental Verification of the Overhauser Nuclear Polarization Effect. *Phys. Rev.* **1956**, *102* (4), 975−980.
(24) Van Der Heijden, G. H. A.; Kentgens, A. P. M.; Van Bentum, P. J. M. Liquid State Dynamic Nuclear Polarization of Ethanol at 3.4 T (95 GHz). *Phys. Chem. Chem. Phys.* **2014**, *16* (18), 8493−8502.
(25) Barnes, R.; Sun, S.; Fichou, Y.; Dahlquist, F. W.; Heyden, M.; Han, S. Spatially Heterogeneous Surface Water Diffusivity around Structured Protein Surfaces at Equilibrium. *J. Am. Chem. Soc.* **2017**, *139* (49), 17890−17901.
(26) Neugebauer, P.; Krummenacker, J. G.; Denysenkov, V. P.; Parigi, G.; Luchinat, C.; Prisner, T. F. Liquid State DNP of Water at 9.2 T: An Experimental Access to Saturation. *Phys. Chem. Chem. Phys.* **2013**, *15* (16), 6049−6056.
(27) Enkin, N.; Liu, G.; Tkach, I.; Bennati, M. High DNP Efficiency of TEMPONE Radicals in Liquid Toluene at Low Concentrations. *Phys. Chem. Chem. Phys.* **2014**, *16* (19), 8795−8800.
(28) Neudert, O.; Mattea, C.; Spiess, H. W.; Stapf, S.; Münnemann, K. A Comparative Study of ^{1}H and ^{19}F Overhauser DNP in Fluorinated Benzenes. *Phys. Chem. Chem. Phys.* **2013**, *15* (47), 20717−20726.
(29) Loening, N. M.; Rosay, M.; Weis, V.; Griffin, R. G. Solution-State Dynamic Nuclear Polarization at High Magnetic Field. *J. Am. Chem. Soc.* **2002**, *124* (30), 8808−8809.
(30) Carver, T. R.; Slichter, C. P. Polarization of Nuclear Spins in Metals. *Phys. Rev.* **1953**, *92* (1), 212−213.
(31) Dubroca, T.; Smith, A. N.; Pike, K. J.; Froud, S.; Wylde, R.; Trociewitz, B.; McKay, J.; Mentink-Vigier, F.; van Tol, J.; Wi, S.; Brey, W.; Long, J. R.; Frydman, L.; Hill, S. A Quasi-Optical and Corrugated Waveguide Microwave Transmission System for Simultaneous Dynamic Nuclear Polarization NMR on Two Separate 14.1 T Spectrometers. *J. Magn. Reson.* **2018**, *289*, 35−44.
(32) Orlando, T.; Dervişoğlu, R.; Levien, M.; Tkach, I.; Prisner, T. F.; Andreas, L. B.; Denysenkov, V. P.; Bennati, M. Dynamic Nuclear Polarization of ^{13}C Nuclei in the Liquid State over a 10 T Field Range. *Angew. Chemie - Int. Ed.* **2019**, *58* (5), 1402−1406.
(33) Liu, G.; Levien, M.; Karschin, N.; Parigi, G.; Luchinat, C.; Bennati, M. One-Thousand-Fold Enhancement of High Field Liquid Nuclear Magnetic Resonance Signals at Room Temperature. *Nat. Chem.* **2017**, *9* (7), 676−680.
(34) Reinhard, M.; Levien, M.; Bennati, M.; Orlando, T. Large ^{31}P-NMR Enhancements in Liquid State Dynamic Nuclear Polarization

https://doi.org/10.1021/acs.jpclett.3c01732
J. Phys. Chem. Lett. 2023, 14, 7059−7064

through Radical/Target Molecule Non-Covalent Interaction. *Phys. Chem. Chem. Phys.* **2022**, *25* (1), 822−828.
(35) Griesinger, C.; Bennati, M.; Vieth, H. M.; Luchinat, C.; Parigi, G.; Höfer, P.; Engelke, F.; Glaser, S. J.; Denysenkov, V.; Prisner, T. F. Dynamic Nuclear Polarization at High Magnetic Fields in Liquids. *Prog. Nucl. Magn. Reson. Spectrosc.* **2012**, *64* (5), 4−28.
(36) Kuzhelev, A. A.; Dai, D.; Denysenkov, V.; Kirilyuk, I. A.; Bagryanskaya, E. G.; Prisner, T. F. Influence of Rotational Motion of Nitroxides on Overhauser Dynamic Nuclear Polarization: A Systematic Study at High Magnetic Fields. *J. Phys. Chem. C* **2021**, *125* (46), 25651−25659.
(37) Rao, Y.; Venkatesh, A.; Moutzouri, P.; Emsley, L. ^{1}H Hyperpolarization of Solutions by Overhauser Dynamic Nuclear Polarization with 13C-1H Polarization Transfer. *J. Phys. Chem. Lett.* **2022**, *13* (33), 7749−7755.
(38) Soundararajan, M.; Dubroca, T.; van Tol, J.; Hill, S.; Frydman, L.; Wi, S. Proton-Detected Solution-State NMR at 14.1 T Based on Scalar-Driven ^{13}C Overhauser Dynamic Nuclear Polarization. *J. Magn. Reson.* **2022**, *343*, No. 107304.
(39) Kuzhelev, A. A.; Dai, D.; Denysenkov, V.; Prisner, T. F. Solid-like Dynamic Nuclear Polarization Observed in the Fluid Phase of Lipid Bilayers at 9.4 T. *J. Am. Chem. Soc.* **2022**, *144* (3), 1164−1168.
(40) Kuzhelev, A. A.; Denysenkov, V.; Ahmad, I. M.; Rogozhnikova, O. Y.; Trukhin, D. V.; Bagryanskaya, E. G.; Tormyshev, V. M.; Sigurdsson, S. T.; Prisner, T. F. Solid-Effect Dynamic Nuclear Polarization in Viscous Liquids at 9.4 T Using Narrow-Line Polarizing Agents. *J. Am. Chem. Soc.* **2023**, *145* (18), 10268−10274.
(41) Leblond, J.; Uebersfeld, J.; Korringa, J. Study of the Liquid-State Dynamics by Means of Magnetic Resonance and Dynamic Polarization. *Phys. Rev. A* **1971**, *4* (4), 1532−1539.
(42) Karyagin, V. V.; Dovgopol, S. P. Frequency Dependence of Dynamic Nuclear Polarization in Viscous Solutions. *Sov. Phys. J.* **1972**, *15* (1), 54−57.
(43) Neudert, O.; Reh, M.; Spiess, H. W.; Münnemann, K. X-Band DNP Hyperpolarization of Viscous Liquids and Polymer Melts. *Macromol. Rapid Commun.* **2015**, *36* (10), 885−889.
(44) Gizatullin, B.; Gafurov, M.; Vakhin, A.; Rodionov, A.; Mamin, G.; Orlinskii, S.; Mattea, C.; Stapf, S. Native Vanadyl Complexes in Crude Oil as Polarizing Agents for in Situ Proton Dynamic Nuclear Polarization. *Energy Fuels* **2019**, *33* (11), 10923−10932.
(45) Gizatullin, B.; Mattea, C.; Stapf, S. Molecular Dynamics in Ionic Liquid/Radical Systems. *J. Phys. Chem. B* **2021**, *125* (18), 4850−4862.
(46) Denysenkov, V.; Dai, D.; Prisner, T. F. A Triple Resonance (e, ^{1}H, ^{13}C) Probehead for Liquid-State DNP Experiments at 9.4 T. *J. Magn. Reson.* **2022**, *337*, No. 107185.
(47) Morris, G. A.; Freeman, R. Enhancement of Nuclear Magnetic Resonance Signals by Polarization Transfer. *J. Am. Chem. Soc.* **1979**, *101* (3), 760−762.
(48) Nowacka, A.; Bongartz, N. A.; Ollila, O. H. S.; Nylander, T.; Topgaard, D. Signal Intensities in ^{1}H-^{13}C CP and INEPT MAS NMR of Liquid Crystals. *J. Magn. Reson.* **2013**, *230*, 165−175.
(49) Kintzinger, J. P.; Zeidler, M. D. Nuclear Magnetic Relaxation Study of Glycerol. *Bunsenges. Phys. Chem.* **1973**, *77* (2), 98−103.
(50) Battiste, J. L.; Wagner, G. Utilization of Site-Directed Spin Labeling and High-Resolution Heteronuclear Nuclear Magnetic Resonance for Global Fold Determination of Large Proteins with Limited Nuclear Overhauser Effect Data. *Biochemistry* **2000**, *39* (18), 5355−5365.
(51) Riek, R.; Wider, G.; Pervushin, K.; Wüthrich, K. Polarization Transfer by Cross-Correlated Relaxation in Solution NMR with Very Large Molecules. *Proc. Natl. Acad. Sci. U. S. A.* **1999**, *96* (9), 4918−4923.
(52) Riek, R.; Fiaux, J.; Bertelsen, E. B.; Horwich, A. L.; Wüthrich, K. Solution NMR Techniques for Large Molecular and Supramolecular Structures. *J. Am. Chem. Soc.* **2002**, *124* (41), 12144−12153.

https://doi.org/10.1021/acs.jpclett.3c01732
J. Phys. Chem. Lett. 2023, 14, 7059−7064

Supporting Information

^{13}C Hyperpolarization of Viscous Liquids by Transfer of Solid-Effect ^{1}H Dynamic Nuclear Polarization at High Magnetic Field

Danhua Dai,[1] Vasyl Denysenkov,[1] Elena G. Bagryanskaya,[2] Victor M. Tormyshev,[2] Thomas F. Prisner[1], Andrei A. Kuzhelev[1]*

[1]*Goethe University Frankfurt am Main, Institute of Physical and Theoretical Chemistry and Center for Biomolecular Magnetic Resonance, Max von Laue Str. 7, 60438 Frankfurt am Main, Germany.* kuzhelev@chemie.uni-frankfurt.de

[2]*N. N. Vorozhtsov Institute of Organic Chemistry, Siberian Branch of Russian Academy of Sciences (SB RAS), Acad. Lavrentiev Avenue 9, 630090 Novosibirsk, Russia.*

This PDF file includes:

Experimental Methods

Sample solutions were prepared by dissolving certain amounts of the sodium salt of the Finland radical in glycerol-$^{13}C_3$ (purchased from Sigma-Aldrich). The radical was synthesized according to a previously described protocol.[1] The concentration of the Finland radical was in the range from 5 to 100 mM and was determined by X-band continuous-wave EPR at room temperature.

^{1}H and ^{13}C DNP/NMR and ^{1}H – ^{13}C INEPT DNP/NMR were performed on a home-built DNP spectrometer based on Bruker Avance II wide-bore spectrometer operating at 9.4 T.[2] Microwaves were generated by a gyrotron (Gycom, Russian Federation) operating at 264 GHz with an output microwave power of 5 W. The DNP probehead is a home-built triple resonance structure (260 GHz/400 MHz/100 MHz).[3] DNP-enhanced and reference NMR FID signals were measured with standard π/2 RF-pulse excitation. INEPT was recorded using the pulse sequence ($\pi/2_x$ ^{1}H) – τ – (π_x ^{1}H) (π_x ^{13}C) – τ – ($\pi/2_{\pm y}$ ^{1}H) ($\pi/2_x$ ^{13}C) – (FID ^{13}C). Refocused INEPT was performed with pulse sequence ($\pi/2_x$ ^{1}H) – τ – (π_x ^{1}H) (π_x ^{13}C) – τ – ($\pi/2_{\pm y}$ ^{1}H) ($\pi/2_x$ ^{13}C) – τ_2 – (π_x ^{1}H) (π_x ^{13}C) – τ_2 – ($\pi/2_x$ /decoupling ^{1}H) (FID ^{13}C). These experiments were carried out by 2-step phase cycling. The π/2 pulse lengths were 34 and 80 μs for ^{1}H and ^{13}C nuclei, respectively. Delays τ and τ_2 in the INEPT experiment were set to $1/4J_{CH}$ and $1/6J_{CH}$, i.e., 1.72 ms and 1.15 ms, respectively. Repetition time was 1 second. The number of scans was 16/128 for ^{1}H DNP/NMR, 9216/61440 for ^{1}H – ^{13}C INEPT DNP/NMR, and 4096/204800 for ^{13}C DNP/NMR, respectively. The enhancements were measured by examination of the signal intensity and were calculated according to $\varepsilon = I_{DNP}/I_{0,H/C} - 1$ for ^{1}H/^{13}C DNP and $\varepsilon = I_{INEPT}/I_{0,C}$ for ^{1}H – ^{13}C INEPT NMR/DNP experiments, respectively, where $I_{0,H}$ and $I_{0,C}$ are Boltzmann ^{1}H/^{13}C polarization levels. Error of the measurements was estimated as 10 %. It was determined by repeating an experiment several times with following statistical averaging.

The ^{1}H/^{13}C NMR T_1 and T_2 relaxation experiments as well as ^{1}H – ^{13}C INEPT NMR were carried out at a magnetic field of 9.4 T and room temperature using the standard Bruker BBI probehead. The volume of the solution in the probehead was around 10 μL. The T_2 and T_1 relaxation times were measured by means of a standard Carr-Purcell-Meiboom-Gill (CPMG) and inversion recovery sequences, respectively. The experiments were performed with and without cw ^{1}H-decoupling. Obtained relaxation curves were fitted to a mono-exponential function (Figures S2-S5). The π/2 pulse lengths were 24 and 29 μs for ^{1}H and ^{13}C nuclei, respectively. Delay τ in the INEPT experiment was set to $1/4J_{CH}$, i.e., 1.72 ms. The repetition time was 2 s. The number of scans was 4/16 for relaxation measurements for ^{1}H/^{13}C, respectively, and 64 for ^{1}H – ^{13}C INEPT NMR.

DNP field profiles

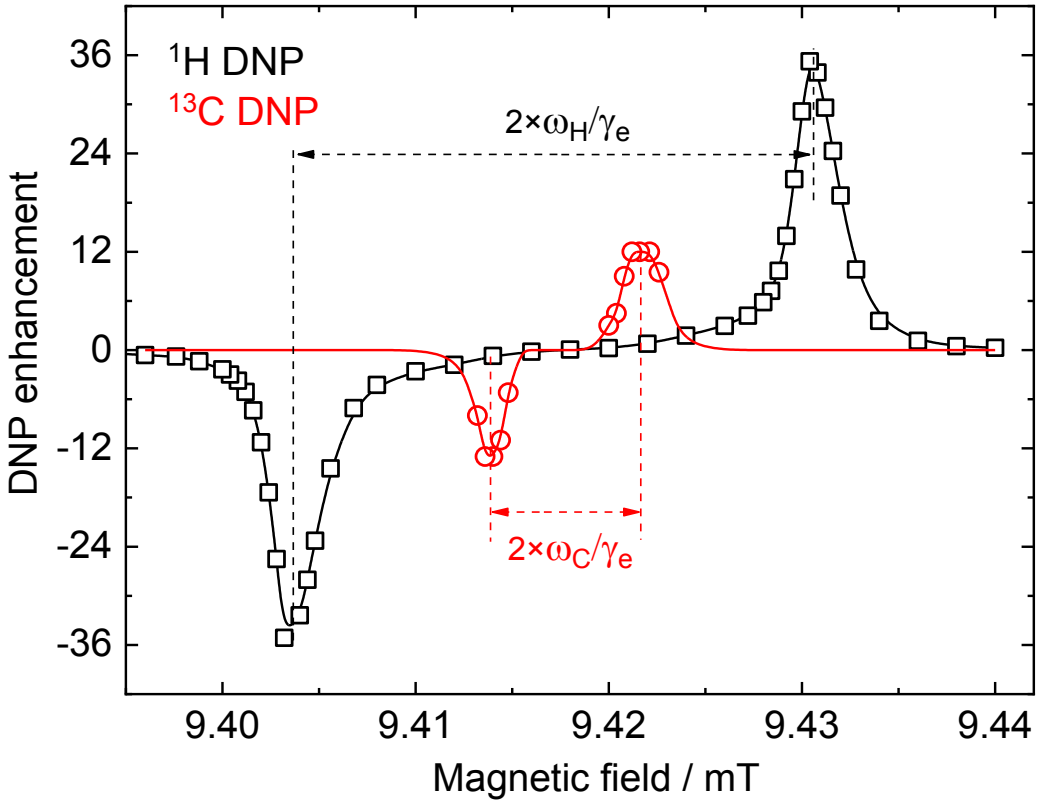

Figure S1. ^{1}H and ^{13}C DNP field profiles for glycerol-$^{13}C_3$ in the presence of 100 mM Finland trityl at a magnetic field of 9.4 T and a temperature of 315 K. The antisymmetric peaks are separated by $2\times\omega_H/\gamma_e$ and $2\times\omega_C/\gamma_e$ for ^{1}H and ^{13}C nuclei, respectively, suggesting that DNP mechanism is the solid effect. The maximum solid-effect DNP enhancements are ±35 and ±12 for ^{1}H and ^{13}C nuclei, respectively.

Nuclear spin relaxation curves

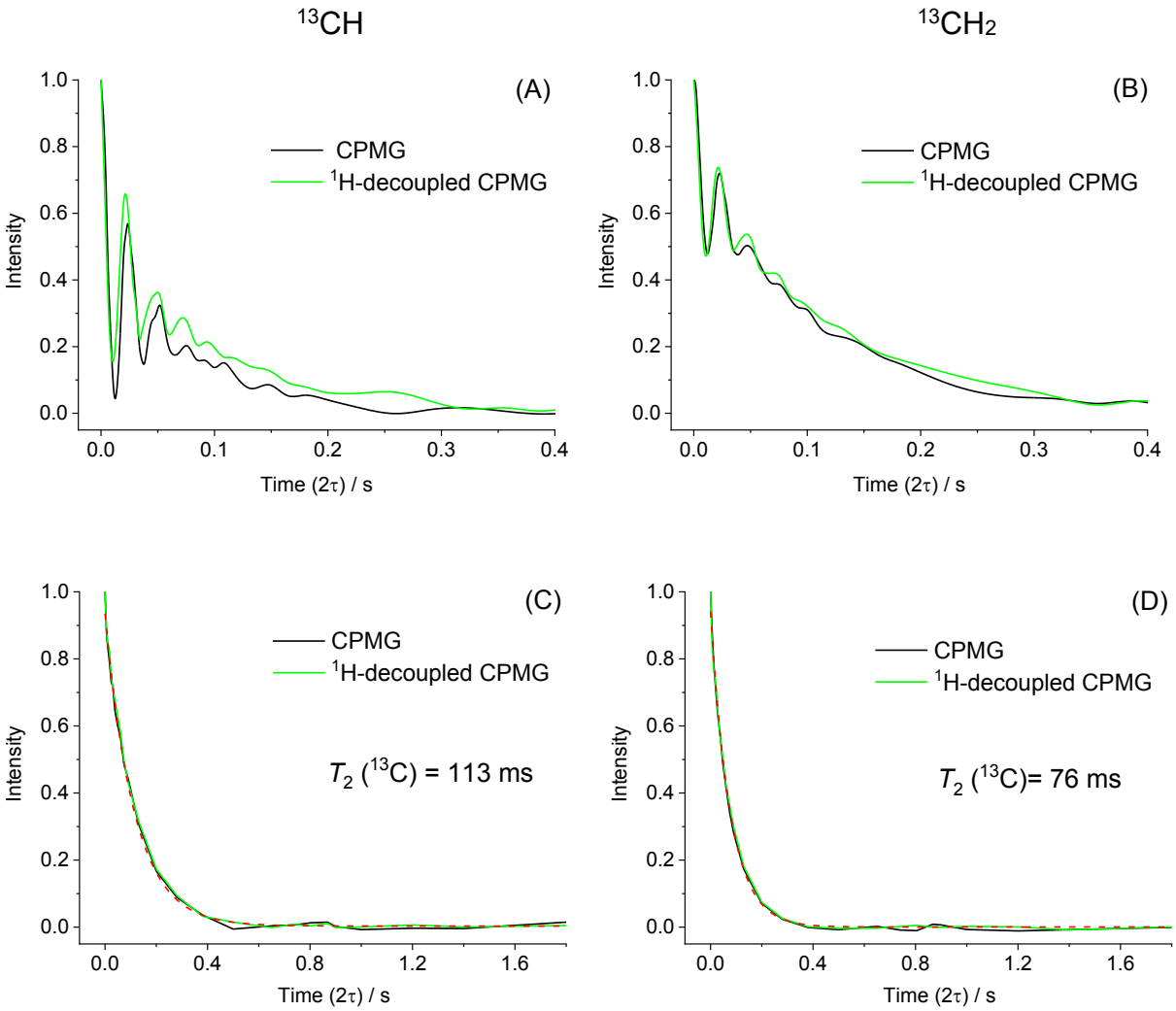

Figure S2. ^{13}C transverse relaxation curves for glycerol-$^{13}C_3$ (A, B) and glycerol (C, D) measured at a magnetic field of 9.4 T and a temperature of 298 K using CPMG (black line) and ^{1}H-decoupled CPMG (green line) pulse sequences. The CPMG experiments with and without proton-decoupling show very similar relaxation curves. The red dashed lines reveal the best-fit mono-exponential curve. For glycerol-$^{13}C_3$ the ^{13}C T_2 relaxation is modulated by the intramolecular spin-coupling (J_{CC} = 40 Hz) between ^{13}C-^{13}C nuclei.

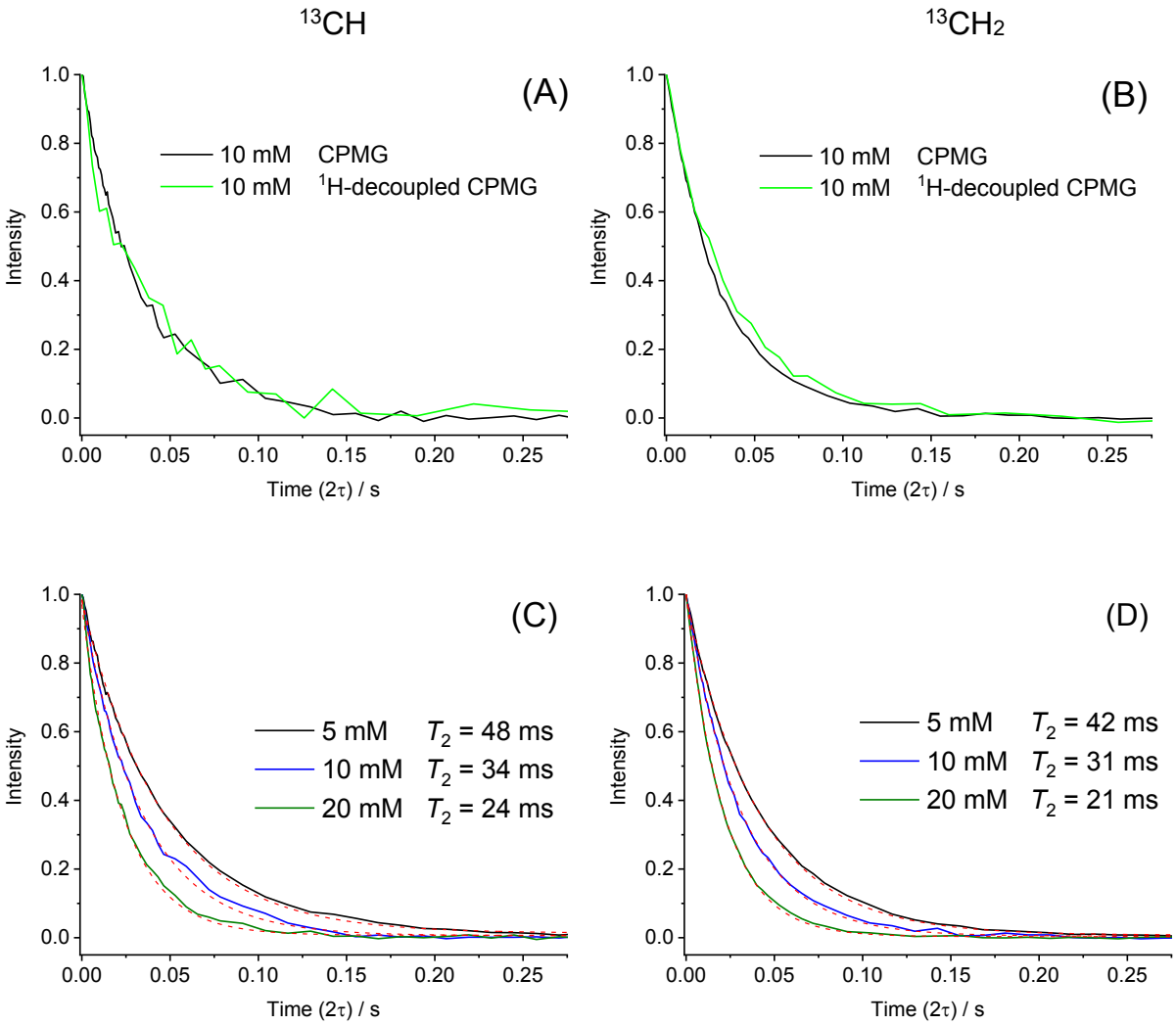

Figure S3. ^{13}C transverse relaxation curves for glycerol-$^{13}C_3$ in the presence of 5, 10, and 20 mM Finland trityl radicals (C, D) measured at a magnetic field of 9.4 T and a temperature of 298 K using CPMG and ^{1}H-decoupled CPMG (A, B, green lines) pulse sequences. The CPMG experiments with and without decoupling show very similar relaxation curves. The red dashed lines reveal the best-fit mono-exponential curve. In the presence of a polarizing agent the T_2 (^{13}C) relaxation curves contain neglectable oscillations.

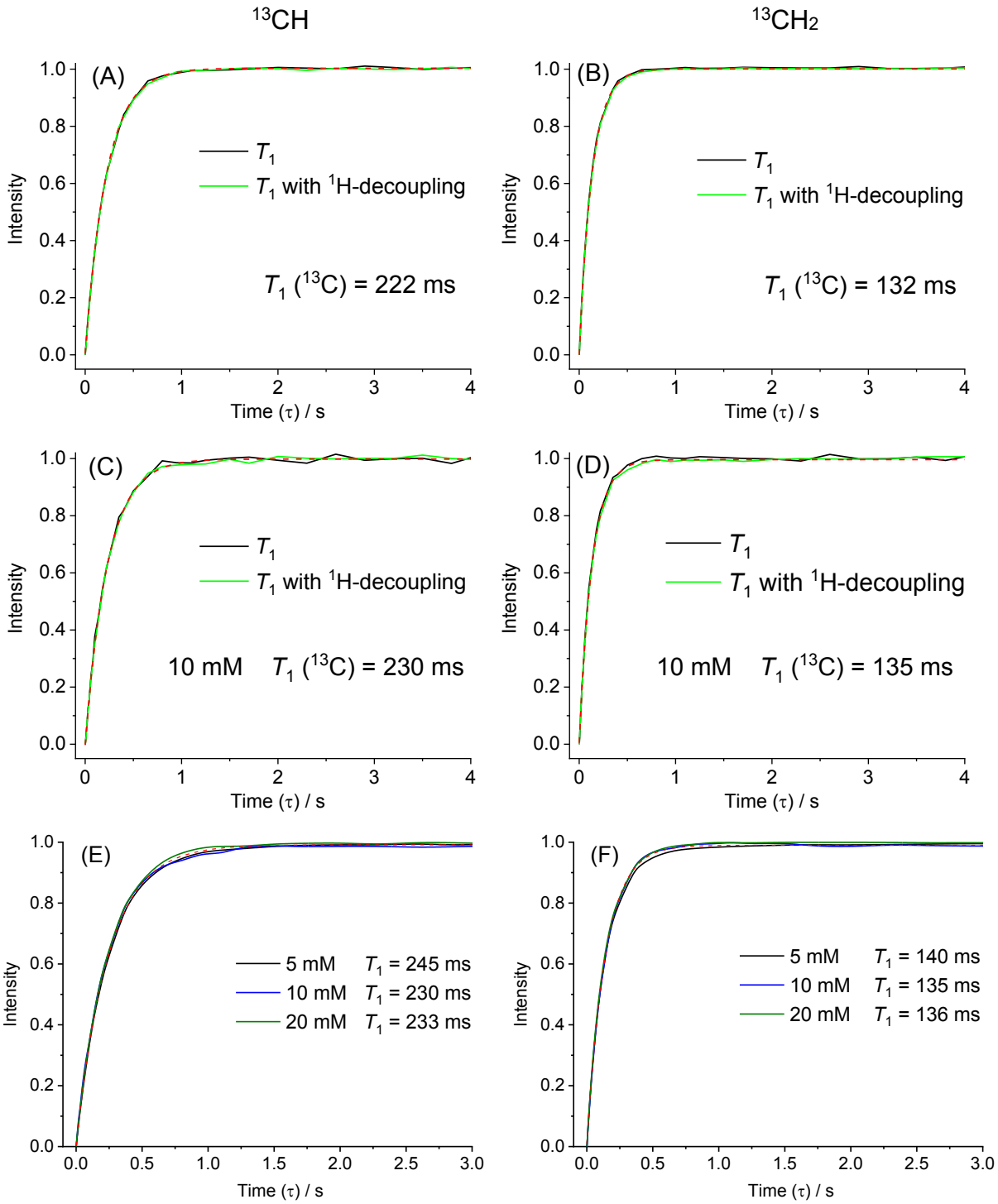

Figure S4. ^{13}C longitudinal relaxation curves for glycerol-$^{13}C_3$ in the absence (A, B) and presence of 10 mM Finland trityl radicals (C, D) measured at a magnetic field of 9.4 T and a temperature of 298 K using inversion recovery with and without ^{1}H-decoupling. (E, F) The T_1 relaxation curves measured by inversion recovery for glycerol-$^{13}C_3$ solution doped with 5, 10, and 20 mM Finland trityl radicals. The red dashed lines show the best-fit mono-exponential curve.

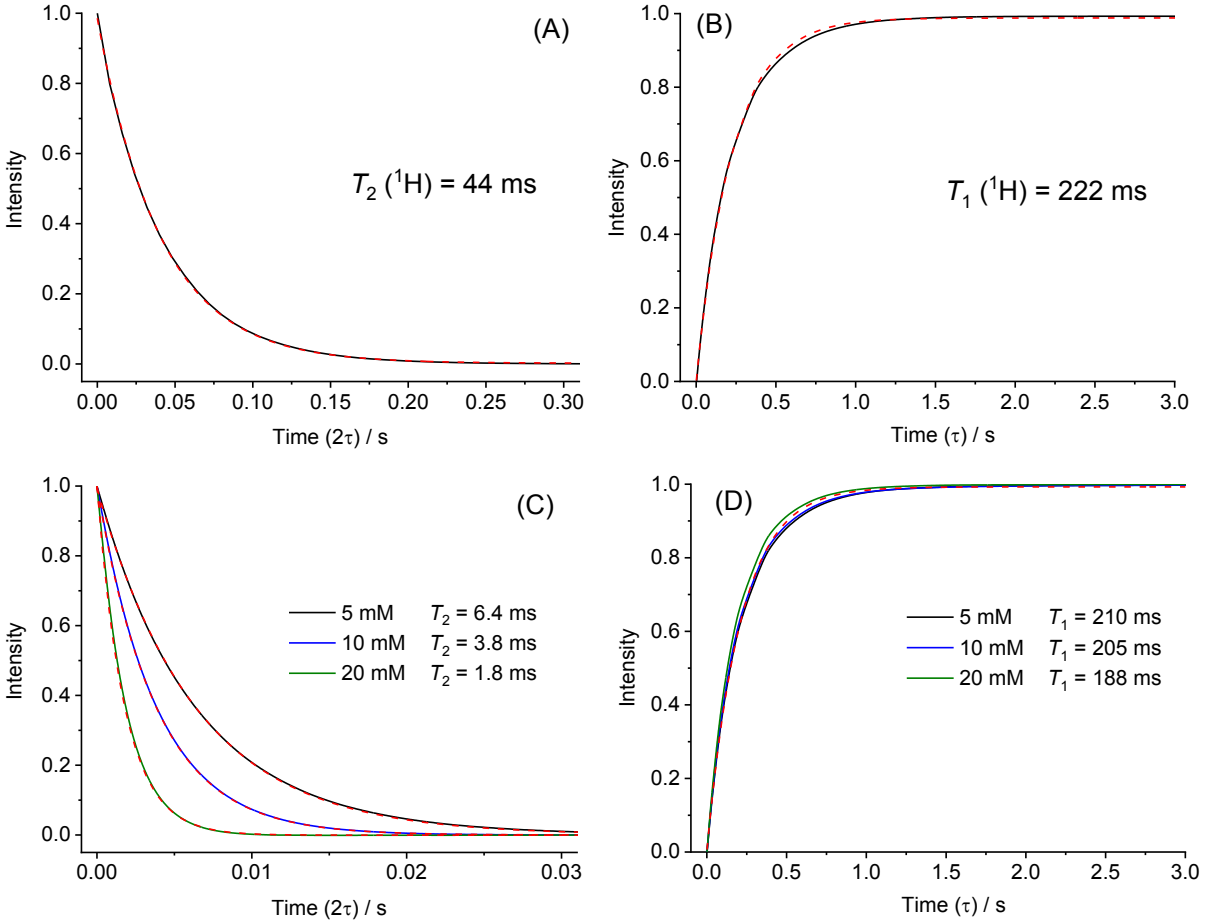

Figure S5. ^{1}H transverse (A,C) and longitudinal (B,D) relaxation curves for glycerol-$^{13}C_3$ in the absence (A, B) and presence of 5, 10, and 20 mM Finland trityl radicals (C, D) measured at a magnetic field of 9.4 T and a temperature of 298 K. The red dashed lines show the best-fit mono-exponential curve.

^{1}H – ^{13}C INEPT NMR using the triple-resonance probehead

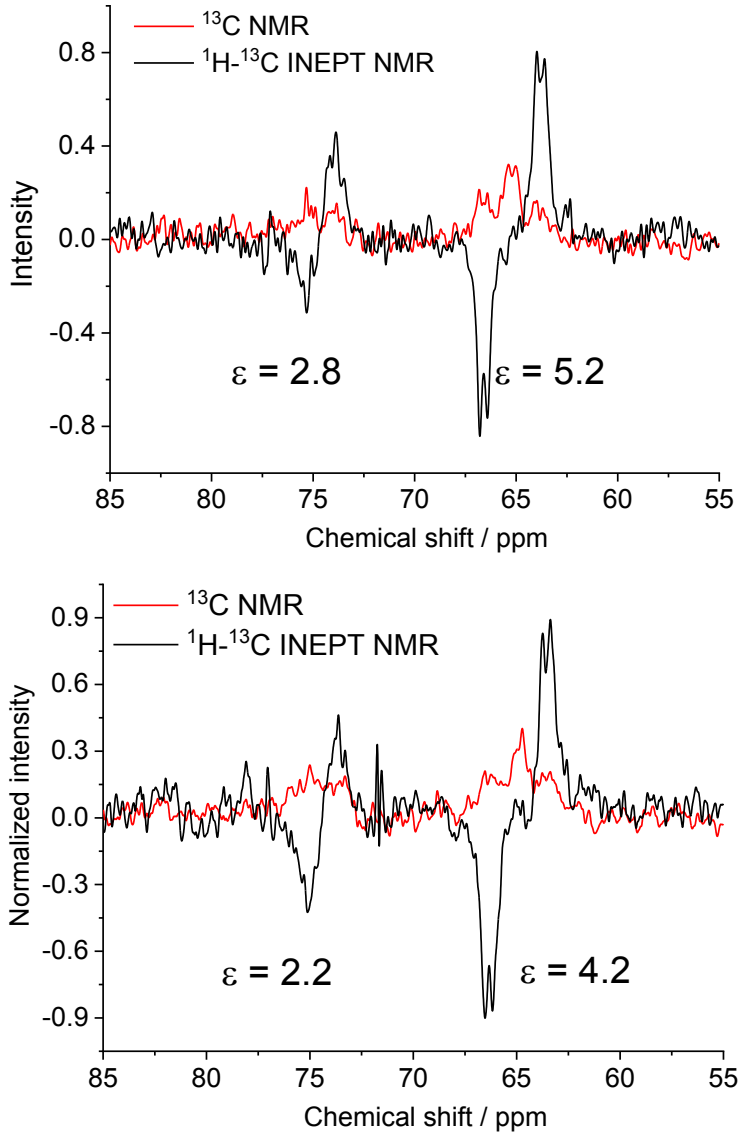

Figure S6. ^{1}H – ^{13}C INEPT NMR (red line) and ^{13}C NMR (black line) spectra obtained at 9.4 T at a temperature of 315 K without microwave irradiation for glycerol-$^{13}C_3$ in the presence of Finland trityl at a concentration of 5 mM (top), 10 mM (bottom). The NMR experiments were performed using the triple-resonance probehead. The spectra were normalized to single scan.

Refocused and ^{1}H-decoupled INEPT

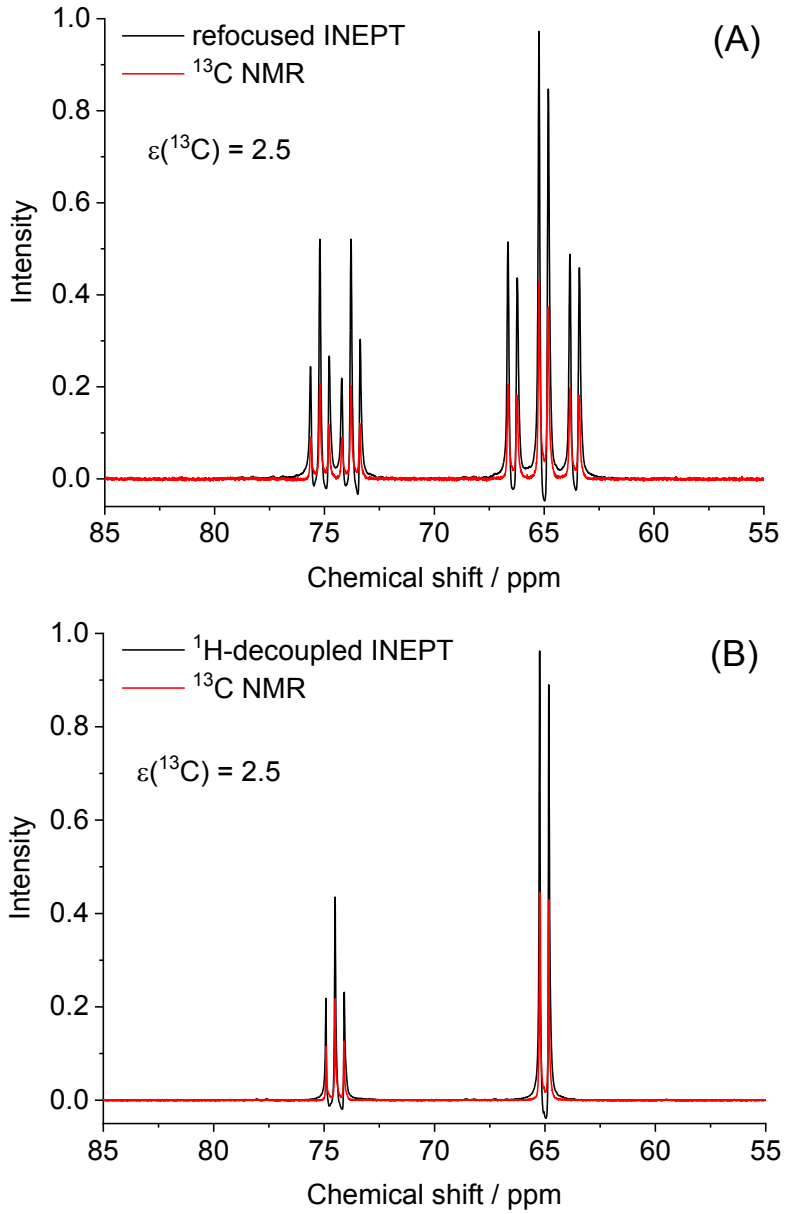

Figure S7. ^{1}H – ^{13}C refocused INEPT NMR (A) and ^{1}H-decoupled refocused INEPT NMR spectra (B) of glycerol-$^{13}C_3$ obtained at 9.4 T and room temperature. The NMR experiments were performed using the Bruker BBI probehead. The spectra were normalized to single scan. The addition pulses and delays in the INEPT sequence causes a decrease in signal strength due to loss of magnetization from relaxation times of both ^{1}H and ^{13}C nuclei. Moreover, severe phase distortions, particularly for CH_2 groups, and J-coupling between ^{13}C-^{13}C nuclei produce anomalous results.

References

(1) Rogozhnikova, O. Y.; Vasiliev, V. G.; Troitskaya, T. I.; Trukhin, D. V.; Mikhalina, T. V.; Halpern, H. J.; Tormyshev, V. M. Generation of Trityl Radicals by Nucleophilic Quenching of Tris(2,3,5,6-Tetrathiaaryl)Methyl Cations and Practical and Convenient Large-Scale Synthesis of Persistent Tris(4-Carboxy-2,3,5,6-Tetrathiaaryl)Methyl Radical. *European J. Org. Chem.* **2013**, *2013* (16), 3347–3355.

(2) Denysenkov, V.; Prandolini, M. J.; Gafurov, M.; Sezer, D.; Endeward, B.; Prisner, T. F. Liquid State DNP Using a 260 GHz High Power Gyrotron. *Phys. Chem. Chem. Phys.* **2010**, *12* (22), 5786–5790.

(3) Denysenkov, V.; Dai, D.; Prisner, T. F. A Triple Resonance (e, ^{1}H, ^{13}C) Probehead for Liquid-State DNP Experiments at 9.4 Tesla. *J. Magn. Reson.* **2022**, *337*, 107185.

9. Summary and outlook

Within the scope of this thesis, the capability of liquid-state DNP at high fields, specifically 9.4 T, was extended from several perspectives as presented in Chapter 4-8.

Scalar OE DNP

OE driven by scalar HFI is of particular interest for liquid-state DNP studies as the mechanism is predicted to be still efficient at high magnetic fields.[23] The ^{13}C enhancements observed on halogenated hydrocarbons were also encouraging.[50,51] The relaxation process driven by scalar HFI depends, on one side, on the spectral density dispersed on the electron Larmor frequency and, on the other side, on the magnitude of the Fermi contact interaction. Given that the magnitude of the Fermi contact interaction is more readily accessible than the spectral density, a methodology to prescreen the potential DNP candidates by measuring their paramagnetic NMR shifts was proposed and examined in the work shown in Section 4.2. On the selected two small biomolecules, imidazole and indole, which exhibit sizable paramagnetic shifts in the presence of nitroxide radicals,[88] we were able to observe significant ^{13}C scalar OE DNP enhancement up to 50 in water and CCl_4, respectively. Based on this prescreening method, further paramagnetic NMR and DNP measurements were performed on a series of amino acids and carbon hydrates. A qualitative relation between the Fermi contact shift and the scalar DNP enhancement was presented. A subsequent collaborative quantum chemical MD study conducted by the He group revealed the sub-ps fluctuation featured by the autocorrelation function of the spin density and suggested that the responsible modulation arises from the intermolecular hydrogen-bond dynamics of the long-living radical-substrate complex.

Utilizing the available published data of paramagnetic NMR shifts, it becomes applicable to exclude numerous less relevant molecules and preliminarily select the

target candidates for subsequent DNP measurements. Nevertheless, the observed enhancement is complicated by the electron spin density distribution on the molecules, the SDF determined by the molecular dynamics, and the counteractive dipolar HFI-driven OE. A quantitative prediction of the scalar DNP efficiency requires a more comprehensive and systematic analysis.[78,102]

SE DNP

As presented in Section 5.2, the SE DNP observed on lipids molecules above the gel-to-liquid-crystalline phase transition temperature provides novel opportunities for liquid-state DNP at high magnetic fields. Unlike OE DNP relying on a dynamical modulation of the HFI, SE in liquids requires the anisotropic HFI not being averaged out by the stochastic motions namely a non-zero state mixing factor as shown in Section 2.4.5. Therefore, it is exploited only in viscous medium.[89-91,103] The nuclear spin forbidden transition, which is partly allowed by the anisotropic HFI as described by the second order perturbation theory, is very inefficient at high magnetic fields. A strong mw nutation frequency provided by a high-quality resonator can partially compensate for this disadvantage. Likewise, a polarizing agent with a narrow EPR linewidth also helps. Theoretical approaches to the SE efficiency in liquids has been performed at low fields[104,105] and high fields[93,94], which suggests that the dipolar correlation time should be longer as the electron transverse relaxation time. This new approach utilizing SE in viscous liquids provides an alternative mechanism to OE in liquids at high fields and could be potentially applicable to macromolecules with relatively slow tumbling.

Dipolar OE DNP

In the case of dipolar OE DNP, we have systematically studied the contribution of inner-sphere rotation to the OE DNP efficiency by utilizing different nitroxide derivatives with distinct ring geometries and substituents as shown in Section 7.2. A regulation of the observed DNP coupling factor on DMSO molecules is observed

by those polarizing agents featuring different rotation correlation times determined by the cw EPR measurements. A dependence of coupling factors on the ring geometry and substituents is absent. With the molecular motions modeled by both inner-sphere rotation and outer-sphere translation, a quantitative match to the experimental results is achieved, which supports the assumed contribution from the rotation of the inner-sphere complex.

As the characteristic time of the inner-sphere rotation might raise concerns about the lifetime of the complex, another model assuming an outer-sphere translation along with the off-centered rotation of radical molecules is examined (see Section 7.3). Similar as the inner- and outer-sphere approach, a quantitative alignment with the experimental observations on DMSO is presented but with a distance of closest approach closer to the value suggested by the radial distribution function from MD simulations. Moreover, our simulations with off-centered rotation were compared with the field-dependent DNP enhancements of water doped with nitroxide radicals achieved at different fields[67,69,95] and gives close results as predicted by MD simulations.[97] Compared with the inner-sphere rotation and outers-sphere translation with centered spins, this model taking into account the off-centered rotation of radical electron spins can also quantitatively predict the DNP coupling factor and is more meaningful in understanding the real physical processes. It can be used in explanation or re-interpretation of the experimental results.

As shown in Section 6.2, we have performed further studies on the lipid bilayers based on the observed ^{1}H DNP in a viscous lipid environment at 9.4 T.[45] By measuring the field profile, DNP enhancements driven by OE and SE were characterized according to their relative offset to the electron Larmor frequency. With a satisfied NMR signal resolution, and an experimental determination of the DNP leakage factor and saturation factor, the individual OE DNP efficiency of water, lipid choline head and acyl chain protons were obtained. Though the coupling factors predicted by the dipolar autocorrelation function exhibit discrepancies to the

experimental observations, the fast dynamics close to the electron Larmor frequency, which is obligated for a successful OE DNP, is well captured by the MD simulations. Further analysis by disentangle the OE and SE contribution considering the dynamical modulated SE and g-tensor broadened OE, which could provide valuable insights of the fast dynamics responsible for the DNP on lipid protons, is engaged. Besides, the MD simulations also suggests the DNP coupling factor of water in liposome sample is contributed mainly by the spin labels flipped to the lipid/water boundary. This is contradictory to the interpretation of previous DNP results obtained at low fields,[106] which also requires further investigations.

Triple-resonance DNP

During this doctoral work, two different triple-resonance DNP experiments were performed, including ^{13}C OE DNP under ^{1}H decoupling performed on sodium pyruvate aqueous solution (see Section 8.2), and ^{13}C NMR of glycerol enhanced by transferring the SE DNP-enhanced ^{1}H spin polarization with a ^{1}H-^{13}C INEPT pulse sequence (see Section 8.3).

The ^{13}C NMR signal of sodium pyruvate enhanced by scalar DNP shows a single peak under ^{1}H decoupling as expected. Notably, slightly different scalar enhancements were observed with ^{1}H decoupling ($\varepsilon_{13C} = 12$) and without ^{1}H decoupling ($\varepsilon_{13C} = 16$). Further investigations are needed to understand whether this is a technical issue or a result of the coupled/decoupled three-spin system.

Using an INEPT pulse sequence, a ^{13}C enhancement up to 45 was achieved by transferring the ^{1}H hyperpolarization generated by SE DNP. It is worth noting that the INEPT-DNP efficiency was constrained by the ^{1}H nuclear transverse relaxation with high radical concentration, which indicates an optimized radical concentration is required for future applications.

These approaches of triple-resonance DNP in liquids provides information for potential integration into the high-dimensional applications of modern NMR.

10. Deutsche Zusammenfassung

Seit ihrer Entdeckung vor mehr als sieben Jahrzehnten[1-3] hat sich die Kernspinresonanz(NMR)-Spektroskopie als ein leistungsstarkes analytisches Werkzeug etabliert, das vielseitige Anwendungen in verschiedenen wissenschaftlichen Disziplinen und Industriezweigen, einschließlich Chemie, Biologie, Materialwissenschaften und Medizin[4-7], aufweist. Sie bietet einen nicht-invasiven Zugang zu den Eigenschaften von Materie auf atomarer Ebene und liefert wertvolle Einblicke in die molekulare Struktur, deren Wechselwirkungen und Dynamiken. Allerdings beinhaltet die NMR eine sehr geringe Wechselwirkungsenergie zwischen den Kernspins und dem externen Magnetfeld, was insbesondere bei Raumtemperaturmessungen deutlich wird. Diese inhärente Eigenschaft der NMR macht sie zu einer zerstörungsfreien Methode, legt jedoch auch Grenzen für ihre Empfindlichkeit fest und beschränkt ihre Möglichkeiten in fortgeschrittenen Anwendungen. Um das Sensitivitätsproblem der NMR anzugehen, wurden enorme Anstrengungen unternommen, um die Intensität der NMR-Signale zu erhöhen. Neben der Weiterentwicklung von Geräten und experimentellen Verfahren[8] wurden in den letzten Jahrzehnten kontinuierlich unterschiedliche Hyperpolarisationstechniken entwickelt, wie die Dynamische Kernpolarisation (DNP) [9], die photochemisch induzierte Dynamische Kernpolarisation (Photo-CIDNP)[10], die Parahydrogen-induzierte Polarisation (PHIP)[11-13] und die optische Anregung von Edelgasen[14].

Unter diesen Hyperpolarisationstechniken wird DNP, genauer gesagt Continuous-Wave (cw) DNP in Flüssigkeiten, der Schwerpunkt dieser Arbeit sein. Als Technik, die Aspekte der NMR-Spektroskopie und der Elektronenspinresonanz(EPR)-Spektroskopie kombiniert, erhöht DNP die Empfindlichkeit der NMR, indem sie die Polarisation von ungepaarten Elektronenspins auf die benachbarten Kernspins überträgt. Mehrere DNP-Mechanismen wurden vorgeschlagen, um die beobachteten

Verstärkungen des NMR Signals in verschiedenen Probensystemen zu erklären. Der erste Mechanismus, der zuerst von Overhauser im Jahr 1953 vorstellte[9] und später experimentell in Lithium verifiziert[15] wurde, beruht auf den Kreuzrelaxations-prozessen der gekoppelten Elektron-Kern(e-N)-Spins und wird als Overhauser-Effekt (OE) DNP bezeichnet. Es ist notwendig, die e-N Hyperfeinwechselwirkung (hfWW) durch stochastische Dynamik zu modulieren, um eine solche Kreuzrelaxation zu induzieren. Diese Modulation ist in molekularen Systemen mit dynamischen e-N Spinpaaren erreichbar, wie zum Beispiel Metallen mit freien beweglichen Elektronen oder Lösungen, die mit Radikalen versetzt sind. Ein weiterer DNP-Mechanismus namens Solid-Effekt (SE) wurde später in di-elektrischen Feststoffen experimentell validiert.[16,17] SE beruht auf der Mischung von Kernspinzuständen in Anwesenheit eines anisotropen hfWW-Feldes. Daher wird er typischerweise in Feststoffproben angewendet, da die anisotropen hfWW in nicht-viskosen Flüssigkeiten vollständig ausgemittelt werden. In Feststoffproben wurden weitere alternative DNP-Mechanismen entdeckt, bei denen ein Kernspin mit zwei oder mehreren Elektronenspins gekoppelt ist. Diese werden als Kreuz-Effekt (CE)[18,19] und thermische Mischung (TM)[20] bezeichnet wurden.

Vor den 1990er Jahren war das wissenschaftliche Interesse hauptsächlich auf DNP-Untersuchungen bei niedrigen Magnetfeldern beschränkt, was sich von der Entwicklung der NMR-Forschung hin zu höheren Magnetfeldern unterschied. Dies war auf theoretische Vorhersagen zurückzuführen, die eine ungünstige DNP-Effizienz aller bekannten DNP-Mechanismen bei hohen Magnetfeldern nahelegten. Ein weiterer Grund ist der Mangel an hochfrequenten Mikrowellen(mw)-Quellen, um den Übergang des Elektronenspins effizient anzutreiben.[21-24]

In den letzten drei Jahrzehnten erlebte die DNP eine Renaissance, bedingt durch die Verfügbarkeit leistungsstarker Gyrotron-mw-Quellen.[25] In Verbindung mit schneller Probenrotation um den magischen Winkel (MAS) hat die DNP in Festkörpern vielfältige Anwendungen von Biomolekülen bis hin zu Materialien bei

hohen Magnetfeldern gefunden.[26,27] Die Dissolution-DNP nutzt die hohe DNP-Effizienz, die bei niedrigen Temperaturen und moderaten Magnetfeldern erreicht wird, und kann durch einen anschließenden schnellen Dissolutionprozess und NMR-Detektion bei hohen Magnetfeldern signifikante Signalverstärkungen liefern.[28,29] Neben den Ansätzen mit cw mw-Strahlung wurden verschiedene gepulste DNP-Techniken entwickelt, um die Effizienzbeschränkungen der DNP-Mechanismen zu umgehen, wie zum Beispiel die "Nuclear Spin Orientation via Electron Spin Locking" (NOVEL),[30,31] DNP im nuklearen Rotationsrahmen[32] sowie die zeitoptimierte gepulste DNP[33].

Jedoch wurde die Anwendung von DNP für Flüssigkeiten im Vergleich zu Festkörperproben bei niedrigen Temperaturen (≈100 K) weit weniger erforscht.[34] Die Hauptherausforderung liegt in der Probenstabilität, die durch starke Erwärmung aufgrund der dielektrischen Verluste von Flüssigkeiten mit hochfrequenten mw-Strahlung verursacht wird. Dieses technische Problem kann effektiv durch die Optimierung des Designs des DNP-Probenkopfes gelöst werden, beispielsweise die Verwendung eines mw-Resonators, der die E- und B-Komponenten der mw trennt, die Verbesserung der Wärmeleitfähigkeit des Probenhalters und die Anwendung aktiver Probenkühlmethoden.[35,36] Diese Modifikationen benötigt zwar eine gewisse Einschränkung des Probenvolumens, ermöglichen aber auch die Trennung der Temperaturschwankungen von der DNP-Effizienz. Darüber hinaus sinkt, ähnlich wie bei den anderen DNP-Mechanismen, die vorhergesagte OE DNP-Effizienz schnell mit zunehmenden Magnetfeldern. Die Spektraldichtefunktion (SDF), die theoretisch die OE DNP-Effizienz bestimmt, wurde aus den hfWW unter molekularen Rotations- und Translationsbewegungen abgeleitet.[37-40] Diese Bewegungen, die durch das klassische Stokes-Einstein-Model mit einer typischen Korrelationszeit von Zehnteln bis Hundertsteln von Pikosekunden beschrieben werden, erklären hinreichend die beobachtete OE DNP-Effizienz bei niedrigen

Magnetfeldern (< 1,5 T), können jedoch keine erhebliche spektrale Dichte bei hohen Magnetfeldern (> 3 T) erzeugen.

Obwohl die ersten Beobachtungen wie erwartet eine gesunkene DNP-Effizienz zeigen,[41-43] hat der Fortschritt der Flüssigkeits-DNP in den letzten Jahren ihr Potenzial bei hohen Magnetfeldern aufgezeigt. Bereits vor Beginn dieser Doktorarbeit wurde erkannt, dass das einfache Model der molekularen Rotation und Translation unzureichend sein könnte, um die DNP-Effizienz bei hohen Feldern zu beschreiben, die besonders empfindlich auf schnelle Fluktuationen reagiert.[44] Das deutlichste Beispiel ist die dipolare hfWW-getriebene ^{1}H OE DNP mit einem Verstärkungsfaktor von -10, die an orientierten Lipiddoppelschichten mit Nitroxidradikalen bei Umgebungstemperaturen und 9,4 T beobachtet wurde.[45] Eine Dynamik mit einer Korrelationszeit $\tau \approx$ 0,6 ps, vergleichbar mit der inversen Elektronen-Larmor-Frequenz ($1/\omega_e$), ist erforderlich, um eine effiziente DNP-Polarisationsübertragung bei diesem Magnetfeld zu erreichen. Allerdings sind die Charakterisierungszeiten für die laterale Diffusion oder axiale Rotation der Lipide um mindestens drei Größenordnungen langsamer,[46-48] was auf eine treibende Kraft aus der lokalen schnellen Dynamik hinweist. Ein weiterer vielversprechender Ansatz bei hohen Magnetfeldern ist die skalare hfWW-getriebene DNP. Theoretisch trägt die skalare hfWW überwiegend zur e-N Zero-Quantum-Kreuzrelaxation bei und hat vernachlässigbare Auswirkungen auf die nukleare Single-Quantum-Relaxation für organische Radikale in Flüssigkeiten.[23] Daher kann die DNP-Effizienz in molekularen Systemen mit dominanter skalare hfWW-induzierter Relaxation auch bei erhöhten Magnetfeldern erheblich bleiben. Ein rechnerischer Ansatz mit Dichtefunktionaltheorie (DFT)-Berechnungen und Molekular-dynamik(MD)-Simulationen hat dieses Potenzial der skalaren DNP bei hohen Magnetfeldern ebenfalls vorhergesagt.[49] Die ersten und auch repräsentativsten experimentellen Nachweise sind die ^{13}C OE DNP, die mit einem Verstärkungsfaktor von bis zu 930 in CCl_4-Lösung bei 3,4 T[50] und bis zu 600 in CBr_4-Lösung bei 9,4

T^{51} beobachtet wurden. Die für skalare DNP verantwortliche Dynamik ist ebenfalls nicht auf molekulare Bewegungen beschränkt. Obwohl der Mechanismus noch diskutiert wird, zeigen experimentelle Beobachtungen, dass OE DNP bei hohen Feldern und niedrigen Temperaturen auch in nichtleitende Festkörpern effektiv ist.[52,53] Eine solche schnelle dynamische Modulation der skalaren hfWW, die für die OE DNP verantwortlich ist, existiert sogar bei 1,2 K.[54]

Im Vergleich zu den in Festkörpern durchgeführt Forschungen, bieten Flüssigkeits-DNP-Messungen einen ergänzenden Einblick in die molekulare Konformation, Dynamik und Substrat-Radikalen-Wechselwirkungen von Molekülen in Lösungen oder sogar in ihrer natürlichen Umgebung. Die Vielfalt aktueller OE DNP-Strategien legt nahe, dass die Flüssigkeits-DNP auch bei eingeschränktem Probenvolumen und Selektivität gegenüber molekularen Systemen ein großes Potenzial hat. In dieser Arbeit wird gezeigt, dass die Flüssigkeits-DNP bei hohen Magnetfeldern, insbesondere bei 9,4 T mit hocheffiziente DNP-Probenköpfen möglich ist.

Skalare OE DNP

Der von skalaren hfWW angetriebene OE ist für Flüssigzustands-DNP-Forschungen von besonderem Interesse, da der von der Theorie vorhergesagte Mechanismus auch bei hohen Magnetfeldern noch effizient ist.[23] Der durch skalare hfWW angetriebene Relaxationsprozess hängt einerseits von der SDF der Dynamik bei der Elektronen-Larmor-Frequenz ab, und andererseits von der Größe der Fermi-Kontakt-Wechselwirkung. Da die Größe der Fermi-Kontakt-Wechselwirkung leichter experimentell zugänglich ist als die Vorhersage der SDF, wurde in der vorliegenden Arbeit (Abschnitt 4.2) eine Methode zur Vorabprüfung potenzieller DNP-Kandidaten durch Messungen ihrer paramagnetischen NMR-Verschiebungen vorgeschlagen und untersucht. Bei den beiden ausgewählten kleinen Biomolekülen, Imidazol und Indol, die in Gegenwart von Nitroxidradikalen beträchtliche paramagnetische Verschiebungen aufweisen,[88] konnten wir eine signifikante ^{13}C-

skalare OE DNP-Verstärkung in Wasser bzw. CCl_4 beobachten. Basierend auf dieser "Screening"-Methode wurden weitere paramagnetische NMR- und DNP-Messungen an einer Reihe von Aminosäuren und Kohlenhydraten durchgeführt. Es wurde ein qualitativer Zusammenhang zwischen der Fermi-Kontakt-NMR Verschiebung und der skalaren DNP-Verstärkungsfaktoren präsentiert. Eine anschließende quantenchemische MD-Studie zeigte die sub-ps-Fluktuationen der Spindichte, und legte nahe, dass die verantwortliche Modulation der hfWW aus der intermolekularen Wasserstoffbrückendynamik des langlebigen Radikal-Substrat-Komplexes resultiert. Durch die Verwendung der vorhandenen veröffentlichten Daten zu den paramagnetischen NMR-Verschiebungen können zahlreiche weniger interessante Moleküle für DNP ausgeschlossen und die Zielkandidaten für nachfolgende DNP-Messungen vorab ausgewählt werden. Dennoch wird der beobachtete ^{13}C-Verstärkungsfaktor durch die Spindichte-Verteilung über die Moleküle, die durch die molekulare Dynamik bestimmte SDF, und die gegengesetzt wirkende OE der über die dipolare hfWW-getriebene wird, kompliziert. Für quantitative Vorhersagen ist deshalb eine umfassendere und systematischere Analyse erforderlich.[78,102]

SE DNP

Wie in Abschnitt 5.2 dargestellt, eröffnet der beobachtete SE (Solid-Effekt) an Lipidmolekülen oberhalb der Lipidphasenübergangstemperatur neue Möglichkeiten für Flüssigkeits-DNP. Im Gegensatz zu OE DNP, das auf einer dynamischen Modulation der hfWW beruht, ist es bei SE in Flüssigkeiten erforderlich, dass die anisotrope hfWW nicht durch die stochastischen Bewegungen ausgemittelt wird. Daher ist SE DNP für viskose Lösungen geeignet.[89-91,103] Die Rate für einen Kernspin-verbotenen Übergang, die durch die anisotrope hfWW teilweise erlaubt wird, wie aus 2. Ordnung Störungstheorie zu ersehen ist, ist bei hohen Magnetfeldern sehr klein. Ein effizienter Resonator mit einer großen mw B_1-Feldstärke kann dieser Nachteil teilweise kompensieren. Ebenfalls würde ein

Radikal mit einer kleinen Linienbreite helfen. Theoretische Ansätze deuten darauf hin, dass für SE DNP die dipolare Korrelationszeit länger sein sollte als die transversale Relaxationszeit des Elektrons.[93,94,104,105] Die neue Anwendung von SE DNP bietet einen alternativen Mechanismus zur OE DNP in Flüssigkeiten bei hohen Magnetfeldern und könnte möglicherweise auf Makromoleküle mit relativ langsamer Rotationsbewegung angewendet werden.

Dipolare OE DNP

Im Kontext von dipolarer OE DNP haben wir den Beitrag der Rotation des Radikals neben der Translationsbewegung zwischen Radikal und Target-Molekül zur OE DNP-Effizienz systematisch untersucht, indem wir verschiedene Nitroxidderivate mit unterschiedlichen Ringgeometrien und Substituenten verwendet haben, wie in Abschnitt 7.2 gezeigt. Eine systematische Abhängigkeit der OE DNP Verstärkung von der Rotationskorrelationszeit der Radikale, die durch cw-EPR-Messungen bestimmt wurde, konnte beobachtet werden. Mithilfe eines Models, das eine 'out-sphere' Translationsbewegung und eine 'inner-sphere' Rotationsbewegung des Radikal-Lösungsmittel-Komplexes enthält, konnte diese Abhängigkeit quantitativ simuliert werden.

Da die charakteristische Zeit des daraus postulierten Radikal-Lösungsmittel-Komplexes von MD-Simulation nicht unterstützt wird, untersuchten wir ein anderes Model, wie in Abschnitt 7.3 beschrieben. Hierbei wurde eine Translationsbewegung mit der Rotation von Radikalen, bei denen das ungepaarte Elektron nicht im Zentrum sitzt, kombiniert. Ähnlich wie beim 'inner-sphere' und 'outer-sphere' Model kann eine quantitative Anpassung an die experimentellen Beobachtungen erreicht werden. Interessanterweise liegt hier der kürzeste Abstand zwischen Kernspin und Elektronenspin näher an der Abstands-Verteilungsfunktion, die aus MD-Simulationen gewonnen wurde. Auch die feldabhängigen OE DNP-Verstärkungsfaktoren, die von TEMPOL in Wasser bestimmt wurden,[67,69,95] können mit diesem Model gut reproduziert werden und stimmen mit der aus MD-

Simulationen bestimmten SDF[97] sehr gut überein. Dieses Model spiegelt die nicht-zentrische Lokalisierung des ungepaarte Elektronenspins in Nitroxidradikalen besser wider und könnte deshalb für diese Radikale eine bessere physikalische Beschreibung des Radikal-Targetmolekül-Paares liefern.

Wie in Abschnitt 6.2 gezeigt, haben wir zusätzliche Untersuchungen an den Lipiddoppelschichten durchgeführt, basierend auf dem beobachteten ^{1}H DNP-Verstärkungen in einer viskosen Lipidumgebung bei 9,4 T.[45] Durch Messung des Feldprofils wurden DNP-Verstärkungen durch OE und SE in Abhängigkeit ihrer relativen Verschiebungen von der Elektronen-Larmor-Frequenz bestimmt. Durch eine zufriedenstellende NMR-Signalauflösung sowie die experimentelle Bestimmung der Leakage- und Sättigungsfaktoren wurde die individuelle OE DNP-Effizienzen für Protonen des Wassers, der Lipid-Cholin-Kopfgruppen oder der Lipid-Acylketten bestimmt. Dadurch wird ein quantitativer Vergleich mit MD-Simulationen ermöglicht. Obwohl die von der dipolaren Autokorrelationsfunktion aus MD-Simulationen vorhergesagten DNP Kopplungsfaktoren noch deutliche Abweichungen von den experimentellen Beobachtungen aufweisen, wird die schnelle Dynamik nahe der Elektronen-Larmor-Frequenz, die für einen erfolgreichen OE DNP Transfer erforderlich ist, von den MD-Simulationen gut erfasst. Eine weitergehende Analyse, bei der der OE- und SE-Beitrag unter Berücksichtigung der dynamisch modulierten SE und der g-Tensor-erweiterten OE getrennt wird, wurde noch nicht abschließend durchgeführt. Diese Modellierung könnte wertvolle Einblicke in die schnelle Dynamik liefern, die für DNP auf Lipidprotonen verantwortlich ist. Darüber hinaus legen die MD-Simulationen auch nahe, dass der DNP-Kopplungsfaktor von Wasserprotonen in der Liposomenprobe hauptsächlich durch die zeitweise an der Lipid/Wasser-Grenze liegenden Spin-Label verursacht wird. Dies steht im Widerspruch zu der Interpretation früherer Ergebnisse bei kleinen Magnetfeldern (0,34 T), die einen kleineren Diffusionskoeffizienten postuliert, was ebenfalls weiterer Untersuchungen bedarf.

Dreifachresonanz-DNP

Es wurden zwei unterschiedliche Dreifachresonanz-DNP-Experimente, einschließlich ^{13}C OE DNP unter ^{1}H-Entkopplung in wässriger Natriumpyruvatlösung (siehe Abschnitt 8.2), und ^{13}C-NMR von Glycin, verstärkt durch SE DNP an ^{1}H zusammen mit einem ^{1}H-^{13}C INEPT-Polarisationstransfer (siehe Abschnitt 8.3), im Rahmen dieser Doktorarbeit durchgeführt. Bemerkenswert ist, dass die INEPT-DNP-Effizienz durch die ^{1}H-Kerntransversalrelaxation bei hoher Radikalkonzentration eingeschränkt wurde, was darauf hindeutet, dass für zukünftige Anwendungen eine optimierte Radikalkonzentration erforderlich ist. Diese ersten Ansätze der Dreifachresonanz-DNP in Flüssigkeiten liefern Informationen für eine mögliche Integration von DNP in der mehrdimensionalen Anwendung der modernen Flüssigkeits-NMR.

11 List of Contributions

A total of 5 published articles in peer-reviewed journals, a submitted manuscript and a summarized manuscript was attached in this dissertation.

11.1 The author's contributions

Publication (1). **Dai, D**., Wang, X., Liu, Y., Yang, X.-L., Glaubitz, C., Denysenkov, V., He, X., Prisner, T. and Mao, J., Room-temperature dynamic nuclear polarization enhanced NMR spectroscopy of small biological molecules in water. *Nat. Commun.* 12, 6880 (2021)

Contributions: The work was prepared in a collaborative manner. The relation between the paramagnetic NMR shift and scalar DNP enhancement was initially proposed by Prof. Jiafei Mao (Institute of Chemistry, Chinese Academy of Sciences). The author performed of the major part of the DNP/NMR experiments including sample preparation and spectra recording. The analysis of the DNP enhancements was performed by the author together with Prof. Jiafei Mao. Dr. Vasyl Denysenkov provides the supports on the probeheads. The quantum mechanical MD simulation and DFT calculations were performed by Prof. Xianwei Wang (Zhejiang University of Technology), Dr. Yiwei Liu (East China Normal University) and Prof. Xiao He (East China Normal University). The author participated in the manuscript preparation including preparation of the figures of DNP spectra and supportive figures related with experiments, and writing the DNP/NMR part.

Publication (2). Kuzhelev, A. A., **Dai, D**., Denysenkov, V. and Prisner, T. F., Solid-like Dynamic Nuclear Polarization Observed in the Fluid Phase of Lipid Bilayers at 9.4 T. *J. Am. Chem. Soc.*, 144, 1164–1168 (2022)

Contributions: The work was prepared in a collaborative manner. The measurement of DNP on viscous lipids with narrow-line radicals is initially proposed by Dr. Andrei Kuzhelev. The author performed of the DNP/NMR experiments together with Dr. Andrei Kuzhelev.

Publication (3). Kuzhelev, A. A., **Dai, D.**, Denysenkov, V., Kirilyuk, I. A., Bagryanskaya E. G. and Prisner, T. F., Influence of Rotational Motion of Nitroxides on Overhauser Dynamic Nuclear Polarization: A Systematic Study at High Magnetic Fields. *J. Phys. Chem. C*, 125, 25651–25659 (2021)

Contributions: The work was prepared in a collaborative manner. The author performed DNP/NMR measurements together with Dr. Andrei Kuzhelev. The EPR experiments were performed by Dr. Andrei Kuzhelev. The analysis and interpretation were performed mainly by Dr. Andrei Kuzhelev.

Publication (4). Denysenkov, V., **Dai, D.** and Prisner, T. F., A triple resonance (e, ^{1}H, ^{13}C) probehead for liquid-state DNP experiments at 9.4 Tesla. *J. Magn. Reson.* 337, 107185 (2022)

Contributions: The work was prepared in a collaborative manner. The development of the probehead and test of the DNP/NMR performance were performed by Dr. Vasyl Denysenkov. The author performed the ^{1}H-decoupling DNP/NMR experiments and the experiments to monitor sample temperature with/without mw irradiation.

Publication (5). **Dai, D.,** Denysenkov, V., Bagryanskaya E. G., Tormyshev, V. M., Prisner, T. F. and Kuzhelev, A. A., ^{13}C Hyperpolarization of Viscous Liquids by Transfer of Solid-Effect ^{1}H Dynamic Nuclear Polarization at High Magnetic Field. *J. Phys. Chem. Lett.* 14, 31, 7059–7064 (2023)

Contributions: The work was prepared in a collaborative manner. The author performed the initial proof of the INEPT-DNP concept. The author performed the DNP/NMR experiments including sample preparation, spectra recording and spectra analysis together with Dr. Andrei Kuzhelev. The author participated in manuscript preparation including preparation of the figures of DNP spectra and supportive figures.

Submitted Manuscript: Sezer, D., **Dai, D.**, and Prisner, T. F., The solid effect of dynamic nuclear polarization in liquids II: Accounting for g-tensor anisotropy at high magnetic fields, *Magn. Reson.* [preprint]: doi.org/10.5194/mr-2023-10, in review (2023)

Contributions: The work was prepared in a collaborative manner. The project was proposed by Dr. Deniz Sezer. The author provided the experimental DNP field profiles and cw EPR spectra, and performed the easyspin simulation. The theoretical work was performed by Dr. Deniz Sezer.

Summarized Manuscript: Overhauser and Solid Effect ^{1}H Dynamic Nuclear Polarization on Liposome at Ambient Temperature and 9.4 T

Contributions: The author performed the DNP/NMR and EPR experiment, deconvoluted the overlapped NMR signal and calculated the DNP coupling factor. The MD simulations were performed by Dr. Deniz Sezer. The calculation of the dipolar autocorrelation function and the resulted coupling factor from MD trajectories were performed by the author.

11.2 List of Presentations in Conferences

Oral Contributions:

- 22nd International Society for Magnetic Resonance Meeting (ISMAR), "^{1}H Overhauser DNP of Lipids at 9.4 Tesla" (online presentation), August 2021, Osaka, Japan,
- (Invited) 43rd FGMR Annual Discussion Meeting, "Overhauser DNP on small biomolecules in water at 9.4 T", September 2022, Karlsruhe, Germany

Poster Contributions:

- HYP18 conference, September 2018, Southampton, UK
- IPTC institute symposium, March 2019, Hirschegg, Austria
- EUROISMAR (Joint conference of EUROMAR and ISMAR), August 2019, Berlin, Germany
- EFEPR school, November 2019, Brno, Czech Republic
- SMNMR conference, May 2023, Nanjing, China

List of Reference

1 Rabi, I. I., Zacharias, J. R., Millman, S. & Kusch, P. A New Method of Measuring Nuclear Magnetic Moment. *Phys Rev* **53**, 318-318 (1938).

2 Purcell, E. M., Torrey, H. C. & Pound, R. V. Resonance Absorption by Nuclear Magnetic Moments in a Solid. *Phys Rev* **69**, 37-38 (1946).

3 Bloch, F. Nuclear Induction. *Phys Rev* **70**, 460-474 (1946).

4 Chien, P.-H., Griffith, K. J., Liu, H., Gan, Z. & Hu, Y.-Y. Recent Advances in Solid-State Nuclear Magnetic Resonance Techniques for Materials Research. *Annual Review of Materials Research* **50**, 493-520 (2020).

5 Shimada, I., Ueda, T., Kofuku, Y., Eddy, M. T. & Wüthrich, K. GPCR drug discovery: integrating solution NMR data with crystal and cryo-EM structures. *Nature Reviews Drug Discovery* **18**, 59-82 (2019).

6 Marion, D. An Introduction to Biological NMR Spectroscopy. *Molecular & Cellular Proteomics* **12**, 3006-3025 (2013).

7 Emwas, A.-H., Roy, R., McKay, R. T., Tenori, L., Saccenti, E., Gowda, G. A. N., Raftery, D., Alahmari, F., Jaremko, L., Jaremko, M. & Wishart, D. S. NMR Spectroscopy for Metabolomics Research. *Metabolites* **9** (2019).

8 Ardenkjaer-Larsen, J. H., Boebinger, G. S., Comment, A., Duckett, S., Edison, A. S., Engelke, F., Griesinger, C., Griffin, R. G., Hilty, C., Maeda, H., Parigi, G., Prisner, T., Ravera, E., van Bentum, J., Vega, S., Webb, A., Luchinat, C., Schwalbe, H. & Frydman, L. Facing and overcoming sensitivity challenges in biomolecular NMR spectroscopy. *Angew. Chem. Int. Ed.* **54**, 9162-9185 (2015).

9 Overhauser, A. W. Polarization of nuclei in metals. *Phys. Rev.* **92**, 411-415 (1953).

10 Kaptein, R., Dijkstra, K. & Nicolay, K. Laser photo-CIDNP as a surface probe for proteins in solution. *Nature* **274**, 293-294 (1978).

11 Bowers, C. R. & Weitekamp, D. P. Transformation of Symmetrization Order to Nuclear-Spin Magnetization by Chemical Reaction and Nuclear Magnetic Resonance. *Physical Review Letters* **57**, 2645-2648 (1986).

12 Eisenschmid, T. C., Kirss, R. U., Deutsch, P. P., Hommeltoft, S. I., Eisenberg, R., Bargon, J., Lawler, R. G. & Balch, A. L. Para hydrogen induced polarization in hydrogenation reactions. *J Am Chem Soc* **109**, 8089-8091 (1987).

13 Richardson, P. M., Parrott, A. J., Semenova, O., Nordon, A., Duckett, S. B. & Halse, M. E. SABRE hyperpolarization enables high-sensitivity 1H and 13C benchtop NMR spectroscopy. *Analyst* **143**, 3442-3450 (2018).

14 Walker, T. G. & Happer, W. Spin-exchange optical pumping of noble-gas nuclei. *Reviews of Modern Physics* **69**, 629-642 (1997).

15 Carver, T. R. & Slichter, C. P. Polarization of Nuclear Spins in Metals. *Phys. Rev.* **92**, 212-213 (1953).

16 Jeffries, C. D. Polarization of Nuclei by Resonance Saturation in Paramagnetic Crystals. *Phys Rev* **106**, 164-165 (1957).

17 Abragam, A. & Proctor, W. G. Une Nouvelle Methode de Polarization Dynamique des Noyaux Atomiques dans les Solides. *Comptes Rendus Hebdomadaries des Seances de L'Academia des Sciences* **246**, 2253-2256 (1958).

18 Kessenikh, A. V., Lushchikov, V. I., Manenkov, A. A. & Taran, Y. V. PROTON POLARIZATION IN IRRADIATED POLYETHYLENES. **Vol: 5** (1963).

19 Hwang, C. F. & Hill, D. A. Phenomenological Model for the New Effect in Dynamic Polarization. *Physical Review Letters* **19**, 1011-1014 (1967).

20 Abragam, A. & Goldman, M. Principles of dynamic nuclear polarisation. *Rep. Prog. Phys.* **41**, 395-467 (1978).

21 Wind, R. A., Duijvestijn, M. J., van der Lugt, C., Manenschijn, A. & Vriend, J. Applications of dynamic nuclear polarization in 13C NMR in solids. *Prog Nucl Mag Res Sp* **17**, 33-67 (1985).

22 Goldman, M. *Spin Temperature and Nuclear Magnetic Resonance in Solids*. (Clarendon Press, 1970).

23 Hausser, K. H. & Stehlik, D. Dynamic nuclear polarization in liquids. *Adv. Magn. Reson.* **3**, 79-139 (1968).

24 Müller-Warmuth, W. & Meise-Gresch, K. Molecular Motions and Interactions as Studied by Dynamic Nuclear Polarization (DNP) in Free Radical Solutions. *Adv. Magn. Reson.* **11**, 1-45 (1983).

25 Becerra, L. R., Gerfen, G. J., Temkin, R. J., Singel, D. J. & Griffin, R. G. Dynamic nuclear polarization with a cyclotron resonance maser at 5 T. *Phys. Rev. Lett.* **71**, 3561--3564 (1993).

26 Ni, Q. Z., Daviso, E., Can, T. V., Markhasin, E., Jawla, S. K., Swager, T. M., Temkin, R. J., Herzfeld, J. & Griffin, R. G. High frequency dynamic nuclear polarization. *Acc. Chem. Res.* **46**, 1933-1941 (2013).

27 Corzilius, B. High-field dynamic nuclear polarization. *Annu. Rev. Phys. Chem.* **71**, 143-170 (2020).

28 Ardenkjaer-Larsen, J. H. On the present and future of dissolution-DNP. *J Magn Reson* **264**, 3-12 (2016).

29 Ardenkjaer-Larsen, J. H., Fridlund, B., Gram, A., Hansson, G., Hansson, L., Lerche, M. H., Servin, R., Thaning, M. & Golman, K. Increase in signal-to-noise ratio of > 10,000 times in liquid-state NMR. *Proc. Natl. Acad. Sci. U.S.A.* **100**, 10158-10163 (2003).

30 Van Den Heuvel, D., Henstra, A., Lin, T.-S., Schmidt, J. & Wenckebach, W. T. Transient oscillations in pulsed dynamic nuclear polarization. *Chem Phys Lett* **188**, 194-200 (1992).

31 Can, T. V., Walish, J. J., Swager, T. M. & Griffin, R. G. Time domain DNP with the NOVEL sequence. *J Chem Phys* **143**, 054201 (2015).

32 Farrar, C. T., Hall, D. A., Gerfen, G. J., Rosay, M., Ardenkjær-Larsen, J. H. & Griffin, R. G. High-Frequency Dynamic Nuclear Polarization in the Nuclear Rotating Frame. *J Magn Reson* **144**, 134-141 (2000).

33 Tan, K. O., Yang, C., Weber, R. T., Mathies, G. & Griffin, R. G. Time-optimized pulsed dynamic nuclear polarization. *Science Advances* **5**, eaav6909 (2019).

34 Denysenkov, V. P. & Prisner, T. F. Liquid-state Overhauser DNP at high magnetic fields. *Emagres* **8**, 41-54 (2019).

35 Denysenkov, V. P., Prandolini, M. J., Krahn, A., Gafurov, M., Endeward, B. & Prisner, T. F. High-field DNP spectrometer for liquids. *Appl. Magn. Reson.* **34**, 289-299 (2008).

36 Denysenkov, V., Dai, D. & Prisner, T. F. A triple resonance (e, 1H, 13C) probehead for liquid-state DNP experiments at 9.4 Tesla. *Manuscript submitted for publication* (2021).

37 Solomon, I. Relaxation processes in a system of two spins. *Phys. Rev.* **99** (1955).

38 Hwang, L.-P. & Freed, J. H. Dynamic effects of pair correlation functions on spin relaxation by translational diffusion in liquids. *J. Chem. Phys.* **63** (1975).

39 Bloembergen, N. Proton relaxation times in paramagnetic solutions. *The Journal of Chemical Physics* **27**, 572-573 (1957).

40 Ayant, Y., Belorizky, E., Aluzon, J. & Gallice, J. Calcul des densités spectrales résultant d'un mouvement aléatoire de translation en relaxation par interaction dipolaire magnétique dans les liquides. *Journal de Physique* **36**, 991-1004 (1975).

41 Loening, N. M., Rosay, M., Weis, V. & Griffin, R. G. Solution-State Dynamic Nuclear Polarization at High Magnetic Field. *J Am Chem Soc* **124**, 8808-8809 (2002).

42 Höfer, P., Parigi, G., Luchinat, C., Carl, P., Guthausen, G., Reese, M., Carlomagno, T., Griesinger, C. & Bennati, M. Field Dependent Dynamic Nuclear Polarization with Radicals in Aqueous Solution. *J Am Chem Soc* **130**, 3254-3255 (2008).

43 Prandolini, M. J., Denysenkov, V. P., Gafurov, M., Endeward, B. & Prisner, T. F. High-field dynamic nuclear polarization in aqueous solutions. *J. Am. Chem. Soc.* **131**, 6090-6092 (2009).

44 Prisner, T., Denysenkov, V. & Sezer, D. Liquid state DNP at high magnetic fields: Instrumentation, experimental results and atomistic modelling by molecular dynamics simulations. *J Magn Reson* **264**, 68-77 (2016).

45 Jakdetchai, O., Denysenkoy, V., Becker-Baldus, J., Dutagaci, B., Prisner, T. F. & Glaubitz, C. Dynamic nuclear polarization-enhanced NMR on aligned lipid lilayers at ambient temperature. *J. Am. Chem. Soc.* **136**, 15533-15536 (2014).

46 Ellena, J. F., Lepore, L. S. & Cafiso, D. S. Estimating lipid lateral diffusion in phospholipid vesicles from carbon-13 spin-spin relaxation. *J. Phys. Chem. A* **97**, 2952–2957 (1993).

47 Filippov, A., Orädd, G. & Lindblom, G. Lipid lateral diffusion in ordered and disordered phases in raft mixtures. *Biophys J* **86**, 891-896 (2004).

48 Klauda, J. B., Roberts, M. F., Redfield, A. G., Brooks, B. R. & Pastor, R. W. Rotation of Lipids in Membranes: Molecular Dynamics Simulation, 31P Spin-Lattice Relaxation, and Rigid-Body Dynamics. *Biophys J* **94**, 3074-3083 (2008).

49 Kücük, S. E. & Sezer, D. Multiscale computational modeling of 13C DNP in liquids. *Phys. Chem. Chem. Phys.* **18**, 9353-9357 (2016).

50 Liu, G. Q., Levien, M., Karschin, N., Parigi, G., Luchinat, C. & Bennati, M. One-thousand-fold enhancement of high field liquid nuclear magnetic resonance signals at room temperature. *Nat. Chem.* **9**, 676-680 (2017).

51 Orlando, T., Dervisoglu, R., Levien, M., Tkach, I., Prisner, T. F., Andreas, L. B., Denysenkov, V. P. & Bennati, M. Dynamic nuclear polarization of C-13 nuclei in the liquid state over a 10 Tesla field range. *Angew. Chem. Int. Ed.* **58**, 1402-1406 (2019).

52 Can, T. V., Caporini, M. A., Mentink-Vigier, F., Corzilius, B., Walish, J. J., Rosay, M., Maas, W. E., Baldus, M., Vega, S., Swager, T. M. & Griffin, R. G. Overhauser effects in insulating solids. *J. Chem. Phys.* **141**, 064202 (2014).

53 Lelli, M., Chaudhari, S. R., Gajan, D., Casano, G., Rossini, A. J., Ouari, O., Tordo, P., Lesage, A. & Emsley, L. Solid-State dynamic nuclear polarization at 9.4 and 18.8 T from 100 K to room temperature. *J. Am. Chem. Soc.* **137**, 14558-14561 (2015).

54 Ji, X., Can, T. V., Mentink-Vigier, F., Bornet, A., Milani, J., Vuichoud, B., Caporini, M. A., Griffin, R. G., Jannin, S., Goldman, M. & Bodenhausen, G. Overhauser effects in non-conducting solids at 1.2 K. *J Magn Reson* **286**, 138-142 (2018).

55 Bertini, I., Luchinat, C. & Parigi, G. *Solution NMR of Paramagnetic Molecules : Applications to Metallobiomolecules and Models*. (Elsevier Science Ltd., Amsterdam, 2001).

56 Levitt, M. H. *Spin dynamics: basics of nuclear magnetic resonance*. (John Wiley & Sons, 2013).

57 Abragam, A. *The principles of nuclear magnetism*. (Clarendon Press, Oxford, 1961).

58 Keeler, J. *Understanding NMR spectroscopy*. (John Wiley & Sons, 2010).

59 Carrington, A. & McLachlan, A. D. *Introduction to magnetic resonance, with applications to chemistry and chemical physics*. (Harper & Row, New York, 1967).

60 Di Rocco, H. & Cruzado, A. The voigt profile as a sum of a gaussian and a lorentzian functions, when the weight coefficient depends only on the widths ratio. *Acta Physica Polonica A* **122**, 666-669 (2012).

61 Fermi, E. Über die magnetischen Momente der Atomkerne. *Zeitschrift für Physik* **60**, 320-333 (1930).

62 Bloembergen, N., Purcell, E. M. & Pound, R. V. Relaxation Effects in Nuclear Magnetic Resonance Absorption. *Phys Rev* **73**, 679-712 (1948).

63 Schneider, D. & Freed, J. Spin relaxation and motional dynamics. *Advances in Chemical Physics: Lasers, Molecules, and Methods* **73**, 387 (1989).

64 Stoll, S. & Schweiger, A. EasySpin, a comprehensive software package for spectral simulation and analysis in EPR. *J Magn Reson.* **178**, 42-55 (2006).

65 Salikhov, K. Contributions of exchange and dipole–dipole interactions to the shape of EPR spectra of free radicals in diluted solutions. *Appl Magn Reson* **38**, 237-256 (2010).

66 Armstrong, B. D. & Han, S. A new model for Overhauser enhanced nuclear magnetic resonance using nitroxide radicals. *The Journal of Chemical Physics* **127** (2007).

67 Türke, M. T. & Bennati, M. Saturation factor of nitroxide radicals in liquid DNP by pulsed ELDOR experiments. *Phys. Chem. Chem. Phys.* **13**, 3630-3633 (2011).

68 Wind, R. A., Lock, H. & Mehring, M. 13C knight shift saturation and 1H dynamic nuclear polarization in a polycrystalline sample of the organic conductor (fluoranthenyl)2PF6. *Chem. Phys. Lett.* **141** (1987).

69 Neugebauer, P., Krummenacker, J. G., Denysenkov, V. P., Parigi, G., Luchinat, C. & Prisner, T. F. Liquid state DNP of water at 9.2 T: an experimental access to saturation. *Phys. Chem. Chem. Phys.* **15**, 6049-6056 (2013).

70 Redfield, A. G. The Theory of Relaxation Processes* *This work was started while the author was at Harvard University, and was then partially supported by Joint Services Contract N5ori-76, Project Order I in *Advances in Magnetic and Optical Resonance*, 1-32 (Academic Press, 1965).

71 Goldman, M. Formal Theory of Spin–Lattice Relaxation. *J Magn Reson* **149**, 160-187 (2001).

72 Gupta, A., Stait-Gardner, T., Moghaddam, M. J. & Price, W. S. Dipolar relaxation revisited: A complete derivation for the two spin case. *Concepts in Magnetic Resonance Part A* **44**, 74-113 (2015).

73 Bennati, M., Parigi, G., Luchinat, C. & Türke, M. T. Water 1H relaxation dispersion analysis on a nitroxide radical provides information on the maximal signal enhancement in Overhauser dynamic nuclear polarization experiments. *Phys. Chem. Chem. Phys.* **12**, 5902-5910 (2010).

74 Lipari, G. & Szabo, A. Model-free approach to the interpretation of nuclear magnetic resonance relaxation in macromolecules. 1. Theory and range of validity. *J Am Chem Soc* **104**, 4546-4559 (1982).

75 Palmer, A. G., III. NMR Characterization of the Dynamics of Biomacromolecules. *Chemical Reviews* **104**, 3623-3640 (2004).

76 Neugebauer, P., Krummenacker, J. G., Denysenkov, V. P., Helmling, C., Luchinat, C., Parigi, G. & Prisner, T. F. High-field liquid state NMR hyperpolarization: a

combined DNP/NMRD approach. *Phys. Chem. Chem. Phys.* **16**, 18781-18787 (2014).

77 van Bentum, P. J. M., van der Heijden, G. H. A., Villanueva-Garibay, J. A. & Kentgens, A. P. M. Quantitative analysis of high field liquid state dynamic nuclear polarization. *Phys Chem Chem Phys* **13**, 17831-17840 (2011).

78 Levien, M., Hiller, M., Tkach, I., Bennati, M. & Orlando, T. Nitroxide Derivatives for Dynamic Nuclear Polarization in Liquids: The Role of Rotational Diffusion. *The Journal of Physical Chemistry Letters* **11**, 1629-1635 (2020).

79 Ayant, Y., Belorizky, E., Fries, P. & Rosset, J. Effet des interactions dipolaires magnétiques intermoléculaires sur la relaxation nucléaire de molécules polyatomiques dans les liquides. *Journal de Physique* **38**, 325-337 (1977).

80 Müller-Warmuth, W., Van Steenwinkel, R. & Noack, F. Dynamic nuclear polarization experiments on 19F in solutions and their interpretation by the 'pulse model' of molecular collisions. *Z. Naturforsch. A* **23**, 506-513 (1968).

81 Stehlik, D. & Hausser, K. H. Relaxation und dynamische Kernpolarisation von Protonen in freien Radikalen. *Zeitschrift für Naturforschung A* **22**, 914-928 (1967).

82 Schweiger, A. & Jeschke, G. *Principles of pulse electron paramagnetic resonance*. (Oxford university press, 2001).

83 Hovav, Y., Feintuch, A. & Vega, S. Theoretical aspects of dynamic nuclear polarization in the solid state–the solid effect. *J Magn Reson* **207**, 176-189 (2010).

84 Wenckebach, W. T. *Essentials of dynamic nuclear polarization*. (Spindrift Publications, 2016).

85 Denysenkov, V. & Prisner, T. Liquid state dynamic nuclear polarization probe with Fabry-Perot resonator at 9.2 T. *J. Magn. Reson.* **217**, 1-5 (2012).

86 Denysenkov, V., Dai, D. & Prisner, T. F. A triple resonance (e, (1)H, (13)C) probehead for liquid-state DNP experiments at 9.4 Tesla. *J Magn Reson* **337**, 107185 (2022).

87 Wang, X., Isley, W. C., Salido, S. I., Sun, Z., Song, L., Tsai, K. H., Cramer, C. J. & Dorn, H. C. Optimization and prediction of the electron-nuclear dipolar and scalar interaction in H-1 and C-13 liquid state dynamic nuclear polarization. *Chem. Sci.* **6**, 6482-6495 (2015).

88 Qiu, Z. W., Grant, D. M. & Pugmire, R. J. Paramagnetic C-13 shifts induced by the free-radical Tempo .2. nitrogen-heterocycles. *J. Am. Chem. Soc.* **106**, 557-563 (1984).

89 Leblond, J., Uebersfeld, J. & Korringa, J. Study of the Liquid-State Dynamics by Means of Magnetic Resonance and Dynamic Polarization. *Physical Review A* **4**, 1532-1539 (1971).

90 Karyagin, V. & Dovgopol, S. Frequency dependence of dynamic nuclear polarization in viscous solutions. *Soviet Physics Journal* **15**, 54-57 (1972).

91 Neudert, O., Reh, M., Spiess, H. W. & Münnemann, K. X-Band DNP Hyperpolarization of Viscous Liquids and Polymer Melts. *Macromolecular Rapid Communications* **36**, 885-889 (2015).

92 Sezer, D., Prandolini, M. J. & Prisner, T. F. Dynamic nuclear polarization coupling factors calculated from molecular dynamics simulations of a nitroxide radical in water. *Phys. Chem. Chem. Phys.* **11**, 6626-6637 (2009).

93 Sezer, D. Non-perturbative treatment of the solid effect of dynamic nuclear polarization. *Magn. Reson.* **4**, 129-152 (2023).

94 Sezer, D. The solid effect of dynamic nuclear polarization in liquids. *Magn. Reson.* **4**, 153-174 (2023).

95 Kryukov, E. V., Pike, K. J., Tam, T. K. Y., Newton, M. E., Smith, M. E. & Dupree, R. Determination of the temperature dependence of the dynamic nuclear polarisation enhancement of water protons at 3.4 Tesla. *Phys Chem Chem Phys* **13**, 4372-4380 (2011).

96 Okuno, Y., Schwieters, C. D., Yang, Z. & Clore, G. M. Theory and Applications of Nitroxide-based Paramagnetic Cosolutes for Probing Intermolecular and Electrostatic Interactions on Protein Surfaces. *J Am Chem Soc* **144**, 21371-21388 (2022).

97 Sezer, D. Rationalizing Overhauser DNP of nitroxide radicals in water through MD simulations. *Phys. Chem. Chem. Phys.* **16**, 1022-1032 (2014).

98 Gafurov, M. TEMPOL as a polarizing agent for dynamic nuclear polarization of aqueous solutions. *Magnetic Resonance in Solids. Electronic Journal* **15**, 13103 (2013).

99 Cho, C. H., Urquidi, J., Singh, S. & Robinson, G. W. Thermal Offset Viscosities of Liquid H2O, D2O, and T2O. *The Journal of Physical Chemistry B* **103**, 1991-1994 (1999).

100 Kuzhelev, A. A., Dai, D., Denysenkov, V., Kirilyuk, I. A., Bagryanskaya, E. G. & Prisner, T. F. Influence of Rotational Motion of Nitroxides on Overhauser Dynamic Nuclear Polarization: A Systematic Study at High Magnetic Fields. *The Journal of Physical Chemistry C* **125**, 25651-25659 (2021).

101 Küçük, S. E., Neugebauer, P., Prisner, T. F. & Sezer, D. Molecular simulations for dynamic nuclear polarization in liquids: a case study of TEMPOL in acetone and DMSO. *Phys Chem Chem Phys* **17**, 6618-6628 (2015).

102 Levien, M., Reinhard, M., Hiller, M., Tkach, I., Bennati, M. & Orlando, T. Spin density localization and accessibility of organic radicals affect liquid-state DNP efficiency. *Phys Chem Chem Phys* **23**, 4480-4485 (2021).

103 Kuzhelev, A. A., Denysenkov, V., Ahmad, I. M., Rogozhnikova, O. Y., Trukhin, D. V., Bagryanskaya, E. G., Tormyshev, V. M., Sigurdsson, S. T. & Prisner, T. F. Solid-Effect Dynamic Nuclear Polarization in Viscous Liquids at 9.4 T Using Narrow-Line Polarizing Agents. *J Am Chem Soc* **145**, 10268-10274 (2023).

104 Papon, P., Motchane, J. L. & Korringa, J. Unitary Theory of Dynamic Polarization of Nuclear Spins in Liquids and Solids. *Phys Rev* **175**, 641-649 (1968).

105 Leblond, J., Papon, P. & Korringa, J. Stochastic Theory of Dynamic Spin Polarization in Viscous Liquids with Anisotropic Electron-Spin Relaxation. *Physical Review A* **4**, 1539-1549 (1971).

106 Kausik, R. & Han, S. Dynamics and state of lipid bilayer-internal water unraveled with solution state 1H dynamic nuclear polarization. *Phys Chem Chem Phys* **13**, 7732-7746 (2011).

Appendix I. List of Abbreviations

BDPA	1,3-**B**is**d**iphenylene-2-**P**henyl**A**llyl
CBr_4	Carbon tetrabromide
CCl_4	Carbon tetrachloride
CE	**C**ross **E**ffect
CSA	**C**hemical **S**hift **A**nisotropy
cw	**c**ontinuous-**w**ave
DFT	**D**ensity **F**unctional **T**heory
DMSO	**D**i**m**ethyl **S**ulf**o**xide
DNP	**D**ynamic **N**uclear **P**olarization
DQ	**D**ouble-**Q**uantum
e-N	**e**lectron-**N**uclear
ELDOR	**El**ectron **Do**uble **R**esonance
EPR	**E**lectron **P**aramagnetic **R**esonance
FID	**F**ree **I**nduction **D**ecay
FP	**F**abry–**P**érot
FT	**F**ourier **T**ransformation
FWHM	**F**ull **W**idth at the **H**alf **M**aximum
HC	**H**elical-**C**ylindrical
HFI	**H**yper**f**ine **I**nteraction
hfWW	**h**yper**f**ein-**W**echsel**w**irkung
HSCS	**H**ard **S**pheres with **C**entered **S**pin
HSOS	**H**ard **S**pheres with **O**ff-centered **S**pin
INEPT	**I**nsensitive **N**uclei **E**nhanced by **P**olarization **T**ransfer
MD	**M**olecular **D**ynamics

mw	**m**icro**w**ave
NMR	**N**uclear **M**agnetic **R**esonance
NMRD	**N**uclear **M**agnetic **R**elaxation **D**ispersion
NOVEL	**N**uclear **O**rientation **v**ia **E**lectron spin **L**ocking
OE	**O**verhauser **E**ffect
PHIP	**P**ara**h**ydrogen-**I**nduced **P**olarization
Photo-CIDNP	**Photoc**hemically-**I**nduced **D**ynamic **N**uclear **P**olarization
rdf	**r**adian **d**istribution **f**unction
rf	**r**adio**f**requency
SABRE	**S**ignal **A**mplification **b**y **R**eversible **E**xchange
SDF	**S**pectral **D**ensity **F**unction
SE	**S**olid **E**ffect
SI	**S**ystème **I**nternational
SQ	**S**ingle-**Q**uantum
T_1	longitudinal relaxation time constant
T_2	transverse relaxation time constant
TEMPO	2,2,6,6-**te**tra**m**ethyl**p**iperidinyl**o**xyl
TEMPOL	4-Hydroxy-2,2,6,6-**te**tra**m**ethyl**p**iperidinyl**o**xy**l**
TM	**T**hermal **M**ixing
trityl	**tri**phenylme**th**y**l**
ZQ	**Z**ero-**Q**uantum

Appendix II. Declaration

Except where stated otherwise by reference or acknowledgment, the work presented was generated by myself under the supervision of my advisors during my doctoral studies. All contributions from colleagues are explicitly referenced in the thesis.

The following parts of the thesis have been previously published and the co-author agreement has been obtained:

- Figure 3. 1. Schematic representation of the helical-cylindrical double resonance structure.

(Contributor: Dr. Vasyl Denysenkov)

- Figure 3. 2. (A) Schematic representation of the triple resonance structure comprising a Fabry–Pérot mw resonator and a coplanar stripline.

(Contributor: Dr. Vasyl Denysenkov)

- Figure 7. 2. (A) Structures of the different nitroxides used.

(Contributor: Dr. Andrei Kuzhelev)